University of Southampton

Faculty of Engineering and Physical Sciences

School of Engineering and School of Chemistry

Investigating the Use of Silver Nanofluids for Solar Collectors Connected to a Thermal Storage System

DOI: https://doi.org/10.5258/SOTON/T0049

by

Harriet Jill Kimpton

ORCID ID orcid.org/0000-0002-3219-217X

Thesis for the degree of Doctor of Philosophy

[July 2022]

University of Southampton

Abstract

Faculty of Engineering and Physical Sciences

School of Engineering and School of Chemistry

Thesis for the degree of Doctor of Philosophy

Investigating the Use of Silver Nanofluids for Solar Collectors Connected to a Thermal Storage System

by

Harriet Jill Kimpton

This work focuses on a potential decarbonising solution for heating and hot water, namely enhanced volumetric based solar thermal capture with silver nanofluids combined with thermal storage. This was shown to be a feasible solution for UK homes < median demand of 12,000 kW h y^{-1}, > average roof area of 15 m^2, space for a thermal store and utilising an enhanced efficiency collector > 70 % efficiency. Morphologically distinct nanofluids were synthesised with different optical properties, including for the first time experimentally, a novel broadband silver absorber produced by combining three silver nanofluids. The morphology was assessed using transmission electron microscopy (TEM), the potential absorption efficiency estimated using UV-vis and UV-vis-IR spectrophotometry and the performance measured in static testing utilising a solar simulator. To assess the nanofluids suitability for the application, one potential stabilisation strategy, namely SiO_2 coating was evaluated. The stability of the nanofluids, colloidal (storage in the dark at 4 °C ≤ 603 days), elevated temperature (70 °C), under simulated sunlight and natural sunlight was measured. The stability of the novel broadband absorber under flow conditions was also evaluated.

The uncoated silver nanofluids showed a measured efficiency in the static solar simulator of ≈ 84 % for the novel silver broadband absorber and ≈ 85 % for the less dilute silver nanoprisms similar to the estimations from UV-vis spectrophotometry (< 10 % difference). In contrast the SiO_2 coated silver nanoprisms had a measured performance of 72 % – 77 % lower than the estimations obtained from the UV-vis spectrophotometry. The stability testing showed the nanofluids to be morphologically unstable and in the case of the silver nanoprisms unstable to aggregation in the longer term natural sunlight tests. Coating with SiO_2 reduced the morphological stability questioning the use of this stabilisation strategy. Although this work has highlighted the importance of application relevant stability testing it is currently not possible to recommend the use of these silver nanofluids for solar and elevated temperature applications.

List of Publications

1. Kimpton, H., Zhang, X., Stulz, E., 2021. The temperature stability and development of a broadband silver nanofluid for solar thermal applications. Energy Reports, 7, 87-96, https://doi.org/10.1016/j.egyr.2021.02.049 (Kimpton et al., 2021).
2. Kimpton, H., Stulz, E., Zhang, X., 2020. Silver nanofluids based broadband solar absorber through tuning nanosilver geometries. Solar Energy, 208, 515-526, https://doi.org/10.1016/j.solener.2020.08.018 (Kimpton et al., 2020b).
3. Kimpton, H., Cristaldi, D.A., Stulz, E., Zhang, X., 2020. Thermal performance and physicochemical stability of silver nanoprism-based nanofluids for direct solar absorption. Solar Energy, 199, 366-376, https://doi.org/10.1016/j.solener.2020.02.039 (Kimpton et al., 2020a).
4. Kimpton, H., Zhang, X., Stulz, E., 2020. Decarbonising heating and hot water using solar thermal collectors coupled with thermal storage: The scale of the challenge. Energy Reports, 6, 25-34, https://doi.org/10.1016/j.egyr.2020.02.024 (Kimpton et al., 2020c)
5. Holland, A., Kimpton, H., Cruden, A., Wills, R., 2018. CuHCF as an electrode material in an aqueous dual-ion Al^{3+}/K^{+} ion battery. Energy Procedia, 151, 69-73, https://doi.org/10.1016/j.egypro.2018.09.029 (Holland et al., 2018)

Table of Contents

List of Tables

List of Figures

List of Accompanying Materials

Data-set for all the Tables and Figures in thesis available at:

https://doi.org/10.5258/SOTON/D2312

Research Thesis: Declaration of Authorship

Print name: Harriet Jill Kimpton

Title of thesis: Investigating the Use of Silver Nanofluids for Solar Collectors Connected to a Thermal Storage System

I declare that this thesis and the work presented in it are my own and has been generated by me as the result of my own original research.

I confirm that:

1. This work was done wholly or mainly while in candidature for a research degree at this University;
2. Where any part of this thesis has previously been submitted for a degree or any other qualification at this University or any other institution, this has been clearly stated;
3. Where I have consulted the published work of others, this is always clearly attributed;
4. Where I have quoted from the work of others, the source is always given. With the exception of such quotations, this thesis is entirely my own work;
5. I have acknowledged all main sources of help;
6. Where the thesis is based on work done by myself jointly with others, I have made clear exactly what was done by others and what I have contributed myself;
7. Parts of this work have been published as:-

[(Kimpton et al., 2020a; Kimpton et al., 2020b; Kimpton et al., 2020c, 2021)

Signature: ..... Date: July 2022

Acknowledgements

I would like to acknowledge the support of my supervisors Xunli Zhang and Eugen Stulz, who let me investigate using silver nanofluids in solar thermal collectors. I would also like to thank the University of Southampton for funding my research and all in the Energy Storage and Its Applications Centre for Doctoral Training (CDT), especially Andy Cruden, Tracey McNeilly and all the CDT students both past and present in Southampton and Sheffield. I would like to thank the Bioengineering Microfluidic Group especially Andrea Cristaldi, Tom Mabey, Fatih Yanah, Bilal Mughal, and Sel Gultakin, for all their help over the years. I would also like to acknowledge the support of all the researchers in laboratory 5003, especially Sam Beddoe for showing me how to use the spectrophotometer on floor 2. I would also like to specifically acknowledge Thomas Mercier for his assistance with the light intensity measurements of the small solar simulator and Zheng Jiang for the use of the solar simulator. Thanks also go to Rachel McKerracher for the laboratory induction for laboratory 1013 and other support over the years and Andy Westerman for all his assistance with finding equipment and ordering supplies. I would like to acknowledge the Bio-imaging Unit Southampton General Hospital for supplying me with many TEM grids and training me on the Hitachi TEM microscope. I would also like to thank the glass and engineering workshops at the University of Southampton, the Chemistry Stores, the IT department, the engineering administration office, especially Katherine Day and all the staff in the PGR office.

Finally, I would like to thank my family and friends for all their emotional support over the years when I was crazy enough to do a second PhD, especially Iman, Tone, Tafa, Tab, Meg, Isabel and Jess and all my Art club friends.

Definitions and Abbreviations

Abbreviations

au	Arbitrary units
ASHP	Air source heat pump
B	Back
BF	Base-fluid or dispersion medium
CHP	Combined Heat and Power
COP	Coefficient of performance
ct	Centrifuged
DASC	Direct absorption solar collector
DEA	Diethylamine
DLS	Dynamic light scattering
DLVO	Derjaguin, Landau, Verwey and Overbeek
DMA	Dimethylamine
ET	Extra-terrestrial
ETC	Evacuated tube collector
F	Front
FPC	flat plate collector
GHG	Greenhouse gas
GSHP	Ground source heat pump
HP	Heat pipe
HW	Hot water
IHP	Inner Helmholtz plane

ISTES	Inter-seasonal thermal energy store
LTES	Latent heat thermal store
M	cation
Md	Middle
MHA	16-mercaptohexadecanoic acid
MPTMS	3-mercaptopropyl trimethoxysilane
M_w	Weight average molecular weight
MWCNT	Multi-walled carbon nanotube
NF	Nanofluid
NP	Nanoparticle
NPr	Nanoprism
NS	Nanosphere
OHP	Outer Helmholtz plane
PCM	Phase change material
PG	1, 2-propanediol or propylene glycol
ppm	Parts per million
PV	Photovoltaic
PVP	Polyvinylpyrrolidone
PVT	Combined PV and thermal collector
r.c.f.	Relative centrifugal force
rpm	Revolutions per minute
SEM	Scanning electron microscopy
SGC	Stern-Gory-Chapman
SSL	Simulated sunlight

STC	Solar thermal collectors
STES	Sensible thermal energy store
TCS	Thermochemical store
TES	Thermal energy storage
TEM	Transmission electron microscopy
TEOS	Tetraethoxysilane
TSCD	Tri sodium citrate di-hydrate
vol	Volume
v/v	Volume / Volume
WF	Working fluid (heat transfer fluid)
wt.	Weight
X	Anion

Symbols

a_1	Heat loss coefficient / W m^{-2} K^{-1}
a_2	Temperature dependence of the heat loss coefficient / W m^{-2} K^{-2}
A	Area / m^2
Ab	Absorbance / au
c	Heat capacity / kJ kg^{-1} K^{-1} or J kg^{-1} K^{-1}
C	Concentration
d	diameter or distance / nm, µm, cm or m
D	Half width between the upper and lower measurement limits
df	Degrees of freedom
E	Energy / J
F	Force / N

FF	Fill factor
F(statistic)	Standard ANOVA *F* statistic
G	Gibbs free energy / kJ mol^{-1}
G_s	Solar irradiance / W m^{-2}
H	Enthalpy / kJ mol^{-1}
I	Current / A
I_L	Light intensity / W m^{-2}
I_{rad}	Solar Irradiation / kW h m^{-2}
K	Equilibrium constant (ratio of partial pressures)
k	Coverage factor
m	Mass / kg
$\dot{m}$	Mass flow rate / kg s^{-1}
MSE	Mean square due to error
MST	Mean square between different groups
N	Number of particles / measurements
p_v	Partial vapour pressure / bar
P	Power / W or W m^{-2}
q	Heat energy / kJ
Q	Heat energy / kW h
r	Radius / m
R_s	Solar reflectance / %
R^2	R-squared statistic
s	Sample variance
S	Entropy / kJ mol^{-1} K^{-1}

T	Temperature / K or °C
T_m	Transmittance / %
$T(value)$	T-test statistic value
U	Expanded Uncertainty
u	Velocity / m s^{-1}
u_R	Relative Uncertainty
V	Volume / m^3
v	Voltage / V
Y	Measurement or observation
$\bar{Y}$	Mean or average value
α	Surface solar absorption / %
β	Angle of surface to horizontal / °
Δ	Change in variable
κ	Extinction coefficient / cm^{-1} or m^{-1}
λ	Wavelength / m or μm or nm
μ_d	Viscosity of the dispersion medium / kg m^{-1} s^{-1}
η	Efficiency / %
ψ	Surface potential / V or mV
ρ	Density / kg m^{-3}
ρ_{TES}	Storage density / kW h m^{-3}
σ	Standard deviation
ϕ	Volume fraction / dimensionless
Φ_e	Radiant flux or radiant heat flow rate / W
ζ	Zeta potential / V or mV

Subscripts / superscripts

AA	Average annual
Ab	Absorbed
Amb	Ambient
BF	Base-fluid
c	Collector
com	Combined
cs	Circumsolar
d	Dispersion medium
D	Demand
dir	Direct
ET	Extra-terrestrial
equil	Equilibrium
f	Specific
gd	Ground diffuse
Heat	Heating
hem	Hemispherical
HW	Hot-water
i	Incident
in	Inlet
max	Maximum
N	Number
Norm	Normalised
oc	Open circuit

opt	Optical
out	Outlet
p	Particle
PE	Photo-conversion
prod	Products
quad	Quadrupole
r	Repulsive
R	Reflected
react	Reactants
rel	Relative
sc	Short circuit
sk	Sky diffuse
t	Transmitted
TES	Thermal energy store
Tran	Transfer fluid
Ts	Total (stored)
w	Water
λ	Wavelength
ϑ	Standard value (for thermodynamic constants)

Constants

c_0	Speed of light = 2.998×10^{8} m s^{-1}
g	Acceleration due to gravity = 9.81 m s^{-2}
k_B	Boltzmann constant = 1.381×10^{-23} J K^{-1}
R	Ideal gas constant = 8.314 J mol^{-1} K^{-1}

Chapter 1 Introduction

This Chapter provides a brief introduction to the thesis. It starts be giving some context, illustrating the importance of the area, the current situation, the possible solutions and the focus of this research including the research gaps, key research questions, aims and objectives. The Chapter then concludes with describing the structure of the thesis.

1.1 Brief Context

There is a requirement to decarbonise the process for providing heating and hot water (HW) in the UK and elsewhere, with an ambitious target of 100 % reduction in greenhouse gas emissions by 2050 for the UK (Climate Change Committee, 2019a; Department for Business Energy and Industrial Strategy, 2019a), and an interim target of 68 % reduction by 2030 (UK Government, 2021b). At present, firm polices published by the government only account for about 20 % of this reduction (Climate Change Committee, 2021b). This shows how challenging this goal is compared to the original UK target of 80 % reduction in greenhouse gas (GHG) emissions by 2050 (Department for Business Energy and Industrial Strategy, 2017a; UK Government, 2008).

1.1.1 Contribution of domestic heating and hot water to green-house gas emissions

In the UK, 29 % – 30 % of primary energy consumption in 2018 was for domestic use (Department for Business Energy and Industrial Strategy, 2019b). Heating and HW for homes is 24 % – 25 % of the total energy use in the UK and 15 %– 18 % of GHG emissions (Climate Change Committee, 2019b; Department for Business Energy and Industrial Strategy, 2017a, b). The remaining 4 % of energy use in homes is for appliances and lighting. There is a need to completely decarbonisation this to meet the new climate change obligations of 100 % reduction in GHG emissions by 2050 (compared to 1990 levels) (Department for Business Energy and Industrial Strategy, 2017a, 2019a; UK Government, 2008). However, emissions from homes actually rose in 2017 by 1 % and by 7 % in 2020 (Climate Change Committee, 2021b) and only 1 million homes have low carbon heating (mainly wood stoves or biomass) (Climate Change Committee, 2019b). With a total housing stock of 29 million homes in the UK, decarbonising represents quite a task.

The situation in other countries is also challenging. Demand for heat in the range of 40 °C – 60 °C represents 20 % of US final energy use (Mellor et al., 2018) and over 50 % of energy consumed globally is finally used as heat (International Energy Agency, 2020a), of which about 25 % of this is

heating in buildings. Worldwide the amount of solar thermal is about 470 GW_{th} of thermal capacity but this only met about 2.1 % of heating and HW demand in 2018.

1.1.2 Main sources of emissions and progress with decarbonisation in the UK

The UK is not currently meeting its decarbonisation heating target of 12 % heating from renewables by 2020 (Energy and Climate Change Committee, 2016).There has been minimum progress on improved insulation and switching to low carbon heating (Climate Change Committee, 2021b) and the delayed Governments heat and building strategy has only recently been published (Climate Change Committee, 2021a; UK Government, 2021a). Currently the main source of emissions is from gas used to provide heating, HW and cooking where 66 % of fuel use in the domestic sector is gas and 1.5 % is solid fuel with the rest being electricity and other fuels (Department for Business Energy and Industrial Strategy, 2017b). Since 1990 although the overall number of houses has increased the number of people per household has decreased leading to lower usage per household (Department for Business Energy and Industrial Strategy, 2017c). When combined with other factors such as energy efficiency improvements and increased energy cost this has led to a drop in emissions from houses by about 15 % since 1990 (Department for Business Energy and Industrial Strategy, 2017a, b). This drop in emissions needs to accelerate considerably in the next 30 years if the net zero target by 2050 is to be reached. However, the drop in gas usage has ceased for all housing types since 2016 (Department for Business Energy and Industrial Strategy, 2020). There is hence an urgent need to address this lack of progress.

1.1.3 Potential solutions

There are a number of potential decarbonising solutions for domestic heating and HW. This will be covered in more detail in Section 2.3.2 but briefly includes: Heat pumps, improved insulation, combined heat and power (CHP), thermal storage and other forms of storage, improved solar capture and replacing gas with hydrogen. In reality most of these decarbonising solutions with need to be used in conjunction with one or more of the other options for example heat pumps with thermal storage, improved insulation and heat pumps.

This research focuses on the use of thermal solar energy capture combined with thermal storage. The feasibility of this solution for a temperate climate such as the UK will be explored at the start of the literature review (Section 2.3).The initial research questions that this part of the literature review will attempt to answer is:

How feasible is a decarbonising solution for heating and hot water based on solar thermal capture combined with a thermal energy store for homes in the UK?

What is the role of enhanced solar capture on this feasibility?

To possibly make the proposed decarbonisation strategy of solar thermal capture combined with thermal energy storage (TES) more attractive it may be beneficial to enhance the amount of solar thermal energy that can be captured by a given collector area. Solar thermal collectors (STCs) can be of various designs (discussed in detail in Section 2.5), and can use a surface absorber to absorb the solar energy or use a volume of liquid to directly absorb the sunlight (volumetric absorption). This research focuses on the latter collector design as a means of potentially enhancing the amount of solar energy captured by combining this design with the use of nanofluids (a nanofluid is an engineered dilute colloid consisting of nanoparticles (NPs) suspended in a suitable base-fluid). A number of different NFs have been proposed for use in solar collectors. These will be discussed in Section 2.7, but can be divided based on the type of nanoparticle (NP) in the NF. For this research one type of NP, namely silver was investigated.

1.2 Research Gaps

1.2.1 Introduction

This Section looks at the key research gaps, firstly for STCs and then for the TES. Finally, this Section details the focus of this thesis.

1.2.2 Solar thermal collectors (STCs)

There are a number of technical challenges preventing the utilisation of nanofluids in solar applications. For a nanofluid to be suitable for use in a STC it must be able to remain stable over the lifetime of the collector for ≈ 20 years (or for a 3 y – 5 y period with a facile method of replacing in a maintenance cycle) whilst being subjected to multiple daily heating / cooling cycles, solar radiation (in the case of volumetric absorption) and shear forces associated with pumping. Stability of the NF is hence a major challenge (Gorji and Ranjbar, 2017a). Other challenges include cost due to production limitations (Mahian et al., 2013; Muhammad et al., 2016), increase pressure drop due to viscosity (Mahian et al., 2013; Ranga Babu et al., 2017), erosion and corrosion (Gorji and Ranjbar, 2017a) and lack of information on long term toxicity (Gorji and Ranjbar, 2017a). The toxicity of the nanofluids can also be effected by their age or stability with dissolution of the NPs into the base-fluid (BF) potentially occurring with time leading to an increase in toxicity (Kittler et al., 2010). There is also an issue with the preparation technique significantly influencing the performance of the NFs (Babar and Ali, 2019) further complicating the study and optimisation of NFs for solar applications.

For silver NFs the problem of stability is further enhanced, as the silver NPs are known to change size and shape due to photo conversion (Jin et al., 2001; Xue et al., 2008). Aggregation may also occur (Otanicar et al., 2013), hence a method is needed to stabilised the silver NPs not just from aggregation but to prevent shape change. One method of stabilising the NP is to coat the NP with a suitable coating forming a hybrid NP (He et al., 2019; Taylor et al., 2018). One such coating is SiO_2. At present, there is a lack of knowledge on the sunlight stability of these SiO_2 coated silver NPs, with limited reports on sunlight and temperature stability of SiO_2 nanodiscs (Hjerrild et al., 2018; Taylor et al., 2018). Long-term stability is likely to be dependent on many factors including, the synthesis process of the NF, the BF used, the nature, size and shape of the particles present, the thickness and consistency of any coating, and the presence and nature of any stabilising agents.

In addition, the optical properties of silver are not ideal as it only absorbs the sunlight over a narrow wavelength window and is hence not a broadband solar absorber. However, the surface plasmonic response of silver NPs, similar to other metal NPs is highly dependent on the size and shape of the NPs in the NF (Aherne et al., 2008; Haber and Sokolov, 2017; Ledwith et al., 2007). It should therefore be possible to tailor the synthesis of the silver NF to produce a broadband absorber more suitable for solar applications. This concept has been investigated numerically using a broadband mixture comprising of five different silver NP geometries giving an absorption efficiency of 95 % - 98 % over the range of 300 nm – 2500 nm (Mallah et al., 2018). Although broadband absorbers based on gold NFs have been assessed for solar applications experimentally (Du and Tang, 2016; Jeon et al., 2014; Jeon et al., 2016), experimental studies on broadband absorbers based on silver have not been carried out.

1.2.3 Thermal storage

There are three main types of TES (discussed in Section 2.4), a sensible thermal energy store (STES), a latent heat thermal store (LTES) and a thermochemical store (TCS). Of these TCS may be the most suitable for this application but it is the least technically mature. Key research gaps for TCS include the requirement for further research at a materials level to find and quantify a suitable active material or couple with sufficient energy density, hydrothermal stability and cyclability at the potential system operating conditions (Scapino et al., 2017b). In addition, an improved knowledge and understanding of reactor design factors is needed (Aydin et al., 2015; Hawwash et al., 2017). A better understanding of various safety issues such as side reactions, toxicity and corrosion is also required (Aydin et al., 2015; Scapino et al., 2017b). Finally, performance analysis studies including assessment of efficiency, dynamics of heat release (Walsh et al., 2020) and economics (Aydin et al., 2015) are needed, however, for these studies to be

effective, work on standardising the testing methods employed is first required (International Energy Agency, 2020b).

1.2.4 Scope of this thesis

This thesis focuses on the NF for use in a volumetric STC. It assesses silver based NFs for their suitability for solar applications firstly by evaluating experimentally their performance and then by looking at their stability under application relevant conditions. It also attempts for the first time to produce experimentally a broadband silver NF absorber by synthesising and combining together different silver NFs with distinct geometries. It then assesses this broadband absorber both for its potential ability to enhance solar thermal capture and for its stability. It also investigates one potential stabilisation method for silver based NFs, namely SiO_2 to see how this affects the photo-conversion shape change associated with silver.

1.3 Key Research Questions

From this scope the following research questions were derived:

What is the potential for silver NFs to enhance the amount of solar thermal energy captured and how can silver based NFs be tailored to improve further this potential enhancement?

What are the effects of application relevant conditions on the stability of the silver NFs for solar thermal capture and how does one potential mitigation or stabilisation strategy change these effects?

1.4 Aim and Objectives

1.4.1 Aim

This work focuses on one potential decarbonising solution for heating and hot water, namely, enhanced solar thermal capture for use in conjunction with thermal storage. It aims to increase the efficiency of solar thermal collectors by investigating silver nanofluids. It estimates the potential performance experimentally and highlights the importance of stability testing, hence showing some of the challenges to commercialisation for enhanced efficiency volumetric absorbers based on silver nanofluids.

1.4.2 Objectives

The objectives of this project are:

1. To synthesis silver nanofluids, producing various silver geometries that give a range of nanofluids with distinct optical properties.
2. Using suitable methods to assess the thus produced silver nanofluids for potential solar performance and stability under application relevant conditions.
3. To experimentally produce a broadband silver based nanofluid and evaluate the potential performance and stability of this broadband absorber.
4. To investigate a potential stabilisation method for silver nanofluids, namely coating the silver nanoparticles with SiO_2, showing that these hybrid nanofluids can be synthesised consistently.
5. To measure, using suitable methods, the potential performance and stability of these hybrid nanofluids for use in enhanced efficiency volumetric absorbers comparing the results to those obtained for the silver nanofluids and the silver broadband absorber.
6. Hence to demonstrate some of the potential barriers to commercialisation of enhanced efficiency volumetric absorbers using silver, a broadband absorber nanofluid based on silver, and hybrid SiO_2 coated silver nanofluids as examples.

1.5 Structure of the Thesis

The structure of this thesis is organised as follows. Following the introduction the first main Chapter 2 the literature review starts by evaluating the feasibility of the proposed decarbonising solution to answer the two research question provided in Section 1.1.3. It then details in more depth the relevant literature on thermal storage, solar thermal collectors, colloidal theory, and nanofluids (NFs) in solar thermal collectors. The literature review finishes with a brief summary.

Chapter 3 details the experimental methods including further literature pertaining specifically to silver NFs and the synthesis of hybrid silica coated silver NFs. The synthesis methods used in this thesis are then given. Characterisation methods are then detailed followed by how the potential solar performance of the NFs was calculated and measured. Finally, the various application relevant stability tests used to evaluate the stability of the NFs are presented.

Chapter 4 gives the results obtained from investigating the synthesis of silver NFs and the subsequent calculations of the potential performance of the silver NFs obtained from the spectrophotometry. This Chapter includes the development of a novel broadband silver based absorber produced by combining three NFs with distinct morphologies.

Chapter 5 presents the results obtained from measuring the efficiencies of the developed silver NFs using static tests in the solar simulator, comparing the results obtained with those of the

proceeding Chapter. The results from the various different stability trials using silver NFs are then detailed including the testing of the novel broadband NF under flow conditions.

The last main working Chapter, Chapter 6, looks at a potential stabilisation strategy namely coating the silver NPs with SiO_2. It starts by developing a coating protocol to consistently coat silver nanoprisms with SiO_2. This is followed by an estimation of the potential efficiency from the spectroscopy, measurement of the performance in static tests and the results of the stability trials. The developed coating protocol is then modified and the effect on the resulting elevated temperature stability assessed. Finally, this Chapter looks briefly at extending the established coating protocol to SiO_2 coat the novel developed broadband absorber NF and the subsequent colloidal stability of this NF.

Chapter 7 provides an overall discussion tying together the results obtained from the three main results Chapters and discussing the implications of the findings in this thesis.

This thesis then finishes with some conclusions and outlook.

Chapter 2 Literature Review

2.1 Publication from this Chapter

1. Kimpton, H., Zhang, X., Stulz, E., 2020. Decarbonising heating and hot water using solar thermal collectors coupled with thermal storage: The scale of the challenge. Energy Reports, 6, 25-34, https://doi.org/10.1016/j.egyr.2020.02.024 (Kimpton et al., 2020c)

2.2 Introduction

This literature review is divided into a number of parts. Firstly, the feasibility of the proposed decarbonising solution based on enhanced thermal solar capture connected to a suitable storage system is presented (Kimpton et al., 2020c). Secondly, the various types of thermal storage are detailed. This chapter then discusses solar thermal collectors. Some colloidal and nanofluid theory is then described. This is followed by a Section looking at the use of nanofluids in solar collectors. The Chapter concludes with a brief Summary.

More detailed literature pertaining to evaluation methods and silver nanofluids in particular are presented in Chapter 3.

2.3 Feasibility of Proposed Decarbonising Solution

2.3.1 Introduction

As mentioned in the introduction (Section 1.1), decarbonising domestic heating and HW is important to meet climate change obligations, however it is challenging. To understand if the proposed decarbonising solution would be feasible it is necessary to assess if enough solar thermal energy can be captured from a reasonable roof area and what the nature and size of a potential store would be, both now and in the future. To this end a feasibility study was carried out (Kimpton et al., 2020c).

Firstly, this Section looks at the advantages and disadvantages of a number of different alternative decarbonising solutions. It then details the methodology and results of the feasibility study on the proposed solution pertaining to this work. Subsequent Sections (namely 2.4 and 2.5) give more details on thermal energy storage (TES) and solar thermal collectors (STCs).

2.3.2 Potential decarbonising solutions

There are a number of different potential decarbonising solutions for heating and HW. The UK has a temperate climate, with an average monthly annual temperature range of ≈ 5 °C to 18 °C and a total annual solar irradiance of ≈ 750 kW h m^{-2} – 1100 kW h m^{-2} (on a horizontal surface, 2015 to 2017 climate values (Dhimish et al., 2018)).Given the age of the housing stock, the complexity and reliance on gas it is likely that no one solution would be ubiquitous for all homes in the UK. The heavy reliance on gas in the UK has actually intensified since 1990 with the number of homes connected to the gas network increasing from 14 million in 1990 to 23.9 million in 2019. It is also likely that any solution will be costly, and disruptive to retrofit, with retrofit costs more than 5 times that of new build (Climate Change Committee, 2019b). However, the UK government has recently stated that it wants to stop the sale of new gas boilers by 2035 and will provide £450 million over 3 years to reduce the upfront costs of low-carbon heating systems (UK Government, 2021b).

The first potential decarbonising solution is the use of heat pumps. A heat pump is a device that moves thermal energy from one place to another normally in the opposite direction to the spontaneous heat flow from a colder outside space to the warmer space inside a building like a refrigerator in reverse (The Renewable Energy Hub, 2021). At present in the UK in 2018 there were only about 35,000 air source heat pumps (ASHPs) and 10,000 ground source heat pumps (GSHPs) including non-domestic installations (Department for Business Energy and Industrial Strategy, 2019b). If these were to have a significant effect on the level of emissions 19 million – 23 million heat pumps would be needed by 2050 (Climate Change Committee, 2019a; Rosenow et al., 2018). The government has set an ambitious target of 600,000 heat pump installations per annum by 2028 (UK Government, 2021b) and 1.7 million per annum by the mid-2030s (UK Government, 2021a), > 10 times the entire current installed capacity. However, if the majority of these were ASHPs (the cheaper and less disruptive option) this level of heat pump use would cause major issues for the electricity grid with a possible peak demand of 330 GW and a minimum demand in summer of less than 30 GW (Sansom, 2012). To provide enough electricity to meet this heat demand would require more than doubling of the UK electricity generation capacity with much of this enhanced capacity only needed in the winter. In addition, the electricity grid would need reinforcing to cope with the additional seasonal power levels (Sansom, 2012). Finally, the electricity used for the heat pumps would need to come from sustainable sources such as wind or biomass otherwise the net impact of using heat pumps would be no significant decrease in emissions. This would be challenging without significant electrical energy storage on the electricity grid to cope with the intermittent electrical output from these renewable sources.

The second decarbonising solution is the use of better home insulation. This is not a standalone solution and needs to be used in combination with another solution if 100 % reduction in emissions is to be achieved. At best insulating all homes could save up to 27 % of demand (technically feasible) or more realistically 18 % - 25 % (Department for Business Energy and Industrial Strategy, 2017c; Rosenow et al., 2018). Even when combined with heat pumps it is estimated that the combined technically feasible reduction in emissions would be 75 % and not the 100 % target, unless all the electricity used is from green sources. This is the technically feasible level of reductions and as such is unlikely to be economically viable.

The third potential decarbonising solution is the use of combined heat and power (CHP). This is where the excess heat from power generation or industry is used to provide heating and HW to nearby homes. In 2018 there were only 129 residential group heating schemes in the UK providing just 481 MW of thermal power output (Department for Business Energy and Industrial Strategy, 2019b). However, although the efficiency of fuel conversion is greater than for electricity alone at about 70 %, the majority of the fuel used for CHP is gas (69 %) with the rest being primarily biomass with some anaerobic digestion. Worldwide also most district heat networks are carbon intensive with a large number relying on coal as an energy source (International Energy Agency, 2020a). Unless CHP uses renewable sources for its electricity generation such as concentrated solar power, biomass or anaerobic digestion it does not offer a means of decarbonisation. In addition, it is very difficult to recover and utilise any excess heat generated from some renewable electricity generation such as photovoltaic (PV) and wind. Finally, CHP is only useful where there is a high density of buildings otherwise the piping costs and heat losses through the system become too significant to make it worthwhile. At best therefore CHP offers a limited means of decarbonisation for a small proportion of the housing stock, in cities close to a pre-existing source of wasted heat such as from industry or biomass electricity generation.

The fourth tool that could be utilised to help decarbonisation of heating and HW is solar thermal energy. Only 1.5 % of the renewable heat initiative in the UK in 2018 was used for solar thermal. This equates to 48,434 MW h (Department for Business Energy and Industrial Strategy, 2019b). There are two main methods of utilising solar thermal power; one is the use of concentrated solar thermal energy to generate electricity and the other is the direct use of thermal energy gained from sunlight. The latter decarbonising solution is the main focus of this thesis and will be discussed in more detail in the following sections. To be effective as a decarbonising solution, firstly, enough solar thermal energy needs to be collected from a reasonable roof area and, secondly, as the energy from solar is intermittent a means of storing the collected thermal energy is needed. The simplest of these is a HW tank.

Many of the above solutions benefit from being combined with thermal storage, whether that is the use of small scale storage such as HW tanks to utilise solar energy generated in the day time in the evening or the use of thermal storage in a CHP system to help balance supply and demand (Lele, 2016). This will be discussed in more detail in Section 2.4.

The final possible decarbonising solution is the replacement of gas in the gas network with hydrogen. There are two main issues with this solution. The first is the ability of the existing gas network to work effectively with a high proportion of hydrogen. It is estimated that on the transmission network the current hydrogen addition limit is 10 %, on the distribution network, 50 % and for end of use appliances up to 20 % – 50 % hydrogen could be used (Gondal, 2019). This existing gas network could therefore be used to reduce but not eliminate the GHG emission from heating and HW. The second main issue is that the hydrogen used needs to come from a green source and not from natural gas or oil. Green hydrogen can be produced by using excess renewable energy to electrolysis water, producing hydrogen. However, these are intermittent sources of energy to produce hydrogen. Without active management of these intermittent sources, considerable variation in the quality of the gas into the network can result leading to network issues (Ekhtiari et al., 2020). In addition, the amount of renewable electricity generation would need to be increased to provide enough capacity to produce the green hydrogen. This would require 305 TW h extra electricity generation if electrolysing hydrogen was used and the heat network was switched to hydrogen rather than heat pumps (approximately 900 TW h per annum compared with current generation of 300 TW h in 2017, and a scenario of using heat pumps for all heating by 2050 of 600 TW h) (Climate Change Committee, 2019a).

2.3.3 Current and potential future demand

With a focus on domestic demand for heating and hot water (HW) for housing, the current median gas usage in the UK in 2015 and in 2018 for England and Wales for an individual household is 12,000 kW h (Department for Business Energy and Industrial Strategy, 2017c, 2020). There is a wide range associated with this median which is correlated with the size of the property, with larger properties tending to have higher demand. Another important factor is the number of people in the property, with more people leading to higher demand. In addition, the type and age of property affect the demand, with bungalows tending to have higher, flats lower, and older properties greater demand.

In the future there is likely to be about a 21 % – 25 % demand reduction due to efficiency improvements such as insulation (Climate Change Committee, 2019a; Rosenow et al., 2018). However, this efficiency improvement also includes boiler efficiencies improvements so should be

treated with caution. Hence a more realistic demand reduction would be just below this range at ≈ 20 %. Some of the factors limiting the future efficiency improvements include the age of the current housing stock, the low percentage of new build properties and the cost and complexity of retrofitting efficiency improvements to existing housing (Climate Change Committee, 2019b).

To estimate if the proposed decarbonising solution is viable a number of parameters need to be estimated. The values used in the estimation are given in Table 2-1.

Table 2-1. Values for parameters needed to estimate feasibility.

Parameter	Value used	Comment	Reference
Annual Energy demand Q_D / kW h y^{-1}	12,000	Median UK gas value from 2015. Median England and Wales gas value from 2018	(Department for Business Energy and Industrial Strategy, 2017c, 2020)
Annual HW demand Q_{HW} / kW h y^{-1}	3,200	Value from literature actually 3216 kW h y^{-1}. Summer HW taken as ½ Q_{HW}	(Greening and Azapagic, 2014)
Average annual solar irradiation $I_{rad(AA)}$ / kW h m^{-2} y^{-1}	1,100	Average value from two sources = 1093.5 kW h m^{-2} y^{-1} in a temperate climate for inclined (≥ 30 °) south facing collectors with no shading. Area is actual surface area	(Ayompe et al., 2011; Greening and Azapagic, 2014)
Current solar collector efficiency η_c for a flat plate collector (FPC) / %	45.9	Average of two values (46.1 % and 45.6 %)	(Ayompe and Duffy, 2013; Ayompe et al., 2011)
Current solar collector efficiency η_c for an evacuated tube collector (ETC) (heat pipe) / %	60.7	Commercial system in temperate climate	(Ayompe et al., 2011)
Average UK roof area available for solar collectors A_c / m^2	15	Estimated value	(Freeman et al., 2015)

2.3.4 Solar collector typical efficiency

A standard commercial thermal solar collector (STC) has an efficiency of about 46 % (Ayompe and Duffy, 2013), that is still higher than the typical efficiency of photovoltaic (PV) panels which is 15 % -20 % (Lewis, 2007; Mellor et al., 2018). But thermal energy is not as adaptable. However, for supplying heat it is ideal as there are no conversion loses. Unfortunately there is a discrepancy between time of generation and demand, hence storage is vital. If thermal collectors could be made more efficient then they may be able to capture enough energy for subsequent longer term storage.

2.3.5 Types of thermal energy store (TES)

For this decarbonising solution to be feasible inter-seasonal storage is vital to allow the shifting of summer generation to the winter, when it is needed. An inter-seasonal thermal energy store (ISTES) is possibly the best way of doing this. There are three main types of thermal storage (TES) namely, sensible thermal energy store (STES), latent heat thermal store (LTES) and thermochemical store (TCS). Typical parameters for these three types of TES are given in Table 2-2.

Table 2-2. Typical TES parameters. * - top value of 100 % impossible but quoted directly from International Renewables Agency IRENA (represents top of likely range).

Parameter	**STES**	**LTES**	**TCS**
Storage density ρ_{TES} / kW h m^{-3} (International Renewable Energy Agency (IRENA), 2013)	25	100	300
Efficiency η_{TES} / %	50 - 90	75 -90	75 – 100* (International Renewable Energy Agency (IRENA), 2013)
Assumptions / comments (see Section 2.4)	No loss of heat with time (unless very large and super insulated this is unlikely (de Jong et al., 2016))	Active PCM has a suitable transition temperature and the majority of the store contains active material	Salt hydrate used gives an output temperature suitable for HW (65 °C) (Donkers et al., 2017)

2.3.6 Scenarios considered

In order to assess the feasibility of collecting enough solar energy and then storing it for subsequent use in a suitable ISTES, it is necessary to estimate the total volume of the thermal store required and the amount of thermal energy needed to be captured to change this store. To this end, six different scenarios were considered (Table 2-3).

A demand reduction of 21 % – 25 % is considered feasible by others (Climate Change Committee, 2019a) hence in this work a conservative value of 20 % was used for scenarios 5 and 6. The values for storage efficiency η_{TES} used were the top and bottom of the range for TCS given in Table 2-2. Scenario 1 represents the 2015 median UK gas usage in the UK and the 2018 gas usage for England and Wales (Department for Business Energy and Industrial Strategy, 2017c, 2020) and has hence been included although it represents an impossible η_{TES} of 100 % (likewise Scenario 2). The value of η_{TES} of 75 % for the other 4 scenarios is more realistic and represent the bottom end of the range reported in Table 2-2 for TCS. Scenarios 5 and 6 represent likely future scenarios for

capture and storage respectively. Scenarios 2, 4 and 6 that exclude summer HW would need a more complicated system design to allow for a summer bypass to the TES.

Table 2-3. Scenarios considered.

Scenario	η_{TES} / %	Excluding summer HW / yes or no	Demand reduction / %	Energy to be stored annually Q_{Ts} / kW h
1	100	No	0	12,000
2	100	Yes	0	10,400
3	75	No	0	16,000
4	75	Yes	0	13,867
5	75	No	20	12,800
6	75	Yes	20	11,093

2.3.7 Calculations

The volume of the thermal store V_{TES} in m^3 is given by (adapted from (Dincer, 2002; Ibrahim et al., 2008; MacKay, 2008)):

$$V_{\mathrm{TES}} = \frac{Q_{\mathrm{Ts}}}{\rho_{\mathrm{TES}}}$$

Equation 2-1

where ρ_{TES} is the volumetric storage density of the TES store in kW h m^{-3}. The total energy to be stored Q_{Ts} in kW h is (adapted from (Dincer and Rosen, 2011):

$$Q_{\mathrm{Ts}} = Q_{\mathrm{D}} \frac{\eta_{\mathrm{TES}}}{100}$$

Equation 2-2

where η_{TES} is the efficiency of the TES in % and the energy demand Q_D in kW h is:

$$Q_{\mathrm{D}} = Q_{\mathrm{Heat}} + Q_{\mathrm{HW}}$$

Equation 2-3

where Q_{Heat} is the heating energy requirement and Q_{HW} is the HW energy demand both in kW h. Typical values for volumetric storage density ρ_{TES} and η_{TES} for the three types of TES are given in Table 2-2. Values for Q_D and Q_{HW} are given in Table 2-1. These values were used in conjunction with Equation 2-1, Equation 2-2 and Equation 2-3 to calculate the maximum size of TES required for the six scenarios. During sunny periods the heat from the STC panels is used (via a heat exchanger) to charge the store. For all three storage types it was assumed that the store would be charged and discharged completely only once per annum. In reality, it is likely that the store will be partially discharged and recharged on numerous occasions throughout the year, so the assumption of one discharge per annum represents the worst-case scenario and hence maximum store size needed. Also excluded from the calculation is any electrical energy required to operate

the thermal store, such as for pumps and heat exchangers. The electrical energy need for this is likely to be low (< 5 %) compared to the total needed for heating and hot water (Hoekstra et al., 2020).

The energy output from the solar collector Q_c in kW h is (adapted from (MacKay, 2008):

$$Q_c = I_{rad(AA)} A_c \frac{\eta_c}{100}$$

Equation 2-4

where $I_{rad(AA)}$ is the average annual solar irradiation per unit area in kW h m^{-2}, A_c is the area of the collector in m^2 and η_c is the collector efficiency (%). Values for the solar and demand parameters used to assess the feasibility of this solution are given in Table 2-1. Equation 2-4 in conjunction with the values in Table 2-1 were used to calculate the size of collector needed to collect enough energy in a year to satisfy scenarios 1, 3 and 5 for a range of different values of collector efficiency η_c. In addition, the reverse calculation was carried out, starting with the collector efficiency and hence determining the amount of energy captured Q_c for a range of collector areas. These results were then compared to the average UK roof area available of 15 m^2 to assess the feasibility of capturing enough solar energy from an average UK home to meet the storage energy demand Q_{Ts} (plus summer HW demand). Again, any electrical energy required to operate the pump for the collector are excluded from the calculations. The η_c is also related to the input and output temperature of the collector and system and the flow rate of the fluid through the collector. At high flow rates, the temperature rise through the collector is lower and hence thermal losses are reduced (Solar Ratings and Certification Corporation, 2020). However, the output temperature from the collector may then not be high enough to provide hot water (65 °C). These factors have not been considered in this feasibility study as they are hard to generalize and depend on the final system and collector design but losses can be significant at nearly 20 % in some cases (Ayompe and Duffy, 2013). Good design, with short well-insulated pipe lengths, close proximity of the collector and store, an efficient heat exchanger, and as low an output temperature as practicable will all help to minimise but not in reality eliminate these losses.

2.3.8 Area of collector needed to meet demand

To determine the potential size of thermal collector required to capture enough solar energy to charge a TES, only Scenarios 1, 3 and 5 were considered as the collector would still need to capture enough energy to meet summer HW demand even if this energy does not need subsequent storage. The calculated area of collector needed versus the efficiency of the collector for the three scenarios considered is shown in Figure 2-1 and Q_c versus roof area for various different values of η_c in Figure 2-2. The UK average roof area of 15 m^2 is highlighted for

illustration. A value of $\eta_c \geq 78$ % is required to capture the energy required for Scenario 5. This value is greater than the maximum η_c obtainable for an ETC in Table 2-1 of 61 %. As such it is optimistic to suggest that the average roof area in the UK can capture enough energy to fully meet the total heating and HW demand even with a demand reduction of 20 % (scenario 5). With the highest current η_c for a heat pipe ETC of 61 % an area of >19 m^2 of collector would be required for Scenario 5. For current FPCs the position is even worse with 15 m^2 only capturing 7590 kW h and > 25 m^2 required to capture enough for Scenario 5. A more realistic possible η_c = 70 % for an enhanced thermal capture system such as the one investigated in this research would need a roof area of slightly less than 16 m^2, marginally above the UK average for Scenario 5. The potential efficiency improvement for STCs is discussed more in Section 2.5.

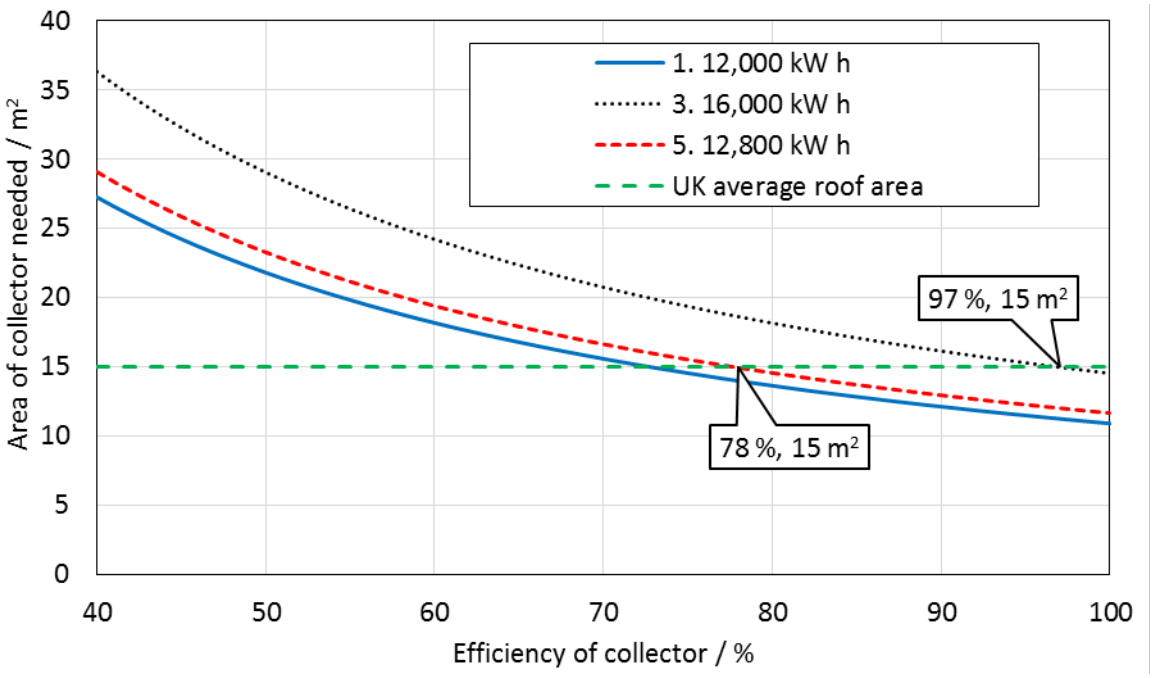

Figure 2-1 Area of collector needed for Scenarios 1, 3 and 5. The average UK roof area of 15 m^2 (Freeman et al., 2015) is also shown.

If energy demand remains at current levels an unattainable efficiency of 97 % is needed with a roof area of 15 m^2. A η_c of 70 % would need a roof area of about 21 m^2 and the current heat pipe ETCs would need an available roof area of ≈ 24 m^2. Hence, demand reduction is again vital to facilitate the feasibility of capturing enough solar energy in combination with improving η_c to ≥ 70 % potentially by the use of nanofluid direct absorption solar collectors (DASCs).

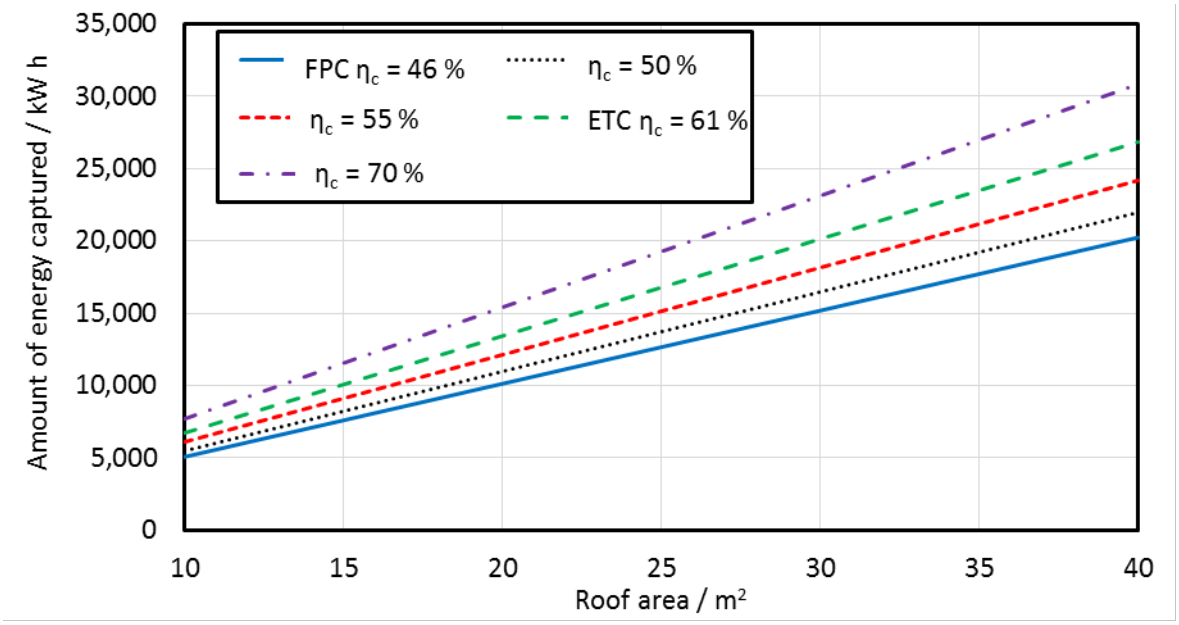

Figure 2-2 Amount of energy captured at different values of collector efficiency η_c. The flat plate collector(FPC) and evacuated tube collector (ETC) values are from (Ayompe and Duffy, 2013; Ayompe et al., 2011).

2.3.9 Size of store needed

Using the storage density values for the three different TES types given in Table 2-2, the size of the store needed for the six different scenarios investigated (Table 2-3) is shown in Figure 2-3. Even with the impossible assumption of no losses with time, STES is not a viable option for ISTES. LTES becomes a more feasible option but would still require a storage volume of 111 m^3 for scenario 6 (for illustrative purposes this equates to a cube with a side length of 4.8 m) that would only be feasible if the store was located underground and well insulated. The storage volume required for a TCS store is much more reasonable with a storage volume of 37 m^3 for scenario 6 (cube side length = 3.33 m). Although still large this store could be located above ground and hence becomes more viable for retrofitting to existing housing stock. To meet current demand with a feasible η_{TES} of 75 % even TCS would require a store size of 46 m^3 (scenario 4) which equates to a cube side length of 3.6 m. Hence, demand reduction is vital to make ISTES viable even if TCS is used.

In reality, therefore, capturing enough thermal energy and placing it in a TCS ISTES for subsequent winter use is hence only likely to become viable for homes in the UK if the following three conditions are met:

1. A below median demand of < 12,000 kW h y^{-1}
2. An above average roof area of > 15 m^2
3. Enough space to house a large (≤ 46 m^3) TCS ISTES

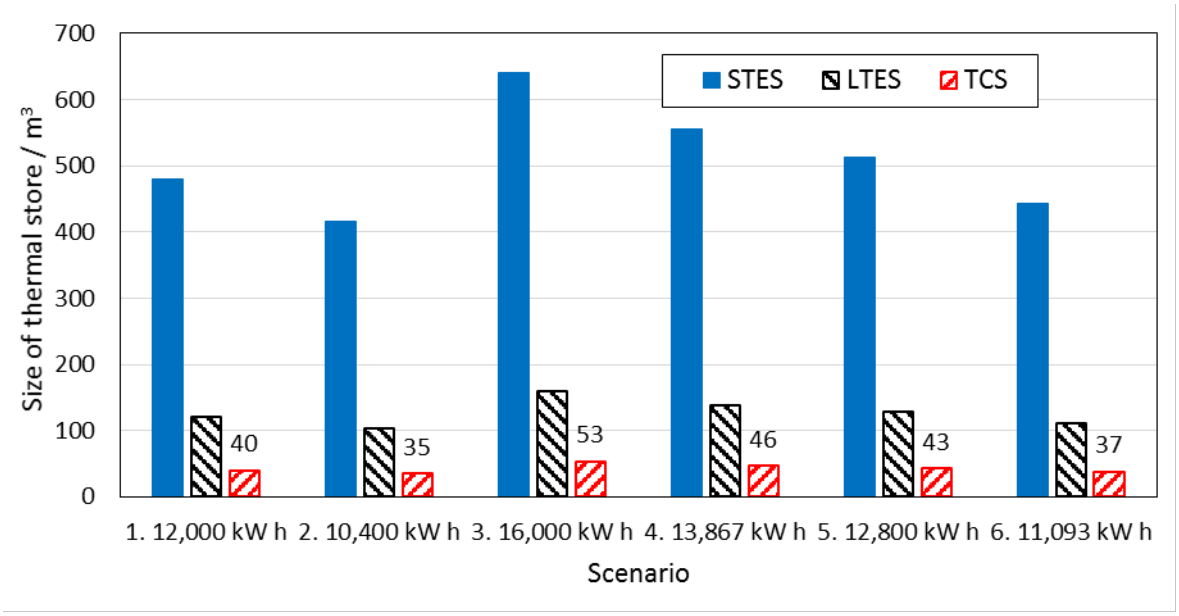

Figure 2-3 Size of thermal energy store (TES) needed for the six different scenarios for the three types of thermal storage, sensible thermal energy storage (STES), latent thermal energy store (LTES) and thermochemical store (TCS). The ρ_{TES} values used are from (International Renewable Energy Agency (IRENA), 2013).

If the amount of solar radiation was much lower (for example a property in North Scotland) the amount of roof area required would be larger, unless the demand was also reduced or the efficiency improved to compensate for the lower amount of sunlight available. Hence, the conclusions that a less than median demand and above average roof area is needed would still be valid but the exact numbers would be slightly different. There will also in reality be losses throughout the system in the pumps, pipes and heat exchangers. These losses would have the same effect as a reduction in solar radiation leading to a need for a larger collector area, a more efficient collector or a greater reduction in demand.

For the store, assuming only one charge / discharge cycle leads to a larger store size than might actually be the case. In contrast, any reduction in storage efficiency or storage density would lead to a smaller TCS ISTES size being proposed than is actually achievable. These factors effectively cancel each other out so would not dramatically affect the conclusion that a large TCS ISTES is needed of about the size suggested here. More details of TES systems are given in Section 2.4.

2.3.10 Summary

A decarbonising solution, based on enhanced solar thermal capture connected to a suitable ISTES comprising a TCS, has been proposed for providing a low-carbon heating and HW option for the average UK home. This solution is only feasible for homes with a less than median demand (< 12,000 kW h y^{-1}), a larger than average roof area (> 15 m^2) and enough space for a large TCS

(≤ 46 m^3). A realistic increase in collector efficiency to 70 % could capture enough solar energy from 16 m^2 to meet the storage requirements for a 20 % reduction in demand (12,800 kW h).

Although the proposed solution is feasible it would not suit every house in the UK and will hence need to be used as a complimentary system to sit alongside the other decarbonising solutions such as heat pumps and low carbon district heating CHP systems discussed in Section 2.3.2. In addition, to being feasible in the UK it is likely that such a system could also be suitable for other countries with similar climatic conditions and demand levels.

2.4 Thermal Energy Storage (TES)

2.4.1 Introduction

This Section firstly looks at some of the advantages of thermal energy storage (TES). It then looks at the three main types of TES, Sensible TES (STES), Latent heat TES (LTES) and Thermochemical TES (TCS). It then focuses on TCS looking firstly at the thermodynamics of TCS salt hydrates (given in Appendix A, Section A.1), then the material challenges (Appendix A, Section A.2), ideal material specification (Section A.3), the use of mixed TCS systems (Section A.4) and finally, system design considerations. This Section concludes with a brief Summary.

2.4.2 Advantages of thermal storage

Although thermal storage is not as adaptable as other forms of storage such as batteries its cost per kW h of storage capacity is considerably less. Battery costs in 2014 were between \$200 kW^{-1} h^{-1} – \$900 kW^{-1} h^{-1} (Feldman et al., 2016; Jorgenson et al., 2016) but have now dropped to about \$90 kW^{-1} h^{-1} – \$140 kW^{-1} h^{-1} and future costs are likely to now fall to about \$40 kW^{-1} h^{-1} – \$70 kW^{-1} h^{-1} (Armand et al., 2020; Duffner et al., 2021; Statista, 2022) Even with this lower cost a battery to provide 11,000 kW h of storage (for scenario 6 Table 2-3) would cost over \$400,000. The use of batteries to provide ISTES with a once per annum discharge is hence not economically viable.

TES is considerably cheaper (Mellor et al., 2018), with one of the more expensive molten salt storage for concentrated solar power costing \$15 kW^{-1} h^{-1} – \$27 kW^{-1} h^{-1} (Jorgenson et al., 2016). This is still not economically viable for an ISTES for scenario 6. However, other forms of TES such as water, rocks or many of the salt hydrates used for TCS are considerably cheaper and the active material costs for a store for scenario 6 using a salt hydrate such as K_2CO_3 would be ≈ \$15,000 (cost for K_2CO_3 ≈ \$1 kg^{-1} (Alibaba, 2020), density 750 kg m^{-3}).

With the final output requirement being heat there is also no conversion losses associated with storing as thermal energy and subsequently using that thermal energy. In contrast, using batteries would require the conversion of electrical energy to thermal energy, incurring losses.

2.4.3 Sensible TES (STES)

Sensible TES (STES) uses a materials heat capacity to store energy, with a material with a high heat capacity being advantageous according to the formula (Dincer and Rosen, 2011):

$$q = \rho c_f V \Delta T$$

Equation 2-5

where q is the heat energy stored in kJ, ρ is the density of the storage material in kg m^{-3}, c_f is the specific heat capacity of the material in the required temperature range in kJ kg^{-1} K^{-1} (c_f is dependent on temperature), V is volume in m^3 and ΔT is change in temperature in K or °C.

The active material for the store needs to be stable to thermal cycling, not toxic or reactive and to not change phase over the designed operating temperature range. In addition, it should also ideally be low cost. The thermal store needs to be well insulated. The best efficiencies are obtained with large store sizes (lower surface to volume ratios), short storage times and high levels of insulation. Some properties of common materials used for STES are shown in Table 2-4. The most familiar forms of STES are home HW tanks and electrical storage heaters. Material choice depends on application, for instance although water has a high heat capacity and is suitable for HW tanks it has a lower maximum operating temperature and density compared to some of the other materials in Table 2-4. This makes it not suitable for home storage heaters which require a high storage density, hence materials with a higher maximum operating temperature and density such as cast iron or steel are used (see Table 2-4). This allows for a greater ΔT and ρ in Equation 2-5 and hence a smaller storage volume V for a given q (Department for Business Energy and Industrial Strategy, 2016; Romero, 2013). Other examples of STES include solar ponds and various forms of ground STES such as borehole TES and aquifer TES.

A solar pond is a specific example of a STES that combines the capture of solar energy with STES (Abdullah et al., 2016; Al-Nimr and Al-Dafaie, 2014; Amouei Torkmahalleh et al., 2017; Sarathkumar et al., 2017; Simic and George, 2017; Spyridonos et al., 2003). These normally work on the principal of a change in density of salt water to inhibit convection and trap collected solar thermal energy in the bottom dense salt layer. A heat pump extracts this energy. Although relatively cheap to construct, they have low energy density and are very difficult to keep stable in practice with issues due to evaporation and maintenance of the salt gradient (Abdullah et al., 2017; Amouei Torkmahalleh et al., 2017; Sarathkumar et al., 2017). Nanofluids can be used to

improve the capture of solar energy into a solar pond (Al-Nimr and Al-Dafaie, 2014) but a large volume of nanofluid would be needed to store enough energy to provide more than just a small incremental improvement in heat pump coefficient of performance (COP). They are unlikely to be useful for STES in a temperate climate.

Table 2-4 Properties of STES materials. Data from (Dincer and Rosen, 2011; Gil et al., 2010).

Material	Maximum temperature	Density / kg m^{-3}	Heat capacity / kJ kg^{-1} K^{-1}
NaCl	500	2160	0.85
Cast iron	400	7200	0.56
Cast Steel	700	7800	0.60
Magnesium fire bricks	1200	3000	1.15
Mineral oil	300	770	2.6
Nitrate salts	565	1870	1.6
Carbonate salts	850	2100	1.8
Liquid sodium	530	850	1.3
Water	100	1000	4.2

Borehole TES is another common form of STES with ground source heat pumps (GSHPs) being a specific example of this type of storage which uses heat pumps to reduce system temperature and hence losses (Hesaraki et al., 2015; Kaygusuz and Ayhan, 1999; Kuang et al., 2003). In this type of STES the ground acts as the storage media and vertical boreholes are drilled to allow heat to be transferred in and out of the store (Rad and Fung, 2016). The efficiency of this type of STES is 40 % – 60 %, but it is relatively cheap and can be easily adapted. For example the storage size can be increased just by adding more boreholes to the system. However it does require stable ground conditions with a low level of ground water flow rate and it can take a number of years to fully change the store (especially for larger stores). It is usually applied to single family homes or smaller buildings (Pellegrini et al., 2019) but has been used in a number of larger community based projects.

Borehole STES has been combined with STCs in a number of large scale projects (Flynn and Sirén, 2015; Rad and Fung, 2016; Sibbitt et al., 2015; Sibbitt et al., 2012). One example of a community heating project employing borehole STES and STCs is the Drake landing solar community project in Canada which consists of 52 homes with solar thermal and heat pumps connected to a borehole STES (Sibbitt et al., 2015; Sibbitt et al., 2012). This purpose built community scheme provides over 90 % of the heating and HW requirements from solar thermal energy. A number of other community heating projects in Germany and Sweden utilising borehole STES with STCs and

solar fractions of 50 % - 60 % (the amount of heating load supplied by the solar collectors) have also been built (Rad and Fung, 2016).

Aquifer STES is a storage system that uses the groundwater to store thermal energy by the use of two or more groundwater wells. It is suitable for larger buildings such as offices, airports and hospitals, with a balanced energy demand for heating and cooling over the year (Hoekstra et al., 2020; Pellegrini et al., 2019). They tend to have a slightly higher storage density and efficiency than borehole STES but need a low groundwater flow and suitable water chemistry in the aquifer (Rad and Fung, 2016).

Like borehole STES there are a number of examples of aquifer STES being combined with solar thermal and combined photovoltaic-thermal (PVT) systems, however there is still a lack of knowledge with the practical operation of such systems which can lead to lower performance than expected (Pellegrini et al., 2019).

Other less common and more expensive larger scale STES systems include large underground HW stores and gravel / water stores. These tend to have higher storage density than borehole and aquifer STES but require containment of the storage medium in a tank. This adds considerably to the cost as soil has to be extracted and the tank needs insulating (Rad and Fung, 2016).

All of the STES systems considered here work best for mid – low temperature systems for use in conjunction with heat pumps. As such they would be difficult to retrofit to existing buildings. In addition, longer term storage such as ISTES leads to considerable losses with time with almost all the heat being lost from a 100,000 L tank after 4 months of storage time (de Jong et al., 2016). The large volume needed for STES for ISTES is also an issue (see Figure 2-3). This would make borehole and even aquifer STES unsuitable in areas with a high density of housing such as cities (Pellegrini et al., 2019).

2.4.4 Latent heat TES (LTES)

LTES relies on utilising a phase change as a means of storing energy (Farid et al., 2004). Advantages compared to STES include higher storage capacity, lower storage volume and isothermal operation (Abokersh et al., 2018). An ideal PCM for LTES should have the properties outlined in Table 2-5. However, no actual PCM material has all of these characteristics (see Table 2-6). Inorganic PCMs include salt hydrates such as zinc chloride hydrate (Agyenim et al., 2010; Zalba et al., 2003), organic PCMs encompass materials such as organic acids and paraffin waxes (Agyenim et al., 2010; Farid et al., 2004).

The properties of a PCM can be improved by encapsulation, composite materials (Kaygusuz and Ayhan, 1999) and by using various additives including silver nanoparticles to improve specifically thermal conductivity (Dincer and Rosen, 2011). In addition, a number of physical methods can be used to enhance the heat transfer from a PCM LTES, these include the addition of tapes or fins (Farid et al., 2004; Kaygusuz and Ayhan, 1999). Various system designs exist for LTES, these include incorporating the PCM in the building (Reddy et al., 2018), the solar collector (Abokersh et al., 2018) or the STES such as a water tank. Stand-alone LTES are also possible with a LTES placed around or within the heat exchanger. Most LTES systems proposed aim at shifting the generation from use by a time period of minutes to hours rather than for ISTES.

Table 2-5 Ideal PCM characteristics for LTES (adapted from (Abokersh et al., 2018)).

Properties	**Ideal PCM characteristics**
Thermal	High latent heat, specific heat and thermal conductivity. Suitable operating temperature
Physical	Low density variation on phase change, no super-cooling on freezing, high density
Chemical	Stable, non-flammable, non-toxic
Economical	Inexpensive

Table 2-6 Properties of some PCMs. Data adapted from (Agyenim et al., 2010; Farid et al., 2004; Zalba et al., 2003).

Material	**Heat Capacity / kJ kg^{-1} K^{-1}**	**Latent Heat / kJ kg^{-1}**	**Density / kg m^{-3}**	**Thermal Conductivity / W m^{-1} K^{-1}**
Water	4.2	333	1000	2.4 (liquid), 0.61 (solid)
Inorganic PCM	2.0	230	1600	0.4 – 5.0
Organic PCM	2.0	190	800	0.15 – 0.35

2.4.5 Principle of thermochemical store (TCS) for TES

The final type of thermal storage TCS is very different in operation as the two components of a reversible chemical reaction or sorption process are separated on charging, stored at room temperature when charged and combined together again on discharge (International Energy Agency, 2014). The principal is shown schematically in Figure 2-4 using salt hydrates as examples.

There are two different types of TCS system, open where only one of the two components are stored and closed (see Figure 2-4), where both of the two components are stored separately and sealed from the atmosphere (Scapino et al., 2017b). A closed system has to be used if one or both of the components are toxic, such as ammonia based reactions or if there is the potential of toxic side reactions, such as the formation of H_2S when using Na_2S as illustrated in Figure 2-4 (Donkers

et al., 2017; Scapino et al., 2017b). A closed system has a lower system storage density due to the need to store both components but can be more easy to control (Cabeza et al., 2017).

As the components are stored separately, there are very low losses with time making TCS ideal for ISTES. In addition, TCS has a higher possible storage density ρ_{TES} of 300 kW h m^{-3} (see Table 2-2), again making it more suitable for ISTES. However, at present TCS is at a research stage of development with problems being found with the reaction kinetics, choice of chemical reaction, and plant design significantly reducing the percentage of active storage media in a given volume, decreasing the energy density (Aydin et al., 2015; Prieto et al., 2016). Thermodynamic information on suitable materials for TCS are available in some cases (Donkers et al., 2016; Donkers et al., 2017) but these do not give an understanding of the material stability and kinetics with multiple cycling of the reaction, hence the need for experimental studies with appropriate apparatus to approximate as closely as possible real life reactors. Table 2-7 gives examples of some proposed TCS systems and illustrates the larger amount of energy available per kg of active material for TCS versus STES (compare reaction enthalpy with heat capacity). This literature review will focus on salt hydrates as these have the highest density and hence potential ρ_{TES}.

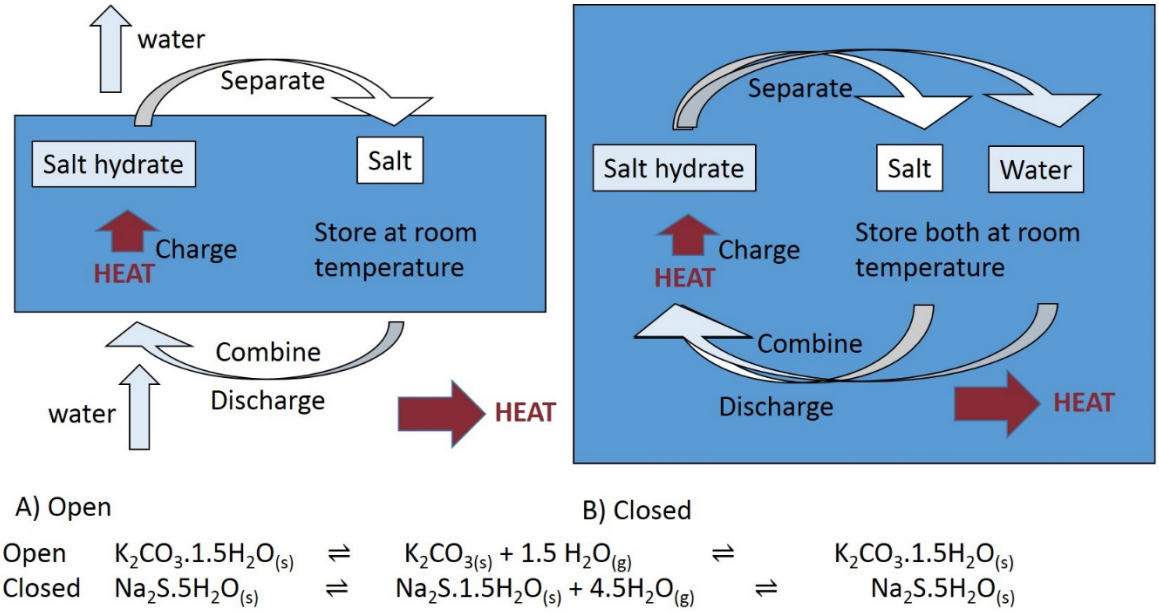

Figure 2-4 Schematic of a salt hydrate thermochemical store (TCS) showing, (A) An open system and (B) A closed system with examples of both (adapted from (de Jong et al., 2014; Donkers et al., 2017; Mamani et al., 2018)).

Table 2-7 Properties of some proposed TCS materials. Data from (Aydin et al., 2015).

Material	**Reaction enthalpy / kJ kg^{-1}**	**Heat capacity *c* / kJ kg^{-1} K^{-1}**	**Density *ρ* / kg m^{-3}**
Calcium chloride hydrate	433.6	3.06	2100
Silica gel	1380	1.13	600
Zeolite	1107	1.07	650

It is estimated that with an active material storage capacity of 2 GJ m^{-3} corresponding to a material storage capacity of about 1 GJ m^{-3} the requirements for ISTES for a passive house could be met by a storage system of 10 m^3 (Donkers et al., 2017). This would give a total storage capacity of 2778 kW h. This figure is lower than the one estimated in Section 2.3.9, but is for the specific example of a highly efficient purpose built passive house rather than the more ubiquitous retrofit scenarios considered in Section 2.3.

The thermodynamics of salt hydrates for TCS are detailed in Appendix A, Section A.1 and shows that controlling the dehydration and rehydration reactions is critical for these stores. It also casts doubt on the high η values quoted in Table 2-2 due to the energy required to evaporate water from a liquid to a vapour.

A salt hydrate for use in TCS needs to fulfil a number of demanding material criteria. These are discussed in Appendix A, Section A.2 with an ideal material specification being given in Section A.3 (Table A.1). No single salt hydrate matches this ideal specification. Therefore mixed salt hydrate systems need consideration. There is limited knowledge of these mixed salt systems with only a small number having been investigated for TCS (see Appendix A, Section A.4).

2.4.6 TCS – system design

Even when a suitable salt hydrate is chosen for a TCS store, the design of that store needs careful consideration. The main challenge is providing a means of ensuring the efficient addition and removal of water vapour from the solid salt hydrate, silica gel or zeolite. For this reason a number of researchers have focused on liquid based systems such as LiBr, NaCl and LiCl (Hamdan et al., 2013; Zhang et al., 2014). These tend to have lower potential storage densities than salt hydrates and operate on a slightly different system with two tanks – one at a higher salt concentration and the other more dilute according to the formula (where charging occurs from left to right):

$$MX.N_{(initial)}H_2O_{(weak\ solution)} + \Delta Q \rightleftharpoons MX.N_{(final)}H_2O_{(strong\ solution)} + H_2O_{(gas)}$$

Equation 2-6

These liquid based systems can be used for either heating or cooling (Ibrahim et al., 2018) and can reach storage density values of up to 110 kW h m^{-3} (compare to the value of 300 kW h m^{-3} for salt hydrates in Table 2-2) with high efficiencies (Zhang et al., 2014). They have also been proposed for use with STCs as they need lower regeneration temperatures than salt hydrates (Gómez-Castro et al., 2018; Shukla and Modi, 2017).

On a systems level there needs to be a better knowledge and understanding of reaction design factors. Hence, significant work is required on optimisation of the reactor design to ensure high

levels of actual storage density and efficiency (Aydin et al., 2015). For example, a prototype pilot scale closed TCS system based on the closed system reaction in Figure 2-4 at present gives a system storage density of 50 kW h m^{-3} but could reach a storage density of 278 kW h m^{-3} with further optimisation according to the authors (de Jong et al., 2016), which is comparable with the value for ρ_{TES} in Table 2-2. This optimisation is mainly around the packing arrangement of the salt hydrate and heat exchangers within the module design, which for the pilot scale demonstrator was far from ideal (i.e. rectangular heat exchangers in a circular cross-section).

2.4.7 Summary

The main two advantages of thermal energy storage (TES) are the cost and the lack of energy conversion efficiency losses. However, although the most technologically mature there are issues with using STES for ISTES, namely the size of the store required and the amount of losses from a STES with time. For LTES there are issues with finding a PCM with high conductivity and a suitable transition temperature. LTES is mainly used for shifting demand from generation by hours rather than days as would be required for an ISTES. TCS on the other hand appears to be the most suitable TES type for ISTES, with mixed salt hydrate systems perhaps being one way of overcoming some of the material limitations identified. Further key challenges and research gaps for TES systems are discussed in Section 2.8.3.

2.5 Solar Thermal Collectors (STCs)

2.5.1 Introduction

STCs need an efficient method of capturing as much solar thermal energy as possible and a means of transferring that energy to where it is needed (either to be used directly or stored for future use) (Tian and Zhao, 2013).

STCs are normally classified by temperature (low ≤ 120 °C, medium 120 °C to 400 °C and ≥ 400 °C high (Goel et al., 2020)), with higher temperature STCs using a method to concentrate the solar energy. These higher temperature collectors normally track and focus sunlight onto a smaller area, increasing the solar concentration and hence temperature. The primary output from these concentrated STCs is steam for power generation.

This review focuses on low temperature STCs for generation of thermal rather than electrical energy via steam generation, with concentrated STCs for power generation being outside of the main focus. It examines the STCs themselves rather than looking at the whole system, i.e. the STC, heat transfer mechanism and integration with thermal storage.

This Section initially gives some details on the electromagnetic spectrum and then define some of the important concepts pertaining to volumetric absorption and collector efficiency. Working fluids and volumetric absorption are then discussed. This Section then details the main types of STCs. Finally, a summary of this Section is given. More details of nanofluids in STCs is given in Section 2.7.

2.5.2 Electromagnetic spectrum

There is a nearly fixed intensity of solar radiation outside of the Earth's atmosphere. The extra-terrestrial (ET) solar irradiance $G_{s(\mathrm{ET})}$ in W m^{-2} is a measure of this solar radiation per unit time on a unit area of surface perpendicular to the electromagnetic wave direction just outside of the Earth's atmosphere. It is ≈ 1370 W m^{-2} (Duffie and Beckman, 2013). This ET radiation is wavelength (λ) dependent and has a characteristic spectral distribution. It should be noted that light intensity (I_L) is also measured in W m^{-2} but is not always the same as irradiance G_s. I_L is the intensity of the light on a plane perpendicular to the direction of the light (per unit area), whereas solar irradiance G_s is the solar radiation on a unit area of surface which is not necessarily perpendicular to the direction of light.

The situation at ground level is more complex, as the Earth's atmosphere absorbs and scatters some of the radiation. For this reason the total radiation is divided by convention into a number of different parts. These are the direct (dir), circumsolar (cs), sky diffuse (sk) and ground diffuse (gd). The $G_{s(\mathrm{dir})}$ is the radiation on a unit surface area that is nearly perpendicular to the surface (0.5 ° divergent cone). The $G_{s(\mathrm{cs})}$ is the radiation from a slightly wider cone (± 2.5 °) - $G_{s(\mathrm{dir})}$. The $G_{s(\mathrm{sk})}$ is the irradiance on a surface that comes from radiation scattered by the sky and $G_{s(\mathrm{gd})}$ is the irradiance arising from solar radiation reflected from the ground (ASTM, 2012; British Standards Insitution (BSI), 2018; Duffie and Beckman, 2013). A schematic of the different types of solar radiation incident on a surface is shown in Figure 2-5.

The total or hemispherical solar irradiance $G_{s(\mathrm{hem})}$ in W m^{-2} is the sum of the other types of solar radiation received per unit area on a planar surface from a solid angle of 2π sr (Steradian) i.e. a hemisphere:

$$G_{s(\mathrm{hem})} = G_{s(\mathrm{dir})} + G_{s(\mathrm{cs})} + G_{s(\mathrm{sk})} + G_{s(\mathrm{gd})}$$

Equation 2-7

Like $G_{s(\mathrm{ET})}$ the irradiance on a surface at ground level also varies with λ. About 97 % – 99 % of hemispherical solar radiation is in range 0.3 µm – 3 µm (British Standards Insitution (BSI), 2018). The λ dependence of $G_{s,\lambda(\mathrm{ET})}$, $G_{s,\lambda(\mathrm{dir\,+\,cs})}$ and $G_{s,\lambda(\mathrm{hem},\,\beta\,=\,37\,^\circ)}$ are shown in Figure 2-6. The effect of the atmosphere on reducing the amount of solar radiation especially at certain values of λ can be

seen along with the addition effect of diffuse radiation and a change in the angle the collector is to the horizontal (compare $G_{s,\lambda(\text{dir + cs})}$ with $G_{s,\lambda(\text{hem, }\theta = 37\,^\circ)}$).

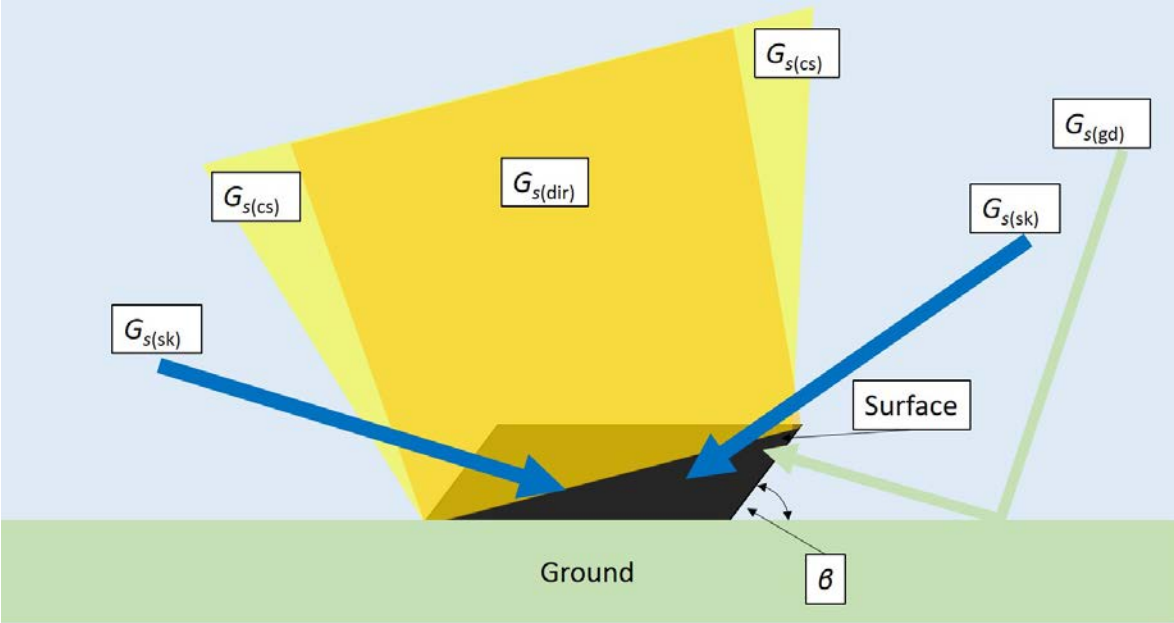

Figure 2-5 Illustration of the types of solar radiation incident on a surface of unit area (irradiance). The angle of the surface to the horizontal is shown as θ.

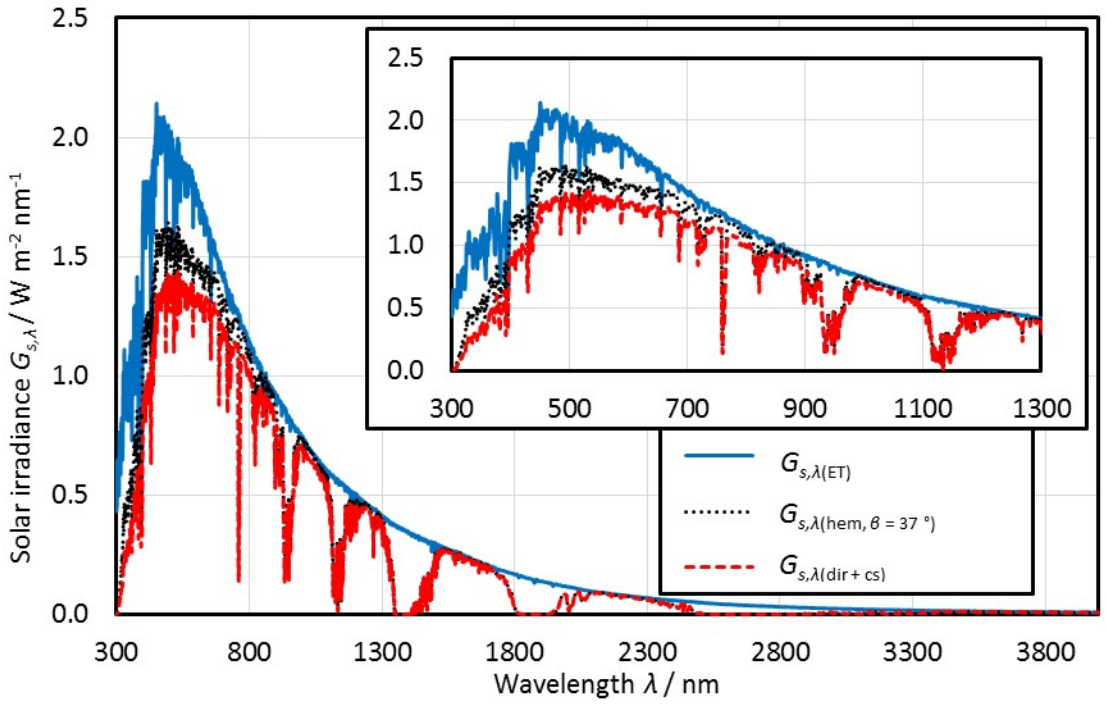

Figure 2-6 The wavelength (λ) dependence of the solar spectrum. The insert shows a magnification of the region from 300 nm – 1300 nm. Adapted from (ASTM, 2012).

2.5.3 Surface absorption versus bulk (volumetric) material absorbance properties

When the solar radiation hits a surface or volume of fluid it is either absorbed, reflected, scattered or refracted. Care needs to be taken when comparing surface absorption and bulk

absorption properties. Surface solar absorption α (%) is the amount of radiant solar flux absorbed divided by radiant flux or radiant heat flow rate received (British Standards Insitution (BSI), 1996):

$$\alpha = \frac{\Phi_e^{\mathrm{Ab}}}{\Phi_e^{\mathrm{i}}}$$

Equation 2-8

where Φ_e^{Ab} is the radiant flux absorbed in W and Φ_e^{i} is the incident radiant flux. Likewise surface solar reflectance (R_s) is the amount of radiant solar flux reflected divided by Φ_e^{i}:

$$R_s = \frac{\Phi_e^{\mathrm{R}}}{\Phi_e^{\mathrm{i}}}$$

Equation 2-9

where Φ_e^{R} is the radiant flux reflected in W.

In contrast, volumetric absorbance (*Ab*) in arbitrary units (au) actually measures attenuation through a material, which can be caused by absorption, reflection, scattering and other processes. It is not a surface property but measures the bulk material and is defined as:

$$Ab = \log\frac{\Phi_e^{\mathrm{i}}}{\Phi_e^{\mathrm{t}}} = -\log\frac{\Phi_e^{\mathrm{t}}}{\Phi_e^{\mathrm{i}}} = -\log T_m$$

Equation 2-10

where Φ_e^{i} is the incident radiant solar flux in W and Φ_e^{t} is the transmitted radiant solar flux and T_m is the transmittance in % and is equal to:

$$T_m = \frac{\Phi_e^{\mathrm{t}}}{\Phi_e^{\mathrm{i}}}$$

Equation 2-11

When the light entering the sample is not from sunlight (as in the case of a spectrometer) *Ab* at a given λ is still related to the power intensity of the light entering the sample (P_i) in W m^{-2} and the power intensity of the light that passes through the sample P_t according to the formula (Khullar et al., 2014; Sheffield Hallam University, 2019):

$$Ab_{(\lambda)} = \log\frac{P_{\mathrm{i}(\lambda)}}{P_{\mathrm{t}(\lambda)}} = -\log\frac{P_{\mathrm{t}(\lambda)}}{P_{\mathrm{i}(\lambda)}}$$

Equation 2-12

As *Ab* is not a surface property its value depends on the path length of the light through the sample. According to the Beer-Lambert law *Ab* is then directly related to the molar concentration of the optically active species, C_{opt} in the sample and the distance the light travels through the

sample, *d* in cm. The constant of proportionality is called the extinction coefficient or the molar extinction coefficient (κ) normally in cm^{-1} (Jeon et al., 2016; Modest, 2003):

$$Ab = \kappa d C_{\mathrm{opt}}$$

Equation 2-13

Strictly speaking, the measured *Ab* is the attenuation through the sample and as such comprises of absorption and scattering. However, for solutions and for colloids containing small nanoparticles (NPs) the amount of scattering is zero or very low and can sometimes be excluded from calculations (Otanicar et al., 2011). For larger NPs (≈ 50 nm) the contribution from scattering can become significant (≈ 50 %) and hence the value of κ can change dramatically (Paramelle et al., 2014a, b).

The issue of determining κ for colloidal solutions or NFs is further complicated by the fact that the value of C_{opt} is related to the amount and size of the NPs and not the initial molar concentration of the ions in solution. For monodispersed spherical silver samples the diameter can be determined from transmission electron microscopy (TEM) and the number of particles determined by titrating the dissolution of the silver particles with a cyanide solution (Paramelle et al., 2014a). Other issues with NFs and colloids will be discussed further in Section 2.6.

2.5.4 Collector efficiencies

Many papers and commercial specifications for STCs give values for collector efficiencies η. However, considerable care needs to be applied when evaluating these headline results and comparing between different work. There are seven different efficiency formulas in the ISO standard for solar collectors alone (British Standards Institution (BSI), 2013). For example the instantaneous hemispherical efficiency η_{hem} is defined as:

$$\eta_{\mathrm{hem}} = \frac{\dot{m} c_{\mathrm{f}} \Delta T}{A_{\mathrm{c}} G_{s(\mathrm{hem})}}$$

Equation 2-14

where $\dot{m}$ is the mass flow rate of the fluid in the collector in kg s^{-1}, c_f is the specific heat capacity of the fluid in J kg^{-1} K^{-1}, ΔT is the change in temperature in °C (or K) between the inlet (T_{in}) and outlet (T_{out}) of the collector ($T_{out} - T_{in}$), A_c is the collector area in m^2 and $G_{s(hem)}$ is the hemispherical solar irradiance in W m^{-2} (British Standards Institution (BSI), 2013).

Even more care needs to be applied to values for commercial STC ηs. For commercial STCs a zero loss or peak collector η_{peak} is often quoted (Mellor et al., 2018; Solar Ratings and Certification Corporation, 2020) along with values for the heat loss coefficient a_1 derived from the equation:

$$\eta_{\text{hem}} = \eta_{\text{peak}} - a_1\left(\frac{T_{\text{Tran}} - T_{\text{Amb}}}{G_{s(\text{hem})}}\right) - a_2\left(\frac{T_{\text{Tran}} - T_{\text{Amb}}}{G_{s(\text{hem})}}\right)^2$$

Equation 2-15

where η_{peak} is the zero loss or peak efficiency, a_1 the heat loss coefficient in W m^{-2} K^{-1}, a_2 the temperature dependence of the heat loss coefficient in W m^{-2} K^{-2}, T_{Tran} is the average temperature of the heat transfer fluid and T_{Amb} the air temperature around the collector (both in either K or °C). Values as high as 84.8 % for η_{peak} are obtainable (Solar Ratings and Certification Corporation, 2020) but this does not represent the likely η_{hem} for this collector in non-ideal conditions with different flow rates, different input and output temperatures and solar irradiance.

2.5.5 Working or heat transfer fluids

All STCs, whether they utilise a selective surface or not, require a working or heat transfer fluid to transfer the heat energy to the point of use. If a secondary heat exchanger is not used then the working fluid needs to be the same as the fluid needing heating, for example water in domestic HW collector or air in a heating system, giving an open loop system where the fluid is not recirculated (Duffie and Beckman, 2013).

Examples of working fluids (WF) include air, water, water with various additives like ethylene glycol and or propylene glycol (to depress the freezing point), glycerol and various oils for higher temperature heat transfer (Hjerrild et al., 2018; Otanicar et al., 2009).

To be ideal as a WF the fluid needs high thermal conductivity, low viscosity, low thermal expansion, and to not freeze or boil (except in the case of heat pipes) within the operating range of the STC. In addition, it needs to be non-corrosive, non-toxic and stable to thermal cycling.

A heat pipe (HP) is a specific design of STC which will be discussed in more detail in Section 2.5.7. The WFs employed in these collectors are low boiling point liquids such as ethanol (Azad, 2012) although higher boiling point WFs can also be used as the WF in the HP is maintained at low pressure (Kumar et al., 2017). The HPs are connected to a manifold, where the WF in the HP STC condenses onto a separate pipe running through the manifold containing a different WF to transfer the heat to where it is needed.

In addition, if the WF also acts as the solar absorber, as in the case of volumetric or direct absorber solar collectors (DASCs), the fluid needs to absorb as much solar radiation as possible. Most commonly employed working fluids have poor optical absorption, with the most common, water only absorbing about 13 % of the available solar radiation (Otanicar et al., 2009).

Using NPs in the WF producing a stable engineered colloidal suspension or nanofluid (NF) can improve the thermal conductivity (Alim et al., 2013; Taylor et al., 2013) and the optical properties, however, their use may cause an increase in viscosity and a reduction in stability to thermal cycling. The different types of NFs studied and their effect on the various properties of the working fluid will be described in more detail in Section 2.7. Further details on colloidal stability are given in Section 2.6.

2.5.6 Volumetric absorbance or direct absorption solar collector (DASC)

DASCs were first proposed in the 1970s (Minardi and Chuang, 1975) and utilise a volume of liquid to collect solar energy rather than an absorbing surface (Gupta et al., 2015a), thus referred to as volumetric absorption. This increases the efficiency of the collector by 6 % – 10 % versus a flat plate collector (FPC) (Nasrin et al., 2015; Turkyilmazoglu, 2016) and also simplifies the construction (Otanicar and Golden, 2009; Otanicar et al., 2010; Tyagi et al., 2009). This increase in efficiency is due to a reduction in thermal conduction and convection resistance within the collector as well as a reduction in radiative and convective losses from the front face of the STC (Mallah et al., 2019; Sreekumar et al., 2022). Initially the working fluid employed suffered from low absorption of solar energy (Otanicar et al., 2009). To combat this micro-particles of carbon black or Indian ink were employed (Gorji and Ranjbar, 2016). However, these suffered from problems with blocking of pumps, erosion, and sedimentation (Kazemi-Beydokhti et al., 2014; Khullar et al., 2014). Research therefore focused on using smaller NPs (Taylor et al., 2013). These provide a larger surface area for absorption as well as potentially enhancing and tuning absorption especially if the NPs or NFs employed in the DASC contain electromagnetically absorbing surface plasmonic species like silver and gold (Chen et al., 2016; Gorji and Ranjbar, 2016). NPs can also improve the thermal conductivity of the WF (Iyahraja and Rajadurai, 2015; Lee et al., 2016) but this enhancement is said to only contribute a small amount to the improved performance for volumetric absorbers (Gorji and Ranjbar, 2016). The light interactions with a NF in a volumetric collector and with a NP are shown schematically in Figure 2-7.

The principle of volumetric absorption can be used in conjunction with any of the three main types of STCs described in the following subsection, namely flat plate collectors (FPCs), evacuated tube collectors (ETCs) and heat pipes (HPs) with some modifications to the design.

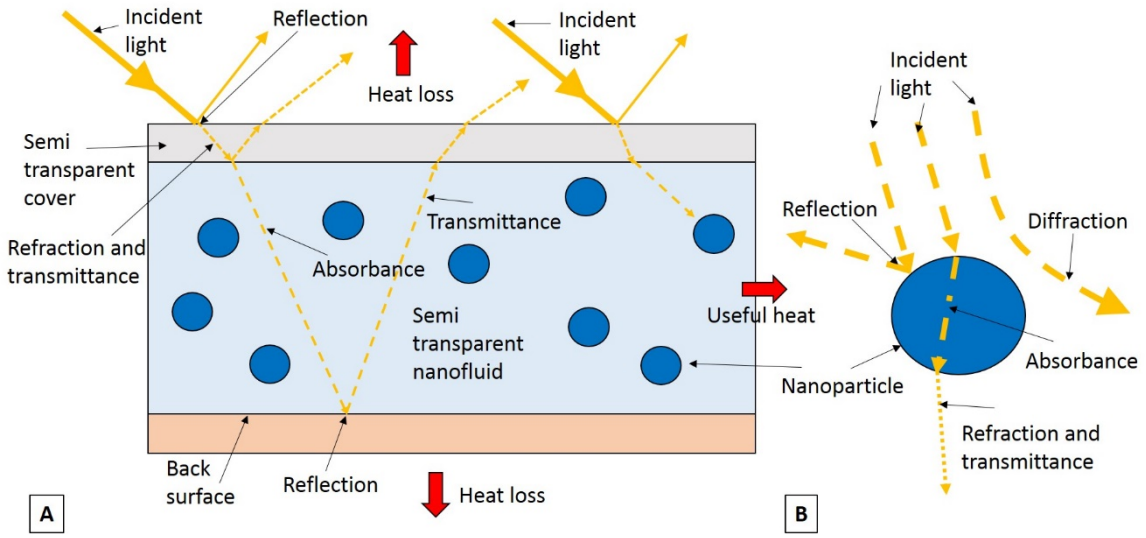

Figure 2-7 Schematics of light interactions with (A) A semi-transparent nanofluid and (B) A nanoparticle. Not to scale (the diameter of the NP at typically < 100 nm is significantly less than the depth of NF which is typically about 10 mm). Adapted from (Honnerova et al., 2017; Modest, 2003; Otanicar et al., 2011).

2.5.7 Types of collectors

There are three main types of geometry employed for STCs, the simplest being FPCs. ETCs are a slight modification with a vacuum tube being employed to reduce heat losses. The final type, HPs are a variation of ETCs where a low boiling point fluid is employed in the actual STC and heat transfer occurs via condensation of this fluid onto a manifold running along the top of the collector containing the WF (Duffie and Beckman, 2013). Dry connections can be used between each vacuum tube and manifold allowing easy replacement of the vacuum tubes, however, the collector must be maintained at an angle to allow the fluid in the tube to evaporate (Selvakumar et al., 2010).

For the FPC utilising a surface absorber a number of configurations are possible with one configuration shown schematically in Figure 2-8 A. Here, two glass covers are shown to reduce heat losses by convection and radiative heat losses from the hot surface absorbing plate (Ajeena et al., 2022; Kumar et al., 2021). In this configuration the copper pipes containing the WF are inserted into the insulation and then welded to the underside of the surface absorber plate. The insulation reduces the heat loss from the back face of the collector. The heat is transferred from the hot absorbing plate via conduction and convection to the WF (Gorji and Ranjbar, 2017a; Sreekumar et al., 2022). Other variations include bending the absorber plate around the pipes, or placing the copper pipes above the insulation.

In contrast, the DASC (Figure 2-8 B), has a much simpler construction. Unlike the FPC with a surface absorber, the DASC relies on radiative heat transfer and has almost no conduction and

convection losses in the main part of the collector. The gradual absorption of the solar radiation throughout the depth of the fluid in the DASC leads to the nanofluid being more thermally homogeneous with a lower temperature front face and hence less losses due to convection and radiation from the top of the collector (Kumar et al., 2021; Mallah et al., 2019). Again in contrast to a surface absorber, convection only has a marginal role in a volumetric absorber and energy losses are primarily due to incomplete absorption of the solar radiation, losses from the scattering of the incident light by the NPs and some small losses to the surroundings from convection and radiation. Like the surface absorber there are again possible design variations, such as changing the nature of the back surface behind the nanofluid. If this is a surface absorber any light that passes through the nanofluid can be absorbed by the back surface, potentially improving the efficiency and ensuring the hottest part of the collector is away from the front face. If the back surface is mirrored this reflects the unabsorbed light back through the nanofluid, again increasing the absorption efficiency for a smaller depth of nanofluid. In both Figure 2-8 A and B two glass covers are shown. In some cases only one cover is used. This reduces the cost but has a detrimental effect on the efficiency. The volume between the two glass covers can also contain an inert gas or even be evacuated to create a vacuum (this is hard to maintain for a FPC – hence ETC).

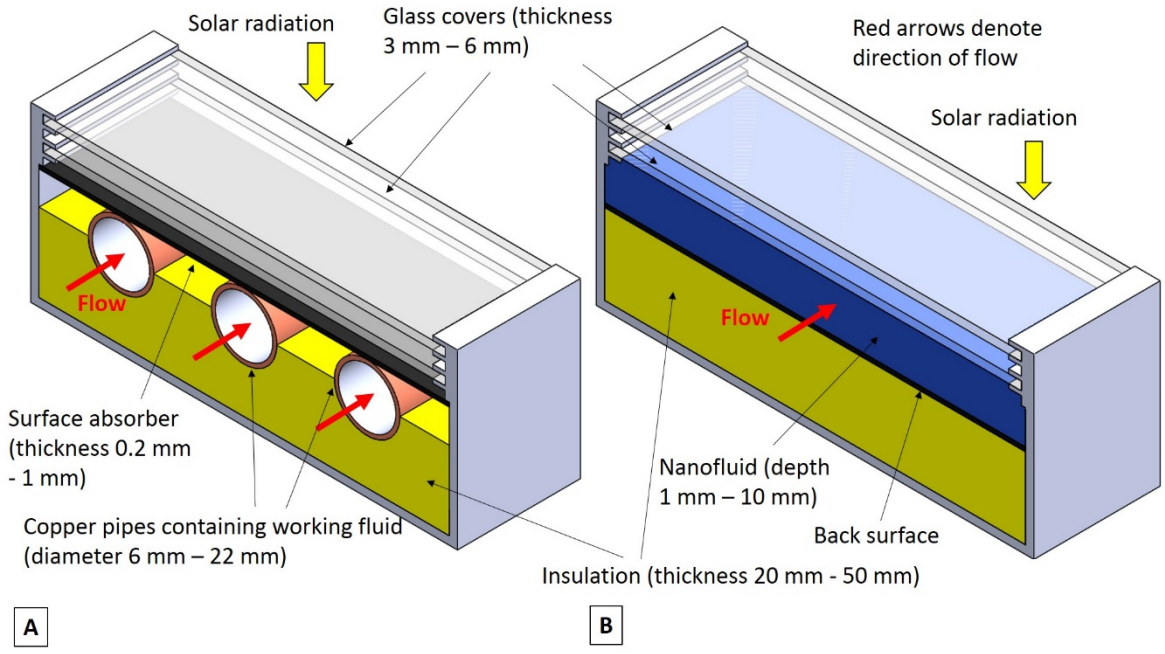

Figure 2-8 Schematics of a FPC, (A) With a surface absorber and (B) A FPC, DASC containing a nanofluid. Typical dimensions are shown in brackets. Typical collector area = 1 m x 1.5 m per module (Deng et al., 2016; Hawwash et al., 2018; Noghrehabadi et al., 2016).

Although more expensive, ETC collectors can reach a higher temperature due to the better vacuum insulation. The simplest type of ETC is illustrated in Figure 2-9 where the working or nanofluid flows once through the collector. Other variations include using a U-shaped pipe to

allow both the inlet and outlet to be co-located at the same end of the vacuum tube. In the case of surface absorption a curved absorber can be used (a flat absorber is shown in Figure 2-9 A) allowing the sunlight to hit the collector plate at the optimum angle throughout the day, making the output potentially more consistent (Selvakumar et al., 2010) and more efficient over a wider range of operating conditions (Zambolin and Del Col, 2010) but they may not be the most suitable collector design for every system (Budihardjo and Morrison, 2009). Disadvantages of an ETC include more expensive construction, a reduction in surface area and issues with sealing the vacuum tube. For the volumetric absorber in this configuration the reduction in area and hence volume of absorber can be significant (depends on diameter of glass tube) and the advantage of the simplified construction may also be lost both due to the difficulty in maintain the seal around the glass pipe and the size of glass pipe required.

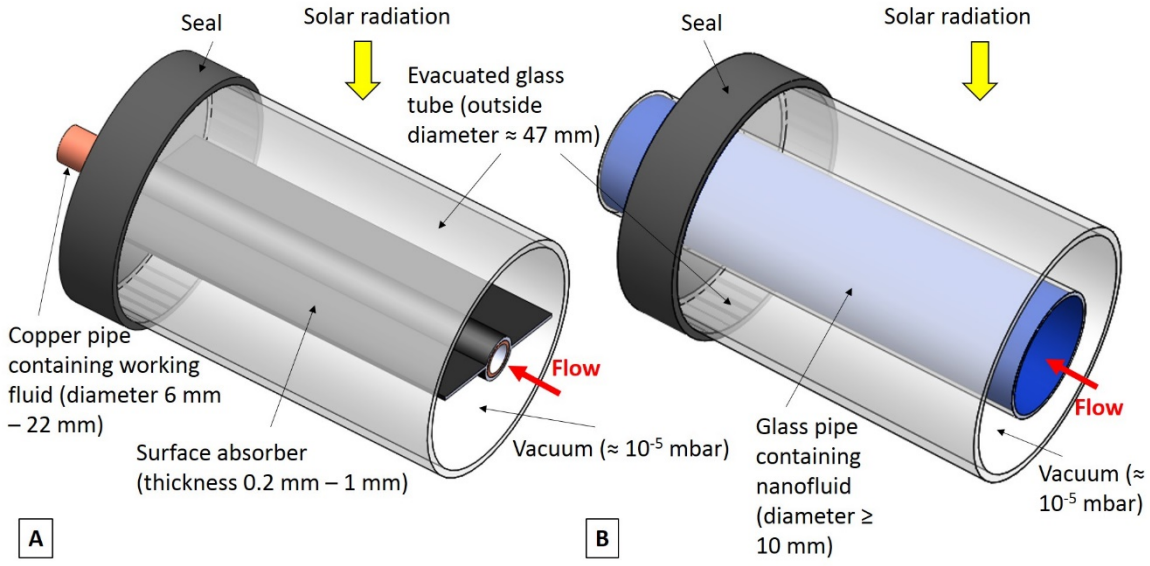

Figure 2-9 Schematics of an ETC, (A) Using a surface absorber and (B) A volumetric absorber with a nanofluid. Typical dimensions and vacuum level shown in brackets. Typical length of glass tube = 1 m – 1.5 m (Ayompe et al., 2011; Mehta and Rane, 2013).

For the final type of collector a HP (Figure 2-10), using a direct absorber would result in an even greater reduction in surface area. For this reason only a surface absorber collector is illustrated in Figure 2-10. This is because a reduced volume of liquid in a partial vacuum is used to fill the HP (a charging volume of about 32 % is common (Han and Rhi, 2011)). This allow the fluid in the heat pipe to evaporate in the evaporator section to form a vapour, which is then condensed again in the condenser section, transferring the heat to the WF in the manifold. Dry connections can be used between each tube in the collector and the WF in the manifold fluid allowing easy replacement of the vacuum tubes, however, the collector must be maintained at an angle to allow the fluid in the tube to evaporate (Selvakumar et al., 2010). Nanofluids can be used in the actual HP to increase the rate of evaporation, however, their use is extremely challenging as the fluid within the HP has to boil to transfer the heat to the condenser section. This can lead to rapid

aggregation of the nanoparticles and issues with deposition of the NF onto the sides and the wicks inside the HP (Han and Rhi, 2011) leading to a significant deterioration in performance.

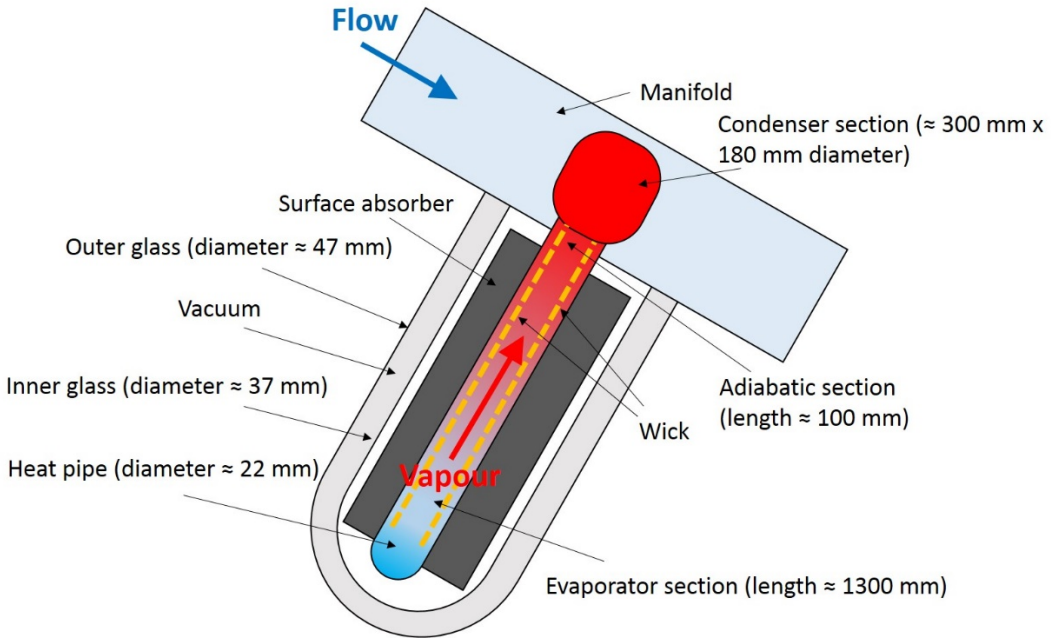

Figure 2-10 Schematic of a heat pipe (HP) with a surface absorber. Adapted from (Kumar et al., 2017; Shafieian et al., 2019). Typical dimensions shown in brackets (Chopra et al., 2018; Ozsoy and Corumlu, 2018).

2.5.8 Summary

This Section provides details of the solar spectrum, showing the λ dependence of the incident light. The difference between bulk and surface absorption is then shown. Issues with evaluating collector efficiencies are then discussed followed by some details about the various working fluids (WFs) that can be used. Volumetric absorption is then described, showing the complex interactions between a NP in a NF and the incident light. The three main geometries of STCs, namely FPC, ETC and HPs are then described, highlighting the difficulties of using volumetric absorbers rather than a selective absorbing surface in both ETCs and HPs.

2.6 Colloidal and Nanofluid (NF) Theory

2.6.1 Introduction

In this Section colloidal and nanofluid (NF) theory is briefly described. Firstly, the definition of a colloid is given with some examples. Secondly, the forces acting on a particle in a colloid are detailed. Colloidal stability is then discussed and finally, the Stern-Gory-Chapman double layer theory is illustrated. A short summary is given at the end of the Section.

2.6.2 Definition of a colloid

A colloid is a suspension of a particle of one phase within a different phase. The range of particle sizes normally referred to as colloidal are between 5 nm and 50 µm. Colloids are often solid particles dispersed in a liquid medium but can be other phases. The main types of colloids with some examples are given in Table 2-8. A NF is a specific example of a solid colloidal suspension with a particle size of ≤ 100 nm in a liquid medium (Taylor et al., 2013).

Table 2-8 Types of colloids (adapted from (Pashley and Karaman, 2004)).

Dispersion medium or base-fluid (BF)	Dispersed phase	Name	Example
Gas	Solid	Solid aerosol	Dust, smoke
Gas	Liquid	Liquid aerosol	Sprays, fogs
Liquid	Solid	Colloidal solution or "sol", paste at high solid concentration	Silver sol, NF, toothpaste
Liquid	Liquid	Emulsion	Milk, paint
Liquid	Gas	Foam	Foams
Solid	Solid	Solid suspension	Coloured plastics, some metal alloys
Solid	Liquid	Solid emulsion	Opal, pearl
Solid	Gas	Solid foam	Expanded polystyrene

2.6.3 Forces acting on the particles in a colloid

There are three main forces that act on fine particles in solution (Pashley and Karaman, 2004). These are:

1. Gravitational forces – This depends on relative density between the particles and the medium they are dispersed in. Gravitational forces cause particles to be raised or to settle.
2. Drag or viscous forces due to the medium or fluid the particles are in having to be forced apart as the particles move through the fluid
3. Forces due to kinetic Brownian motion

The terminal or limiting velocity of the particle can be calculated. At this velocity the gravitational forces will equal the drag forces, hence for a spherical particle of radius *r* (Pashley and Karaman, 2004):

$$F_{\text{drag}} = 6\pi r u \mu_{\text{d}} = F_{\text{gravity}} = \frac{4\pi r^3 g(\rho_{\text{p}} - \rho_{\text{d}})}{3}$$

Equation 2-16

where F_{drag} is the viscous drag force in N. $F_{gravity}$ is the gravitational force again in N, u is the limiting or settling velocity of the particle in m s^{-1}, g is the acceleration due to gravity in m s^{-2}, μ_d is the viscosity of the dispersion medium or BF (e.g. water) in kg m^{-1} s^{-1}, ρ_p and ρ_d are the densities of the particle and the dispersion medium respectively in kg m^{-3}. From Equation 2-16 it can be seen than generally small particles and particles with similar densities to the dispersion medium are more stable.

Equation 2-16 does not account for the third force arising from Brownian motion. The amount of Brownian motion will be dependent on the temperature of the system. As the particles move they will collide with each other. The particles are likely to have van der Waals attractive forces between each other and hence on colliding together with agglomerate and are therefore more likely to settle out (larger radius r). The relative number of particles that will aggregate (N_{rel}) is given by (Cosgrove, 2010):

$$N_{\mathrm{rel}} = \exp\left(-\frac{E_{\mathrm{r}}}{k_B T}\right)$$

Equation 2-17

where E_r is the repulsive energy of interaction in J, k_B is the Boltzmann constant in J K^{-1}, and T is temperature in K. A value of about 25 x k_BT gives several months of stability (without any other factors).

2.6.4 Colloid stability

Colloids are always metastable (Pashley and Karaman, 2004). However, an opposing repulsive electrostatic force can be generated to offset the attractive Van der Waals forces. This forms the bases of the DLVO colloid theory (from Derjaguin, Landau, Verwey and Overbeek), which states that the total force acting on a particle in a colloid will be comprised of the Van der Waals forces and the electrical double layer forces (Cosgrove, 2010; Polte, 2015).

The properties of the particle surface are very important. This is because a large number of small particles give a high surface area (Cosgrove, 2010). The interface area between a uniform sized spherical particle and the medium (A) in m^2 can be defined as:

$$A = \frac{3\phi V_{\mathrm{Total}}}{r}$$

Equation 2-18

where ϕ is the volume fraction of the particle. V_{Total} in m^3 is the volume of the system and r is the particle radius in m. Hence, the larger the volume fraction (the more concentrated the colloid) and the smaller the particle size the greater the surface area. Understanding the surface chemistry of the particle and the interactions of this surface with the dispersive media is hence vital for colloidal stability.

2.6.5 Stern-Gory-Chapman (SGC) double layer theory

The first theory to describe the behaviour of a charged particle in an electrolyte / solution was the Helmholtz model (Cosgrove, 2010; Pashley and Karaman, 2004). This assumed a linear potential change from the surface of the particle to the point of closest approach of the solvated counter ion. This model was refined by Gouy-Chapman, where the ions were considered as point charges and the potential changes in an exponential decay across an extended diffuse layer before reaching the potential of the bulk solution. Finally, the double layer Stern-Gory-Chapman (SGC) was proposed. This allows for counter-ions to become specifically adsorbed onto the charged surface as well as allowing for the closest approach of the hydrated ions forming two distinct layers. The potential changes linearly across the first compact layer and exponentially across the diffuse layer. The differences between the three different models is show schematically in Figure 2-11.

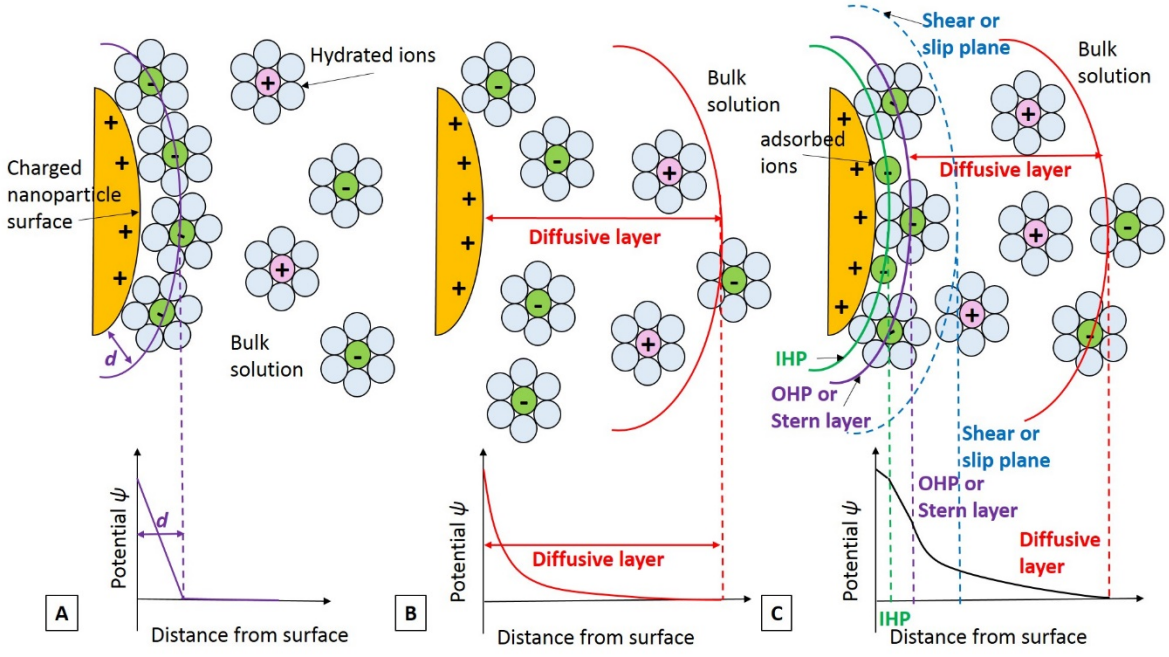

Figure 2-11 Schematics of charged particle models showing (A) Helmholtz model, (B) Gouy-Chapman model and (C) SGC model. IHP is the inner Helmholtz plane and OHP the outer Helmholtz plane. The change in potential ψ is also shown. Adapted from (Hunter, 1981; Tiwari and Uzun, 2015).

In Figure 2-11 C the shear or slip plane is shown separate to the position of the outer Helmholtz (OHP) or stern plane (this is the plane which corresponds to the zeta (ζ) potential. Normally the ζ

potential is the same as the Stern potential but this is not always the case (Hunter, 1981) especially if a bulky polymer is also absorbed on the surface – causing the shear plane or ζ potential to be displaced. When the SGC model is combined with the DVLO theory a total interaction potential is obtained resulting in a curve with a maxima representing the aggregation barrier that two particles need to overcome in order to aggregate. The height of this barrier determines the colloidal stability (Polte, 2015) for electrostatic stabilisation.

However, colloids can also be stabilised using steric stabilisation. This is where large molecules such as surfactants or polymers are absorbed onto the surface of the colloidal particle. The DVLO theory can hence be extended to include another repulsive force term for the steric stabilisation. Unlike electrostatic stabilisation, steric stabilisation does not depend on the colloid particle size but depends on the nature of the polymer, its concentration and the solubility of the polymer in the BF, with a more soluble polymer leading to less aggregation (Polte, 2015).

2.6.6 Summary

A colloid is a suspension of a particle of one phase in a medium of another phase with a NF being a specific example of a solid particle of ≤ 100 nm in a liquid phase. There are 3 main forces acting on a particle in a colloid. These need to be balanced to ensure colloidal stability. Both electrostatic and steric stabilisation can be used to balance these forces, with the Stern-Gory-Chapman double layer theory being used to describe electrostatic stabilisation.

2.7 Nanofluids (NFs) in Solar Collectors

2.7.1 Introduction

NFs can be used in both selective surface STCs and in volumetric absorbers. Firstly, this Section looks at the two main methods of preparing NFs, it then details the four main types of NFs employed. This Section then concludes with looking at the important properties of NFs for use with selective surface absorbers and in DASCs for volumetric absorbance with a brief summary being given at the end of the Section. Further details of specifically Ag NFs are given in Chapter 3.

2.7.2 Preparation methods

There are two main methods of preparing NFs; these are the one-step and the two-step methods.

The two-step method involves using ultrasound to suspend pre-prepared NPs in the BF or dispersion medium with or without a surfactant to impart steric stability (Bandarra Filho et al.,

2014; Gorji and Ranjbar, 2016, 2017b; Otanicar et al., 2010; Roy et al., 2015; Xuan et al., 2014). Issues with this method include temperature stability of the surfactant and oxidation of metal NPs (Gorji and Ranjbar, 2017a; Taylor et al., 2013). This two-step method of preparation is said to increase the level of aggregation on exposure to temperature (Otanicar et al., 2013).

In the one-step method, NPs are produced in situ by using a reducing agent either using a batch or continuous microfluidics method (Carboni, 2014; Carboni et al., 2013; Chen et al., 2016). They are then stabilised using various capping agents such as PVP and citrate (Tang et al., 2015; Tsuji et al., 2012). An issue with the one-step method is the presence of other chemicals in the NF. For hybrid NFs (a NF with more than one NP type) sometimes one of the NPs is prepared using the one-step method. The other type of NP is then added (Hjerrild et al., 2016; Sani et al., 2015; Zeng and Xuan, 2018) either as a solid NP or as an already prepared NF (Zeiny et al., 2018). Another variation of the one-step method is the use of a preliminary seeding step to produce small NPs that are then grown by the addition of the seed to another solution containing a suitable reducing agent (Crisostomo et al., 2017; Taylor et al., 2018). The preparation of silver NFs by the one-step method will be discussed further in Section 3.4.

2.7.3 Types of nanofluids (NFs)

The NFs used in solar applications can be classified into four main groups, those using carbon-based NPs, those using metal oxide NPs, those using metal NPs, and hybrid NFs containing single NPs comprised of more than one component or mixtures of two or more different NPs. This Section will only detail some of the studies carried out. The performance of the different NFs will be discussed in more detail in Sections 2.7.4 and 2.7.5.

For the carbon-based NFs the NFs are normally prepared by the two-step method as the carbon has to be functionalised in order to make a stable NF especially in polar BFs such as water. Some of the studies that have been carried out on carbon-based NFs are detailed in Appendix B, Table B.1. Overall carbon-based NFs tend to exhibit broadband absorption over the visible part if the solar spectrum and appear black in colour.

Some of the studies on metal oxide based NFs for solar applications are shown in Appendix B Table B.2. Like carbon-based NFs the majority of metal oxide based studies utilise the two-step preparation method. Unlike carbon-based NFs metal oxide NFs tend to have sharper absorption peaks and are not broadband absorbers. For example the wavelength of the absorption maximum λ_{max} = 830 nm for CuO, 400 nm for TiO_2, 370 nm for ZnO, 400 nm for CeO_2 and 620 nm for Fe_2O_3 (Milanese et al., 2016a, b).

Four main metallic nanoparticles have been studied, namely, copper (Luo et al., 2014), nickel (Gorji and Ranjbar, 2017a), silver and gold. The silver based NFs will be discussed further in Section 3.4. One of the issues with metal nanoparticles is preventing oxidation of the metal prior to inclusion in the base-fluid to form the NF, especially if the two-step preparation method is used and for copper and nickel it is likely that the nanoparticles will have a thin layer of oxide particularly if dispersed in an aqueous BF. Unlike carbon and metal oxide NFs, gold and silver NFs are mainly prepared by the one-step method. Some studies of gold NFs all in water BF prepared by the one-step method are shown in Appendix B Table B.3.

The final type of NF is hybrids. The use of hybrid NFs either containing two different types of particles or a single particle type comprised of more than one compound are an increasing area of study (Babar and Ali, 2019; Che Sidik et al., 2017; Dhinesh Kumar and Valan Arasu, 2018; Ranga Babu et al., 2017). The reasons for utilising a hybrid NF rather than a mono-nanofluid are numerous but can be to change the optical properties (for example to produce a broadband absorber by combining different metal oxide NFs), impact greater stability, reduce the cost, and change the thermo-physical properties (thermal conductivity, viscosity, specific heat and density) of the NF. As there are so many proposed hybrid NFs this review will focus on silver containing hybrids only. These are discussed in Appendix B, Section B.2 and Section 3.6.2.

2.7.4 Use of nanofluids (NFs) with surface absorbers

NFs can be used in conjunction with selective surfaces as the WF to enhance the efficiency of heat transfer, mainly by enhancing the thermal conductivity of the WF (Alim et al., 2013) but also by increasing the convective heat transfer due to Brownian motion (Sreekumar et al., 2022). A small mass of nanoparticles is required (< 5 % by volume). When combined with the transfer base-fluid the nanoparticles should form a stable non-aggregating nanofluid.

Some authors have reviewed the level of thermal enhancement obtained with NFs (Kakaç and Pramuanjaroenkij, 2009; Murshed et al., 2008; Murshed et al., 2011; Wang and Mujumdar, 2007; Yu and Xie, 2012). Part of the improvement in thermal transfer efficiency is due to an increase in thermal conductivity of the nanofluid (Kazemi-Beydokhti et al., 2014; Xie et al., 2011). Other factors which affect the transfer of heat include convective heat transfer due to increased Brownian motion of the particles and an increase in effective surface area of the particles within the fluid, however thermal conductivity enhancement is believed to be the most important factor (Xie et al., 2011) and research has tended to focus on this (Wang and Mujumdar, 2007).

The enhancement of thermal conductivity is related to the nature of the particles (Sharma et al., 2011; Tawfik, 2017) within the NF and the temperature of measurement, with higher

temperatures leading to higher thermal conductivity (Iyahraja and Rajadurai, 2015). Comparisons with the same temperature BF are therefore vital (Xie et al., 2011). Higher thermal conductivity NPs (such as MWCNT and metals) also tend to give rise to greater thermal conductivity enhancements for the NF but this is not always the case (Das, 2017). Smaller particles also lead to a greater enhancement and the presence of surfactants reduces the level of enhancement. If the surfactant is added to stabilise the nanofluid this will initially lead to an increase in thermal conductivity which will then reduce as excess surfactant is added (Xie et al., 2011). The pH of the NF can also affect the stability of the NF and the surface charge on the nanoparticles within the fluid and hence effect thermal conductivity (Kazemi-Beydokhti et al., 2014; Xie et al., 2011). Sonication can increase the movement of particles and the temperature, explaining in part the wide range of improvements reported in the literature (Muhammad et al., 2016; Wang and Mujumdar, 2007; Xie et al., 2011).

To achieve high enhancements of thermal conductivity, the concentrations of NPs in the NF tend to be greater than those used to change the optical properties of the NF with many studies looking at NP concentrations in the range of 0.1 % – 5 % vol (Tawfik, 2017). In many studies an increase in concentration leads to increased thermal conductivity (Das, 2017). However, these higher concentrations can lead to issues with increased viscosity and maintaining a stable NF (Oliveira et al., 2019). The higher concentrations utilised can also lead to aggregation of the NPs, which causes the enhancement in thermal conductivity to be reduced (Tawfik, 2017; Zayed et al., 2019).

2.7.5 Use for volumetric absorbance and direct absorption solar collectors (DASCs)

In a volumetric absorber the primary mechanism of heat transfer is via radiative heat transfer as there are minimal conduction and convection resistances within the collector (Mallah et al., 2019). Hence with volumetric absorption, and no selective absorbing surface, the efficiency of the STC is directly related to the absorption characteristics of the WF employed with broadband absorbance being the primary goal for STCs (Goel et al., 2020). The use of an appropriate absorbing NF is therefore vital to improve the efficiency of these STCs.

There are in the literature a number of reviews on the optical properties of NFs for solar applications (Ahmad et al., 2017; Gorji and Ranjbar, 2017a). To enhance solar absorbance, the ideal NF needs to absorb solar radiation strongly over the broad range of the solar spectrum with a low concentration of nanoparticles to prevent nanoparticle aggregation in the fluid (Jeon et al., 2014; Sharaf et al., 2019). Although graphite and some metal oxide based NFs tend to achieve broadband absorption, they require ≈ 5 times the concentration of metal based NFs (Hjerrild et

al., 2016) enhancing possible aggregation. Metal based NFs, however, exhibit strong absorption at lower reagent concentrations but tend to have a narrow absorption peak (Du and Tang, 2016).

Although volumetric absorption potentially offers enhanced efficiency improvements not many studies have compared directly the performance of a DASC containing NFs with that of a conventional FPC with an absorbing surface with many researchers quoting efficiency improvements compared to a BF without NPs rather than to a FPC with an absorbing surface. One numerical study compared a DASC containing Cu NPs with the same geometric set-up with a black painted surface instead of direct absorption and found a 8 % – 10 % improvement in photo conversion efficiency (Nasrin et al., 2015). Another, in this case experimental study, compared the temperature rise of a selective surface absorber directly to a DASC with the same geometry in a small scale static test in a solar simulator and found the DASC containing MWCNT NF showed a greater and more even temperature rise but did not extend their work by calculating the differences in η between the two systems (Khullar et al., 2014).

Even when η improvements are evaluated compared to the BF for DASCs containing NPs there is a wide range of improvements quoted in the literature (Murshed et al., 2011; Yu and Xie, 2012). For example for silver NF one of the lowest improvements quoted in the literature is 5 % (Otanicar et al., 2010) and one of the highest is 144 % (Bandarra Filho et al., 2014). This is because the geometry of the experimental set-up strongly influences the results obtained even when similar NFs are evaluated. Considerable caution must therefore be used when comparing the results of one study with another.

2.7.6 Summary

There are two main methods for preparing NFs; the one-step and the two-step method. The four main types of NFs are carbon-based, metal oxides, metals and hybrids. Of these only carbon and some metal oxides tend to offer broadband absorbance which is required for most volumetric applications. For applications with a selective surface absorber, thermal conductivity is one of the most important characteristics of the NF, however there is a large range of results reported in the literature and considerable care needs to be taken when comparing one study with another. This is also the case with volumetric absorption reported efficiency improvements. There is also a lack of investigations directly comparing the performance of volumetric and surface absorbers with many studies reporting improvements compared to the BF without NPs rather than compared to a selective surface.

2.8 Summary

A short summary of the main points covered and the findings from each of the Sections in this Chapter is given in Table 2-9.

Table 2-9 Chapter 2 Summary.

Section	**Points covered / Outcome**
Feasibility of proposed decarbonising solution	Viable for some homes in the UK (≤ median energy use, > average roof area, enough space for a TES)
Thermal storage (TES)	3 types described – focus on thermochemical TES (TCS) using salt hydrates
Solar thermal collectors (STC)	Details nature of solar spectrum, the concept of volumetric absorption including the absorption formula, and efficiency calculations. The working fluids used in STCs and three main types of STCs (FPC, ETC and HP) are then described
Colloidal and Nanofluid (NF) theory	Definition of a colloid and NF, forces acting on the particles in a colloid. Types of stabilisation are electrostatic (SGC double layer theory) and steric
Nanofluids in Solar Collectors	Preparation methods described, four main types of NFs, carbon-based NPs, metal oxide NPs, metal NPs and hybrids. In STCs with a surface absorber the most important property of the NF appears to be thermal conductivity, for volumetric absorption optical properties are important

Chapter 3 Experimental Methods

3.1 Publications from this Chapter

1. Kimpton, H., Stulz, E., Zhang, X., 2020. Silver nanofluids based broadband solar absorber through tuning nanosilver geometries. Solar Energy, 208, 515-526, https://doi.org/10.1016/j.solener.2020.08.018 (Kimpton et al., 2020b).
2. Kimpton, H., Cristaldi, D.A., Stulz, E., Zhang, X., 2020. Thermal performance and physicochemical stability of silver nanoprism-based nanofluids for direct solar absorption. Solar Energy, 199, 366-376, https://doi.org/10.1016/j.solener.2020.02.039 (Kimpton et al., 2020a).
3. Kimpton, H., Zhang, X., Stulz, E., 2021. The temperature stability and development of a broadband silver nanofluid for solar thermal applications. Energy Reports, 7, 87-96, https://doi.org/10.1016/j.egyr.2021.02.049 (Kimpton et al., 2021).

3.2 Introduction

This Chapter details the experimental methods used in this thesis. It presents the main methods used throughout this thesis and describes the various parameters that are investigated. Further specific sample details are then provided in the relevant subsequent results and discussion Chapters.

It starts by listing all the chemicals employed. Next some literature pertaining to silver NF synthesis and hybrid NFs containing silver is described. This is followed by the actual synthesis methods used for producing silver NFs including work undertaken to develop a broadband absorber based on silver NFs and an assessment of the consistency of the batch manufacturing process. The methods for coating silver NPs with SiO_2 are subsequently presented, starting with a short review of the literature, followed by the methods investigated in this thesis and the variations undertaken on the developed coating method. The characterisation methods employed are then detailed again starting by briefly reviewing the potential evaluation methods. After this the methods used to calculate and measure the potential solar performance of the NFs are provided. Next the methods used to investigate the stability of the resultant NFs are detailed. The last main Section of this Chapter gives an assessment of the uncertainty associated with the methods employed. Finally, a summary is given at the end of the Chapter.

3.3 Chemicals

All chemicals were purchased from Sigma Aldrich except where explicitly stated. They were all used directly as supplied without modification. All water employed was ultra-pure Milli-Q quality with a resistivity of ≤ 18.2 MΩ cm, both to ensure reproducibility of results and to prevent accidental contamination of the synthesis.

3.3.1 Silver nanofluid synthesis

The chemicals used to synthesis the silver nanofluids were:

Silver nitrate ($AgNO_3$ 99 %), tri sodium citrate di-hydrate (TSCD), polyvinylpyrrolidone (PVP, weight average molecular weight $M_w \approx 29{,}000$ g mol^{-1}), hydrogen peroxide (H_2O_2 30 wt. %) and sodium borohydride ($NaBH_4$, 99 %).

3.3.2 SiO_2 coating procedure

The chemicals used for the Stöber SiO_2 coating procedure were:

16-mecaptohexadecanoic acid (MHA) (2 batches), tetraethoxysilane (TEOS), dimethylamine (DMA) solution (40 % v/v) and absolute ethanol (from Fisher Scientific).

The chemicals used for the water-glass SiO_2 coating procedure were:

3 mercaptopropyl trimethoxysilane (MPTMS), sodium metasilicate ($Na_2SiO_3.5H_2O$).

3.3.3 Other chemicals

1, 2-propanediol (or propylene glycol) (PG).

3.4 Literature Review on Silver Nanofluids (NFs)

The literature concerning the one-step synthesis of Ag NFs is described in this Section. The literature on hybrid NFs is given in Appendix B, Section B.2 with further literature specifically on SiO_2 coating of silver NPrs given in Section 3.6.2.

For silver NFs the one-step production technique involves the reduction of silver nitrate in the presence of stabilising agents and a reducing agent. To make non-spherical prisms hydrogen peroxide can also be used to selectively etch different faces of the spheres during manufacture (Carboni et al., 2013; Carboni et al., 2016). The reduction of silver in the presence of sodium

borate as the reducing agent is given in Equation 3-1 and the use of hydrogen peroxide as a selective etch in Equation 3-2. There are different kinetics involved in these two reactions with Equation 3-1 occurring almost instantaneously, whereas Equation 3-2 occurs more slowly due to H_2O_2 being stable in solution in the neutral form. This reaction takes ≈ 10 minutes – 30 minutes to initialise depending on if PVP is present in the solution or not (PVP acts as a capping agent or steric barrier slowing the silver and H_2O_2 reaction) (Carboni, 2014). In this reaction citrate can be used not only as a stabilising agent but as a buffering agent to remove the nitric acid formed in the reduction step (Equation 3-1). This use of citrate is shown in Equation 3-3 (Carboni, 2014).

$$NaBH_4 + 8AgNO_3 + 4H_2O \rightleftharpoons Na[B(OH)_4] + 8Ag^{(0)} + 8HNO_3$$

Equation 3-1

$$2Ag^{(0)} + H_2O_2 + 2H^+ \rightleftharpoons 2Ag^+ + 2H_2O$$

Equation 3-2

$$Na_3C_3H_5O(COO)_3 + HNO_3 \rightleftharpoons Na_2HC_3H_5(COO)_3 + NaNO_3$$

Equation 3-3

A photo-induced method can also be employed (Jin et al., 2003; Stamplecoskie and Scaiano, 2010; Tang et al., 2015; Tang et al., 2013). Suitable stabilising agents include citrate (Ledwith et al., 2007; Metraux and Mirkin, 2005; Moreira et al., 2013; Ung et al., 1998), PVP (Brandon et al., 2014; Graf et al., 2003; Mirzaei et al., 2016; Salehi et al., 2013; Yan et al., 2016), bis(p-sulphonatophenyl) phenylphosphine dihydrate dipotassium (BSPP) (Jin et al., 2003; Metraux and Mirkin, 2005; Xue et al., 2007) and poly-sodium 4-styrenesulfonate (PSSS) (Brandon et al., 2014; Crisostomo et al., 2017; Hjerrild et al., 2016; Hjerrild et al., 2018). Apart from citrate which gives electrostatic stabilisation the majority of these stabilising agents provide steric stabilisation and their addition has been shown to affect the long term stability of the silver NF and the duration of the reaction but not the growth mechanism of the reaction (i.e. not the shape) (Polte, 2015).

Suitable reducing agents include sodium borohydride (Carboni et al., 2016; Ledwith et al., 2007; Metraux and Mirkin, 2005; Mirzaei et al., 2016; Moreira et al., 2013; Torres et al., 2007; Ung et al., 1998; Yan et al., 2016), ascorbic acid (Brandon et al., 2014; Chen et al., 2016; Crisostomo et al., 2017; Hjerrild et al., 2016; Hjerrild et al., 2018; Ledwith et al., 2007), hydrazine (Salehi et al., 2013) and whiskey (Otari et al., 2016). NFs can also be produced using a plasma discharge process(Lee et al., 2016).

It is also possible to use a variation of the one-step method using an initial seeding method, producing small spherical silver particles, which are then subsequently grown (Crisostomo et al.,

2017; Haber and Sokolov, 2017; Hjerrild et al., 2016; Hjerrild et al., 2018; Ledwith et al., 2007; Tang et al., 2015). A stabilising agent such as poly-vinyl alcohol can also be added at the seeding and or growth stage to stabilise the final NPs shape and size (Walshe et al., 2019). The order in which the reagents are added together can also be varied with one research group adding the PVP and the silver nitrate together first (Torres et al., 2007). These researchers in contrast to others found no destabilisation of the resultant NF with exposure to ambient light for 1 month.

3.5 Silver Nanofluid (NF) Synthesis Methods

3.5.1 Introduction

This Section details the actual silver NF synthesis methods used in this thesis. It also broadly discusses the various parameters that have been investigated. Further individual sample details are then given in Chapter 4 and Chapter 5. Firstly, the synthesis methods for silver nanospheres (Ag NSs) and nanoprisms (Ag NPrs) are given. This is followed by a Section on the development of a silver based broadband absorber. The final main subsection presents a short investigation undertaken to measure the consistency of the batch synthesis method. This Section then concludes with a brief summary.

3.5.2 Batch synthesis method for nanospheres (Ag NSs)

The batch synthesis method using a starting concentration of 0.1 mM silver and electrostatically stabilised with TSCD only was as follows:

A 48 mL solution containing TSCD (0.1 M, 0.75 mL) and silver nitrate ($AgNO_3$, 0.05 M, 0.1 mL) was stirred vigorously at room temperature. After 7 minutes stirring a freshly prepared solution of sodium borohydride ($NaBH_4$, 6.25 mM, 2 mL) was rapidly injected. After about 5 minutes the solution changed through yellow to orange-brown.

To produce TSCD and PVP stabilised Ag NSs the synthesis was nearly identical except the initial solution also contained PVP (0.7 mM, 0.75 mL) and the reaction took longer changing to orange-brown after 20 minutes - 30 minutes.

All reagents in the synthesis where scaled accordingly to produce more concentrated NFs up to a starting concentration of Ag of 0.8 mM.

The resulting NFs containing Ag NS were evaluated using transmission electron microscopy (TEM) (Section 3.7.1) and UV-vis spectroscopy (Section 3.7.2).

3.5.3 Batch synthesis method for nanoprisms (Ag NPrs)

Again both TSCD and TSCD with PVP stabilised NF containing Ag NPrs were produced.

For the TSCD stabilised Ag NPrs with a starting silver molarity of 0.1 mM, 48 mL of solution containing TSCD (0.1 M, 0.75 mL), silver nitrate ($AgNO_3$, 0.05 M, 0.1 mL) and hydrogen peroxide (H_2O_2, 30 wt. %, 9.77 M (USP Technologies, 2021), 0.25 mL) was stirred vigorously at room temperature. After 7 minutes stirring a freshly prepared solution of sodium borohydride ($NaBH_4$, 25 mM, 2 mL) was rapidly injected. After about 5 minutes, the solution changed through yellow to orange-brown, then green-blue through to blue after several more minutes. The ratio of silver ions to sodium borohydride in this synthesis is 1: 10 which is similar to that employed by Tang et al (Tang et al., 2015) of 1: 8, Panzarasa et al (Panzarasa, 2015) of 1: 9.8 and the same as that employed by Zhang et al (Zhang et al., 2011) and Carboni et al (Carboni, 2014).

The formulation and synthesis for PVP and TSCD stabilised Ag NPrs was identical except that the initial solution also contained PVP (0.7 mM, 0.75 mL). The reaction was much slower with it taking ≈ 25 minutes - 30 minutes for the solution to change from light yellow. After 30 minutes, the reaction then proceeded rapidly finally forming a blue solution.

Unlike the Ag NSs it was not possible to produce more concentrated NFs containing Ag NPrs with a suitable absorption maxima (λ_{max}) at > 750 nm directly. Therefore to produce more concentrated NFs containing Ag NPrs the NF solution was centrifuged at 12,857 relative centrifugal force (r.c.f.) (10,000 revolution per minute (rpm)) for 15 minutes and the supernatant removed. For the Ag NPrs stabilised with both TSCD and PVP the force was increased to 16,168 r.c.f. (13,000 rpm) and the centrifuging time extended to 30 minutes. The resulting Ag NPrs were then re-dispersed with sonication (using a Fisher Scientific sonicating water bath Type FB 15051) for 10 minutes in the appropriate lower amount of Milli-Q water or other BF to obtain the final NF at the desired concentration. When the NF has been concentrated by centrifuging and re-dispersing this will be made clear in Chapter 4 and Chapter 5 when the results are discussed.

The resulting NFs were characterised using UV-vis and UV-vis-IR spectroscopy (see Section 3.7.2) and TEM (Section 3.7.1). Solar performance and stability were evaluated using the methods described in Sections 3.8 and 3.9.

3.5.4 Development of a broadband silver nanofluid absorber

To enhance solar absorbance, the ideal NF needs to absorb solar radiation strongly over the broad range of the solar spectrum with a low concentration of NPs to prevent aggregation of the NPs in the fluid (Jeon et al., 2014; Sharaf et al., 2019). Although graphite and metal oxide based NFs tend

to achieve broadband absorption, they require ≈ 5 times the concentration of metal based NFs (Hjerrild et al., 2016) enhancing possible aggregation. Metal based NFs, however, exhibit strong absorption at lower reagent concentrations but tend to have a narrow absorption peak (Du and Tang, 2016). To overcome these limitations, a blended NF consisting of different gold NPs (Du and Tang, 2016; Jeon et al., 2014; Jeon et al., 2016) and with silver NPs (Mallah et al., 2018) have been shown to be suitable for volumetric absorption.

The position of the maximum absorption peak (λ_{max}) for silver can be tailored by changing the size and shape of the NPs (Haber and Sokolov, 2017). It should therefore be possible to combine difference silver NPs with a range of selected sizes and shapes to produce a NF which absorbs over a broad spectral range. This has been shown to be possible numerically but not experimentally by others (Mallah et al., 2018) although interestingly, Walshe et al "accidentally" produced a silver NF with two different absorption peaks at approximately 430 nm and 600 nm which gave a good photo-thermal conversion efficiency of 70 % - 90 % depending on NP concentration (Walshe et al., 2019).

The Ag NPrs recipe shown in Section 3.5.3 (stabilised with both TSCD and PVP) was used as a starting point to investigate this possibility, with the aim of producing two other NFs with different morphologies and hence λ_{max} that could be combined with the existing Ag NPrs (stabilised with TSCD and PVP) NF to give a broadband absorber with absorption over a broad spectral range. Ideally the three NFs should be able to be combined together without having to concentrate any of the constituent NFs by centrifuging. Further understanding of the synthesis was required in order to develop suitable recipes for these two other NFs.

The solar intensity varies asymmetrically with λ as illustrated in Figure 2-6 with the highest intensity at about 530 nm (ASTM, 2012). The intensity then decreases with increasing λ. Over 85 % of the energy is associated with λ < 1300 nm. Hence, one of the NFs needs to have a strong absorption at about 500 nm (designated short λ) with a high enough reagent concentration of silver to allow this NF to be combined with the other two NFs to produce a peak at 500 nm, but still considerable absorption over as much of the rest of the spectrum as possible. A peak at 500 nm rather than at 530 nm was chosen to still provide sufficient absorption in the 400 nm – 500 nm range, due to the narrow width of the absorption peak for silver. The second NF needs to exhibit a λ_{max} somewhere between 500 nm and 850 nm; an ideal target for this NF would be approximately 650 nm – 750 nm (designated mid λ). The final NF would be the already developed Ag NPr NF with a λ_{max} in the 850 nm – 950 nm range (designated long λ).

A number of researchers have investigated the effect of various reagents used in the thermal synthesis of anisotropic silver NPs (Dong et al., 2010; Metraux and Mirkin, 2005; Zhang et al., 2011)

with somewhat conflicting results, where some researcher argued that the stabilising agent tri-sodium citrate was vital to producing Ag NPrs (Dong et al., 2010; Metraux and Mirkin, 2005), whereas others stated that hydrogen peroxide concentration was the most important shape determining reagent (Zhang et al., 2011). Increasing the amount of reducing agent $NaBH_4$ in the solution also leads to a red-shift in λ_{max} producing NPrs (Dong et al., 2010). NPrs can also be produced using a seeding process, where small spherical seeds of silver are used to subsequently grow larger anisotropic particles.

Firstly, using the long λ (Ag NPrs stabilised with TSCD and PVP) as a starting point, the effect of overall concentration of reagents was investigated. If Ag NPrs with a λ_{max} close to 850 nm could be obtained from a solution using higher concentrations of reagents, this gives more flexibility for the two other NFs to be developed as the overall silver reagent concentration in the mixture needs to be ≈ 3 times the initial concentration used for the long λ Ag NPrs recipe (see Section 3.5.3) to give enough broadband absorbance. If increasing the concentration of reagents fails to give the same λ_{max} then this would indicate that the synthesis involved a complex reaction (this is likely given the conflicting literature on the role of the different reagents), increasing the difficulty of developing other NFs.

The effect of changing the amount of hydrogen peroxide in the Ag NPrs recipe was then investigated as this could be a pivotal reagent (Zhang et al., 2011). It was hoped that λ_{max} would vary linearly from 400 nm (no hydrogen peroxide – Ag NS recipe stabilised with TSCD and PVP – Section 3.5.2) to ≈ 900 nm (Ag NPrs recipe (with PVP) – long λ). This would allow the other two NFs to be produced by varying just this reagent.

The effect of changing the Ag to $NaBH_4$ ratio was then considered. For these experiments, the effect of concentration at a lower Ag: $NaBH_4$ ratio of 1: 5 was first studied. Then the initial silver nitrate reagent concentration was trebled to 0.3 mM, and the ratio of Ag: $NaBH_4$ further reduced. Others have found that increasing the $NaBH_4$ level leads to a red-shift in λ_{max}, so a decrease should lead to a blue-shift (Dong et al., 2010). The effect of reducing the H_2O_2 level at the lower Ag to $NaBH_4$ ratio of 1: 5 was also evaluated. It was hoped that this investigation would yield a synthesis recipe for either the mid λ (λ_{max} = 650 nm - 750 nm) and or the short λ NF (λ_{max} ≈ 500 nm) at an appropriate silver reagent concentration to combine with the other NFs without further processing.

The ability to tailor λ_{max} after a NF had been synthesised by adding more $NaBH_4$ to an already prepared seed solution was then investigated. As it is possible to produce an anisotropic Ag NPr starting from a spherical Ag NS seed (Haber and Sokolov, 2017) it should be possible to change the position of λ_{max} by adding more reducing agent to an already prepared anisotropic seed NF. As

the $NaBH_4$ was added as a solution this also had the effect of changing the final molarities of the other chemicals in the solution as well as the final ratio of Ag: $NaBH_4$. In addition, to looking at the effect of adding just more reducing agent, the effect of adding both $NaBH_4$ and more $AgNO_3$ solution to an already prepared seed solution was also investigated.

To produce the broadband mixture, the three most suitable NF recipes for long λ, mid λ and short λ were selected and the synthesis repeated to check method consistency. The UV-vis-IR spectra was recorded using the UV-vis-IR-1 spectrophotometer (see Section 3.7.2), diluting the NFs to an appropriate level to prevent saturation of the detector in the spectrophotometer. The broadband mixture was then designed using the ASTM G173 solar spectrum (ASTM, 2012) as reference over a λ range of 300 nm - 1350 nm as described in Section 3.8.2 to calculate the absorption efficiency ($\eta_{Ab(300\ nm\ -\ 1350\ nm)}$) for a number of different mixtures and the optimum mixture selected for further testing. TEM analysis of the three optimal NFs and the mixture was undertaken to understand the morphology. Details of how the TEM measurements were undertaken are given in Section 3.7.1.

The performance of the mixture and component NFs was then measured in the solar simulator according to the method described in Section 3.8.3, using set-up B and comparing the efficiencies obtained from the UV-vis-IR spectra with those obtained from the solar simulator. The change in the UV-vis-IR spectra with exposure to simulated sunlight (SSL) was also measured to assess the stability of the broadband mixture and its components (see Section 3.9.4).

The component NFs and optimum broadband mixture were remade and the stability to temperature also determined according to the method described in Section 3.9.3. The effect of flow on the broadband mixture was then evaluated using the method described in Section 3.9.6. In order to evaluate the effect of flow a number of different batches of each component NF were needed to produce sufficient volume of the broadband mixture. This allowed an assessment of the batch consistency of the three different synthesis recipes to be undertaken (see Section 3.5.5). The long term colloidal stability over a period of 8 months of the component NFs (diluted to an appropriate level for UV-vis-IR spectroscopy) and the broadband mixture were also measured according to the method described in Section 3.9.2.

3.5.5 Consistency of batch synthesis

As mentioned in the previous Section (Section 3.5.4) in order to produce enough of the broadband absorber mixture to undertake testing under flow conditions it was necessary to synthesis a larger volume of the broadband mixture. In order to do this a number of different

batches of the long λ, mid λ and short λ NFs were made and combined together to give sufficient volume. This gave an opportunity to assess the consistency of the batch synthesis method.

In total 20 batches of 30 mL of the long λ NF, 8 x 30 mL batches of the mid λ NF and 12 x 30 mL batches of the short λ NF were produced over a relatively short timeframe of < 7 days. This allowed for an assessment of the consistency of the synthesis for these three NFs to be made while all the other variables such as batch size (kept constant for this work at 30 mL), age of chemicals and laboratory conditions, which could affect the synthesis were kept as consistent as possible.

This knowledge of the consistency of the batch processes for these three NFs was then used as a benchmark, to allow comparison with all other batches of these NFs that were produced at different times throughout the thesis. The results of this benchmarking process are given in Section 4.7, along with a discussion on the reproducibility of the broadband absorber mixture. The reproducibility of the NS synthesis is discussed separately in Section 4.3.

3.5.6 Summary

A short summary of the experimental synthesis methods covered in this Section and the main points covered in the proceeding silver NF literature Section is given in Table 3-1.

Table 3-1 Summary of main points covered in this and the proceeding Section.

Subsection	**Covered**
Ag NPs literature	One-step method
Ag NS synthesis	Methods for TSCD and TSCD with PVP stabilised Ag NSs
Ag NPrs synthesis	Methods for TSCD and TSCD with PVP stabilised Ag NPrs
Development of broadband absorber	Parameters investigated – concentration, H_2O_2 amount, ratio of Ag: $NaBH_4$ – timing of $NaBH_4$ addition – long, mid and short λ NFs combined to give broadband mixture
Consistency of batch process	Batches of 20 x long λ, 8 x mid λ and 12 x short λ used to measure batch variation

3.6 Silver nanofluid (NF) Synthesis Methods Containing SiO_2 coated Silver Nanoprisms (SiO_2@Ag NPrs)

3.6.1 Introduction

This Section starts by reviewing the literature on the main SiO_2 coating methods for NPs. Next it describes the development of a suitable SiO_2 coating synthesis method. The resulting optimised

coating procedure is then presented followed by a description of modifications made to the parameters in this multi-step synthesis aimed at improving the Ag NP stability. This Section concludes with a summary.

3.6.2 SiO_2 coating - literature review

Stability of the resultant NPs could be increased by coating with a thin shell of silica producing a composite NP. Silica coating can be achieved by using a water-glass method using aqueous sodium silicate or a Stöber process using tetraethoxysilane (TEOS) in a base catalysed reaction in ethanol (Brandon et al., 2014; Graf et al., 2003; Lismont et al., 2015). The Stöber process is a liquid chemical method involving the hydrolysis and subsequent condensation of silica alkoxide in an alcoholic solution in the presence of water, with ammonia as a catalyst (Lismont et al., 2015). The hydrolisation reaction is shown in Equation 3-4 and the subsequent condensation reaction in Equation 3-5 (Carboni, 2014). The thickness of the coating can be changed either by varying the reaction time (Lismont et al., 2015) or the amount of TEOS (Kang et al., 2015).

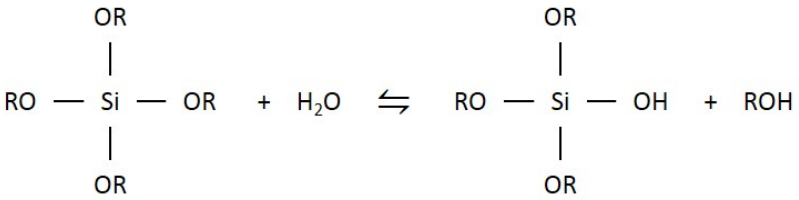

Equation 3-4

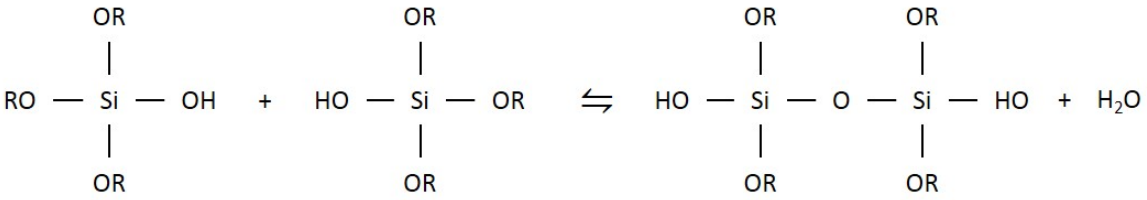

Equation 3-5

The water-glass method can be used on its own to produce a thin coating or as a precursor step to deposit a thin layer of silica prior to using the Stöber process to thicken the coating (Brandon et al., 2014; Crisostomo et al., 2017; Hjerrild et al., 2018). One group of researchers produced a large volume (4.5 L) of silica coated nanodiscs for subsequent solar testing using this combined method (Crisostomo et al., 2017). This appears to be the largest volume of silica coated silver NPs in the literature. Issues with the water-glass method include long reaction times, reaction reliability with a strong pH dependence, and inhibition in the presence of strong capping agents such as PVP (Ung et al., 1998).

For the TEOS Stöber method, utilisation of a stabilising or capping agent can prevent aggregation and degradation of the NPs on transferring to the alcoholic solution. These include polyvinylpyrrolidone (PVP) (Graf et al., 2003), surfactants (Lismont et al., 2015) and stronger coupling agents or primers such as organosilanes (Crisostomo et al., 2017; Hjerrild et al., 2018) for example 3-aminopropyltrimethoxysilane (Ung et al., 1998) with amino or thiol groups. Carboni used 16-mercaptohexadecanoic acid (MHA) as a coupling agent to produce SiO_2@Ag NPrs (Carboni, 2014) as it forms a strong bond to the silver particles and helps to protect the particles from etching in the presence of ammonia ions. To this end he also investigated using different ammonia containing compounds as a catalyst for the TEOS step of the process and found that dimethylamine (DMA) gave better results than diethylamine (DEA) (Carboni et al., 2013).

Other researchers have also examined the synthesis for coating silver NPs with SiO_2 (Brandon et al., 2014; Carboni, 2014; Carboni et al., 2016; Radloff and Halas, 2001; Ung et al., 1998; Xue et al., 2007; Zmijan et al., 2014) with one group of researchers suggesting a very novel synthesis method employing whisky as the reducing agent (Otari et al., 2016).

Even when coated with silica the long-term stability of the NFs to both temperature and sunlight is relatively unknown with only one group of researchers having investigated stability to temperature and sunlight of SiO_2 coated silver nanodiscs in glycerol BF (Hjerrild et al., 2018) and water (Taylor et al., 2018). They found that UV exposure had a more detrimental effect than temperature alone in glycerol.

3.6.3 Development of synthesis methods

Two different methods were investigated aiming at coating Ag NPrs with SiO_2. Ag NPrs were chosen as the starting NP to investigate SiO_2 coating as they were larger than Ag NS and hence easier to centrifuge, facilitating the development of a suitable coating synthesis. One method investigated was based on the water-glass method whereas the other method focused on the Stöber process. For both methods investigated the ability of the synthesis method to produce consistent SiO_2 coatings onto the Ag NPrs were assessed using TEM (see Section 3.7.1). The change in the UV-vis spectrum following coating was also measured using UV-vis spectroscopy (Section 3.7.2) as this may give an indication that the coating process was causing aggregation of the NPrs or a change in λ_{max} as a result of shape change of the NPrs or the coating itself affecting the absorption.

For the water-glass method Ag NPrs stabilised with just TSCD were used as the presence of PVP may inhibit the formation of a coating using the water-glass method (Ung et al., 1998). The procedure was as follows:

To a 50 mL solution of Ag NPrs in water produced using a concentration of 0.1 mM Ag, a solution containing 3-mercaptopropyl trimethoxysilane (MPTMS, 0.075 mL, 10 mM) was added. This was then stirred for 20 minutes and sodium metasilicate ($Na_2SiO_3.5H_2O$, 1 mL, 2.86 mM) added. The reaction was then allowed to proceed for 48 h with stirring.

To obtain the final NF, the solution was then centrifuged at 12857 r.c.f. (10,000 rpm) for 30 minutes and re-dispersed into the desired volume of BF, sonicating for 10 minutes to ensure even distribution of the coated Ag NPrs.

The experiments and the results of investigating the water-glass method are discussed in further detail in Section 6.2.

The Stöber method investigated was based on the protocol of Lismont et al (Lismont et al., 2015) but with significant modifications as this procedure had only been carried out on Ag NSs. The ammonia hydroxide used by Lismont was replaced with DMA to prevent etching of the triangular Ag NPrs (Carboni, 2014) and MHA was added to stabilise the surface. The Stöber coating procedure resulting from using this modified protocol is given in Section 3.6.4. The main differences between this Stöber process and the one employed by Carboni (Carboni, 2014) were that firstly in the Lismont method, the MHA was added to the Ag NPrs before the first centrifuging step. Secondly, the capped Ag NPrs were re-dispersed into a known small quantity of water in the adapted Lismont protocol, whereas no extra water was used in the Carboni synthesis. Thirdly, more TEOS was used in the adapted Lismont synthesis and it was not diluted prior to addition. Finally, the reaction was stopped by adding excess ethanol followed by centrifuging in the modified Lismont synthesis but not in the Carboni protocol, where the reaction was halted by centrifuging and re-dispersing into water.

To arrive at this protocol a number of different parameters within the protocol were investigated. These include the amount of TEOS used, the amount of MHA and the reaction time. Further details of the initial experiments conducted in order to arrive at a suitable SiO_2 coating protocol by adapting the synthesis of Lismont et al are given in Section 6.3 along with the results of these experiments.

3.6.4 Optimised Stöber SiO_2 coating procedure

The optimised procedure employed in this thesis to coat Ag NPrs with SiO_2 based on the work of Lismont et al (Lismont et al., 2015) was as follows, starting with 25 mL of Ag NPrs (TSCD and PVP stabilised) aqueous NF (made using an initial silver concentration of 0.1 mM Ag):

An ethanolic solution of MHA (1.0 mL, 1.0 mM) was added to 25 mL of the Ag NPrs solution giving a final MHA concentration of 40 µM. This was shaken for 5 minutes and then centrifuged at 16,168 r.c.f. (13,000 rpm) for 30 minutes to remove the excess PVP and TSCD. The supernatant was removed and the sample re-dispersed in 1.5 mL Milli-Q water. To this, 67.5 µL of TEOS was added. This was mixed and then injected into 25 mL of absolute ethanol containing 2.66 mL of 40 % DMA solution. The reaction was allowed to proceed for 30 minutes with stirring (600 rpm). After 30 minutes the reaction was stopped by adding excess ethanol (20 mL). The resultant solution was centrifuged at 12857 r.c.f. (10,000 rpm) for 15 minutes and the nanoparticles re-dispersed three times into ethanol to remove as much of the excess SiO_2 as possible. Finally, the SiO_2@Ag NPrs were re-dispersed into the appropriate BF volume with sonication for 10 minutes to give the NF.

The morphology of the SiO_2@Ag NPrs were evaluated by TEM (see Section 3.7.1) and any changes in the UV-vis spectra noted using the method described in Section 3.7.2.

The performance of the SiO_2@Ag NPrs when exposed to SSL was determined using set-up A in the solar simulator as described in Section 3.8.3. The performance of a NF containing SiO_2 only was also evaluated using set-up A as it was not possible to remove all the excess SiO_2 from the SiO_2@Ag NPrs NF. The NF containing SiO_2 was produced using the same protocol as the SiO_2@Ag NPrs except that the protocol was started at the point of adding the TEOS to a known quantity of water. The stability of the SiO_2@Ag NPrs were determined according to the methods described in Section 3.9.

An attempt was also made to coat the broadband absorber mixture developed in Section 3.5.4 with SiO_2 by increasing the length of the initial centrifuge step (the broadband mixture contains smaller NPs) to 3 h and scaling all the reagents in the synthesis to account for the difference in the starting molarity of the broadband absorber NF. Further details of the trial and the results are given in Section 6.6.

3.6.5 Modifications to coating procedure – aimed at understanding stability

The optimised Stöber SiO_2 coating procedure shown in Section 3.6.4 was modified to investigate the effect on the resultant stability of changing various parameters in the protocol. The stability of the resultant NFs were assessed using the temperature stability protocol described in Section 3.9.3. The parameters investigated in the protocol are shown schematically in Figure 3-1. The aim of changing the synthesis parameters was to attempt to improve the temperature stability of the resultant SiO_2@Ag NPrs. The investigation therefore focused on the parameters that were more

likely to effect the stability, such as the inclusion of an extra purification step and the removal of oxygen from the resulting NF.

In addition, the temperature /colloidal stability of the uncoated Ag NPrs in water plus some of the reagents (DMA and MHA) used in the coating synthesis was measured to aid in the understanding of the role of the various reagents on the coating process by assessing changes in the UV-vis spectrum with time to see if the reagent either protected the Ag NPrs or lead to increased dissolution / shape changes of the Ag NPrs.

Further details of the experiments conducted and the results are given in Chapter 6, Section 6.5.

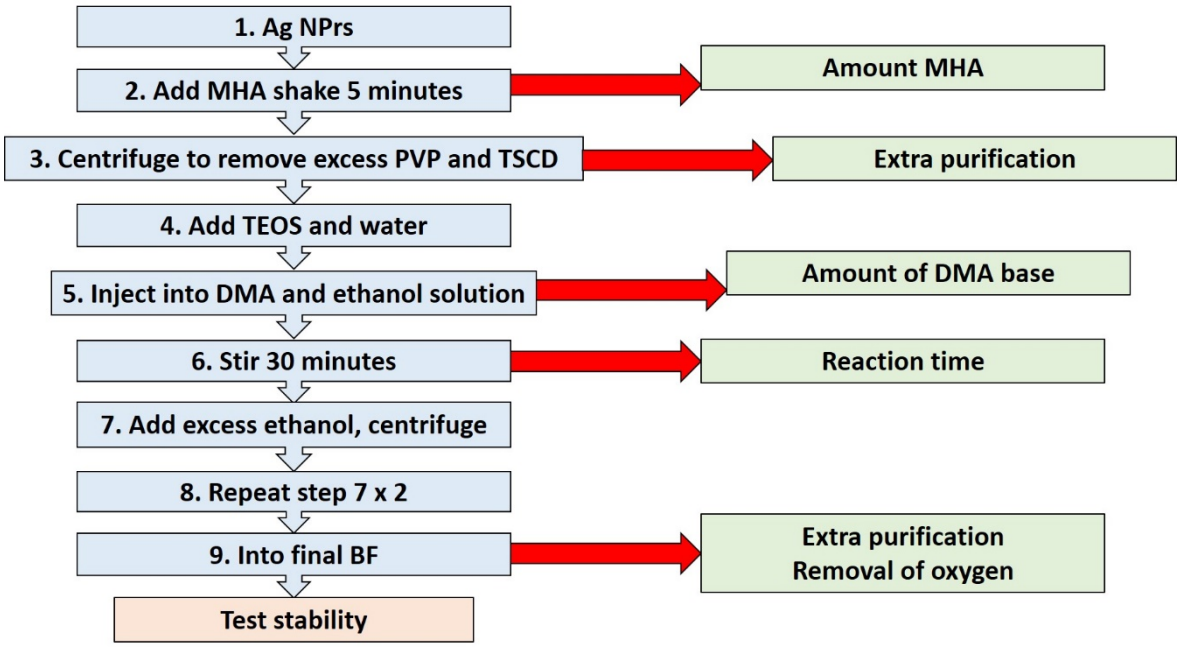

Figure 3-1 SiO_2 coating protocol (shown in light blue) and parameters investigated (light green).

3.6.6 Summary

A short summary of the main points covered in this Section is given in Table 3-2.

Table 3-2 Summary of SiO_2 coating of Ag methods Section.

Subsection	Covered
SiO_2 coating of NPs literature	2 main methods – Water-glass and Stöber process
Development of suitable SiO_2 coating procedure	2 methods investigated – one based on water-glass method, the other on the Stöber process
Optimised SiO_2 coating protocol	Details optimised method used for SiO_2 coating of Ag NPrs
Modifications to protocol	Parameters investigated – Detailed in Figure 3-1

3.7 Characterisation

This Section describes the actual methods employed in this thesis namely TEM and UV-vis / UV-vis-IR spectroscopy. Other potential methods that could have been used are discussed in Appendix C, Section C.1.

3.7.1 Transmission electron microscope (TEM) analysis

A Hitachi HT7700 100 kV was used for TEM analysis. Samples were prepared on Formvar and carbon coated 200 mesh Cu/Pd grids by drop-casting the colloid solution and allowing the base-fluid to evaporate. Digimizer software was used to further analyse the samples using the TEM image scale bar to calibrate the line length. Manual size measurement of individual NPs was employed, dividing the particles into different shape categories. For triangular particles, the length of the longest side of the triangle was measured and for discs or spheres, the diameter. Some TEM grids were specially prepared to assess the thickness of the NPs by drop casting a larger volume of solution onto the grid. The thickness of the NPs was then measured across the smallest dimension of the edge-on NPs in the TEM micrograph.

For SiO_2 coated samples the total diameter of the coated samples was measured, along with the length of the silver particle inside the SiO_2 coating and the coating thickness. In addition, the percentage of single-cored (containing only one silver NP), multi-cored (containing two or more silver NPs), and particles with no silver in the middle (SiO_2 only NPs) was determined along with the percentage of multi-cored versus single-cored (excluding the SiO_2 only NPs). Finally, the number and size of not SiO_2 coated Ag NP were measured and compared to the total number and size of the SiO_2 coated Ag NPs. Using more than one image of each sample provided a statistically adequate number of measurements.

3.7.2 UV-vis and UV-vis-IR

A number of different cuvettes were used for the UV-vis and UV-vis-IR measurements. For more concentrated NFs a 1 mm path length quartz cuvette with a chamber volume of 350 µL was utilised. In addition, some measurements on more concentrated NF were carried out by using a Malvern instrument ZEN0040 cuvette rotated through 90 ° to give a path length of 4 mm.

This cuvette was also used in its normal configuration of 10 mm path length (minimum volume 40 µL) for less concentrated NFs. Other 10 mm path length cuvettes employed were, a quartz 3 mL sample volume cuvette, a polystyrene macro-cuvette (2.5 mL – 4.5 mL volume), and another

smaller volume cuvette (Fisherbrand polystyrene Semi Micro cuvette, Product code 105941750 1 mL sample volume).

Most NF samples were tested as made. However, some samples were diluted with Milli-Q water to keep the absorbance below 2 au and prevent saturation of the spectrophotometer employed. The cuvette and any dilution details will be clearly stated when the UV-vis or UV-vis-IR results are presented.

Three different UV-vis and UV-vis-IR spectrophotometers were used. For UV-vis spectroscopy a Varian Cary 300 Bio spectrophotometer (denoted UV-vis-1) was used over a wavelength (λ) of 200 nm to either 850 nm or 900 nm with base-fluid and cuvette correction. A scan rate of 600 nm min^{-1}, with a step of 1 nm, and a time per step of 0.1 s was employed. For UV-vis-IR measurements either a Perkin Elmer Lambda 750S UV-Vis-IR spectrophotometer over a λ of 300 nm to 1350 nm (or 1300 nm) with a scan rate of 204.74 nm min^{-1} and a step of 1 nm per scan was used (denoted UV-vis-IR-1) or an AvaLight – Hal lamp and Avaspec - 2048 with AvaSoft 8.10 software UV-Vis-IR spectrophotometer with an integration number of 1.05 ms and 1000 averages over a λ of 330 nm to 1100 nm (denoted UV-vis-IR-2). All measurements for the NFs were undertaken with BF and cuvette correction.

To understand the effect of changing the spectrophotometer, a comparison between the spectrophotometers was undertaken measuring the same samples in two of the spectrophotometers on the same day. The full results are given in Appendix C, Section C.2. There were some differences between the spectrophotometers in the < 400 nm and > 872 nm, but the main part of the spectrum (400 nm – 850 nm) was broadly comparable.

3.8 Performance Evaluation

3.8.1 Introduction

To evaluate the potential performance of the NFs for solar thermal applications, two main methods were employed. The first method was to calculate the potential efficiency of the NF from the UV-vis or UV-vis-IR data obtained. The second method was to measure the performance in static tests using a solar simulator to monitor in real time the temperature rise of the NFs. These two methods are detailed in this Section.

3.8.2 Calculating efficiency from absorption spectra

The $G_{s,\lambda(\mathrm{dir+cs})}$ spectrum shown in Figure 2-6 (ASTM, 2012) was used as a reference spectrum to calculate the efficiency of absorption (η_{Ab}) from the absorption spectra obtained using either UV-vis or UV-vis-IR. It was assumed that $G_{s,\lambda(\mathrm{dir+cs})}$ in W m^{-2} was equal to the light intensity I_L, the radiant flux Φ_e^{i} (Equation 2-10) per unit area or the power of the light incident on the sample (P_{i}) from Equation 2-12 (British Standards Insitution (BSI), 1996; Khullar et al., 2014) and rearranging to give the power absorbed ($P_{\mathrm{Ab}(\lambda)}$) in W m^{-2} at a given wavelength:

$$P_{\mathrm{Ab}(\lambda)} = P_{\mathrm{i}(\lambda)} - \frac{P_{\mathrm{i}(\lambda)}}{10^{\mathrm{Ab}_\lambda}}$$

Equation 3-6

where $P_{\mathrm{i}(\lambda)}$ is the incident power intensity at λ or solar irradiance $G_{s,\lambda(\mathrm{dir+cs})}$ at λ in W m^{-2} taken from the reference spectrum (ASTM, 2012) and Ab_λ is the measured absorbance at λ (au) from the UV-vis or UV-vis-IR measurement of the sample.

The absorption efficiency ($\eta_{\mathrm{Ab}(\lambda = x\ \mathrm{nm} - \lambda = y\ \mathrm{nm})}$) of the sample over a given λ range ($\lambda = x$ to $\lambda = y$) is then obtained by dividing the sum of the power absorbed by the sample by the total incident power over the λ range measured, according to the formula (Du and Tang, 2016; Duffie and Beckman, 2013; Modest, 2003):

$$\eta_{\mathrm{Ab}(\lambda=x\ \mathrm{nm} - \lambda=y\ \mathrm{nm})} = \frac{\sum_{\lambda=x\ \mathrm{nm}}^{\lambda=y\ \mathrm{nm}} P_{\mathrm{Ab}(\lambda)}}{\sum_{\lambda=x\ \mathrm{nm}}^{\lambda=y\ \mathrm{nm}} P_{\mathrm{i}(\lambda)}} \times 100$$

Equation 3-7

For example when the sample was measured using UV-vis-IR-1 (see Section 3.7.2), the λ range was x = 300 nm to y = 1350 nm and Equation 3-7 would be:

$$\eta_{\mathrm{Ab}(300\ \mathrm{nm} - 1350\ \mathrm{nm})} = \frac{\sum_{\lambda=300\ \mathrm{nm}}^{\lambda=1350\ \mathrm{nm}} P_{\mathrm{Ab}(\lambda)}}{\sum_{\lambda=300\ \mathrm{nm}}^{\lambda=1350\ \mathrm{nm}} P_{\mathrm{i}(\lambda)}} \times 100$$

Equation 3-8

where $\sum_{\lambda=300\ \mathrm{nm}}^{\lambda=1350\ \mathrm{nm}} P_{\mathrm{i}(\lambda)}$ = 793.1 W m^{-2} from the $G_{s,\lambda(\mathrm{dir+cs})}$ reference spectrum. This accounts for 88.1 % of the power of the total solar spectrum from 280 nm to 4000 nm ($\sum_{\lambda=280\ \mathrm{nm}}^{\lambda=4000\ \mathrm{nm}} P_{\mathrm{i}(\lambda)}$ = 900.2 W m^{-2}).

The efficiency $\eta_{\mathrm{lamp}(330\ \mathrm{nm} - 1100\ \mathrm{nm})}$ (or $\eta_{\mathrm{lamp}(330\ \mathrm{nm} - 900\ \mathrm{nm})}$ for samples measured using UV-vis-1) for the solar simulator lamp was also calculated in a similar manner to allow direct comparison between

the efficiency values obtained from measuring the photo-conversion efficiency and those obtained by spectroscopy. More details of this is given in Section 3.8.3.

3.8.3 Measurement of photo-conversion efficiency using a solar simulator

The solar simulator (Figure 3-2) that was employed consists of a xenon light source (type PLS SXE300) and stabilised power supply (type CHF-XM-500W) both manufactured by "Perfect Light" (China). The light has an output power of 50 W over a spectral range of 300 nm - 2500 nm and a light spot diameter of 30 mm - 63 mm. It was cooled by a radial cooling module and metal fan and when used in conjunction with the stabilised power supply has a light instability of ± 6 % (dimensions of metal light box are 160 mm x 210 mm x 200 mm). The setting on the power supply was kept constant throughout each set of experiments. The spectra obtained from the Xenon lamp was measured using a portable spectrophotometer (an Avantes AvaSpec-ULS2048 portable spectrophotometer with a range of 330 nm to 1100 nm and AvaSoft 8 software) and compared to sunlight to show that the lamp gave a good approximation to sunlight exposure. In order to prevent saturation of the spectrophotometer the aperture was reduced from 9 mm to 1 mm.

For some samples to allow direct comparison between the calculated absorption efficiency obtained using spectroscopy and the efficiency obtained from monitoring the rate of change of temperature with time (the photo-conversion efficiency) in the solar simulator this spectra was used to find the absorption efficiency of the sample $\eta_{\text{lamp(330 nm - 1100 nm)}}$ in %. This was calculated by using this spectra along with the spectroscopy spectra to find $P_{\text{Ab}(\lambda)}$ (see Section 3.7.2 for measurement details and Equation 3-6) and adapting Equation 3-7 to give Equation 3-9 where $\sum_{\lambda=330\text{ nm}}^{\lambda=1100\text{ nm}} P_{\text{i lamp}(\lambda)}$ is the incident power intensity of the lamp over the wavelength range 330 nm – 1100 nm in W m^{-2}. As the spectrophotometer does not give a power intensity, the spectra obtained for the lamp was normalised, and the area under the spectral curve used to approximate $\sum_{\lambda=330\text{ nm}}^{\lambda=1100\text{ nm}} P_{\text{i lamp}(\lambda)}$.

$$\eta_{\text{lamp}(330\text{ nm} - 1100\text{ nm})} = \frac{\sum_{\lambda=330\text{ nm}}^{\lambda=1100\text{ nm}} P_{\text{Ab}(\lambda)}}{\sum_{\lambda=330\text{ nm}}^{\lambda=1100\text{ nm}} P_{\text{i lamp}(\lambda)}} \times 100$$

Equation 3-9

When the spectral data was obtained using UV-vis-1 (λ range ≤ 900 nm), Equation 3-9 was adapted to give $\eta_{\text{lamp(330 nm - 900 nm)}}$.

A Schneider Electric NSYCRN325150 steel box from Farnell (dimensions 300 mm L x 250 mm H x 150 mm D – shown open in Figure 3-2 B) was modified to cover the light source and provide

consistent placement of the sample test holder. The distance from the light source to the front face of the samples was 180 mm.

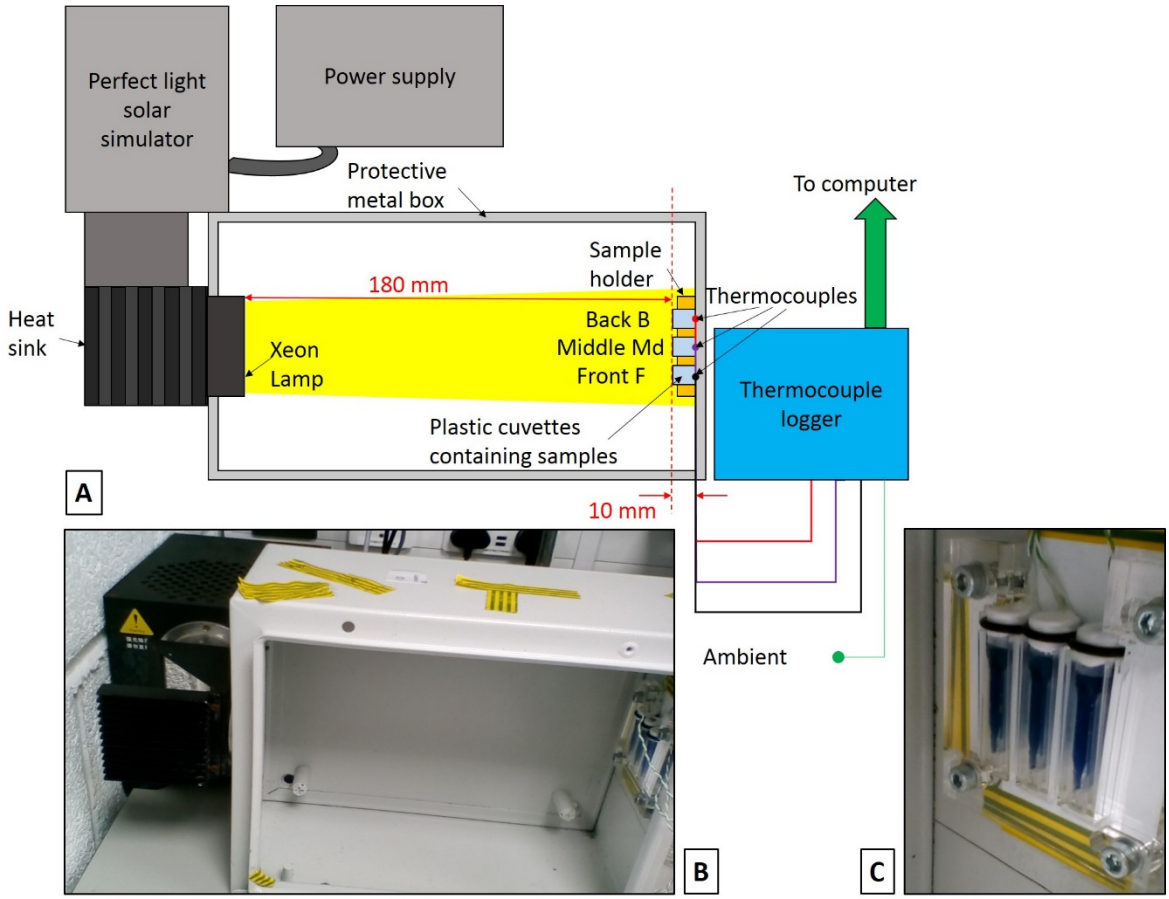

Figure 3-2 Details of the solar simulator set-up showing (A) Schematic of solar simulator set-up, (B) Photograph of set-up (with the protective box open – showing 3 samples in the sample holder) and (C) Close up of 3 NF samples in the Perspex sample holder (Set-up A).

An 80 mm x 80 mm x 10 mm sample holder was designed (Figure 3-3 A) and laser cut from Perspex and bolted to the steel box using 10 mm bolts (shown in Figure 3-2 C) so that the centre of the sample holder was in the centre of the light beam. The front face of the holder was 182 mm from the lamp.

The temperature of the samples was monitored in real time using RS PRO type K thermocouples of 0.6 mm diameter (temperature range -50 °C to +250 °C) with a welded grounded junction conforming to IEC 60584 standard. The thermocouples were placed 10 mm from the front face of the samples. The thermocouples were connected to a National Instruments NI9211 thermocouple data logger utilising Labview software. This was connected to a computer.

As the lamp had to be changed during the course of this work, two different experimental set-ups were used (denoted set-up A and set-up B).

For the solar simulator set-up A, the solar flux incident (I_L) on the samples was measured using a Voltacraft PL-110 SM solar meter and found to be 1500 W m^{-2}. Each sample of 1.5 mL was placed in a disposable solvent resistant micro cuvette (Malvern instruments ZEN0040 – wavelength range 230 nm - 900 nm). The minimum volume of the cuvette was 40 µL with a path length of 10 mm. A thermocouple was placed at the back of each cuvette and the cuvette lid added. The samples were then sealed with PTFE tape, parafilm and O-rings to reduce evaporation. A schematic of the cuvette is given in Figure 3-3 B and a photograph of three NF samples prior to testing is shown in Figure 3-2 C. Three samples were tested at the same time.

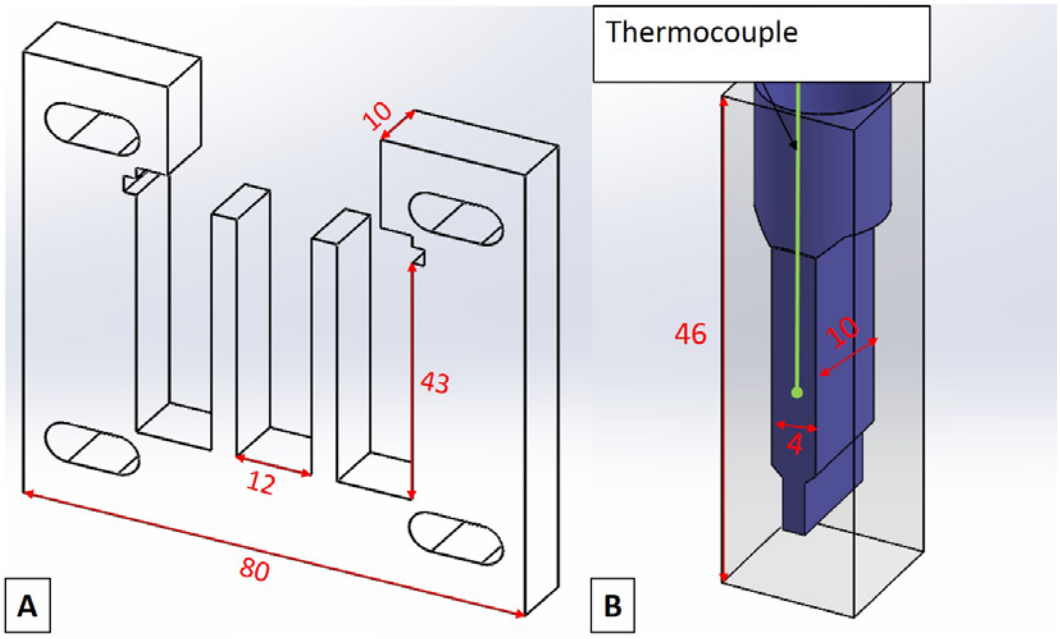

Figure 3-3 Detail of (A) Sample holder and (B) ZEN0040 cuvette. All dimensions in mm.

For set-up A the testing procedure was as follows: three 1.5 mL samples of the same nanofluid type were placed in three cuvettes and the UV-vis spectra recorded by rotating the cuvette through 90° giving a path length of 4 mm (to prevent saturation of the Varian Cary spectrophotometer). The thermocouples were added and the cuvettes sealed. These were placed in the sample holder bolted to the steel box with one sample in the front (F) position, one in the middle (Md) and the final sample at the back (B). The starting temperature of the NFs was recorded for a minimum of 30 s prior to switching on the simulator for one hour while the temperature was monitored. The samples were allowed to cool and removed from the sample holder. The UV-vis spectra were recorded using the Varian Cary spectrometer (UV-vis-1 see Section 3.7.2) in the same manner as the initial spectra. The samples were then placed back in the sample holder with each sample moved by one position and the procedure repeated to give the required total exposure time (moving each sample by one position following each hour of exposure). This allowed an assessment of the stability of the NF to SSL to be evaluated (See Section 3.9.4).

For set-up B the light intensity was measured using a "ReRA system" (manufacturers designation – Re stands for the type of reference cell used for the calibration and RA for the place of calibration, see Appendix C.3) calibrated silicon PV cell connected to a Keighley Power supply. Details of the measurement technique and results are given in Appendix B, Section C.3.

For set-up B, one cuvette containing 3 mL of sample was placed in the middle Md position in the sample holder with the thermocouple 10 mm from the front face of the sample. The sample was sealed using blue tack and parafilm to prevent evaporation. Photographs of the samples in the cuvettes for set-up A and set-up B are shown in Figure 3-4.

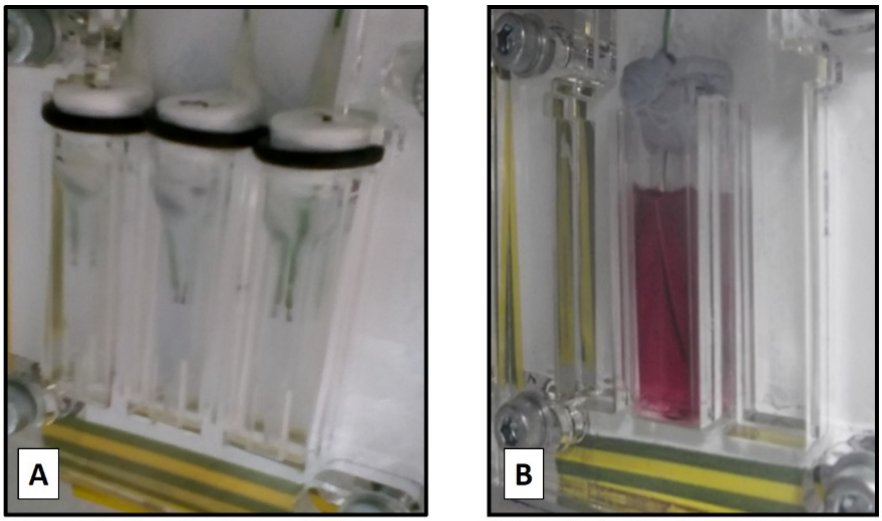

Set-up A, 3 x 1.5 mL samples in ZEN0040 micro-cuvettes with dimensions – 46 mm H x 4 mm W x 10 mm D

Set-up B, 1 x 3 mL sample in cuvette with internal dimensions – 45 mm H x 10 mm W x 10 mm D

Figure 3-4 Detail of cuvettes used for (A) Set-up A and (B) Set-up B.

The testing procedure for set-up B was: Each sample was exposed to simulated sunlight (SSL) for a period of 10 minutes, cooled and the measurement repeated two more times on the same sample giving a total exposure time of 30 minutes. Care was taken to ensure the starting temperature of the sample was as consistent as possible at 25 °C ± 1.5 °C.

For Set-up A the change in temperature (ΔT) was calculated taking the starting temperature as the average of the 30 s prior to the lamp being switched on, whereas for set-up B the starting temperature was taken as the average temperature for 10 s prior to the lamp being switched on. The slope of the graph $\Delta T/\Delta t$ was calculated in the linear region between t = 90 s and t = 150 s for set-up A and in the linear range over the time period t = 91 s to 211 s for set-up B. For a dilute NF the heat capacity and the mass of NF can be approximated by the heat capacity and mass of the BF (Jin et al., 2016). Hence (Equation 3-10):

$$\eta_{\mathrm{PE}} = \frac{m_{\mathrm{w}} c_{\mathrm{w}} \Delta T}{I_L A \Delta t}$$

Equation 3-10

where η_{PE} is the photo-conversion efficiency in %, which is a ratio of the internal energy increase to the total incident solar radiation. c_w is the heat capacity of the base-fluid in J kg^{-1} K^{-1}, m_w is the mass of the BF in kg, ΔT is the change in temperature in K, I_L is the incident radiative light intensity in W m^{-2}, A is the surface area exposed in m^2 and Δt is the change in time in s. Hence, for a given system where I_L, A, c_w and m_w are constant η_{PE} is proportional to the rate of temperature rise in the linear part of the graph.

The differences between the two set-ups and the values of the constants used in Equation 3-10 are shown in Table 3-3. The value for c_w was taken as the average value between 20 °C and 40 °C for water from (Engineering Toolbox, 2004). The mass of the NF was assumed to be the same as the BF and calculated from the volume employed (measured with a micro-pipette) using a density ρ of 1000 kg m^{-3}. The surface area A was calculated from the volume (either 1.5 mL or 3 mL) and the thickness of sample, which was 10 mm in both cases.

Table 3-3 Comparison between solar simulator set-up A and set-up B. For an understanding of measurement sensitivity see uncertainty analysis (Section 3.10 and Appendix C.4).

Parameter / detail	**Symbol**	**Unit**	**Set-up A**	**Set-up B**
Incident radiative light intensity	I_L	W m^{-2}	1500	1191
Volume of sample used	V	mL	1.5	3
Surface area exposed	A	m^2	0.00015	0.0003
Heat capacity	c_w	J kg^{-1} K^{-1}	4182	4182
Mass of base-fluid	m_w	kg	0.0015	0.003
Number of samples tested together	-	-	3	1
Time used for calculation of average starting temperature	t	s	30	10
Time range of slope $\Delta T/\Delta t$ calculation	t	s	90 - 150	91 - 211
Length of individual test	t	minutes	60	10

3.8.4 Summary

The two methods used to evaluate the potential performance of the NFs were, the calculation of the absorption efficiency (η_{Ab}) from the UV-vis or UV-vis-IR spectrum and the measurement of the photo-conversion efficiency (η_{PE}) using temperature monitoring and a solar simulator. There were two different set-ups used for the solar simulator (Set-up A and Set-up B).

3.9 Stability Testing

3.9.1 Introduction

In order for the developed NFs to be suitable for use in a SC they need to be stable under application relevant conditions. To assess the NFs a number of different stability tests were undertaken. The first was an assessment of the baseline colloidal stability under ideal storage conditions. The second method was an assessment of the effect on the stability of exposure to an elevated temperature consistent with a temperature that might be experienced in a STC. The third and fourth methods looked at the NFs stability when exposed to either simulated sunlight or natural sunlight. The next stability tests looked at the effect of fluid flow on the NF. Finally, the potential effect of changing to a more suitable BF for solar applications was assessed. This Section then concludes with a short summary.

3.9.2 Colloid stability

The stability of the NFs under ideal storage conditions of 4 °C in the dark was assessed. The method was as follows:

Samples of the NFs (1 mL or 3 mL) were placed into polystyrene macro-cuvettes (3 mL volume) or into Fisherbrand polystyrene Semi Micro cuvettes (1 mL sample volume). The UV-vis or UV-vis-IR spectrum was then recorded using the method described in Section 3.7.2. The samples were then stored in the dark at 4 °C for a period of ≈ 1.5 months - 20 months. The samples were then removed from storage and re-measured using UV-vis-IR-2. For some NF samples interim UV-vis-IR measurements were also undertaken.

3.9.3 Stability at elevated temperatures

To assess the temperature stability of the NF, 1.5 mL samples of each NF were placed in 1.5 mL Eppendorfs. The UV-vis or UV-Vis-IR spectrum for each samples was then measured and the Eppendorfs placed in an Eppendorf Thermomixer Comfort which was maintained at a temperature of 70 °C for the duration of the test. The samples were periodically removed and the UV-Vis or UV-Vis-IR spectrum measured. For details of the UV-vis and UV-vis-IR spectrophotometers and setting employed see Section 3.7.2. For some samples the morphological changes associated with exposure to temperature were also assessed using TEM (see Section 3.7.1) by taking TEM subsamples prior to and after exposure.

3.9.4 Stability with exposure to simulated sunlight

To assess the stability of the NFs to SSL under static conditions (i.e. no flow) the solar simulator was used. For details of the solar simulator see Section 3.8.3. The UV-vis or UV-vis-IR spectra were recorded prior to placing the NF samples in the sample holder in the solar simulator. The samples were then exposed to SSL for a set length of time (with periodic removal to measure the UV-vis / UV-vis-IR spectrum). After exposure the UV-vis or UV-vis-IR measurements were repeated.

To assess the morphological changes occurring on exposure to SSL TEM micrographs were taken prior to and after exposure according to the protocol described in Section 3.7.1.

3.9.5 Stability with exposure to natural sunlight

To ascertain the longer-term stability of the NFs, outdoor exposure tests were undertaken on some of the NF samples. Two different sets of these outdoor exposure tests were conducted (denoted natural sunlight trial 1 and trial 2).

The first natural sunlight trial 1 took place over a two week period between 2nd June and 16th June 2018 in Southampton in the UK. The samples faced due south and were angled at 30 ^{o} to the horizontal. The sample volume was 3 mL and the sample containers were glass with a plastic lid to prevent evaporation. UV-vis spectroscopy was undertaken prior to and after exposure.

The second trial 2 was carried out for a period of 5 weeks from 21st August to 25th September 2018 in Southampton in the UK. The samples faced due south and were angled at 30 ^{o} to the horizontal. The sample volume was 1.5 mL and the sample containers were glass with a screw on plastic lid to prevent evaporation. The samples were sealed carefully with 2 x parafilm to further prevent evaporation. UV-vis spectroscopy was undertaken prior to and after exposure.

3.9.6 Effect of fluid flow

To evaluate the effect of fluid flow a flow cell was constructed for use in the solar simulator. Details of the set-up used in the solar simulator and the flow cell are given in Figure 3-5 and Figure 3-6. The flow cell, manufactured in the glass workshop at Southampton University consisted of a 10 mm internal diameter inner borosilicate glass tube surrounded by a second glass tube of diameter 30 mm. The air within the gap between the two glass tubes was removed to help reduce the heat loss through the flow cell. The overall length of the evacuated part of the flow cell was 90 mm (see Figure 3-5). Two thermocouples (RS PRO type K thermocouples of 0.6mm diameter (temperature range -50 °C to +250 °C) with a welded grounded junction conforming to IEC 60584 standard) were placed within the flow cell 80 mm apart. RS Pro-silicon

transparent silicone tubing of internal bore size 8 mm (Part number 667-8450) was connected to each end of the flow cell. This was then connected to a male tee-hose coupling from RS components (part number 795-411). One end of the tee-coupling was connected to more silicone tubing and the other end containing the thermocouple wire was sealed with water proof black silicone sealant (Silcoset 158 from RS components –part number 283-426). The distance from the evacuated part of the flow cell and the tee-coupling was 67 mm (see Figure 3-5). The joins between the silicon hose and the flow cell were secured with cable ties to prevent the connections from moving when the flow cell was taken in and out of the solar simulator test rig.

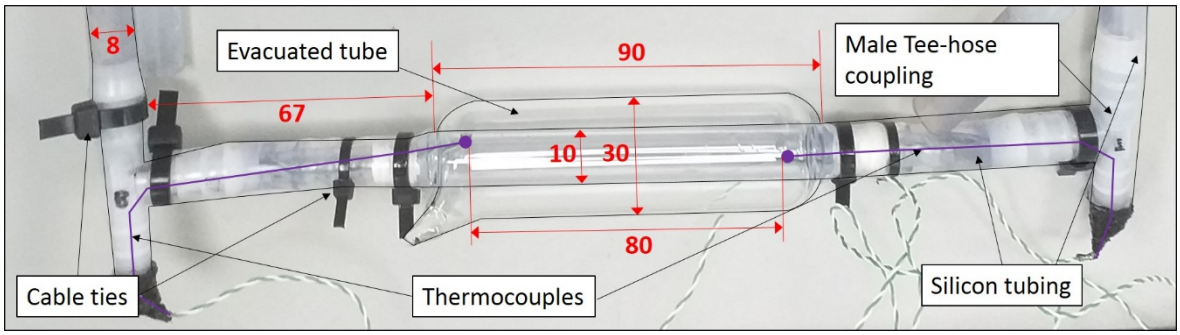

Figure 3-5 Detail of flow cell. All dimension (in red) in mm. Diameters are internal diameters.

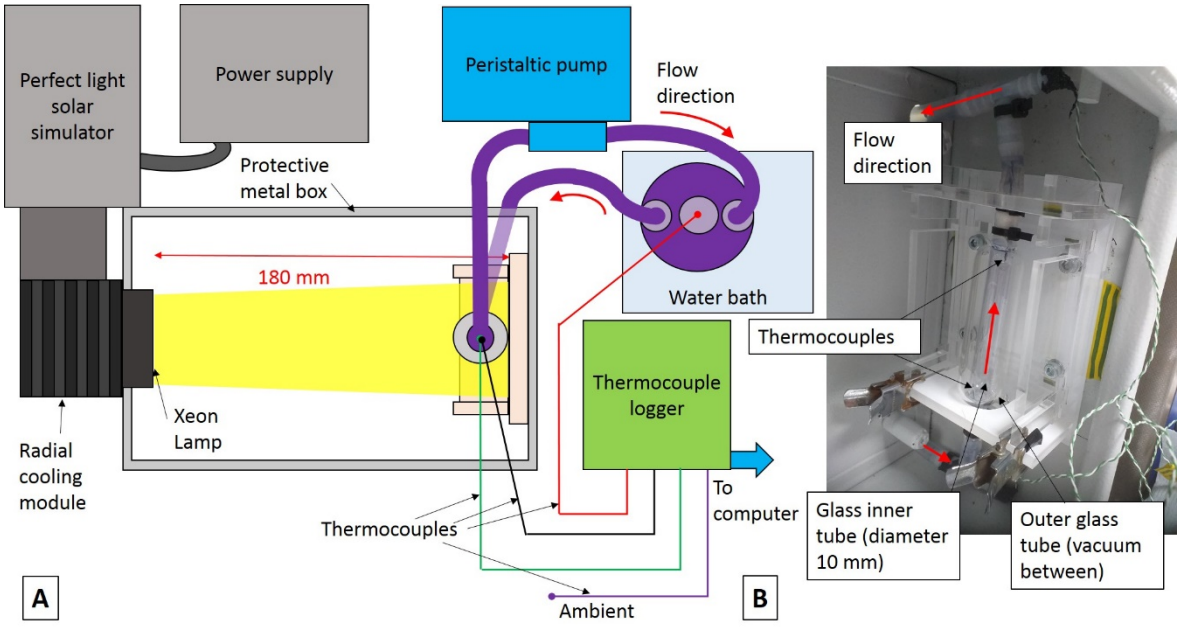

Figure 3-6 Detail of experimental set-up to assess flow showing (A) Schematic of solar simulator set-up and (B) Photograph showing flow cell in the solar simulator. Red arrows denote the direction of flow.

The flow cell was mounted in the Schneider Electric NSYCRN325150 steel box from Farnell (dimensions 300 mm L x 250 mm H x 150 mm D) using a modified Perspex holder to allow consistent placement of the flow cell in relationship to the lamp. Two holes were drilled in the steel box to allow the tubing to exit. The silicone tubing connected to the bottom of the flow cell was passed through this hole and into a three port 100 mL round bottomed flask which was

placed into a water bath (Fisher Scientific sonicating water bath type FB 15051) to maintain a set temperature (see Figure 3-6). The silicone tubing from the top of the flow cell was passed through the top hole in the metal box and into the flask in the water bath via a peristaltic pump (type Watson Marlow Sci Q 323). The direction of flow was from the bottom of the flow cell to the top. This is illustrated in Figure 3-6 A and B. Another thermocouple was placed in the round bottomed flask, with its end submerged in the solution to be tested, and held in place using a glass stopper. The flask, tubing and top of the water bath were covered with aluminium foil to reduce evaporation.

The flow rate of water through the set-up was measured for various different values of rpm on the peristaltic pump and a graph plotted to calculate the flow rate. Even at the lowest rpm setting on the pump the flow rate was ≈ 0.25 mL s^{-1} (actual value 0.238 mL s^{-1} using the equation of best fit of $y = 0.076x + 0.0104$ where x = value of rpm setting on pump and y = flow rate in mL s^{-1}, R^2 (R-squared statistic) = 0.997). This equates to a time between the two thermocouples in the flow cell of only about 16 s. Any differences measured between T_{in} (bottom thermocouple) and T_{out} (top thermocouple) are therefore likely to be very small especially for the BF only and possibly within the measurement error even with the evacuation of the air in the space around the central flow cell to prevent heat loss. Hence, although the intention had been to estimate performance of the NFs under flow conditions as well as stability this was not possible with this set up.

To evaluate the stability of the NFs under flow conditions the experimental procedure was as follows:

Prior to commencing the test 1 mL of sample was used to measure the UV-vis-IR spectra at $t = 0$, where t is time (using a Fisherbrand polystyrene Semi Micro cuvette, Product code 105941750 with 10 mm path length) and UV-vis-IR-1 (see Section 3.7.2). An 82 mL sample of either water BF or NF was placed in the round bottomed flask and the thermocouple and silicone tubing from the flow cell added. The pump was then switch on to prime the flow cell with liquid. When the flow cell was filled the pump was switched off.

The stability of the NF to flow only was then determined. The pump was switch on with a flow rate of 0.238 mL s^{-1} (3 rpm) and the NF pumped through the flow rig with the water bath switched off. The system was allowed to run for a total time of 480 mins (8 h), with periodical removal of 1 mL for UV-vis-IR measurements. The NF was then removed from the flow rig and Milli-Q water used to flush the flow rig to clean it. A final UV-vis-IR spectrum was recorded.

The effect of both temperature and flow on the NF was then evaluated. A further 82 mL of NF was placed in the round bottomed flask after removing a 1 mL $t = 0$ sample for UV-vis-IR testing. The

flow cell was primed and the flow was turned off. The water bath was then set to a temperature of 70 °C. The peristaltic pump was then switch on again (at a setting of 3 rpm equating to 0.238 mL s^{-1}) when the temperature measured by the thermocouple immersed in the round bottomed flask had reached 30 °C. The system was allowed to run for a total time of 360 minutes (6 h) with periodical removal of a 1 mL sample for UV-vis-IR measurement. When each sample was removed the temperature of the thermocouple in the round bottomed flask were noted. Due to heat losses in the flow rig and cell the maximum temperature obtained in the NF in the round bottomed flask was 59.8 °C although the set temperature on the water bath was 70 °C. The water bath and pump were switch off after 360 minutes and the NF allowed to cool. The NF was then removed from the flow cell, tubing and flask and the system cleaned with Milli-Q water.

The stability of the NF to flow combined with SSL was then evaluated. Again another 82 mL of NF was placed in the round bottomed flask, with the water bath switch off (again removing a t = 0 sample for UV-vis-IR measurement). The tubing from the flow cell and the thermocouple were added and the flow cell primed. The pump (0.238 mL s^{-1} or 3 rpm) and the solar simulator lamp were then switch on for a period of 30 minutes. The lamp used was the same as for set-up B in Section 3.8.3 (I_L = 1191 W m^{-2}). A UV-vis-IR sample was then removed and the flow only continued for 30 minutes. The lamp was then switch back on for 30 minutes and the cycle repeated (30 minutes SSL with flow followed by 30 minutes flow only). This cycling method was used to prevent the lamp in the solar simulator from overheating. The cycles were then repeated until the total exposure to SSL was 240 minutes (4 h). The NF was then removed and the flow rig cleaned with Milli-Q water.

The combined effect of SSL, temperature and flow was then determined. A t = 0 UV-vis-IR sample was removed and 82 mL of NF placed in the flask. The water bath was set to 70 °C and the flow cell primed. The experiment was then started when the temperature of the NF in the flask had reached 30 °C. The pump was switched on (0.238 mL s^{-1} or 3 rpm) and the NF pumped around the system. After 30 minutes of flow a UV-vis-IR sample was removed and the solar simulator lamp was switch on for 30 minutes. Another UV-vis-IR sample was taken, the lamp switch off and the NF allowed to circulate for 30 minutes. This cycle was repeated until the total time of exposure to SSL was 150 minutes and the total exposure to temperature was 330 minutes. A final UV-vis-IR sample was removed and the pump, water bath and lamp switched off. The NF was removed and the system cleaned.

Throughout all the above experiments the temperature of all four thermocouples, T_{in} (the temperature at the bottom of the flow cell), T_{out} (the temperature at the top of the flow cell), T_{flask}

(the temperature of the fluid in the round bottomed flask) and $T_{ambient}$ (the laboratory temperature) were recorded.

To assess the effect of the different conditions on the morphology of the NPs, TEM samples were taken prior to exposure and after exposure for all four exposure conditions (after flow only, after flow and SSL, after flow and temperature and after flow, temperature and SSL). Details of how the TEM measurements were conducted are given in Section 3.7.1).

3.9.7 Effects of changing base-fluid (BF)

To illustrate the potential issue of changing the BF employed to one that is more suitable for solar applications, uncoated Ag NPrs stabilised with TSCD and PVP were centrifuged (ct) at 12,857 r.c.f. (10,000 rpm) for 30 minutes (3 samples) and re-dispersed into ¼ the volume of either a different BF propylene glycol (PG) or water. The initial UV-vis spectra were recorded. The samples was exposed to a temperature of 70 °C for 6 h using the method described in Section 3.9.3. The UV-vis spectra were then re measured.

3.9.8 Summary

A short summary of this Section illustrating the differences between the various stability tests undertaken is given in Table 3-4. In all cases the stability was assessed using a combination of TEM and UV-vis or UV-vis-IR measurements.

Table 3-4 Summary of Stability testing conditions and Subsections.

Subsection	**Covered**
Colloid Stability	Stability to 4 °C in the dark
Elevated temperature	Stability to a temperature of 70 °C
Simulated sunlight (SSL)	Static tests in solar simulator
Natural Sunlight exposure	Two different trials – trial 1 (2 weeks) and trial 2 (5 weeks)
Effect of fluid flow	Set-up for flow testing detailed – conditions assessed – flow alone, flow + temperature, flow + temperature + SSL
Changing BF	Effect on stability to temperature of changing the BF to propylene glycol (PG)

3.10 Uncertainty Analysis

Uncertainty analysis was carried out according to the method described in Bell (Bell, 2001). The method and a summary of the results are given in Appendix C, Section C.4, with the full Type B (uncertainty associated with measurement technique) results being given in Appendix D, and the

Type A (uncertainty due to sample variation) results in Appendix E. One of the largest measurement uncertainties were associated with the determination of η_{PE} using the solar simulator, which gave an expanded uncertainty (Type A + Type B) of 8.24 % – 10.37 % for set-up B and 10.21 % – 10.36 % for set-up A. Another large measurement uncertainty was for the measurement of the size of the NPs using TEM which gave an expanded uncertainty of 2.96 % - 11.82 %.

3.11 Summary

A short summary of the main Sections in this Chapter is given in Table 3-5.

Table 3-5 Chapter 3 Summary.

Section	**Points covered / Outcome**
Chemicals	All chemicals used listed
Silver NFs literature	One-step synthesis method
Silver NF synthesis	Methods for Ag NSs and Ag NPrs, development of a broadband Ag NF absorber based on three separate NFs, measurement of consistency of batch synthesis
Coating of Ag NP with SiO_2	Literature on potential methods – 2 methods identified. Development of a protocol – 1 water-glass method and 1 Stöber method investigated. Optimised protocol presented. Modifications to this optimised protocol described
Characterisation	Two methods used – TEM and UV-vis or UV-vis-IR spectroscopy
Performance evaluation	Two methods. First calculating η_{Ab} from UV-vis or UV-vis-IR spectroscopy. Second measuring η_{PE} using solar simulator (2 set-ups – Set-up A and Set-up B)
Stability Testing	Colloidal stability (4 °C dark), elevated temperature (70 °C), simulated sunlight (SSL), natural sunlight (2 trials), effect of fluid flow (flow alone, flow + temperature, flow + temperature + SSL), changing BF
Uncertainty Analysis	Highest uncertainty associated with measuring η_{PE} using the solar simulator (≤ 10.37 %) and the size analysis in the TEM (≤ 11.82 %)

Chapter 4 Silver Nanofluid (NF) Synthesis

4.1 Publications from this Chapter

1. Kimpton, H., Stulz, E., Zhang, X., 2020. Silver nanofluids based broadband solar absorber through tuning nanosilver geometries. Solar Energy, 208, 515-526, https://doi.org/10.1016/j.solener.2020.08.018 (Kimpton et al., 2020b).
2. Kimpton, H., Cristaldi, D.A., Stulz, E., Zhang, X., 2020. Thermal performance and physicochemical stability of silver nanoprism-based nanofluids for direct solar absorption. Solar Energy, 199, 366-376, https://doi.org/10.1016/j.solener.2020.02.039 (Kimpton et al., 2020a).
3. Kimpton, H., Zhang, X., Stulz, E., 2021. The temperature stability and development of a broadband silver nanofluid for solar thermal applications. Energy Reports, 7, 87-96, https://doi.org/10.1016/j.egyr.2021.02.049 (Kimpton et al., 2021).

4.2 Introduction

This Chapter presents the results obtained from investigating the synthesis of Ag NPs for the preparation of silver nanofluids (NFs). It starts by describing the results obtained from the nanosphere (NS) synthesis stabilised by tri-sodium citrate di-hydrate (TSCD) and by TSCD with polyvinylpyrrolidone (PVP). It then assesses how Ag NFs containing NSs might perform in a volumetric absorber by calculating the efficiency η_{Ab} for various different concentrations and path lengths (or depth of fluid). The UV-vis and TEM results obtained for the synthesis of Ag nanoprisms (NPrs) using the methods described in Section 3.5.3 are then presented along with the calculation of the potential η_{Ab} for these NFs.

This Chapter then details the results of the investigation into the synthesis with the aim of producing two other Ag NP synthesis methods that would give two different morphologies and hence λ_{max} that could then be combined with the Ag NPrs to produce a broadband absorber covering a broad spectral range.

The following Section 4.6 uses the UV-vis spectra obtained from these additional NF along with the spectra from the Ag NPrs to calculate the potential η_{Ab} for a number of different mixtures of the three NFs. The optimum is then selected and the potential combined UV-vis spectrum for this NF calculated. This is then compared to the actual spectrum obtained from combining the three NFs together. The potential η_{Ab} for this novel mixture is then assessed.

Section 4.7 then presents the results of repeating the synthesis of the three different NFs used for the broadband absorber to assess the level of variability obtained and hence highlight any potential issues with the developed recipes and the effect any variation in the repeatability may have on the resultant broadband absorber mixture.

Finally, the conclusions obtained from the results described in this Chapter are given, along with a discussion on the implications and a brief summary.

4.3 Ag Nanospheres (NS)

This Section presents the UV-vis results obtained from undertaking the NS synthesis using the method described in Section 3.5.2. It then details the results of calculating the η_{Ab} for a number of different concentrations and path lengths, followed by a short discussion. A summary is given at the end of the Section.

The results from repeating the NS synthesis over a range of starting concentrations of Ag are summarised in Figure 4-1 for both NS stabilised with only TSCD and NS stabilised with both TSCD and PVP. It was possible to produce stable Ag NS nanofluids with an initial concentration of 0.8 mM Ag when both TSCD and PVP were used as stabilising agents, but not when only TSCD was present, illustrating the stability advantage gained from using both stabilising agents.

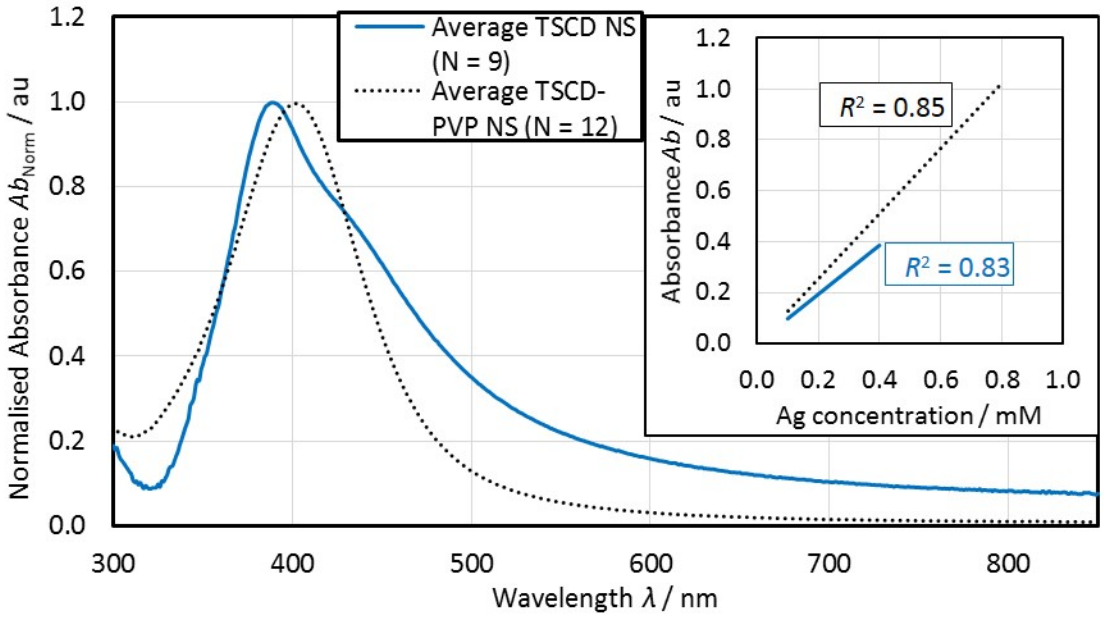

Figure 4-1 UV-vis spectra of Ag NS stabilised with TSCD and with TSCD-PVP. The average normalised data (Ab_{Norm}) for 3 concentrations of Ag TSCD NS (0.1 mM, 0.2 mM and 0.4 mM, number of samples N = 9) and for 4 concentrations of Ag TSCD-PVP NS (0.1 mM, 0.2 mM, 0.4 mM and 0.8 mM, N = 12) are shown. The insert shows how the absorption value changes with Ag concentration (for a 1 mm path length cuvette). All measured using UV-vis-1.

For the NS TSCD samples λ_{max} was 389 nm (standard deviation σ = 1.9 nm, N = 9) and for the NS TSCD-PVP samples λ_{max} was slightly red-shifted to a value of 402 nm (σ = 2.8 nm, N = 12). This difference was significant using a two-sample t-test (See Appendix F, Section F.1 for definition). The shape of the curve was also different with the NS TSCD samples exhibiting a broader absorption peak with a shoulder at ≈ 425 nm which was absent for the NS TSCD-PVP samples. The reduction in the width of the peak produced has also been seen by others when PVP is used in addition to TSCD (Zhang et al., 2011).

There was also more variation in the value of maximum absorption (Ab_{max}) for the TSCD NS samples compared to the NS TSCD-PVP samples. This is reflected in the lower value of R^2 obtained for the regression analysis shown in Figure 4-1 of 0.83 compared to R^2 = 0.85 for the TSCD-PVP NS samples on the concentration versus absorbance inserted graph. The gradient of the regression analysis for the TSCD NS samples was also less, showing that the TSCD NS synthesis was producing a broader lower absorbance as the initial concentration of Ag in the synthesis was increased.

TEM analysis of one of the 0.4 mM Ag TSCD-PVP NS samples (Figure 4-2) showed the majority of NPs were small and spherical with an average size of 5.1 nm (σ = 2.7 nm, N = 100, range = 2.2 nm – 17.9 nm) which is a smaller average size than would be suggested from the UV-vis λ_{max} of 402 nm which should correspond to a NP diameter of ≈ 20 nm (Paramelle et al., 2014a). Although the mean value was considerably lower than this literature figure the maximum particle size obtained was similar. It should be noted that this literature value is for TSCD only stabilised Ag NS rather than TSCD and PVP stabilised Ag NSs. Others have found that the particle size decreases as the amount of PVP is increased for a similar Ag NS synthesis utilising $NaBH_4$ as the reducing agent but without using TSCD (Mirzaei et al., 2016). Hence the presence of PVP may account for some of the reduction in size observed.

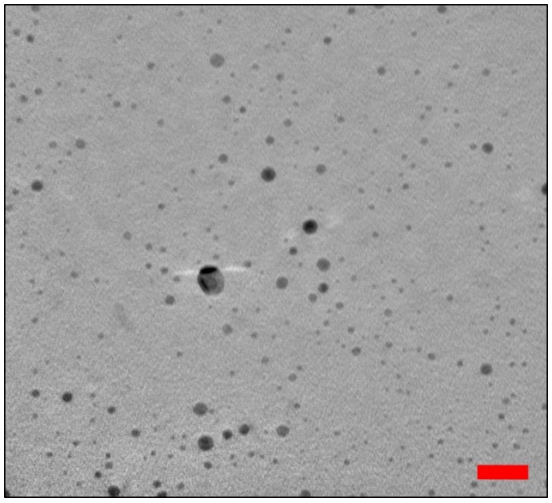

Figure 4-2 TEM micrograph of Ag TSCD-PVP NS. Red scale bar = 20 nm.

4.3.1 Nanospheres - absorption efficiency

The power absorbed by the NF containing NS were calculated according to the method described in Section 3.8.2 using Equation 3-6. The results for a number of different NS NFs are shown in Figure 4-3, using two different path lengths of 10 mm and 1 mm. The 10 mm path length spectra were scaled from the 1 mm spectra using the Beer-Lambert law, which states that there is a linear relationship between absorbance (*Ab*) and path length for low concentration solutions (Sheffield Hallam University, 2019).

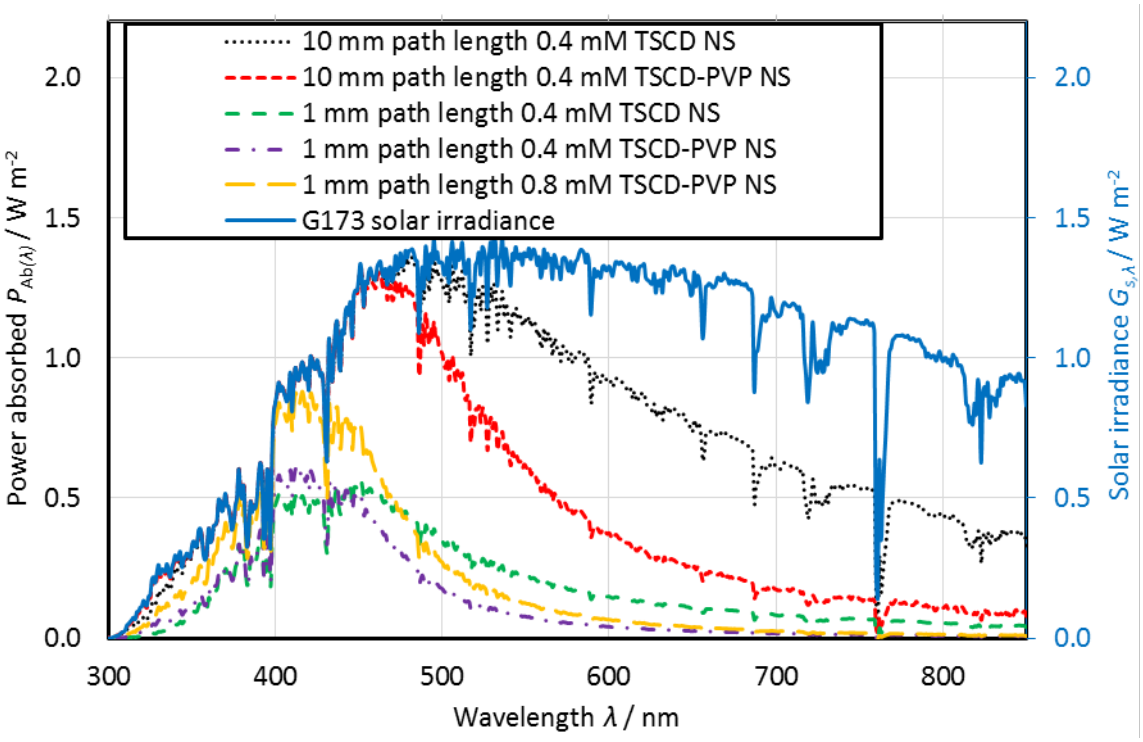

Figure 4-3 Amount of power absorbed P_{Ab} of the G173 ($G_{s,\lambda(dir+cs)}$) by the NS NFs at different Ag starting concentrations and path lengths. The secondary vertical axis is for the G173 solar spectrum taken from (ASTM, 2012). The 10 mm path length data is calculated from the 1 mm data using the Beer Lambert law (Sheffield Hallam University, 2019).

The efficiency $\eta_{Ab(300\ nm\ -\ 850\ nm)}$ was also calculated by modifying Equation 3-7 to give:

$$\eta_{\mathrm{Ab(300\ nm-850\ nm)}} = \frac{\sum_{\lambda=300\ \mathrm{nm}}^{\lambda=850\ \mathrm{nm}} P_{\mathrm{Ab}(\lambda)}}{\sum_{\lambda=300\ \mathrm{nm}}^{\lambda=850\ \mathrm{nm}} P_{\mathrm{i}(\lambda)}} \times 100$$

Equation 4-1

This only accounts for ≈ 62 % of the solar spectrum. Therefore to give an indication of the efficiency over the total spectrum $\eta_{Ab(280\ nm\ -\ 4000\ nm)}$ was also calculated assuming no absorption outside of the measured 300 nm – 850 nm range again by modifying Equation 3-7 to give:

$$\eta_{\mathrm{Ab(280\ nm-4000\ nm)}} = \frac{\sum_{\lambda=300\ \mathrm{nm}}^{\lambda=850\ \mathrm{nm}} P_{\mathrm{Ab}(\lambda)}}{\sum_{\lambda=280\ \mathrm{nm}}^{\lambda=4000\ \mathrm{nm}} P_{\mathrm{i}(\lambda)}} \times 100$$

Equation 4-2

This underestimates the total efficiency as the BF water absorbs in the near infrared region. The results for the calculated η_{Ab} are shown in Table 4-1. Increasing the concentration or the path length increases η_{Ab}. The NS stabilised with TSCD only gave higher η_{Ab} values than the TSCD-PVP samples (at the same path length and concentration). This is because the TSCD only NSs absorbed over a broader spectral range (see Figure 4-1). Even the highest concentration of 0.4 mM Ag TSCD NS only achieved a $\eta_{Ab(300\ nm\ -\ 850\ nm)}$ of 71.7 % with a 10 mm path length. The actual performance of this NF would be less but greater than the 44.1 % estimated for $\eta_{Ab(280\ nm\ -\ 4000\ nm)}$ in Table 4-1. Sani et al obtained an efficiency of 37 % over the range 280 nm – 2000 nm for a more dilute (0.1 g L^{-1}) Ag NF containing NS calculated from the transmission spectrum and extinction coefficient (Sani et al., 2015), broadly similar to this result.

If the path length was increased still further the efficiency would not increase dramatically as the NF would still fail to absorb much of the longer λ light. The only way to increase the efficiency would be to broaden the width of the absorption peak by the use of a broadband absorber. This could be achieved by combining the Ag NSs with another NF with a strong absorption at longer λs such as $CsWO_3$ (Liu et al., 2020) or by the use of different morphologies of Ag particles. The development of a silver broadband absorber is discussed further in Sections 4.5 and 4.6.

Table 4-1 Estimated η_{Ab} values for various NS NFs.

Sample	**Path length / mm**	**$\eta_{Ab(300\ nm\ -\ 850\ nm)}$ / %**	**Estimated $\eta_{Ab(280\ nm\ -\ 4000\ nm)}$ / %**
0.4 mM TSCD	1	18.4	11.3
0.4 mM TSCD-PVP	1	12.7	7.8
0.8 mM TSCD-PVP	1	19.1	11.7
0.4 mM TSCD	10	71.7	44.1
0.4 mM TSCD-PVP	10	44.2	27.2

With the low potential efficiency of NFs based solely on NS it is unlikely that a volumetric absorber using only Ag NS would provide enough advantage compared to a standard FPC utilising a selective surface. Others have investigated using Ag NS for solar applications and have suggested that Ag NS could be used as an optical filter in combined PVT applications to provide more thermal output while still maintaining a high electrical output (Abdelrazik et al., 2019).

4.3.2 Summary

To summarise, this Section has shown that the Ag NS synthesis method consistently produces NS with a low variation in λ_{max}. In addition, utilising PVP can increase the stability of the NS NFs allowing more concentrated NFs to be synthesised and producing a narrower absorption peak. However, this narrower absorption peak has a detrimental impact on η_{Ab}. Even when the broader spectral response of the Ag TSCD NS is used to calculate η_{Ab}, the resultant value is unlikely to be high enough to make a NF based solely on NSs to be suitable for enhancing solar capture.

4.4 Ag Nanoprisms (Ag NPrs)

This Section presents the results obtained from the batch synthesis of Ag NPrs using the method described in Section 3.5.3. Firstly, the results without PVP are presented, comparing the before and after centrifuged samples. Secondly, the Ag NPrs stabilised with TSCD and PVP UV-vis and TEM results are given again including a discussion on the effects of centrifuging. The results of calculating the power absorbed and hence the η_{Ab} are then presented along with a debate on the implications for solar capture. A short summary is provided at the end of the Section.

The results of repeating the Ag NPr synthesis without PVP specified in Section 3.5.3, nine times are shown in Figure 4-4. Three of the nine samples were then centrifuged and re-dispersed into water to ¼ the original volume. These were measured using a 1 mm path length cuvette. Figure 4-4 shows these three samples separately before and after centrifuging. The after centrifuging spectra have been adjusted to allow direct comparison of the results.

For the original 9 samples the average λ_{max} was 798 nm (σ = 31.5 nm, N = 9, range = 748 nm – 848 nm (error bars in Figure 4-4)) and the average Ab_{max} was 1.318 au (σ = 0.101 au, N = 9, range = 1.195 au – 1.513 au). The three samples before centrifuging had an average λ_{max} of 769 nm (σ = 19.1 nm, range = 749 nm – 787 nm) and an average Ab_{max} of 1.320 au (σ = 0.168 au, range = 1.206 au – 1.513 au). After centrifuging the average λ_{max} blue-shifted to a value of 756 nm (σ = 9.8 nm, range = 745 nm – 762 nm) and the Ab_{max} dropped to a value of 1.155 au (σ = 0.188 au, range = 1.045 au – 1.372 au). Using a two-sample t-test (not a paired t-test as the samples measured were different sub-samples) this blue-shift and drop in Ab_{max} following centrifuging was not significant. The results from more centrifuged samples would be needed to check if there was indeed no change following centrifuging.

The results of repeating the Ag NPr synthesis using both TSCD and PVP are shown in Figure 4-5. Two different batch sizes were produced, 50 mL (20 repeats) and 25 mL (3 repeats). The 25 mL samples were measured on the UV-vis-IR-1 spectrophotometer, whereas all the other samples

were measured on the UV-vis-1 spectrophotometer. Six of the twenty 50 mL samples were centrifuged at 16,168 r.c.f. (13,000 rpm) for 30 minutes and re-dispersed into ¼ volume of water. These six samples are also shown separately in Figure 4-5 before and after centrifuging. The after centrifuging results have been adjusted to account for the different cuvette path length and volume of NF. In addition, to investigate the consistency of the batch manufacturing process (see Section 3.5.5) 20 x 30 mL batches of Ag TSCD-PVP NPrs (long λ NF) were produced. The results from these 20 samples will be presented in Section 4.7.

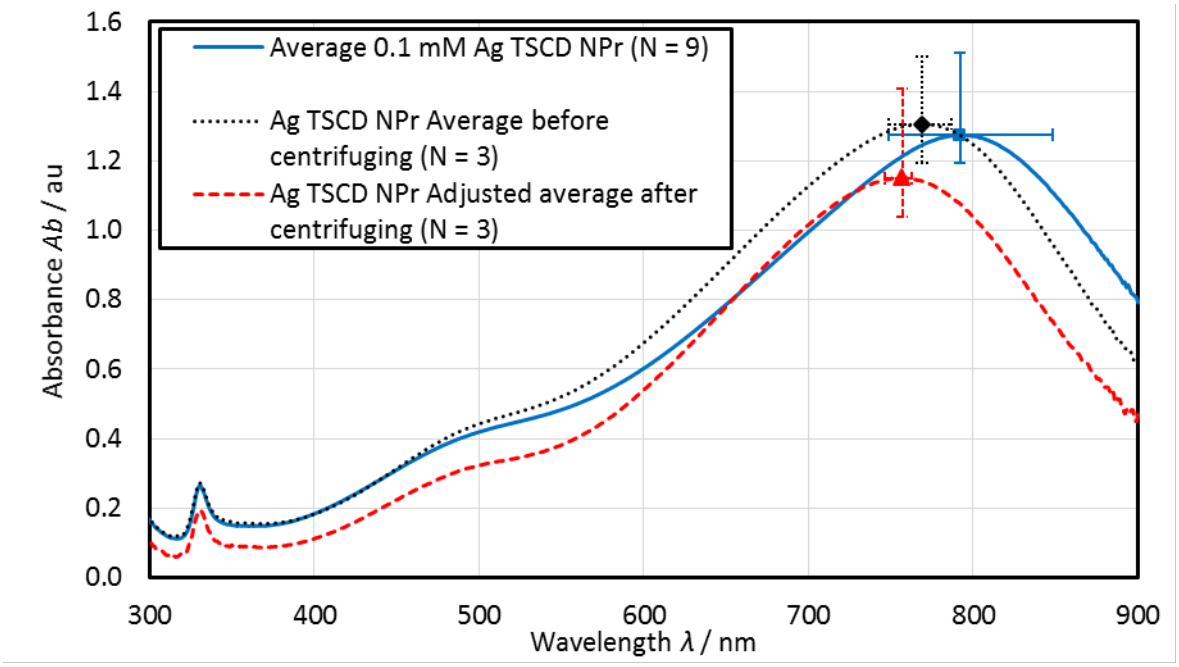

Figure 4-4 UV-vis spectra for Ag NPr stabilised with TSCD. All measured on UV-vis-1. The average 0.1 mM (N = 9) and the average before centrifuging all measured with a 10 mm path length quartz cuvette. The data for the after centrifuging samples has been adjusted for volume and cuvette path length (original spectra recorded using ¼ volume samples and a 1 mm cuvette). The error bars show the range of results obtained at the maximum absorbance.

For the 20 x 50 mL samples the average λ_{max} was 858 nm (σ = 28.9 nm, N = 20, range = 812 nm – 900 nm) and Ab_{max} was 1.4202 au (σ = 0.1560 au, N = 20, range = 1.1114 au – 1.8054 au). This represents about a 60 nm red-shift in λ_{max} compared to the Ag TSCD NPr only samples and a small increase in Ab_{max}. This difference in λ_{max} was significant according to a two-sample t-test but the slight increase in Ab_{max} was not. It is also similar in size and direction of shift to the results reported by Carboni (Carboni, 2014) for Ag NPr synthesis with and without PVP.

Similar to the Ag TSCD NPr samples there was a drop in Ab_{max} with a blue-shift in λ_{max} after centrifuging. However, in contrast both the reduction in Ab_{max} of about 30 % and the 30 nm blue-shift in λ_{max} following centrifuging were significant (using a two-sample t-test). This may have been due to the additional stability of the Ag TSCD-PVP NPr which required a higher centrifuge force and time in order to aggregate enough for the supernatant to be removed. Even with this increase in centrifuging parameters the drop in Ab_{max} due to loss of NPrs was still significant and

clearly demonstrates the additional stability to aggregation of the Ag NPrs stabilised with both TSCD and PVP. The blue-shift in λ_{max} following centrifuging may have been caused by the harsher centrifuging conditions leading to a rounding of the corners of the NPrs. Others have also found that a blue-shift of ≈ 40 nm occurs after 2 h centrifuging at 14,000 r.c.f. (Zeng et al., 2010). Changing the sharpness of the corners has been shown numerically to cause a blue-shift in λ_{max} of up to 200 nm (Kelly et al., 2003).

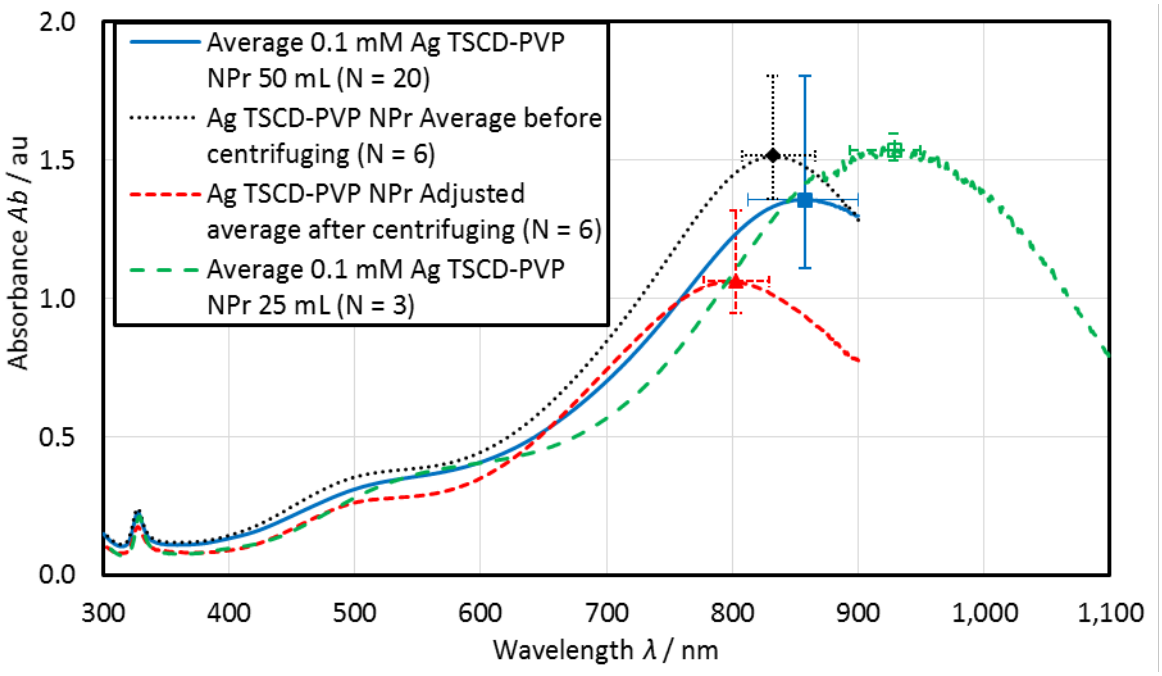

Figure 4-5 UV-vis spectra for Ag NPr stabilised with TSCD and PVP. All measured on UV-vis-1 except the Ag NPr 25 mL samples (measured on UV-vis-IR-1). All the non-centrifuged samples measured with a 10 mm path length cuvette. The data for the after centrifuging samples has been adjusted for volume and cuvette path length (original spectra recorded using ¼ volume samples and a 1 mm cuvette). The error bars show the range of results obtained at the maximum absorbance.

When the batch volume of the synthesis was reduced to 25 mL (in the same sized flask) there was a significant (according to a two-sample t-test) red-shift in λ_{max} of ≈ 70 nm compared to the 50 mL batches (see Figure 4-5). There was also a small but not significant increase in average Ab_{max}. This potential red-shift caused by changing the batch volume (perhaps improving the stirring rate) will be discussed further in Section 4.7 were the results of the 30 mL batch volume samples are presented. However, it should be treated with some caution as the 50 mL spectra were recorded using UV-vis-1 (maximum λ = 900 nm) and the 25 mL spectra were measured using UV-vis-IR-1 (maximum λ = 1350 nm). Hence, λ_{max} may have been occurring outside of the measurement range (> 900 nm) for some of the 20 samples (4 samples had a λ_{max} ≈ 900 nm), blue-shifting the average, σ and range of results presented.

Typical TEM micrographs of the Ag TSCD-PVP NPr are shown in Figure 4-6. Size analysis of the particles was undertaken according to the method described in Section 3.7.1. The results are summarised graphically in Figure 4-7. The full results are given in Appendix G.1.

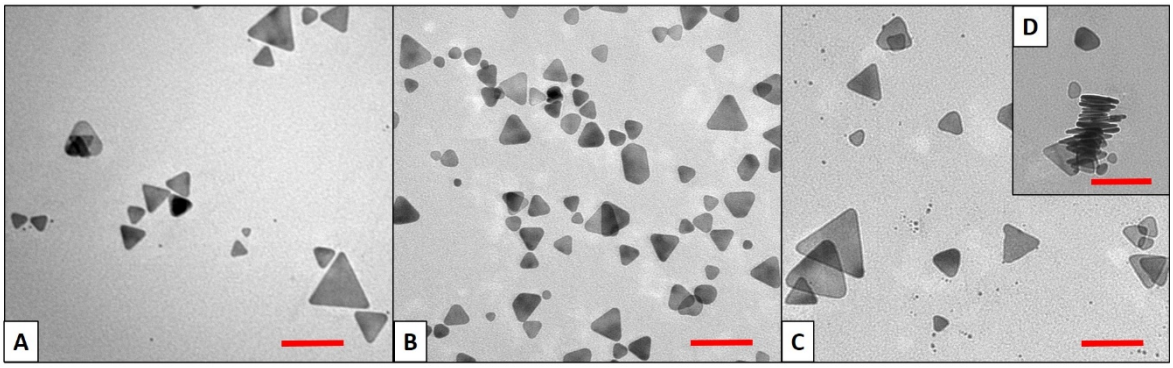

Figure 4-6 TEM micrographs of (A) Ag TSCD-PVP NPr 50 mL, (B) Ag TSCD-PVP NPr after centrifuging and concentrating to ¼ volume, (C) Ag TSCD-PVP NPr 25 mL and (D) insert showing edge of Ag TSCD-PVP NPr 25 mL. All red scale bars = 100 nm.

From Figure 4-7 it can be seen that for the 50 mL batch volume of Ag TSCD-PVP NPr the majority of the particles were triangles or rounded cornered triangles. The average size (i.e. the average length measured from corner to corner) for the triangles was 48.2 nm (σ not shown in Figure 4-7 was 16.7 nm, N = 339). The rounded cornered triangles had a slightly smaller average size of 38.8 nm (σ = 14.4 nm, N = 143).

The effect of centrifuging was to increase the relative amount of rounded cornered triangles and other particles, and to reduce the size of both the triangles and the rounded cornered triangles. Two-sample t-tests showed that this size difference was significant (see Appendix G.1.1 for full results).

Changing the batch volume from 50 mL to 25 mL appears to have increased the relative amount and size of the triangles to 69 % and 52.2 nm (σ = 17.6 nm, N = 153 see Appendix G.1). In contrast the size of the rounded cornered triangles and other particles was reduced. All the size changes were significant according to two-sample t-tests (for average differences and range of the differences see Appendix G.1.1). Varying the batch size in the same sized container could influence the amount of oxygen present in the solution (different surface to volume ratio). This is known to influence the selective etching and growth of the NPrs during manufacture perhaps because of the conversion of Ag to Ag^+ (Xue et al., 2008). The thickness of the NPs (see Figure 4-6 D) was also measured for this sample and found to be 5.87 nm ± 2.62 nm (N = 102).

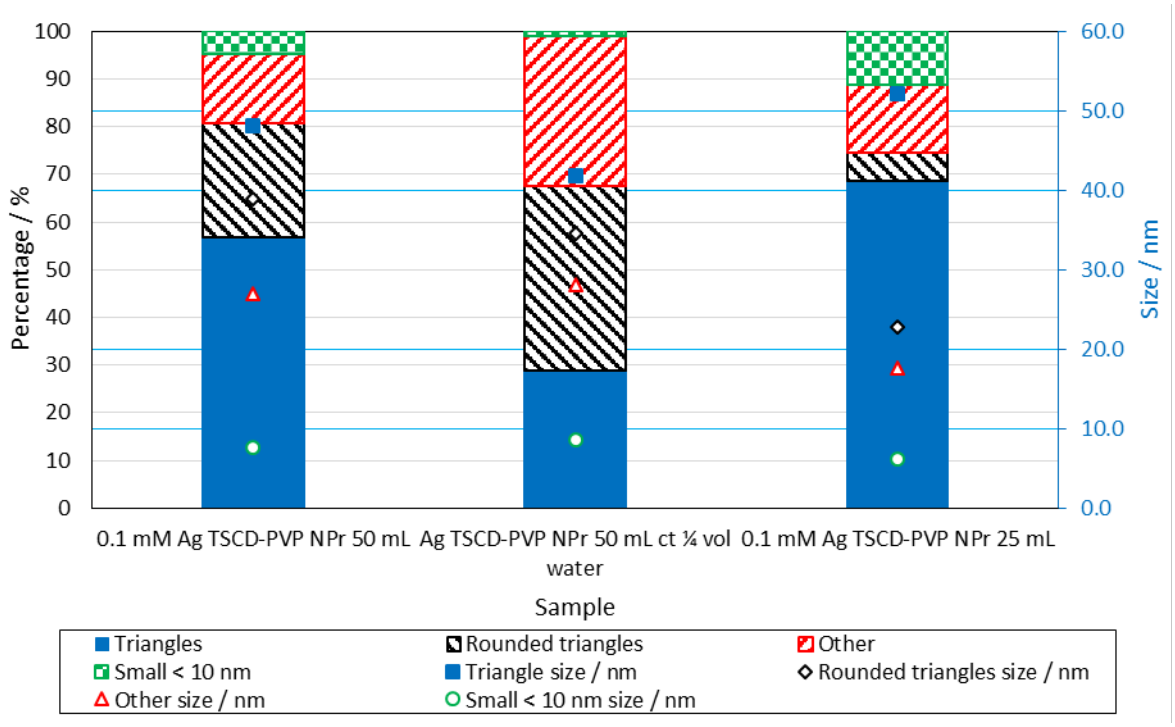

Figure 4-7 Summary of TEM size analysis for Ag TSCD-PVP NPr. The percentage of each particle type is shown on the primary vertical axis and the average size of each particle type on the secondary vertical axis.

When these morphological changes are related to the average λ_{max} it can be seen that an increase in size and amount of triangles leads to an increase in λ_{max}. This agrees with the numerical work of others (Kelly et al., 2003).

4.4.1 Absorption efficiency – nanoprisms (Ag NPrs)

The power absorbed by the NFs containing Ag NPrs were calculated according to the method described in Section 3.8.2 using Equation 3-6. The results for a number of different NFs containing Ag NPrs stabilised with TSCD only are shown in Figure 4-8, using a path length of 10 mm. The actual after centrifuging results were calculated from the 1 mm UV-vis-1 spectra using the Beer-Lambert law (Sheffield Hallam University, 2019). The adjusted after centrifuging results allow for the direct comparison of the effect of the reduction in Ab_{max} for the centrifuged samples.

The corresponding graph for the Ag TSCD-PVP NPrs samples is shown in Figure 4-9. Both the 0.1 mM Ag NPrs absorbed the majority of the spectral power in the longer λ range but failed to absorb much of the power in the short and medium λ range (< 650 nm – 700 nm). The adjusted centrifuged results showed a reduction in power absorbed due to the decrease in the value of Ab_{max}. However, when the effect of increasing the concentration of NPrs as in the actual centrifuged samples is considered (over a 10 mm path length, re-dispersed in ¼ the volume of water) it can be seen that these ≈ 4 x concentrated samples absorb all the long λ light and much of the medium and short λs.

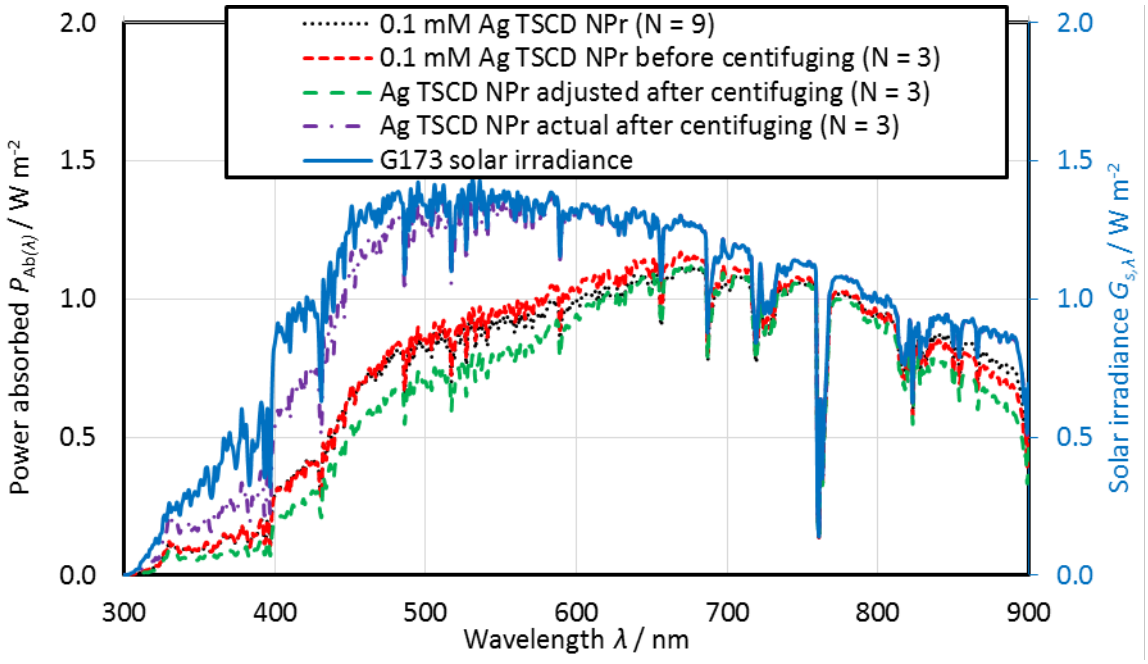

Figure 4-8 Amount of power absorbed P_{Ab} of the G173 ($G_{s,\lambda(dir+cs)}$) by the Ag TSCD NPrs using a path length of 10 mm. The secondary vertical axis is for the G173 solar spectrum taken from (ASTM, 2012). The adjusted centrifuged samples are calculated assuming that the NPrs were re-dispersed in the same volume as the before centrifuged samples. For the actual after centrifuging NF, the 1 mm path length UV-vis-1 spectra have been adjusted to a 10 mm path length.

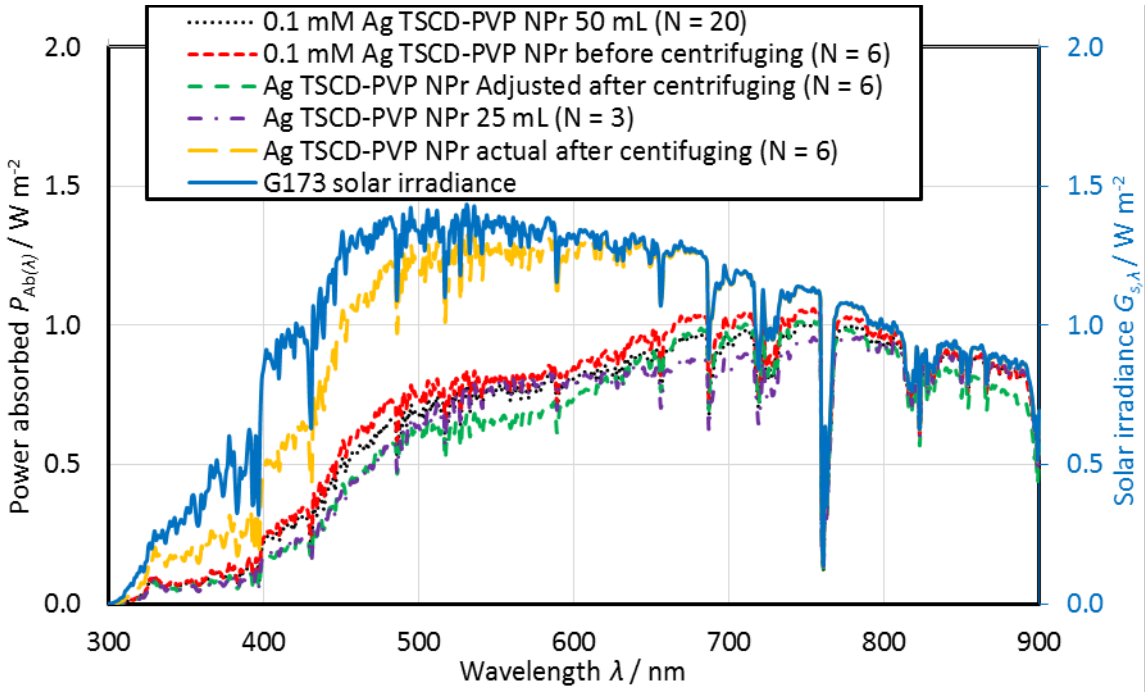

Figure 4-9 Amount of power absorbed P_{Ab} of the G173 ($G_{s,\lambda(dir+cs)}$) with a 10 mm path length by the Ag TSCD-PVP NPr. The secondary vertical axis is for the G173 solar spectrum taken from (ASTM, 2012). The adjusted centrifuged samples are calculated assuming that the NPrs were re-dispersed in the same volume as the before centrifuged samples. For the actual after centrifuging NF the 1 mm path length UV-vis-1 spectra have been adjusted to a 10 mm path length.

In a similar manner to the NS the value of $\eta_{Ab(300\ nm\ -\ 900\ nm)}$ was calculated by modifying Equation 3-7 to give:

$$\eta_{\mathrm{Ab\ (300\ nm-900\ nm)}} = \frac{\sum_{\lambda=300\ \mathrm{nm}}^{\lambda=900\ \mathrm{nm}} P_{\mathrm{Ab}(\lambda)}}{\sum_{\lambda=300\ \mathrm{nm}}^{\lambda=900\ \mathrm{nm}} P_{\mathrm{i}(\lambda)}} \times 100$$

Equation 4-3

This only accounts for ≈ 66 % of the solar spectrum. $\eta_{\mathrm{Ab(280\ nm\ -\ 4000\ nm)}}$ was also calculated assuming no absorption outside of the measured 300 nm – 900 nm range again by modifying Equation 3-7 to give:

$$\eta_{\mathrm{Ab(280\ nm-4000\ nm)}} = \frac{\sum_{\lambda=300\ \mathrm{nm}}^{\lambda=900\ \mathrm{nm}} P_{\mathrm{Ab}(\lambda)}}{\sum_{\lambda=280\ \mathrm{nm}}^{\lambda=4000\ \mathrm{nm}} P_{\mathrm{i}(\lambda)}} \times 100$$

Equation 4-4

This underestimates the total efficiency as the BF water absorbs in the near infrared region. The results are shown in Table 4-2. If these results are compared to the best performing NS in Table 4-1 of 0.4 mM Ag TSCD NS with the same 10 mm path length of 71.7 % for $\eta_{\mathrm{Ab(300\ nm\ -\ 850\ nm)}}$ it can be seen that the NPrs have a greater or similar η_{Ab} to this even with a lower starting concentration of Ag of 0.1 mM. With a similar Ag molar concentration (as for the centrifuged actual results), $\eta_{\mathrm{Ab(300\ nm\ -\ 900\ nm)}}$ is greater being > 90 %. This is because the NPrs have a higher and broader spectral response than the NS (compare Figure 4-1, Figure 4-4 and Figure 4-5).

Table 4-2 Estimated η_{Ab} values for various NPr NFs using a 10 mm path length.

Sample	**$\eta_{\mathrm{Ab(300\ nm\ –\ 900\ nm)}}$ / %**	**Estimated $\eta_{\mathrm{Ab(280\ nm\ –\ 4000\ nm)}}$ / %**
0.1 mM Ag TSCD NPr (*N* = 9)	73.8	48.9
0.1 mM Ag TSCD NPr before centrifuging (*N* = 3)	75.0	49.7
Ag TSCD NPr adjusted after centrifuging	67.4	44.7
Ag TSCD NPr actual after centrifuging (¼ the volume)	94.4	62.6
0.1 mM Ag TSCD-PVP NPr 50 mL (*N* = 20)	65.6	43.5
0.1 mM Ag TSCD-PVP NPr before centrifuging (*N* = 6)	69.2	45.9
Ag TSCD-PVP NPr adjusted after centrifuging	61.3	40.6
0.1 mM Ag TSCD-PVP NPr 25 mL (*N* = 3)	62.3	41.3
Ag TSCD-PVP NPr actual after centrifuging (¼ the volume)	91.7	60.8

A NF comprising of a high concentration of Ag NPrs may therefore be a suitable NF for enhancing solar capture. However, because a more concentrated NF is employed, aggregation of the NPrs with time is more likely. In addition, utilising a more concentrated NF may cause the incident light

in the longer λ region to be absorbed in a thin surface layer of the NF rather than throughout the bulk of the NF causing more radiative heat losses to the environment (Taylor et al., 2013). This would reduce η_{Ab} in practice. The actual performance and stability to spectral changes and aggregation for such a NF based on Ag NPrs is discussed further in Chapter 5.

Even by utilising a more concentrated Ag NPr NF it can be seen from Figure 4-8 and Figure 4-9 that not all the power in the 300 nm – 500 nm is absorbed. It may therefore be prudent and possible to improve this potential η_{Ab} still further by utilising a broadband absorber, tailored to absorb as much of the spectrum as possible with a lower overall NP concentration. The development and measurement of such a broadband absorber is discussed further in Sections 4.5 and 4.6.

4.4.2 Summary

The synthesis method for Ag NPrs produced NPrs with a $\lambda_{max} > 750$ nm and a broader spectral response than for the Ag NS synthesis. There was more variation in λ_{max} (≈ 100 nm) than for the NSs. Adding PVP had the effect of both stabilising the resultant NFs (longer centrifuging time needed) and red-shifting $\lambda_{max} \approx 70$ nm. Centrifuging had the effect of blue-shifting the position of λ_{max} and reducing Ab_{max}. TEM analysis showed that this blue-shift was possibly caused by the rounding of the corners of the triangles and a reduction in particle size. However, by centrifuging a more concentrated NF could be produced. This had the advantage of increasing the possible η_{Ab}, potentially making these NFs suitable for enhancing solar capture in a volumetric absorber.

4.5 Investigating Additional Synthesis Methods

The aim of this investigation was to determine two additional Ag NP synthesis methods that could be used to produce Ag NPs with distinct geometries and hence λ_{max} with the aim of demonstrating the possibility of producing a broadband silver absorber by combining the two developed NFs with the already established Ag NPrs NF.

Firstly, the results of the effect of overall reagent concentration will be discussed, followed by the effect of changing the amount of hydrogen peroxide as this is thought to be a pivotal reagent (Zhang et al., 2011). The results of investigating the effect of changing the Ag to $NaBH_4$ ratio will then be debated. Results from investigating the use of an anisotropic seed, followed by the addition of more reducing agent and more silver are then discussed.

Finally, the most suitable selected methods are shown, along with a check on the consistency of the developed synthesis methods, and a short summary of the main finding from this Section.

The results from investigating the effect of overall concentration are detailed in Appendix H, Section H.1. These show an inability to produce nanoparticles with a λ_{max} > 800 nm at higher reagent concentrations. This is in contrast to the NS synthesis discussed in Section 4.3 and suggests that controlling the morphology of the resultant NPs for the NPrs synthesis to produce a peak at λ_{max} > 800 nm is likely to be problematic due to a complex relationship between each of the reagents during the synthesis, which is affected not only by the ratio of the various reagents to each other but also by their overall concentrations in the solution.

When the amount of hydrogen peroxide was reduced at the lowest Ag concentration of 0.1 mM, there was a blue-shift in λ_{max} and a drop in Ab_{max} (full details and results in Appendix H, Section H.2). It was therefore not possible to produce a NF with a high Ab_{max} at a λ_{max} of ≈ 500 nm just by varying the H_2O_2 level.

Full details of the experiments and results investigating the effect of reducing the silver to reducing agent $NaBH_4$ ratio are given in Appendix H, Section H.3. By halving the ratio from 1: 10 to 1: 5 while also increasing the concentration of all the reagents by three times (0.3 mM Ag) it was possible to produce a NF with a λ_{max} in the 650 nm -750 nm range, a high value of Ab_{max} and a high enough Ag concentration to allow for it to be combined without further processing. This would be a suitable recipe for a mid λ NF. However, it was not possible to identify a suitable recipe for the short λ NF (λ_{max} ≈ 500 nm and a high value of Ab_{max}) from these experiments.

As mentioned in Section 3.5.4 as others have been able to produce an anisotropic Ag NPr starting from a spherical Ag NS seed (Haber and Sokolov, 2017), the effect of adding more reducing agent $NaBH_4$ to an already prepared seed NF was investigated to see how this would change λ_{max}.

Five different seed solutions were evaluated. The full list of seed solutions is given in Appendix H, Section H.4, along with results obtained. Surprisingly there was a blue-shift in λ_{max} when more $NaBH_4$ was added similar to the blue-shift observed when the level of H_2O_2 was varied. This again emphasizes the complex nature of the synthesis reaction, with $NaBH_4$ normally acting as the reducing agent, whereas H_2O_2 acts as an oxidising agent to selectively etch the surface of the developing NP. As more $NaBH_4$ was added, λ_{max} was further blue-shifted and Ab_{max} reduced. For one of the seed solutions there was a good linear fit when both λ_{max} and Ab_{max} were plotted against total $NaBH_4$ amount (relative to Ag) (see Figure H.6), however the other 4 NFs investigated did not show this linear relationship. In fact for one of the seeds (seed Z = 0.4 mM Ag TSCD-PVP NP, 1: 5 Ag: $NaBH_4$, 100 % H_2O_2), Ab_{max} increased rather than decreased potentially due to the presence of unreacted Ag in the original NF, making this seed plus 4 aliquots of $NaBH_4$ a potential recipe for the short λ NF (with λ_{max} = 523 nm and Ab_{max} = 1.121 au see Appendix H, Figure H.8).

However, to give enough absorption in the 400 nm – 500 nm range a λ_{max} < 500 nm would be more suitable.

Details of the experiments undertaken to investigate adding both $AgNO_3$ and $NaBH_4$ to an already synthesised seed and the results obtained are given in Appendix H, Section H.4. Again as more $NaBH_4$ and $AgNO_3$ were added there was a blue-shift in λ_{max} to ≈ 500 nm and a drop in Ab_{max} (even when the increase in Ag concentration is taken into account). However, adding both $AgNO_3$ and $NaBH_4$ to an already synthesised seed appears to be a suitable means of producing the desired short λ NF with a λ_{max} at ≈ 500 nm (average of 4 samples in Figure H.9 is 480 nm) even with the drop in Ab_{max} as the overall reagent concentration of Ag was higher allowing for more flexibility in the broadband mixture recipe.

4.5.1 Selected recipes

After investigating the synthesis, there was one possible recipe for the mid λ NF and three for the short λ NF. The three possible recipes for the short λ NF were all produced using a starting seed. The first used seed Z + 4 x aliquots of $NaBH_4$ (see Appendix H) and gave a λ_{max} of 523 nm and Ab_{max} of 1.121 au (at 1: 4 dilution). The second and third options were both produced by adding $AgNO_3$ and $NaBH_4$ to an already prepared seed and gave very similar results (see Table H.6). The final option utilising less additional $NaBH_4$ was chosen as it had a higher final Ag molarity.

The synthesis for the three selected NF was repeated to check method consistency. The results and details of the final three NF are given in Table 4-3 and Figure 4-10. All three NFs exhibited a different spectral response with three clearly distinct λ_{max} ranges. The repeat synthesis for all three showed the methods were consistent with a maximum σ for the long λ NF λ_{max} of 31.8 nm and a maximum σ for the short λ NF Ab_{max} of 0.061 au. A further discussion on the repeatability of the synthesis methods is given in Section 4.7 where all three synthesises are repeated multiple times. The results of investigating the morphology of the three selected NFs using TEM will be detailed in Section 4.6.3 when the morphology of the resultant broadband mixture is also discussed.

Table 4-3 Three selected recipes for the NFs to be used for the broadband silver NF absorber.

Parameter	**Short λ**	**Mid λ**	**Long λ**
Target λ_{max} range / nm	≈ 500	650 - 750	> 850
Recipe	0.3 mM Ag TSCD-PVP NP, 1: 5 Ag: $NaBH_4$, 50 % H_2O_2 seed + Ag + ½ $NaBH_4$	0.3 mM Ag TSCD-PVP NP, 1: 5 Ag: $NaBH_4$, 100 % H_2O_2	0.1 mM Ag TSCD-PVP NPr 25 mL recipe from Section 3.5.3
Average λ_{max} / nm	468	667	929

Parameter	Short λ	Mid λ	Long λ
$\sigma\,\lambda_{max}$ / nm	24.8	7.9	31.8
Dilution ratio for UV-vis measurement	1: 5	1: 3	none
Average Ab_{max} / au	0.708	1.342	1.577
$\sigma\,Ab_{max}$ / au	0.061	0.030	0.031
N	3	3	3

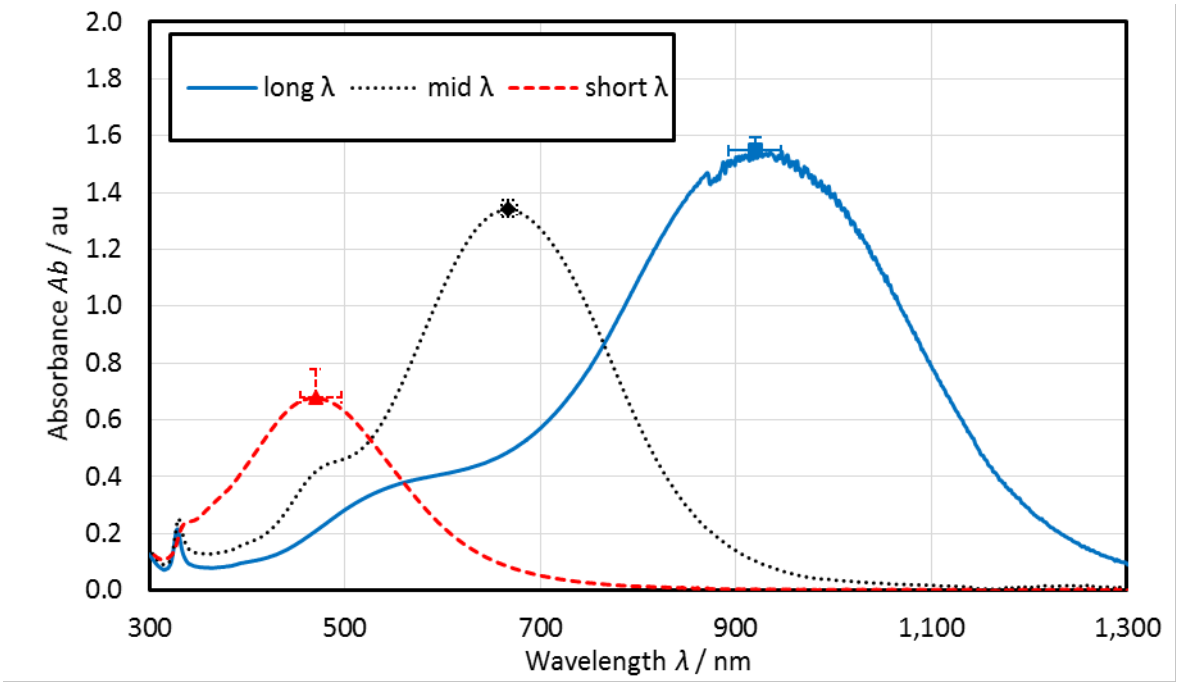

Figure 4-10 UV-vis-IR spectra for the final selected three NFs to be used in the broadband absorber. The error bars show the range of results obtained at the maximum absorbance for the three repeat synthesis. Measured using UV-vis-IR-1 and a 3 mL 10 mm path length disposable cuvette. The mid λ and short λ samples have been diluted as detailed in Table 4-3.

In summary, this Section has highlighted the difficulties with investigating and controlling the Ag NF synthesis, due to the complex reactions that occur to give the different NP shapes. However, it was possible to develop two synthesis methods to produce constantly, a mid λ NF (target λ_{max} = 650 nm – 750 nm) and a short λ NF (target $\lambda_{max} \approx$ 500 nm).

4.6 Silver Broadband Absorber

4.6.1 Introduction

In this Section the potential power absorbed by the three component NF is used as a starting point to estimate η_{Ab} and hence the best combination of the NFs to give broadband absorption over as much of the spectrum as possible. The potential UV-vis spectral response for this absorber is then calculated and compared to the actual spectra obtained for the repeat synthesis of the

components and mixture. The η_{Ab} for this mixture is then estimated and compared to the previous results and those obtained for the Ag NPrs. Finally, the results of investigating the morphology of the two newly developed NF and the mixture using TEM are given along with a brief summary of the Section.

4.6.2 Broadband – calculation of absorption efficiency

In this thesis as described in Section 3.8.2 the measured absorption was used directly to calculate the power absorbed rather than the extinction coefficient used by others (Jeon et al., 2014). This approach, on one hand, overcame the difficulty of estimating the extinction coefficient for non-spherical metallic particles (while only spherical and nanorods have been estimated previously) (Gorji and Ranjbar, 2017a; Jeon et al., 2014). It was valid as absorption was representative of extinction coefficient for NFs of low particle loading without aggregation (i.e. with insignificant scattering effect)(Gorji and Ranjbar, 2015, 2017a). On the other hand, it was difficult to compare the results obtained with those reported through extinction coefficient estimation.

The power absorbed by the three component NFs relative to the incident solar irradiance is shown in Figure 4-11.

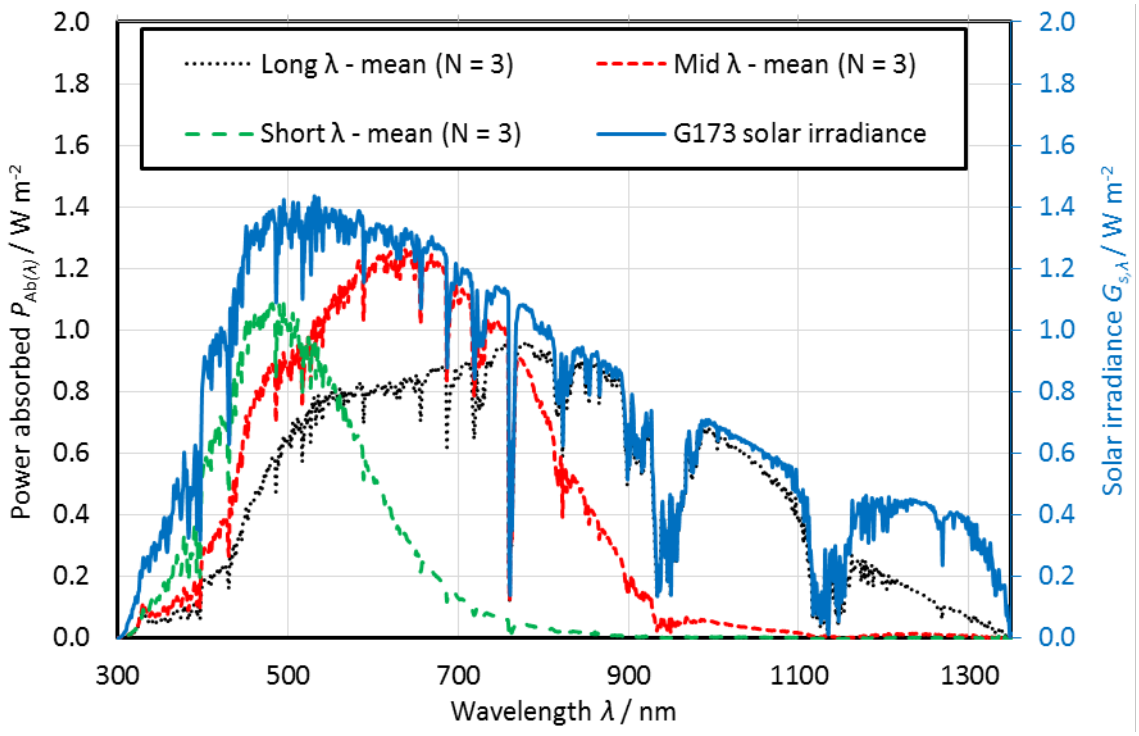

Figure 4-11 Amount of power absorbed P_{Ab} of the G173 ($G_{s,\lambda(dir+cs)}$) with a 10 mm path length by the three component NFs. The secondary vertical axis is for the G173 solar spectrum taken from (ASTM, 2012). The results shown use the diluted components used for the UV-vis-IR measurements.

For the short λ NF, the majority of the power was absorbed in the 300 nm – 600 nm range with negligible power absorbed outside of this region. As the calculation was undertaken using the

diluted NFs used for the UV-vis-IR measurements rather than the actual NF, the actual short λ NF would absorb more of the power in this region than illustrated in a similar manner as the 0.4 mM Ag TSCD-PVP NS 10 mm path length sample in Figure 4-3. The curve for the mid λ NF was broader and even when diluted still absorbed a large proportion of the power in the 600 nm – 800 nm region. The long λ NFs were not diluted prior to measurement and absorbed over a broader region with the majority of the power being absorbed in the 800 nm – 1100 nm range.

Various different η_{Ab} calculations were undertaken using both the diluted component NFs and the undiluted NFs. These are given in Appendix H, Section H.5. The maximum $\eta_{Ab(300\ nm\ -\ 1350\ nm)}$ obtained was 74.12 % (average of 3 values shown in Table H.7) for the undiluted mid λ NF. When calculated over the smaller λ range of 300 nm -900 nm to allow comparison with the Ag NPr samples in Table 4-2, this NF type gave an average $\eta_{Ab(300\ nm\ -\ 900\ nm)}$ of 92.9 % similar to the best NF in Table 4-2 of 94.4 %.

To design the broadband mixture $\eta_{Ab(300\ nm\ -\ 1350\ nm)}$ for a number of different mixtures was calculated using Equation 3-8. The results are shown in Appendix H, Section H.6. The selected calculated combination was 30 % short λ, 20 % mid λ and 50 % long λ (shown in bold in Table H.8) which gave a $\eta_{Ab(300\ nm\ -\ 1350\ nm)}$ of 82.52 %. This mixture was chosen rather than the optimum mixture of 20 % short λ, 30 % mid λ and 50 % long λ ($\eta_{Ab(300\ nm\ -\ 1350\ nm)}$ = 83.14 %) as it minimised the amount of the mid λ NF (which was least stable with storage, see Section 5.4).

The choice of recipe for the short λ NF was also checked by calculating $\eta_{Ab(300\ nm\ -\ 1350\ nm)}$ for the selected 30 % short λ, 20 % mid λ and 50 % long λ mixture using the other two options for the short λ NF. The selected short λ recipe gave a slightly higher $\eta_{Ab(300\ nm\ -\ 1350\ nm)}$ than the other two options (see Table H.9).

To allow comparison with the Ag NPr efficiency calculations given in Table 4-2 and the data obtained from measuring the broadband mixture in the solar simulator, other efficiencies were also calculated for the various potential mixtures. These are given in Table H.10. The value for $\eta_{Ab(300\ nm\ -\ 900\ nm)}$ of 91.09 % for the selected broadband mixture was similar to the value obtained for the centrifuged Ag TSCD-PVP NPrs re-dispersed into ¼ the volume of water of 91.7 % (Table 4-2) and to the maximum $\eta_{Ab(300\ nm\ -\ 900\ nm)}$ value obtained for the undiluted mid λ NF of 92.9 %.

The η_{Ab} results calculated for this broadband absorber consisting of three NF was lower than the efficiency results obtained numerically for a 5 component broadband mixture of 94.7 % to 98.2 % over a λ range of 300 nm – 2500 nm, with improved absorption compared to this broadband mixture in the > 1000 nm region due to the use of Ag nanorods (Mallah et al., 2018). However,

these quoted efficiencies were for a depth of fluid of 100 mm rather than the 10 mm calculated here and were based on numerical estimation of the extinction and absorption spectra.

It is likely that the silver concentration for the broadband mixture is lower than the centrifuged NPrs sample and slightly lower than the mid λ NF (2.47 mM versus 3.0 mM). This could give the broadband absorber an advantage in terms of stability. In addition, as the absorption profile is more closely matched to the solar spectrum compared to the centrifuged Ag TSCD-PVP NPrs, any issues with the absorption primarily occurring close to the front face (in the longer λ region) of the NF giving rise to more heat losses will be reduced (Taylor et al., 2013).

Finally, the value of $\eta_{Ab(300\ nm\ -\ 1350\ nm)}$ for the broadband absorber of 82.52 % was greater than the largest value of $\eta_{Ab(300\ nm\ -\ 1350\ nm)}$ of 74.12 % obtained for the component NFs suggesting that the broadband absorber will give a slightly improved performance in reality than its individual components. The actual performance of the developed broadband mixture compared to the centrifuged Ag TSCD-PVP NPr samples and to its component NFs will be discussed further in Section 5.5 where the performance of the NFs under simulated sunlight will be described.

4.6.3 Broadband – UV-vis-IR

Figure 4-12 shows the results of calculating the absorbance for the mixture based on the spectra obtained for the short, mid and long λ components along with the actual spectra obtained when the mixture was measured. Again, the mean values are shown with the error bars depicting the range of the primary λ_{max}. For the actual mixture there was a red-shift of about 100 nm in the secondary λ_{max} corresponding to the mid λ component (leading to a decrease in Ab_{max} at ≈ 600 nm and an increase at ≈ 750 nm) compared to the calculated value (this was consistent for all three repeats). The primary λ_{max} due to the short λ component in contrast was similar for both the calculated and measured spectra. The cause of the red-shift in the secondary λ_{max} is unknown and is additional information which is obtained by carrying out experimental studies.

The power absorbed by the calculated and measured broadband mixture is shown in Figure 4-13. When compared to the three component NFs (Figure 4-11), it can be seen that both the measured and actual broadband mixture absorbs a larger proportion of the power than each of the three components over a broader wavelength range up to about 1100 nm. In the 1100 nm – 1350 nm range the performance of the mixture reduced, with only a small proportion of the incident solar power being absorbed. The reasons for this are two-fold, firstly the amount of long λ, which is only a weak absorber in this region, in the broadband mixture is only 50 % this reduces the power absorbed in this region due to the Ag NPs. Secondly, as base-line correction for the BF was used to undertake the UV-Vis-IR measurements any absorption due to the BF water in this region would

not be accounted for. As water absorbs more strongly in this region (Mallah et al., 2018), this leads to an under estimation of the power absorbed by the combination of the Ag NPs and the BF (i.e. the NF) above 1100 nm.

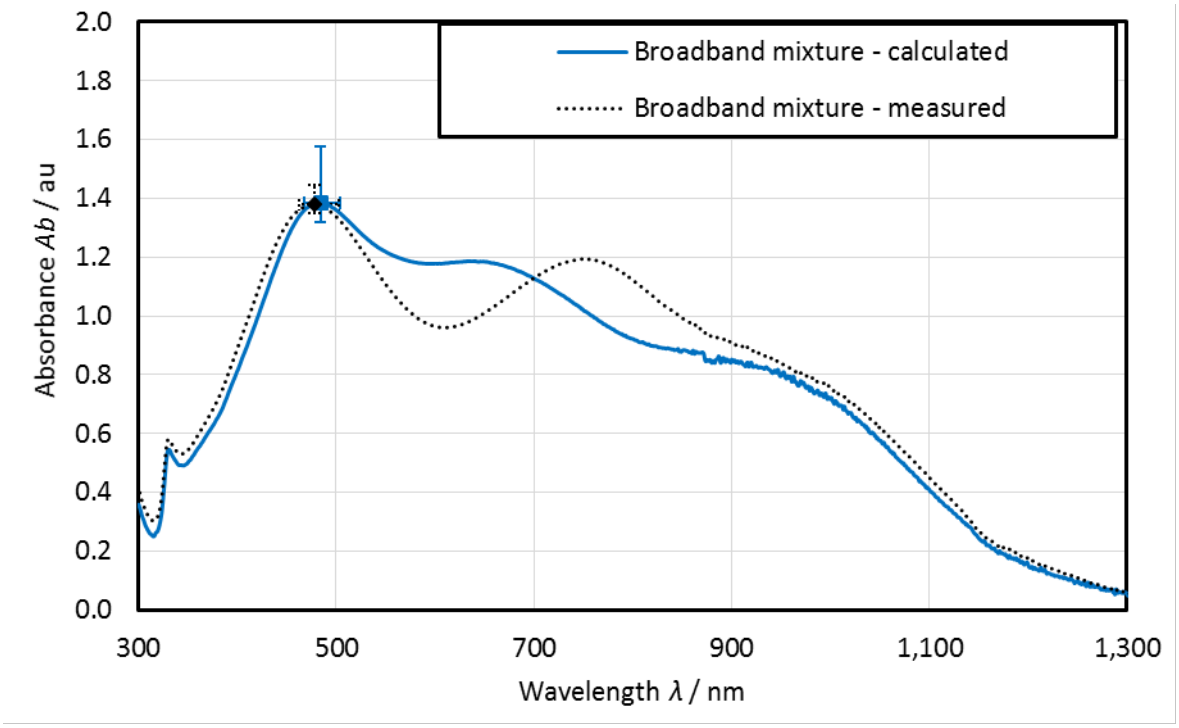

Figure 4-12 Calculated and measured spectra for the broadband mixture (30 % short λ, 20 % mid λ and 50 % long λ). The calculated spectra was obtained from the individual spectra for the component NFs. The error bars show the range of results obtained at the maximum absorbance for the three repeat synthesis. Measured using UV-vis-IR-1 and a 3 mL 10 mm path length disposable cuvette.

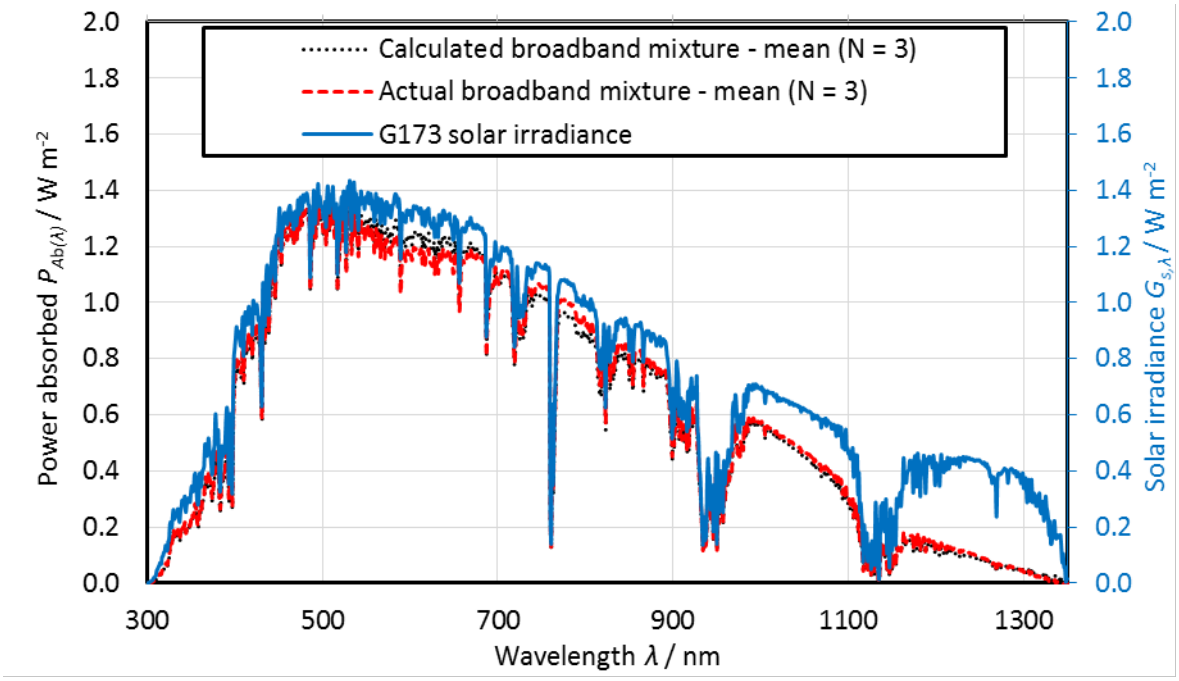

Figure 4-13 Amount of power absorbed P_{Ab} of the G173 ($G_{s,\lambda(dir+cs)}$) with a 10 mm path length by the broadband mixture (calculated and measured). The secondary vertical axis is for the G173 solar spectrum taken from (ASTM, 2012).

In a similar manner to the component NFs, various different η_{Ab} calculations were undertaken. The complete results are given in Appendix H, Section H.7. The measured broadband absorber gave a slightly higher mean value of 83.05 % for $\eta_{Ab(300\ nm\ -\ 1350\ nm)}$ (average of three results in Table H.11) than the calculated mixture. Although there were some differences in the UV-vis-IR spectra between the calculated and measured broadband absorber (see Figure 4-12), when a two-sample t-test was undertaken on the $\eta_{Ab(300\ nm\ -\ 1350\ nm)}$ results comparing the calculated to the measured broadband mixture, there was found to be no significant difference.

4.6.4 Broadband and components – TEM

TEM micrographs of two of the component NFs (the short λ and mid λ NFs) and the broadband mixture consisting of 30 % short λ, 20 % mid λ and 50 % long λ are shown in Figure 4-14. A TEM micrograph of the long λ NF has already been given in Figure 4-6 C and D (Ag TSCD-PVP NPr 25 mL). Size analysis of the particles was undertaken as described in Section 3.7.1 and the results are summarised in Figure 4-15 with the full results being given in Appendix G, Section G.2. The results for the long λ NF have been repeated for easy reference although they have already been illustrated in Figure 4-7 (full results for the long λ sample in Section G.1).

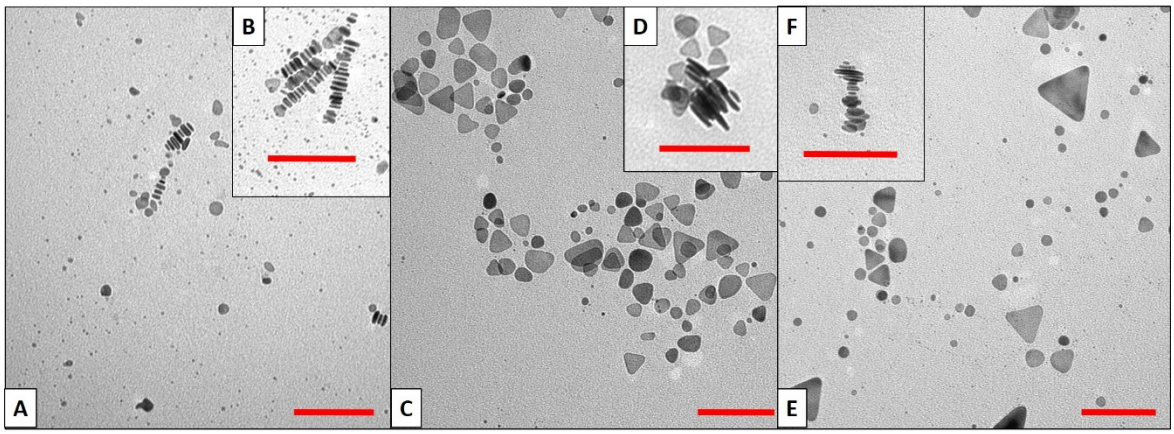

Figure 4-14 TEM micrographs of (A) Short λ NF, (B) insert showing edge of short λ, (C) Mid λ NF, (D) insert showing edge of Mid λ, (E) Broadband mixture (30 % short λ, 20 % mid λ and 50 % long λ) and (F) insert showing edge of broadband mixture NPs. All red scale bars = 100 nm.

Figure 4-15 shows that there were distinct morphological differences between the three NFs used for the broadband absorber. The short λ NF contained mainly small (< 10 nm) particles and slightly larger disc-like particles (diameter 15.9 nm ± 4.2 nm, thickness 5.0 nm ± 1.1 nm). The mid λ NF consisted of mainly small triangles (mean size 27.5 nm ± 7.6 nm) and rounded cornered triangles (mean size 23.7 nm ± 6.7 nm), with a particle thickness of 4.7 nm ± 1.3 nm, whereas the long λ NF as mentioned previously was mainly triangles with a mean size of 52.2 nm and particle thickness of 5.9 nm ± 2.6 nm. The broadband mixture contained all the different types of particles, with larger sharp cornered triangles, smaller rounded corner triangles, disc-like particles and small

(< 10 nm) particles being present. The particle thickness for the broadband mixture was 4.1 nm ± 1.23 nm.

To further investigate the effect of making the broadband mixture on the sizes of the different types of particles two-sample t-tests were undertaken, comparing in turn the broadband mixture particles with the same particle type in each of the component NFs. The results are given in Section G.2.1.

The largest difference in size that was significant was for the triangle particle size of the broadband mixture when compared to the long λ triangle size (31.16 nm for the broadband mixture and 52.2 nm for long λ). This difference was expected as the broadband mixture contained the mid λ NF, which had a smaller average triangle size of 27.47 nm. Conversely as expected the mid λ triangles were found to be significantly smaller than the broadband mixture triangles (using a two-sample t- test).

Surprisingly, there was found to be a significant difference in thickness of the particles in the broadband mixture when compared to its component NFs, with the broadband mixture containing particles that were on average thinner than all the component NFs. However, although significant the difference was of the order of 1 nm, so could be partly due to measurement uncertainty.

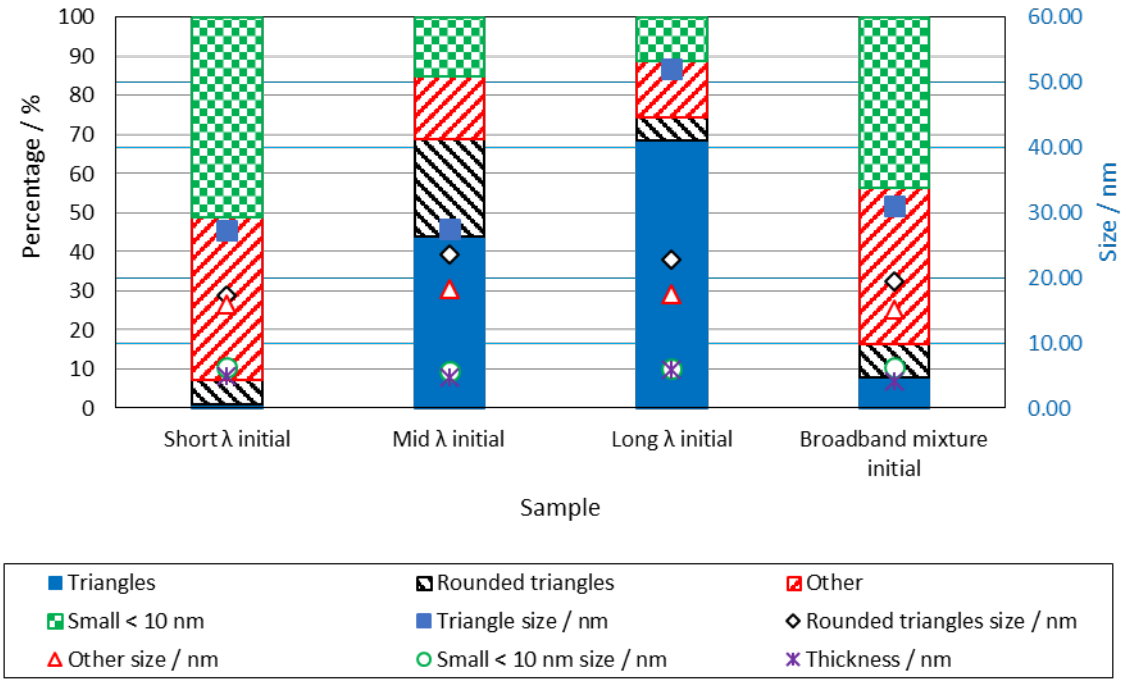

Figure 4-15 Summary of TEM size analysis for the broadband mixture and its component NFs. The percentage of each particle type is shown on the primary vertical axis and the average size of each particle type on the secondary vertical axis.

4.6.5 Summary

The calculation of η_{Ab} for the broadband absorber showed the potential performance of the mixture to be similar to that obtained for the centrifuged Ag NPrs but with a lower silver concentration making the broadband absorber a possible candidate for enhanced solar collection. When the actual broadband mixture was produced by combining the component NFs there were some differences between the calculated and measured spectra obtained showing the additional knowledge that is gained by undertaking experimental studies. This is to the author's best knowledge the first study to have investigated experimentally a broadband absorber based only on different morphologies of Ag NPs. The TEM analysis confirmed the dissimilar morphologies, with the short λ NF containing small and flat disc like particles with a diameter of ≈ 16 nm, the mid λ NF containing small triangles and rounded corner triangles whereas the long λ NF (Section 4.4) mainly comprised of triangles with an edge length of ≈ 50 nm. The mixture as expected contained all the types of NPs.

4.7 Reproducibility of Batch Synthesis

This Section presents the results of investigating the repeatability of the batch manufacturing process for the three component NFs used to produce the broadband absorber. Firstly, the results of repeating the short λ synthesis are summarised, followed by the mid λ NF and the long λ NF. The resultant broadband mixture obtained from combining all the separate batches together is then described and compared to the broadband mixture obtained previously. TEM results are then presented. This Section then concludes with a short discussion on the fitness for purpose of the methods and a summary.

4.7.1 Reproducibility of component nanofluids

The results of undertaking 12 repeat synthesises of the short λ NF are given in Appendix I, Section I.1 using a 30 mL batch size. The results were consistent with those shown in Figure 4-10 with no significant differences in either λ_{max} or Ab_{max} between the two groups of samples (using a two-sample t-test see Appendix F, Section F.1 for t-test definition).

For the Mid λ NF, 8 repeat synthesises were carried out again using a 30 mL rather than 25 mL batch volume. The results (Appendix I, Section I.2) show a ≈ 80 nm range for λ_{max} between samples with a similar average to that obtained in Figure 4-10 of 673 nm. However, when the same samples were re-measured after storage at 4 °C in the dark for 2 weeks (stored diluted, 0.3 mL in 1 mL), there was a blue-shift in average λ_{max} of ≈ 80 nm. Ab_{max} values for the 30 mL batch repeats were similar in both average and range to those obtained previously in Figure 4-10.

The 8 samples were combined together and measured. Just after diluting the combined λ_{max} was similar to the initial average obtained being 659 nm but Ab_{max} was slightly lower. However after being stored diluted and re-measured λ_{max} had again blue-shifted by ≈ 50 nm to 610 nm. The blue-shift observed may therefore be partly due to diluting the mid λ NF to undertake UV-vis measurements. This lack of stability of the mid λ NF will be discussed further in Chapter 5.

To check if any of the differences between the groups of batches of the mid λ samples was significant, analysis of variance (ANOVA) was undertaken as described in Appendix F.2. This is similar to carrying out a t-test but for more than two samples (in this case 3, mid λ 25 mL, mid λ 30 mL and mid λ 30 mL after 2 weeks storage). The λ_{max} results (Appendix I, Section I.2.1) show the after storage samples to be significantly different to the 25 mL and 30 mL batches, which were the same as each other.

Repeat batches (N = 20) of the long λ NF (Ag NPrs) were undertaken using a 30 mL batch volume. The results are provided in Appendix I, Section I.3. For λ_{max} there was an almost 200 nm range of results obtained (average λ_{max} = 889 nm, range 802 nm – 997 nm). This is a large variation in λ_{max} even when the reactions were carried out as consistently as possible and illustrates clearly the problems of controlling the batch synthesis method. Others have shown numerically that a 200 nm blue-shift in λ_{max} can occur when the corners of the prisms become rounded (Kelly et al., 2003), so the sharpness of the corners of the triangles may be influencing λ_{max}. In addition, Carboni also obtained about a 200 nm range when he repeated a similar Ag NPr batch synthesis stabilised with both TSCD and PVP using a 50 mL batch volume (Carboni, 2014).

To check the effect of the 30 mL batch size ANOVA (method described in Section F.2) was undertaken comparing the 30 mL batches to the 50 mL and 25 mL batches (results in Appendix I, Section I.3.1). λ_{max} was significantly blue-shifted for the 50 mL batch size compared to the 25 mL batch (same as t-test in Section 4.4), but the 30 mL batch was not significantly different from either the 25 mL or the 50 mL batch suggesting that the difference may have been only due to the different number of samples in each group.

There was also a large range of results obtained for Ab_{max} (average 1.586 au range 1.364 au – 1.885 au). However, given the noise associated with the measurement > 872 nm (artefact of change of lamp in UV-vis-IR-1) this result should be treated with caution. ANOVA also showed a significant difference compared to the 50 mL batch volume for Ab_{max}, potentially due to the different spectrophotometer (range 200 nm – 900 nm) used for the 50 mL samples.

4.7.2 Reproducibility of broadband absorber

When the combined short, mid and long λ 30 mL batch samples were mixed together to produce the broadband mixture, the resultant broadband mixture was different to that obtained from the 25 mL batches (Figure 4-16). Except for the 25 mL batches the broadband mixture was similar to the value obtained from calculating the likely spectrum from the components. The differences appear to be due to the stability of the mid λ NF.

When trying to account of the cause of the differences it was discovered that the broadband mixture from the 25 mL batches was combined 4 days after synthesising the component NFs, whereas the larger volume of combined broadband mixture from the 30 mL batches was mixed 12 days after synthesising the individual NFs. The potential lack of stability of the mid λ NF may therefore be part of the cause of the difference in the spectra. The stability of the mid λ NF will be discussed further in Chapter 5.

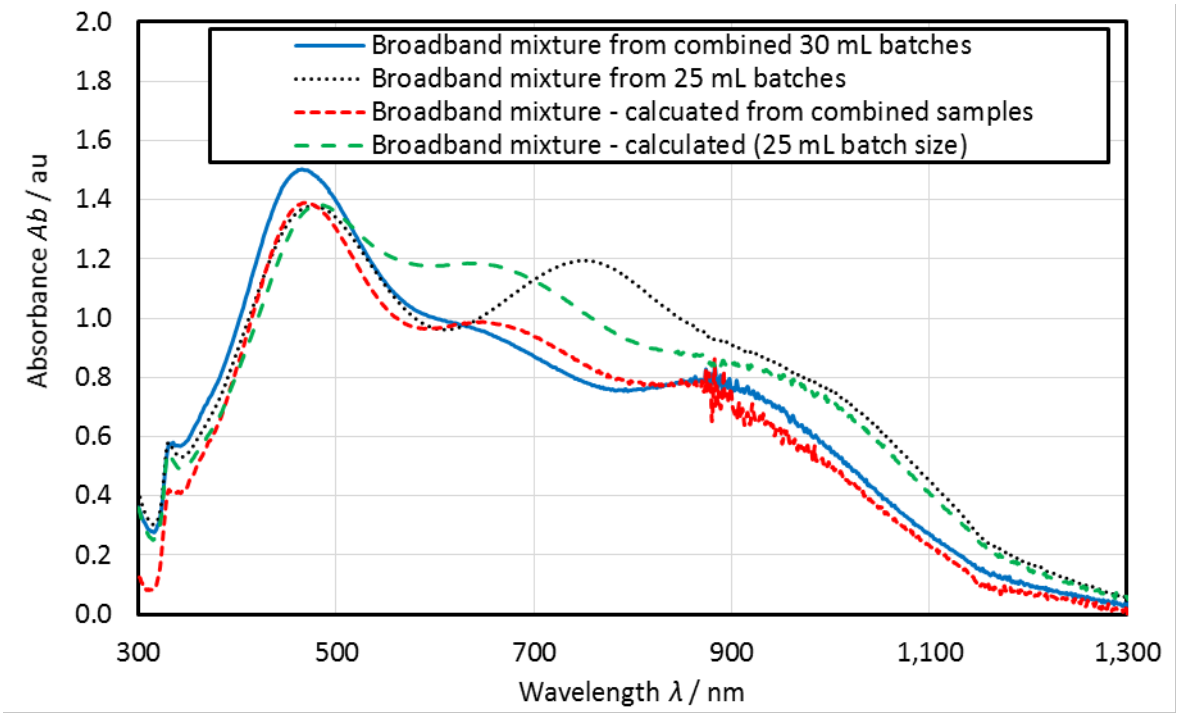

Figure 4-16 Calculated and measured spectra for the broadband mixture. The 25 mL batch data from Figure 4-12 have be included for ease of comparison. Measured using UV-vis-IR-1 and a 3 mL 10 mm path length disposable cuvette.

4.7.3 TEM analysis

TEM micrographs of the component NFs made using the 30 mL batch volume and the resultant combined broadband mixture are shown in Figure 4-17. The size analysis is summarised in Figure 4-18 (full results in Appendix G, Section G.3). On comparing with the broadband mixture and components produced using a 25 mL batch volume (Figure 4-14) it can be seen that the combined

short λ NF had slightly more of the other shaped particles (54 % versus 42 %) and less small particles. The thickness of the combined short λ particles was 4.1 nm (slightly less than the 25 mL short λ NF). The combined mid λ contained less triangles (15 % versus 44 %) than the mid λ (25 mL) NF and more other and small particles. The particle thickness was similar to the short λ NF at 4.1 nm again slightly less than the 25 mL mid λ NF. The combined long λ NF comprised of slightly less triangles (63 % versus 69 %) and slightly more other shaped particles (19 % versus 14 %) than the 25 mL batch size long λ NF with a similar particle thickness of 5.6 nm. The resultant combined broadband mixture contained slightly more other shaped particles (50 % versus 40 %), rounded triangles and triangles than the broadband mixture produced using the 25 mL component batch sizes. The particle thickness was 4.4 nm ± 0.7 nm.

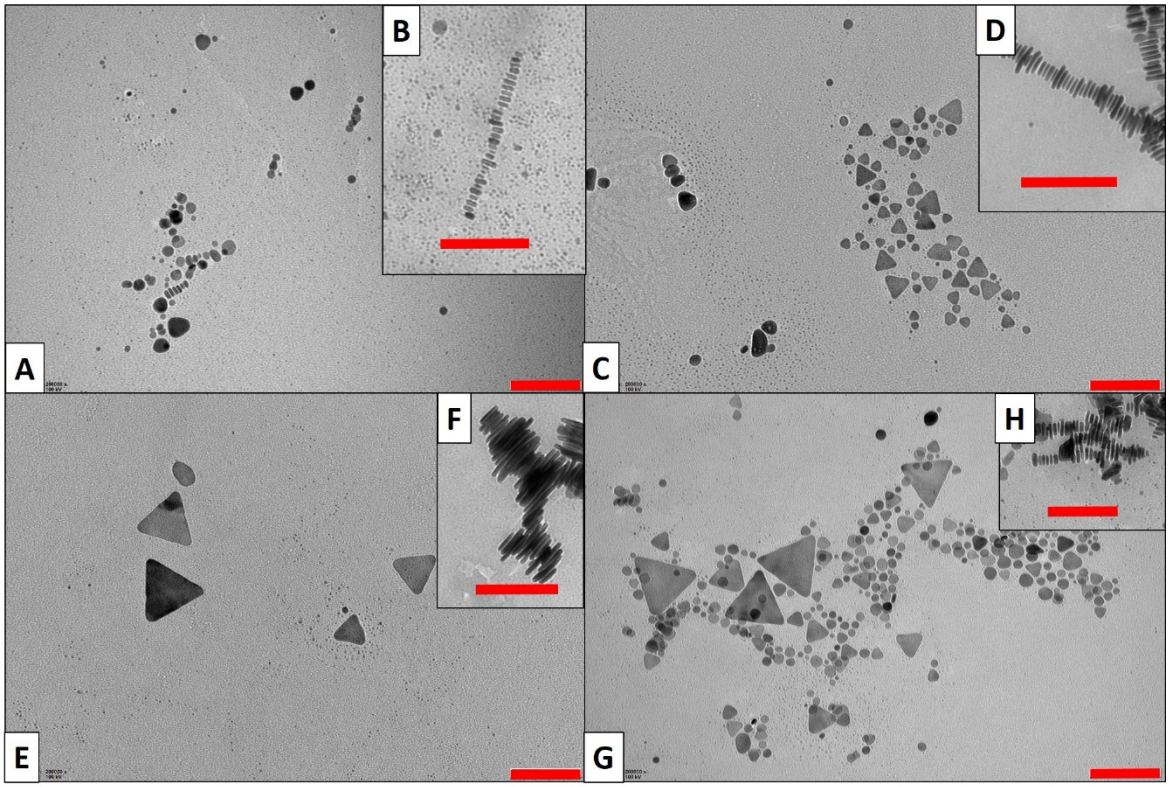

Figure 4-17 TEM micrographs of (A) Combined short λ NF, (B) insert showing edge of combined short λ, (C) Combined mid λ NF, (D) insert showing edge of combined mid λ, (E) Combined long λ NF, (F) insert showing edge of combined long λ, (G) Combined broadband mixture and (H) insert showing edge of combined broadband mixture. All red scale bars = 100 nm.

To compare the sizes from the 25 mL batches with the combined 30 mL batches, two-sample t-tests were undertaken using the method described in Section F.1. The complete results are given in Appendix G, Section G.3.1. The largest significant differences were obtained for the long λ NF, rounded triangles and other particles, which were both significantly smaller for the samples produced from the 25 mL batches. However the size of the majority of the particles (i.e. the triangles) were not significantly different for the long λ NFs. The comparison of the sizes for the mid λ samples showed significant fairly large differences in size for the triangles and rounded

triangles, with the combined mid λ giving rise to smaller triangles and rounded triangles. This decrease in size supports the blue-shift observed in the UV-vis spectrum of this sample (Figure I.2) compared to the 25 mL mid λ batches (Carboni, 2014).

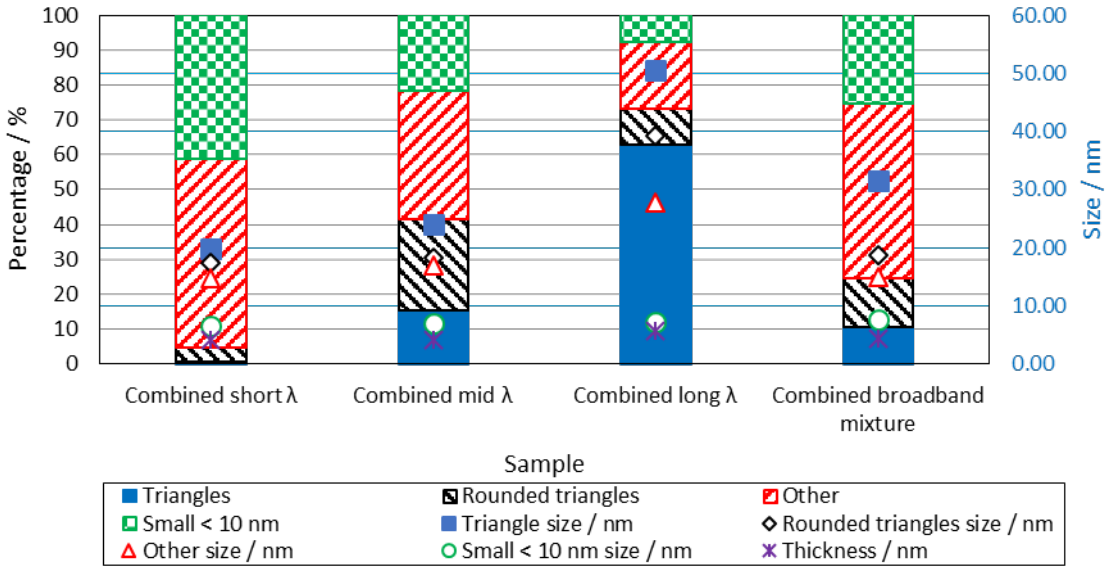

Figure 4-18 Summary of TEM size analysis for the combined broadband mixture and its component NFs (made using a 30 mL batch volume). The percentage of each particle type is shown on the primary vertical axis and the average size of each particle type on the secondary vertical axis.

4.7.4 Summary

Of the three synthesis methods only the short λ method gave consistent results for λ_{max}, Ab_{max} and the TEM size and shape distribution. The mid λ synthesis varied by ≈ 80 nm in λ_{max} and there were potential issues with the stability of this NF with storage at 4 °C in the dark (to be discussed further in Chapter 5), especially when diluted for the UV-vis measurements. The variation in λ_{max} for the long λ NF was even greater (≈ 200 nm), illustrating the difficulties in reproducing the geometry of the nanoprisms accurately. Although these results are consistent with those seen by others (Carboni, 2014), this batch method requires considerable improvement to allow accurate tuning of λ_{max}. One possible solution would be to use a continuous flow reactor to control the mixing better, potentially leading to more constant results (Carboni et al., 2013).

When the component NFs were combined there were some differences obtained in the resultant broadband mixture spectra. The position of the primary peak corresponding to the short λ NF was similar but the secondary peak due to the mid λ NF was blue-shifted. This may be due to the instability of the mid λ NF. Further synthesis development focused primarily on improving the stability of the mid λ NF would therefore be needed to produce consistently the broadband absorber.

4.8 Conclusions, Implications and Overall Summary

4.8.1 Conclusions

For the NS, the stability to aggregation of the NFs were improved by adding PVP in addition to TSCD, allowing for more concentrated NFs to be produced. However, the potential solar performance of the NS TSCD-PVP NFs was reduced compared to the NS NFs without PVP. Even without PVP the lack of a broad spectral absorbance for NFs containing only Ag NS would make them unsuitable on their own for enhancing solar capture.

For the Ag NPrs there was considerably more variation in λ_{max} illustrating the difficulties in controlling the batch synthesis method to produce Ag NPrs consistently. Again the addition of PVP showed an increased stability to aggregation than the Ag NPrs manufactured without PVP. In addition, λ_{max} was red-shifted compared to the non PVP containing samples. Centrifuging to produce a more concentrated NF lead in contrast to a blue-shift in λ_{max} potentially due to the rounding of the corners of the prisms and a reduction in particle size. When the possible solar performance of the centrifuged Ag NPrs was estimated high values of η_{Ab} were obtained making these NFs potentially suitable for enhancing solar capture.

By varying the amount and timing of the reagents added during the synthesis of silver NFs it allowed for the development of recipes to produce 2 additional morphologies of silver nanoparticles, which gave distinct absorption profiles covering a broad range of wavelengths. These two NFs were combined with the Ag TSCD-PVP NPr NF (long λ) to give a broadband absorber tailored to the incident solar radiation. This is to the author's knowledge the first study to deliberately synthesise and measure using UV-vis a broadband absorber based on silver NFs and demonstrates the principal. A potentially better performing broadband absorber based on 5 different types of silver nanoparticles has been designed by others using a numerical study but that broadband absorber was not synthesised experimentally (Mallah et al., 2018). A broadband TiO_2 coated silver NS NF was also produced by Li et al for enhanced steam generation containing a much greater NP fraction (200 ppm) and hence possibly considerable NP aggregation, which may have been the cause of the broad spectral response they reported (Li et al., 2017). This broadband absorber was hence not based on different morphologies of silver.

The potential performance of the broadband mixture in solar applications was estimated ($\eta_{Ab(300\ nm\ -\ 900\ nm)}$ = 92.9 %) and was similar to that obtained for a more concentrated NF based on centrifuged Ag NPrs and to one of its component NFs (mid λ), but the broadband mixture is likely to have advantages in terms of stability and reduced heat loss due to the lower concentration of silver and better matching with the solar spectrum.

When the reproducibility of the batch synthesis methods for the three NFs used to produce the broadband absorber was investigated only the short λ synthesis produced consistent results. The mid λ synthesis appeared to have problems with stability and the long λ synthesis produced a large variation in λ_{max} of ≈ 200 nm. There were also issues with consistency of the final broadband mixture potentially caused by the lack of stability of the mid λ NF.

4.8.2 Implications

Although a more concentrated Ag NPr NF and the developed broadband absorber have been shown to offer potential for enhancing η_{Ab} and hence solar thermal capture, the actual performance of these NFs needs to be measured. This will be discussed in Chapter 5.

The work in this Chapter has hinted that there may be an issue with the stability on storage of the developed mid λ NF. Further work on measuring the stability of the Ag NPrs, the component NFs and the broadband absorber mixture under application relevant conditions would be needed before these NFs could be recommended for use in solar collectors. This will also be discussed in Chapter 5.

As only the synthesis method for the short λ NF was shown to be consistent enough to be fit for purpose, further work on the synthesis methods for the more problematic morphologies such as those of the mid λ and long λ NFs is required. This is of lower priority than the measurement of the actual performance and an assessment of the stability of the NFs under application relevant conditions. If the developed NFs are found to have either a low actual performance or significant stability issues this would preclude their use in solar applications and no amount of work on improving the consistency of the synthesis methods would change this.

4.8.3 Summary

A short summary of the main points covered in this Chapter and the conclusions is given in Table 4-4.

Table 4-4 Chapter 4 Summary.

Section	**Covered**	**Conclusions / outcomes**
Ag NS	Synthesis of Ag NS with / without PVP, calculation of η_{Ab}	λ_{max} ≈ 400 nm with low variation. PVP improves stability to aggregation but reduces broadness of peak reducing η_{Ab}. η_{Ab} too low for enhanced capture

Section	Covered	Conclusions / outcomes
Ag NPrs	Synthesis of NPrs with / without PVP, morphology (TEM), effect of centrifuging, calculation of η_{Ab}	λ_{max} > 750 nm with high (≈ 100 nm) variation. ≈ 50 nm triangles produced. Centrifuging gives blue-shift in λ_{max}, adding PVP gives red-shift. Centrifuging leads to a rounding of the corners of the triangles and a reduction in particle size. η_{Ab} for more concentrated centrifuged samples high, giving potential for solar applications
Investigating synthesis	Effect of overall concentration, changing H_2O_2 amount, Ag: $NaBH_4$ ratio and timing of reagent addition investigated	Highlighted difficulties with investigating synthesis. Two methods for a short λ and a mid λ NF developed
Silver broadband absorber	η_{Ab} used to design broadband absorber. Actual mixture made and measured. η_{Ab} calculated. TEM undertaken on broadband mixture and components	Novel broadband mixture = 30 % short λ, 20 % mid λ, 50 % long λ. η_{Ab} similar to centrifuged Ag NPrs but Ag concentration lower. TEM – short λ – disc like particles ≈ 16 nm, mid λ – small rounded triangles and triangles, mixture all types.
Reproducibility of batch synthesis	Batches of 30 mL of 12 x short λ, 8 x mid λ, and 20 x long λ, combined broadband absorber produced and compared to previous results. TEM compared to previous	Only short λ consistent, mid λ potential issues with stability, long λ large ≈ 200 nm variation in λ_{max}. Issues with repeatability of broadband absorber due to stability of mid λ NF.

Chapter 5 Silver Nanofluid (NF) Performance and Stability

5.1 Publications from this Chapter

1. Kimpton, H., Stulz, E., Zhang, X., 2020. Silver nanofluids based broadband solar absorber through tuning nanosilver geometries. Solar Energy, 208, 515-526, https://doi.org/10.1016/j.solener.2020.08.018 (Kimpton et al., 2020b).
2. Kimpton, H., Cristaldi, D.A., Stulz, E., Zhang, X., 2020. Thermal performance and physicochemical stability of silver nanoprism-based nanofluids for direct solar absorption. Solar Energy, 199, 366-376, https://doi.org/10.1016/j.solener.2020.02.039 (Kimpton et al., 2020a).
3. Kimpton, H., Zhang, X., Stulz, E., 2021. The temperature stability and development of a broadband silver nanofluid for solar thermal applications. Energy Reports, 7, 87-96, https://doi.org/10.1016/j.egyr.2021.02.049 (Kimpton et al., 2021).

5.2 Introduction

The performance of various Ag NFs obtained from static tests in a solar simulator is presented in this Chapter along with the results of assessing the stability of the Ag NFs under application relevant conditions.

Firstly, the literature pertaining to performance of Ag NFs both when used in conjunction with a surface absorber, and when used for volumetric absorption is presented. This is followed by a brief examination at any stability studies that have been carried out on Ag NFs in the literature.

The next Section 5.5 details the results of measuring the thermal performance of five different water based Ag NFs in static tests in the solar simulator. The temperature rise is measured and used to estimate the photo-conversion efficiency (η_{PE}) which is then compared to the efficiency η_{Ab} values calculated in Chapter 4 and to literature.

The final main Section in this Chapter presents the results obtained from the various stability trials undertaken, roughly in order of ascending severity, thus building a picture of the potential stability issues that would need to be addressed if Ag NFs were to be used for solar applications. Firstly, the results of measuring the stability under ideal storage conditions of 4 °C in the dark are given (colloidal stability). This is followed by an assessment of the stability with exposure to an

elevated temperature of 70 °C. The effects of simulated sunlight (SSL) and natural sunlight exposure are then discussed. What happens to the Ag broadband absorber NF under flowing conditions (i.e. potential mechanical damage) is then illustrated. This Section concludes with the potential issues of changing from a water base-fluid (BF) to propylene glycol (PG) a more suitable BF for solar applications.

This Chapter finally finishes with some conclusions, implications and a summary.

5.3 Literature Review on Performance of Nanofluids (NFs)

This subsection briefly describes the literature on performance of NFs in solar collectors. It looks firstly at any literature on the performance of solar collectors containing a selective surface absorber. Literature pertaining to the performance of volumetric or DASCs is then presented.

5.3.1 Performance when used with a selective surface absorber

For silver NFs used in conjunction with surface absorbers to improve heat transfer a number of researchers have investigated the enhancement in thermal conductivity obtained. One group of researchers found a thermal conductivity improvement of between 9 % – 18 % for silver NFs containing up to 1000 ppm of silver (Salehi et al., 2013) while another group measured a 12 % improvement for a silver NF containing dendritic silver NPs (Lee et al., 2016). Similar levels of enhancement were also found for Ag in a different BF of ethylene glycol (9 % – 18 %) (Sharma et al., 2011). This may imply that the BF does not affect the thermal conductivity but this is not correct with lower thermal conductivity BFs tending to give a larger enhancement (Xie et al., 2011). It should be noted that the concentration of NPs required to show thermal conductivity enhancement tend to be considerably higher than the concentrations used for volumetric absorption. Of the metals used for NFs, silver has the highest thermal conductivity and is hence likely to show the greatest enhancement in thermal conductivity when used in a NF (Babar and Ali, 2019).

A number of studies (both numerical and experimental) have estimated the potential collector η_{PE} improvements that would be obtained from using NFs in FPCs obtaining improvements of 0 % - 22 % depending on how the estimation was undertaken (see Section 2.5.4 for a discussion on the issues with comparing results for η estimations) and the nature and concentration of NF investigated (Alim et al., 2013; Nasrin and Alim, 2014; Polvongsri and Kiatsiriroat, 2014; Roy et al., 2015).

5.3.2 Performance when used as a volumetric or direct absorber

As discussed in Section 2.7.5, considerable care needs to be taken when comparing the performance results obtained from different studies. The highest value of η_{PE} obtained for a volumetric absorber utilising a broadband Ag NF was 95 % - 98 % in a numerical study by Mallah et al (Mallah et al., 2018), whereas other studies using Ag NFs have obtained η_{PE} values of the order of ≈ 35 % – 55 % less than or similar to current FPC (Amjad et al., 2018; Chen, M. et al., 2017; Gorji and Ranjbar, 2016; Liu et al., 2020). These studies quoting lower η_{PE} values all used Ag NS rather than Ag NPrs or a broadband Ag NF. Ag NS have been shown in Section 4.3.1 to be unsuitable on their own to enhance η, however, two of them (Chen, M. et al., 2017; Liu et al., 2020) did investigate the use of a hybrid NF containing Ag to broaden the absorption peak and hence enhance η_{PE}. Walshe et al "accidently" produced an Ag NF (i.e. a broadband Ag NF) containing two absorption peaks at ≈ 430 nm and 600 nm, which gave a η_{PE} of 70 % – 90 % depending on NF concentration (Walshe et al., 2019). The tailoring of the NF to provide absorbance over a wide spectral range is hence vital to improve η_{PE}.

Even though the NF utilised provides broadband absorbance there is a lack of studies that directly compare the performance of a FPC with a volumetric absorber. Of the studies that do (not using Ag NF), one found an enhancement (Nasrin et al., 2015), the other a reduction (Li et al., 2016). Further larger scale studies would therefore be needed on volumetric collectors with optimised NF absorption characteristics and geometries before volumetric systems can be recommended for enhancing efficiency.

5.4 Literature Review on Stability Studies of Nanofluids (NFs)

This subsection presents some of the literature pertaining to stability studies. It focuses on stability studies undertaken using Ag NFs. As discussed in Section 2.8.2, stability of the NF for solar applications is a major challenge especially for silver NFs.

Only a handful of papers appear to have investigated the effect of temperature and or light on Ag NFs and hybrid Ag NFs for solar applications. Some others have looked at both heat and light as a way of producing anisotropic Ag NPs and hence tend to focus on short timeframes and on NF solutions that enhance rather than reduce the rate of change. For assessing colloidal stability many researchers rely on zeta-potential measurements (see Appendix C, Section C.1), which is not suitable for NFs that are sterically stabilised and those that do assess longer term colloidal stability do not always provide sufficient experimental details of the storage conditions. In addition, colloidal stability tends not to be the main focus of the paper presented and hence any

NF storage studies to assess colloidal stability are buried within the paper text (or supplementary information) making a thorough review of the literature problematic.

A number of studies that have either assessed colloidal stability or exposed silver NF to heating or light are summarised in Appendix K, Table K.1. The most relevant of these studies is the work of Taylor et al (Taylor et al., 2018) on Ag nanodiscs and SiO_2 coated Ag nanodiscs in water BF. They investigated the effect of heat, UV light and SSL. In a different paper by the same group they also exposed the SiO_2 coated NFs to natural sunlight under flow conditions and mentioned that the NF were stable for 9 months, but no storage conditions were given and the UV-vis spectra before and after natural sunlight exposure / flow conditions were not provided (Crisostomo et al., 2017).

Even less information is available on the stability of Ag NFs under flowing rather than static conditions. Zeng et al (Zeng et al., 2010) used centrifuging at different rates as a surrogate to investigate mechanical / flow damage finding that an increase in r.c.f. lead to a greater blue-shift in the UV-vis spectra and a rounding of the corners (assessed using TEM) of the triangular NPs in a similar manner to elevated temperature exposure.

Given the general lack of stability trial data in the literature, there is an urgent need to undertake more stability trials under application relevant conditions for Ag NFs so that any future improvements due to an appropriate stabilisation strategy can be quantified.

5.5 Silver Nanofluids Performance under Simulated Sunlight (SSL)

5.5.1 Introduction

The thermal performance of various NFs obtained from direct measurement of the temperature rise using the solar simulator is described in this Section. Initially the results obtained for the technique using repeat measurements of water to determine the base-line performance are presented. The subsequent two subsections then give the results for the five Ag NFs evaluated using this technique with the first of these subsections providing the results obtained using set-up A in the solar simulator and the second set-up B. For all the NFs the photo-conversion efficiency η_{PE} is calculated directly from the temperature measurements and compared to the efficiency results obtained from the UV-vis spectra and from literature. A short summary then completes this Section.

This is one of the first studies to measure directly the temperature rise in a solar simulator of anisotropic Ag NFs with strong absorbance in the near-IR wavelength (> 750 nm) and the first study to measure an Ag broadband absorber NF by combining three different anisotropic Ag NFs.

5.5.2 Solar simulator set-up

This subsection describes the results of undertaking repeat measurements of the water BF in the solar simulator using the two different set-ups described in Section 3.8.3 and the subsequent efficiency η_{PE} calculations. This gives a base line performance that can be used for comparison with the subsequent testing of the different NFs.

The emission spectra of the solar simulator compared to sunlight is shown in Appendix J, Figure J.1 and is broadly comparable over the range measured, although the lamp has some notable differences especially a large peak at $\lambda \approx 825$ nm. To account for the differences between the spectrums $\eta_{lamp(330\ nm\ -\ 1100\ nm)}$ was calculated to allow for comparison of η_{PE} with the UV-vis estimations (see Section 3.8.3).

For set-up A and set-up B the reproducibility of the method was tested by repeat measurements of the water temperature. For set-up A (full results in Appendix J, Table J.1), the average temperature change ΔT was 18.7 °C - 21.8 °C after 1 h in the solar simulator (dependent on position) and the slope of the graph $\Delta T/\Delta t$ was 0.016 °C s^{-1}– 0.020 °C s^{-1}. The pooled standard deviation (pooled σ) for ΔT was 1.096 °C, and 0.0015 °C s^{-1} for the slope $\Delta T/\Delta t$. However, the position of the sample in the simulator was found to be a significant factor with the sample in the middle (Md) position having consistently higher values. It was therefore necessary to rotate the batches in the simulator in a consistent manner to ensure that each batch of each type of NF had the same amount of time in each position over the total number of testing cycles. This allowed a statistical analysis of the results. For set-up B (full results in Table J.2), $\Delta T/\Delta t$ was lower at 0.006 °C s^{-1} with a lower σ of 0.0003 °C s^{-1} due to only using the middle position and undertaking less repeats ($N = 3$ versus $N = 27$).

The subsequent calculation of η_{PE} for water using set-up B gave an average value of 20.51 % (using Equation 3-10 and the values given in Table 3-3 – full results in Table J.2). When the same calculation was performed for set-up A for water there was found to be a considerable difference in the results obtained with the values of η_{PE} being much greater for set-up A (Average = 44.8 %). This discrepancy is likely to be due to the measurement of the intensity of the lamp I_L for set-up A. For set-up A the lamp intensity was measured using a Voltacraft PL-110 SM solar meter. This meter is designed for measuring sunlight and has a relative spectral sensitivity maximum at ≈ 940 nm. It then uses an algorithm to calculate the intensity of the whole spectrum assuming the shape of the spectra is the same as sunlight. However, the lamp output was significantly different in the > 800 nm range (see Figure J.1), making this measurement of I_L suspect. It was not possible to double check the measurement for set-up A using the "ReRA System" calibrated silicon cell used to measure I_L for set-up B as the solar simulator power supply and lamp had broken and

been repaired in the interim period between measurements. It should be noted that although the results from the solar simulator tests using set-up A have been published (Kimpton et al., 2020a), the subsequent calculation of η_{PE} using the erroneous figure of 1500 W m^{-2} was not carried out at this time and only the values of ΔT and $\Delta T/\Delta t$ were presented and discussed.

The η_{PE} value of 20.51 % in set-up B was therefore used as a control value for water and this value used to estimate I_L for set-up A and hence η_{PE} for the subsequent NFs tested using set-up A.

5.5.3 Silver Nanoprisms

This subsection presents the results obtained by undertaking repeat measurements of an Ag NPrs NF using set-up A in the solar simulator comparing the results to water (Section 5.5.2) and any literature values available. The η_{PE} of this NF is calculated and compared to the results obtained directly from the UV-vis spectra efficiency calculations in Section 4.4.1.

The measurement of mean change in temperature ΔT on exposure to SSL using set-up A for Ag TSCD-PVP NPrs centrifuged and re-dispersed into ¼ volume of water are shown in Figure 5-1 along with the values for the water BF. Both the Ag NPrs and water showed an initial linear increase in temperature, followed by a levelling out of the temperature rise. The Ag NPr NF reached a maximum average ΔT of 36 °C – 44 °C, whereas the water only showed a rise of 19 °C – 22 °C after 1 h.

The results from the SSL exposure were analysed using response surface methodology utilising Minitab 17.3.1 (for a brief description of response surface methodology see Appendix F, Section F.3). The results (Appendix J, Section J.3, and Figure J.2) show that the batch number (1 - 3) and time (1 h - 9 h) did not significantly affect ΔT. However, the nature of the NF and the position in the solar simulator caused ΔT variations. The mean results in Figure 5-1 showed that the middle Md sample position for set-up A (see Figure 3-2) gave a larger ΔT than the other two positions. In addition, the Ag NPr NF had a much higher final temperature and slope, $\Delta T/\Delta t$ than water (see Appendix J, Table J.4 for results). The increase in ΔT for the NF was about double that of water and the value of $\Delta T/\Delta t$ was ≈ three times that of water.

The results obtained were higher than those observed by Otanicar et al (Otanicar et al., 2010) and Hjerrild et al (Hjerrild et al., 2016), but of a similar magnitude to others (Al-Nimr and Al-Dafaie, 2014; Bandarra Filho et al., 2014; Chen et al., 2016). This may be attributed to the test geometry and NF Ag concentration used in this work that was optimised to maximize the NF absorption of the solar radiation. In contrast, Ag NPs are known to increase the thermal conductivity of the fluid (Lee et al., 2016; Roy et al., 2015; Salehi et al., 2013). This is likely to have a detrimental effect on

ΔT at 3600 s with an increase in thermal conductivity leading to an enhancement of losses to the surroundings and a lower stagnation temperature. This may explain why the improvement in the slope $\Delta T/\Delta t$ was larger than the improvement in ΔT.

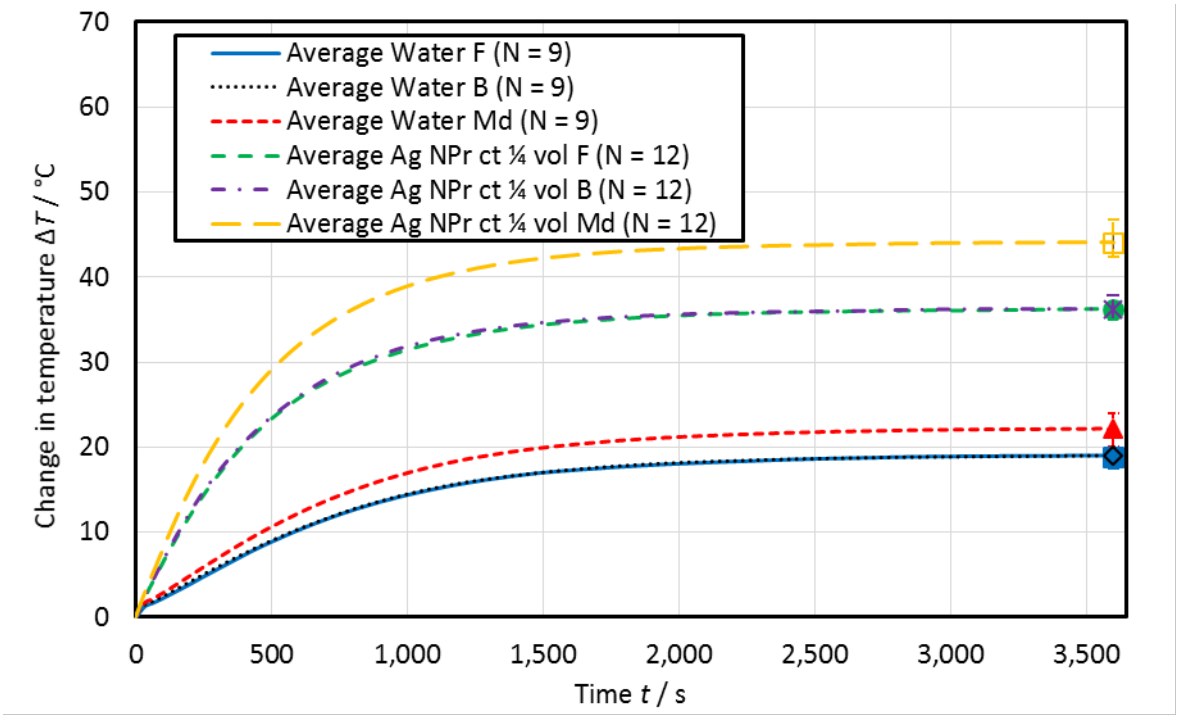

Figure 5-1 Mean change in temperature (ΔT) as a function of SSL exposure time using set-up A. Position in solar simulator = Back (B), middle (Md) and Front (F). The error bars show the range in results for ΔT at t = 3600 s.

When the value of η_{PE} for the Ag NPr NF was estimated using the 20.51 % value for water and compared to the calculated $\eta_{lamp(330\ nm\ -\ 900\ nm)}$ obtained from the UV-vis data, η_{PE} was > 80 % and $\eta_{lamp(330\ nm\ -\ 900\ nm)}$ was > 90 % (see Table J.5). Although it appears that the $\eta_{lamp(330\ nm\ -\ 900\ nm)}$ results were greater, when the measurement uncertainty of ≈ 10 % (see Table E.4 and Table E.5) is taken into consideration the results obtained from the two methods are similar. Comparing the value of η_{PE} with the calculated η value in Table 4-2 of 91.7 % for the same NF also shows good agreement between the two methods of estimating performance. The similarity of the results obtained therefore enables calculations based on UV-Vis measurements to be used with confidence for the rapid identification and screening of NFs for their potential performance in solar applications.

A less concentrated (0.1 mM) Ag TSCD-PVP NPr NF (long λ) was also measured in the solar simulator using set-up B. The results from this NF will be discussed in Section 5.5.4 along with the results for the broadband NF and its other component NFs (short λ and mid λ).

In summary, the centrifuged Ag TSCD-PVP NPr NF produced a temperature rise of ≈ 40 °C after 1 h, approximately twice that of water alone and an efficiency η_{PE} of ≈ 80 % - 85 % again higher

than the ≈ 20 % for water. This result for the Ag NPrs was comparable with that obtained from UV-vis measurements.

5.5.4 Broadband Absorber

This subsection presents the results of measuring the temperature rise of the novel broadband absorber NF and its three component NFs, short, mid and long λ when subjected to SSL using set-up B in the solar simulator. This temperature rise is then used to estimate the η_{PE}. The results obtained are compared to those obtained directly from the UV-vis spectra (see Section 3.8.2) and to literature.

The thermal performance of the broadband absorber and its component NFs subject to SSL exposure was measured by monitoring the temperature rise over a period of 10 minutes using set-up B (see Section 3.8.3). The results are shown in Figure 5-2, along with the profile for water. The initial temperature recorded at the start of each experiment was 25.7 °C (σ = 0.6 °C, N = 39). The NFs all exhibited an initial linear temperature rise with time, followed by a decrease in the rate of temperature rising. The trend indicated that, if the time of the experiments was extended, the temperature profile would level out as the stagnation temperature was reached (i.e. the rate of heat loss became equal to the rate of heat gain) as seen in Figure 5-1 for set-up A.

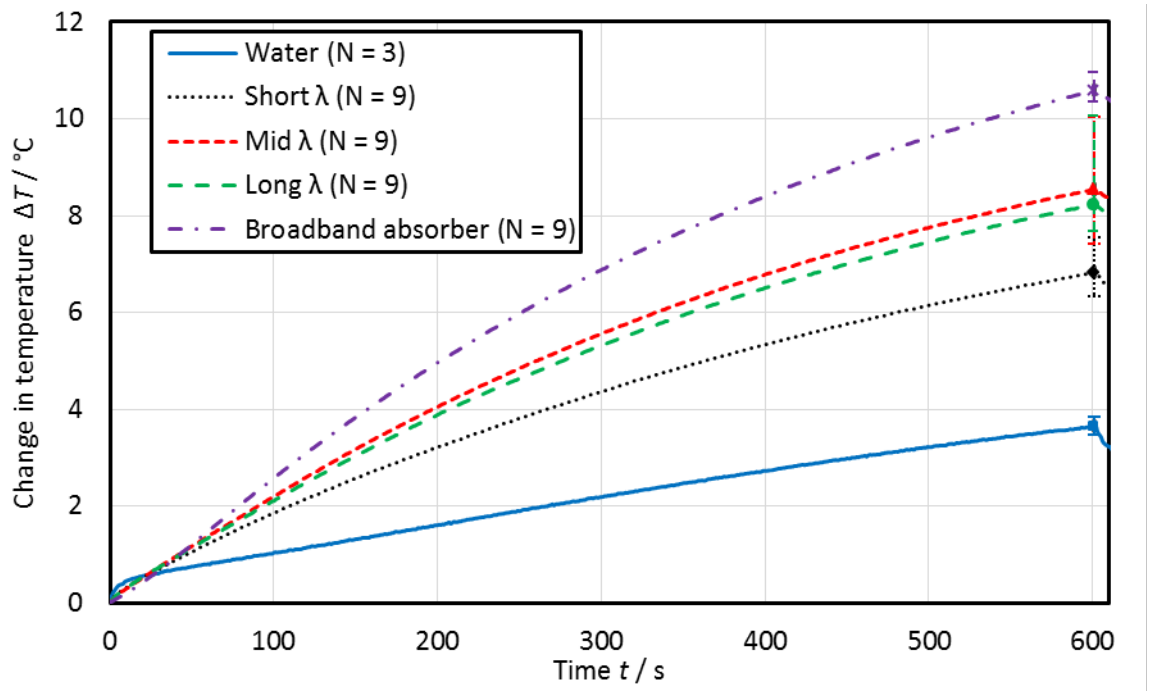

Figure 5-2 Mean change in temperature (ΔT) as a function of SSL exposure time using set-up B. The error bars show the range in results for ΔT at t = 600 s.

As shown in Equation 3-10, with a given absorber and irradiation source, the thermal performance is determined by $\Delta T/\Delta t$, the initial slope of the linear temperature rise. Therefore,

for these experiments it was not deemed necessary to continue the experiment beyond the linear rise stage, or until the saturation temperature was reached. In addition, if care had not been taken to maintain a consistent starting temperature of the NF, there may have been some variation in the length of the linear portion of the graph, requiring that the slope was calculated over a smaller Δt. However, it should not greatly affect the value of η_{PE} obtained (especially when the experimental uncertainties of ≈ 10 % are considered), unless a significantly higher starting temperature at or near the stagnation temperature was used leading to no linear region on the graph. Further investigation of the effect of starting temperature would be needed to confirm this.

All of the NFs exhibited a significantly greater ΔT than water with the broadband NFs showing the largest increase, followed by the mid λ, long λ and then the short λ NF. The value of $\eta_{lamp(330\ nm - 1100\ nm)}$ was calculated for the 3 component NFs using the initial spectra, a spectra obtained after 4 weeks storage in the dark and the spectra obtained after SSL testing to give $N = 9$ and the value of η_{PE} estimated using Equation 3-10 and the parameters in Table 3-3. For the broadband absorber NF the spectra calculated from the component NFs was also used to calculate $\eta_{lamp(330\ nm - 1100\ nm)}$ giving $N = 12$. To ascertain the relative performance of the four different NFs ANOVA was undertaken on the η results (see Appendix F.2). The results are shown in Table 5-1. The η_{PE} for water (shown in Appendix J, Table J.2) were also used in the ANOVA tests for η_{PE} and gave a confidence interval of 14.61 % – 26.34 % and a grouping letter of D.

From Table 5-1 there can be seen to be good agreement between the results especially if the measurement uncertainty for the two methods are considered (≈ 10 % for η_{PE} and 2.9 % – 7.2 % for $\eta_{lamp(330\ nm - 1100\ nm)}$ see Appendix E).

As discussed in Section 4.6.2, there is no direct comparison between the results obtained here and those with a blended mixture of gold by Jeon et al (Jeon et al., 2016) who used extinction coefficients for calculation under different conditions, such as using a computer model to calculate η under flow conditions based on static experimental data. Interestingly, their blended gold absorber appeared to give a comparable level of maximum efficiency at about 80 % - 85 %, which is similar to the results obtained in this study (83.77 %).

In addition, the Ag NF with the two absorption peaks produced by Walshe et al (essentially a mixture with an absorbance covering the range 300 nm - 750 nm) also gave a η_{PE} value of about 90 %, similar to this study (Walshe et al., 2019). These results were also obtained from static testing while using different sample geometry and testing protocol. The numerical study by Mallah et al (Mallah et al., 2018) produced better results for efficiency than this study at a lower concentration but with a longer path length employed (up to 98 % for a 10 cm path length). The

absorption obtained in the near IR range was better for the NF they proposed containing Ag nanorods. To give a true comparison to their work a five component NF with the same concentrations, NP types and ratio of components would need to be synthesised and tested using the same geometry as they proposed. In fact, in their conclusions they acknowledge the importance of conducting experimental studies on these blended NFs.

Table 5-1 Calculated values of $\eta_{lamp(330\ nm\ -\ 1100\ nm)}$ and η_{PE} for the NFs tested using set-up B. For the calculation of $\eta_{lamp(330\ nm\ -\ 1100\ nm)}$ for the broadband absorber the calculated spectral data has also been included (hence N = 12 rather than 9). The ANOVA results are also given where means that do not share the same letter are significantly different.

NF tested	**Short λ (diluted 1: 5)**	**Mid λ (diluted 1: 3)**	**Long λ**	**Broadband absorber**
Mean $\eta_{lamp(330\ nm\ -\ 1100\ nm)}$ / %	46.29	73.97	57.82	92.75
$\sigma\ \eta_{lamp(330\ nm\ -\ 1100\ nm)}$ / %	4.61	2.02	1.78	1.37
$\eta_{lamp(330\ nm\ -\ 1100\ nm)}$ 95 % confidence interval for the mean / %	44.49 – 48.10	72.17 – 75.78	56.01 – 59.62	91.18 – 94.31
$\eta_{lamp(330\ nm\ -\ 1100\ nm)}$ grouping	D	C	B	A
N for $\eta_{lamp(330\ nm\ -\ 1100\ nm)}$	9	9	9	12
Mean η_{PE} / %	47.68	65.05	62.46	83.77
$\sigma\ \eta_{PE}$ / %	4.68	7.58	4.49	2.29
η_{PE} 95 % confidence interval for the mean / %	44.31 – 51.05	61.68 – 68.42	59.09 – 65.83	80.40 – 87.14
η_{PE} grouping	C	B	B	A
N for η_{PE}	9	9	9	9

When the results for the broadband absorber are compared to those obtained for the more concentrated Ag NPr NF tested using set-up A, the results were the same according to a two-sample t-test (see Section F.1 for t-test definition) for the samples tested in the middle Md position in the solar simulator (83.77 % for the broadband absorber, 84.81 % for the Ag TSCD-PVP NPr centrifuged and re-dispersed into ¼ volume of water – see Appendix J, Table J.4). The likely concentration of Ag in the broadband absorber is lower than the Ag NPr NF so may offer some advantage in terms of colloidal stability. This will be discussed further in Section 5.6.

In summary, all of the NFs produced a greater temperature rise and slope $\Delta T/\Delta t$ than water when measured in the solar simulator using set-up B. The subsequent efficiency η_{PE} calculations for the NFs showed the diluted short λ NF to have the lowest η_{PE}, followed by the mid λ and long λ NF which gave similar results. The broadband absorber produced the highest η_{PE} of the 4 NFs giving a value of 83.77 % similar to that obtained for the more concentrated centrifuged Ag NPrs. The results were comparable with those found via UV-vis spectra and with any relevant literature results.

5.5.5 Conclusions / Summary

The NFs all exhibited a larger temperature rise and rate of temperature rise ($\Delta T/\Delta t$) in the solar simulator than water alone. They all achieved a greater photo-conversion efficiency η_{PE} compared to water (20.51 %) illustrating their potential for enhancing solar capture. The order of η_{PE} for the five NFs tested was short λ < mid λ ≈ long λ < broadband absorber (83.77 %) ≈ centrifuged Ag NPrs re-dispersed into ¼ volume water (84.81 % middle position). Both the centrifuged Ag NPr NF and the broadband NF may therefore be suitable for enhancing solar capture.

This is one of the first attempts to measure in static solar simulator tests Ag NPrs with a λ_{max} > 750 nm and the first study to measure directly the performance of the developed novel Ag based broadband absorber produced from combining three different Ag NFs.

The results for η_{PE} were similar to those calculated directly from the UV-vis spectra ($\eta_{lamp(330\ nm\ -\ 1100\ nm)}$ or $\eta_{lamp(330\ nm\ -\ 900\ nm)}$). The similarity of the results obtained enables calculations based on UV-vis measurements to be used with confidence for the rapid identification and screening of NFs for their potential in DASC applications.

However, considerable care needs to be taken when calculating η_{PE} as the value obtained is very dependent on the accuracy of the measurement of the light intensity I_L. This uncertainty can be offset to some extent by checking the value obtained with that given from UV-vis measurements providing an additional benefit of utilising complementary techniques for the determination of efficiency.

5.6 Stability Testing

5.6.1 Introduction

This Section presents the results of undertaking stability testing of the various different Ag NFs. The results are given approximately in order of harshness of the testing regime building a picture of the potential stability issues that would make Ag NFs unsuitable for solar and potentially other applications.

The stability under ideal storage conditions (4 °C in the dark) is discussed first. This is followed by an evaluation of the effect of elevated temperature on the various NFs. Next the change in the UV-vis spectra and morphology of the NFs following exposure to simulated sunlight (SSL) are provided. The effect of a longer duration test, namely natural sunlight is then presented. How the broadband absorber NF changes under flow conditions is then discussed. The last main subsection illustrates how a change in BF from water to a more suitable BF, propylene glycol (PG), affects the

elevated temperature stability of the Ag NPrs. This Section concludes with an overall summary of all the stability test results.

5.6.2 Silver nanofluid colloid stability

The effect of long term storage under ideal conditions (4 °C in the dark) on the UV-vis spectra is presented in this subsection. This gives an indication of the colloidal stability, with a reduction in peak height (Ab_{max}) indicating instability to aggregation and any changes in the position of the maximum peak (λ_{max}) suggesting morphological instability. Of the stability trials, storage in the dark at 4 °C represents the least harsh condition assessed. Hence, any instability noted in these trials would indicate the potential unsuitability of Ag and especially anisotropic Ag NFs for any applications that required the NF to be stable for many months or years. As a number of different NFs and samples were assessed after storage in the dark the full results are presented in Appendix K with this subsection giving a summary of the main findings. Firstly, the results for the NFs with only one spectral peak (such as NS and NPrs) are discussed. The way the spectral response for the broadband absorber NF changed with storage is then presented. This subsection finishes with a discussion and summary.

Where possible the results were compared to any literature results, however, as discussed in Section 5.4, this was not always possible due to a lack of long term stability trials in the literature. In addition, although there is sometimes relevant literature, colloidal stability is very dependent on the nature of the NPs, the BF used and the presence of any stabilising agent so it can be hard to compare data from different studies.

The full results of assessing the colloidal stability of various different Ag NFs by storing in the dark at 4 °C (see Section 3.9.2) are given in Appendix K, Section K.2.

In terms of colloidal stability (stability to aggregation or sedimentation with time), only the Ag NS stabilised with only TSCD showed a reduction in Ab_{max} of > 25 % with storage (see Figure K.1). This demonstrates the advantage of using PVP in addition to TSCD as a colloidal stabilising agent and showed that all the NFs produced with PVP had good stability to aggregation or sedimentation with storage under ideal conditions even after ≈ 600 days. Ozsoy and Corumlu saw a 50 % reduction in Ab_{max} for their Ag NS NF after 1 y of storage in the dark (Ozsoy and Corumlu, 2018) similar to the least stable Ag TSCD NS samples, unfortunately the storage temperature was not mentioned and insufficient synthesis details were provided to know what if any stabilising agents they had used.

In contrast, for some of the NFs measured, the stability to morphological changes (assessed by measuring the change in λ_{max}) was not as good (see Figure K.2). The Ag NS were stable in terms of morphological changes (< ± 20 nm shift ≈ 150 days), as were the centrifuged Ag TSCD-PVP NPrs. Unfortunately the centrifuged Ag NPrs were only measured for ≈ 50 days, so further testing would be needed to confirm this morphological stability. Sharma et al (Sharma et al., 2011) in contrast saw a red-shift in λ_{max} in the first 15 days of storage for their Ag NS followed by a period of morphological stability (15 further days). However, this work is not directly comparable to this study as their NS were in ethylene glycol BF and were considerably more concentrated that the NFs assessed in this work.

The short λ NFs were the next most stable having a red-shift in λ_{max} of < 45 nm after 603 days (see Figure K.2). In contrast, with extended storage the more dilute Ag NPr NFs (long λ) showed a blue-shift in λ_{max} of up to 90 nm after 603 days of storage at 4 °C. There was considerable variation in the data obtained, with some samples showing no change in λ_{max} after 239 days and other Ag NPr samples having a change in λ_{max} of > 40 nm at the same time point. The least stable NF in terms of change in λ_{max} was the mid λ NF which exhibited a rapid initial blue-shift in λ_{max} of ≈ 100 nm. These morphological changes then slowed as the storage time was extended giving a ≈ 130 nm blue-shift in total after 603 days storage. Again like the Ag NPrs there was considerable variation in the level of change observed between individual samples.

For the broadband absorber NF the changes in morphology with storage time (up to a maximum of ≈ 600 days at 4 °C in the dark) were assessed visibly by comparing the UV-vis spectra, rather than just looking at the change in λ_{max} and Ab_{max} for the primary peak. The full results are given in Appendix K, Section K.2.1. Three of the 7 batches tested showed no change in spectra after a short (23 days) storage period. After an extended storage period (up to 603 days) all of the 7 broadband absorber batches investigated exhibited an increase in the Ab_{max} of the primary peak at ≈ 460 nm of between 10 % and 60 % and a red-shift in λ_{max} of ≈ 20 nm – 50 nm for this peak. The shoulder corresponding to the mid λ NF appeared to be blue-shifting in position leading in some cases to it becoming less pronounced and in 3 of the 7 samples the shoulder corresponding to the long λ NF was also blue-shifted by ≈ 100 nm. The other 4 broadband NFs tested showed no large change in the position of this shoulder. The changes in the broadband absorber with storage time reflect those observed for the component NFs also again with the same large variation between repeat samples.

It had been hoped that this work would start to show an improvement in stability of the broadband absorber NF versus the more concentrated centrifuged Ag NPrs. Unfortunately with both the broadband absorber and the centrifuged Ag NPrs being stable over a relative short

timeframes of < 50 days and the fact that the centrifuged Ag NPrs were only tested for < 50 days this was not possible. In addition, with the main changes being morphological resulting in a blue-shift in λ_{max}, rather than aggregation any increase in stability due to a lower concentration of Ag in the broadband absorber would not occur. Finally, the lack of morphological stability of the mid λ NF, and to a lesser extent the long λ NF has a detrimental effect on the stability to morphological changes of the broadband absorber, suggesting that rather than being more stable the broadband absorber could be less stable to morphological changes than the centrifuged Ag NPrs. Further testing would be needed to confirm this.

The lack of morphological stability of some of the NFs even under ideal storage conditions (significantly less harsh than those needed in a solar collector) also illustrates the extent of the stability issue for Ag NFs and shows that stability to morphological changes is one of the main issues precluding the use of these NFs for any applications that require long term NF stability. If NFs based on Ag are to be used in solar collectors they would require NF that are stable for >> 1 y (and preferably ≈ 20 years) as a minimum.

This is, to the author's knowledge, the first study to look at the effect of storage times > 1 year on the UV-vis spectral response for a range of Ag NFs including anisotropic NPs. It serves to illustrate the amount of further work required in this area, firstly to try and understand the reasons for the large variation observed between repeat samples and secondly to investigate appropriate stabilising strategies to improve the morphological stability.

In summary, the NFs stabilised with both TSCD and PVP were stable to aggregation (< 25 % reduction in Ab_{max}) for a period of ≤ 603 days under ideal storage conditions (4 °C in the dark). However, not all the NFs were stable to morphological changes with the mid λ and long λ NFs being the least stable. The stability of the resultant broadband absorber was strongly influenced by the lack of morphological stability of these two NFs.

5.6.3 Silver nanofluid stability at elevated temperatures

This subsection presents the results of assessing the stability of various different NFs to an elevated temperature of 70 °C. This represents a more harsh testing condition than used in the proceeding subsection. Firstly, the UV-vis results obtained for the NFs with only a single main absorption peak are discussed. Again like for the colloidal stability assessment for these NFs this subsection gives a summary of the main findings with the full results being given in Appendix K, Section K.3. The UV-vis results for the broadband absorber NF are then presented.

This subsection then looks more closely at the morphological changes occurring on exposure to an elevated temperature of 70 °C, using TEM to assess the broadband absorber and three component NFs before and after exposure. A short summary then completes this subsection.

A number of different NFs were assessed for their stability at an elevated temperature of 70 °C using the protocol given in Section 3.9.3. The UV-vis results are given in Appendix K, Section K.3 for all of the NF that were assessed by comparing the λ_{max} and Ab_{max} obtained after exposure to a temperature of 70 °C with the initial λ_{max} and Ab_{max}. Two-sample t-tests (see Appendix F, Section F.1) were also used to determine the significance of any changes (different sub-sets of samples re-measured so two-sample rather than paired t-test used).

It was expected that as the NFs were exposed to higher temperatures, the NPs within the fluid would have more energy and hence be closer to the aggregation barrier reducing the stability to aggregation with a resultant decrease in Ab_{max} (Polte, 2015). This was not found to happen for any of the NFs tested (Figure K.11 and Figure K.13), with a number of the NFs instead showing a small but significant increase in Ab_{max} (maximum increase 24 %). Unfortunately the NFs stabilised with just TSCD were only tested for 3 h at 70 °C. Further testing over an extended period would be needed to definitely show stability to aggregation at elevated temperatures and check if there were any difference seen between samples stabilised with only TSCD and those stabilised with both TSCD and PVP.

However, in a similar manner to the colloidal stability data, it was found that some of NFs were not stable to morphological changes (change in λ_{max}) with exposure to elevated temperatures (Figure K.10 and Figure K.12). Both the Ag TSCD-PVP NS and the short λ NFs showed no change in λ_{max}, whereas the Ag TSCD NS exhibited a small (12 nm) significant red-shift. The mid λ NF in contrast rapidly changed on exposure, giving a 60 nm – 120 nm blue-shift within the first hour of exposure to a temperature of 70 °C. The rate of change in λ_{max} then slowed. Taylor et al (Taylor et al., 2018) also obtained a blue-shift in λ_{max} of ≈ 170 nm after exposure to a temperature of 80 °C for their Ag nanodiscs similar to the size of the change seen here, however, in contrast to this work they also found that aggregation of the nanodiscs occurred. This may have been due to the longer testing time and higher temperature employed in their study.

For the various Ag NPr samples evaluated, the changes in λ_{max} were more complicated (Figure K.12). It was thought to be perhaps due to a complex relationship between the amount of TSCD present in the NF, the starting λ_{max}, and the concentration of Ag in the NF, with the Ag NPr NFs that had been centrifuged for a longer time, resulting in a decrease in TSCD in the solution and a blue-shift in the starting λ_{max}, being stable to morphological changes. In contrast the most concentrated Ag NPr NFs, centrifuged for a short time perhaps resulting in a higher concentration

of TSCD, were the least stable and showed a rapid blue-shift in λ_{max} of ≈ 90 nm. Others have found that the amount of TSCD present effects the amount and rate of morphological change when Ag NFs are exposed to elevated temperatures and or sunlight (Tang et al., 2013) supporting this argument. However, further testing would be required to confirm and investigate the importance of the different contributing factors to the shape evolution of Ag NPrs with exposure to elevated temperatures.

Zeng et al (Zeng et al., 2010) saw a 320 nm blue-shift in λ_{max} after 9 h at 80 °C (from 770 nm to 450 nm) for Ag NPrs stabilised with both TSCD and PVP, a considerably greater change than seen in this study perhaps due to both the increased temperature used and the presence of more TSCD and ascorbic acid in their NF.

Similar to colloidal stability the broadband absorber NFs were assessed by visually comparing the UV-vis spectra obtained initially before and after exposure to an elevated temperature. The average results are shown in Figure 5-3.

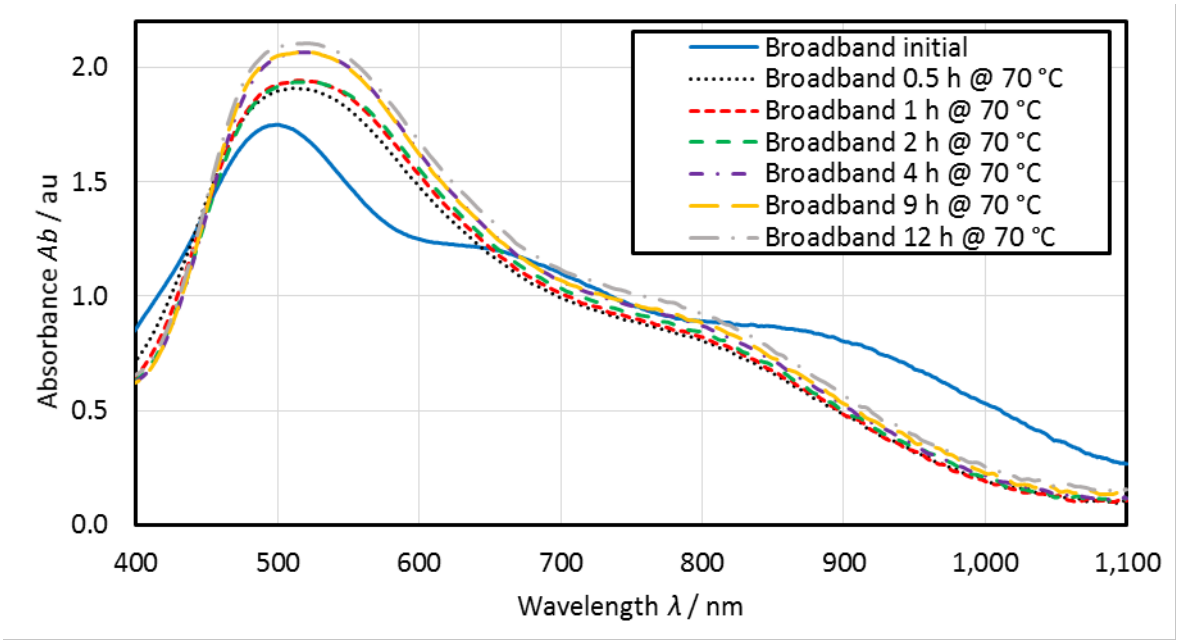

Figure 5-3 Change in the UV-vis-IR spectra for the broadband absorber NF with exposure to an elevated temperature of 70 °C. The average spectra obtained at each time point is shown (N = 6 for the initial and t = 0.5 h time points whereas N = 3 for all other time points).

At elevated temperatures, there was an initial rapid change in the shape of the spectra with the primary peak at ≈ 490 nm increasing, red-shifting by ≈ 20 nm – 40 nm and becoming broader. The shoulder corresponding to the mid λ NF disappeared and the longer λ shoulder corresponding to the long λ NF red-shifted by ≈ 70 nm. The same trends continued to happen with further exposure but at a slower rate. These changes were similar to some of those seen when the colloidal stability of the broadband absorber was assessed (see Section 5.6.2) but more rapid and pronounced. This reflects the severity of the testing condition used.

The change in spectra obtained for the broadband absorber following exposure to elevated temperature will have an effect on the potential η for the broadband absorber. The amount of sunlight absorbed at $\lambda > 800$ nm and $\lambda < \approx 440$ nm will decrease, whereas even more of the energy in the ≈ 440 nm - 670 nm range will be absorbed. However, the broadband absorber already absorbs the majority of the solar energy in this region so it is likely that η will reduce overall. This will be discussed further in Section 5.6.4, where the η values before and after exposure to SSL will be presented.

TEM micrographs of the broadband absorber and 3 component NFs after 4 h of exposure to an elevated temperature of 70 °C are shown in Figure 5-4 and the corresponding summary of the analysis in Figure 5-5 (complete TEM results given in Appendix G, Section G.4, including two-sample t-test results investigating the change in size of the different type of NPs following temperature testing).

By correlating Figure 5-5 with the initial TEM analysis (shown in Figure 4-15) and looking at any significant size changes (Table G.12) obtained from the t-test analysis, it can be seen that the majority of the changes following exposure to elevated temperature were changes in shape rather than size. The largest significant size difference in Table G.12 was ≈ 3 nm for the rounded cornered triangles in the broadband absorber NF, with the temperature exposed rounded corner triangles being larger. If the larger triangles in the broadband absorber were becoming rounded with temperature exposure this would increase both the percentage of rounded corner triangles and the average size of rounded triangles which is indeed the case (rounded triangles after exposure 25 %, before 14 %, triangles after 6 %, before 11 %). Zeng et al (Zeng et al., 2010) also found that there was no significant change in size of their Ag NPrs with aging at temperature, with the primary change being the rounding of the corners, which they attributed to atomic migration rather than oxidative etching. Similarly Taylor et al attributed their blue-shift in λ_{max} to a rounding of their nanodiscs rather than a change in size (Taylor et al., 2018).

Although there was no noticeable change in λ_{max} following exposure to temperature for the short λ NF, there were some differences in morphology with the after temperature exposure short λ NF containing more rounded triangles and less small particles. Ab_{max} did increase for this NF by about 24 %. The relative amount of rounded triangles and small particles may therefore be causing an increase in Ab_{max} rather than a shift in λ_{max}. Further studies would be needed to confirm this.

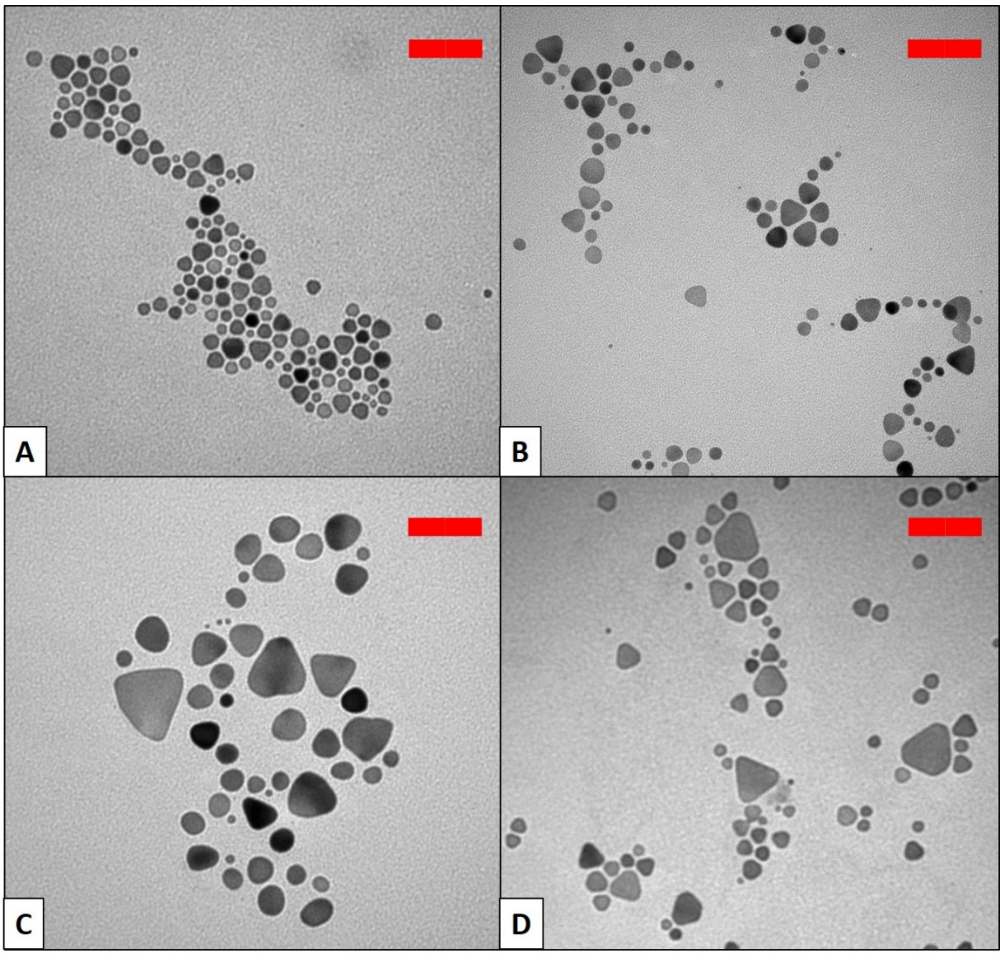

Figure 5-4 TEM micrographs after 4 h at 70 °C of (A) Short λ NF, (B) Mid λ NF, (C) Long λ NF, and (D) Broadband mixture. All red scale bars = 100 nm.

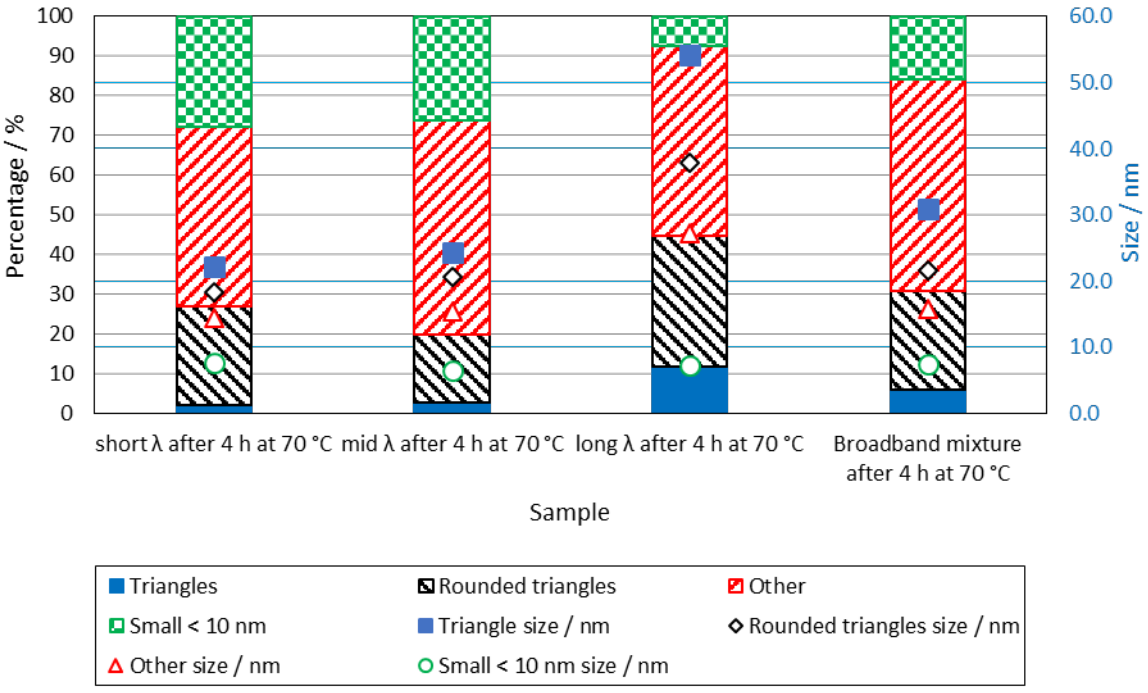

Figure 5-5 TEM analysis after 4 h at 70 °C for the broadband mixture and component NFs.

For the mid λ NF the percentage of triangles decreased and the amount of other shaped particles increased. This would result in a blue-shift in λ_{max}, which was indeed seen. The number of triangles also decreased for the long λ NF from 63 % to 12 %, again accounting for the blue-shift in λ_{max} observed (see Figure K.12 and Table K.3).

Although it was hoped that the broadband absorber would offer advantages in terms of stability due to its lower Ag concentration than the concentrated centrifuged Ag NPrs this was not found to be the case in these elevated temperature trials. This was due to aggregation not being the main failure mechanism. The lack of centrifuging to remove any excess TSCD for the broadband absorber versus the centrifuged Ag NPrs appeared to be actually having a detrimental effect on the stability to morphological changes with the centrifuged more concentrated Ag NPrs being more stable than the broadband absorber. Further elevated temperature testing of the broadband absorber after centrifuging and re-dispersal would be needed to confirm this. However, centrifuging to remove excess TSCD may improve the morphological stability but it would have a detrimental effect on the broadband nature of the absorber, potentially rounding the corners of the sharp triangles, resulting in a blue-shift in the position of the shoulder corresponding to the long λ NF and a loss of initial performance at > 900 nm.

Both the Ag NS and the short λ NF were stable over the short timeframe tested here. They may therefore be appropriate NFs for use in applications where stability to elevated temperatures ≈ 70 °C was important. However, they are not on their own suitable for enhanced solar absorption in volumetric absorbers due to their narrow absorption band and lack of absorption efficiency (see Section 4.3.1 and Section H.5).

The centrifuged Ag NPrs may also be suitable for elevated temperature applications but further work is needed to understand the differences between samples observed. Testing over a longer time period would also be required. They may be suitable for volumetric absorption as their photo-conversion efficiency η_{PE} is high but further stability testing would be needed to confirm this. This will be discussed in the following Sections.

Further work on the elevated temperature stability of the mid λ and long λ is required before the broadband absorber can be recommended for use in elevated temperature applications.

In summary, this subsection has presented the results of assessing the stability of various NF to an elevated temperature of 70 °C. All the NFs were stable to aggregation over the timeframe tested but some were not morphologically stable. Again like for colloidal stability the least stable NFs were the mid and long λ NFs predominately due to a rounding of the triangular corners of the NPs (from the TEM results) rather than a change in NP size. This is the first study to assess the effect of

elevated temperature on a broadband Ag NF, showing that at present this NF is not stable to morphological changes with temperature exposure due to the instability of the mid and long λ component NFs.

5.6.4 Silver nanofluids stability with exposure to simulated sunlight

An increasingly harsh exposure scenario of simulated sunlight (SSL) is used in this subsection to evaluate the stability of various different Ag NFs. The changes in UV-vis spectra with exposure to SSL are firstly given followed by a discussion of the effect on the efficiency (η) of these changes. The TEM analysis of the various NPs following exposure are then presented. This subsection then concludes with a short discussion and summary.

One Ag NPr NF type (3 repeats) was exposed to simulated sunlight (SSL) for a period of 12 h using the solar simulator set-up A under static conditions (see Sections 3.8.3 and 3.9.4). The broadband absorber and component NFs (short, mid and long λ) were exposed for a shorter time of 0.5 h using set-up B. To assess the stability with exposure to SSL the change in peak position (λ_{max}) and height (Ab_{max}) following exposure was calculated for all of the NFs except the broadband absorber. The results for λ_{max} are shown in Figure 5-6 and the changes in Ab_{max} are summarised in Table 5-2 (the actual before and after UV-vis spectra are given in Appendix K, Section K.4)

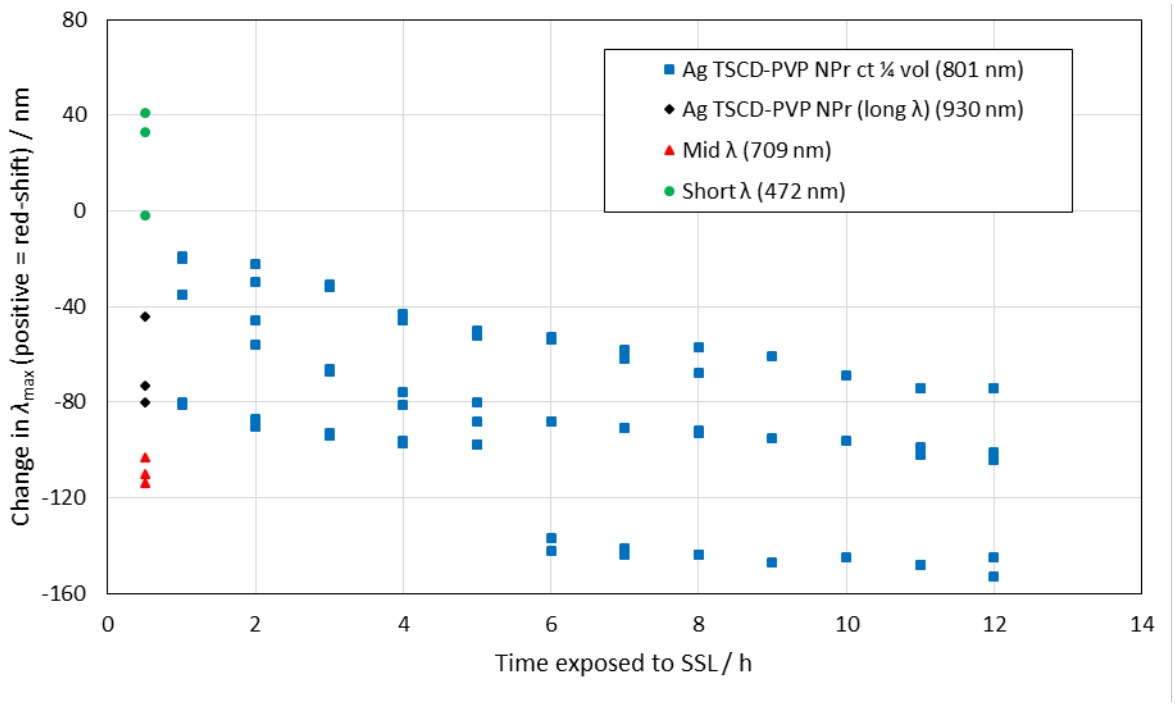

Figure 5-6 Change in λ_{max} with exposure to simulated sunlight (SSL). The Ag TSCD-PVP NPr ct ¼ volume was tested using set-up A. The other NFs were tested using set-up B. Repeat samples (N = 3) were evaluated (for Ag TSCD-PVP NPr ct ¼ vol replica measurements were undertaken at some time points). The starting λ_{max} is shown in brackets.

For the Ag TSCD-PVP NPrs centrifuged and re-dispersed into ¼ volume of water there was a blue-shift in λ_{max}, which increased as the time of exposure increased giving an average blue-shift of 109 nm (σ = 34 nm, N = 6) after 12 h exposure. In contrast Ab_{max} only increased by 7.1 %, showing the more concentrated centrifuged Ag NPrs to be stable to aggregation but not morphological changes over the time period tested.

Table 5-2 Change in Ab_{max} following exposure to SSL for various NFs.

Parameter	**Ag TSCD-PVP NPr ct ¼ vol**	**Ag TSCD-PVP NPr (long λ)**	**Mid λ (diluted 1: 3)**	**Short λ (diluted 1: 5)**
Average change in Ab_{max} / % (positive = increase)	7.1	-5.7	8.8	44.7
σ / %	6.7	0.6	1.1	5.1
N	3	3	3	3
Exposure time / h	12	0.5	0.5	0.5
Solar simulator set-up	Set-up A	Set-up B	Set-up B	Set-up B

The direction of change was the same for the less concentrated Ag NPrs (long λ) NF, however, the magnitude of the blue-shift was greater being 66 nm after only 0.5 h (compared to the centrifuged Ag NPr 1 h data of 45 nm). This shows the centrifuged Ag NPrs to be potentially slightly more morphologically stable when exposed to SSL than the non-centrifuged Ag NPr NFs in agreement with the elevated temperature results in Section 5.6.3. This is especially true when it is also considered that the intensity of the simulated sunlight used in set-up A was considerably greater than that used in set-up B (see Section 5.5.2).

Like for the elevated temperature stability trials the mid λ NF was more unstable to morphological changes than the long λ NF, giving a similar blue-shift in λ_{max} of 109 nm after 0.5 h as that obtained by the centrifuged Ag NPrs after 12 h.

In contrast to the other NFs tested, the short λ NF exhibited a small red-shift in λ_{max} of 24 nm (σ = 23 nm, N = 3) but a large increase in Ab_{max} of 44.7 % (see Table 5-2). This small red-shift was not seen in the elevated temperature tests but a similar, abate smaller, rise in Ab_{max} of 29 % was.

The magnitude of the changes in λ_{max} with SSL exposure were in all cases comparable to (in the case of the mid λ NF) or larger than those seen in the temperature stability trials reflecting the harshness of the testing conditions, with the NFs being exposed to both light and elevated temperatures in the solar simulator.

The UV-vis spectra for the broadband absorber NF before and after exposure to SSL using set-up B for 0.5 h are shown in Figure 5-7. In a similar manner as following testing at an elevated temperature (see Figure 5-3), the height of the primary peak increased and slightly red-shifted

and the shoulder corresponding to the long λ NF blue-shifted. However, unlike for the temperature testing the shoulder corresponding to the mid λ NF although blue-shifted was still apparent. This may have been partly due to the different position of the mid λ NF shoulder in the initial broadband absorber being at a longer λ for the broadband absorber before SSL testing compared to the broadband absorber samples used for temperature testing.

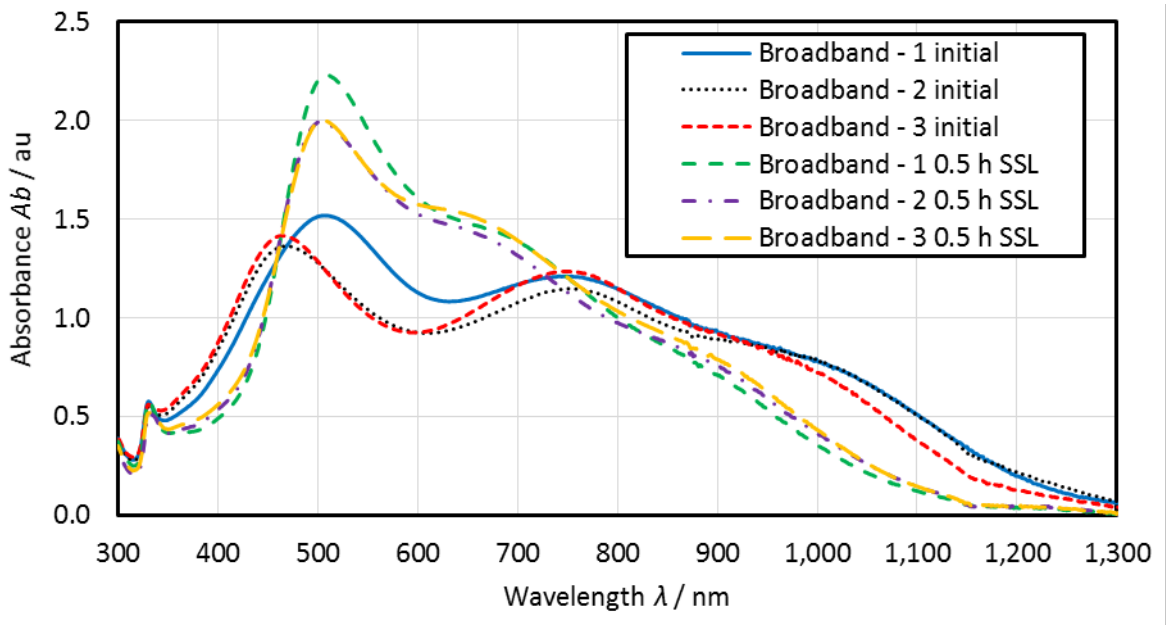

Figure 5-7 Change in the UV-vis-IR spectra for the broadband absorber NF (3 samples –denoted – 1, - 2 and – 3) with exposure to SSL using set-up B in the solar simulator. Measured using the UV-vis-IR-1 spectrophotometer (10 mm path length).

To understand the implications of the various changes in spectra following SSL exposure, various different η calculations were carried out. The results are given in Appendix K, Table K.4 and Table K.5. The $\eta_{\text{lamp(330 nm - 900 nm)}}$ for the centrifuged Ag NPrs exposed for 12 h using set-up A appears to increase from 92 % to 99 %. However this results should be treated with some caution as it does not account for any reduction in power absorbed > 900 nm and the centrifuged Ag NPrs were not measured > 900 nm. The broadband absorber also showed a small increase in $\eta_{\text{lamp(330 nm - 1100 nm)}}$ following SSL exposure of ≈ 3 % (92 % to 95 %), however, when the efficiency was calculated over a larger range (see Table K.5) a decrease of ≈ 3 % – 7 % was observed (depending on sample and η value used). This illustrates clearly the care that is required when comparing different efficiency calculations.

This work suggests that the broadband absorber and the more concentrated centrifuged Ag NPrs NF both offer similar advantages in terms of efficiency change with the centrifuged Ag NPrs perhaps being slightly better. However further testing over a broader wavelength range and for a longer time would be needed to confirm this. A longer testing time may result in more aggregation of the NPs in the more concentrated NF giving the broadband absorber NF an

advantage. Conversely a longer testing time may give a greater shift in the position of the peak corresponding to the long λ NF in the broadband absorber due to more TSCD being present, reducing further the performance > 900 nm, leading to the centrifuged Ag NPrs performing better in the long term.

TEM micrographs before and after SSL testing for the centrifuged Ag TSCD-PVP NFs are shown in Figure 5-8, and a summary of the size analysis is given in Figure 5-9 (full TEM results in Appendix G, Section G.5). Before exposure the analysis resulted in 29 % triangles (average size 41.75 nm ± 10.64 nm, N = 620), 39 % rounded cornered triangles (average size 34.52 nm ± 10.21 nm, N = 833), 31 % other shaped particles (average size 28.19 nm ± 13.51 nm, N = 677) and 1 % small (> 10 nm). After exposure the relative number of triangles reduced to 6 % and the size increased to 48.70 nm (significant according to a two-sample t-test, see Table G.16). The amount of rounded cornered triangles stayed about the same at 32 %, but their average size again increased to 41.70 nm (again significant). The amount of other shaped particles increased to 59 % and their size increased significantly to 32.23 nm. The amount of small (< 10 nm) particles also increased slightly.

The increase in size of the rounded cornered triangles can be explained in part by the rounding of the corners of the larger triangles with exposure, shifting these larger particles into the rounded cornered triangle category hence increasing the average size. This also explains in part the increase in size of the particles in the other category. However, this cannot be the reason for the increase in size of the particles in the triangle category. This increase in size only occurred for two of the three samples tested (see Figure 5-9) so may be an artefact of the measurement technique (hard to judge how representative the TEM images analysed are of the sample as a whole). In fact if a two-sample t-test is undertaken comparing the size of all the particles measured before with all particles afterwards, although the size of the particles is significantly greater after exposure to SSL, the magnitude of that difference is only ≈ 1.2 nm, which is less than the uncertainty associated with the measurement technique (see Appendix E).

Hence the main morphological changes for the centrifuged Ag NPs were a rounding of the sharp corners of the triangles forming rounded corner triangles and other disc like shapes. This rounding of the corners of the triangles was also seen for the long λ NF after only 0.5 h exposure to SSL (TEM micrographs in Figure 5-10 and summary of TEM analysis in Figure 5-11, full results in Appendix G, Section G.5). The percentage of triangles dropped from 69 % to 32 % (compare Figure 4-15 to Figure 5-11), whereas the size stayed the same at ≈ 50 nm (not significantly different according to a two-sample t-test see Table G.17). The amount of rounded cornered triangles and

other particles also increased for the long λ NF following SSL exposure. Again the average size of these particles increased significantly in a similar manner as for the centrifuged Ag NPrs.

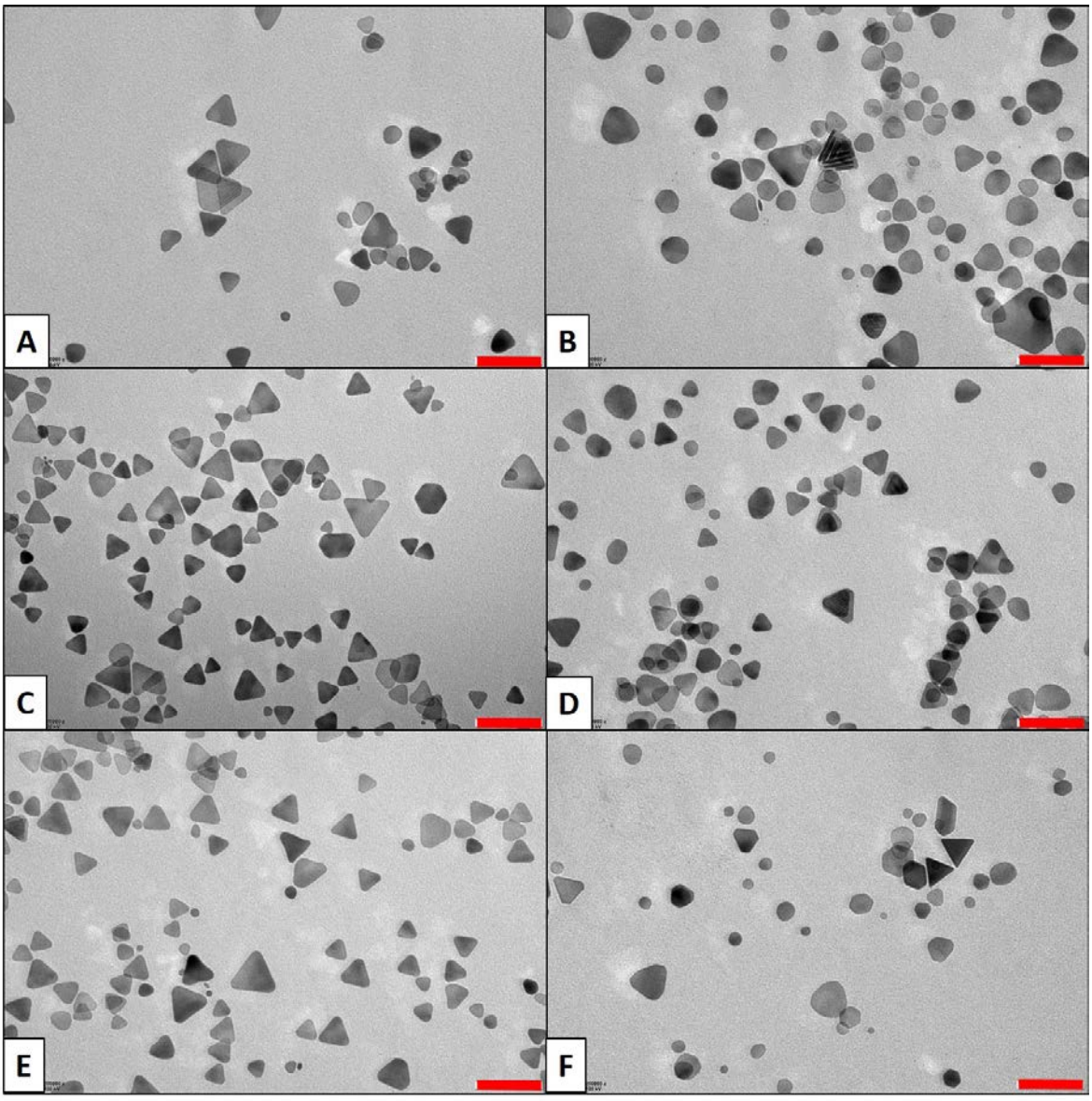

Figure 5-8 TEM micrographs of (A) Ag TSCD-PVP NPr ct ¼ vol water - 4 initial, (B) Ag TSCD-PVP NPr ct ¼ vol water - 4 after 12 h SSL, (C) Ag TSCD-PVP NPr ct ¼ vol water - 5 initial, (D) Ag TSCD-PVP NPr ct ¼ vol water - 5 after 12 h SSL, (E) Ag TSCD-PVP NPr ct ¼ vol water - 6 initial, and (F) Ag TSCD-PVP NPr ct ¼ vol water - 6 after 12 h SSL. All red scale bars = 100 nm.

For the mid λ NF, the percentage of triangles dropped from an initial value of 44 % to 11 %, the amount of rounded cornered triangles stayed about the same (25 % before, 20 % after) and the amount of other disc like particles increased from 16 % to 57 %. Both the other and small (< 10 nm) increased slightly in size following SSL (two-sample t-test results in Table G.17).

Dissimilar to that observed with temperature exposure, there were no large changes in the morphology of the short λ NFs. There were slightly more other shaped particles at 47 % following SSL than before at 42 % and slightly less small (< 10 nm) particles at 48 % versus 51 %. There were

no significant differences in particle size. Ab_{max} did increase for this NF by 45 %, a larger increase than seen on exposure to an elevated temperature of 70 °C. The change in morphology seen for the temperature samples cannot therefore be attributed to the increase in Ab_{max} as previously suggested.

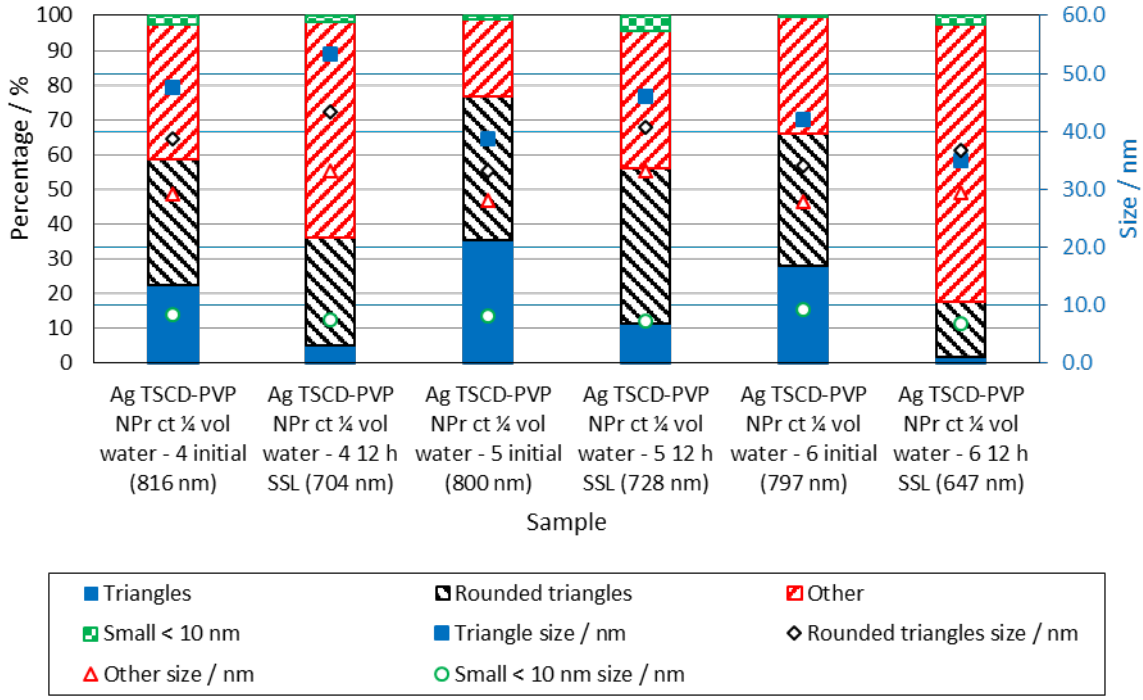

Figure 5-9 TEM analysis before and after 12 h SSL (using set-up A) for Ag TSCD-PVP NPr centrifuged and re-dispersed in ¼ volume of water. The value of λ_{max} obtained is shown in brackets.

For the broadband absorber (TEM micrograph shown in Figure 5-10 and analysis summary in Figure 5-11), the size and relative amount of each particle type did not change following exposure to SSL for 0.5 h using set-up B (the largest change in relative amount was for the triangles which changed from 8 % to 6 %). The only change in size that was significant (see Table G.17) was the thickness, which increased slightly following exposure. However the magnitude of this increase was only 0.46 nm, which is within the measurement uncertainty so is probably an artefact rather than a real increase.

The lack of differences seen in the TEM analysis for the broadband absorber mixture illustrates the lack of sensitivity of this technique compared to UV-vis measurements for detecting small morphological changes, especially when analysing a NF with a broad spectral response, containing a wide range of particle geometries.

When Taylor et al exposed a nanofluid containing Ag nanodiscs to UV light they observed a large number of small Ag particles (Taylor et al., 2018), and a rounding of the corners of their NPs. Although rounding of the corners was seen in this work no additional clusters of small (< 10 nm) particles were observed for any of the NFs following exposure to a broad spectrum light source.

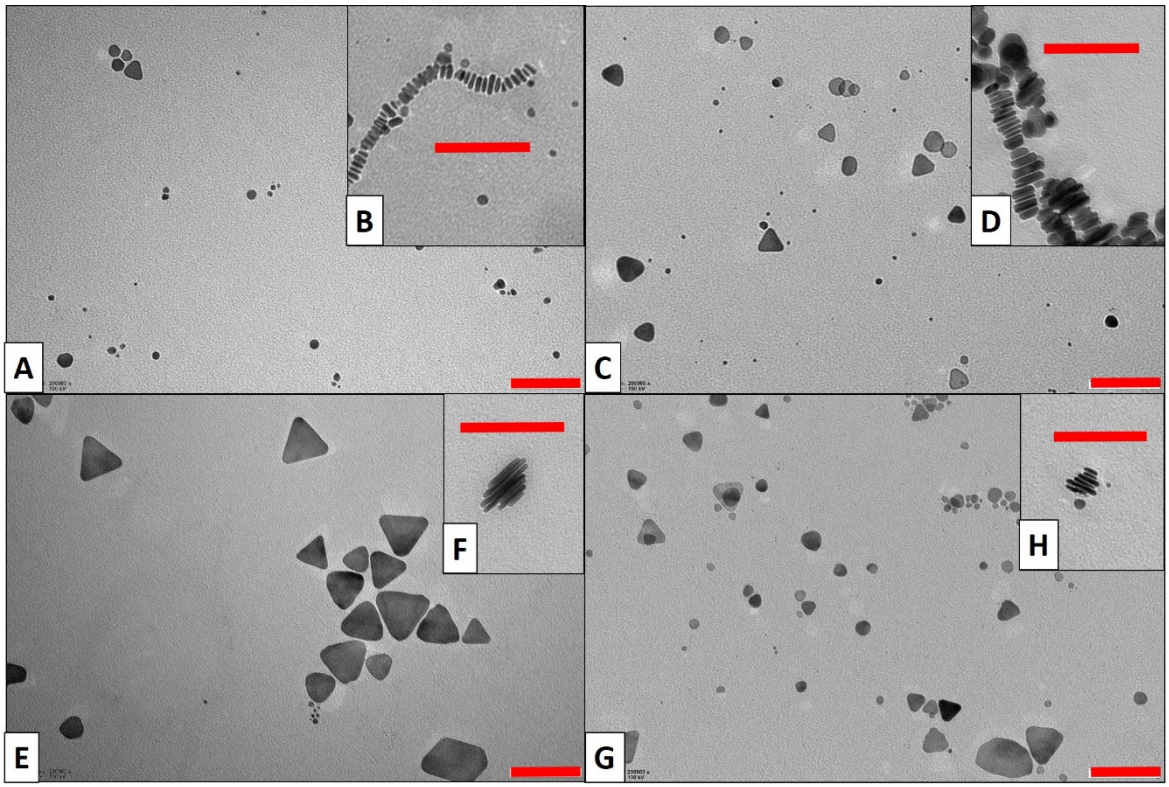

Figure 5-10 TEM micrographs after 0.5 h exposure to SSL of (A) Short λ, (B) insert showing edge of short λ, (C) Mid λ, (D) insert showing edge of mid λ, (E) Long λ, (F) insert showing edge of long λ, (G) Broadband absorber NF, and (H) insert showing edge of broadband absorber. All red scale bars = 100 nm.

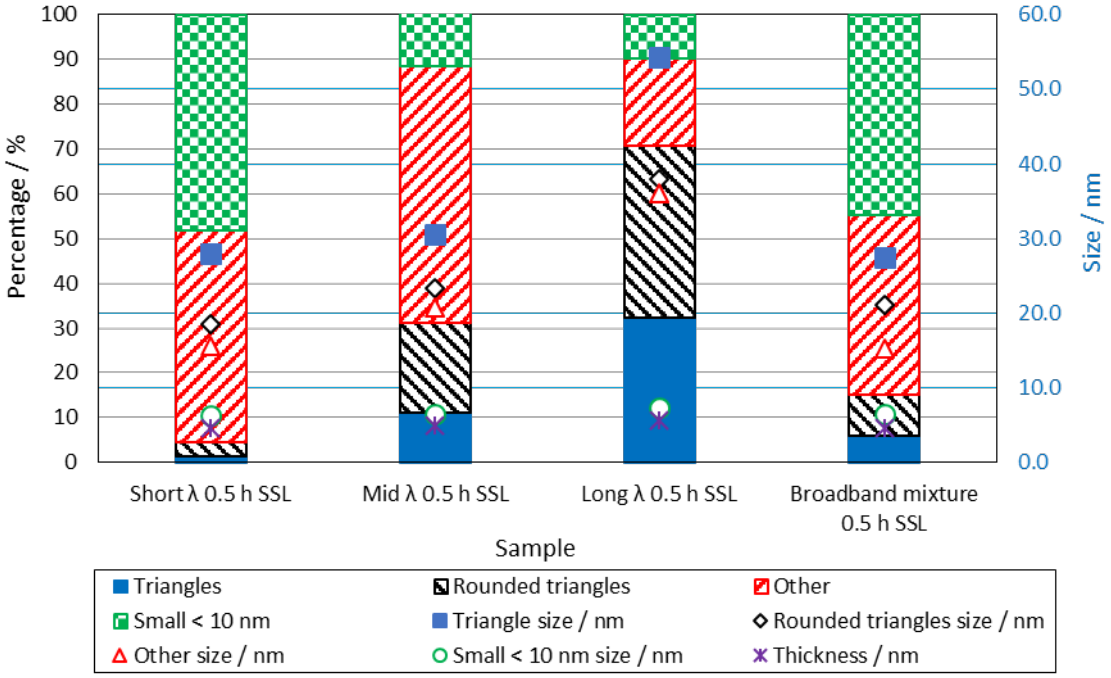

Figure 5-11 TEM analysis after 0.5 h SSL (using set-up B) for the broadband absorber mixture and its three component NFs.

This work also contrasts with the work of Tang et al (Tang et al., 2013) who managed to produce Ag NPrs by irradiating Ag nanodiscs with light (a red-shift in λ_{max}). However, when they used a solution containing no additional TSCD they did not observe this change, showing that the

magnitude, rate and direction of any change in peak position is strongly influenced by the amount of TSCD present in solution (Tang et al., 2015).

This subsection presents the results of assessing the stability of a number of NF following exposure to SSL. Although stable to aggregation over the short timeframe tested, none of the NFs were stable to morphological changes. All the changes were in the same directions as those observed for the elevated temperature trials but of a larger magnitude (even with a shorter testing time). The short λ NF exhibited a small red-shift in λ_{max} but a large increase in Ab_{max}. In contrast the other NFs containing more triangular shaped NPs all showed a large blue-shift in λ_{max} even after only 0.5 h of exposure, but no large increase in Ab_{max}. The broadband absorber appeared to be less stable to morphological changes than the centrifuged Ag NPrs NF tested. This was thought to be perhaps due to more TSCD being present in the broadband absorber NF.

5.6.5 Silver nanoprisms stability when exposed to natural sunlight

The way in which the UV-vis spectra changes following exposure to natural sunlight for Ag NPrs is detailed in this subsection. The results are presented, followed by a short discussion and summary.

Two separate natural sunlight exposure trials were undertaken. The duration of the first trial (denoted trial 1) was 2 weeks and the second trial (trial 2) was 5 weeks (see Section 3.9.5). In both cases the NF tested was Ag TSCD-PVP NPrs centrifuged and re-dispersed into ¼ the volume of water.

The results obtained from the two trials were similar (see Figure 5-12). For trial 1, Ab_{max} decreased by 73 % on average (range 39 % – 97 %, N = 3), while λ_{max} blue-shifted by ≈ 80 nm. For trial 2, Ab_{max} decreased by 57 % (range 17 % – 96 %, N = 8), with a blue-shift in λ_{max} of ≈ 60 nm. There was a large variation in drop in Ab_{max} between the different samples in the same trial.

The large drop in Ab_{max} for the majority of samples following exposure to natural sunlight suggests that aggregation of the particles within the NF is occurring (eye-visible seeds were observed in some samples within the NF after exposure in both trials confirming this supposition). Comparison with the SSL results for the centrifuged Ag NPrs (see Figure 5-6) showed that the blue-shift in λ_{max} was similar (60 nm - 80 nm for natural sunlight testing and 74 nm – 153 nm for SSL after 12 h). The drop in Ab_{max}, however, was not (see Table 5-2). This suggests that initial shape modification of the NPs was a faster process than aggregation, occurring within the time period of the SSL trials, whilst aggregation took longer to occur becoming only obvious after the prolonged natural sunlight exposure trials. It also indicates that the rate of shape alteration was fastest when the NF

was first exposed to solar radiation, as the shift in λ_{max} was similar for both the SSL and natural sunlight trials.

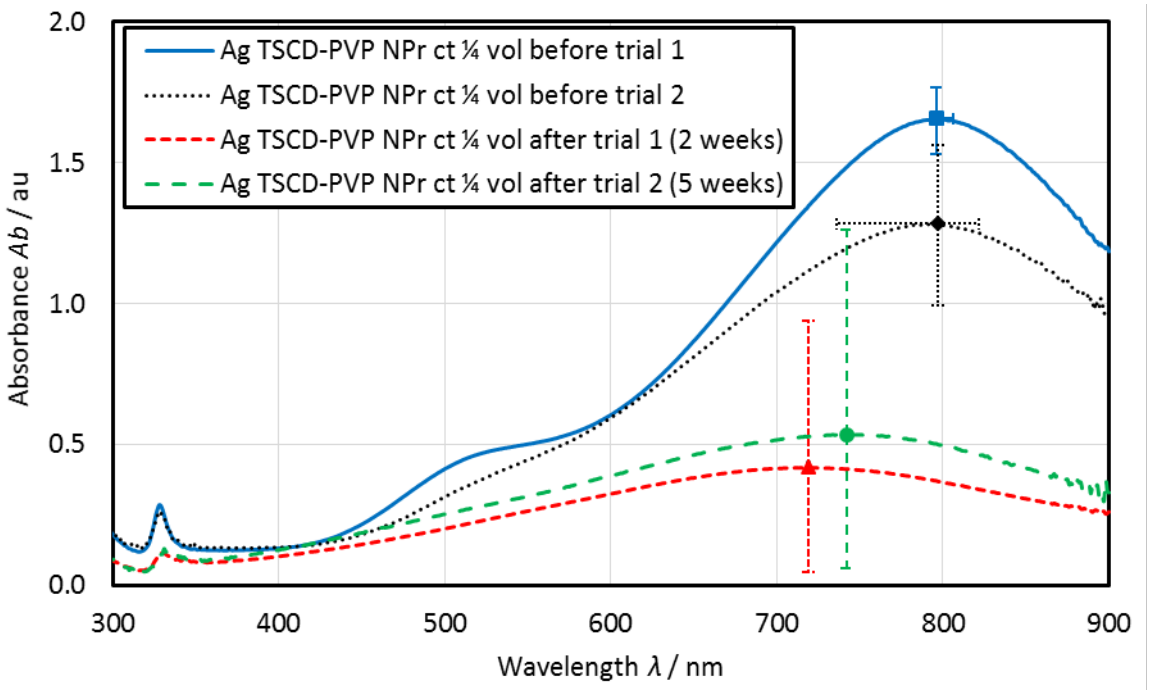

Figure 5-12 UV-vis spectra of Ag TSCD-PVP NPrs centrifuged and re-dispersed into ¼ volume of water before and after exposure to natural sunlight for either 2 weeks (trial 1) or 5 weeks (trial 2). Measured using UV-vis-1. The error bars show the range of results obtained at the maximum absorbance (the *x* error bars after sunlight exposure are excluded as it was difficult to determine λ_{max}).

Taylor et al also found that their Ag nanodisc NFs were initial stable to aggregation on heating to 80 °C but started to aggregate after prolonged heating (> ≈ 27 h), supporting the hypothesis that aggregation is a slower process (Taylor et al., 2018). Tang et al also observed large changes in λ_{max} on sunlight exposure for 18 h but no significant drop in Ab_{max} again suggesting that shape evolution is a faster process than aggregation (Tang et al., 2015).

It would have been useful to undertake further natural sunlight exposure trials on the broadband absorber and component NF (along with repeat trials of the centrifuged Ag NPrs) to determine how the NF concentration and the level of TSCD present in the NF affects the longer term stability to aggregation. However, the broadband absorber NF would have to be orders of magnitude more stable that the Ag NPrs tested here to make it suitable for solar applications (would need to be stable to aggregation for >> 2 weeks in sunlight). Given the lack of morphological stability of the broadband absorber in the shorter term SSL tests and the similarity of the stabilising agents used to those employed in the Ag NPr NF this is extremely unlikely.

This is the first study available in the current literature to examine the change in UV-vis spectra for Ag NPrs following exposure to natural sunlight and shows the benefit of carrying out various different types and lengths of stability tests. One other study assessed the photo-conversion of Ag

NPs in natural sunlight but only for ≤ 18 h so did not see the level of aggregation observed in these longer timeframe trials (Tang et al., 2015).

This subsection presents the results of assessing the stability of Ag NPrs by the use of natural sunlight trials. Unlike for the other stability trials conducted significant aggregation of the NPrs was observed. It clearly demonstrates the fact that morphological changes are a quicker process than aggregation, and provides significant information that is not obtained utilising shorter or less severe testing conditions.

5.6.6 Effects of fluid flow on the silver broadband absorber

This subsection details the results obtained when one Ag NF, specifically the broadband NF was exposed to flow, flow plus elevated temperature, flow plus SSL and flow plus both elevated temperature and SSL. Firstly, the UV-vis spectra before and after exposure are shown followed by pictures of the deconstructed flow cell and associated pipework after testing. The TEM analysis after exposure then follows. This subsection concludes with a summary.

The effect of fluid flow on the stability of the Ag broadband absorber NF was determined using the protocol described in Section 3.9.6. Due to the large volume of NF required for the experiments, only the broadband absorber NF was tested (total amount of broadband NF for the flow tests = 1.2 L).Four different conditions were evaluated, flow only, flow plus elevated temperature, flow plus SSL and flow plus elevated temperature and SSL.

The UV-vis-IR results for the least harsh condition, flow only are shown in Figure 5-13. Over the limited time period tested flow only (flow rate = 0.238 mL s^{-1}) did not change the UV-vis-IR spectra. In should be noted that there was a time lag of 36 days between testing repeat 1 and 3. This therefore also shows the short term colloidal stability of the broadband absorber when stored at 4 °C in the dark (compare initial repeat 1 with repeat 3) and agrees with the colloidal stability results in Section 5.6.2 following 23 days storage.

The effect of both an elevated temperature and flow on the UV-vis-IR spectra is shown in Figure 5-14. The primary peak (initial λ_{max} ≈ 480 nm) red-shifted by about 30 nm - 40 nm and Ab_{max} increased by ≈ 11 % for this peak after 6 h exposure to both an elevated temperature and flow. The shoulder corresponding to the mid λ NF at ≈ 650 nm started to become less pronounced after 1 h and had completely disappeared after 6 h. The shoulder corresponding to the long λ NF blue-shifted by ≈ 30 nm. On comparing with the elevated temperature results (Figure 5-3) the red-shift in the primary peak and the increase in Ab_{max} were similar to those seen after only 2 h at 70 °C but the blue-shift in the position of the long λ shoulder was less (≈ 70 nm for the 70 °C results in

Figure 5-3). Although the water bath was set to 70 °C the maximum sample temperature in the round bottomed flask reservoir was ≈ 60 °C. The NF also cooled as it passed through the tubing into the flow cell and back into the reservoir. The time at this lower elevated temperature was therefore considerably less that for the static elevated temperature tests in Figure 5-3. Zeng et al (Zeng et al., 2010) found that the temperature strongly effected the blue-shift in λ_{max} observed with a lower temperature giving a smaller blue-shift. It is likely therefore that the lower temperature seen by the broadband absorber NF in the flow rig explains the reduction in Ab_{max} increase for the primary peak and the magnitude of the blue-shift in the shoulder corresponding to the long λ NF compared to the static 70 °C results.

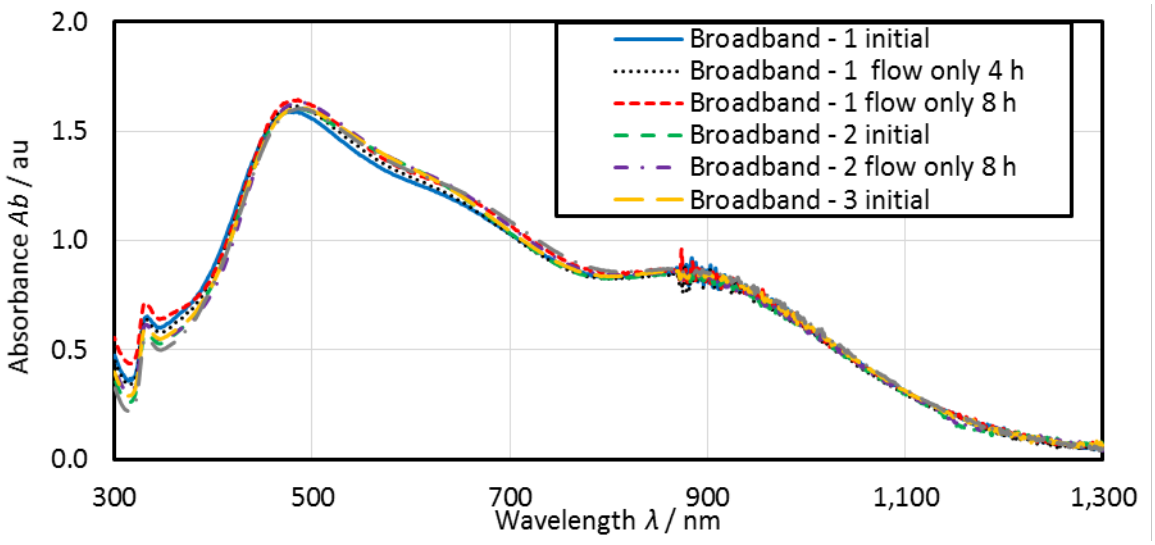

Figure 5-13 UV-vis-IR spectra of the broadband absorber NF before and after being subjected to a flow rate of 0.238 mL s^{-1} for 8 h (3 repeats shown). Measured using a 1 mL plastic cuvette of 10 mm path length and UV-vis-IR-1.

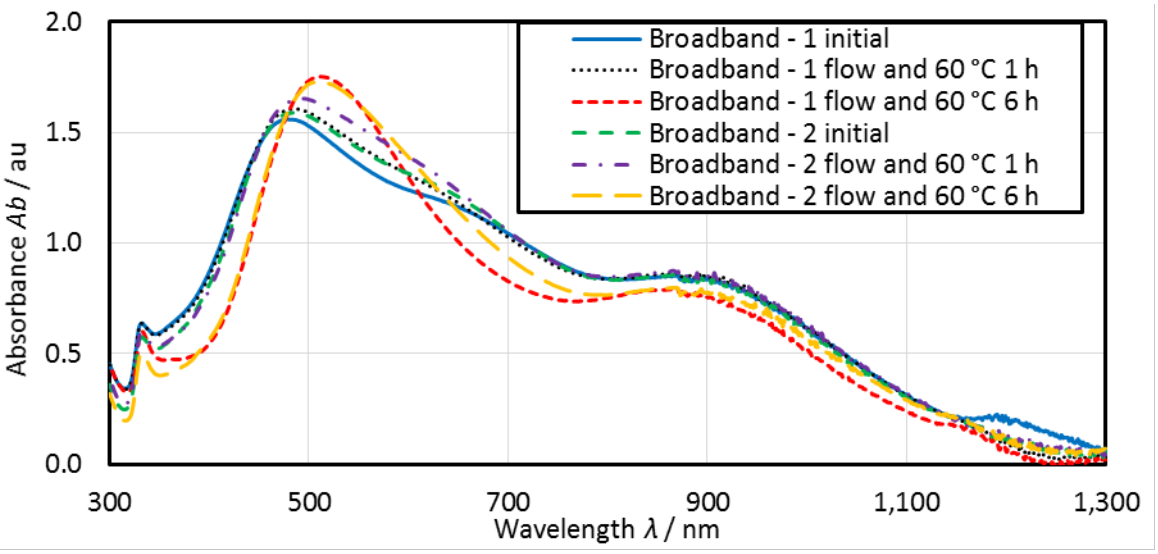

Figure 5-14 UV-vis-IR spectra of the broadband absorber NF before and after being subjected to a flow rate of 0.238 mL s^{-1} for 6 h combined with an elevated temperature of ≈ 60 °C (2 repeats shown). Measured using a 1 mL plastic cuvette of 10 mm path length and UV-vis-IR-1.

When the broadband absorber NF was subjected to flow with SSL exposure (potentially harsher conditions than flow plus elevated temperature) the red-shift in the primary peak was similar at 30 nm - 40 nm (shown in Figure 5-15) but the increase in Ab_{max} for this primary peak was greater at ≈ 40 % after 4 h exposure to SSL (7.5 h of flow). This increase in Ab_{max} was greater than that seen after 4 h in the static elevated temperature tests of ≈ 20 % (Figure 5-3) but similar to that seen (45 %) after 0.5 h of SSL in the static tests in Figure 5-7. The static SSL tests expose the sample to both SSL and elevated temperature so are harsher than the SSL and flow conditions. As mentioned previously (Section 3.9.6) the time in the flow cell was ≈ 16 s and there was < 2 °C difference between the thermocouple at the bottom of the rig and the top thermocouple. Therefore the SSL and flow samples were only exposed to SSL and flow and not SSL and elevated temperature like the static SSL samples.

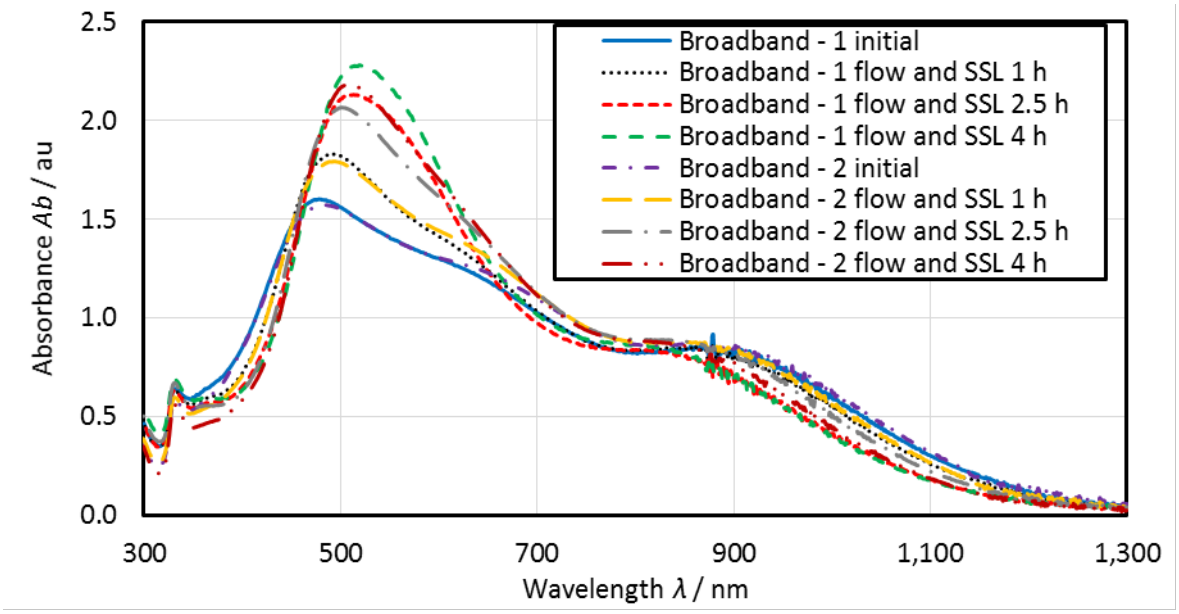

Figure 5-15 UV-vis-IR spectra of the broadband absorber NF before and after being subjected to a flow rate of 0.238 mL s^{-1} for 7.5 h combined with simulated sunlight (SSL) for up to 4 h. Measured using a 1 mL plastic cuvette of 10 mm path length and UV-vis-IR-1.

The blue-shift in the shoulder corresponding to the long λ NF for the flow and SSL samples (Figure 5-15) was ≈ 50 nm which was slightly greater than that seen for flow and temperature (Figure 5-14 but less than that seen for the static elevated temperature of ≈ 70 nm (Figure 5-3) and static SSL tests of ≈ 80 nm – 100 nm (Figure 5-7).

Like the elevated static temperature tests the shoulder corresponding to the mid λ NF disappeared on exposure to flow plus SSL. This was in contrast to the SSL static tests but may have been due to the different starting spectra for the SSL static tests (the initial broadband absorber NF had a secondary peak at ≈ 750 nm corresponding to the mid λ NF absent from the initial broadband absorber spectra for the flow tests).

The final testing condition assessed the impact of flow, elevated temperature and periodic exposure to SSL. The initial and after exposure spectra are shown in Figure 5-16. There was a similar red-shift in the position of the primary peak of 30 nm – 40 nm with an increase in Ab_{max} for this peak of ≈ 33 %. The disappearance of the shoulder corresponding to the mid λ NF was also observed as was a ≈ 70 nm blue-shift in the shoulder corresponding to the long λ NF.

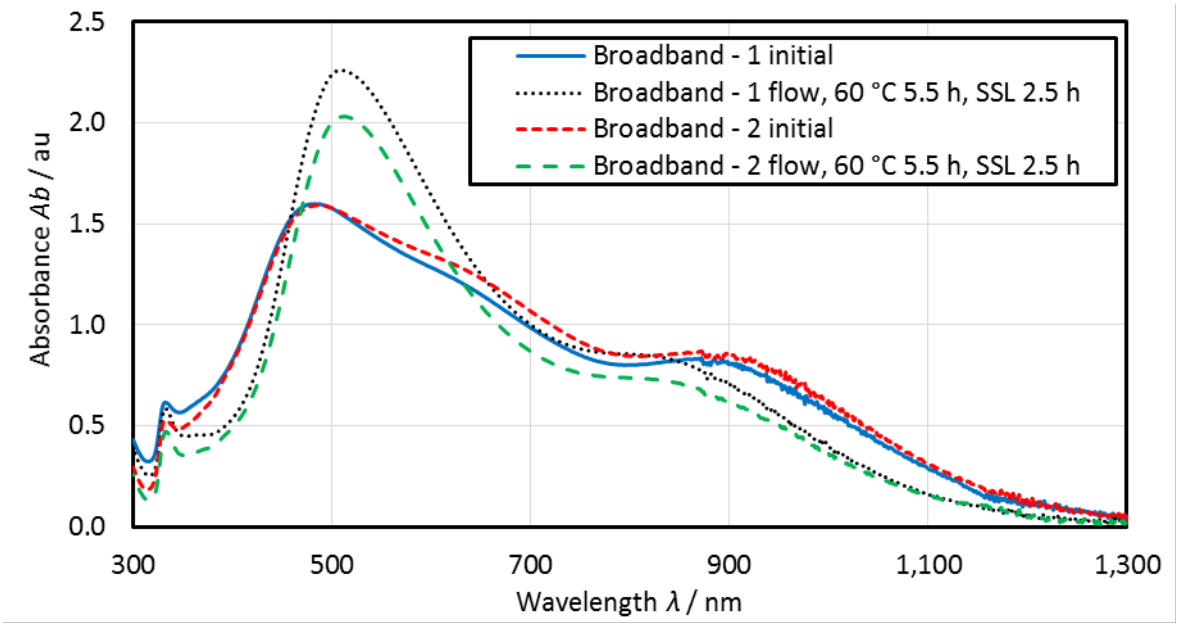

Figure 5-16 UV-vis-IR spectra of the broadband absorber NF before and after being subjected to a flow rate of 0.238 mL s^{-1} for 5.5 h combined with an elevated temperature of ≈ 60 °C and SSL for 2.5 h (2 repeats). Measured using a 1 mL plastic cuvette of 10 mm path length and UV-vis-IR-1.

The increase in Ab_{max} for the primary peak was similar to that seen with flow plus SSL after 2.5 h exposure to SSL (30 % increase see Figure 5-15) but the blue-shift in the long λ shoulder was slightly greater. This blue-shift was similar to that seen for the static elevated temperature and SSL samples.

Although it was hoped to understand more about how the broadband absorber NF changed by undertaking these experiments looking at the effect of fluid flow, the amount of additional insight gathered from the UV-vis-IR spectra is questionable. The lack of change of the spectra with flow over the limited timeframe tested implies that the NF is stable. However, this may not have been the case if the testing had be continued for longer. In addition, the change in the spectra obtained following the harsher exposure conditions of flow plus temperature, flow plus SSL and the combination of all three were similar (but < that seen after the same testing time) to the static results. The static SSL tests also allow for the measurement of the temperature rise allowing the potential efficiency to be calculated. In addition, the sample volume for the static tests is considerably lower.

However, even after cleaning the flow cell and associated pipework multiple times with water, NP residues could be clearly seen coating the sides of the tubes and the flow cell after testing.

Pictures of the flow cell, pipework, thermocouple and reservoir are shown in Figure 5-17. The purple / grey colouration shows the deposits to be thickest at points were the flow is restricted or slowed (for example on passing through the pump (Figure 5-17 C), however, some deposition was also apparent on most types of material (the silicon tubing, plastic thermocouple and glass flow cell).

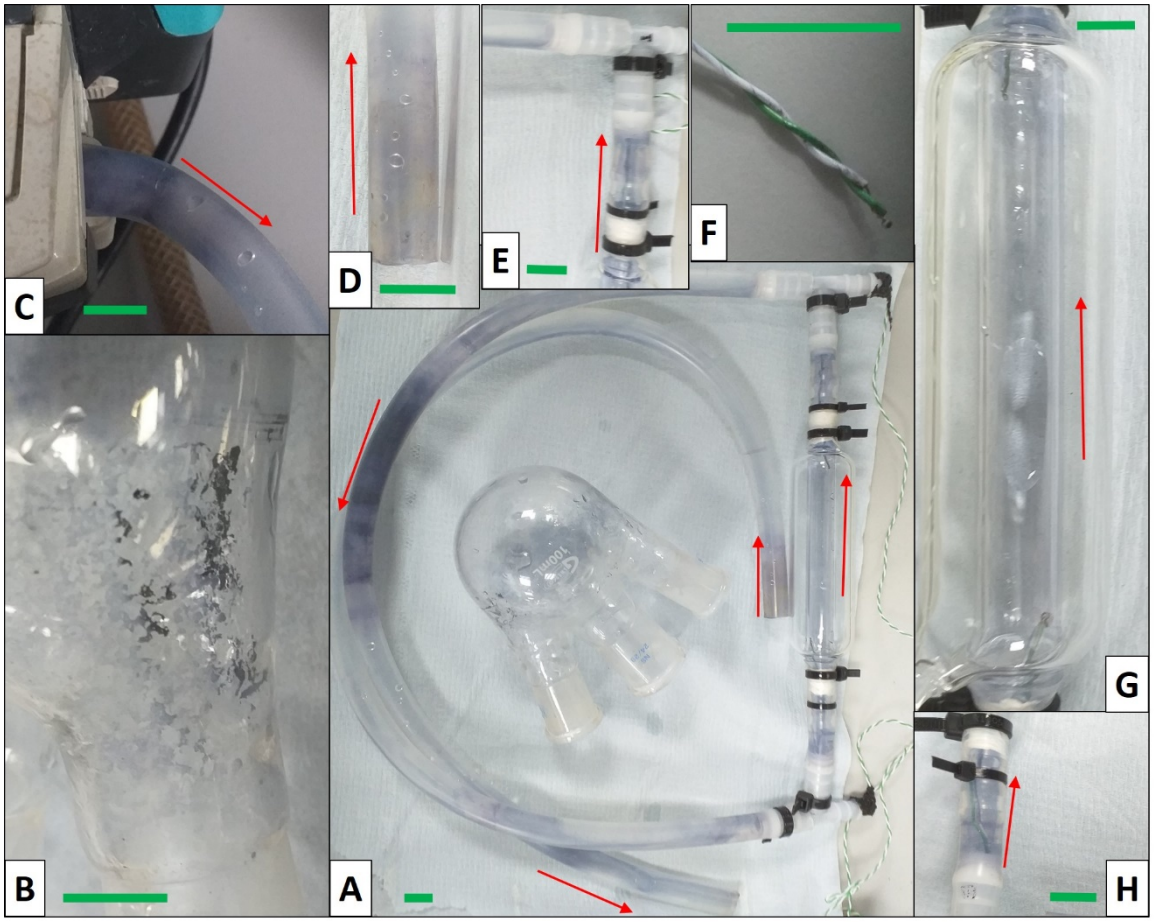

Figure 5-17 Photographs of the flow rig after use showing (A) The flow cell, associated piping and flask, (B) Detail of deposits on the side of the round bottomed flask reservoir, (C) The tubing exiting the peristaltic pump, (D) The bottom of the inlet tube placed in the round bottomed flask, (E) Detail of the connection tube at the top of the flow cell, (F) One of the thermocouples after testing, (G) Flow cell after testing, and (H) Detail of the connection tube at the bottom of the flow cell. The red arrows denote the direction of flow. All green scale bars = 10 mm.

Given the lower concentration of Ag in the broadband absorber NF compared to the centrifuged and re dispersed in ¼ volume Ag NPrs it is likely that if this more concentrated NF had been tested it too would have deposited on the sides of the pipework (and maybe to a greater extent). Although no drop in Ab_{max} was observed in these limited trials it is likely that the amount of this deposit will increase with exposure time, leading to a more dilute NF and an eventual drop in absorbance. It will also become increasingly difficult for the light to pass through the deposit (especially if it becomes thick enough to become silvery as shown in Figure 5-17 B and hence a

reflector) into the bulk of the NF negating the advantages of volumetric absorption leading to lower efficiencies with time.

This deposition of NPs on the surfaces was not observed in the static tests and is additional information that has been obtained from the flow testing.

The results of the TEM analysis before and after flow testing are summarised in Figure 5-18, with the complete results being given in Appendix G, Section G.6. The initial broadband NF contained 11 % triangles (size 31.6 nm), 14 % rounded cornered triangles (size 18.6 nm), 50 % other shaped particles (size 14.9 nm) and 25 % small (< 10 nm) particles.

However all of the "after" testing samples including those of flow alone contained considerably less triangles. This was not expected, given the lack of change in the UV-vis-IR spectra for the flow only samples. There was a considerable time gap between preparing the "after" testing samples and measuring (4 months), due to issues with the availability of the TEM. Zeng et al (Zeng et al., 2010) showed that triangular Ag NPrs were unstable on TEM grids and were transformed into irregular shaped particles after a period of 2 months, whereas round Ag discs were not, with a shape dependent surface migration mechanism being proposed. Hence, it is likely that the TEM samples had degraded prior to analysis accounting for the differences in relative amounts shown in Figure 5-18.

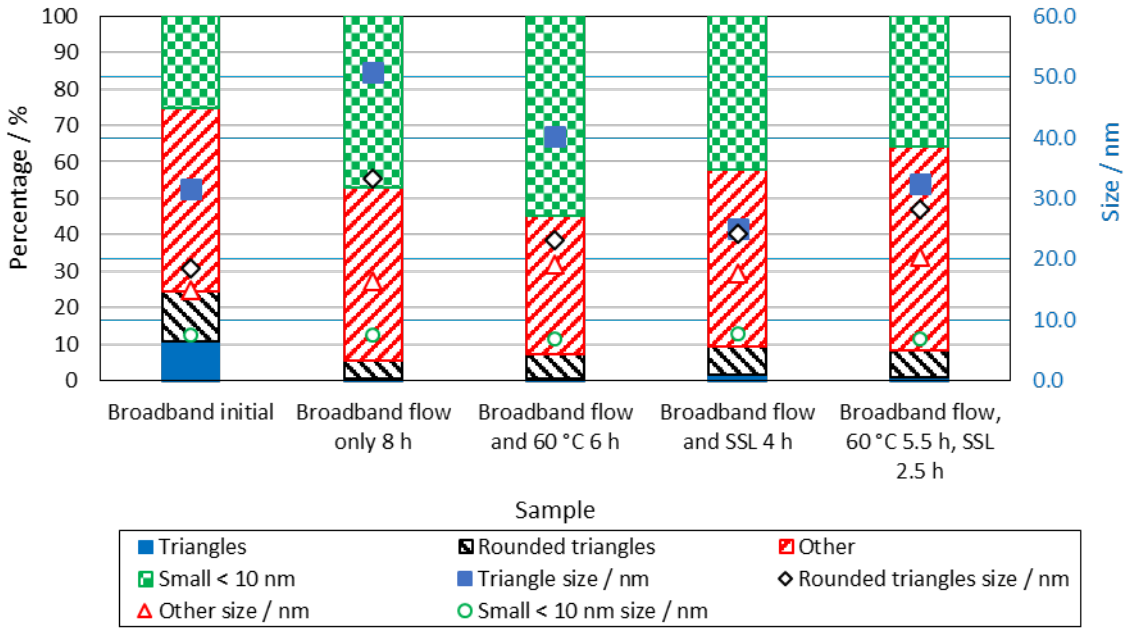

Figure 5-18 TEM analysis after flow, flow and elevated temperature (60 °C), flow and SSL and flow, elevated temperature and SSL for the broadband absorber mixture NF.

This lack of morphological stability of the triangular NPrs even when not in a liquid and deposited on a TEM grid (stored in the dark) clearly further illustrates issues with using them for any application that requires the triangular Ag NPrs to be morphologically stable with time.

Others have assessed the performance of Ag NS (Otanicar et al., 2010) and Ag nanodiscs (Crisostomo et al., 2017) under flow conditions but none have looked at the change in the NF following exposure. Zeng et al (Zeng et al., 2010) did look at the effect of mechanical damage on the UV-vis spectra but used centrifuging as a surrogate for flow rather than constructing a flow rig. This is hence, to the author's knowledge the only study to assess the stability of a broadband Ag NF under flow conditions.

Assessing the Ag broadband absorber NF under flow conditions has shown the NF to be stable to flow only over the limited duration of this test (8 h). Flow conditions with elevated temperature, with SSL and with both gave similar results to the static SSL and elevated temperature tests but the level of change at the same time point was less. The flow tests did, however, identify a potential issue with NPs being deposited on the surfaces of the pipework and flow rig during the testing, especially in regions where the flow was slowest or constricted. Finally, the TEM analysis showed that the triangular Ag NPrs were not stable even when deposited on a TEM grid (i.e. not in a NF). This indicates that stabilising this particular morphology would be very challenging.

5.6.7 Effects of changing base-fluid (BF)

The potential issues with changing the BF from water to one more suitable for solar applications, namely propylene glycol (PG) are shown in this subsection. The UV-vis spectra before and after exposure to an elevated temperature of 70 °C for centrifuged Ag TSCD-PVP NPrs in both water and PG are shown and discussed.

Both ethylene glycol (Kim et al., 2006; Sharma et al., 2011; Silvert et al., 1996; Silvert et al., 1997) and propylene glycol (PG) (Park et al., 2011) can act as reducing agents in the synthesis of Ag NS instead of $NaBH_4$ at temperatures of > 120 °C. It is likely therefore that when the BF is changed to one more suitable for solar applications such as ethylene glycol or PG that this will have an effect on the stability to temperature of the Ag NPs. As it is not thought possible to produce Ag NPrs with diols (Darmanin et al., 2012) it is likely that λ_{max} will blue-shift rapidly on heating Ag NPrs as more NS are produced even at a lower temperature of 70 °C. The presence of PVP in the solution may also affect the reaction with PVP known to have a size controlling effect on the NS produced at temperature in ethylene glycol. In addition, it can also act as a reducing agent with Ag NPs being produced at ≈ 100 °C in the presence of high concentrations of PVP only in water BF (Silvert et al., 1996).

There is, a lack of knowledge of the effect of adding already synthesised Ag NPs to either ethylene glycol or PG and then heating to a lower temperature than used in the synthesis protocols. One study looked at the effect of exposure to temperatures ≤ 45 °C on the optical properties for Ag NS in ethylene glycol (Otanicar et al., 2013) finding an increase in transmittance but no shift in λ_{max}.

Other studies have assessed ethylene glycol and water BF with Ag NS coated with TiO_2 (He et al., 2019) and PG BF with SiO_2 coated Ag NS (Huang et al., 2021) for PVT applications but do not appear to have undertaken any sunlight or elevated temperature stability trials.

To illustrate the potential issues of changing the BF the protocol described in Section 3.9.7 was followed to investigate the effect of a temperature of 70 °C on the UV-vis spectra for Ag NPrs stabilised with both TSCD and PVP, centrifuged and re-dispersed into ¼ volume of either PG BF or water.

UV-vis spectra showing the average results obtained (for three replicates) are presented in Figure 5-19. For the Ag NPrs re-dispersed into water there was a small blue-shift in λ_{max} of ≈ 20 nm and no drop in Ab_{max}. This blue-shift in λ_{max} was not significant according to a two-sample t-test (Appendix F Section F.1). This result agrees with the result obtained for the centrifuged Ag TSCD-PVP NPr samples in Section 5.6.3 (see also Figure K.12), even although the starting value of λ_{max} occurred at a higher wavelength (891 nm versus 773 nm).

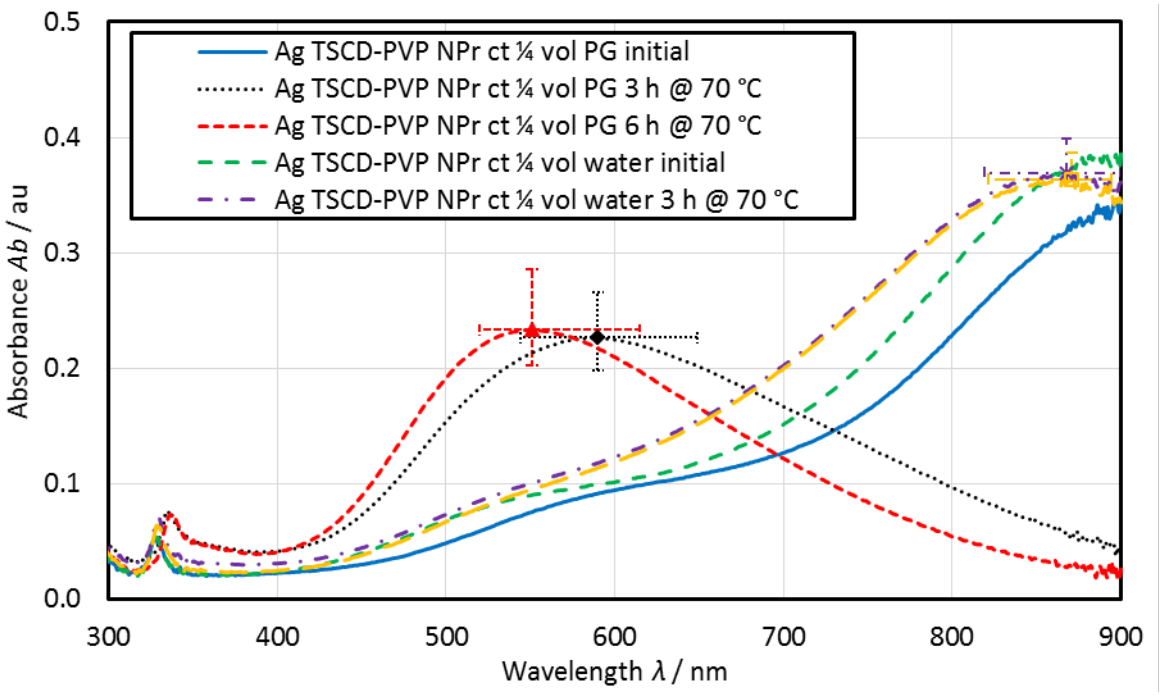

Figure 5-19 UV-vis spectra before and after exposure to a temperature of 70 °C for Ag TSCD-PVP NPrs centrifuged at 12,857 r.c.f. (10,000 rpm) for 30 minutes and re-dispersed into either ¼ volume of PG or water. All samples measured on UV-vis-1 with a 1 mm path length quartz cuvette. Average results shown. Error bars show range of results obtained at the maximum absorbance (N = 3).

In contrast the Ag NPrs re-dispersed into PG exhibited a large blue-shift in λ_{max} after 3 h exposure to a temperature of 70 °C of ≈ 300 nm, and a corresponding drop in Ab_{max} of ≈ 35 %. After another 3 h testing there was a continued blue-shift in λ_{max} of ≈ 30 nm - 45 nm (total average shift 334 nm ± 49 nm, N = 3), but no further decrease in Ab_{max} with Ab_{max} actually increasing slightly as the peak became less broad (see Figure 5-19).

The changes in both λ_{max} and Ab_{max} were greater than all the changes observed for the water BF NFs with exposure to elevated temperature (see Section 5.6.3) clearly demonstrating the potential stability issue of changing the BF to one more suitable for solar applications.

5.6.8 Summary / Conclusions

For the colloidal stability (4 °C in the dark), all the NFs stabilised with both TSCD and PVP were stable to aggregation even after 603 days of storage, demonstrating the benefit of using an additional stabilising agent, namely PVP to prevent aggregation. Unfortunately not all the NFs tested were stable to morphological changes even under these ideal conditions with the mid λ and long λ NFs showing the greatest change. This had a subsequent effect on the morphological stability of the broadband absorber.

When the NFs were exposed to an elevated temperature of 70 °C, they again revealed good stability to aggregation over the timeframe tested. The harsher testing conditions exasperated the morphological instability of the mid λ, long λ and broadband absorber NFs. TEM analysis showed these morphological changes to be due to the rounding of the corners of the NPs rather than a change in NP size. However, the centrifuged Ag NPrs were more resistant to morphological changes perhaps due to the removal of excess TSCD on centrifuging.

When the even harsher static SSL tests were used to assess the stability of the centrifuged Ag NPrs, the broadband absorber NF and its component NFs, the changes observed were in the same directions as those seen in the elevated temperature tests but of a larger magnitude over a shorter testing time. The broadband absorber NF again appeared to be less stable to morphological changes than the centrifuged Ag NPrs NF.

The natural sunlight trials in contrast to the other trials undertaken showed significant aggregation of the Ag NPrs. This indicates that morphological changes occur more rapidly than aggregation and provides further information that is not obtained from the shorter timeframe trials. This illustrates the benefits of utilising complementary methods to assess stability.

The Ag broadband absorber NF was found to be stable to fluid flow over the 8 h tested. When flow was combined with elevated temperature and or SSL the results were similar to those

observed in the static elevated temperature and SSL tests but of a lower magnitude at the same time point. However, NPs were found to deposit on the surfaces within the test rig especially at points where the flow was slower or constricted. The irreversible deposition of NPs from the NF could have serious consequences in terms of efficiency reduction with time and is additional information not gathered from the static tests. The after flow TEM results also indicated that the sharp cornered Ag NPrs were not even morphologically stable when not in solution, potentially affecting the use of Ag NPrs for other applications that require morphological stability.

Finally, when Ag NPrs were re-dispersed into an alternative BF more suitable for solar applications, namely PG the blue-shift in λ_{max} with elevated temperature exposure were considerably greater than that seen with water again indicating further stability challenges for Ag NFs. There was also a large reduction in Ab_{max} suggesting aggregation as well as morphological changes were occurring in the alternative BF.

5.7 Conclusions, Implications and Overall Summary

5.7.1 Conclusions

This is one of the first studies to measure in static solar simulator tests Ag NPrs with a λ_{max} > 750 nm and the first study to measure directly the performance of the developed novel Ag based broadband absorber produced from combining three different morphologies of Ag NFs. It is also one of the few studies to investigate the stability of anisotropic Ag NPrs using a variety of complementary tests and the only study to look at the stability of the developed novel broadband absorber NF. The use of longer timeframe trials such as the natural sunlight tests and the long term storage trials under ideal conditions is also unusual.

In the static solar simulator tests all the five NFs evaluated exhibited a greater ΔT and $\Delta T/\Delta t$ than water alone. They all consequently had a greater photo-conversion efficiency (η_{PE}) than the 20.51 % obtained for water clearly indicating their potential for enhancing solar thermal capture. The order of η_{PE} for the five NFs tested was short λ (47.68 %) < mid λ (65.05 %) ≈ long λ (62.46 %) < broadband absorber (83.77 %) ≈ centrifuged Ag NPrs re-dispersed into ¼ volume water (84.81 % middle position). Both the short and mid λ NF were diluted for these tests.

These results were similar to those obtained from direct calculation of $\eta_{lamp(330\ nm\ -\ 1100\ nm)}$ or $\eta_{lamp(330\ nm\ -\ 900\ nm)}$ from the UV-vis spectra. This allows calculations based on UV-vis measurements to be used with confidence for the rapid identification and screening of NFs for their potential in DASC applications. Utilising these two complementary techniques to calculate the potential

efficiency also has the added benefit of reducing the uncertainty of the η_{PE} calculation which is highly dependent on the accurate measurement of the lamp intensity.

The stability studies undertaken in this work have started to address the urgent need for more information on Ag NF stability and will serve as a useful bench mark to quantify any future improvements in stability obtained from an appropriate stabilisation strategy. All the water BF Ag NFs stabilised with both TSCD and PVP were stable to aggregation in all of the stability trial except the longer timeframe natural sunlight trials, suggesting that aggregation is a slower process than morphological changes and illustrating the advantage of undertaking a variety of stability tests utilising differing timeframes.

Even under ideal storage conditions (4 °C in the dark), not all the NFs evaluated were morphologically stable, with the most unstable two NFs (the mid and long λ NFs) exhibiting a rapid blue-shift in λ_{max} and a rounding of the corners of the NPs. The magnitude and speed of this change was dependent on the stability test conditions with the more harsh conditions giving a more rapid, larger change. The rounding of the corners of the Ag NPrs was even seen after several months when the NPrs were deposited onto a TEM grid rather than being in a fluid. As both the mid and long λ NF were not morphologically stable this influenced the stability of the resultant broadband absorber NF.

The centrifuged Ag NPrs were more resilient to morphological changes than the less concentrated broadband absorber in both the elevated temperature and static SSL trials perhaps due to the centrifuging removing excess TSCD, which is known to have a detrimental effect on the stability.

Although stable to flow alone over a short timeframe of 8 h, the Ag broadband absorber NF was not morphologically stable when subjected to flow with elevated temperature and or SSL reflecting the results obtained in the static tests. The magnitude and speed of change was less than that seen in the static tests questioning the added information gained from the more experimentally complex flow testing. However, the flow tests did show that NPs were being irreversibly deposited onto the surfaces of the testing equipment from the NF at points of low flow and constricted flow. This was additional information not obtained from the static tests.

Even the slightly more stable centrifuged Ag NPrs (compared to the broadband absorber NF) demonstrated a large rapid blue-shift in λ_{max} of ≈ 300 nm and a drop in Ab_{max} of 30 % - 40 % when an alternative BF of PG rather than water was used suggesting that the Ag NPs react with this BF causing both morphological changes and aggregation.

5.7.2 Implications

The actual performance of the more concentrated centrifuged Ag NPr NF and the broadband absorber NF were both shown to be potentially high enough for enhancing solar capture and agreed well with the calculated results obtained in Chapter 4. However, actual measurements of performance of larger scale volumetric SCs containing these NFs would be required to check if this enhanced performance occurred in practice comparing the results obtained directly with the best commercial STCs available.

Even if the performance of these collectors was found to be suitable for enhancing solar capture the issue of NF stability would still need to be addressed. Without a morphologically stable NF it would be impossible to recommend that STCs based on Ag NFs are used even if they do offer significant advantages in terms of performance. An appropriate stabilising strategy for Ag based NFs is hence urgently needed. One such strategy could be the use of a SiO_2 coating to protect the surface of the Ag NP and potentially prevent the rounding of the corners of the NPs. The development of a SiO_2 synthesis method, the measurement of its performance and an assessment of the stability of the SiO_2 coated Ag NPs will be discussed further in Chapter 6.

Moreover, even with an appropriate stabilisation strategy it would still be extremely challenging to improve the stability of the NFs enough to make then suitable for solar applications as several orders of magnitude improvement is needed to give ≈ 20 years of service (or 3 y – 5y with periodic complete replacement of the NF).

Although the stability testing undertaken here has increased the amount of knowledge of Ag NF stability, further work is required over longer timeframes using the more harsh testing conditions such as elevated temperature and SSL exposure. This may firstly improve the understanding of how the morphological changes vary with testing time and secondly allow aggregation to occur in these accelerated tests in a similar manner to the aggregation observed in the longer term natural sunlight tests.

Further work on the role of TSCD within the NF is also required. If it was possible to remove all the TSCD from the NF, this could prevent or significantly reduce the morphological changes occurring even with light exposure, conversely it may increase the propensity to aggregation as there would no longer be any electrostatic stabilisation in the colloid.

Finally, further work on the stability of the Ag NPrs when not in solution is needed. Any instability of Ag NPrs when not in solution would preclude the use of these shapes of NPs for any other application requiring morphological stability with time unless a means of stabilising the shape when deposited on a surface can be found.

5.7.3 Summary

A short summary highlighting the main Sections covered in this Chapter and the conclusions is given in Table 5-3.

Table 5-3 Chapter 5 Summary.

Section	Covered	Conclusions / outcomes
Performance literature	Performance with a surface absorber Performance in a volumetric STC	Surface absorber – Ag NFs increase thermal conductivity, η_{PE} improvements of 0 % – 22 % Volumetric – best potential η_{PE} = 95 % – 98 % (numerical study). Need broadband absorbance to enhance η_{PE}. Also a need to compare to commercial FPCs
Stability literature	Literature measuring stability of Ag NFs	Lack of stability trial data on Ag NFs in the literature, especially long term storage trials and natural sunlight testing
Measuring performance in the solar simulator	Solar simulator set-up (measurement of water), Ag NPrs, broadband absorber NF and components temperature rise and η_{PE} calculation	All NF > ΔT than water (η_{PE} = 20.51 %). η_{PE} for the five NFs tested was short λ (47.68 %) < mid λ (65.05 %) ≈ long λ (62.46 %) < broadband absorber (83.77 %) ≈ centrifuged Ag NPrs re-dispersed into ¼ volume water (84.81 % middle position). Results similar to η_{Ab} obtained from UV-vis measurements. Care needed in the measurement of I_L
Stability testing	In approximate order of ascending severity. Colloidal stability (ideal, dark, 4 °C), elevated temperature (70 °C), SSL stability, natural sunlight trials, effect of fluid flow and changing the BF to PG	All water Ag NFs showed good stability to aggregation except in natural sunlight trials. Aggregation a slower process than morphological changes. All not morphologically stable in SSL tests (worst mid and long λ NFs – rapid blue-shift in λ_{max} - rounding of corners of NPs – not even stable under ideal conditions and Ag NPrs not stable on TEM grid). Rate and magnitude of change dependent on harshness of testing regime and type of NP in NF. Reducing TSCD amount may improve stability. Broadband not stable due to instability of mid and long λ NFs. Deposition of NPs on surfaces in flow test. PG BF more aggressive – rapid ≈ 300 nm blue-shift in λ_{max} and drop in Ab_{max} ≈ 35 % on exposure to 70 °C for centrifuged Ag NPrs. Ag NFs not at present suitable for solar applications due to lack of stability

Chapter 6 SiO_2 Coated Silver Nanofluids (NFs)

6.1 Publications from this Chapter

1. Kimpton, H., Cristaldi, D.A., Stulz, E., Zhang, X., 2020. Thermal performance and physicochemical stability of silver nanoprism-based nanofluids for direct solar absorption. Solar Energy, 199, 366-376, https://doi.org/10.1016/j.solener.2020.02.039 (Kimpton et al., 2020a).

6.2 Introduction

The focus of this Chapter is on investigating the coating of silver nanoparticles with silica to produce hybrid nanofluids that may offer advantages in terms of stability, allowing SiO_2 coated silver nanoparticles to be used for solar applications.

Firstly, the results obtained from the development of a suitable coating protocol are described, looking at two potential SiO_2 coating methods, namely the water-glass method and one based on the Stöber process utilising tetraethoxysilane (TEOS) in an ethanolic base catalysed reaction.

Section 6.4 then looks at repeating the SiO_2 coating protocol developed in the proceeding Section to check the reproducibility of the synthesis using Ag NPrs as the starting nanofluid (NF). The potential performance of this hybrid SiO_2@Ag NPr NF is then estimated from the UV-vis spectra and compared to the actual performance obtained from static tests in the solar simulator. This Section then describes the results obtained from assessing the stability of this NF, roughly in order of ascending severity of the stability trial, starting with the colloidal stability, then elevated temperature exposure, simulated sunlight (SSL) testing and finally, natural sunlight exposure trials.

The next Section assesses the impact of several coating protocol modifications on the temperature stability of the resultant SiO_2@Ag NPr NF. Firstly, the effect of adding an extra purification is described along with the reduction in oxygen level in the NF. Secondly, the role of the capping agent, namely 16-mecaptohexadecanoic acid (MHA) is investigated, along with the effect of reducing the amount of the base, dimethylamine (DMA). Finally, the effect of reducing the time of the base catalysed step is evaluated.

The last main Section 6.6, describes the results obtained when the starting NF used for SiO_2 coating was the broadband absorber developed in Chapter 4, Section 4.6.

This Chapter finishes with some conclusions, implications and a summary.

6.3 Development of Synthesis Methods

This Section provides details of the initial investigations undertaken aimed at developing a suitable synthesis method to consistently coat Ag NPrs with SiO_2. The results obtained for the first of the two methods assessed, namely the water-glass method are described first. Secondly, the results obtained using the second Stöber TEOS method are detailed. A short summary then completes this Section.

6.3.1 Water-glass method

In the water-glass method described in Section 3.6.3, the aim was to produce a thin SiO_2 coating onto the Ag NPrs, which could then be used on its own or combined with the Stöber process to produce a thicker SiO_2 layer. The capping agent 3-mercaptopropyl trimethoxysilane (MPTMS) was used to prepare the surface of the NPs for subsequent SiO_2 coating and the subsequent reaction allowed to proceed for a long time (48 h) to produce a coating that could be observed using TEM.

In total three different sets of experiments were undertaken. These are described in more detail in Appendix L, Section L.1. The first two sets of experiments used the protocol described in Section 3.6.3, and the third looked at increasing the amount of MPTMS by 5 x as this may produce more elevated temperature resistant NFs (Hjerrild et al., 2018).

Following the addition of the capping agent MPTMS for the first group of experiments (Figure 6-1), there was a small red-shift in λ_{max} of ≈ 10 nm. After SiO_2 coating using the water-glass procedure, centrifuging and re-dispersing into ¼ volume of water BF there was a further red-shift in λ_{max} of ≈ 20 nm and a significant drop in Ab_{max} of ≈ 35 %. This drop in Ab_{max} was greater than that seen for uncoated Ag TSCD NPrs (also shown in Figure 6-1), centrifuged and re-dispersed into water. When re-dispersed into an alternative BF, PG, the drop in Ab_{max} was even larger (≈ 78 %).

To investigate this drop in Ab_{max}, a second set of experiments were undertaken (see Appendix L, Section L.1). Following SiO_2 coating there was a small drop in Ab_{max} of ≈ 15 %, however, when these samples were subsequently centrifuged the drop in Ab_{max} was greater (≈ 40 %) showing that even though the length of the centrifuging time was increased compared to the uncoated Ag NPrs (30 minutes compared to 15 minutes) it was still not long enough to prevent loss of product.

When the amount of MPTMS was increased, the drop in Ab_{max} following SiO_2 coating using the water glass method prior to centrifuging was even greater (Figure L.1) at ≈ 65 %. The red-shift on coating was also larger at ≈ 60 nm. Centrifuging and re-dispersing into an alternative BF of 50 %

PG and water resulted in an almost complete loss of product. Further optimisation of the centrifuging conditions and protocol is therefore required.

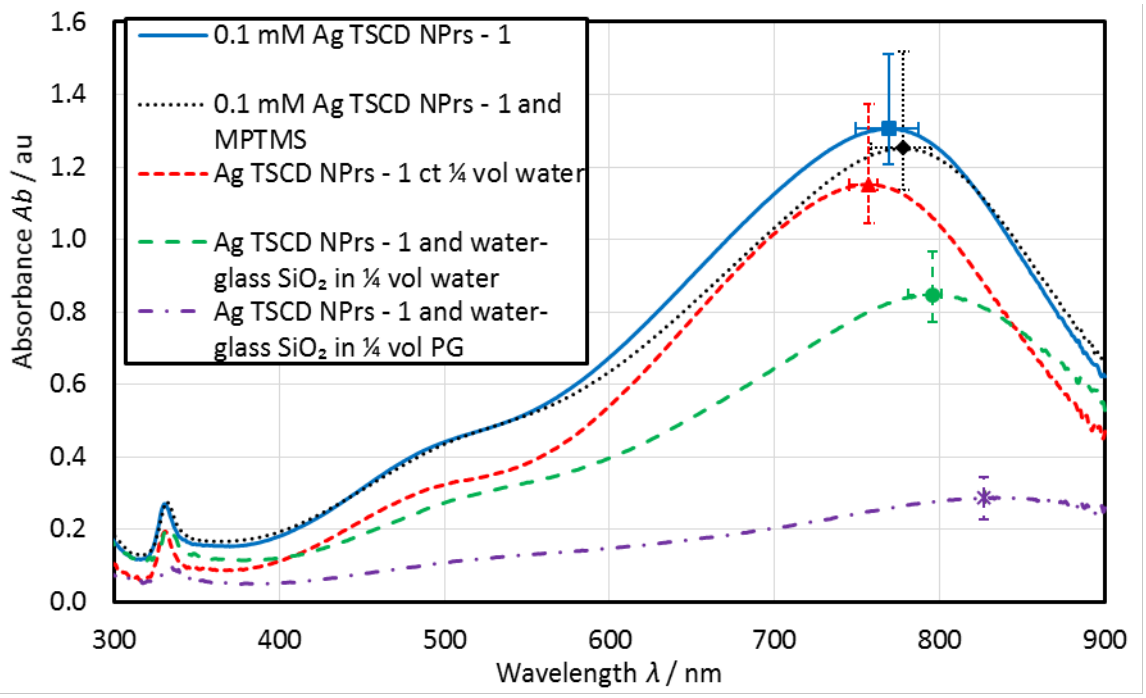

Figure 6-1 UV-vis-IR spectra before and after using the water-glass method to coat the Ag NPrs with SiO_2. All measured using UV-vis-1. The centrifuged results (¼ vol samples) have been adjusted for cuvette and volume. Average results shown (N = 3). Error bars depict range of results obtained at the maximum absorbance.

When the NFs from the first set of experiments were tested for their stability to an elevated temperature of 70 °C using the protocol described in Section 3.9.3, there was no significant change (according to two-sample t-tests) in either λ_{max} or Ab_{max} (full results in Section L.1) in either water or PG BF. This is an improvement in stability to elevated temperature compared to the uncoated Ag NPrs in PG (Figure 5-19). However, the result in PG should be treated with some caution due to the low broad nature of the spectra for the water-glass SiO_2@Ag NPr PG NFs.

Conversely, when the SiO_2@Ag NPr water-glass water BF NFs were subjected to SSL for 2 h using set-up A in the solar simulator (Figure 6-2) there was a ≈ 45 nm blue-shift in λ_{max} and a ≈ 38 % reduction in Ab_{max} accompanied by the formation of a low secondary peak at ≈ 425 nm. This change following SSL exposure was very different to that observed for the uncoated Ag NPrs which showed no large reduction in Ab_{max}, a slightly larger blue-shift in λ_{max} of ≈ 55 nm (average value from Figure 5-6 after 2 h exposure) and no additional peak at ≈ 425 nm (Figure K.14). Using the water-glass SiO_2 procedure, increased the level of NP aggregation (drop in Ab_{max}), lead to the formation of Ag NS (peak at 425 nm) and still resulted in a rounding of the NPrs (blue-shift in λ_{max}) following SSL exposure compared to the uncoated Ag NPrs.

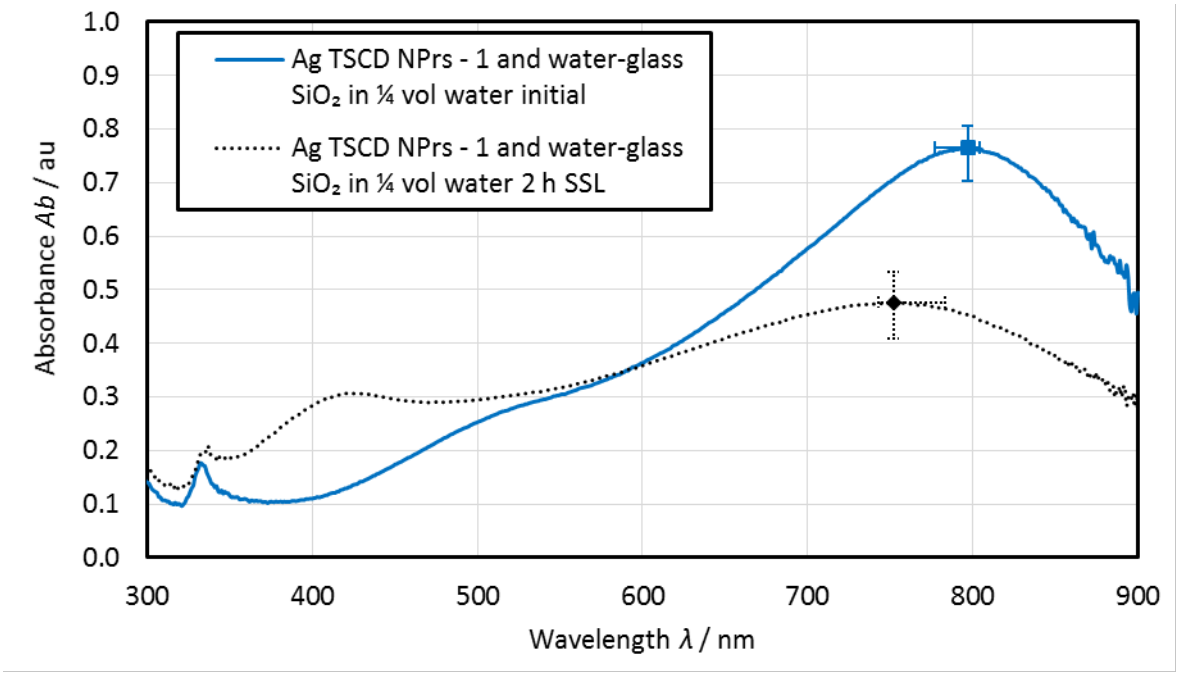

Figure 6-2 UV-vis spectra before and after exposure to SSL for 2 h using set-up A in the solar simulator. Measured using UV-vis-1. Average of three results shown with error bars depicting the range of results at the maximum absorbance.

TEM micrographs of the NPs after application of the SiO_2 water-glass procedure are given in Figure 6-3 (a summary of the size analysis results is given in Appendix L, Figure L.2, with complete TEM results in Appendix G, Section G.7). A thin incomplete coating of SiO_2 was observed after centrifuging and re-dispersal into water for the first set of experiments (Figure 6-3 A). When exposed to SSL there were more rounded cornered triangles and smaller particles, with some etching of the NPrs on the side of the triangles being apparent (Figure 6-3 B). When more MTPMS was used (Figure 6-3 C) a more complete thin (≈ 4 nm) coating was formed in water BF and there was evidence of aggregation of the NPs as well as etching along the sides of the triangular NPs. In an alternative BF of 50 % PG / water mix, more dissolution of the particles occurred (Figure 6-3 D) and the coating appeared thinner and less consistent. Although using more MTPMS appears to increase the coating thickness, the loss of product even prior to centrifuging is concerning. Further work on optimising the water-glass coating method is therefore required in order to produce a consistent coating without dissolution of the NPs especially if PG rather than water is used as the BF.

These TEM micrographs appeared similar to those presented by Taylor et al for their water-glass SiO_2@Ag nanodiscs in water (Taylor et al., 2018). However, they observed a blue-shift in λ_{max} of ≈ 80 nm following exposure to a temperature of 80 °C for 30 h and no change following exposure to UV light only (not heat and SSL as in this case). They also in contrast saw a drop in Ab_{max} and the presence of a secondary peak at ≈ 400 nm for their uncoated Ag nanodiscs following UV light exposure.

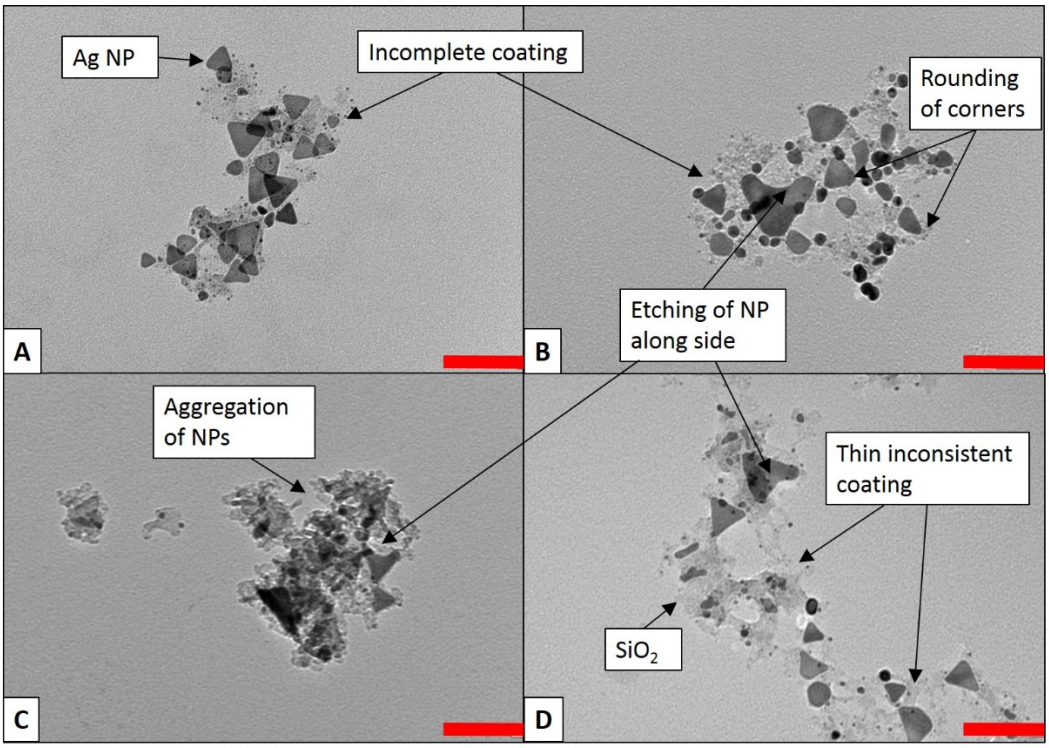

Figure 6-3 TEM micrographs after water-glass method of (A) Ag TSCD NPrs – 1 and water-glass SiO_2 in ¼ volume water initial, (B) After SSL for 2 h, (C) Ag TSCD NPrs – 3 and 5 x MPTMS, water-glass SiO_2 in water, and (D) in a mixture of water / 50 % PG. All red scale bars = 100 nm.

In summary, although the water-glass method of SiO_2 coating appeared to improve the elevated temperature stability especially in PG BF, the SSL stability results were worse than for the uncoated Ag NPrs and a thin incomplete coating of SiO_2 was produced. There was also significant loss of product following both the coating procedure (especially when using 5 x MPTMS and / or PG BF) and centrifuging. Considerable further work on the synthesis method, perhaps utilising an alternative capping agent or combining with the Stöber coating process to produce a thicker more complete coating is required. Even then it is unlikely that using the water-glass method would increase the level of stability of the resultant NF enough (especially given the poor SSL stability even in water BF) to allow it to be recommended as a SiO_2 coating method suitable for Ag NPrs NFs to make their use in solar applications possible.

6.3.2 Stöber SiO_2 coating method

To arrive at the Stöber SiO_2 coating method detailed in Section 3.6.4, a number of parameters were initially investigated. These were, the amount of TEOS used (4 concentrations), the amount of capping agent MHA (2 concentrations) and the time of the TEOS stage (60 minutes, 30 minutes and 15 minutes). The success of the coating protocol was assessed using a combination of UV-vis and TEM analysis, with the best protocol being the one with the highest Ab_{max}, the most consistent complete SiO_2 coating and the lowest amount of multi-cored NPs (those containing ≥ 2 Ag NPs within one shell). Further trials as detailed in Section 3.6.5 were then undertaken with the

aim of improving the resultant stability to elevated temperature of the SiO_2@Ag NPrs. The results of these will be discussed in Section 6.5.

The same Ag NPr NF (5 mL) was used for each experiment (50 mL total batch volume). TEM analysis was undertaken on this starting NF (see Appendix G, Table G.22) and showed the starting NF to mainly contain triangles (63 %) with a size of 49.13 nm (σ = 16.17 nm, N = 196). These results were consistent with those seen previously for Ag TSCD-PVP NPrs produced using a 50 mL batch volume (Figure 4-7).

The UV-vis results obtained for the 4 different TEOS concentrations investigated (16 mM, 10 mM, 8 mM, 1.6 mM) are shown in Figure 6-4 along with the spectra for the uncoated Ag NPrs. The time of the TEOS stage and the amount of MHA were both kept constant at 60 minutes and 20 µM. Prior to coating (0.1 mM Ag TSCD-PVP NPr), Ab_{max} was 1.49 au and λ_{max} was 899 nm similar to those seen previously for Ag TSCD-PVP NPrs produced using a 50 mL batch volume (Figure 4-5).

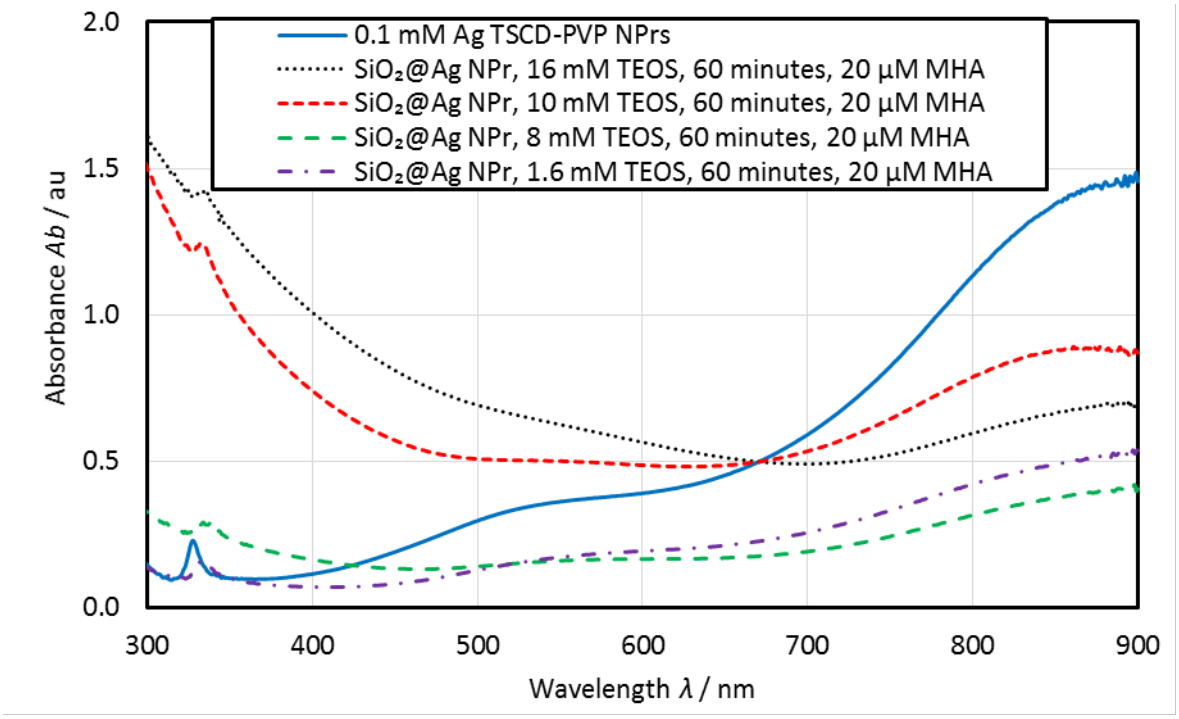

Figure 6-4 UV-vis spectra before and after application of the Stöber coating process investigating the effect of TEOS concentration. Measured using UV-vis-1 and a 10 mm path length quartz cuvette.

After SiO_2 coating using the Stöber method and repeat centrifuging with re-dispersal into the same volume of water BF, there was a reduction in Ab_{max} for the Ag NPr peak at ≈ 900 nm, but an increase in the absorbance < 600 nm for the samples produced using the highest concentrations (16 mM and 10 mM) of TEOS. This was due to incomplete removal of the SiO_2 NPs even with repeat centrifuging. The lowest decrease in Ab_{max} for the Ag NPr peak was observed for the sample produced using 10 mM TEOS.

Typical TEM micro-graphs of the SiO_2@Ag NP are shown in Figure 6-5 (complete TEM analysis results in Appendix G, Section G.8). The highest concentration of TEOS (16 mM Figure 6-5 A) gave rise to an inconsistent thickness of SiO_2 coating (average coating thickness 46.48 nm, σ = 35.01 nm, N = 52) and clumping of the NPs leading to a high percentage of multi-cored NPs and considerable difficulty in analysis of the micro-graphs.

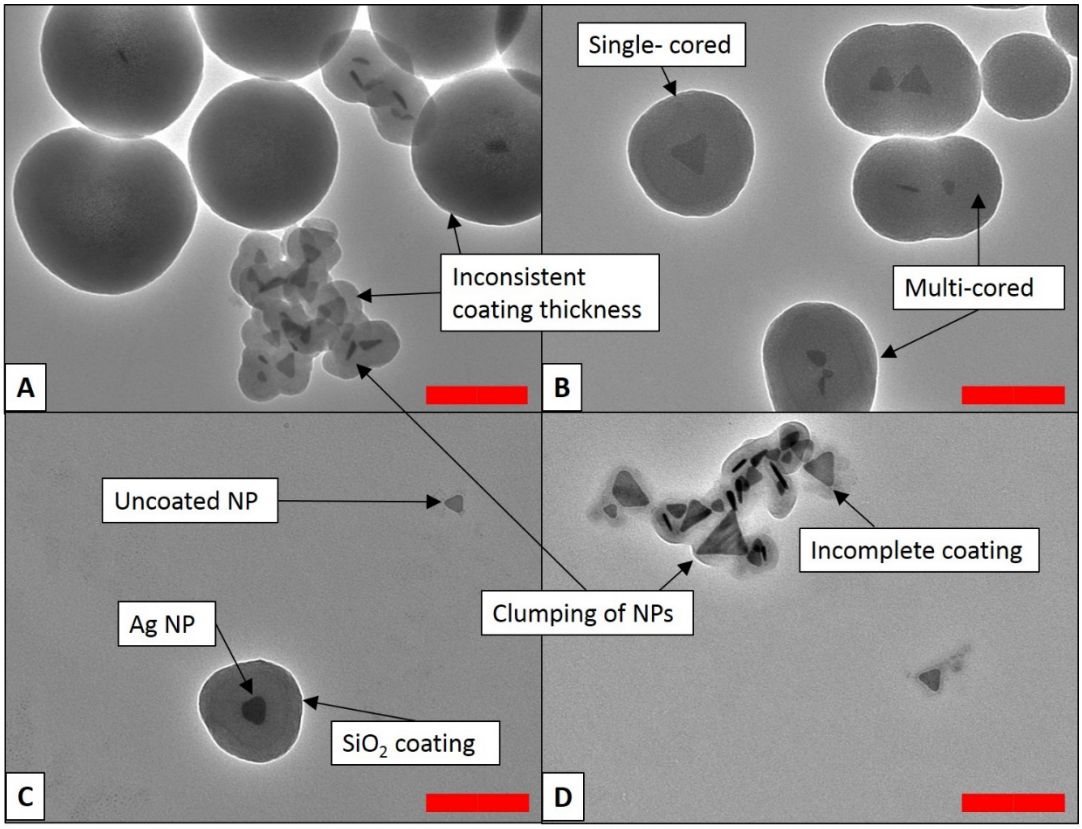

Figure 6-5 TEM micrographs after TEOS SiO_2 coating using (A) 16 mM TEOS, (B) 10 mM TEOS, (C) 8 mM TEOS, and (D) 1.6 mM TEOS. All using 20 µM MHA and 60 minutes TEOS reaction time. All red scale bars = 200 nm.

The 10 mM TEOS sample had a more constant SiO_2 coating of thickness 85.99 nm (σ = 8.67 nm, N = 227) and less multi-cored NPs (3 multi-cored NPs shown in Figure 6-5 B). When the amount of TEOS was reduced to 8 mM there were more Ag particles with an incomplete coating (one such particle is illustrated in Figure 6-5 C) and again more aggregation of the NPs, resulting in a higher percentage of multi-cored particles and a greater variation in the coating thickness (average value 52.59 nm, σ = 18.65 nm, N = 74). Further reducing the TEOS concentration to 1.6 mM resulted in a thin (21.89 nm, σ = 9.47 nm, N = 61) incomplete SiO_2 coating (Figure 6-5 D). The optimum concentration of TEOS would therefore appear to be 10 mM although further repeat experiments would be needed to confirm this.

This concentration of TEOS was then used to assess the effect of reducing the time of the TEOS stage as this may impact the coating thickness (Lismont et al., 2015) and of doubling the amount of capping agent MHA in the hope of reducing the number of multi-cored NPs. The UV-vis results

from these experiments are shown in Figure 6-6 (the uncoated Ag NPr and the 60 minutes, 20 µM MHA spectra from Figure 6-4 are reproduced for ease of comparison). Again in all cases following coating there was a decrease in Ab_{max} for the Ag NPr peak at ≈ 870 nm – 900 nm and an increase in the absorbance in the < 600 nm region due to the presence of SiO_2. Reducing the time of the TEOS stage appeared to increase the reduction in Ab_{max} (compare the 60 minute, 20 µM MHA with the 30 minute, 20 µM MHA and the 30 minute, 40 µM MHA with the 15 minute, 40 µM MHA). Increasing the MHA concentration in contrast reduces the reduction in Ab_{max} (compare the two 30 minute spectra).

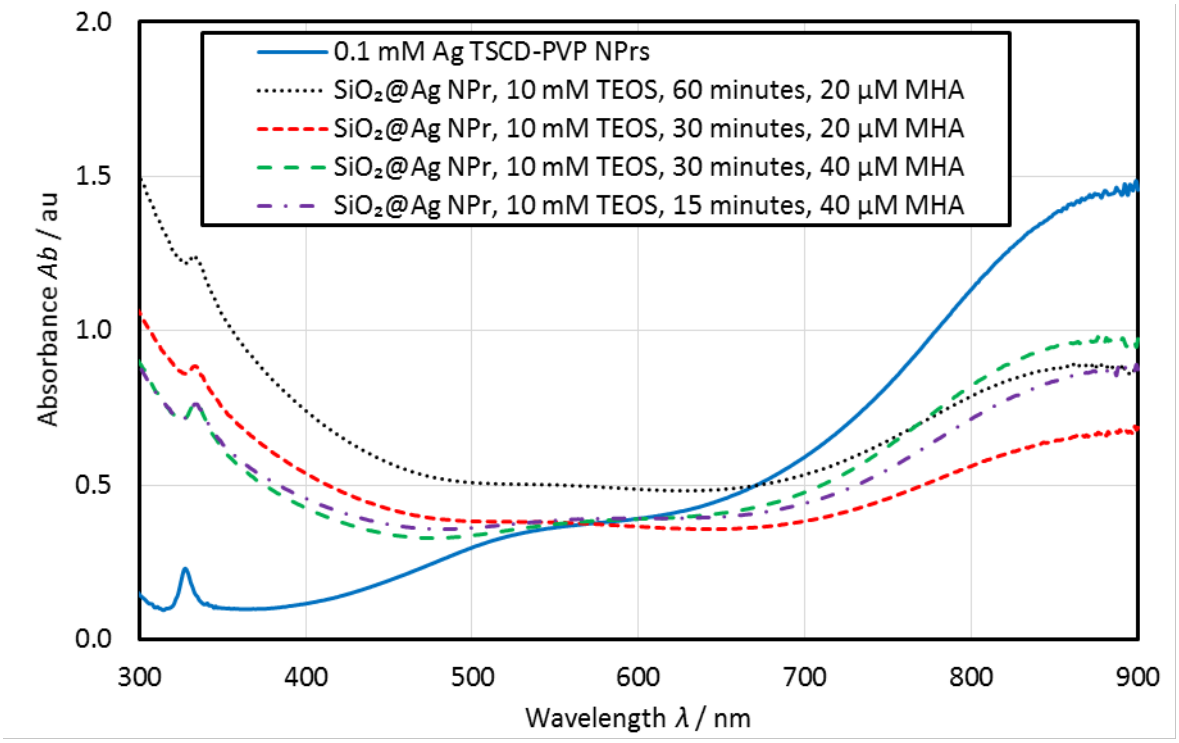

Figure 6-6 UV-vis spectra before and after application of the Stöber TEOS coating process investigating reducing the reaction time of the TEOS stage and increasing the concentration of capping agent MHA. Measured using UV-vis-1 and a 10 mm path length quartz cuvette.

TEM micro-graphs of the before coating Ag TSCD-PVP NPrs and the experiments investigating timing of the TEOS stage and amount of MHA are shown in Figure 6-7 (full TEM analysis in Appendix G, Section G.8). The dominance of the triangular shape prior to coating is shown in Figure 6-7 A. After SiO_2 coating, the SiO_2 coating around the central Ag NP is apparent, along with the presence of multi-cored NPs and SiO_2 only NPs (no Ag NP in the middle). Increasing the amount of MHA reduced the average coating thickness and reduced the variation slightly from 84.49 nm ± 10.03 nm to 61.09 nm ± 6.97 nm (significant according to a two-sample t-test, average different = 23.40 nm). The amount of multi-cored NPs was also reduced from 36 % to 25 %. In contrast the time of the TEOS step, although it reduced the average SiO_2 thickness slightly, this reduction was only significant for the 40 µM MHA samples (the 15 minute sample was 4.57 nm thinner at 56.52 nm than the 30 minute sample according to a two-sample t-test). This contrasts

to the finding of Lismont et al (Lismont et al., 2015) who found that halving the reaction time from 30 minutes to 15 minutes reduced their coating thickness from 60 nm to 40 nm. However, they employed no capping agent, coated Ag NS and used ammonia rather than DMA as the base so their synthesis differed. A graphical summary of the SiO_2 coating thickness for all the Stöber TEOS initial experiments is given in Appendix L, Section L.2 along with a graphical representation of the percentage of multi-cored NPs and the amount of uncoated Ag NPs observed.

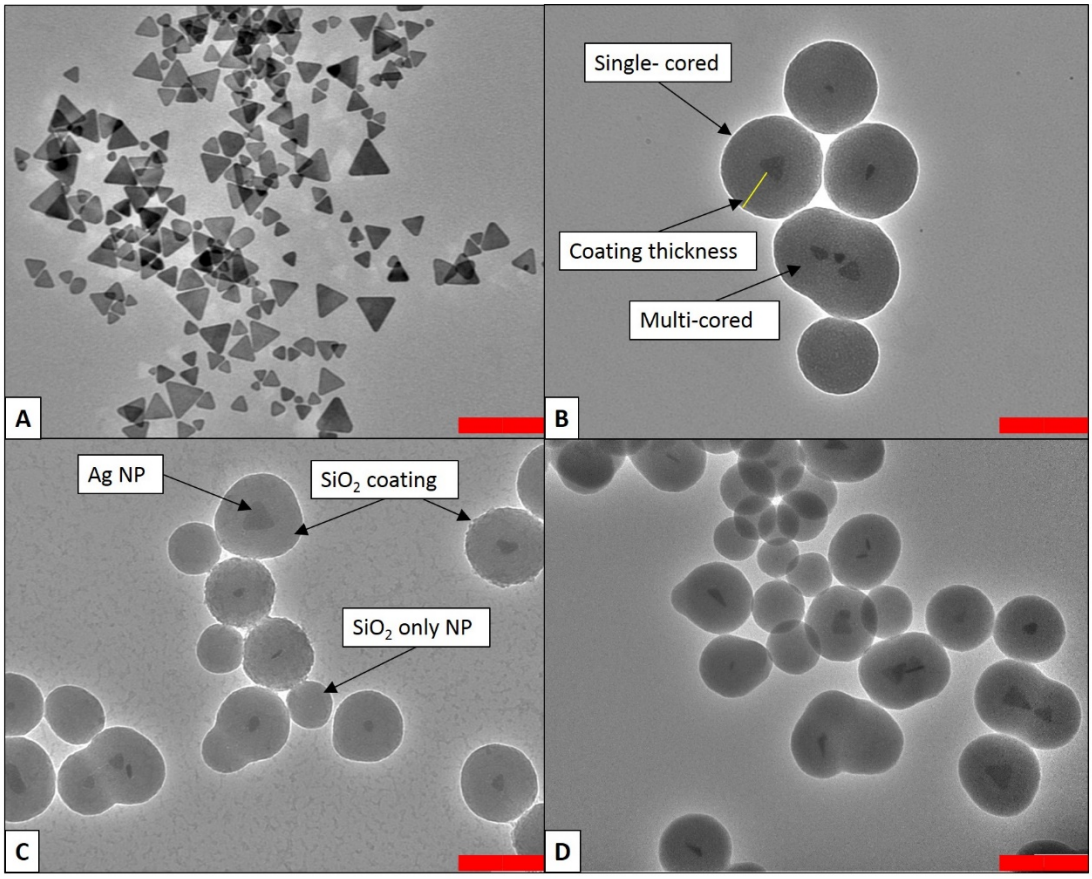

Figure 6-7 TEM micrographs of (A) before, and (B - D) after TEOS SiO_2 coating using (B) 10 mM TEOS, 30 minutes, 20 µM MHA, (C) 10 mM TEOS, 30 minutes, 40 µM MHA, and (D) 10 mM TEOS, 15 minutes, 40 µM MHA. All red scale bars = 200 nm.

From these preliminary experiments it would appear that the best concentration of TEOS to employ would be 10 mM with 40 µM MHA for 30 minutes. However, given the conflicting effect of MHA and time it would have also been useful to repeat the 60 minute experiments using the higher MHA level. This developed optimum protocol also needs scaling and repeating to produce enough more concentrated SiO_2@Ag NPr NF for stability testing to ascertain if SiO_2 coating does increase the stability of the resultant NF to make it more suitable for solar applications.

6.3.3 Summary

Using the water-glass method produced a thin incomplete SiO_2 coating, which had slightly improved elevated temperature stability especially in an alternative BF, compared to the

uncoated Ag NPrs. However, the stability in simulated sunlight tests was worse. Considerable further method development would therefore be needed to make this method suitable for SiO_2 coating of Ag NPrs.

The TEOS Stöber method in contrast produced a thick SiO_2 coating with the best protocol identified as 10 mM TEOS with 40 µM MHA for 30 minutes. This method now needs to be scaled and repeat synthesises undertaken to test the consistency of the protocol and the subsequent stability of the SiO_2@Ag NPrs NFs produced. This will be the focus of the next Section.

6.4 SiO_2 Coated Silver Nanoprisms (SiO_2@Ag NPrs) Produced using the Developed Stöber Coating Procedure

This Section presents the results obtained from SiO_2@Ag NPrs produced using the developed Stöber coating procedure described in Section 3.6.4. Firstly, the results of repeating the synthesis are described. The calculation of the efficiency from the UV-vis spectra is then presented, followed by the actual performance of the SiO_2@Ag NPrs measured in static tests in the solar simulator. The results of testing the stability of the SiO_2@Ag NPrs follow, starting with the lease severe testing environment, namely colloidal stability, then elevated temperature stability, simulated sunlight (SSL) stability and finally, the results of exposing the SiO_2@Ag NPrs to natural sunlight. A brief summary and some conclusions then complete this Section.

6.4.1 Measurements of nanofluids (NFs) as synthesised

The initial volume of NF employed was increased from the 5 mL used in Section 6.3.2 to 25 mL and the optimised Stöber TEOS procedure (40 µM MHA, 10 mM TEOS for 30 minutes, see Section 3.6.4) repeated 12 times (1 sample was repeated using the smaller batch size of 5 mL).

The UV-vis results before and after application of a SiO_2 coating using the developed Stöber coating procedure are summarised in Table 6-1 (full results in Appendix M, Section M.1). The average change in both Ab_{max} and λ_{max} were calculated from summing the difference before and after coating for each individual sample, allowing σ for the change to be calculated. After SiO_2 coating there was a drop in Ab_{max} of ≈ 40 %, but no change in λ_{max} on average. The drop in Ab_{max} seen in Section 6.3.2 of ≈ 34 % (Figure 6-6) and the blue-shift in λ_{max} of 23 nm was within the range of reductions observed for these repeats.

TEM analysis (summarised in Table 6-2, full results in Appendix M, Section M.1 and Appendix G, Section G.9), showed the Ag NPs to be coated with a layer of SiO_2 with a consistent average thickness of 51.24 nm (range of average thickness for all 9 samples = 46.31 nm to 54.39 nm -

Figure G.3), thinner than seen in the preliminary work in Figure 6-5 C of 61.09 nm and thinner than that obtained by Lismont et al of ≈ 60 nm after 30 minutes reaction time (Lismont et al., 2015). One TEM sample (excluded from the average results given in Table 6-2), exhibited a much thicker coating of 80.58 nm ± 6.43 nm. However, like the preliminary work this sample was produced using a lower batch volume of 5 mL rather than the 25 mL volume used for all the other samples. It hence appears that the batch volume is affecting the thickness of the coating but further work would be needed to confirm this. The amount of multi-cored NPs was also the same or lower than seen previously when the larger batch volume was used. The repeat sample (SiO_2@Ag NPr – 7) produced using the lower 5 mL starting NF volume contained the most multi-cored NPs at 49 % (see Figure M.3), suggesting that increasing the batch volume (perhaps improving the stirring consistency) has reduced the amount of NP aggregation and hence the amount of multi-cored NPs present.

Table 6-1 Summarised UV-vis results for Ag TSCD-PVP NPrs before and after SiO_2 coating using the developed Stöber TEOS procedure (10 mM TEOS, 40 µM MHA, 30 minutes). Some samples were sub-divided after coating for subsequent testing, hence *N* after coating = 19 rather than 12.

Parameter	**Average**	**Range**	***σ***	***N***
Ab_{max} before coating / au	1.452	1.192 to 1.653	0.137	12
Ab_{max} after coating / au (adjusted for dilution and cuvette)	0.911	0.377 to 1.262	0.272	19
Change in Ab_{max} / % (positive = increase)	-40.1	-72 to -22	15.4	19
λ_{max} before coating / nm	849	796 to 928	42	12
λ_{max} after coating / nm	844	793 to 906	42	19
Change in λ_{max} / nm (positive = red-shift)	0.4	-24 to 34	18.5	19

Table 6-2 TEM analysis after SiO_2 coating using the developed Stöber TEOS procedure (SiO_2@Ag NPr, 10 mM TEOS, 30 minutes, 40 µM MHA). Average results for 9 samples shown (sample 7 has been excluded as was made using a lower batch volume). The average λ_{max} from the UV-vis = 848 nm ± 48 nm (*N* = 9).

Measurement type	**%**	**% excluding SiO_2 NPs**	**Average size / nm**	**Maximum / nm**	**Minimum / nm**	***σ* / nm**	***N***
Single-cored	36	92	134.43	194.23	81.13	17.15	1260
Multi-cored	3	8	137.34	201.39	69.25	20.32	113
SiO_2 only	61	-	87.67	132.66	35.72	14.64	2140
SiO_2 coating thickness	-	-	51.24	68.46	26.32	5.05	1449
Ag inside	98	-	35.53	87.95	8.21	12.01	1451
Ag free	2	-	17.74	36.77	7.51	8.20	30

In summary, the developed Stöber TEOS method resulted in a drop in Ab_{max}, no shift in λ_{max} and a consistent SiO_2 coating thickness of ≈ 50 nm with a low percentage of uncoated Ag NPs and multi-cored NPs.

6.4.2 Calculating efficiency from absorption spectra

The power absorbed by the NFs containing SiO_2@Ag NPrs was calculated according to the method described in Section 3.8.2 using Equation 3-6, with a 10 mm path length. The average results are shown in Figure 6-8. The result obtained for the Ag TSCD-PVP NPrs centrifuged and re-dispersed in ¼ volume of water are also reproduced from Figure 4-9 for ease of comparison. As the SiO_2@Ag NPr NFs showed an increase in absorption in the < 550 nm region due to the presence of SiO_2 in the NF, the amount of power absorbed in this region was enhanced compared to the Ag TSCD-PVP NPrs (see Figure M.1).

The efficiency $\eta_{Ab(300\ nm\ -\ 900\ nm)}$ was calculated using Equation 4-3 and gave an average value of 98.5 % (σ = 1.1 %, N = 7 – full results in Appendix M, Section M.1.2). As this only accounts for ≈ 66 % of the solar spectrum, $\eta_{Ab(280\ nm\ -\ 4000\ nm)}$ was also calculated assuming no absorption outside of the measured 300 nm – 900 nm range using Equation 4-4 and gave an average value of 65.3 % (σ = 0.7 %, N = 7). These values were both higher than those obtained for Ag TSCD-PVP NPrs centrifuged and re-dispersed into ¼ volume water of 91.7 % and 60.8 % (see Table 4-2) and reflect the enhanced absorption obtained in the < 550 nm region due to the presence of SiO_2.

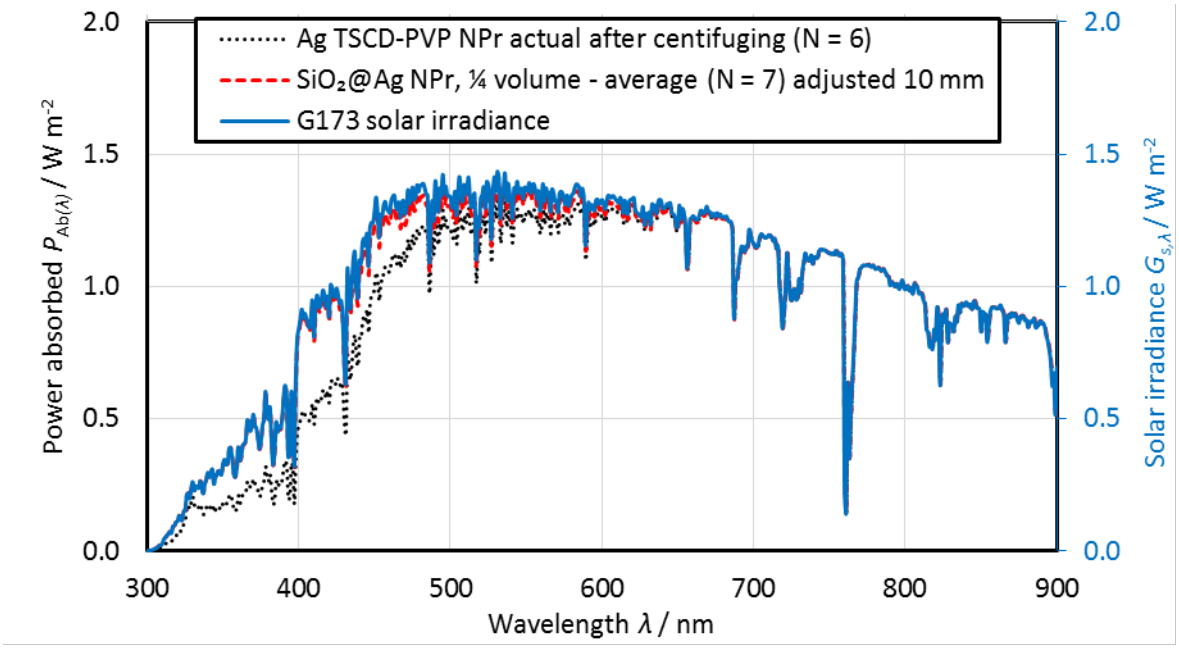

Figure 6-8 Amount of power absorbed P_{Ab} of the G173 ($G_{s,\lambda(dir\ +\ cs)}$) with a 10 mm path length by the SiO_2@Ag NPrs (average for 7 samples shown). The power absorbed by centrifuged Ag TSCD-PVP NPrs is also shown reproduced for ease of comparison from Figure 4-9. The secondary vertical axis is for the G173 solar spectrum taken from (ASTM, 2012).

6.4.3 Performance under SSL

This subsection presents the results obtained from undertaking repeat measurements of both a NF containing SiO_2@Ag NPrs and one containing SiO_2 only using set-up A in the solar simulator. The results are compared to water and to those obtained previously for Ag NPrs (Section 5.5.3). The η_{PE} of both NFs is calculated and the value obtained for the SiO_2@Ag NPrs compared to the efficiency values calculated directly from the UV-vis spectra (Section 6.4.2).

Although SiO_2@Ag nanodiscs (λ_{max} < 600 nm) produced using the water-glass method have been measured by others in static solar simulator tests (Hjerrild et al., 2016), SiO_2@Ag NPrs with a λ_{max} > 750 nm and a coating thickness of ≈ 50 nm have not been measured and compared directly to both the efficiency calculations obtained from UV-vis measurements and to uncoated Ag NPrs.

The mean change in temperature ΔT on exposure to SSL using set-up A for these two NFs and for water BF are shown in Figure 6-9. All the fluids exhibited an initial linear increase in temperature, followed by a levelling out of the temperature rise. The SiO_2@Ag NPr NF reached a maximum average ΔT of 35 °C – 42 °C, whereas the SiO_2 NF only showed a rise of 20 °C – 24 °C and water a 19 °C – 22 °C rise after 1 h. This maximum ΔT for the SiO_2@Ag NPr NF was slightly lower than the 36 °C – 44 °C seen for the Ag NPr NF in Figure 5-1.

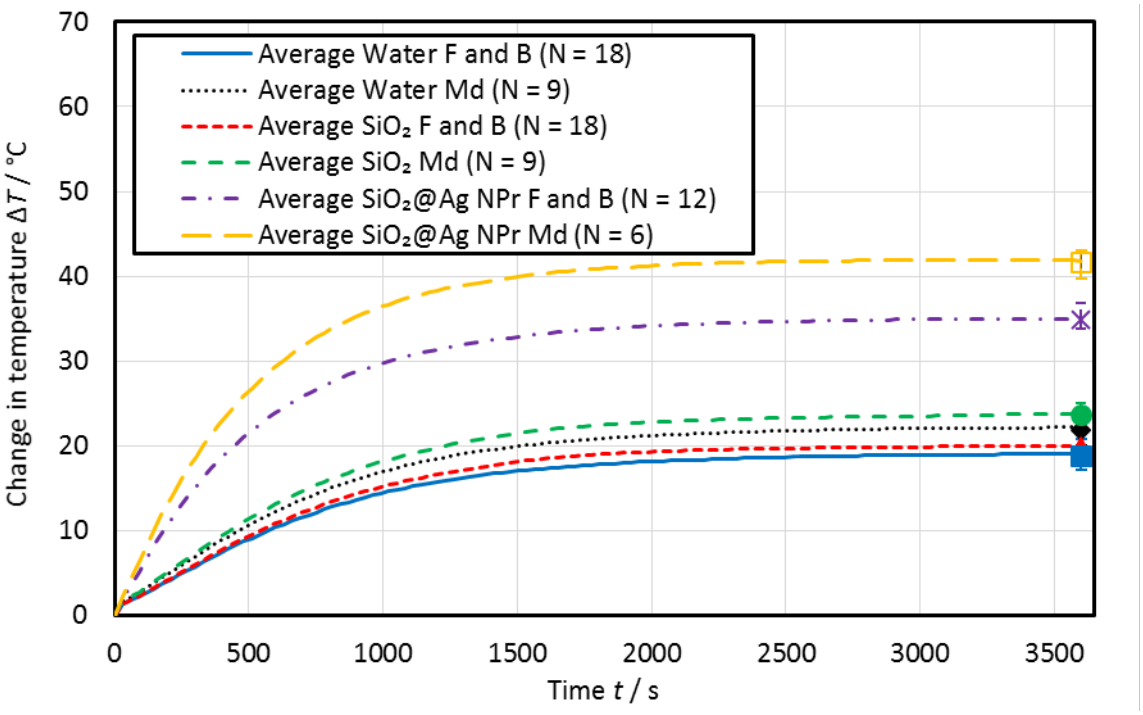

Figure 6-9 Mean change in temperature (ΔT) as a function of SSL exposure time using set-up A for water, SiO_2 only NF, and SiO_2@Ag NPrs. Position in solar simulator = Back (B), middle (Md) and Front (F). The error bars show the range in results for ΔT at t = 3600 s.

In a similar manner to the Ag NPr NF in Section 5.5.3 the results from the SSL exposure were analysed using response surface methodology (results in Appendix J, Section J.4). Both the type of

fluid and the position in the solar simulator caused Δ*T* variations, whereas the batch number and time did not significantly effect Δ*T*. The middle Md sample position gave a larger Δ*T* and the SiO_2@Ag NPr NF had a much higher final temperature and slope Δ*T*/Δ*t* than both water and the SiO_2 only NF (Table J.7 and Table J.8).

When the value of η_{PE} for the SiO_2@Ag NPr NF was estimated using the 20.51 % value for water and compared to the calculated $\eta_{lamp(330\ nm\ -\ 900\ nm)}$ obtained from the UV-vis data, η_{PE} was > 70 % and $\eta_{lamp(330\ nm\ -\ 900\ nm)}$ was > 95 % (see Table J.9). The value of η_{PE} for the SiO_2 only NF was in contrast much lower at < 25 %, clearly showing the advantage of using a NF containing Ag NPrs.

For the SiO_2@Ag NPr NF it appears that the $\eta_{lamp(330\ nm\ -\ 900\ nm)}$ results were greater than the estimated η_{PE} values even when the measurement uncertainties are taken into consideration. The $\eta_{lamp(330\ nm\ -\ 900\ nm)}$ results agree well with the calculated $\eta_{Ab(300\ nm\ -\ 900\ nm)}$ value of 98.5 % in Section 6.4.2 but not with the lower η_{PE} estimations obtained from direct measurement. The estimation of η_{PE} was also lower than the > 80 % value obtained for the Ag NPrs in Section 5.5.3, whereas both the $\eta_{lamp(330\ nm\ -\ 900\ nm)}$ and $\eta_{Ab(300\ nm\ -\ 900\ nm)}$ values would suggest that η_{PE} for the SiO_2@Ag NPrs should have been greater than for the Ag NPrs. The reason for this reduction may be due to the addition of the non-conducting SiO_2 coating and the increase in size of the NPs both of which would reduce the thermal conductivity (see Section 2.7.4). The additional size could also lead to increased scattering of the incident light, which would perhaps lead to more thermal losses to the surroundings (Mallah et al., 2019). It may also be partly due to the NF absorbing the majority of the incident light in the first part of the path length of the cuvette. This would lead to a less thermally homogeneous NF with potentially a hotter front surface and therefore more convection and radiative losses to the environment reducing the measured η_{PE} (see Section 2.5.7). With the reasons unclear for the lower actual performance of the SiO_2@Ag NPrs further investigation is required. It does, however, in contrast to both the Ag NPr and the broadband absorber results question the confidence that can be attributed to calculations based on UV-vis measurements for rapid screening of NFs for their potential performance in solar applications.

In summary, this subsection has presented the results obtained from assessing the actual performance of the SiO_2@Ag NPrs in a solar simulator. The value of η_{PE} obtained was lower than expected from the calculations based on the UV-vis spectra at ≈ 73 % – 77 %, questioning the confidence that can be attributed to these estimations.

6.4.4 Colloidal Stability

Given the general lack of colloidal stability information available in the literature discussed in Section 5.4, this subsection attempts to address this by investigating the colloidal stability of

SiO_2@Ag NPrs in water base-fluid produced using the optimised procedure described in Section 3.6.4 comparing the results obtained to the uncoated Ag NPrs in Section 5.6.2.

The colloidal stability of the SiO_2 coated Ag NPrs was assessed using the protocol described in Section 3.9.2 using both UV-vis and TEM. The UV-vis gives an indication of the colloidal stability, with a reduction in peak height (Ab_{max}) indicating instability to aggregation and any changes in the position of the maximum peak (λ_{max}) suggesting morphological instability. Of the stability trials, storage in the dark at 4 °C represents the least harsh condition assessed. The samples were tested for a maximum period of 51 days. A summary of the UV-vis results after > 38 days storage is given in Table 6-3 with the full results in Appendix M, Section M.3.

Table 6-3 Summarised colloidal stability results for all SiO_2@Ag NPr NF samples stored in the dark at 4 °C for > 38 days.

Parameter	**Average**	**Range**	***σ***	***N***
Storage time / days	46	38 to 51	5	5
Change in Ab_{max} (positive = increase) / %	-17	-39 to -5	13	5
Change in λ_{max} (positive = red shift) / nm	-60	-110 to -30	39	5

There was on average a reduction in Ab_{max} and a blue shift in λ_{max} suggesting that the NFs were both unstable to aggregation and morphological changes (both changes were significant according to paired t-tests). This was in contrast to the uncoated centrifuged Ag TSCD-PVP NPrs in Section 5.6.2 which showed no significant change in either Ab_{max} or λ_{max} after ≈ 50 days. It is also in contrast to the 10 day stability results of ≤ 3.3 % drop in transmission reported by Huang et al for their SiO_2@Ag NS in a mixed BF of propylene glycol and cobalt sulphate (Huang et al., 2021) and to the work of Crisostomo et al who saw a < 5 nm shift in λ_{max} after 9 months for their SiO_2@Ag nanodiscs (Crisostomo et al., 2017). The application of a SiO_2 coating therefore seems to have reduced rather than enhanced the NFs colloidal stability.

Three samples were analysed using TEM after storage in the dark at 4 °C for ≈ 50 days. The TEM results for these three samples are summarised in Table 6-4 (full results in Appendix G, Section G.10 and typical micro-graphs in Appendix M, Figure M.5). Following storage the percentage of multi-cored NPs had increased from 8 % to 11 % (compare Table 6-2 with Table 6-4) and the size of the Ag NP inside the SiO_2 shell had reduced by ≈ 7 nm (this size reduction was significant according to a two sample t-test). This suggests that the Ag NPs are dissolving inside the SiO_2 shell. The micro-graphs in Figure M.5 confirm this hypothesis.

Table 6-4 TEM analysis on SiO_2@Ag NPr re-dispersed into ¼ volume of water after storage for ≈ 50 days in the dark at 4 °C. Average results for 3 samples shown. The average λ_{max} from the UV-vis = 778 nm ± 45 nm (N = 3).

Measurement type	**%**	**% excluding SiO_2 NPs**	**Average size / nm**	**Maximum / nm**	**Minimum / nm**	**σ / nm**	***N***
Single-cored	36	77	128.49	173.05	81.10	13.71	267
Multi-cored	11	23	128.67	175.74	78.23	18.39	80
SiO_2 only	53	-	87.59	118.76	51.82	13.55	394
SiO_2 coating thickness	-	-	50.76	69.94	31.64	5.57	455
Ag inside	97	-	28.56	69.71	4.41	13.33	456
Ag free	3	-	19.41	48.17	6.35	12.39	12

In summary, the SiO_2@Ag NPrs were not stable to aggregation (reduction in Ab_{max}) or morphologically stable (change in λ_{max}) with storage in the dark at 4 °C for > 38 days. TEM results showed that the Ag NPs appeared to be dissolving inside the SiO_2 shells. The application of a SiO_2 coating therefore seems to have reduced rather than enhanced the colloidal stability of Ag NPrs.

6.4.5 Stability with exposure to elevated temperature

This subsection presents the results of assessing the stability of the SiO_2 coated Ag NPrs to an elevated temperature of 70 °C and again addresses the urgent need for more stability testing of Ag based NFs identified in Section 5.4. Elevated temperature represents a more harsh testing condition than used in the proceeding subsection. Firstly, the UV-vis results are discussed followed by the results of assessing the NFs after temperature exposure using TEM. Like for the proceeding subsection this Section gives a summary of the results obtained with the full results for the UV-vis testing being provided in Appendix M, Section M.4 and the TEM results in Appendix G, Section G.11.

Three different concentrations of SiO_2@Ag NPr NFs were assessed for their stability at an elevated temperature of 70 °C using the protocol given in Section 3.9.3. There were SiO_2@Ag NPrs re-dispersed into the same volume of water following coating as the original NF, a NF with a similar concentration (adjusted to give an Ab_{max} of ≈ 0.8 au with a 10 mm path length cuvette prior to temperature testing – labelled as SiO_2@Ag NPr diluted) and a more concentrated NF re-dispersed into ¼ volume of water after coating.

All three different concentrations of NFs showed a reduction in Ab_{max} with exposure to elevated temperature of between 0 % – 32 % over a period of 18 h (Figure M.7). This might suggest that the NFs are not stable to aggregation / dissolution of Ag NPrs resulting in a drop in Ab_{max}. However, there was considerable variation between individual samples of the same NF resulting

in no significant difference in change in Ab_{max} with temperature exposure compared to the Ag TSCD-PVP NPr (long λ NF) after 9 h of testing (according to analysis of variance calculations – see Section M.4.1). The average decrease in Ab_{max} (18 %) after 18 h exposure to 70 °C was similar to that seen after storage for > 38 days in the dark at 4 °C of 17 % (see Table 6-3). This shows the increased severity of the testing condition.

None of the SiO_2@Ag NPr NFs tested were stable to morphological changes (change in λ_{max}) with exposure to elevated temperature, with the more concentrated NF being significantly less stable (according to ANOVA testing see Section M.4.1). Unlike the unstable, uncoated, Ag NP NFs (see Figure K.12), there was no rapid initial blue-shift in λ_{max} with exposure followed by a decrease in the rate of change. Instead the blue-shift for the two more dilute NFs was almost linear with time (Figure M.6). Although the response for the more concentrated SiO_2@Ag NPr NF appeared to be more linear than that of the uncoated Ag NFs there was considerable variation between individual samples leading to a low value of R^2 for the linear fit (the least stable sample had an ≈ blue-shift of 256 nm, the most stable an ≈ blue-shift of 141 nm after 18 h at 70 °C). To facilitate comparison with the uncoated stability results the data obtained after 9 h exposure was compared using analysis of variance (ANOVA). This showed the SiO_2@Ag NPr, ¼ volume NF (the most concentrated NF) to have a significantly greater blue-shift (162.7 nm on average) than the other two SiO_2 coated NFs, which had a similar blue-shift in λ_{max} to the least stable of the uncoated Ag NFs (the mid λ and long λ).

Compared to the colloidal stability data in Table 6-3, the blue-shift in λ_{max} after 9 h at 70 °C was greater on average (80 nm after ≈ 50 days storage compared to 108 nm after 9 h), with the most concentrated NF being considerably worse (163 nm average blue-shift). This again illustrates the increased severity of the testing condition.

To understand the change in morphology more, TEM analysis was undertaken. The full results are given in Appendix G, Section G.11. In total 4 samples were assessed after 18 h exposure to a temperature of 70 °C (1 of SiO_2@Ag NPr, ¼ volume, 2 of the SiO_2@Ag NPr diluted and 1 of the SiO_2@Ag NPr NF). The more concentrated SiO_2@Ag NPr, ¼ volume NF showed the SiO_2 coating to be almost completely absent (only one particle was still seen to be coated) and the free Ag NPs had all changed from being triangular to being disc like or small particles, suggesting that the increased temperature was causing both destruction of the SiO_2 coating and shape change of the Ag NPs.

Of the other three samples assessed, 2 still contained a significant proportion of SiO_2@Ag NPs whereas the other sample only contained ≈ 5 % of SiO_2@Ag NPs. Porosity of the SiO_2 coating could clearly be seen even in the still coated NPs. This porosity of the coating and the absence of

the coating around the Ag NPs is illustrated in Figure 6-10, where the two SiO_2@Ag NPr diluted samples are shown.

Exposure to an elevated temperature of 70 °C therefore seems to be causing the SiO_2 coating to break apart leaving the Ag NPs exposed and vulnerable to further shape change resulting in a large blue-shift in λ_{max} and a small change in Ab_{max}. The time taken for this to occur may in part be the cause of the difference in change in λ_{max} with time compared to the uncoated Ag NPs, resulting in a less rapid initial blue-shift in λ_{max}.

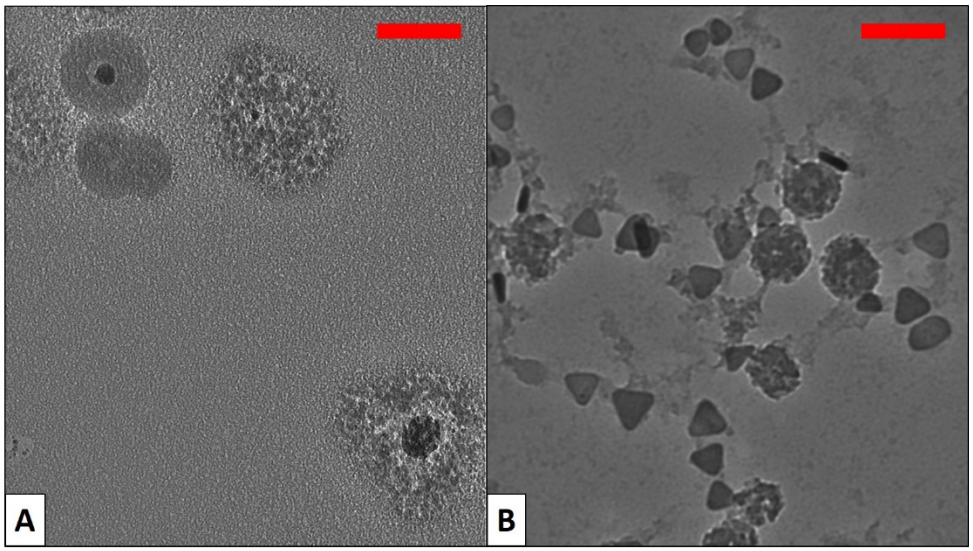

Figure 6-10 TEM micrographs of the standard TEOS SiO_2 coating after exposure to a temperature of 70 °C for 18 h showing (A) SiO_2@Ag NPr-10, and (B) SiO_2@Ag NPr-12, both NFs diluted to give an Ab_{max} of ≈ 0.8 au prior to temperature testing. All initially produced using 40 µM MHA and 10 mM TEOS for 30 minutes. All red scale bars = 100 nm.

The application of a SiO_2 coating hence appears to have reduced rather than enhanced the morphological temperature stability of the Ag NFs. This is in contrast to the work of Taylor et al (Taylor et al., 2018) who saw an enhancement in the morphological stability of their SiO_2 coated Ag nanodiscs on exposure to an elevated temperature of 80 °C and no breaking up of their coating. However, they produced their TEOS coated nanodiscs by first applying a thin SiO_2 coating using the water-glass method. It may therefore be possible to combine the water-glass method discussed in Section 6.3.1 with the developed TEOS method to enhance the temperature stability. This would require further investigation.

Even although Taylor et al (Taylor et al., 2018) managed to enhance the thermal stability, they still saw an ≈ 70 nm blue-shift following exposure to 80 °C for ≈ 30 h. Hence, even with combining the water-glass and TEOS method together it is unlikely that it will be possible to enhance the thermal stability enough to produce a NF comprised of SiO_2@Ag NPs that would be suitable for use for many years in an elevated temperature environment.

This subsection presents the results obtained from investigating the elevated temperature stability of SiO_2@Ag NPrs. The SiO_2@Ag NPrs appeared less morphologically stable than their uncoated Ag NPr counterparts with the SiO_2 coating becoming more porous and even dissolving with exposure to a temperature of 70 °C.

6.4.6 Stability with exposure to SSL under static conditions

An increasingly harsh exposure scenario of simulated sunlight (SSL) is examined in this subsection to evaluate the stability of SiO_2@Ag NPr NF re-dispersed into ¼ volume of water using the solar simulator set-up A under static conditions (see Sections 3.8.3 and 3.9.4). The changes in UV-vis spectra (λ_{max} and Ab_{max}) with exposure to SSL are firstly given followed by a discussion of the effect on the efficiency (η) of these changes. The TEM analysis following exposure is then presented. This subsection then concludes with a short discussion and summary.

One exposure to SSL there was a rapid blue-shift in λ_{max} (Figure 6-11) within the first hour of exposure of on average 163 nm (similar to that seen with elevated temperature testing after 9 h exposure). The rate of change then reduced with the average blue-shift in λ_{max} being 240 nm ± 66 nm after 6 h (Table 6-5). There was considerable variation between samples with one sample (SiO_2@Ag NPr – 2) being especially unstable (before and after SSL exposure average spectra provided in Appendix M, Figure M.8). This blue-shift was greater than the 109 nm shift seen for Ag TSCD-PVP NPrs after 12 h SSL exposure (Section 5.6.4) suggesting that the addition of a SiO_2 coating has reduced rather than enhanced the morphological stability. It was also greater than that seen following storage in the dark at 4 °C (80 nm blue-shift) and following exposure to a temperature of 70 °C (160 nm blue-shift after 9 h) reflecting the increased harshness of the testing conditions.

In contrast there was no consistent change in Ab_{max} even after 6 h exposure (Table 6-5). This suggests that the NFs were stable to aggregation.

To understand the potential implications of the spectral changes following SSL exposure $\eta_{lamp(330\ nm - 900\ nm)}$ was calculated using the 6 h spectra. The results (Table 6-5) suggest that there may be a small increase in $\eta_{lamp(330\ nm - 900\ nm)}$ of 1 % (unlikely to be significant given the measurement uncertainty). This result should be treated with extreme caution given both the fact that the NFs were only measured over the 200 nm – 900 nm range and the lack of correlation between η_{PE} and $\eta_{lamp(330\ nm - 900\ nm)}$ discussed in Section 6.4.3.

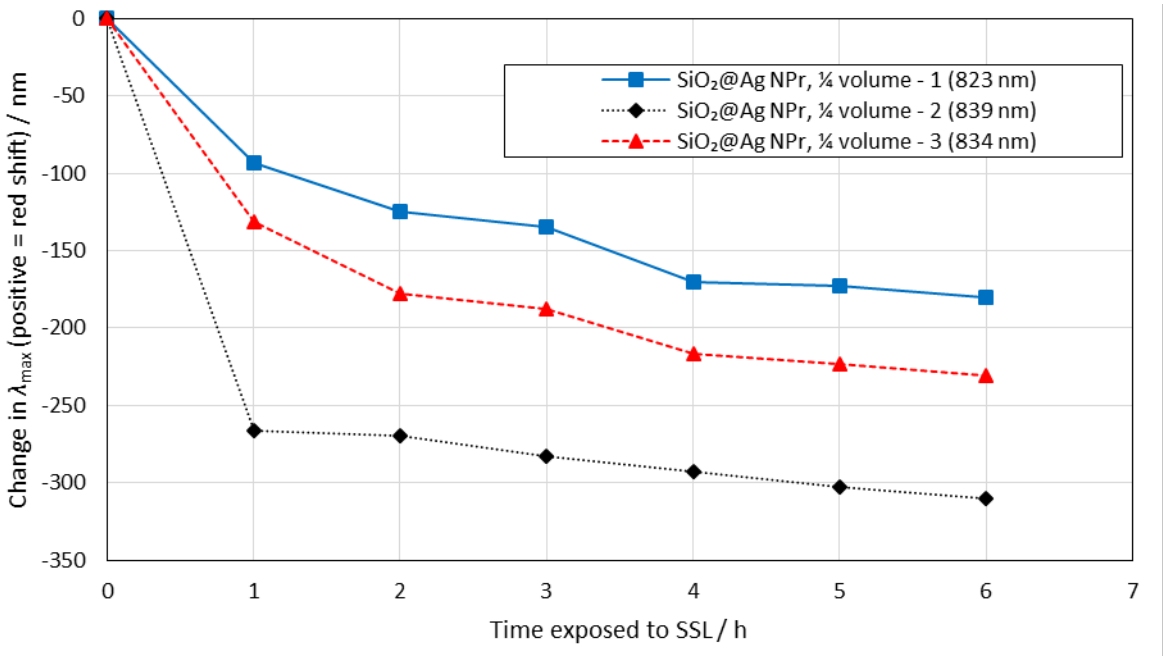

Figure 6-11 Change in λ_{max} with exposure to simulated sunlight (SSL) for SiO_2@Ag NPrs re-dispersed into ¼ volume of water (compared to volume of starting NF). Tested using set-up A. The starting value of λ_{max} is shown in brackets.

Table 6-5 Summarised results for SiO_2@Ag NPr NF re-dispersed into ¼ volume of water (compared to pre-coated NF volume) after 6 h exposure to SSL.

Parameter	**Average**	**Range**	***σ***	***N***
Change in Ab_{max} (positive = increase) / %	-1	-19 to 19	19	3
Change in λ_{max} (positive = red shift) / nm	-240	-360 to -180	66	3
Change in $\eta_{lamp(330\ nm - 900\ nm)}$ (positive = increase) / %	1.04	0.72 to 1.26	0.28	3

TEM after exposure to SSL for 6 h was used to further understand the morphological changes. The TEM results are summarised in Table 6-6 (full results in Appendix G, Section G.12 and typical micro-graphs in Appendix M, Figure M.9). Following SSL exposure the percentage of multi-cored NPs had increased from 6 % to 23 % (compare Table 6-6 with Table G.49) and the size of the Ag NP inside the SiO_2 shell had reduced by ≈ 10 nm (this size reduction was significant according to a two sample t-test - Table G.53). This suggests that the Ag NPs are dissolving inside the SiO_2 shell. The micro-graphs in Figure M.9 confirm this hypothesis. This increase in multi-cored particles and reduction in size were both greater than seen in the storage trials reflecting the increased harshness of the SSL testing regime. As the Ag NPs dissolve they become both smaller and more rounded accounting for the large blue-shift in λ_{max} observed.

In addition, the number of free Ag NPs has increased from 0 % to 3 % and the thickness of the SiO_2 coating has reduce slightly by 4 nm, suggesting that the SiO_2 coating is both dissolving and breaking apart (Figure M.9 C shows free Ag NPs and some broken-up SiO_2 coatings). The breaking up of the SiO_2 coating was not as pronounced as that seen for the elevated temperature stability tests, perhaps reflecting the shorter exposure time and the lower maximum temperature the

samples reached in the SSL tests (≈ 65 °C for < 6 h). It may also be that the SSL (perhaps from the short λ, UV portion of the light) is cross linking the SiO_2 coating leading to it being more resistant to breaking up in a similar manner to that seen by Taylor et al (Taylor et al., 2018). The decrease in the thickness of the coating shell may in fact be due to this effect rather than dissolution of the SiO_2. However, unlike Taylor et al there was no large increase in Ab_{max}, suggesting that if this cross linking was occurring the amount was much lower than observed by Taylor et al, reflecting both the different testing regime used (UV light) and coating protocol employed.

Table 6-6 TEM analysis on SiO_2@Ag NPr re-dispersed into ¼ volume of water after exposure to SSL for 6 h using set-up A in the solar simulator. Average results for 3 samples shown. The average λ_{max} from the UV-vis = 592 nm ± 58 nm (N = 3).

Measurement type	**%**	**% excluding SiO_2 NPs**	**Average size / nm**	**Maximum / nm**	**Minimum / nm**	**σ / nm**	***N***
Single-cored	38	77	135.41	176.49	91.38	13.82	207
Multi-cored	11	23	134.57	167.29	81.07	17.97	62
SiO_2 only	51	-	96.56	132.10	57.33	13.13	280
SiO_2 coating thickness	-	-	48.88	65.20	24.05	5.93	352
Ag inside	97	-	25.21	59.51	4.38	10.39	352
Ag free	3	-	36.81	18.86	74.46	14.90	12

This subsection presents the results of assessing the stability of SiO_2@Ag NPr NFs to SSL. Although stable to aggregation over the short timeframe tested, they were not morphologically stable resulting in a rapid blue-shift in λ_{max} > uncoated Ag TSCD-PVP NPr NFs and > SiO_2@Ag NPr samples stored at 4 °C in the dark or exposed to an elevated temperature of 70 °C. The addition of a SiO_2 coating is hence reducing the morphological stability of the NFs rather than enhancing it, making these NFs not suitable for solar applications. The main morphological changes appeared to be the dissolution and rounding of the Ag NPs inside the SiO_2 coating, although there was also some evidence of the SiO_2 coating breaking up.

6.4.7 Stability with exposure to natural sunlight

The way in which the UV-vis spectra changes following exposure to natural sunlight for SiO_2@Ag NPrs is detailed in this subsection. The results are presented, followed by a short discussion and summary.

Two separate natural sunlight exposure trials were undertaken. The duration of the first trial (denoted trial 1) was 2 weeks and the second trial (trial 2) was 5 weeks (see Section 3.9.5). In both cases the NF tested was SiO_2@Ag NPrs re-dispersed into ¼ the volume of water (compared to original NF volume).

The results obtained from the two trials were similar (see Figure 6-12). For both trials Ab_{max} decreased by an average of 9 % (range -22 % to 30 %, N = 13) showing the NF to be relatively stable to aggregation over the timeframe tested. This is in contrast to the uncoated Ag NFs (Figure 5-12), which showed a marked decrease in Ab_{max}.

However, they were not morphologically stable, with trial 1 showing a blue-shift in λ_{max} of 181 nm (range 146 nm to 216 nm N = 3) and trial 2 showing a blue-shift of 171 nm (range 151 nm to 199 nm, N = 10). In both cases the blue-shift was greater than the 60 nm – 80 nm seen for the uncoated Ag NPrs after exposure to natural sunlight. When compared with the SSL stability results, the blue-shift was the same (according to a two sample t-test) as that obtained for SiO_2@Ag NPrs after 6 h exposure (Figure 6-11). This suggests that the morphological change occurred when the SiO_2@Ag NPrs were first exposed to solar radiation. These results are in contrast to those of Taylor et al who saw an increase in Ab_{max} and no change in λ_{max} after exposure to UV light (not natural sunlight) for their SiO_2@Ag nanodiscs (Taylor et al., 2018).

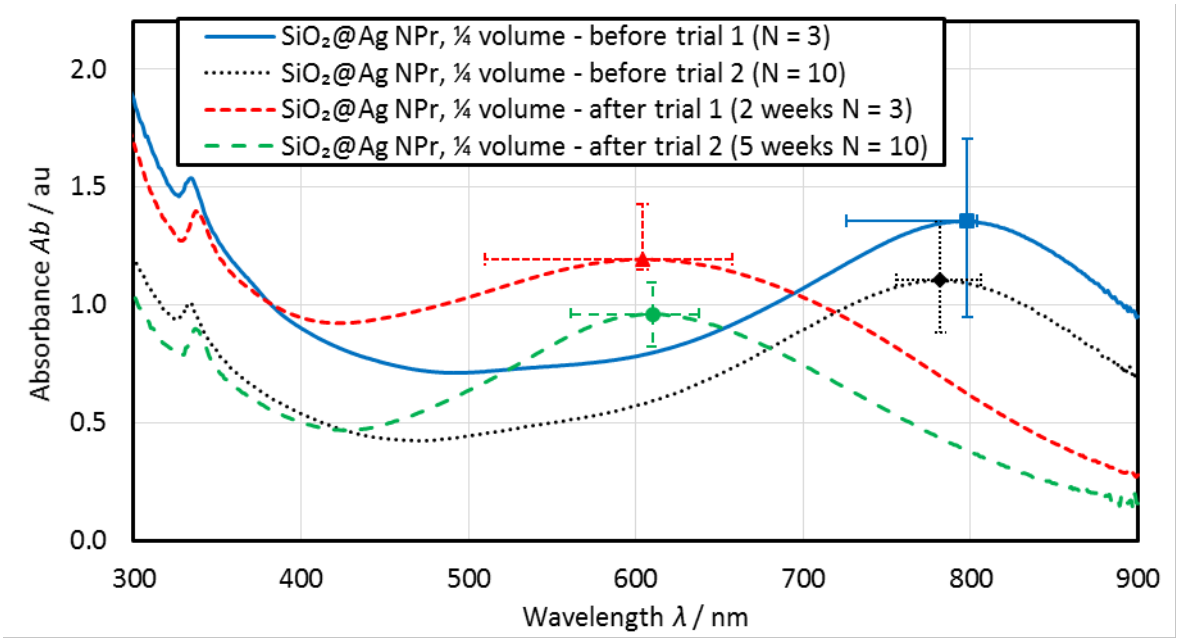

Figure 6-12 UV-vis spectra of SiO_2@Ag NPrs re-dispersed into ¼ volume of water compared to original NF volume before and after exposure to natural sunlight for either 2 weeks (trial 1) or 5 weeks (trial 2). Measured using UV-vis-1 and a 4 mm path length cuvette. The error bars show the range of results obtained at the maximum absorbance.

This is one of the only trials to assess the stability of SiO_2@Ag NPrs to natural sunlight exposure and gave similar results to those obtained for the SSL trials over a shorter timeframe. The morphological changes were greater than the uncoated Ag NPrs but the level of aggregation was improved. This shows one potential improvement obtained by using the developed SiO_2 coating compared to uncoated Ag NPrs. However, the large level of morphological changes observed would still preclude these SiO_2@Ag NPr NFs from use in solar applications.

6.4.8 Conclusions / Summary

This Section presents the results obtained from repeat synthesis of SiO_2@Ag NPrs using the developed Stöber TEOS method described in Section 3.6.4. These showed a drop in Ab_{max}, no shift in λ_{max} and a consistent SiO_2 coating thickness of ≈ 50 nm with a low percentage of uncoated Ag NPs and multi-cored NPs.

Calculating the absorption efficiency $\eta_{Ab(300\ nm\ -\ 900\ nm)}$ from the UV-vis spectra gave an average value of 98.5 % higher than the value obtained for Ag NPrs due to enhanced absorption in the < 500 nm region. However the actual performance, η_{PE} obtained from measurements in the solar simulator was lower than expected from these UV-vis calculations at ≈ 73 % – 77 %, questioning the confidence that can be attributed to these estimations.

Stability testing showed the SiO_2@Ag NPrs were not stable to aggregation (reduction in Ab_{max}) or morphologically stable (change in λ_{max}) with storage in the dark at 4 °C for > 38 days with the TEM results suggesting that the Ag NPs were dissolving inside the SiO_2 shells. The application of a SiO_2 coating therefore seems to have reduced rather than enhanced the colloidal stability of Ag NPrs. In a similar manner with exposure to an elevated temperature the SiO_2@Ag NPrs appeared less morphologically stable than their uncoated Ag NPr counterparts with the SiO_2 coating becoming more porous and even dissolving. With exposure to SSL the story was similar with the SiO_2@Ag NPrs being less morphologically stable than uncoated Ag TSCD-PVP NPrs, however, the main changes appeared to be the dissolving and rounding of the corners of the NPs inside the SiO_2 shells rather than increased porosity and dissolution of the SiO_2 coating itself. This is one of the only trials to assess the stability of SiO_2@Ag NPrs to natural sunlight exposure and gave similar results to the SSL trials. The morphological changes were > than the uncoated Ag NPrs but the level of aggregation was improved. This shows one potential improvement obtained by using the developed SiO_2 coating compared to uncoated Ag NPrs. However, the large level of morphological changes observed would still preclude these SiO_2@Ag NPr NFs from use in solar applications.

6.5 Modifications to coating procedure

This Section investigates the effect on the elevated temperature stability of SiO_2@Ag NPrs produced by carrying out various modifications to the established TEOS Stöber coating procedure given in Section 3.6.4. Firstly, the effects of adding an extra purification step and reducing the oxygen level in the final NF are investigated. The role of the capping agent MHA is then evaluated along with the effect of reducing the concentration of the base DMA in the base catalysed hydrolysis step. Finally, an assessment of the effect of reducing the time of this base catalysed step is examined. This Section then finishes with a brief summary and conclusion.

6.5.1 Adding extra purification and reducing amount of oxygen

An extra purification step was added to the standard optimised Stöber coating procedure to ascertain if this had any effect on the resultant temperature stability of the SiO_2@Ag NPr NF. The extra purification step was added either at step 3 in the procedure (initial extra purification) or at step 9 (final extra purification) as shown in Figure 3-1. Full experimental details and results are given in Appendix N, Section N.1 (initial TEM results in Appendix G, Section G.13). The results show that although there was a slight increase in the amount of multi-cored NPs (containing more than one Ag NP), the SiO_2 coating thickness was similar at ≈ 50 nm and there was no difference in the elevated temperature stability of the NFs after 6 h exposure to a temperature of 70 °C.

The presence of oxygen is known to affect the manufacture of silver nanoparticles especially Ag NPrs with some authors specifically removing oxygen during the production of Ag NPrs (Stamplecoskie and Scaiano, 2010; Xue et al., 2007; Xue et al., 2008). The role of oxygen is thought to be the conversion of Ag into Ag^+ and hence it controls the selective etching and growth of the prisms during manufacture (Xue et al., 2008). In addition, removing the oxygen from already formed uncoated Ag NPrs is known to reduce the shape change observed on heating (Tang et al., 2013). Hence an attempt was made to reduce the level of oxygen in the resulting NF to ascertain if this would change the temperature stability. This was done by bubbling argon through the NF prior to exposure to a temperature of 70 °C. The UV-vis results (Appendix N, Section N.1) show that reducing the level of oxygen had no effect on the elevated temperature stability even after 18 h exposure to a temperature of 70 °C.

In summary, neither adding an extra purification step nor reducing the level of oxygen changed the temperature stability of SiO_2@Ag NPrs.

6.5.2 Understanding the role of the various reagents

This subsection presents an overview of the results obtained from a number of experiments investigating the role of the capping agent, MHA and the base, DMA used in the base catalysed ethanoic step in the developed Stöber SiO_2 coating procedure. Further experimental details and results are given in Appendix N, Section N.2.

Figure 6-13 shows the values of Ab_{max} obtained when MHA and DMA are added to an already prepared Ag NPr NF, just after addition of the reagent, after storage in the dark at 4 °C, and after subsequent exposure to an elevated temperature of 70 °C. Without any reagent added Ab_{max} drops by ≈ 5 %. With just DMA added, Ab_{max} decreases rapidly (≈ 93 % reduction after ≈ 16 h at 4 °C). When just MHA is added Ab_{max} also decreases but at a slower rate (≈ 45 % after ≈ 16 h at

4 °C). Heating at 70 °C results then in a further small ≈ 10 % reduction. When MHA followed by DMA are added the reduction is similar to that seen for MHA alone and clearly shows the role of the MHA capping agent in preventing dissolution of the Ag NPrs in the DMA base.

If the optimised Stöber coating procedure in Section 3.6.4 was undertaken without using any MHA (experimental details and UV-vis results in Appendix N, Section N.2), there was a large reduction in Ab_{max} of 68 % – 83 % following SiO_2 coating. After subsequent exposure to a temperature of 70 °C, there was a further reduction in Ab_{max} resulting in almost no absorption. TEM analysis (Appendix G, Section G.14.1), showed aggregation of the NPs and a thin inconsistent SiO_2 coating thickness (illustrated in Figure 6-14 B). This again showed the importance of the capping reagent MHA in both preventing Ag NP dissolution and aggregation of the NPs (for comparison the TEM micrograph for the optimised procedure using 40 µM MHA is given in Figure 6-14 A).

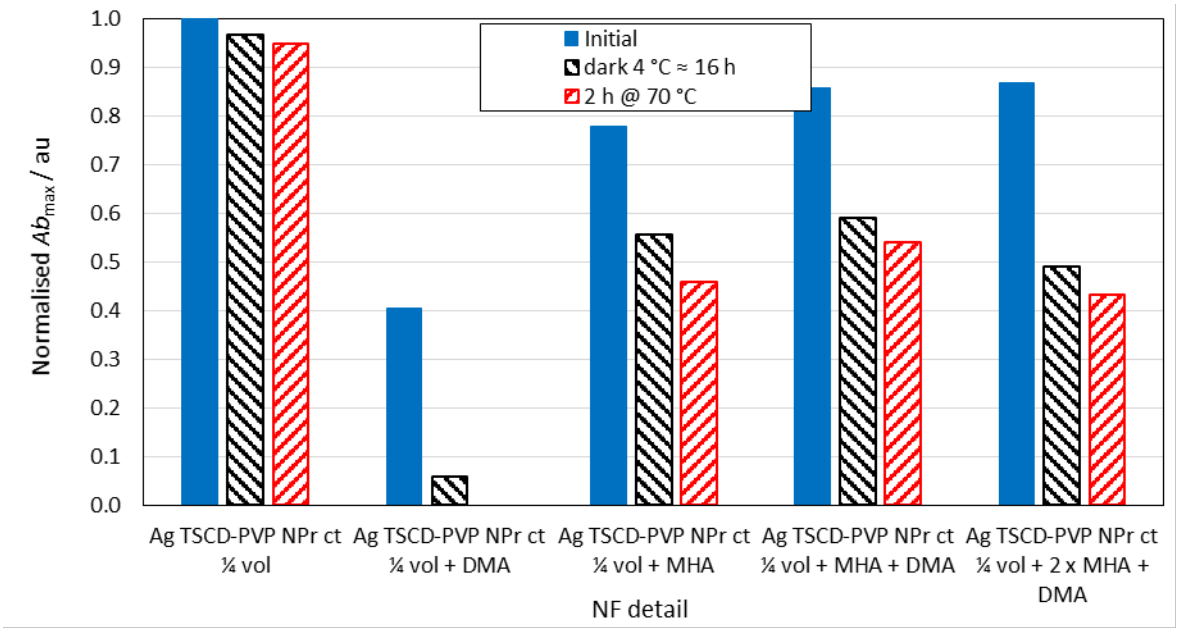

Figure 6-13 Effect of the reagents DMA and MHA on Ab_{max}. Ab_{max} has been normalised to the initial value for the Ag TSCD-PVP NPr centrifuged and re-dispersed in ¼ volume of water and adjusted to account for the NF concentration. Measured using UV-vis-1 and a 1 mm path length quartz cuvette.

To investigate further the effect of MHA, the optimised coating procedure was followed using a higher concentration of 160 µM MHA. The after coating samples were assessed using UV-vis and TEM. The samples were then subjected to an elevated temperature of 70 °C for 6 h and the resultant changes in UV-vis compared to samples produced using 40 µM MHA (the normal amount). The UV-vis results (Appendix N, Section N.2) showed no significant differences compared to the 40 µM MHA samples both just after SiO_2 coating and after exposure to an elevated temperature. There were also no significant differences (according to a two-sample t-test) in the morphologies of the NPs (TEM results in Appendix G, Section G.14.2). Changing the

concentration of MHA to 160 µM in the optimised coating process therefore did not alter the final NF produced showing the synthesis to be relatively insensitive to MHA concentration in the range 40 µM – 160 µM MHA.

Finally, the effect of reducing the concentration of the DMA base by ¼ was evaluated (experimental details in Appendix N, Section N.2). When this lower concentration of base was used there was a substantial drop to Ab_{max} following coating of 49 % – 63 %. TEM analysis showed the coating produced to be thinner, more inconsistent (one sample average thickness ≈ 14 nm, the other ≈ 38 nm), with more uncoated free silver NPs and aggregation of the NPs being present (TEM results in Appendix G, Section G.14.3, illustrated in Figure 6-14 C and D). The results obtained following exposure to an elevated temperature of 70 °C for 12 h were inconclusive but still suggested that the NFs were unstable to elevated temperature. Further repeat experiments using this lower concentration of base would be needed to confirm these finding but given the reduction in Ab_{max} observed it is unlikely that SiO_2@Ag NPrs produced using a lower concentration of DMA would offer any improvement compared to the optimised procedure given in Section 3.6.4. Hjerrild et al also found no improvement in temperature stability by either increasing or decreasing DMA levels for their SiO_2@Ag nanodiscs in glycerol (Hjerrild et al., 2018).

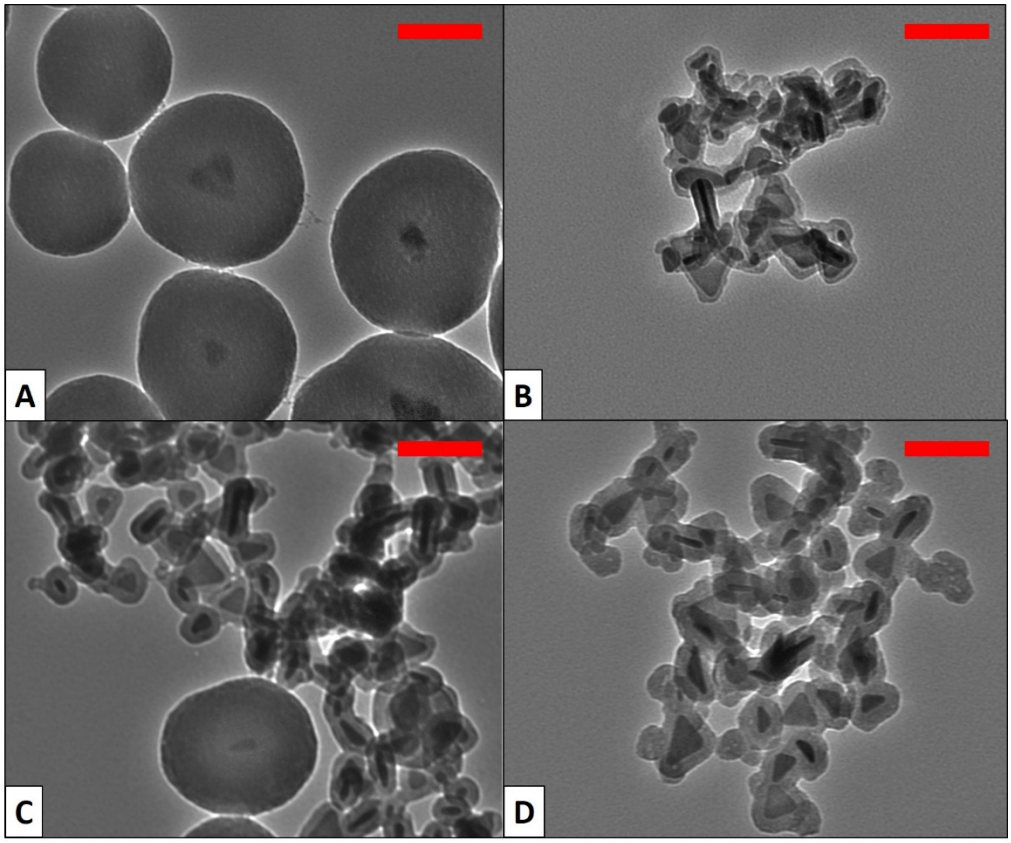

Figure 6-14 TEM micrographs of (A) SiO_2@Ag NPr, optimised procedure 8 mL NF volume, (B) SiO_2@Ag NPr, no MHA, ¼ volume DMA, (C) SiO_2@Ag NPr, 40 µM MHA, ¼ volume DMA and (D) SiO_2@Ag NPr, 160 µM MHA, ¼ volume DMA. 10 mM TEOS for 30 minutes in all cases. All red scale bars = 100 nm.

In summary, this subsection has looked in more detail at the role of MHA and DMA, finding that the capping agent MHA is vital to produce consistent SiO_2@Ag NPrs, however, the procedure appears insensitive to MHA concentration in the range 40 µM – 160 µM MHA. Reducing the concentration of DMA base results in a reduction in absorbance and a thin inconsistent SiO_2 coating. These NFs still appear to be unstable when exposure to elevated temperatures although further repeat experimentation is needed to confirm this.

6.5.3 Timing of TEOS step

According to Lismont et al (Lismont et al., 2015), when the reaction time is reduced a thinner SiO_2 coating should be produced. However, there is limited knowledge of how a thinner coating might perform in stability tests. Hence this subsection looks at firstly how reducing the reaction time affects the UV-vis spectra and morphology of the SiO_2@Ag NPrs produced and secondly the effect that this reduction in reaction time has on the elevated temperature stability of the resultant NFs. An overview of the results is presented in this subsection with further details of the UV-vis results in Appendix N, Section N.3 and TEM results in Appendix G, Section G.14.4.

Two shorter reaction times of 1 minute and 5 minutes were evaluated and compared to the standard 30 minute reaction time used in the optimised Stöber procedure (Section 3.6.4). Following SiO_2 coating there was a large reduction in Ab_{max}, which was greatest for the 1 minute reaction time at 84 %. This reduction was greater than the 40 % reduction observed for the 30 minute reaction time (Table 6-1). TEM analysis showed the SiO_2 coating thickness to be significantly thinner, with the 1 minute reaction time producing an average coating thickness of ≈ 12 nm (illustrated in Figure 6-15 A), and the 5 minutes reaction time a thickness of ≈ 28 nm (Figure 6-15 B). This thickness after 5 minutes was similar but slightly thicker than the ≈ 23 nm coating observed by Lismont et al after the same reaction time (Lismont et al., 2015).

After exposure to an elevated temperature of 70 °C, there was a blue-shift in λ_{max}, of on average 59 nm (1 minute reaction time), and 86 nm (5 minute reaction time) after 9 h exposure. Although at first these results appear to be a slight improvement compared to the 30 minute samples of 91 nm blue-shift after 9 h (Table M.6), ANOVA testing showed the differences to be not significant. There were also some changes in Ab_{max}, but these changes were not consistent and again not significantly different according to ANOVA testing when compared to the same level of dilution, 30 minute samples.

TEM analysis after exposure to an elevated temperature of 70 °C for 18 h showed the NPs to be no longer coated with SiO_2, although there was some evidence of SiO_2 still being present (Figure 6-15 C and D). The morphology obtained was similar to that found for the uncoated long λ NF

after 4 h at 70 °C, with ≈ 10 % triangles, 23 % – 30 % rounded triangles and 34 % – 39 % other shaped particles (Figure G.4).

In summary, this subsection gives an overview of the results obtained using shorter TEOS reaction times of 1 minute and 5 minutes. Although thinner SiO_2 coatings were produced, the results obtained after exposure to a temperature of 70 °C were not significantly different to those obtained using a reaction time of 30 minutes.

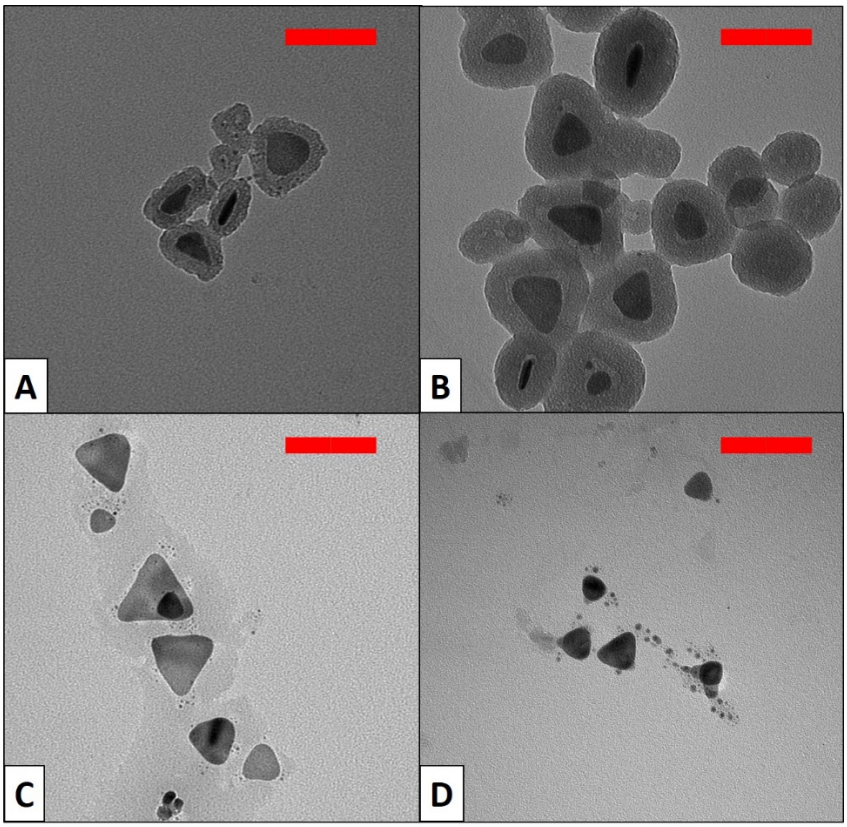

Figure 6-15 TEM micrographs of (A) SiO_2@Ag NPr, as synthesised, 1 minute reaction time, (B) SiO_2@Ag NPr, as synthesised, 5 minutes reaction time, (C) SiO_2@Ag NPr, 1 minute reaction time, after 18 h @ 70 °C and (D) SiO_2@Ag NPr, 5 minutes reaction time, after 18 h @ 70 °C. All red scale bars = 100 nm.

6.5.4 Conclusions / Summary

Neither the addition of an extra purification step nor reducing the level of oxygen changed the elevated temperature stability of SiO_2@Ag NPrs. Although the presence of the capping agent was shown to be vital to produce consistent SiO_2@Ag NPrs, the procedure appeared insensitive to MHA concentration in the range 40 µM – 160 µM MHA. Reducing the concentration of DMA base resulted in a reduction in absorbance and a thin inconsistent SiO_2 coating. These NFs still appeared to be unstable when exposure to elevated temperatures although further repeat experimentation is needed to confirm this. Finally, although reducing the time of the TEOS reaction step produced thinner SiO_2 coatings, the elevated temperature stability of these thinner

SiO_2@Ag NPrs was not significantly different to the thicker SiO_2@Ag NPrs produced using a reaction time of 30 minutes.

Hence, none of the modifications to the SiO_2 coating procedure investigated in this Section improved the elevated temperature stability, leaving the SiO_2@Ag NPrs still unsuitable for use in elevated temperature environments such as those found in solar applications.

6.6 Coating of the Broadband Absorber

This Section presents the results obtained from an attempt to coat the broadband absorber NPs with SiO_2 by modifying the developed Stöber TEOS method. The UV-vis-IR results are discussed first, followed by the potential performance calculated from the UV-vis-IR spectra. The TEM results are then provided. This subsection then concludes with a look at the colloidal stability of the SiO_2@broadband NF and a brief summary.

To attempt to coat the broadband absorber NF with SiO_2, the initial centrifuge step was increased to 3 h at 16,168 r.c.f. (13,000 rpm) to try and sediment all the smaller particles. The MHA concentration was increased to 98.8 µM (the broadband NF had a Ag molarity of 0.247 mM versus 0.1 mM for the Ag TSCD-PVP NPr NF). The amount of water used, the amount of TEOS, ethanol and DMA were also scaled in a similar manner to account for the difference in molarity of the broadband absorber NF.

Even after increasing the centrifuging time it was not possible to sediment all the smaller particles. This is shown in Figure 6-16, where it can be seen that the supernatum still contained a significant amount of Ag NPs with a $\lambda_{max} \approx 490$ nm and an $Ab_{max} \approx 0.32$ au (measured with a 10 mm cuvette). The use of a higher speed centrifuge or a further increase in centrifuging time would hence be required to remove all the small particles. However, this may further damage the larger NPrs within the broadband absorber leading to loss of absorption > 800 nm. It may therefore be better to optimise the centrifuging conditions for each of the component NFs in the broadband absorber separately, coat with SiO_2 and then combine. Further work on this would be needed.

The UV-vis-IR spectra of the broadband absorber before and after SiO_2 coating is also shown in Figure 6-16. Coating with SiO_2 resulted in ≈ 50 nm red-shift in the primary peak and a small reduction in Ab_{max} of ≈ 2 %. There was also a reduction in the level of absorption > 700 nm and a disappearance of the small shoulder corresponding to the mid λ NF.

The effect of these changes on the potential performance of the SiO_2@broadband NF was calculated (results in Appendix O) and show the SiO_2@broadband NF to give a potential

$\eta_{Ab(300\ nm - 1300\ nm)}$ of 81.95 % and a $\eta_{Ab(300\ nm - 900\ nm)}$ of 92.36 % similar to those obtained previously for the broadband mixture of 91.09 % (Table H.10) and the value obtained for the centrifuged Ag TSCD-PVP NPrs re-dispersed into ¼ the volume of water of 91.7 % (Table 4-2).

TEM analysis was undertaken on the SiO_2@broadband NF (full results in Appendix G, Section G.13) and show the coating thickness to be the same at 50.62 nm as seen previously for the optimised Stöber SiO_2@Ag NPrs (Table 6-2). However, the percentage of SiO_2 only NPs was reduced and the percentage of multi-cored NPs increased. A typical TEM micrograph of the SiO_2@broadband is shown in Figure 6-17, illustrating one of these multi-cored NPs along with some single-cored SiO_2@Ag NPs and one SiO_2 only NP. Further optimisation of the coating procedure would be required to reduce the percentage of multi-cored NPs obtained perhaps by introducing a sonication step just prior to the addition of the TEOS to break up the NP clump obtained after centrifuging. This may reduce the amount of multi-cored NPs but would require further investigation.

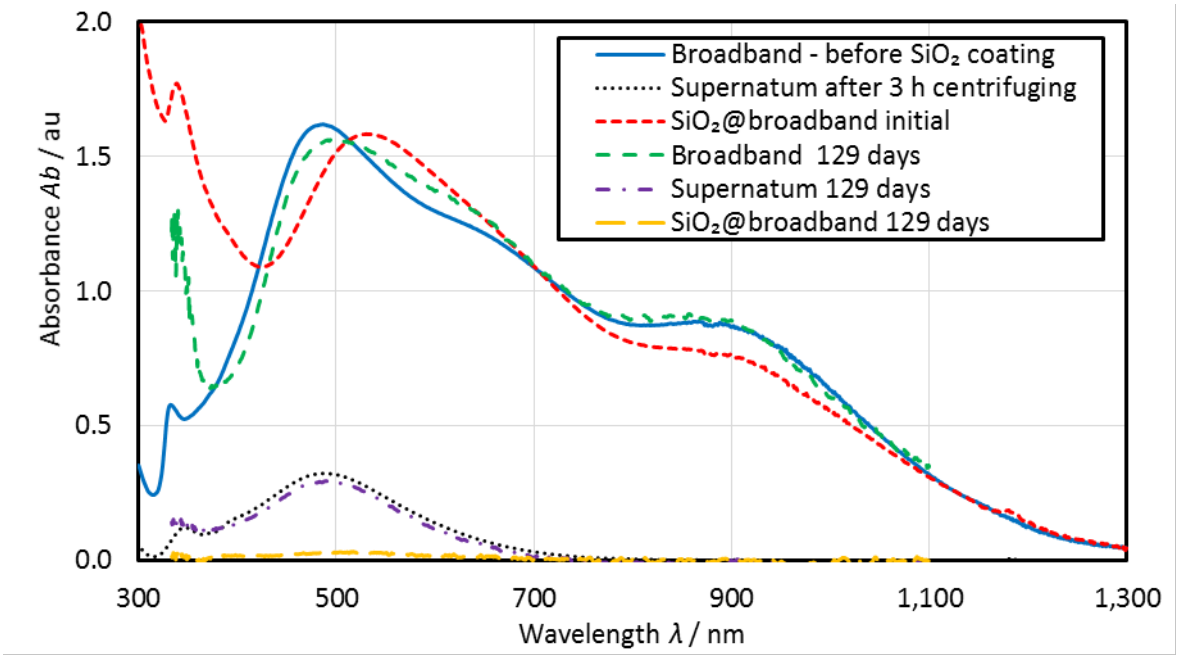

Figure 6-16 UV-vis-IR spectra for the broadband absorber before and after SiO_2 coating using the developed Stöber TEOS method and after storage in the dark at 4 °C. The supernatum after 3 h centrifuging at 16,168 r.c.f. (13,000 rpm) is also shown. Before storage measured using the UV-vis-IR-1 and after using UV-vis-IR-2 (10 mm path length).

The uncoated broadband NF, the SiO_2@broadband NF and the supernatum obtained after 3 h centrifuging were all stored in the dark at 4 °C for 129 days and their colloidal stability assessed using UV-vis-IR and the procedure described in Section 3.9.2. The results (also shown in Figure 6-16) show the broadband NF and the dilute supernatum to both be relatively unchanged whereas the absorbance of the SiO_2@broadband NF had dropped to almost zero over the same period.

Pictures of the three NFs following storage (Figure 6-18) show that the NPs in the SiO_2@broadband NF had settled to the bottom of the cuvette, accounting for the absorbance drop. This may have been due to a combination of the removal of the TSCD and PVP stabilising agents and the increase in size and hence mass of the SiO_2@NPs.

This sedimentation of the NPs may not occur in practice in a flowing NF in a solar collector, however it does illustrate instability of the NF which could increase the propensity of the NPs to deposit on the surfaces of the collector in a similar way to that already seen in the flow testing of the uncoated broadband NF in Section 5.6.6.

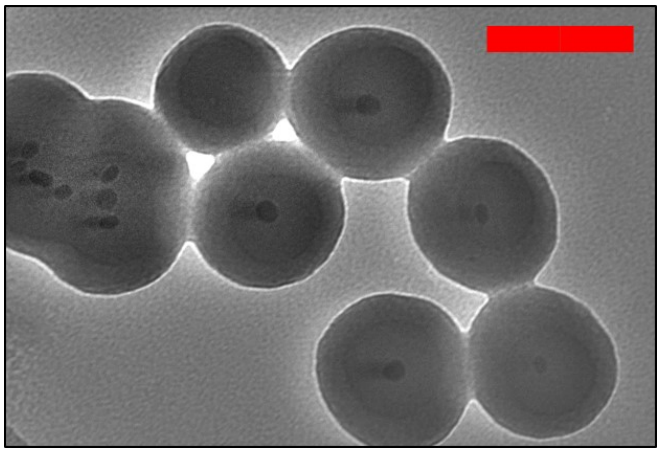

Figure 6-17 TEM micrograph of SiO_2@broadband NF. Red scale bar = 100 nm.

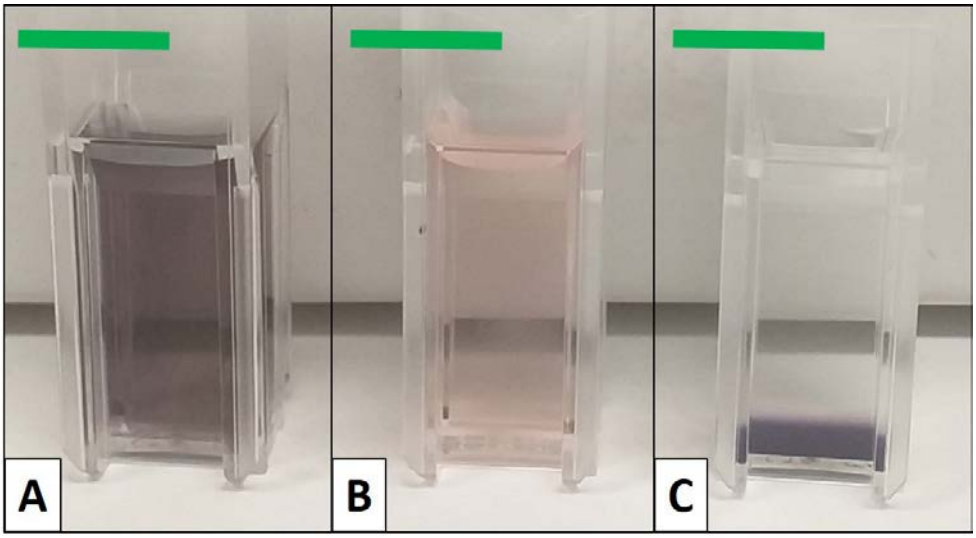

Figure 6-18 Photographs of (A) The broadband absorber NF, (B) The supernatum and (C) SiO_2@broadband NF after storage in the dark at 4 °C for 129 days. All green scale bars = 10 mm.

In summary, this Section shows that although it is possible to SiO_2 coat the NPs in the broadband absorber NF considerable further work is required to optimise the coating procedure. In addition, the lack of colloidal stability of the SiO_2@broadband NF is concerning and may have implications for the use of this NF in solar collectors.

6.7 Conclusions, Implications and Summary

6.7.1 Conclusions

This is one of the first studies to measure in static solar simulator tests SiO_2@Ag NPrs with a λ_{max} > 750 nm and a SiO_2 coating thickness of ≈ 50 nm produced by using a TEOS Stöber coating technique only, and to compare the results obtained to calculations based on the UV-vis spectra and to uncoated Ag NPrs.

It is also one of the only studies to provide comprehensive stability data on ≈ 50 nm thick SiO_2 coating on Ag NPrs produced using just a Stöber coating procedure under application relevant conditions and as such helps address the urgent need to undertake more stability trials.

It is the first attempt to SiO_2 coat a broadband absorber produced from combining three different morphologies of Ag NFs and to assess the colloidal stability of the thus produced NF.

To develop a suitable coating protocol, two different methods were assessed. The first water-glass method produced a thin incomplete SiO_2 coating, which, although slightly improving the elevated temperature stability compared to uncoated Ag NPrs, had a detrimental effect on the SSL stability. The second method, based on a Stöber TEOS hydrolysis, produced consistent thicker SiO_2@Ag NPrs. The optimum level of TEOS was found to be 10 mM with a reaction time of 30 minutes.

Repeat synthesis using this optimised Stöber method produced a consistent coating thickness of ≈ 50 nm, and a low percentage of free Ag NPs and multi-cored NPs (containing > 1 Ag NP). However, while there was no change in λ_{max} on coating, there was a loss of product in all cases with Ab_{max} dropping.

Calculations of $\eta_{Ab(300\ nm\ -\ 900\ nm)}$ from the UV-vis spectra gave an average value of 98.5 % > than the value obtained for Ag NPrs. However, the measured efficiency η_{PE} was lower at 73 % – 77 %, questioning the confidence that can be applied to the UV-vis calculations for these hybrid NFs.

Stability testing showed the SiO_2@Ag NPrs to be less morphologically stable in all the stability tests than their uncoated Ag NPr counterparts. They were also less stable to aggregation (drop in Ab_{max}) in the colloidal stability tests but more stable to aggregation in the natural sunlight tests. Attempts to improve the stability by modifying the optimised coating protocol although highlighting the importance of using a capping agent (in this case MHA) did not show any significant change in the morphological elevated temperature stability.

Investigating the morphological changes using TEM showed the Ag NPs to be dissolving inside the SiO_2 shell in the SSL exposure trials, but in the elevated temperature trials the SiO_2 shell was also seen to become more porous and even to dissolve leading to a high percentage of free Ag NPs.

It was possible to coat the broadband absorber with SiO_2, producing an ≈ 50 nm SiO_2 shell thickness, however, the colloidal stability of the NF produced was poor, with sedimentation of the SiO_2@Ag NPs occurring after 129 days at 4 °C in the dark.

Given the lack of morphological stability of the SiO_2@Ag NPrs it would appear that 50 nm SiO_2 coatings produced using the Stöber process are not a suitable means of stabilising Ag NPrs for solar or elevated temperature applications.

6.7.2 Implications

In contrast to the uncoated Ag NFs investigated in Chapter 5, the lack of agreement between the efficiency calculations based on the UV-vis measurements and the measurement of the efficiency in the static solar simulator for these SiO_2@Ag NPrs is of concern and could have implications for others investigating hybrid coated NPs.

Also of concern is the increase in the morphological instability of the SiO_2@Ag NPrs compared to the uncoated Ag NPrs. This questions the use of SiO_2 as an appropriate stabilising strategy. It may be that the morphological stability could be improved by combining the water-glass method with the TEOS method to produce a thin SiO_2 layer next to the NP and a more porous SiO_2 outer layer. This would require further method development and investigation. However, even if an improvement in the morphological stability is achieved the level of improvement required is enormous (need to survive for ≈ 20 years on a roof) and hence unlikely.

The lack of colloidal stability to aggregation and sedimentation (drop in Ab_{max}) is also an issue as it may increase the propensity for SiO_2@Ag NPs to deposit on the surfaces of any solar collector in a similar manner to the deposition of the Ag NPs seen in the flow testing in Section 5.6.6. Further work on producing a stable NF after coating is therefore required.

A different coating strategy to stabilise the Ag NPs is hence needed if Ag NP NFs are to be used in solar collectors. It may be that a thin 2 nm TiO_2 coating may work better (He et al., 2019; Li et al., 2017). This would require further investigation. However, given that colloids are always metastable (Pashley and Karaman, 2004) it would still be very challenging to find an appropriate stabilisation strategy which would prevent degradation over the 20 + years life-span of a solar collector even if a strategy of periodic (3 y – 5 y) complete replacement of the NF was employed.

6.7.3 Summary

A short summary highlighting the main Sections covered in this Chapter and the conclusions is given in Table 6-7.

Table 6-7 Chapter 6 Summary.

Section	**Covered**	**Conclusions / outcomes**
Development of synthesis method	2 methods – 1 based on water-glass, other Stöber TEOS method	Water-glass - thin incomplete SiO_2 coating, better temperature stability at 70 °C compared to uncoated Ag NPrs, worse SSL stability Stöber - ≈ 61 nm thick SiO_2 coating – best recipe, 10 mM TEOS with 40 µM MHA for 30 minutes
Optimised SiO_2 coating	Reproducibility, calculation of η_{Ab} from UV-vis, measurement of η_{PE}, stability testing	Reproducible coating thickness of ≈ 50 nm (12 repeats), with low % of uncoated Ag and multi-cored NPs $\eta_{Ab(300\ nm\ -\ 900\ nm)}$ from UV-vis > uncoated at 98.5 %, however, η_{PE} lower at ≈ 73 % – 77 % Stability – morphologically more unstable in all tests compared to uncoated, more stable to aggregation in natural sunlight exposure trials
Modifications to developed SiO_2 coating method	Changes made – adding extra purification, reducing O_2 level, changing MHA and DMA amount, reducing time of reaction	Capping agent MHA vital to produce consistently coated Ag NPrs. Reducing reaction time gave thinner SiO_2 layer. All modifications did not significantly change the elevated temperature stability of the resultant NF
SiO_2 coating of broadband absorber	Initial trial aimed at SiO_2 coating the broadband absorber and colloidal stability of SiO_2@broadband NF	Possible to coat broadband absorber but further method development required. Lack of colloidal stability of SiO_2@broadband NF after 129 days @ 4 °C in the dark

Chapter 7 Overall Discussion

7.1 Introduction

It has been suggested that all relevant technologies exist today to decarbonise the energy sector (International Energy Agency, 2021). However, this relies on widespread adoption of heat pumps and a significant increase in solar thermal HW heaters from 250 million worldwide in 2020 to 1,200 million by 2050 and a step change in rate of improvements in building efficiency. Unfortunately, given that HW accounts for ≈ ¼ of the annual energy demand (see Table 2-1) the latest UK government strategy does not prioritise solar thermal as a means of assisting decarbonisation (UK Government, 2021a).

This Chapter firstly summarises and then considers the implications of the results obtained within this thesis for STCs aimed at increased efficiency. It then looks at the broader picture, discussing other ways of increasing the number or utility of STCs to help reach the 4 – 5 x increase in STCs required by 2050. The focus then shifts to the future importance of thermal storage. A brief summary and a description of the publications from this thesis then complete this Chapter.

7.2 Summary of Results Obtained

This subsection collates together and summarises the results obtained in both Chapter 5 and Chapter 6. It starts with the performance results and then gives a summary of the stability testing results.

A summary of the performance of the seven nanofluids tested in this thesis and water is given in Table 7-1. Both the results from calculating the efficiency from the UV-vis spectra and from the static tests in the solar simulator are given. The values obtained for η_{PE} are also compared directly to the value obtained for water. The improvement in η_{PE} for all the nanofluids can clearly be seen, with the nanofluids containing the plasmonic Ag NPs exhibiting a much greater enhancement than the nanofluid containing only SiO_2. For the uncoated silver nanofluids the greatest improvements are seen for the nanofluids that exhibit a broad, strong spectral response (i.e. a high value of η_{lamp}) illustrating clearly how the potential performance of a volumetric absorber STC is dominated by the optical characteristics of the nanofluid as discussed in Section 2.7.5.

However, this is not the case for the hybrid SiO_2 coated Ag NPr NF tested, which showed a reduction in measured η_{PE} compared to the expected result calculated from the UV-vis spectra. As

discussed in Section 6.4.3 the reason for this discrepancy is unclear and requires further investigation.

Table 7-1 Summary of results obtained for the performance of the 7 NFs and water tested in this thesis. For further details of the results see Table 5-1, Table J.5 and Table J.9.

Fluid	**Mean $\eta_{lamp(330\ nm\ -\ 1100\ nm)}$ or $\eta_{lamp(330\ nm\ -\ 900\ nm)}$ / %**	**Mean η_{PE}/ %**	**% improvement in η_{PE} relative to water / %**
Water	-	20.51	0
SiO_2 only NF	-	24.40	19
Short λ NF	46.29	47.68	132
Long λ NF (0.1 mM Ag NPr)	57.82	62.46	204
Mid λ NF	73.82	65.05	217
SiO_2@Ag NPrs NF re-dispersed into ¼ volume water (middle position)	98.84	77.28	277
Broadband absorber NF	92.75	83.77	308
Ag NPrs centrifuged and re-dispersed into ¼ volume water (middle position)	91.72	84.81	313

The results from both Chapter 5 and Chapter 6 for the stability tests are summarised in Table 7-2. The lack of stability of the NFs tested in this thesis can clearly be seen, emphasising the importance of stability testing under application relevant conditions and showing that the stabilisation strategy of SiO_2 coating via the Stöber process investigated in this work is not a suitable means of stabilising Ag NPs for solar or elevated temperature applications.

Table 7-2 Summary of stability test results.

Stability test	**Uncoated Ag NFs (Chapter 5)**	**SiO_2 coated Ag NF (Chapter 6)**
Colloidal (4 °C in the dark)	All with TSCD and PVP stable to aggregation. Least morphologically stable mid λ NF, long λ NF and broadband absorber	Not stable to aggregation or morphologically stable, Ag NPs dissolving inside SiO_2 coating
Elevated temperature of 70 °C	Stable to aggregation, morphological instability of mid λ NF, long λ NF and broadband absorber exasperated. Centrifuged Ag NPrs more morphologically stable.	Less morphologically stable than uncoated. SiO_2 coating becoming more porous and dissolving
Exposure to SSL	All morphologically unstable	Stable to aggregation but less morphologically stable than uncoated
Natural sunlight trials	Aggregation of Ag NPrs	Less morphologically stable but more stable to aggregation than uncoated
Fluid flow	Broadband absorber stable to flow but not when combined with elevated temperature or SSL	-

Stability test	Uncoated Ag NFs (Chapter 5)	SiO_2 coated Ag NF (Chapter 6)
Changing BF to PG	Less stable to both aggregation and morphological changes	-

7.3 Implications for Enhanced Solar Capture

Although volumetric absorbers may offer advantages in terms of efficiency improvements their long term stability is questionable. Silver is probably one of the worst in terms of morphological stability but it does illustrate well the issues of using NFs in volumetric absorbers. On the other hand carbon NFs, although potentially more morphologically stable, need a higher NF concentration to give enough absorption. Their stability to aggregation may hence be problematic especially when exposed to multiple heating cycles and sunlight. Two studies have assessed the colloidal stability of MWCNTs with one showing a 4 % – 14 % drop in absorption after 50 days (Sarsam et al., 2017) and the other ≤ 40 % after 240 days (Hordy et al., 2014). This is without temperature and sunlight exposure showing that even carbon NFs suffer from stability issues and would be problematic to commercialise.

The stabilisation strategy of SiO_2 coating investigated within this thesis had a detrimental effect on the morphological stability, showing it to be an unsuitable method of improving stability. A different stabilisation strategy is hence needed if Ag NPs are to be used for solar or heat applications. Even if a suitable stabilisation strategy could be found it is still unlikely that this will increase the stability of the resultant NF enough to make it suitable for enhanced efficiency solar capture over a 20 year collector lifespan. A strategy of periodic complete replacement of the NF in the collector could be employed but even then it would be challenging to increase the stability enough to make it last for the 3 y to 5 y needed for this scenario. This strategy would also have system design implications (would need a facile method of completely removing and replacing the NF) and would increase the lifetime cost of the collector (maintenance and NF cost).

The additional mass of the volumetric absorbers on a roof may also be an issue especially for the large collector areas needed for decarbonising heating as well as hot water (HW) and especially if the NF used needs to be dilute to prevent stability issues (hence a greater path length and greater weight).

NFs can also be used for enhanced heat transfer in FPCs and ETCs with a selective surface absorber. These NFs would not need optical morphological and sunlight stability, but would need to be stable under flow conditions and with temperature cycling. However, the concentration of the NFs for thermal conductivity enhancement tends to be higher (see Section 2.7.4), so although Ag NSs which are more temperature stable may then be shown to be feasible after further longer-

term temperature experiments, the increased NF concentration needed could give rise to other stability issues. Further investigation would then be needed to see if the resulting increase in thermal conductivity and convective heat transfer gave enough of an advantage to justify further work.

Given the significant challenges that need to be overcome in order to make NF based STCs a reality, the concept of enhanced solar thermal capture using volumetric absorption discussed within this thesis is impractical as a means of decarbonising by 2050.

A different mechanism for enhancing the efficiency is hence needed, however, there are other means of improving STCs to allow more widespread adoption. These will be discussed further in the next Section.

7.4 Other Solar Design Options

With the now rapidly increasing need to decarbonise it may be prudent to focus on more widespread deployment of cheaper less efficient STCs to supplement mainly HW production rather than STCs for both heating and HW. An example of this is to improve the insulation on a flat plate collector giving it a comparable performance to a evacuated tube collector at 70 % of the cost (Beikircher et al., 2015).

There may also be scope for government incentives to encourage widespread uptake. This may lead to higher volume manufacturing and a reduction in costs similar to how the costs of solar PV have decreased in recent years.

However, the design of the solar collector and the HW storage system needs to consider the household use profile and after sales support to actually get the decarbonising benefit, increase consumer satisfaction and encourage further uptake (Gill et al., 2015). This need for a tailored system increases complexity and hence cost, limiting the ability to reduce costs.

Another way of increasing the amount of energy from a STC would be to increase the area rather than the efficiency. For example the building walls can be used rather than the roof to heat air to improve the efficiency of mechanical heat recovery systems and as a supplement to heat pumps (SPECIFIC, 2021; TATA Steel, 2021). These are presently mainly for commercial buildings and are not a stand-alone system, relying on a heat pump to decarbonise but they could be used for domestic systems. Widespread adoption of this type of technology would make heat pumps more efficient reducing the amount of electricity needed and hence facilitating decarbonisation.

These sort of solutions will become increasingly important as the amount of heat pumps increase together with an increase in the number of electrical vehicles, both adding stress to the existing electricity network.

7.5 Implications for Thermal Storage

Thermal storage will become increasingly important. It is estimated that a HW tank of 700 L – 800 L would be needed to shift heating demand for an individual homeowner by about 1 h so other forms of storage such as a latent heat thermal energy store (LTES) and a thermochemical store (TCS) will become imperative (Wilson et al., 2013) with the proposed increased use of heat pumps. Inter-seasonal storage (ISTES) will also become increasingly vital to balance the disparity between winter and summer.

Further research on TCS is hence important to produce more working pilot scale demonstrators that can then be commercialised in the 2030s to help balance the electricity grid as the number of heat pumps increases worldwide. However, even then salt hydrate TCS systems are unlikely to be developed enough for mass deployment in the timeframe needed for initial decarbonisation, they may find certain niche applications. It may therefore be prudent to concentrate the TCS research initially on liquid based systems (even although they have lower energy storage density) as these may in practice be easier to engineer and hence take less time to commercialise (see Section 2.4.6).

Anything that reduces the overall electricity demand, such as an increase in the number of solar thermal HW systems will also help reduce the future stress on the electricity grid. In addition, there needs to be a move away from combination boilers and high power electrical showers providing instant HW (which would require hydrogen or high power resistive heaters to decarbonise) towards HW tank systems that could then be used in conjunction with STCs as these do not have such an instantaneously detrimental impact on electrical grid stability.

HW tanks for use with solar thermal collectors are an existing technology, but there is perhaps scope to make these cheaper, easier to install, or sized differently (either smaller perhaps by using LTES or TCS where space is limited, or larger to provide some storage for space heating) to encourage widespread adoption.

Again thermal storage can be used with heat pumps for heating systems, with GSHPs being an already existing example. However, there may be scope to reduce the cost of these by combining with other thermal storage solutions such as HW tanks, LTES or TCS to make them cheaper, more efficient or more flexible offering greater utility to the consumer. It may also be possible to

combine GSHPs with STCs to reduce the cost or amount of supplementary electrical energy required.

7.6 Summary and Publications

This Chapter has provided a summary of the thesis results and given context for the work undertaken, describing the issues with volumetric absorbers using NFs and the use of NFs as heat transfer fluids. It has then looked at other ways of improving the uptake of STCs, such as policy incentives and cost reductions. The importance of thermal storage as a balancing mechanism is then discussed along with the suggestion that further work should focus on TCS systems and initially mainly on liquid based TCS.

A number of papers were published during the completion of this thesis. The novelty and focus of each of these different publications is given in Table 7-3 and the graphical abstracts for publications 1, 2 and 3 in Figure 7-1, Figure 7-2 and Figure 7-3.

Table 7-3 Summary of publications.

Publication number	**Title**	**Novelty and focus**
1	The Temperature Stability and Development of a Broadband Silver Nanofluid for Solar Thermal Applications (Kimpton et al., 2021)	Details the development of three silver based nanofluids with distinct morphologies, the subsequent combining of these nanofluids to produce a broadband absorber and an assessment of the elevated temperature stability of this broadband absorber and its component nanofluids
2	Silver nanofluids based broadband solar absorber through tuning nanosilver geometries (Kimpton et al., 2020b)	Assesses the performance of a novel silver broadband absorber made by combining three different silver based nanofluids both by utilising UV-vis-IR measurements to calculate the performance and by measuring that performance in static solar simulator tests
3	Thermal performance and physicochemical stability of silver nanoprisms-based nanofluids for direct solar absorption (Kimpton et al., 2020a)	First time nanofluids based on silver nanoprisms and SiO_2 coated silver nanoprisms have been assessed for their performance and stability under application relevant conditions
4	Decarbonising Heating and Hot Water Using Solar Thermal Collectors Coupled with Thermal Storage: The Scale of the Challenge (Kimpton et al., 2020c)	Ties together the use of silver nanofluids (NF) to enhance solar thermal capture with the use of an inter-seasonal thermal store. Looks at the feasibility of the numbers and assesses if this could be a possible decarbonising solution for the UK.

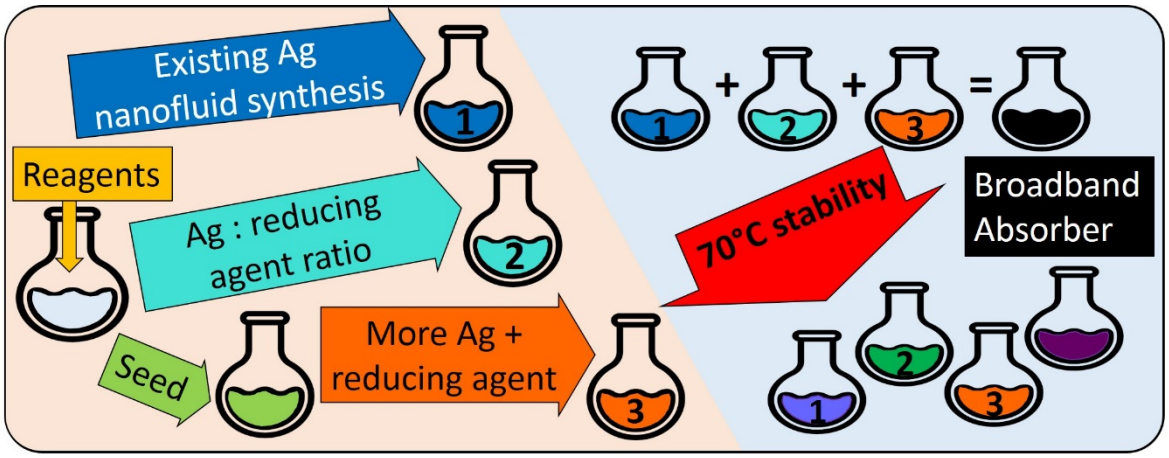

Figure 7-1 Graphical abstract for publication 1, The Temperature Stability and Development of a Broadband Silver Nanofluid for Solar Thermal Applications (Kimpton et al., 2021).

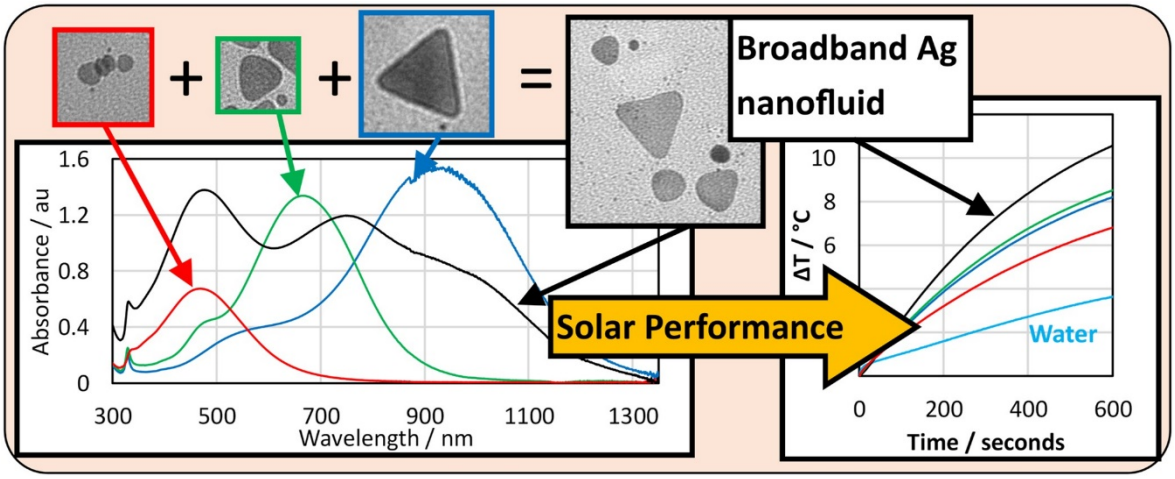

Figure 7-2 Graphical abstract for publication 2, Silver nanofluids based broadband solar absorber through tuning nanosilver geometries (Kimpton et al., 2020b).

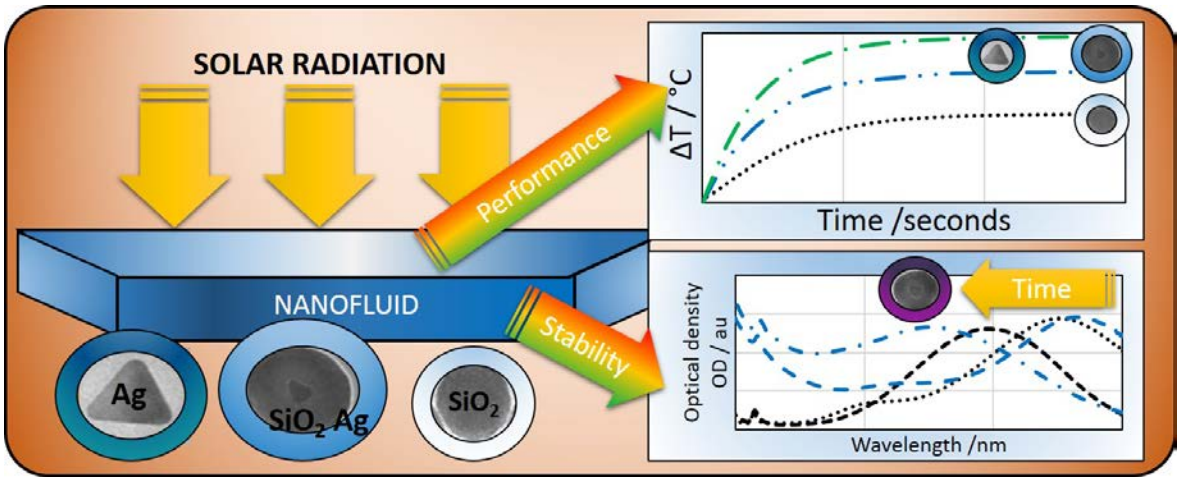

Figure 7-3 Graphical abstract for publication 3, Thermal performance and physicochemical stability of silver nanoprisms-based nanofluids for direct solar absorption (Kimpton et al., 2020a).

Chapter 8 Conclusions

The feasibility study on the proposed decarbonising solution of enhanced solar thermal capture connected to a suitable inter seasonal store highlighted the scale of the challenge facing the UK to decarbonise heating and hot water, but showed that the proposed solution could be applicable for some homes in the UK (greater than average roof area, lower than median demand and enough space for a large inter-seasonal store). However, this solution is not technically mature at present with a need for considerable research into long-term stability of nanofluids for solar thermal applications and for further research into suitable inter seasonal storage.

The focus of this thesis was on the enhancing of solar thermal capture by the use of silver nanofluids in a volumetric absorber.

Silver nanosphere based nanofluids had a lack of broad spectral absorbance and were shown from UV-vis calculations to be unsuitable on their own for enhancing solar capture. In contrast, although there were difficulties in controlling the batch synthesis method for silver nanoprisms, nanofluids containing nanoprisms did show a sufficiently broad absorption profile, making them potentially suitable for enhanced solar capture.

Synthesis methods were developed for two additional nanofluids containing distinct morphologies and hence absorption profiles which when combined with the silver nanoprism nanofluid produced experimentally for the first time a novel broadband absorber. From UV-vis measurements this broadband absorber nanofluid was also shown to offer potential for enhancing solar thermal efficiency. A synthesis protocol to consistently coat silver nanoprisms with ≈ 50 nm layer of SiO_2 was also developed as a possible morphological stabilisation strategy. This nanofluid were also shown from UV-vis measurements to enhance efficiency.

This is one of the first studies to measure in static solar simulator tests silver nanoprism nanofluids with a $\lambda_{max} > 750$ nm, and ≈ 50 nm thick SiO_2 coated silver nanoprisms produced using just a Stöber synthesis method. It is the first study to measure directly the performance of the developed novel silver based broadband absorber produced from combining three different morphologies of silver nanoparticles. It is also one of the few studies to investigate the stability of anisotropic silver nanoprisms using a variety of complementary tests and the only study to look at the stability of the developed novel broadband absorber nanofluid. The use of longer timeframe trials such as the natural sunlight tests and the long term storage trials under ideal conditions is also unusual.

In the static solar simulator tests all the six silver nanofluids evaluated had a greater photo-conversion efficiency than water clearly indicating their potential for enhancing solar thermal capture. The results were similar to those obtained from calculations based on UV-vis measurements for the uncoated silver nanofluids potentially allowing these calculations to be used for rapid screening of nanofluids. However, this was not the case for the hybrid SiO_2 coated silver nanoprism nanofluid which showed a reduction in measured performance compared to the calculated value.

The stability studies undertaken in this work have started to address the urgent need for more information on silver nanofluid stability. All the water based uncoated silver nanofluids were stable to aggregation in all the stability trials except the longer timeframe natural sunlight trials, suggesting that aggregation is a slower process than morphological changes and illustrating the advantage of undertaking a variety of stability tests utilising differing timeframes. However, they were not morphologically stable, with the harsher stability tests resulting in a larger change. When an alternative base fluid of propylene glycol (more suitable for solar applications) was used, the elevated temperature stability was even worse.

The SiO_2 coated silver nanoprisms were less morphologically stable than their uncoated counterparts. They were more stable to aggregation in the longer term natural sunlight tests, but they and the SiO_2 coated broadband absorber were less stable to aggregation in the colloidal stability tests. Dissolving of the silver nanoprisms and even dissolution of the SiO_2 coating with elevated temperature was found from TEM analysis to be the main failure mechanisms.

Given the lack of morphological stability and stability to aggregation it would appear that 50 nm SiO_2 coatings produced using the Stöber process are not a suitable means of stabilising silver nanofluids for solar or elevated temperature applications.

Overall this work has highlighted that measuring performance of the nanofluids is only part of the picture. It shows the vital importance of carrying out stability tests under realistic conditions for these and other nanofluids for solar and other applications. Assessing the morphological changes obtained under different exposure conditions has also lead to further insights into the failure mechanisms for these nanofluids.

The lack of morphological stability illustrated in this thesis, is the main barrier to commercialisation for enhanced efficiency volumetric absorbers based on silver. At present the silver nanofluids studied here cannot be recommended for use in solar and elevated temperature applications due to this lack of stability.

Chapter 9 Outlook

By producing experimentally for the first time a broadband absorber based on combining 3 morphologically distinct silver nanofluids this thesis has shown one of the potential practical issues that could occur when different nanofluids are mixed. This was the inconsistent shifting of the secondary peak primarily due to the instability of the mid λ NF. Producing this NF experimentally also allowed the broadband nanofluid to be both measured for its potential performance and tested for stability under application relevant conditions. This showed that although this NF was suitable to potentially enhance solar capture its lack of morphological stability was an issue. These insights would not have been gained from a numerical study.

The similarity of the performance results obtained for the five uncoated silver NFs in terms of potential efficiency obtained from the two complimentary methods employed in this thesis suggested that UV-vis measurements could be used as a rapid screening tool to evaluate NFs for their potential in solar applications. In contrast, the lower measured performance of the SiO_2 coated silver nanoprisms compared to that expected from UV-vis calculations is intriguing and suggests that efficiency calculations obtained from UV-vis alone are not suitable for evaluating SiO_2 coated metallic silver nanoparticles for their solar performance. This is a key insight, which may have relevance to other researchers looking at coated hybrid NPs for solar applications.

The focus of this thesis on measuring stability under application relevant conditions using a variety of complementary tests has led to insights into the failure mechanisms. One of these is the information that for these silver NFs, morphological changes occur rapidly, whereas aggregation is a slower process, only becoming apparent in the longer term natural sunlight trials. Other failure mechanism insights came from the investigation into one possible stabilisation strategy, namely SiO_2 coating. Here it was shown that the 50 nm thick SiO_2 coating produced in this work was not preventing the morphological changes, with dissolution of the silver nanoparticles inside the coating, and with elevated temperature, dissolution of the SiO_2 coating itself occurring. All of these insights could be useful for others looking at developing a testing protocol to investigate their nanofluids for stability and for those investigating SiO_2 coating as a possible stabilisation strategy.

In the future, both solar thermal collectors and thermal energy storage will be of increasing importance worldwide as countries move to lower carbon energy systems. However, it is unlikely that the main types of collectors employed are based on volumetric absorbers as it would be commercially challenging to develop stable nanofluids in a realistic timeframe.

If volumetric absorbers using silver are to be investigated further an alternative stabilising strategy is needed such as TiO_2 coating, however, even then it may be too challenging to increase the stability enough to make silver and volumetric absorbers a viable option. The observation regarding the lack of agreement between the two techniques used to evaluate efficiency in this thesis for the SiO_2 coated nanoprisms could be relevant to any assessment of the potential performance of nanofluids produced utilising this alternative TiO_2 coating.

This work also highlighted issues with the consistency of the batch manufacturing method used to produce the different nanofluids investigated. There is hence, also a need in the case of silver to improve the consistency of the manufacturing methods for the morphologically different nanofluids, however, this is of lesser importance than finding a means of stabilising the nanofluids.

When volumetric absorbers or other collector designs utilising other nanofluids are investigated, stability studies should form an integral part of the study. It is not enough to show an increase in efficiency, the nanofluid must also be capable of performing at the same level for an extended period without maintenance or replacing the nanofluid to make it suitable for solar or heat transfer applications. The insights gained within this thesis may assist others with their stability study designs or with what NFs to investigate.

As the pressure to decarbonise intensifies, rather than just looking at efficiency, it may be prudent to focus on methods to increase the uptake of solar thermal systems, such as reducing collector cost, improving the ease of installation, providing policy incentives and looking at other ways of utilising solar thermal capture to reduce the overall building's energy use. This would greatly assist the decarbonisation efforts as less renewable energy (mainly in the form of electricity) would be needed to be generated elsewhere.

Given the urgency of the decarbonising needed it is likely that any solar thermal capture with thermal storage system will have to be for use in conjunction with another decarbonising solution such as heat pumps. This will help reduce the stress on the existing electricity network with the proposed widespread uptake of heat pumps and will become increasingly vital as the move away from gas space and hot water heating accelerates.

The future importance of thermal storage as a means of assisting decarbonisation is also likely to increase. There will be a growing need to balance the supply of electricity from intermittent renewable sources with demand especially as more of the gas network is electrified with increasing heat pump uptake. Given the seasonal nature of space heating more, longer term, heat storage will be needed.

In the short term this thermal storage is likely to be in the form of GSHPs and the use of more hot water tanks (sensible thermal energy STES). However, this is not ideal for inter-seasonal storage. Although latent heat storage in the form of phase change materials may find certain niche applications to reduce the size of HW tanks, research should focus primarily on the development and commercialisation of thermochemical systems. This would allow these to become a commercial reality and hence greatly assist in the balancing of future inter-seasonal heat supply and demand. It may be that in the medium term it will be easier to develop TCS systems based on liquid reactions as these, although giving a lower energy storage density, may be easier to design and hence implement more widely commercially in a shorter timeframe.

Appendix A Additional Literature on Thermochemical Store (TCS) for Thermal Energy Storage (TES)

This Appendix gives additional information on TCS for TES with a focus on salt hydrates. It initially describes the thermodynamics of salt hydrates. This is followed by a Section on material challenges facing the use of salt hydrates for TCS and a Section detailing an ideal material specification. The Appendix then concludes with a brief look at potential mixed salt hydrate systems.

A.1 TCS – Thermodynamics of Salt Hydrates

For a salt hydrate the basic thermochemical reaction is as shown in Equation A.1 (Rammelberg et al., 2016). MX is the salt (M = cation, X = anion), $N_{initial}$ is the initial number of moles of water (for the anhydrous salt $N = 0$), N_{added} is the number of added moles of water. ΔH is the change in enthalpy in kJ mol^{-1}.

$$MX.(N_{added} + N_{initial})H_2O \rightleftharpoons MX.(N_{initial})H_2O + (N_{added})H_2O \quad \Delta H \text{ is positive (endothermic reaction)}$$

Equation A.1

The forward reaction is endothermic (changing the store) and energy needs to be added i.e. ΔH is positive. The back reaction is exothermic (discharging the store) and energy is released in the form of heat (ΔH is negative). The reaction needs to be reversible to ensure cycle stability. The kinetics of the reaction are also important. One of the key things to influence the kinetics is over hydration, which can lead to deliquescence or the dissolving of the solid hydrate in the excess water (Rammelberg et al., 2016). In addition, if the salt has a low melting point this can cause problems. If the salt melts or forms a solid solution it becomes no longer possible for water to diffuse through the salt during discharge (Scapino et al., 2017b). This reduces the capacity of the store.

Control of the dehydration and hydration is hence vital. This can be achieved by controlling the water vapour partial pressure $p_{v(w)}$ (Ferchaud et al., 2014; Steiger, 2018). At a given pressure (for example 1 bar) the charging or dehydration reaction occurs at a certain temperature T_{equil} (in K) defined by Equation A.2, where ΔH is the change in enthalpy in kJ mol^{-1} and ΔS in the change in entropy in kJ mol^{-1} K^{-1} (Kiyabu et al., 2018).

$$T_{\text{equil}} = \frac{\Delta H}{\Delta S}$$

Equation A.2

If the charging temperature is above T_{equil} then the endothermic dehydration reaction in Equation A.1 will occur and if the temperature is below T_{equil} the reverse exothermic reaction will occur discharging the store and releasing heat. At T_{equil}, ΔG the change in Gibbs free energy in kJ mol^{-1} is 0 hence (Scapino et al., 2017a):

$$\Delta G = \Delta H^{\vartheta} - T\Delta S^{\vartheta} + RT \ln K$$

Equation A.3

where ΔH^{ϑ} is the standard enthalpy change in kJ mol^{-1}, ΔS^{ϑ} is the standard entropy change in kJ mol^{-1} K^{-1}, T is temperature in K, R is the ideal gas constant which is 8.314 J mol^{-1} K^{-1} and K is the ratio of partial vapour pressures (or equilibrium constant (Glasser, 2014b)) of the products ($p_{v(prod)(i)}$ in bar) and the reactants ($p_{v(react)(i)}$) given by Equation A.4.

$$K = \frac{\prod_i p_{\text{v(prod)}(i)}}{\prod_i p_{\text{v(react)}(i)}}$$

Equation A.4

For the charging reaction the hydrated salt MX.$(N_{added} + N_{initial})H_2$O is a solid with low partial pressure p_v hence Equation A.4 simplifies to:

$$K = \frac{p_{\text{v(w)}}}{{p_{\text{v}}}^{\vartheta}}$$

Equation A.5

where $p_{v(w)}$ is the vapour pressure of water in bar and ${p_v}^{\vartheta}$ is the standard reference pressure normally taken as 1 bar (Donkers et al., 2017). Values of ΔH^{ϑ} and ΔS^{ϑ} for a large number of single salt hydrates can be obtained from standard thermochemical tables such as (Chase, 1998; Glasser, 2014a, b) and databases (Deutsch et al., 2016). This allows for the construction of the equilibrium curve by varying T and $p_{v(w)}$. When a salt can exist in a number of different hydrated forms such as for the reaction of MgCl$_2$.$(N_{added} + N_{initial})H_2$O more than one equilibrium line can be calculated. For example with MgCl$_2$.$(N_{added} + N_{initial})H_2$O, $N_{added} + N_{initial}$ can be 1, 2, 4 or 6 giving the following equations and 3 equilibrium lines (Rammelberg et al., 2016; Scapino et al., 2017a). This is illustrated in Figure A.1:

$$MgCl_2.2H_2O \rightleftharpoons MgCl_2.H_2O + H_2O$$

Equation A.6

$$MgCl_2.4H_2O \rightleftharpoons MgCl_2.2H_2O + 2H_2O$$

Equation A.7

$$MgCl_2.6H_2O \rightleftharpoons MgCl_2.4H_2O + 2H_2O$$

Equation A.8

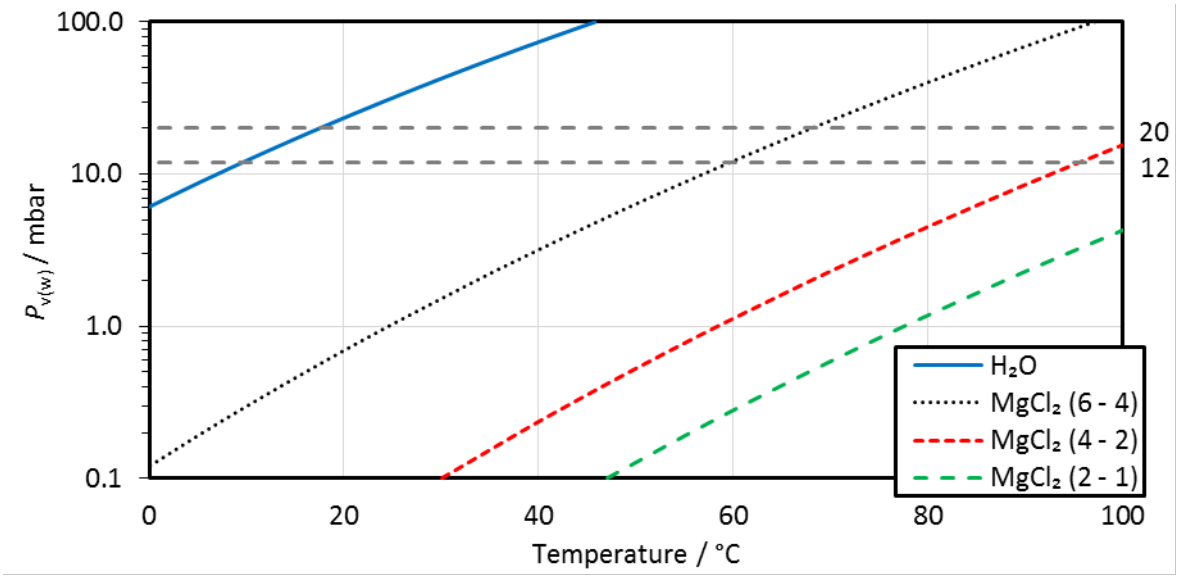

Figure A.1 Equilibrium curves for $MgCl_2$ and H_2O. The data for the $MgCl_2$ curves are taken from (Donkers et al., 2017) and the curve for H_2O is calculated from the steam tables for water (Dean and Lange, 1999). The reference lines at 12 mbar and 20 mbar represent suitable $p_{v(w)}$ values for hydration and dehydration respectively. The numbers in brackets are the change in the number of moles of water.

The 12 mbar value for the hydration (discharging reaction) in Figure A.1 occurs when the water temperature is 10 °C. A supply of water at this temperature is hence needed. Some studies consider that this water could be obtained from using a borehole TES or GSHP for the water required (Donkers et al., 2017). This borehole storage could then also be used to cool the water coming off the salt hydrate on the dehydration or charging cycle leading to a constant 17 °C (equating to 20 mbar) water temperature for dehydration (also shown in Figure A.1). Such a proposal would require the storage of the water and hence turn a system that could be an open system to effectively a closed system (see Figure 2-4) with a knock on effect on both the storage density and the complexity of the system design. However, it is vital to control the water input T and hence $p_{v(w)}$ as this has a direct relationship to the charging and discharging temperature of the TCS.

The standard reaction entropy for each mole of water is roughly constant at 146 J K^{-1} mol^{-1} ± 11 J K^{-1} mol^{-1} (Glasser, 2014b) so the higher the value of N_{added} for a given hydrate the higher the potential amount of energy that can be stored per mole of salt. Hence, many studies have focused on salts with high potential values of N_{added} such as $MgSO_4.7H_2O$ and $MgCl_2.6H_2O$ (Linnow et al.,

2014; N'Tsoukpoe et al., 2014; Rammelberg et al., 2016; Scapino et al., 2017b; Sögütoglu et al., 2018). The molar mass and the density of the highest hydrate can then be used to give an idea of the potential storage density of the salt.

However, although it is possible for the $MgCl_2$ dehydration to lead to only 1 remaining water leading to a total removal of 5 water molecules it is not possible to achieve either the $MgCl_2.2H_2O$ or the $MgCl_2.H_2O$ at an operating temperature less than 100 °C and a $p_{v(w)}$ of 20 mbar. This means that in practice for this salt only Equation A.8 will occur reducing the potential storage density for a store based on $MgCl_2$. This is also the case for many of the other higher hydrate salts (Donkers et al., 2017; Glasser, 2014a, b).

The storage density is also affected by the need to provide energy to the water in order to evaporate it from a liquid to a vapour (N'Tsoukpoe et al., 2014). With the latent heat of vaporisation for water being ≈ 44.6 kJ mol^{-1} (in the range 10 °C - 20 °C) this can have a significant effect on both the storage density and the net efficiency of the store. This requirement makes the η values quoted in Table 2-2 for TCS highly unlikely in practice. In fact N'Tsoukpoe et al quoted values of η between 19.3 % – 38.5 % for the salt hydrates they investigated (N'Tsoukpoe et al., 2014), which is considerably less than the 75 % – 100 % in Table 2-2 (International Renewable Energy Agency (IRENA), 2013). Others have also suggested that the actual storage efficiency for salt hydrates may be ≈ 25 % – 40 % (Trausel et al., 2014). This issue around efficiency needs to be investigated further before TCS can be recommended as the most suitable TES for ISTES.

A.2 TCS – Material Challenges

For a salt hydrate to be suitable for use in TCS it needs to fulfil a number of demanding material criteria. T_{equil} needs to be sufficiently high enough at a reasonable $p_{v(w)}$ to provide HW at about 65 °C on the hydration cycle. T_{equil} for the dehydration or charging cycle also has to occur within a temperature range suitable for regeneration by the solar collector, again at an appropriate $p_{v(w)}$. The theoretical ρ_{TES} for the salt couple based on the highest possible known hydrate should also be as high as possible, provided that as many of the dehydration reactions occur within the appropriate $p_{v(w)}$/ T window (for multiple dehydration reactions such as for $MgCl_2$). However, although desirable, if the T_{equil} is not in the right range, even a salt couple with a high ρ_{TES} would be unsuitable. It should be noted from this that the much studied $MgSO_4.7H_2O$, with a high theoretical ρ_{TES} would be unsuitable as its value of T_{equil} at a $p_{v(w)}$ of 12 mbar is only 24 °C for the hydration reaction (Donkers et al., 2017) from the monohydrate to heptahydrate.

For a salt hydrate reaction to be cycled within a TCS the reaction needs to be reversible with no unwanted side reactions occurring during operation (Liu and Rao, 2017). For example $MgCl_2.2H_2O$

can decompose at temperature forming HCl according to the reaction in Equation A.9 (Rammelberg et al., 2016). This is an irreversible reaction and leads both to the depletion of active material in the store and to the formation of corrosive HCl, both of which are not desirable.

$$MgCl_2.2H_2O \rightarrow MgOHCl.H_2O + HCl$$

Equation A.9

Other salt hydrates that have unwanted side reactions include Na_2S which forms toxic H_2S, and $Mg(NO_3)_2$ which losses N_2 (Donkers et al., 2017).

Deliquescence, the formation of a saturated solution on over hydration is also not desirable. This occurs when a material is very hydroscopic and causes significant issues in a TCS which relies on the passage of air carrying water vapour to charge and discharge the TCS. Deliquescence blocks areas of the store preventing hydration / dehydration leading to reduced storage capacity. To reduce the issue of deliquescence, the salt can be absorbed onto an inert substrate (Frazzica et al., 2020), but this reduces the percentage of active material in the store and hence the storage density.

Melting of the salt within the proposed operating temperature range of the store also prevents the passage of moist air causing the same detrimental effect on the TCS. $CaCl_2.6H_2O$ is such a salt, which has a melting point of 29.8 °C and can also suffer from deliquescence (Rammelberg et al., 2016).

There are a number of other considerations that may preclude a salt hydrate from being useful in a TCS. These include cost of the salt, corrosive nature (for example LiCl (Donkers et al., 2017) is corrosive as is NaOH (Kiyabu et al., 2018)) and toxicity of the salt. It may be possible to mitigate the cost of an expensive material for HW provision by using a cascade TCS consisting of more than one salt hydrate, the cheaper one being used for heating but not HW provision (N'Tsoukpoe et al., 2016). A final consideration is the volume change from the hydrated to dehydrated salt. Large volume changes may cause issues with cycling of the TCS and lead to material degradation over time reducing the storage capacity.

A.3 TCS - Ideal Material Specification

An ideal material specification can be obtained from consideration of the above factors. In drawing up this specification due consideration has been made to the importance of each factor, for example an appropriate value of T_{equil} was considered to be more important than a high storage density. The specification is similar to the one employed by Donkers et al (Donkers et al.,

2017) but with a reduced importance placed on energy storage density. The specification is given in Table A.1.

Table A.1 Ideal TCS Material Specification.

Parameter	**Value**	**Comments / values for $K_2CO_3.1.5H_2O$ (Donkers et al., 2017; Sögütoglu et al., 2018)**
Hydration or discharging T_{equil} / °C	> 65	59
Hydration p_v / mbar	≈ 12	12
Dehydration or charging T_{equil} / °C	< 150	65
Dehydration p_v / mbar	≈ 20	20
Melting point / °C	> dehydration T_{equil}	> 150
Presence of deliquescence	None	None
Side reactions	None	Side reaction with CO_2 does not lead to cycle instability (Sögütoglu et al., 2018)
Maximum hydrate number	As great as possible	1.5
Material Storage density / GJ m^{-3}	> 1 (ideal ≈ 2)	1.3
Toxicity / corrosive	Not toxic / corrosive	Not toxic / corrosive
Cost	Low	Low (common name potash)

The order of the parameters in the table reflects the order of importance of each of the factors. The values for the most suitable single salt hydrate $K_2CO_3.1.5H_2O$ identified and investigated by Donkers et al (Donkers et al., 2017; Sögütoglu et al., 2018) are also shown for comparison. $K_2CO_3.1.5H_2O$ nearly fits this ideal specification. However, the hydration T_{equil} is too low and the material storage density is only just acceptable due to the low hydrate number of 1.5.

A number of reviews of different salt hydrates have been undertaken (Donkers et al., 2017; N'Tsoukpoe et al., 2014; Trausel et al., 2014) and although they all identify possible suitable candidate materials, none match the ideal specification given in Table A.1. It is therefore likely that mixed salt-hydrate systems will need consideration.

A.4 TCS – Mixed Salt Systems

Only a small number of mixed salt systems have been investigated for TCS applications. These include $CaCl_2$ with $MgCl_2$ to change the onset temperature of the unwanted HCl side reaction (Pathak et al., 2016; Pathak et al., 2017; Rammelberg et al., 2013; Rammelberg et al., 2016), $MgCl_2$ with $MgSO_4$ (Posern and Kaps, 2010; Rammelberg et al., 2013; Rammelberg et al., 2016), $MgSO_4$ with $SrCl_2$ (Posern and Osburg, 2017), $CaCl_2$ with $MgBr_2$ (Rammelberg et al., 2013), $CaCl_2$ with

$LiNO_3$ (Sutton et al., 2018) and $CaCl_2$ with $FeSO_4$ (Rammelberg et al., 2013). In addition, mixtures of Na_2SO_4 with $MgSO_4$, KCl with $MgCl_2$ and LiCl with $MgCl_2$ have been studied both in respect to their suitability for TCS and as PCM materials for LTES (Gutierrez et al., 2018; Gutierrez et al., 2017). Doping with a small amount of other salts (alkali nitrates) have also been examined experimentally to reduce the T_{equil} and increase the kinetics of both MgOH and CaOH for higher temperature TCS applications (Shkatulov and Aristov, 2015; Shkatulov et al., 2014).

With K_2CO_3 showing good cycle stability (Sögütoglu et al., 2018), but a slightly too low T_{equil} for HW it may be possible to combine this with another salt to increase T_{equil}. Ideally the same anion should be employed. However, the only plausible candidate for this would be Rb_2CO_3. Rb_2CO_3 is a rare earth salt hydrate and as such is likely to be too costly, especially as a fairly high proportion would be needed to shift T_{equil} by more than 6 °C. The equilibrium curves for K_2CO_3 and Rb_2CO_3 are illustrated in Figure A.2. For pure Rb_2CO_3 (for 1 to 0 H_2O), T_{equil} for the hydration reaction would be 74 °C, which is only 15 °C > K_2CO_3.

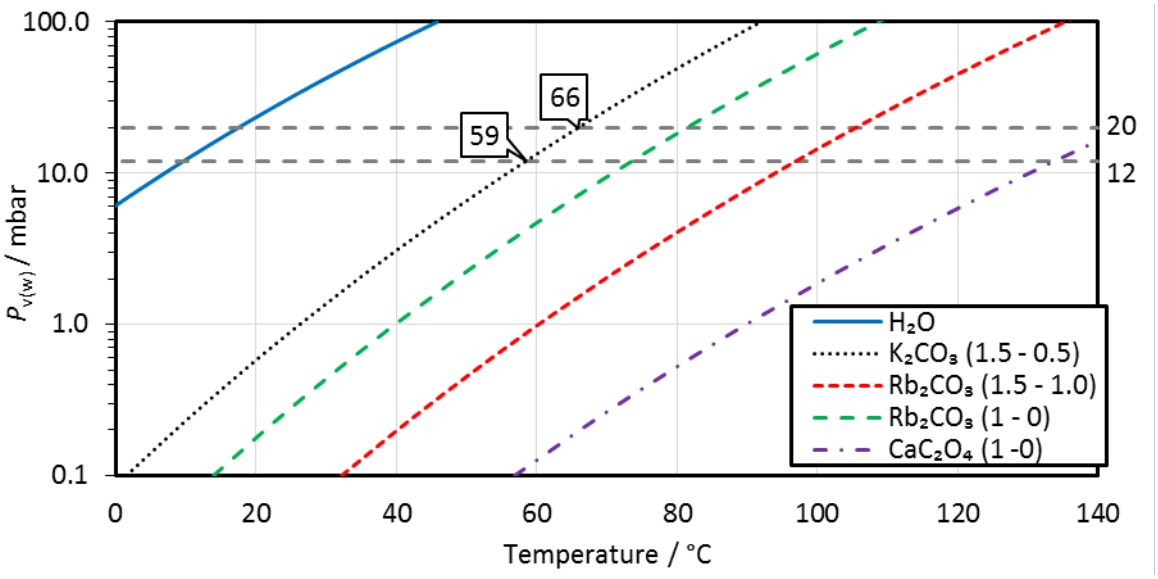

Figure A.2 Equilibrium curves for K_2CO_3, Rb_2CO_3, CaC_2O_4 and H_2O. The data for the salt hydrate curves are taken from (Donkers et al., 2017) and the curve for H_2O is calculated from the steam tables for water (Dean and Lange, 1999). The reference lines at 12 mbar and 20 mbar represent suitable $p_{v(w)}$ values for hydration and dehydration respectively.

Another potential candidate for mixing with K_2CO_3 would be CaC_2O_4. The equilibrium curve for this is also illustrated in Figure A.2. Pure CaC_2O_4 has a T_{equil} above 100 °C for both the hydration and dehydration reactions, because of this its potential for shifting the mixture T_{equil} is much higher at low inclusion levels. It has been investigated on its own for higher temperature TCS applications (Knoll et al., 2017) and has good cycle stability even after 100 cycles. However, CaC_2O_4 is acutely toxic so is not an ideal material (N'Tsoukpoe et al., 2014).

Appendix B Additional Literature Review on Types of Nanofluids

This Appendix gives further details of studies that have been carried out on some of the different types of NFs. Firstly, NFs containing only one species are discussed. Hybrid NFs are then described focussing on silver hybrids only.

B.1 Studies on Different Types of Nanofluids

Some studies on carbon-based NFs are given in Table B.1. Other studies on metal oxide based NFs are shown in Table B.2 while those utilising gold NFs are given in Table B.3. Where the concentration of NPs is shown as a vol % this figure was taken directly from the reference but can be calculated using:

$$\text{vol } \% = \frac{{}^{m_{\mathrm{p}}}/_{\rho_{\mathrm{p}}}}{\left({}^{m_{\mathrm{p}}}/_{\rho_{\mathrm{p}}}\right) + \left({}^{m_{\mathrm{BF}}}/_{\rho_{\mathrm{BF}}}\right)}$$

Equation B.1

where m_{p} is the mass of the NP, ρ_{p} is the NP density, m_{BF} is the mass of base-fluid and ρ_{BF} its density (Li et al., 2020).

Table B.1 Studies on carbon-based NFs for solar applications.

Type of carbon	**BF**	**Concentration of NPs**	**For volumetric absorption / Yes or No**	**Reference**
Graphene	Water	≤ 0.02 wt. %	No	(Ahmadi et al., 2016)
Multi-walled carbon nanotubes	Water	≤ 0.03 vol %	Yes	(Beicker et al., 2018)
Functionalised carbon nanotubes	Ethylene glycol	≤ 0.1 vol %	Yes	(Li et al., 2020)
Functionalised multi-walled carbon nanotubes	Water	≤ 0.1 wt. %	No	(Sarsam et al., 2017)
Functionalised multi-walled carbon nanotubes	Ethylene glycol	≤ 0.64 vol %	Yes	(Tam et al., 2018)
Carbon black	Water	≤ 10 wt. %	Yes*	(Ulset et al., 2018)
Graphite / carbon nanotubes	Texatherm oil	≤ 1 vol %	Yes	(Luo et al., 2014)
Graphene oxide	Water	≤ 0.1 wt. %	Yes	(Chen, L. et al., 2017)

Type of carbon	BF	Concentration of NPs	For volumetric absorption / Yes or No	Reference
Carbon (soot)	Paraffin oil	≤ 2 vol %	Yes	(Singh and Khullar, 2019)

*For steam generation in a concentrated parabolic trough collector – hence very different concentration

Table B.2 Studies on metal oxide based NFs.

Type of metal oxide	BF	Concentration of NPs	For volumetric absorption / Yes or No	Reference
CuO	Water	≤ 1.5 wt. %	No*	(Liu et al., 2013; Lu et al., 2011)
CuO	70 % / 30 % mix of water / ethylene glycol	≤ 0.01 vol % (100 ppm)	Yes	(Karami et al., 2015)
CuO / TiO_2 / ZnO / CeO_2 / Fe_2O_3	Water	≤ 1 vol %	Yes	(Milanese et al., 2016a, b)
Al_2O_3	Water	≤ 0.05 vol %	Yes	(Gupta et al., 2015b, c)
Al_2O_3	Water / ethylene glycol	≤ 2 vol %	No	(Hamid et al., 2015)
Al_2O_3	Water	≤ 3 vol %	No (HP)	(Hassan et al., 2015)
TiO_2	Water	≤ 0.3 wt. %	No	(Chaji et al., 2013)
TiO_2 / SiO_2	Texatherm oil	≤ 3 vol %	Yes	(Luo et al., 2014)
Fe_3O_4	Water	≤ 0.004 vol %	Yes	(Gorji and Ranjbar, 2016, 2017b)
CeO_2 / WO_3	Water	≤ 0.067 vol %	No	(Sharafeldin and Gróf, 2018; Sharafeldin et al., 2017)

*Concentrated solar power with a HP

Table B.3 Studies utilising gold nanofluids.

Type of gold NP	Concentration of NPs	Comment	Reference
Spherical	≤ 0.004 vol %	Static outdoor test – showed instability	(Beicker et al., 2018)
Citrate stabilised, 1-step, 20 nm - 30 nm spherical	≤ 0.04 wt. %	For steam generation in concentrated sunlight	(Amjad et al., 2017)

Type of gold NP	Concentration of NPs	Comment	Reference
Nanorods and nanoellipsoids	≤ 0.001 vol %	Blended mixture – numerical study	(Du and Tang, 2016)
Nanorods of varying aspect ratios	≤ 0.0001 vol %	Blended mixture of aspect ratios to give broadband absorbance	(Jeon et al., 2014; Jeon et al., 2016)
Spheres stabilised by citrate with / without additional poly ethylene glycol stabilisation	≤ 0.1 vol %	Mainly focused on NF stability but also estimates DASC performance numerically	(Sharaf et al., 2019)
Spheres (mean diameter = 13 nm)	≤ 0.0178 vol %	For steam generation in concentrated sunlight	(Wang et al., 2017)
Spheres (mean diameter = 16 nm)	≤ 0.01 wt. %	For steam generation via bubble formation	(Liu et al., 2018)

B.2 Silver Hybrids

There are a large number of hybrid NFs containing silver that have been investigated. For hybrids, the silver can be present as a separate nanoparticle within a NF containing another type of NP, the silver can also be coated with another material making a composite NP or silver can be added to the surface of another NP. These three types of hybrid nanofluids (designated type 1, 2 or 3 for ease of discussion) are illustrated for silver in Figure B.1.

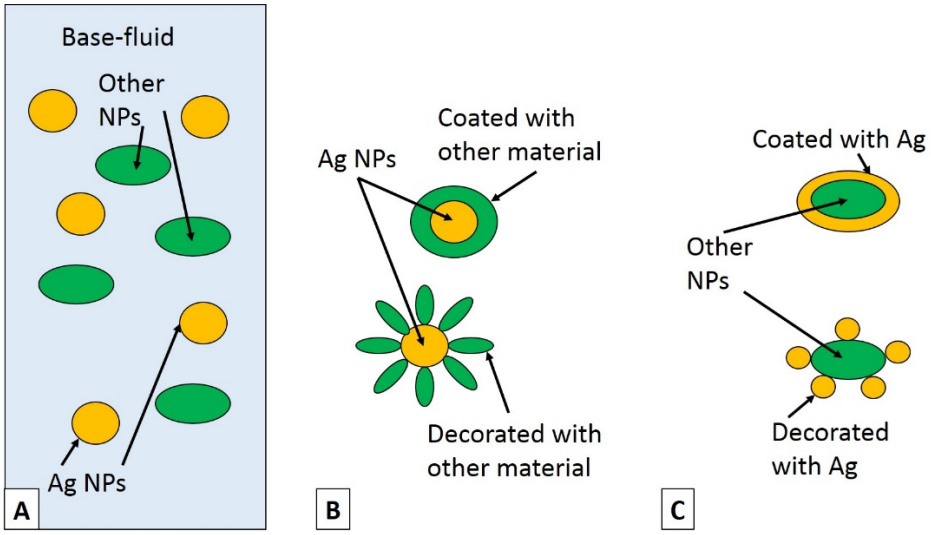

Figure B.1 Schematic of the three different types of silver hybrid nanofluids (A) Type 1 hybrid consisting of a mixture of different NP types, (B) Type 2 hybrid containing Ag NPs either coated or decorated with another material and (C) Type 3 hybrid containing another NP either coated or decorated with Ag.

Details of some of the type 1 hybrid NFs that have been investigated are given in Table B.4 and illustrate the number of different permutations that are possible for type 1 hybrids.

Less different permutations exist in the literature for type 2 hybrid NF containing a silver core. However, the shape of the internal silver NP can be varied as well as the BF employed. Some examples of type 2 hybrid NFs include SiO_2 coating of Ag nanodiscs in water BF (Taylor et al., 2018) or glycerol BF (Hjerrild et al., 2018), and Ag nanospheres with a λ_{max} of 474 nm coated with SiO_2 in a novel BF of propylene glycol (PG) containing $CoSO_4$ (Huang et al., 2021) all for PVT applications. Another example of a type 2 hybrid is 20 nm Ag NPs coated with a thin 2 nm TiO_2 coating in a BF of ethylene glycol / water again for PVT applications (He et al., 2019) or for enhanced solar steam generation (Li et al., 2017).

Table B.4 Type 1 hybrid NFs investigated.

Shape / type of Ag NP	**Other NP used**	**Preparation method**	**Reason for hybrid**	**Reference**
Spherical	Carbon nanohorns	Two-step	Improve thermal properties of NF	(Sani et al., 2015)
Spherical (30 nm – 50 nm)	ZnO (note only a 50: 50 mixture of Ag: ZnO investigated)	Two-step	Thermal conductivity enhancement	(Esfahani et al., 2018)
Spherical (stabilised with PVP)	Graphene nanoplatelets	Two-step (in Propylene glycol / water BF)	To tailor optical properties	(Vallejo et al., 2019)
Spherical (38 nm ± 7 nm)	Gold (10 nm ± 2 nm)	Prepared separately using one-step synthesis and then combined (also bimetallic prepared by one-step investigated)	Enhanced photo-conversion efficiency. Bimetallic performed better than blended hybrid	(Chen, M. et al., 2017)
SiO_2 coated nanodiscs (type 2 hybrid)	Carbon nanotubes	Seeded method to produce Ag nanodiscs followed by SiO_2 coating. The two separate NFs then mixed together	To tailor the absorption properties for PVT applications	(Hjerrild et al., 2016)
Ag coated onto a SiO_2 NP (type 3 hybrid)	Multi walled carbon nanotube (MWCNT)	Different NP prepared separately and combined using two-step preparation method	To produce a broadband absorber	(Zeng and Xuan, 2018)
Spherical (80 nm)	Caesium tungstate oxide hybrid NP (Near infra-red absorber)	Different NPs prepared separately – combined using two-step method	To produce a broadband absorber. BF is ethylene glycol	(Liu et al., 2020)

For the type 3 hybrid NFs with silver on the outside of another NP a large number of different core particles have been investigated. Some of these are illustrated in Table B.5.

Table B.5 Type 3 hybrid NFs investigated.

Inner NP	**Preparation method**	**Reason for hybrid**	**Reference**
TiO_2	Ag added to surface using photo-conversion method – two-step method then used	To improve absorption / optical properties	(Xuan et al., 2014)
Reduced graphene oxide	Ag reduced onto surface of reduced graphene oxide, dried and re-dispersed via two-step preparation method	To improve absorption and heat transfer properties	(Mehrali et al., 2018)
Antimony tin oxide	Ag reduced onto surface of antimony tin oxide hybrid NP, dried and re-dispersed via two-step method using surfactant into water BF	To produce a broadband absorber of a parabolic DASC	(Sreekumar et al., 2020)
CuO	Ag reduced onto surface of prepared CuO particles and then re-dispersed via two-step ultrasonic method into BF	To produce a broadband absorber	(Yu and Xuan, 2018)
Diamond	Ag reduced onto the surface of acid functionalised nanodiamonds	To improve the thermal conductivity	(Oliveira et al., 2019)

Appendix C Additional Information on Experimental Methods

This Appendix contains additional information pertaining to Chapter 3, Experimental Methods. The first Section describes potential evaluation methods, the second gives details of a comparison between the different spectrophotometers used in this study. Information pertaining to the measurement of the intensity of the lamp used in the solar simulator using a calibrated PV cell is then provided. The Appendix then finishes with a description of the method used to evaluate the uncertainty of the various experimental techniques used along with a discussion of the results obtained.

C.1 Potential Evaluation Methods

To evaluate the size of the NPs in the NF there are two main methods available, dynamic light scattering (DLS) and TEM. DLS measures the hydrodynamic size of the NP by looking at the way that light from a laser is scattered through the sample. The typical laser λ used is 633 nm so it may not be a suitable technique for samples with a strong absorption at or around this λ. In addition, using this technique on non-spherical particles can lead to data artefacts (an additional secondary peak in the size distribution is obtained due to the rotational motion of the non-spherical particles). For gold NPs DLS also leads to a 2 x 4 times wider size distribution than TEM measurements (larger standard deviation σ)(Khlebtsov and Khlebtsov, 2011). Even when used to look at spherical Ag NPs stabilised with PVP, DLS can register a large proportion of large hydrodynamic sizes due to the presence of the PVP. These large particles scatter light more than small ones skewing the results obtained (Garcia et al., 2020). DLS also does not give any information on the geometry of the NPs present. However, DLS is a non-destructive technique and allows changes in size distribution with time to be monitored easily so can give information on colloidal stability.

TEM analysis gives significantly more information on the morphology of the NPs present but it becomes more difficult to monitor changes in the sample with time as it is a destructive technique. However, as only a very small sample of NF is needed to provide a TEM sample, some monitoring of changes with time can be achieved by sub-sampling of the NF. As this work is focused on evaluating spectral changes in the Ag NFs with time and relating them to the morphological changes, TEM analysis to give information on size, distribution and geometric shape of the NPs has been chosen as the preferred method.

To evaluate the optical properties of the NF, spectroscopic techniques can be employed. The most suitable of these are UV-vis and UV-vis-IR spectroscopy. This technique can be used to estimate the potential solar performance of a NF (Du and Tang, 2016) for volumetric absorption (see Section 3.8.2). For silver as the position of the absorption peak (λ_{max}) is strongly related to the size and shape of the NP (Aherne et al., 2008; Haber and Sokolov, 2017; Ledwith et al., 2007) this technique will complement the morphological results obtained from TEM measurements. As it is a non-destructive technique it can also be used to monitor changes with time giving information about the stability of the NF and has been used by others to assess stability (Haber and Sokolov, 2017; Tang et al., 2013).

Another method that can be used to assess the stability of a NF is the measurement of ζ potential using an electrophoretic light scattering technique (Xu, 2008) to determine the height of the barrier to aggregation for electrostatic stabilisation (Section 2.6.5). However, it cannot assess the effect of steric stabilisation and in fact any steric stabilisation present may significantly affect the value obtained (Garcia et al., 2020; Hunter, 1981). As it only gives information on the potential stability to aggregation it cannot give an understanding of spectral and morphological changes of the NPs in the NF.

The thermal conductivity of a NF (or other liquid) can be measured using the transient hot wire technique with a low level of uncertainty of below 2 % for NFs (Zhao et al., 2016). However, there are not many commercial transient hot wire instruments available (perhaps because of the very thin wire needed). When the transient hot wire technique is compared to another method for measuring thermal conductivity (namely the laser flash method) there is found to be an order of magnitude difference (Zagabathuni et al., 2016) giving an indication that part of the improvement in thermal conductivity of NFs is due to an increase in Brownian motion (the laser flash method uses a very small volume and hence restricts Brownian motion). Although thermal conductivity enhancement is important for NFs utilised as the heat transfer fluid in surface absorbing STCs (Section 2.7.4), it is of lesser importance in volumetric absorbers, where performance enhancement is based on the optimisation and control of the NFs optical properties.

As mentioned the potential solar performance of the NFs can be estimated from the UV-vis spectra. However it is also possible to measure directly the performance of the NFs for volumetric absorption by using sunlight or various artificial analogues to provide a light source, while measuring simultaneously the temperature rise of the NF. For commercial collectors BS EN ISO 9806 (British Standards Institution (BSI), 2013) describes the test methods employed to measure performance, either utilising sunlight or a solar simulator. These methods can be adapted to give an indication of potential performance for smaller volumes of experimental nanofluids. However,

as mentioned in Section 2.7.5 considerable care needs to be employed when evaluating the results obtained when non-standard test methods have been used.

C.2 Comparison Between Spectrophotometers

To understand the effect of changing the spectrophotometer, a comparison between the spectrophotometers was undertaken measuring the same samples in two of the spectrophotometers on the same day. For this comparison two different long λ Ag NPr (λ range 850 nm – 970 nm) samples and two different mid λ Ag NP (λ range 590 nm – 670 nm) samples were used. The long λ samples were prepared according to the procedure in Section 3.5.3 and tested as made without centrifuging to concentrate. The mid λ samples were prepared according to the protocol described in Section 3.5.4 and 4.5.1 for the mid λ NF used for the broadband absorber and diluted 1 mL in 3 mL final volume for UV-vis and UV-vis-IR measurements. The results of the comparison are shown in Figure C.1.

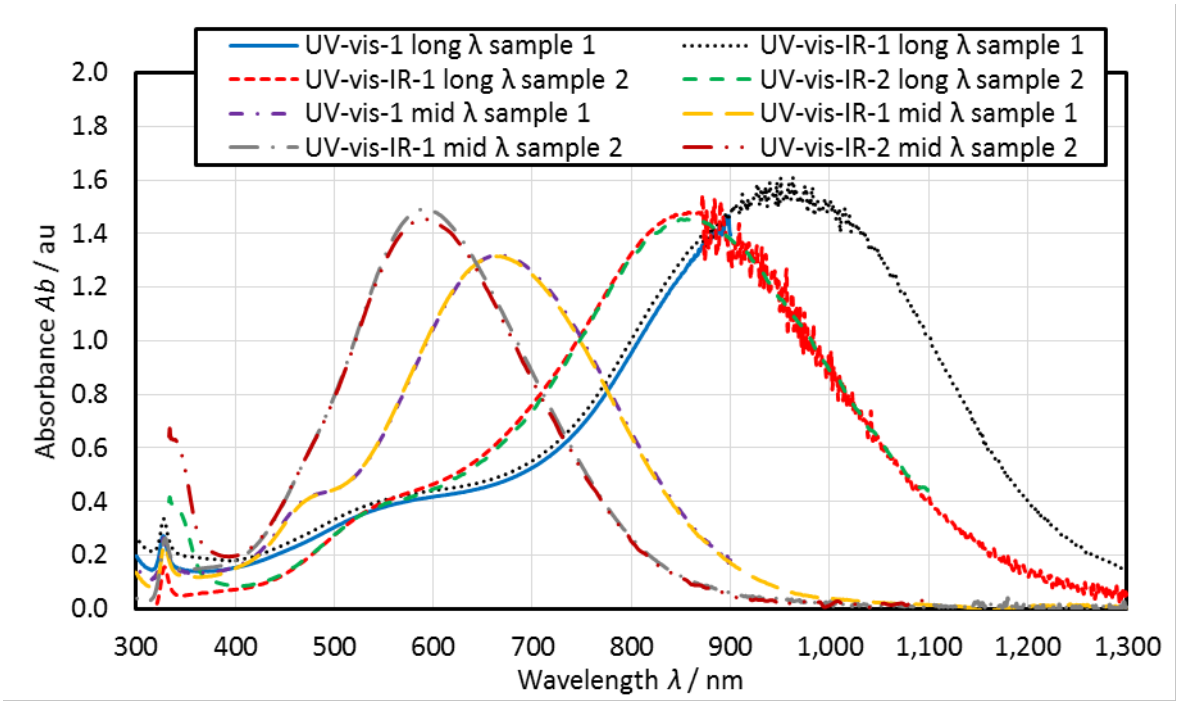

Figure C.1 Comparison of the UV-vis and UV-vis-IR spectra from the different spectrophotometers used. UV-vis-1 = Varian Cary 300 Bio, UV-vis-IR-1 = Perkin Elmer Lambda 750S and UV-vis-IR-2 = AvaLight – Hal lamp and Avaspec -2048. Measured using a polystyrene macro-cuvette (2.5 mL – 4.5 mL volume) with a 10 mm path length.

There were some noticeable differences between the spectrophotometers especially in the 300 nm – 400 nm range for the peak height ($Ab_{max(quad)}$) of the small quadrupole peak (associated with the asymmetric nature of the NPs) especially when the UV-vis-IR-2 spectrophotometer was used. This is understandable as the position of the quadrupole peak ($\lambda_{max(quad)}$) is about 325 nm – 335 nm and is at the limit of the range for this spectrophotometer (range 330 nm – 1100 nm).

The shape of the spectral curves in the > 400 nm range were similar for all the samples tested especially the mid λ samples. For these samples the main peak positions (λ_{max}) were 664 nm and 662 nm for the mid λ sample 1, and 592 nm and 591 nm for the mid λ sample 2, a difference of < 2 nm. The peak height (Ab_{max}) was also similar for the mid λ samples (1.320 au and 1.315 au for mid λ sample 1, 1.493 au and 1.454 au for mid λ sample 2) a difference of < 0.04 au (≈ 2.7 %).

There are larger differences in the λ_{max} for the long λ samples, this is for two reasons. Firstly, the noise associated with the measurements at > 872 nm for UV-vis-IR-1 due to the change in light source in this spectrophotometer at 872 nm. Secondly, for the long λ sample 1, λ_{max} occurs outside of the measurement range for the UV-vis-1 (> 900 nm). These two reasons also lead to larger differences in Ab_{max} for the long λ samples.

C.3 Measuring the Light Intensity (I_L) using a "ReRA System" Calibrated Silicon PV Cell

For set-up B the light intensity was measured using a "ReRA system" calibrated silicon PV cell connected to a Keighley Power supply. The silicon cell was calibrated initially at Radboud University Nijmegen PV measurement facility. This calibration was performed using an NREL calibrated reference cell. This type of reference is suitable for indoor solar simulator applications.

The fill factor (*FF*) of a PV cell is defined as:

$$FF = \frac{v_{\max} I_{\max}}{v_{\mathrm{oc}} I_{\mathrm{sc}}} \times 100$$

Equation C.1

where v_{max} in V is the maximum voltage obtained from the cell, I_{max} is the maximum current (A), v_{oc} is the open circuit voltage and I_{sc} is the short circuit current. This can then be used to calculate the cell efficiency η_{cell}:

$$\eta_{\mathrm{cell}} = \frac{FF v_{\mathrm{oc}} I_{\mathrm{sc}}}{P_{\mathrm{i}}}$$

Equation C.2

where P_i is the power incident on the cell (equivalent to the intensity I_L) in W. As the area of the cell is known this can then be equated to the intensity of the light I_L.

When the value of I_{sc} is equal to the calibration value of the cell the output from the lamp is 1000 W m^{-2}. The calculated value of η_{cell} is then used to determine the new value of P_i and hence I_L with the lamp at the setting used in the experiments from rearranging Equation C.2. The results of measuring I_L using the "ReRA system" calibrated silicon cell are given in Table C.1.

Table C.1 Measurements of I_L / W m^{-2} for set-up B in the solar simulator using a "ReRA System" calibrated silicon cell (area of cell = 3.6 cm^2).

	I_{sc} / mA	V_{oc} / V	I_{max} / mA	V_{max} / V	*FF* / %	η_{cell} / %	P_i / W	I_L / W m^{-2}
Calibration value	89.7	-	-	-	-	-	-	-
Measured value (1000 W m^{-2})	89.9 ± 3.5 (*N* = 4)	0.547	79.55	0.374	60.46	8.26 ± 0.25	0.36	1000
At lamp setting (*N* = 9)	107.46 ± 5.7	0.554	103.14 ± 6.38	0.344 ± 0.02	59.54 ± 2.72	8.26	0.429 ± 0.01	1191.2 ± 40.29

C.4 Uncertainty Analysis

The measurement uncertainty was determined according to the method described in (Bell, 2001) and (Taylor and Kuyatt, 1994). For each measurement type (TEM, UV-vis and UV-vis-IR spectroscopy, performance evaluation and stability testing) the relative uncertainty (u_R) was calculated for each of the Type B (equipment, calibration / resolution) uncertainties assuming a rectangular probability distribution such that:

$$u_R\ (\text{Type B}) = \frac{D}{\sqrt{3}}$$

Equation C.3

where *D* is the half width between the upper and lower measurement limits. The combined Type B uncertainties ($u_{R(com)}$) are then summed using the law of propagation of uncertainty or the root sum of squares method (Taylor and Kuyatt, 1994):

$$u_{R(\text{com})}\ (\text{Type B}) = \sqrt{\sum_i^j \left(u_{Ri}^2 + \cdots u_{Rj}^2\right)}$$

Equation C.4

where the first u_R uncertainty is *i* and the last *j*.

The Type A uncertainties arising from sample variation were calculated assuming a normal distribution of the data such that:

$$u_R\ (\text{Type A}) = \frac{\sigma}{\sqrt{N}}$$

Equation C.5

where σ is the sample standard deviation (in this case expressed as a %) and *N* is the number of measurements.

The Type B were then combined with the Type A (sample variation) uncertainties to give a combined relative uncertainty ($u_{R(\mathrm{com})}$ (Type A + B)) using the root sum of squares method. A coverage factor (k) of 2 (approximately 95 % confidence) was then used to give a final expanded uncertainty (U) where:

$$U = ku_{R(\mathrm{com})}\ (\mathrm{Type\ A + B})$$

Equation C.6

The Type B uncertainties for all of the measurement types are given in Appendix D and the Type A uncertainties in Appendix E along with the final U values using a k value of 2. To limit the number of calculations 35 typical TEM groups of measurements are shown in Appendix E. For the UV-vis and UV-vis-IR measurements only the results of the consistency of batch synthesis (see Section 3.5.5) are shown. For the calculation and measurement of efficiency again a limited sub-set of samples is used to estimate typical Type A uncertainties.

For the TEM measurements $u_{R(\mathrm{com})}$ (Type B) was 1.29 % which would give a value of U (Type B) of 2.58 % using a k value of 2 (see Table D.1). Even with the use of multiple images to increase the number of measurements the particle size variation gave rise to some larger Type A variations and hence U. The range of values for the Type A relative uncertainties for the TEM measurements (based on 35 typical groups of measurements) was 0.72 % – 5.77 % giving rise to U values of between 2.96 % and 11.82 % (Table E.1). These values do not account for any errors associated with choosing the particle shape manually from the TEM image.

The Type B measurement uncertainties for the three different spectrophotometers used for UV-vis and UV-vis-IR characterisation are given in Table D.2 for the uncertainty in measuring λ_{max} and in Table D.3 for the uncertainties associated with measuring Ab_{max}. Even when the variation between the three spectrophotometers utilised is taken into account (using the mid λ samples shown in Figure C.1), the value of $u_{R(\mathrm{com})}$ (Type B) was < 1 %, which would give a value of U (Type B) of < 2 % using a k value of 2 (see Table D.2 and Table D.3 for actual values).

The Type A uncertainties for the three types of NFs used to investigate the consistency of the batch manufacturing process (Section 3.5.5) are all < 2.1 % for both λ_{max} and Ab_{max} (Table E.2 and Table E.3), giving a final U value of < 4.5 % when combined with the Type B uncertainties using a k value of 2. It should be noted that these values are lower than the maximum U values reported in (Kimpton et al., 2020b) of 6.69 % for the UV-vis-IR measurements as they are based on a larger number of samples and the uncertainty associated with the result will decrease as N increases.

The Type B uncertainties in calculating the absorption efficiency $\eta_{\mathrm{lamp(330\ nm\ -\ 1100\ nm)}}$ (see Equation 3-9) are given in Table D.4. The value of $u_{R(\mathrm{com})}$ (Type B) was 1.41 %, which would give a U (Type B)

of 2.81 % using a coverage factor k of 2. Typical Type A uncertainties are given in Table E.4 for repeat measurements of four different NFs over a range of values of λ_{max}. The range of u_R (Type A) was 0.43 % – 3.32 % giving rise to U values of 2.94 % – 7.22 % when combined with the Type B uncertainty using a k value of 2. The largest value of U was associated with the short λ samples, which had a lower value for $\eta_{lamp(330\ nm\ -\ 1100\ nm)}$ and a larger σ.

For the measurement of η_{PE} (see Equation 3-10) using the solar simulator, there were larger Type B uncertainties. These are shown in Table D.5 for set-up A and in Table D.6 for set-up B. For set-up A, $u_{R(com)}$ (Type B) was 4.81 %, which would give a U (Type B) of 9.63 % using k = 2. For set-up B, $u_{R(com)}$ (Type B) was slightly lower at 4.09 %, giving a U (Type B) of 8.18 %. The largest single factor contributing to these uncertainties was the variation in the lamp intensity I_L of the solar simulator.

Typical Type A uncertainties for both solar simulator set-ups are given in Table E.5 using water in all three positions in the solar simulator as an example for set-up A. The examples used for set-up B were water and three samples of the long λ, mid λ, short λ and resultant broadband absorber mixture (for further sample details see Section E.4). For set-up A u_R (Type A) ranged from 1.70 % – 1.91 % giving values of U of 10.21 % – 10.36 %. For set-up B u_R (Type A) ranged from 0.52 % – 3.19 % leading to U values of between 8.24 % and 10.37 %.

Appendix D Type B Measurement Uncertainties

This Appendix gives the results of calculating the Type B (measurements uncertainty arising from anything else apart from directly measured Type A uncertainties, such as those arising from equipment variability, calibration and resolution) uncertainties for the measurement techniques and main calculations undertaken in this thesis using Equation C.4. For Type B measurements the probability distribution is assumed rather than measured as in Type A uncertainties (Bell, 2001). The expanded uncertainty U arising from only the Type B uncertainties is also given. The Type B uncertainties for the TEM technique are given first, followed by those for the UV-vis and UV-vis-IR spectrometry. The Appendix then looks as the Type B uncertainties for calculating $\eta_{\text{lamp(330 nm – 1100 nm)}}$ and η_{PE} for the two solar simulator set-ups.

D.1 Transmission Electron Microscopy (TEM)

The Type B uncertainties for the TEM are given in Table D.1.

Table D.1 Type B uncertainties for TEM measurements.

Source of uncertainty	**Comment**	**Value / ± %**	**Probability distribution**	**Divisor**	**Uncertainty / %**
Calibration of line length (u_{R1})	Resolution of 100 nm line length is 200 pixels – assume to be ± 1 nm	1.00	Rectangular	$D/\sqrt{3}$	0.58
Resolution of TEM (u_{R2})	Assumed to be ± 1 nm for a particle of 50 nm	2.00	Rectangular	$D/\sqrt{3}$	1.15
Combined Type B ($u_{R(com)}$ (Type B))	-	-	Assumed normal	-	1.29
Expanded Type B (U (Type B))	Using a k value of 2 (≈ 95 % confidence)	-	Assumed normal	-	2.58

D.2 UV-vis and UV-vis-IR Spectroscopy – Type B Uncertainties in λ_{max}

The Type B uncertainties in λ_{max} are given in Table D.2 for all the three different spectrophotometers used.

Table D.2 Type B uncertainties in λ_{max} for UV-vis and UV-vis-IR measurements.

Source of uncertainty	**Comment**	**Value / ± %**	**Probability distribution**	**Divisor**	**Uncertainty / %**
UV-vis-1 resolution of λ (u_{R1})	Step rate 1 nm for UV-vis. Maximum uncertainty at 200 nm	0.50	Rectangular	$D/\sqrt{3}$	0.29

Source of uncertainty	Comment	Value / ± %	Probability distribution	Divisor	Uncertainty / %
Spectrophotometer used UV-vis-1 versus UV-vis-IR-1 (u_{R2})	Using mid λ sample 1 - UV-vis-1 λ_{max} = 666 nm, UV-vis-IR-1 λ_{max} = 664 nm 2 samples	0.15	Assumed normal	$\sigma/\sqrt{N}$	0.11
UV-vis Combined Type B ($u_{R(com)}$ (Type B))	-	-	Assumed normal	-	0.31
UV-vis Expanded Type B (U (Type B))	Using a k value of 2 (≈ 95 % confidence)	-	Assumed normal	-	0.62
UV-vis-IR-1 resolution of λ (u_{R1})	Step rate 1 nm for UV-vis-1. Maximum uncertainty at 300 nm	0.33	Rectangular	$D/\sqrt{3}$	0.19
Spectrophotometer used UV-vis-1 versus UV-vis-IR-1 (u_{R2})	Using mid λ sample 1 - UV-vis-1 λ_{max} = 666 nm, UV-vis-IR-1 λ_{max} = 664 nm 2 samples	0.15	Assumed normal	$\sigma/\sqrt{N}$	0.11
Spectrophotometer used UV-vis-IR-1 versus UV-vis-IR-2 (u_{R3})	Using mid λ sample 2 - UV-vis-IR-1 λ_{max} = 592 nm, UV-vis-IR-2 λ_{max} = 591 nm 2 samples	0.08	Assumed normal	$\sigma/\sqrt{N}$	0.06
UV-vis-IR-1 Combined Type B ($u_{R(com)}$ (Type B))	-	-	Assumed normal	-	0.23
UV-vis-IR-1 Expanded Type B (U (Type B))	Using a k value of 2 (≈ 95 % confidence)	-	Assumed normal	-	0.46
UV-vis-IR-2 resolution of λ (u_{R1})	Step rate 1 nm for UV-vis-IR-1. Assume similar sensitivity for UV-vis-IR-2. Maximum uncertainty at 330 nm	0.30	Rectangular	$D/\sqrt{3}$	0.17
Spectrophotometer used UV-vis-IR-1 versus UV-vis-IR-2 (u_{R2})	Using mid λ sample 2 - UV-vis-IR-1 λ_{max} = 592 nm, UV-vis-IR-2 λ_{max} = 591 nm 2 samples	0.08	Assumed normal	$\sigma/\sqrt{N}$	0.06
UV-vis-IR-2 Combined Type B ($u_{R(com)}$ (Type B))	-	-	Assumed normal	-	0.18
UV-vis-IR-2 Expanded Type B (U (Type B))	Using a k value of 2 (≈ 95 % confidence)	-	Assumed normal	-	0.37

D.3 UV-vis and UV-vis-IR Spectroscopy – Type B Uncertainties in Ab_{max}

The Type B uncertainties associated with the determination of Ab_{max} are given in Table D.3.

Table D.3 Type B uncertainties in Ab_{max} for UV-vis and UV-vis-IR measurements.

Source of uncertainty	**Comment**	**Value / ± %**	**Probability distribution**	**Divisor**	**Uncertainty / %**
UV-vis-1 resolution of *Ab* (u_{R1})	Assume similar to *λ* resolution	0.50	Rectangular	$D/\sqrt{3}$	0.29
Spectrophotometer used UV-vis-1 versus UV-vis-IR-1 (u_{R2})	Using mid *λ* sample 1 - UV-vis-1 Ab_{max} = 1.32 au, UV-vis-IR-1 Ab_{max} = 1.315 au. 2 samples	0.19	Assumed normal	$\sigma/\sqrt{N}$	0.13
UV-vis-1 Combined Type B ($u_{R(com)}$ (Type B))	-	-	Assumed normal	-	0.32
UV-vis-1 Expanded Type B (*U* (Type B))	Using a *k* value of 2 (≈ 95 % confidence)	-	Assumed normal	-	0.64
UV-vis-IR-1 resolution of *Ab* (u_{R1})	Assume similar to *λ* resolution	0.50	Rectangular	$D/\sqrt{3}$	0.29
Spectrophotometer used UV-vis-1 versus UV-vis-IR-1 (u_{R2})	Using mid *λ* sample 1 - UV-vis-1 Ab_{max} = 1.32 au, UV-vis-IR-1 Ab_{max} = 1.315 au. 2 samples	0.19	Assumed normal	$\sigma/\sqrt{N}$	0.13
Spectrophotometer used UV-vis-IR-1 versus UV-vis-IR-2 (u_{R3})	Using mid *λ* sample 2 - UV-vis-IR-1 Ab_{max} = 1.493 au, UV-vis-IR-2 Ab_{max} = 1.454 au. 2 samples	1.31	Assumed normal	$\sigma/\sqrt{N}$	0.92
UV-vis-IR-1 Combined Type B ($u_{R(com)}$ (Type B))	-	-	Assumed normal	-	0.98
UV-vis-IR-1 Expanded Type B (*U* (Type B))	Using a *k* value of 2 (≈ 95 % confidence)		Assumed normal	-	1.95
UV-vis-IR-2 resolution of *Ab* (u_{R1})	Assume similar to *λ* resolution	0.50	Rectangular	$D/\sqrt{3}$	0.29
Spectrophotometer used UV-vis-IR-1 versus UV-vis-IR-2 (u_{R2})	Using mid *λ* sample 2 - UV-vis-IR-1 Ab_{max} = 1.493 au, UV-vis-IR-2 Ab_{max} = 1.454 au, 2 samples	1.31	Assumed normal	$\sigma/\sqrt{N}$	0.92
UV-vis-IR-2 Combined Type B ($u_{R(com)}$ (Type B))	-	-	Assumed normal	-	0.97
UV-vis-IR-2 Expanded Type B (*U* (Type B))	Using a *k* value of 2 (≈ 95 % confidence)	-	Assumed normal	-	1.94

D.4 Type B Uncertainty in Calculating $\eta_{lamp(330\ nm - 1100\ nm)}$

Table D.4 given the Type B uncertainties that arise from the calculation of $\eta_{lamp(330\ nm - 1100\ nm)}$ using the Type B uncertainties that were calculated for the spectrophotometers.

Table D.4 Type B uncertainty in calculating $\eta_{\text{lamp(330 nm – 1100 nm)}}$.

Source of uncertainty	**Comment**	**Symbol**	**Uncertainty / %**
Measuring sample spectrum on UV-vis-IR-1 uncertainty in λ_{max}	From Table D.2	u_{R1}	0.23
Measuring sample spectrum on UV-vis-IR-1 uncertainty in Ab_{max}	From Table D.3	u_{R2}	0.98
Measuring solar simulator output on UV-vis-IR-2 uncertainty in λ_{max}	From Table D.2	u_{R3}	0.18
Measuring solar simulator output on UV-vis-IR-2 uncertainty in Ab_{max}	From Table D.3	u_{R4}	0.97
Uncertainty in area = uncertainty in λ_{max} + uncertainty in Ab_{max}	Combining u_{R1} - u_{R4}	$u_{R(com)}$ (Type B)	1.41
Expanded uncertainty (Type B)	Using a k value of 2	U (Type B)	2.81

D.5 Type B Uncertainty in Calculating η_{PE} for the Solar Simulator Set-up A

The Type B uncertainties for each of the parameters in Equation 3-12 (mass m_w, specific heat capacity c_w, light intensity I_L, Area A and change in temperature ΔT) were used to estimate the Type B uncertainty in η_{PE}. The results are given in Table D.5.

Table D.5 Type B uncertainty in calculating η_{PE} for the solar simulator set-up A.

Source of uncertainty	**Symbol**	**Comment**	**Value / ± %**	**Divisor**	**Uncertainty / %**
Change in c_w with temperature	u_{R1}	c_w changes from 4.182 KJ Kg^{-1} K^{-1} to 4.190 KJ Kg^{-1} K^{-1} over temperature range 20 °C – 70 °C	0.19	$D/\sqrt{3}$	0.11
Uncertainty in measuring m_w	u_{R2}	1000 µL Micropipette used to measure amount with accuracy of ± 0.3 %	0.30	$D/\sqrt{3}$	0.17
Change in A with temperature	u_{R3}	Due to thermal expansion of liquid (water thermal expansion used)	4.00	$D/\sqrt{3}$	2.31
Change in I_L due to lamp output variation	u_{R4}	Lamp output varies by ± 6 %	6.00	$D/\sqrt{3}$	3.46
Uncertainty in measuring I_L	u_{R5}	Voltacraft PL-110 SM solar meter ± 10 W m^{-2} for sunlight. Assumed to be 5 x for lamp (similar value to "ReRA system" PV cell)	3.33	$D/\sqrt{3}$	1.92

Source of uncertainty	Symbol	Comment	Value / ± %	Divisor	Uncertainty / %
Uncertainty of temperature measurement because of thermocouples	u_{R6}	Assumed to be ± 0.5 °C which equates to 0.5/20 x 100 % at 20 °C	2.50	$D/\sqrt{3}$	1.44
Combined Type B	$u_{R(com)}$ (Type B)	-	-	-	4.81
Expanded Type B	U (Type B)	Using a k value of 2 (≈ 95 % confidence)	-	-	9.63

D.6 Type B Uncertainty in Calculating η_{PE} for the Solar Simulator Set-up B

The Type B uncertainties in for each of the parameters in Equation 3-12 (mass m_w, specific heat capacity c_w, light intensity I_L, Area A and change in temperature ΔT) were used to estimate the Type B uncertainty in η_{PE}. The results are given in Table D.6.

Table D.6 Type B uncertainty in calculating η_{PE} for the solar simulator set-up B.

Source of uncertainty	Symbol	Comment	Value / ± %	Divisor	Uncertainty / %
Change in c_w with temperature	u_{R1}	c_w changes from 4.1844 KJ Kg^{-1} $K^{-1}$to 4.1796 KJ Kg^{-1} K^{-1} over temperature range 20 °C – 40 °C	0.11	$D/\sqrt{3}$	0.06
Uncertainty in measuring m_w	u_{R2}	1000 µL Micropipette used to measure amount with accuracy of ± 0.3 %	0.30	$D/\sqrt{3}$	0.17
Change in A with temperature	u_{R3}	Due to thermal expansion of liquid (water thermal expansion used)	2.00	$D/\sqrt{3}$	1.15
Variation in I_L due to lamp output variation	u_{R4}	Lamp output varies by ± 6 %	6.00	$D/\sqrt{3}$	3.46
Uncertainty in measuring I_L	u_{R5}	Using “ReRA system” calibrated PV cell I_L is 1191.16 ± 40.29. N is 9	3.38	$\sigma/\sqrt{N}$	1.13
Uncertainty of temperature measurement because of thermocouples	u_{R6}	Assumed to be ± 0.5 °C which equates to 0.5/20 x 100 % at 20 °C	2.50	$D/\sqrt{3}$	1.44
Combined Type B	$u_{R(com)}$ (Type B)	-	-	-	4.09
Expanded Type B	U (Type B)	Using a k value of 2 (≈ 95 % confidence)	-	-	8.18

Appendix E Type A Measurement Uncertainties

This Appendix details the results of calculating the Type A uncertainties using Equation C.5. Type A uncertainties are those arising from repeated direct measurements, where the mean and standard deviation can be calculated and the shape of the probability distribution is known (Bell, 2001), such as those arising from sample variation.

E.1 Transmission Electron Microscopy (TEM)

Table E.1 shows a selection of Type A uncertainties for the TEM measurements along with the expanded uncertainty *U*. Samples that were centrifuged (ct) to concentrate are indicated using the abbreviation ct followed by the concentration ratio and the BF used. The range of values for u_R (Type A) is 0.72 % – 5.77 % (*N* = 35) giving *U* values between 2.96 % and 11.82 %.

Table E.1 Type A uncertainties for TEM measurements and expanded uncertainty *U* using a *k* value of 2.

Sample	**Mean / nm**	**σ / nm**	***N***	**σ Value / ± %**	**u_R (Type A) / %**	**u_R (Type A+B) / %**	***U* / %**
Long λ before testing triangles	52.20	17.57	153	33.66	2.72	3.01	6.02
Long λ before testing rounded triangles	22.77	7.18	13	31.54	2.19	2.54	5.08
Long λ before testing other	17.60	8.00	32	45.47	4.50	4.68	9.37
Long λ before testing < 10 nm	6.13	1.58	25	25.72	2.55	2.86	5.71
Long λ before testing thickness	5.87	2.62	102	44.54	4.41	4.60	9.19
Mid λ before testing triangles	27.47	7.59	157	27.63	2.74	3.02	6.05
Mid λ before testing rounded triangles	23.69	6.67	89	28.15	2.79	3.07	6.14
Mid λ before testing other	18.20	6.66	58	36.58	3.62	3.85	7.69
Mid λ before testing < 10 nm	5.76	1.22	54	21.23	2.10	2.47	4.93
Mid λ before testing thickness	4.70	1.29	75	27.35	2.71	3.00	6.00
Short λ before testing triangles	27.34	15.92	5	58.24	5.77	5.91	11.82
Short λ before testing rounded triangles	17.33	4.46	30	25.71	2.55	2.85	5.71
Short λ before testing other	15.50	4.06	157	26.19	2.59	2.90	5.79
Short λ before testing < 10 nm	6.21	1.51	157	24.31	2.41	2.73	5.46
Short λ before testing thickness	4.97	1.11	143	22.24	2.20	2.55	5.10
Broadband mixture before testing triangles	31.16	13.91	67	44.65	4.42	4.61	9.21

Sample	**Mean / nm**	**σ / nm**	***N***	**σ Value / ± %**	**u_R (Type A) / %**	**u_R (Type A+B) / %**	***U* / %**
Broadband mixture before testing rounded triangles	19.38	5.71	75	29.46	2.92	3.19	6.38
Broadband mixture before testing other	15.25	5.20	157	34.08	3.37	3.61	7.23
Broadband mixture before testing < 10 nm	5.67	1.95	157	34.43	3.41	3.65	7.29
Broadband mixture before testing thickness	4.07	1.23	103	30.29	3.00	3.27	6.53
Long λ ct ¼ vol water repeat 1 before testing triangles	43.71	11.26	208	25.76	2.55	2.86	5.72
Long λ ct ¼ vol water repeat 1 before testing other	29.16	11.41	145	39.13	3.87	4.08	8.17
Long λ ct ¼ vol water repeat 2 before testing triangles	38.18	11.31	414	29.63	2.93	3.21	6.41
Long λ ct ¼ vol water repeat 2 before testing other	27.79	15.12	121	54.42	5.39	5.54	11.08
Long λ ct ¼ vol water repeat 3 before testing triangles	38.52	10.84	773	28.14	2.79	3.07	6.14
Long λ ct ¼ vol water repeat 3 before testing other	27.52	13.85	421	50.32	4.98	5.15	10.29
SiO_2@Ag NPr ct ¼ vol water repeat 1 before testing coating thickness	52.16	4.39	220	8.42	0.83	1.54	3.07
SiO_2@Ag NPr ct ¼ vol water repeat 1 before testing Ag inside	38.90	10.41	220	26.76	2.65	2.95	5.89
SiO_2@Ag NPr ct ¼ vol water repeat 1 before testing SiO_2 particles no Ag core	86.84	13.79	465	15.88	1.57	2.03	4.07
SiO_2@Ag NPr ct ¼ vol water repeat 2 before testing coating thickness	54.39	5.28	232	9.71	0.96	1.61	3.22
SiO_2@Ag NPr ct ¼ vol water repeat 2 before testing Ag inside	31.50	8.06	233	25.59	2.53	2.84	5.69
SiO_2@Ag NPr ct ¼ vol water repeat 2 before testing SiO_2 particles no Ag core	90.98	12.43	274	13.66	1.35	1.87	3.74
SiO_2@Ag NPr ct ¼ vol water repeat 3 before testing coating thickness	52.42	3.82	192	7.28	0.72	1.48	2.96
SiO_2@Ag NPr ct ¼ vol water repeat 3 before testing Ag inside	34.56	9.73	192	28.15	2.79	3.07	6.14
SiO_2@Ag NPr ct ¼ vol water repeat 3 before testing SiO_2 particles no Ag core	88.91	12.53	208	14.09	1.40	1.90	3.80

E.2 UV-vis and UV-vis-IR Spectroscopy

The Type A uncertainties for the UV-vis and UV-vis-IR measurements are shown in Table E.2 and Table E.3 using the long, mid and short λ samples produced to investigate the consistency of the batch process. Short λ samples measured using UV-vis-1, long λ and mid λ samples measured using UV-vis-IR-1.

Table E.2 Type A uncertainties for λ_{max} and expanded uncertainty U using a k value of 2.

Sample	**Mean / nm**	**σ / nm**	**N**	**σ Value / ± %**	**u_R (Type A) / %**	**u_R (Type A+B) / %**	**U / %**
Long λ	888.75	53.47	20	6.02	1.35	1.36	2.73
Mid λ	590.13	35.01	8	5.93	2.10	2.11	4.22
Short λ	458.00	5.89	12	1.29	0.37	0.48	0.96

Table E.3 Type A uncertainties for Ab_{max} and expanded uncertainty U using a k value of 2.

Sample	**Mean / au**	**σ / au**	**N**	**σ Value / ± %**	**u_R (Type A) / %**	**u_R (Type A+B) / %**	**U / %**
Long λ	1.59	0.14	20	9.02	2.02	2.24	4.48
Mid λ	1.33	0.02	8	1.69	0.60	1.15	2.29
Short λ	0.76	0.02	12	2.97	0.86	0.91	1.83

E.3 Type A Uncertainty in Calculating $\eta_{lamp(330\ nm - 1100\ nm)}$

Repeat measurements of three different samples were used as examples to calculate typical Type A uncertainties in the calculation of $\eta_{lamp(330\ nm - 1100\ nm)}$. The samples were the long λ, mid λ, short λ and the corresponding broadband absorber mixture obtained from combining the three NF in the ratio of 30 % short λ, 20 % mid λ and 50 % long λ measured using UV-vis-IR-1. The repeated UV-vis-IR-1 measurements were undertaken on initial (just synthesised), after four weeks in the dark at 4 °C and after 30 minutes testing in the solar simulator. In addition, the calculated value for the broadband mixture obtained from summing the spectra for its component NFs was used giving N = 12 for the broadband mixture. The results are shown in Table E.4.

Table E.4 Type A uncertainties for $\eta_{lamp(330\ nm - 1100\ nm)}$ and expanded U using a k value of 2.

Sample	**Mean / %**	**σ / %**	**N**	**σ Value / ± %**	**u_R (Type A) / %**	**u_R (Type A+B) / %**	**U / %**
Long λ	57.81	1.78	9	3.09	1.03	1.74	3.48
Mid λ	73.97	2.02	9	2.73	0.91	1.67	3.35
Short λ	46.29	4.61	9	9.97	3.32	3.61	7.22
Broadband mixture	92.75	1.37	12	1.48	0.43	1.47	2.94

E.4 Type A Uncertainty in Measuring η_{PE} for Both Solar Simulator Set-up A and Set-up B

Repeat measurements of a 1 mL sample of water in the three positions in set-up A were used to provide an indication of the Type A uncertainties for measuring η_{PE}. Repeat measurements of 3 mL of water, the broadband absorber mixture (30 % short λ, 20 % mid λ, 50 % long λ), long λ, mid λ and short λ NFs (3 samples of each NF, measured 3 times) were used to give an indication of the Type A uncertainties for the solar simulator set-up B (All in the middle Md position in the solar simulator). It should be noted that the maximum temperature rise for set-up A was considerably greater than set-up B due to an increase in the lamp I_L output and an increase in testing time for set-up A. The results for both set-ups and the resultant expanded uncertainties U are given in Table E.5.

Table E.5 Type A uncertainties for η_{PE} and expanded U using a k value of 2 for both solar simulator set-ups.

Sample	**Set-up**	**Mean / °C**	**σ / °C**	**N**	**σ Value / ± %**	**u_R (Type A) / %**	**u_R (Type A+B) / %**	**U / %**
Water in Middle Md position	A	21.83	1.25	9	5.74	1.91	5.18	10.36
Water in Front F position	A	18.68	0.95	9	5.10	1.70	5.10	10.21
Water in Back B position	A	18.75	1.06	9	5.67	1.89	5.17	10.34
3 mL Water in Middle Md position	B	3.64	0.18	3	4.86	2.81	4.96	9.92
Long λ	B	8.23	0.62	9	7.52	2.51	4.80	9.59
Mid λ	B	8.54	0.82	9	9.57	3.19	5.19	10.37
Short λ	B	6.82	0.42	9	6.14	2.05	4.57	9.15
Broadband mixture	B	10.59	0.17	9	1.56	0.52	4.12	8.24

Appendix F Statistical Test Definitions

This Appendix gives details of the various statistical calculations and methods employed in this thesis.

F.1 Definition of t-test

A t-test is a hypothesis test that allows you to compare means. A two-sample t-test allows the comparison between two means from two different sets of samples. The null hypothesis is that the two means are the same. The formula is:

$$T(value) = \frac{\bar{Y}_2 - \bar{Y}_1}{\sqrt{s_{(\text{pooled})}{}^2 \left(\frac{1}{N_1} + \frac{1}{N_2}\right)}}$$

Equation F.1

The computed *T(value)* can be looked up in standard t-tables or using a statistical software package to determine if the results are significant. For this the degrees of freedom needs to be calculated. For a two-sample t-test the degrees of freedom ($df_{(2\ \text{sample})}$) is given as:

$$df_{(2\ \text{sample})} = N_1 + N_2 - 2$$

Equation F.2

$\bar{Y}_1$= Mean of sample set 1 and $\bar{Y}_2$ = Mean of sample set 2, N_1 and N_2 are the number of results in each sample set and $s_{(\text{pooled})}{}^2$ is the pooled sample variance given by the equation:

$$s_{(\text{pooled})}{}^2 = \frac{\sum_{i=1}^{N_1}(Y_i - \bar{Y}_1)^2 + \sum_{j=1}^{N_2}\left(Y_j - \bar{Y}_2\right)^2}{N_1 + N_2 - 2}$$

Equation F.3

where Y_i and Y_j are the measurements or observations.

In contrast a paired t-test can be used to compare the means when the two means are from the same samples re-measured twice. Two examples of when a paired t-test is the more appropriate t-test to use are when a different spectrophotometer is used to measure the same samples again or when a group of samples have been measured before and after exposure to SSL. A paired t-test was only used in this thesis when exactly the same sample was re-measured. If a different sub-sample was removed from the main bulk sample for TEM analysis or UV-vis measurement a two-sample t-test was used instead. In a paired t-test the difference between the two measurement values is calculated:

$$\text{difference} = Y_2 - Y_1$$

Equation F.4

where Y_1 is the first measurement value and Y_2 is the second measurement value for the same sample. The *T(value)* is then given by:

$$T(value) = \frac{\sum \text{difference}}{\sqrt{\frac{N(\sum \text{difference}^2) - (\sum \text{difference})^2}{N-1}}}$$

Equation F.5

where ∑difference is the sum of the differences and *N* is the number of samples. In this case the *df* for the paired t-test ($df_{(\text{paired})}$) is:

$$df_{(\text{paired})} = N - 1$$

Equation F.6

F.2 Analysis of variance (ANOVA)

One way ANOVA is a generalisation of the two-sample t-test for more than two samples. The null hypothesis is that all the means are equal and the alternative hypothesis is that at least one mean is different. Normally equal variances and normally distributed data are assumed for the analysis. Instead of a *T(value)* an *F(statistic)* is used (again this can be looked up in standard tables or using a statistics software package). In this case:

$$F(statistic) = \frac{MST}{MSE}$$

Equation F.7

where *MST* is the mean square between different groups and *MSE* is the mean square due to error.

$$MST = \frac{\sum_{i=1}^{N_{(\text{mean})}} \left({\text{Total}_{(i)}}^2 \Big/ N_i \right) - {\text{Total}_{(\text{All})}}^2 \Big/ N}{N_{(\text{mean})} - 1}$$

Equation F.8

where $\text{Total}_{(i)}$ is the total for one group, $\text{Total}_{(\text{All})}$ is the total for all observations, $N_{(\text{mean})}$ is the number of means, N_i is the number of observations in group *i* and *N* is the total number of observations.

$$MSE = \frac{\sum_{i=1}^{N(\text{mean})} \sum_{j=1}^{N_i} {Y_{ij}}^2 - \sum_{i=1}^{N(\text{mean})} \left({Total_{(i)}}^2 / N_i \right)}{N - N_{(\text{mean})}}$$

Equation F.9

where *MSE* is the mean square due to error and Y_{ij} is an observation or measurement. A standard software package (Minitab version 17.3.1) was used to undertake ANOVA analysis. The output from this software package assigns a different letter to each group that is significantly different from another group.

F.3 Response Surface Methodology

This is similar to a factorial or part factorial experimental design but has added flexibility as more than two levels of a factor can be selected. In addition, non-linearity can be investigated (if three or more levels of one or more continuous factors are used). In order to evaluate a group of experiments using response surface analysis, the experimental set needs to be orthogonal (each variable in the experimental set changed in a consistent manner).

ANOVA is used to build a model of the predicted response for each of the factors in the experimental design. Regression analysis is then undertaken to determine how well the model fits with the data. Any results that do not fit with the predicted response are indicated by analysing the residuals (the difference between the observed results and those predicted by the model).

The results of the model are then used to calculate the main effect of each of the factors changed and the interactions between the factors (if the experimental group has a sufficient number of individual experiments).

A standard software package (Minitab version 17.3.1), was utilised to undertake response surface analysis on appropriate groups of experiments.

Appendix G TEM Size Analysis

This Appendix gives details of the TEM size analysis which was undertaken according to the method described in Section 3.7.1. Firstly, the results for the uncoated silver given. This is then followed by the results for the various SiO_2 coated nanofluids.

G.1 Ag NPr Stabilised with TSCD and PVP

For all the Ag TSCD-PVP NPr samples the particles types were divided into four groups, triangles, rounded cornered triangles, other and small (< 10 nm). A graphic of the types of particles is shown in Figure G.1. The results for three separate samples of Ag TSCD-PVP NPrs (50 mL batch volume) are shown in Table G.1 and the average results for these three samples in Table G.2. The percentage of each sample type, the average, standard deviation (σ) and number of measurements (N) are given. The value of λ_{max} for each of the samples is also shown.

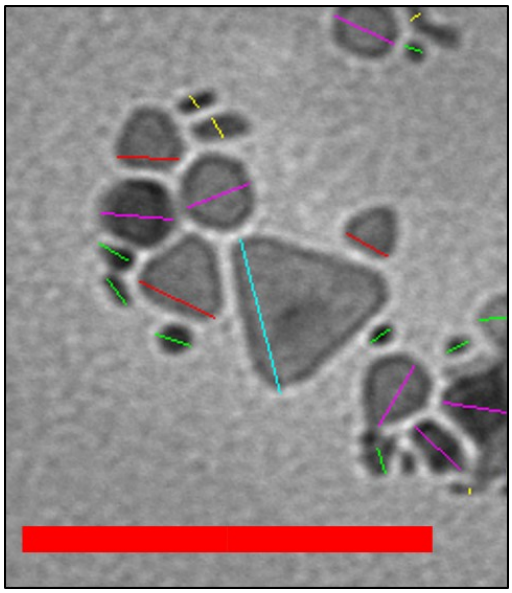

Figure G.1 Graphic showing how the NPs were divided for the Ag NPs. Blue line = triangle, red line = rounded cornered triangle, pink line = other, green line = small and yellow line = thickness (undertaken on some samples see Section G.2). Thick red scale bar = 100 nm.

Table G.1 TEM analysis on Ag TSCD-PVP NPr 50 mL batch volume not centrifuged.

Sample	**Particle shape**	**%**	**Average size / nm**	**σ / nm**	***N***
0.1 mM Ag TSCD-PVP NPr – 8 (λ_{max} = 867 nm)	Triangle	59	42.88	16.83	82
0.1 mM Ag TSCD-PVP NPr – 8 (λ_{max} = 867 nm)	Rounded cornered triangle	17	32.76	16.31	23
0.1 mM Ag TSCD-PVP NPr – 8 (λ_{max} = 867 nm)	Other	14	20.04	12.87	20

Sample	**Particle shape**	**%**	**Average size / nm**	***σ* / nm**	***N***
0.1 mM Ag TSCD-PVP NPr – 8 (λ_{max} = 867 nm)	Small < 10 nm	9	6.90	1.23	13
0.1 mM Ag TSCD-PVP NPr – 10 (λ_{max} = 900 nm)	Triangle	41	52.32	16.74	61
0.1 mM Ag TSCD-PVP NPr – 10 (λ_{max} = 900 nm)	Rounded cornered triangle	32	36.11	9.76	48
0.1 mM Ag TSCD-PVP NPr – 10 (λ_{max} = 900 nm)	Other	21	24.06	7.06	32
0.1 mM Ag TSCD-PVP NPr – 10 (λ_{max} = 900 nm)	Small < 10 nm	5	8.56	1.48	8
0.1 mM Ag TSCD-PVP NPr – 20 (λ_{max} = 899 nm)	Triangle	63	49.13	16.17	196
0.1 mM Ag TSCD-PVP NPr – 20 (λ_{max} = 899 nm)	Rounded cornered triangle	23	42.61	15.42	72
0.1 mM Ag TSCD-PVP NPr– 20 (λ_{max} = 899 nm)	Other	12	33.27	20.03	36
0.1 mM Ag TSCD-PVP NPr – 20 (λ_{max} = 899 nm)	Small < 10 nm	2	8.23	1.73	7

Table G.2 TEM analysis on Ag TSCD-PVP NPr 50 mL batch volume not centrifuged – average results.

Sample	**Particle shape**	**%**	**Average size / nm**	***σ* / nm**	***N***
0.1 mM Ag TSCD-PVP NPr average (λ_{max} = 889nm ± 19 nm)	Triangle	57	48.19	16.70	339
0.1 mM Ag TSCD-PVP NPr average (λ_{max} = 889 nm ± 19 nm)	Rounded cornered triangle	24	38.84	14.40	143
0.1 mM Ag TSCD-PVP NPr average (λ_{max} = 889 nm ± 19 nm)	Other	15	26.91	15.68	88
0.1 mM Ag TSCD-PVP NPr average (λ_{max} = 889 nm ± 19 nm)	Small < 10 nm	5	7.71	1.58	28

Table G.3 shows the TEM analysis on three 50 mL samples of Ag TSCD-PVP NPr after centrifuging at 16,168 r.c.f. (13,000 rpm) for 30 minutes. The average values for these three samples are given in Table G.4.

Table G.3 TEM analysis on Ag TSCD-PVP NPr 50 mL batch volume after centrifuging and re-dispersal into ¼ volume water.

Sample	**Particle shape**	**%**	**Average size / nm**	***σ* / nm**	***N***
Ag TSCD-PVP NPr ct ¼ vol water - 4 (λ_{max} = 816 nm)	Triangle	22	47.58	9.86	83
Ag TSCD-PVP NPr ct ¼ vol water - 4 (λ_{max} = 816 nm)	Rounded cornered triangle	36	38.68	10.74	134
Ag TSCD-PVP NPr ct ¼ vol water - 4 (λ_{max} = 816 nm)	Other	39	29.30	11.33	144
Ag TSCD-PVP NPr ct ¼ vol water - 4 (λ_{max} = 816 nm)	Small < 10 nm	2	8.33	2.56	9

Sample	**Particle shape**	**%**	**Average size / nm**	***σ* / nm**	***N***
Ag TSCD-PVP NPr ct ¼ vol water - 5 (λ_{max} = 800 nm)	Triangle	35	38.64	10.99	192
Ag TSCD-PVP NPr ct ¼ vol water - 5 (λ_{max} = 800 nm)	Rounded cornered triangle	42	33.18	10.54	227
Ag TSCD-PVP NPr ct ¼ vol water - 5 (λ_{max} = 800 nm)	Other	22	28.10	15.05	119
Ag TSCD-PVP NPr ct ¼ vol water - 5 (λ_{max} = 800 nm)	Small < 10 nm	1	8.15	1.87	7
Ag TSCD-PVP NPr ct ¼ vol water - 6 (λ_{max} = 797 nm)	Triangle	28	42.07	9.99	345
Ag TSCD-PVP NPr ct ¼ vol water - 6 (λ_{max} = 797 nm)	Rounded cornered triangle	38	33.98	9.62	472
Ag TSCD-PVP NPr ct ¼ vol water - 6 (λ_{max} = 797 nm)	Other	33	27.82	13.76	414
Ag TSCD-PVP NPr ct ¼ vol water - 6 (λ_{max} = 797 nm)	Small < 10 nm	1	9.33	1.12	7

Table G.4 TEM analysis on Ag TSCD-PVP NPr centrifuged and re-dispersed into ¼ volume water– average results.

Sample	**Particle shape**	**%**	**Average size / nm**	***σ* / nm**	***N***
Ag TSCD-PVP NPr ct ¼ vol water - average (λ_{max} = 804 nm ± 10 nm)	Triangle	29	41.75	10.64	620
Ag TSCD-PVP NPr ct ¼ vol water - average (λ_{max} = 804 nm ± 10 nm)	Rounded cornered triangle	39	34.52	10.22	833
Ag TSCD-PVP NPr ct ¼ vol water - average (λ_{max} = 804 nm ± 10 nm)	Other	31	28.19	13.52	677
Ag TSCD-PVP NPr ct ¼ vol water - average (λ_{max} = 804 nm ± 10 nm)	Small < 10 nm	1	8.58	1.99	23

For the 25 mL batch volume samples only one sample was analysed using TEM (this sample was also the long λ sample used as one of the components for the broadband absorber mixture). The results of the size analysis for this sample is given in Table G.5. An additional TEM sample was also prepared specifically to assess the thickness of the NPs according to the method described in Section 3.7.1. The thickness measurements have been excluded from the percentage of each particle type shown in Table G.5. The average λ_{max} shown in brackets is for the three 25 mL samples shown in Figure 4-5.

Table G.5 TEM analysis on Ag TSCD-PVP NPr 25 mL batch size not centrifuged (long λ). The average λ_{max} for 3 samples is also shown.

Sample	**Particle shape**	**%**	**Average size / nm**	***σ* / nm**	***N***
Ag TSCD-PVP NPr 25 mL (long λ) – (average λ_{max} = 929 nm ± 32 nm)	Triangle	69	52.20	17.57	153
Ag TSCD-PVP NPr 25 mL (long λ) – (average λ_{max} = 929 nm ± 32 nm)	Rounded cornered triangle	6	22.77	7.18	13
Ag TSCD-PVP NPr 25 mL (long λ) – (average λ_{max} = 929 nm ± 32 nm)	Other	14	17.60	8.00	32
Ag TSCD-PVP NPr 25 mL (long λ) – (average λ_{max} = 929 nm ± 32 nm)	Small < 10 nm	11	6.13	1.58	25
Ag TSCD-PVP NPr 25 mL (long λ) – (average λ_{max} = 929 nm ± 32 nm)	Thickness	-	5.87	2.62	102

G.1.1 Significance of differences

To assess whether centrifuging has changed the size of the particles, unpaired two-sample t-tests were undertaken (using the formula given in F.1) comparing the average results obtained from the Ag TSCD-PVP NPr 50 mL samples with the Ag TSCD-PVP NPr centrifuged samples. As different sub-samples were used to produce the TEM micro-grids, two-sample t-tests rather than paired t-tests were used for all the t-tests on the TEM results.

In a similar manner to determine if reducing the batch volume changed the morphology unpaired two-sample t-tests were carried out this time comparing the average Ag TSCD-PVP NPr 50 mL sample to the Ag TSCD-PVP NPr 25 mL sample.

The results for all these t-tests are shown in Table G.6. Only the significantly different results are given along with the average difference and the confidence interval for this difference (at a 95 % confidence level).

Table G.6 Two-sample t-test results for TEM analysis of Ag TSCD-PVP NPr (where sample 2 is significantly smaller than sample 1 the average difference is shown as positive).

Sample 1	**Sample 2**	**Particle type**	**Average difference /nm**	**Range of difference (at 95 % confidence) / nm**
50 mL not centrifuged	50 mL centrifuged	Triangles	6.44	4.70 to 8.18
50 mL not centrifuged	50 mL centrifuged	Rounded triangles	4.37	2.38 to 6.26
50 mL not centrifuged	25 mL not centrifuged	Triangles	-4.01	-0.76 to -7.26
50 mL not centrifuged	25 mL not centrifuged	Rounded triangles	16.07	8.07 to 24.07

Sample 1	Sample 2	Particle type	Average difference /nm	Range of difference (at 95 % confidence) / nm
50 mL not centrifuged	25 mL not centrifuged	Other	9.31	3.56 to 15.06
50 mL not centrifuged	25 mL not centrifuged	Small	1.58	0.71 to 2.45

G.2 Broadband Mixture and Component NFs

For the broadband mixture and two of the component NFs (short λ and mid λ) the particles types were divided into four groups, triangles, rounded cornered triangles, other and small (< 10 nm). The long λ results have already been given in Table G.5.One sample from each NF type was measured and the results are shown in Table G.7. The percentage of each sample type, the average, standard deviation (σ) and number of measurements (N) are given. The average value of λ_{max} for each of the samples is also shown. An additional TEM sample was also prepared specifically to assess the thickness of the NPs according to the method described in Section 3.7.1. The thickness measurements have been excluded from the percentage of each particle type shown in Table G.7.

Table G.7 TEM analysis on the broadband mixture and two of the component NFs. The average λ_{max} for 3 samples is also shown.

Sample	Particle shape	%	Average size / nm	σ / nm	N
Short λ (λ_{max} = 468 nm ± 25 nm)	Triangle	1	27.34	15.92	5
Short λ (λ_{max} = 468 nm ± 25 nm)	Rounded cornered triangle	6	17.33	4.46	30
Short λ (λ_{max} = 468 nm ± 25 nm)	Other	42	15.90	4.16	204
Short λ (λ_{max} = 468 nm ± 25 nm)	Small < 10 nm	51	6.26	1.64	252
Short λ (λ_{max} = 468 nm ± 25 nm)	Thickness	-	4.97	1.11	143
Mid λ (λ_{max} = 667 nm ± 8 nm)	Triangle	44	27.47	7.59	157
Mid λ (λ_{max} = 667 nm ± 8 nm)	Rounded cornered triangle	25	23.69	6.67	89
Mid λ (λ_{max} = 667 nm ± 8 nm)	Other	16	18.20	6.66	58
Mid λ (λ_{max} = 667 nm ± 8 nm)	Small < 10 nm	15	5.76	1.22	54
Mid λ (λ_{max} = 667 nm ± 8 nm)	Thickness	-	4.70	1.29	75
Broadband mixture (30 % short λ, 20 % mid λ, 50 % long λ)	Triangle	8	31.16	13.91	67
Broadband mixture (30 % short λ, 20 % mid λ, 50 % long λ)	Rounded cornered triangle	9	19.38	5.71	75
Broadband mixture (30 % short λ, 20 % mid λ, 50 % long λ)	Other	40	15.12	5.05	347

Sample	Particle shape	%	Average size / nm	σ / nm	*N*
Broadband mixture (30 % short λ, 20 % mid λ, 50 % long λ)	Small < 10 nm	44	6.39	2.16	378
Broadband mixture (30 % short λ, 20 % mid λ, 50 % long λ)	Thickness	-	4.07	1.23	103

G.2.1 Significance of differences

To assess whether the size of the particles had changed when the component NFs were combined to produce the broadband mixture unpaired two-sample t-tests were undertaken (using the formula given in F.1) comparing the broadband mixture to firstly the short λ, then the mid λ, and finally, the long λ NF (results for this NF in Table G.5). The significantly different results of the t-tests are shown in Table G.8.

Table G.8 Two-sample t-test results for TEM analysis of the broadband mixture and its three component NFs (where sample 2 is significantly smaller than sample 1 the average difference is shown as positive). In all cases sample 1 is the broadband mixture.

Sample 2	Particle type	Average difference /nm	Range of difference (at 95 % confidence) / nm
Short λ	Thickness	-0.90	-0.60 to -1.20
Mid λ	Triangles	3.49	0.64 to 6.34
Mid λ	Rounded triangles	-4.31	-2.38 to -6.25
Mid λ	Other	-3.08	-1.60 to -4.56
Mid λ	Small	0.63	0.04 to 1.22
Mid λ	Thickness	-0.63	-0.25 to -1.01
Long λ	Triangles	-21.04	-16.26 to -25.82
Long λ	Other	-2.48	-0.54 to -4.43
Long λ	Thickness	-1.80	-1.24 to -2.36

G.3 Consistency of Batch Synthesis – TEM

For the combined broadband mixture produced from combining the 30 mL batches of the three component NFs (short λ, mid λ and long λ) the particles types were divided into four groups, triangles, rounded cornered triangles, other and small (< 10 nm). The results are shown in Table G.9. The percentage of each sample type, the average, standard deviation (σ) and number of measurements (*N*) are given. The value of λ_{max} is also shown. The λ_{max} for the mid λ NF is the value obtained immediately after diluting the combined mid λ sample given in Table I.3. An additional TEM sample was also prepared specifically to assess the thickness of the NPs according to the

method described in Section 3.7.1. The thickness measurements have been excluded from the percentage of each particle type.

Table G.9 TEM analysis on the broadband mixture and the component NFs produced using a 30 mL batch volume. The λ_{max} for the combined samples is also shown.

Sample	**Particle shape**	**%**	**Average size / nm**	***σ* / nm**	***N***
Combined short *λ* (λ_{max} = 467 nm)	Triangle	1	19.76	1.03	2
Combined short *λ* (λ_{max} = 467 nm)	Rounded cornered triangle	4	17.35	5.49	12
Combined short *λ* (λ_{max} = 467 nm)	Other	54	14.69	4.25	166
Combined short *λ* (λ_{max} = 467 nm)	Small < 10 nm	41	6.54	1.77	126
Combined short *λ* (λ_{max} = 467 nm)	Thickness	-	4.08	0.86	140
Combined mid *λ* (λ_{max} = 659 nm)	Triangle	15	24.06	6.48	65
Combined mid *λ* (λ_{max} = 659 nm)	Rounded cornered triangle	26	18.20	5.25	110
Combined mid *λ* (λ_{max} = 659 nm)	Other	37	16.94	7.57	154
Combined mid *λ* (λ_{max} = 659 nm)	Small < 10 nm	22	7.00	1.66	92
Combined mid *λ* (λ_{max} = 659 nm)	Thickness	-	4.05	0.78	669
Combined long *λ* (λ_{max} = 883 nm)	Triangle	63	50.42	17.50	256
Combined long *λ* (λ_{max} = 883 nm)	Rounded cornered triangle	10	39.18	16.16	42
Combined long *λ* (λ_{max} = 883 nm)	Other	19	27.69	16.90	77
Combined long *λ* (λ_{max} = 883 nm)	Small < 10 nm	8	7.32	1.62	32
Combined long *λ* (λ_{max} = 883 nm)	Thickness	-	5.58	1.04	187
Combined broadband mixture (30 % short *λ*, 20 % mid *λ*, 50 % long *λ*)	Triangle	11	31.60	18.40	84
Combined broadband mixture (30 % short *λ*, 20 % mid *λ*, 50 % long *λ*)	Rounded cornered triangle	14	18.60	5.39	107
Combined broadband mixture (30 % short *λ*, 20 % mid *λ*, 50 % long *λ*)	Other	50	14.90	4.18	394
Combined broadband mixture (30 % short *λ*, 20 % mid *λ*, 50 % long *λ*)	Small < 10 nm	25	7.57	1.75	198
Combined broadband mixture (30 % short *λ*, 20 % mid *λ*, 50 % long *λ*)	Thickness	-	4.37	0.72	322

G.3.1 Significance of differences compared to the 25 mL batch samples

To assess whether the size of the particles had changed compared to the 25 mL batch samples unpaired two-sample t-tests were undertaken (using the formula given in F.1). The significantly different results of the t-tests are shown in Table G.10. It should be noted that although some of the tests resulted in a significant difference, the size in terms of nm of that difference was very

small and may be due to measurement uncertainty rather than a truly significant difference (the t-tests do not account for additional measurement uncertainty inherent in the technique).

Table G.10 Two-sample t-test results for TEM analysis of the combined broadband mixture and its three component NFs compared to the 25 mL initial data in Table G.5 and Table G.7 (where sample 2 is significantly smaller than sample 1 the average difference is shown as positive).

Sample 1	**Sample 2**	**Particle type**	**Average difference /nm**	**Range of difference (at 95 % confidence) / nm**
Short λ (25 mL batch)	Combined short λ	Other	1.21	0.35 to 2.07
Short λ (25 mL batch)	Combined short λ	Thickness	0.89	0.66 to 1.12
Mid λ (25 mL batch)	Combined mid λ	Triangles	3.41	1.29 to 5.53
Mid λ (25 mL batch)	Combined mid λ	Rounded triangles	5.49	3.82 to 7.16
Mid λ (25 mL batch)	Combined mid λ	Small	-1.24	-0.73 to -1.75
Mid λ (25 mL batch)	Combined mid λ	Thickness	0.65	0.45 to 0.85
Long λ (25 mL batch)	Combined long λ	Rounded triangles	-16.41	-7.10 to -25.72
Long λ (25 mL batch)	Combined long λ	Other	-10.09	-3.89 to -16.29
Long λ (25 mL batch)	Combined long λ	Small	-1.19	-0.33 to -2.05
Broadband mixture (25 mL batch)	Combined broadband mixture	Small	-1.18	-0.83 to -1.53
Broadband mixture (25 mL batch)	Combined broadband mixture	Thickness	-0.30	-0.11 to -0.49

G.4 TEM After Exposure to Elevated Temperature

For the broadband mixture and component NFs (short, mid and long λ) after exposure to 70 °C for 4 h the particles types were divided into four groups, triangles, rounded cornered triangles, other and small (< 10 nm). The results are shown in Table G.11. The percentage of each sample type, the average, standard deviation (σ) and number of measurements (N) are given. The average values of λ_{max} obtained after 4 h at 70 °C are also shown in brackets for the three component NFs.

Table G.11 TEM analysis on the broadband mixture and the component NFs after 4 h exposure to a temperature of 70 °C. The average λ_{max} after 4 h at 70 °C is also shown.

Sample	**Particle shape**	**%**	**Average size / nm**	***σ* / nm**	***N***
Short λ after 4 h at 70 °C (λ_{max} = 495 nm)	Triangle	2	22.08	7.64	8
Short λ after 4 h at 70 °C (λ_{max} = 495 nm)	Rounded cornered triangle	25	18.19	3.23	97
Short λ after 4 h at 70 °C (λ_{max} = 495 nm)	Other	46	14.47	3.29	179

Sample	Particle shape	%	Average size / nm	σ / nm	*N*
Short λ after 4 h at 70 °C (λ_{max} = 495 nm)	Small < 10 nm	28	7.67	1.86	109
Mid λ after 4 h at 70 °C (λ_{max} = 562 nm)	Triangle	3	24.36	3.09	6
Mid λ after 4 h at 70 °C (λ_{max} = 562 nm)	Rounded cornered triangle	17	20.49	4.02	40
Mid λ after 4 h at 70 °C (λ_{max} = 562 nm)	Other	54	15.34	3.66	126
Mid λ after 4 h at 70 °C (λ_{max} = 562 nm)	Small < 10 nm	26	6.41	2.05	61
Long λ after 4 h at 70 °C (λ_{max} = 820 nm)	Triangle	12	54.19	22.72	22
Long λ after 4 h at 70 °C (λ_{max} = 820 nm)	Rounded cornered triangle	33	37.87	12.60	62
Long λ after 4 h at 70 °C (λ_{max} = 820 nm)	Other	48	27.19	9.66	90
Long λ after 4 h at 70 °C (λ_{max} = 820 nm)	Small < 10 nm	7	7.12	1.85	14
Broadband mixture (30 % short λ, 20 % mid λ, 50 % long λ) after 4 h at 70 °C	Triangle	6	30.83	10.22	90
Broadband mixture (30 % short λ, 20 % mid λ, 50 % long λ) after 4 h at 70 °C	Rounded cornered triangle	25	21.61	6.74	396
Broadband mixture (30 % short λ, 20 % mid λ, 50 % long λ) after 4 h at 70 °C	Other	53	15.78	5.74	839
Broadband mixture (30 % short λ, 20 % mid λ, 50 % long λ) after 4 h at 70 °C	Small < 10 nm	16	7.43	1.72	249

G.4.1 Significance of differences compared to before exposure to elevated temperatures

To assess whether the size of the particles had changed following exposure to a temperature of 70 °C for 4 h unpaired two-sample t-tests were undertaken (using the formula given in F.1). The significantly different results of the t-tests are shown in Table G.12. It should be noted that although some of the tests resulted in a significant difference, the size in terms of nm of that difference was very small (the largest average difference was ≈ 3 nm) and may be due to measurement uncertainty rather than a truly significant difference (the t-tests do not account for additional measurement uncertainty inherent in the technique).

Table G.12 Two-sample t-test results for TEM analysis of the broadband mixture and its three component NFs after exposure to a temperature of 70 °C compared to the initial data in Table G.9 (where sample 2 is significantly smaller than sample 1 the average difference is shown as positive).

Sample 1	Sample 2	Particle type	Average difference /nm	Range of difference (at 95 % confidence) / nm
Short λ after 4 h at 70 °C	Combined short λ	Small	1.13	0.66 to 1.59

Sample 1	Sample 2	Particle type	Average difference /nm	Range of difference (at 95 % confidence) / nm
Mid λ after 4 h at 70 °C	Combined mid λ	Rounded triangles	2.29	0.48 to 4.10
Mid λ after 4 h at 70 °C	Combined mid λ	Other	-1.60	-3.05 to -0.15
Broadband after 4 h at 70 °C	Combined broadband mixture	Rounded triangles	3.01	1.62 to 4.40
Broadband after 4 h at 70 °C	Combined broadband mixture	Other	0.88	0.25 to 1.52

G.5 TEM After Exposure to Simulated Sunlight (SSL)

For the Ag NFs after exposure to simulated sunlight (SSL) the particle types were divided into four groups, triangles, rounded cornered triangles, other and small (< 10 nm). The results are given in Table G.13 for the Ag NPr NF tested using set-up A in the solar simulator for a total exposure time of 12 h. The percentage of each sample type, the average, standard deviation (σ) and number of measurements (N) are given. The value of λ_{max} obtained after SSL exposure is also shown in brackets. The average results for this Ag NPr NF is given in Table G.14.

The results obtained following a shorter exposure time of 0.5 h using set-up B for the broadband mixture and component NFs (short, mid and long λ) are given in Table G.15. The average values of λ_{max} obtained after 0.5 h SSL exposure are also shown in brackets for the three component NFs. An additional TEM sample was also prepared specifically to assess the thickness of the NPs according to the method described in Section 3.7.1. The thickness measurements have been excluded from the percentage of each particle type.

Table G.13 TEM analysis on Ag TSCD-PVP NPr 50 mL initial batch volume after centrifuging, re-dispersal into ¼ volume water and exposure to SSL for 12 h using set-up A.

Sample	Particle shape	%	Average size / nm	σ / nm	N
Ag TSCD-PVP NPr ct ¼ vol water - 4 after 12 h SSL (λ_{max} = 704 nm)	Triangle	5	53.44	10.08	52
Ag TSCD-PVP NPr ct ¼ vol water - 4 after 12 h SSL (λ_{max} = 704 nm)	Rounded cornered triangle	31	43.32	10.66	315
Ag TSCD-PVP NPr ct ¼ vol water - 4 after 12 h SSL (λ_{max} = 704 nm)	Other	62	33.30	10.70	628
Ag TSCD-PVP NPr ct ¼ vol water - 4 after 12 h SSL (λ_{max} = 704 nm)	Small < 10 nm	2	7.42	1.49	20
Ag TSCD-PVP NPr ct ¼ vol water - 5 after 12 h SSL (λ_{max} = 728 nm)	Triangle	11	46.14	12.62	59

Sample	Particle shape	%	Average size / nm	σ / nm	*N*
Ag TSCD-PVP NPr ct ¼ vol water - 5 after 12 h SSL (λ_{max} = 728 nm)	Rounded cornered triangle	45	40.77	10.01	231
Ag TSCD-PVP NPr ct ¼ vol water - 5 after 12 h SSL (λ_{max} = 728 nm)	Other	40	33.18	12.17	206
Ag TSCD-PVP NPr ct ¼ vol water - 5 after 12 h SSL (λ_{max} = 728 nm)	Small < 10 nm	4	7.23	1.37	23
Ag TSCD-PVP NPr ct ¼ vol water - 6 after 12 h SSL (λ_{max} = 647 nm)	Triangle	2	35.01	7.54	7
Ag TSCD-PVP NPr ct ¼ vol water - 6 after 12 h SSL (λ_{max} = 647 nm)	Rounded cornered triangle	16	36.84	10.72	61
Ag TSCD-PVP NPr ct ¼ vol water - 6 after 12 h SSL (λ_{max} = 647 nm)	Other	80	29.39	10.38	307
Ag TSCD-PVP NPr ct ¼ vol water - 6 after 12 h SSL (λ_{max} = 647 nm)	Small < 10 nm	3	6.96	1.12	10

Table G.14 TEM analysis on Ag TSCD-PVP NPr centrifuged, re-dispersed into ¼ volume water and exposure to SSL for 12 h using set-up A – average results.

Sample	Particle shape	%	Average size / nm	σ / nm	*N*
Ag TSCD-PVP NPr ct ¼ vol water - average after 12 h SSL (λ_{max} = 693 nm ± 37 nm)	Triangle	6	48.70	12.27	118
Ag TSCD-PVP NPr ct ¼ vol water - average after 12 h SSL (λ_{max} = 693 nm ± 37 nm)	Rounded cornered triangle	32	41.70	10.60	607
Ag TSCD-PVP NPr ct ¼ vol water - average after 12 h SSL (λ_{max} = 693 nm ± 37 nm)	Other	59	32.23	11.03	1141
Ag TSCD-PVP NPr ct ¼ vol water - average after 12 h SSL (λ_{max} = 693 nm ± 37 nm)	Small < 10 nm	3	7.25	1.36	53

Table G.15 TEM analysis on the broadband mixture and the component NFs after 0.5 h exposure to SSL using set-up B. The average λ_{max} after exposure is also shown.

Sample	Particle shape	%	Average size / nm	σ / nm	*N*
Short λ after 0.5 h SSL exposure (λ_{max} = 496 nm ± 3 nm)	Triangle	1	27.92	12.10	4
Short λ after 0.5 h SSL exposure (λ_{max} = 496 nm ± 3 nm)	Rounded cornered triangle	3	18.56	6.19	10
Short λ after 0.5 h SSL exposure (λ_{max} = 496 nm ± 3 nm)	Other	47	15.59	4.76	142
Short λ after 0.5 h SSL exposure (λ_{max} = 496 nm ± 3 nm)	Small < 10 nm	48	6.29	2.01	146
Short λ after 0.5 h SSL exposure (λ_{max} = 496 nm ± 3 nm)	Thickness	-	4.62	1.26	67

Sample	Particle shape	%	Average size / nm	σ / nm	*N*
Mid λ after 0.5 h SSL exposure (λ_{max} = 600 nm ± 2 nm)	Triangle	11	30.56	7.21	27
Mid λ after 0.5 h SSL exposure (λ_{max} = 600 nm ± 2 nm)	Rounded cornered triangle	20	23.28	6.07	50
Mid λ after 0.5 h SSL exposure (λ_{max} = 600nm ± 2 nm)	Other	57	20.81	6.37	141
Mid λ after 0.5 h SSL exposure (λ_{max} = 600nm ± 2 nm)	Small < 10 nm	13	6.51	1.87	28
Mid λ after 0.5 h SSL exposure (λ_{max} = 600 nm ± 2 nm)	Thickness	-	4.99	1.46	69
Long λ after 0.5 h SSL exposure (λ_{max} = 864 nm ± 23 nm)	Triangle	32	54.34	15.42	95
Long λ after 0.5 h SSL exposure (λ_{max} = 864 nm ± 23 nm)	Rounded cornered triangle	39	37.91	9.41	114
Long λ after 0.5 h SSL exposure (λ_{max} = 864 nm ± 23 nm)	Other	19	36.13	19.67	57
Long λ after 0.5 h SSL exposure (λ_{max} = 864 nm ± 23 nm)	Small < 10 nm	10	7.34	1.82	29
Long λ after 0.5 h SSL exposure (λ_{max} = 864 nm ± 23 nm)	Thickness	-	5.62	1.60	49
Broadband mixture (30 % short λ, 20 % mid λ, 50 % long λ) after 0.5 h SSL exposure	Triangle	6	27.50	10.31	71
Broadband mixture (30 % short λ, 20 % mid λ, 50 % long λ) after 0.5 h SSL exposure	Rounded cornered triangle	9	21.15	7.39	110
Broadband mixture (30 % short λ, 20 % mid λ, 50 % long λ) after 0.5 h SSL exposure	Other	40	15.31	4.19	475
Broadband mixture (30 % short λ, 20 % mid λ, 50 % long λ) after 0.5 h SSL exposure	Small < 10 nm	45	6.55	2.09	534
Broadband mixture (30 % short λ, 20 % mid λ, 50 % long λ) after 0.5 h SSL exposure	Thickness	-	4.53	0.92	180

G.5.1 Significance of differences compared to before exposure to SSL

To assess whether the size of the particles had changed following exposure to SSL unpaired two-sample t-tests were undertaken (using the formula given in F.1). The significantly different results of the t-tests are shown in Table G.16 for Ag TSCD-PVP NPr centrifuged and re-dispersed into ¼ volume water and in Table G.17 for the broadband and component NF. For the centrifuged Ag TSCD-PVP NPrs there were some significant differences in size after exposure to SSL. Of the differences that were significant only one was significantly smaller after SSL exposure (sample – 6 for the small sized particles). There were only a smaller number of particles measured in this group and the difference was ≈ 2.4 nm so may be due in part to the number of particles measured

and the uncertainty of the measurement technique, which is not taken into account when the t-tests are performed. All the other significant differences showed the particles in that category to be larger following SSL exposure. This makes sense in part if it is considered that the relative number of particles in each category is also changing. The larger triangular particles are becoming more rounded with SSL increasing the average size of the rounded cornered triangles, the slightly larger rounded triangles are becoming even more rounded, increasing the average size of the other particles. However it does not explain fully the increase in size of the triangular particles seen for two of the centrifuged Ag TSCD-PVP NPr samples.

Table G.16 Two-sample t-test results for TEM analysis of the Ag TSCD-PVP NPr centrifuged and re-dispersed into ¼ volume water after exposure to SSL for 12 h using set-up A compared to the initial data in Table G.3 (where sample 2 is significantly smaller than sample 1 the average difference is shown as positive).

Sample 1	**Sample 2**	**Particle type**	**Average difference /nm**	**Range of difference (at 95 % confidence) / nm**
Ag TSCD-PVP NPr ct ¼ vol water – 4 after 12 h SSL	Ag TSCD-PVP NPr ct ¼ vol water – 4 initial	Triangles	5.86	2.38 to 9.34
Ag TSCD-PVP NPr ct ¼ vol water – 4 after 12 h SSL	Ag TSCD-PVP NPr ct ¼ vol water – 4 initial	Rounded triangles	4.64	2.47 to 6.81
Ag TSCD-PVP NPr ct ¼ vol water – 4 after 12 h SSL	Ag TSCD-PVP NPr ct ¼ vol water – 4 initial	Other	4.00	2.04 to 5.96
Ag TSCD-PVP NPr ct ¼ vol water – 5 after 12 h SSL	Ag TSCD-PVP NPr ct ¼ vol water – 5 initial	Triangles	7.50	4.16 to 10.84
Ag TSCD-PVP NPr ct ¼ vol water – 5 after 12 h SSL	Ag TSCD-PVP NPr ct ¼ vol water – 5 initial	Rounded triangles	7.59	5.70 to 9.48
Ag TSCD-PVP NPr ct ¼ vol water – 5 after 12 h SSL	Ag TSCD-PVP NPr ct ¼ vol water – 5 initial	Other	5.08	2.07 to 8.09
Ag TSCD-PVP NPr ct ¼ vol water – 6 after 12 h SSL	Ag TSCD-PVP NPr ct ¼ vol water – 6 initial	Rounded triangles	2.86	0.25 to 5.47
Ag TSCD-PVP NPr ct ¼ vol water – 6 after 12 h SSL	Ag TSCD-PVP NPr ct ¼ vol water – 6 initial	Small	-2.37	-3.55 to -1.19

For the broadband mixture and its components (Table G.17) the only significant differences > 2 nm (average difference) again showed the particle size following SSL exposure to be larger than before exposure. The biggest of the significant differences were for the other and rounded cornered triangles in the long λ NF sample supporting the fact that the larger triangles were becoming more rounded with SSL exposure leading to an increase in average size of the rounded triangles and the larger rounded triangles were becoming more disc like again increasing the average size seen in the other category.

Table G.17 Two-sample t-test results for TEM analysis of the broadband mixture and its three component NFs after exposure to SSL for 0.5 h using set-up B compared to the initial data in Table G.5 (long λ) and Table G.7 (where sample 2 is significantly smaller than sample 1 the average difference is shown as positive).

Sample 1	**Sample 2**	**Particle type**	**Average difference /nm**	**Range of difference (at 95 % confidence) / nm**
Short λ after 0.5 h SSL	Short λ	Thickness	-0.35	-0.69 to -0.01
Mid λ after 0.5 h SSL	Mid λ	Other	2.61	0.62 to 4.60
Mid λ after 0.5 h SSL	Mid λ	Small	0.75	0.07 to 1.43
Long λ after 0.5 h SSL	Long λ	Rounded triangles	15.14	9.80 to 20.48
Long λ after 0.5 h SSL	Long λ	Other	18.53	11.29 to 25.77
Long λ after 0.5 h SSL	Long λ	Small	1.21	0.27 to 2.15
Broadband after 0.5 h SSL	Broadband mixture	Thickness	0.46	0.21 to 0.71

G.6 Effect of Fluid Flow

To assess the effect of fluid flow on the morphology using TEM the particle types were divided into four groups, triangles, rounded cornered triangles, other and small (< 10 nm). The results are given in Table G.18. The percentage of each sample type, the average, standard deviation (σ) and number of measurements (N) are given. It should be noted that the TEM analysis was undertaken on samples that had been prepared 4 months before analysis and the samples may have degraded over this timeframe (Zeng et al., 2010). Comparison with the initial TEM (Table G.9) for the combined broadband mixture and the flow only broadband NF (no change in UV-vis spectra, considerable change in amount of triangles and rounded triangles) supports this hypothesis. For this reason and considering the small number of particles measured in some of the categories (leading to considerable uncertainty about the average measured particle size obtained), t-tests were not undertaken comparing the size of the particles before and after testing.

Table G.18 TEM analysis on the broadband absorber after exposure to flow, flow and elevated temperature, flow and SSL and flow, elevated temperature and SSL.

Sample	**Particle shape**	**%**	**Average size / nm**	***σ* / nm**	***N***
Broadband NF flow only for 8 h	Triangle	1	50.72	15.60	2
Broadband NF flow only for 8 h	Rounded cornered triangle	5	33.22	23.26	14
Broadband NF flow only for 8 h	Other	47	16.41	9.24	132
Broadband NF flow only for 8 h	Small < 10 nm	47	7.46	1.47	132

Sample	Particle shape	%	Average size / nm	σ / nm	*N*
Broadband NF after flow and 6 h at 60 °C	Triangle	1	40.28	10.33	4
Broadband NF after flow and 6 h at 60 °C	Rounded cornered triangle	7	23.23	10.80	36
Broadband NF after flow and 6 h at 60 °C	Other	38	19.24	9.79	207
Broadband NF after flow and 6 h at 60 °C	Small < 10 nm	55	6.96	1.52	298
Broadband NF after flow and 4 h SSL	Triangle	2	25.06	6.43	4
Broadband NF after flow and 4 h SSL	Rounded cornered triangle	8	24.26	10.69	18
Broadband NF after flow and 4 h SSL	Other	48	17.69	9.39	111
Broadband NF after flow and 4 h SSL	Small < 10 nm	42	7.76	1.61	97
Broadband NF after flow, 60 °C for 5.5 h and SSL for 2.5 h	Triangle	1	32.43	20.24	5
Broadband NF after flow, 60 °C for 5.5 h and SSL for 2.5 h	Rounded cornered triangle	7	28.13	10.59	36
Broadband NF after flow, 60 °C for 5.5 h and SSL for 2.5 h	Other	56	20.41	9.65	268
Broadband NF after flow, 60 °C for 5.5 h and SSL for 2.5 h	Small < 10 nm	36	7.01	1.48	172

G.7 Water-glass SiO_2 Coating Method

To assess the morphology of the NFs that had been produced using the water-glass SiO_2 coating method the particle types were divided into four groups, triangles, rounded cornered triangles, other and small (< 10 nm). Where there was a consistent SiO_2 coating on the Ag NP the thickness of the coating was also measured. The results before and after 2 h exposure to SSL are shown in Table G.19 for the water-glass synthesis method given in Section 3.6.3. All these NFs used water as the BF. This method did not produce a consistent thin SiO_2 coating so the coating thickness was not measured. The percentage of each sample type, the average, standard deviation (σ) and number of measurements (*N*) are shown. The average values of λ_{max} obtained from the UV-vis measurements is also shown in brackets (number of samples *N* = 3). It should also be noted that some of the particles in the small category may be SiO_2 rather than Ag.

Table G.19 TEM analysis on Ag TSCD NPrs plus water-glass SiO_2, centrifuged and re-dispersed into ¼ volume of water BF, before and after exposure to SSL for 2 h using set-up A.

Sample	Particle shape	%	Average size / nm	σ / nm	*N*
Ag TSCD NPrs - 1 and water-glass SiO_2 in ¼ vol water initial (λ_{max} = 797 nm)	Triangle	22	38.49	12.18	211

Sample	Particle shape	%	Average size / nm	σ / nm	*N*
Ag TSCD NPrs - 1 and water-glass SiO_2 in ¼ vol water initial (λ_{max} = 797 nm)	Rounded cornered triangle	29	28.97	11.31	276
Ag TSCD NPrs - 1 and water-glass SiO_2 in ¼ vol water initial (λ_{max} = 797 nm)	Other	13	21.22	11.48	122
Ag TSCD NPrs - 1 and water-glass SiO_2 in ¼ vol water initial (λ_{max} = 797 nm)	Small < 10 nm	36	5.25	1.25	350
Ag TSCD NPrs - 1 and water-glass SiO_2 in ¼ vol water 2 h SSL (λ_{max} = 752 nm)	Triangle	3	38.86	11.62	36
Ag TSCD NPrs - 1 and water-glass SiO_2 in ¼ vol water 2 h SSL (λ_{max} = 752 nm)	Rounded cornered triangle	14	28.37	9.30	149
Ag TSCD NPrs - 1 and water-glass SiO_2 in ¼ vol water 2 h SSL (λ_{max} = 752 nm)	Other	36	17.45	9.60	374
Ag TSCD NPrs - 1 and water-glass SiO_2 in ¼ vol water 2 h SSL (λ_{max} = 752 nm)	Small < 10 nm	46	6.41	1.55	478

The results of investigating the morphology using TEM for NFs produced using a modified water-glass method utilising 5 x the amount of capping agent MPTMS in water BF or centrifuged and re-dispersing into a mixed BF containing 50 % PG and water are given in Table G.20. For the SiO_2 coated Ag NPs in water it was just possible to measure the thickness of the SiO_2 coating for some particles. The thickness of this coating has been excluded from the percentage of each particle type. For this sample it was also difficult to accurately determine the particle shapes and sizes due to aggregation of the particles. The average value of λ_{max} (N = 3) is also shown for the water samples but not for the PG / water BF as it was not possible to determine accurately the value of λ_{max} for these samples due to the low value of Ab_{max} obtained.

Table G.20 TEM analysis on Ag TSCD NPrs, with 5 x MPTMS plus water-glass SiO_2 in water BF or centrifuged and re-dispersed into ⅟₁₂ volume water / 50 % PG BF.

Sample	Particle shape	%	Average size / nm	σ / nm	*N*
Ag TSCD NPrs – 3, 5 x MPTMS and water-glass SiO_2 in water (λ_{max} = 866 nm)	Triangle	3	33.31	15.09	7
Ag TSCD NPrs – 3, 5 x MPTMS and water-glass SiO_2 in water (λ_{max} = 866 nm)	Rounded cornered triangle	10	27.28	14.44	23
Ag TSCD NPrs – 3, 5 x MPTMS and water-glass SiO_2 in water (λ_{max} = 866 nm)	Other	26	15.86	7.17	59
Ag TSCD NPrs – 3, 5 x MPTMS and water-glass SiO_2 in water (λ_{max} = 866 nm)	Small < 10 nm	61	6.09	1.41	137
Ag TSCD NPrs – 3, 5 x MPTMS and water-glass SiO_2 in water (λ_{max} = 866 nm)	SiO_2 coating thickness	-	4.33	1.22	38

Sample	Particle shape	%	Average size / nm	σ / nm	*N*
Ag TSCD NPrs – 3, 5 x MPTMS and water-glass SiO_2 in 1/12 volume water / 50 % PG	Triangle	2	28.38	10.65	27
Ag TSCD NPrs – 3, 5 x MPTMS and water-glass SiO_2 in 1/12 volume water / 50 % PG	Rounded cornered triangle	8	21.88	11.43	128
Ag TSCD NPrs – 3, 5 x MPTMS and water-glass SiO_2 in 1/12 volume water / 50 % PG	Other	36	16.30	6.78	568
Ag TSCD NPrs – 3, 5 x MPTMS and water-glass SiO_2 in 1/12 volume water / 50 % PG	Small < 10 nm	54	6.48	1.47	851

G.7.1 Significance of differences for water-glass SiO_2 coating method

To determine whether the size of the particles had changed following exposure to SSL for 2 h unpaired two-sample t-tests were undertaken (using the formula given in F.1). The results of the t-tests are shown in Table G.21. Only the significant results are shown. The largest difference was for the other shaped particles which were on average 3.77 nm smaller following SSL exposure. The only other difference that was significant was for the small < 10 nm category and may be due to measurement uncertainty rather than a truly significant difference (the t-tests do not account for additional measurement uncertainty inherent in the technique).

An assessment of whether the nature of the BF was effecting the size of the particles was also made again using a two-sample t-test. These results are also given in Table G.21, with again only the significant results being shown. The size of the rounded cornered triangles was significantly smaller in the 50 % PG BF than in water by 5.4 nm but there was a large confidence range associated with this due to the small number of rounded triangles measured for the water BF sample. There was also a significant difference in the size of the small particles but this was < 1 nm so may be due the measurement uncertainty.

The effect of increasing the amount of capping agent MPTMS by 5 x on the size of the NPs was also evaluated. Again only the significant results are given in Table G.21. The other shaped particles were smaller by ≈ 5.4 nm when more MPTMS was used, however, this result should be treated with caution as the 5 x MPTMS sample was very difficult to analyse.

Table G.21 Two-sample t-test results for TEM analysis of the water-glass SiO_2 NFs (where sample 2 is significantly smaller than sample 1 the average difference is shown as positive).

Sample 1	**Sample 2**	**Particle type**	**Average difference /nm**	**Range of difference (at 95 % confidence) / nm**
Ag TSCD NPrs - 1 and water-glass SiO_2 in ¼ vol water initial	Ag TSCD NPrs - 1 and water-glass SiO_2 in ¼ vol water after 2 h SSL	Other	3.77	1.70 to 5.84
Ag TSCD NPrs - 1 and water-glass SiO_2 in ¼ vol water initial	Ag TSCD NPrs - 1 and water-glass SiO_2 in ¼ vol water after 2 h SSL	Small	-1.16	-1.36 to -0.96
Ag TSCD NPrs – 3, 5 x MPTMS and water-glass SiO_2 in water	Ag TSCD NPrs – 3, 5 x MPTMS and water-glass SiO_2 in 1/12 volume water / 50 % PG	Rounded triangles	5.40	0.06 to 10.74
Ag TSCD NPrs – 3, 5 x MPTMS and water-glass SiO_2 in water	Ag TSCD NPrs – 3, 5 x MPTMS and water-glass SiO_2 in 1/12 volume water / 50 % PG	Small	-0.39	-0.65 to -0.13
Ag TSCD NPrs - 1 and water-glass SiO_2 in ¼ vol water initial	Ag TSCD NPrs – 3, 5 x MPTMS and water-glass SiO_2 in water	Other	5.36	2.14 to 8.58
Ag TSCD NPrs - 1 and water-glass SiO_2 in ¼ vol water initial	Ag TSCD NPrs – 3, 5 x MPTMS and water-glass SiO_2 in water	Small	-0.84	-1.10 to -0.58

G.8 Development of Stöber SiO_2 Coating Method

To assess the morphology of the Ag NPr prior to coating with SiO_2 using the Stöber TEOS coating method the particle types were divided into four groups, triangles, rounded cornered triangles, other and small (< 10 nm). The results are given in Table G.22 and show the majority of NPs to be triangular in shape with an average size of 49.13 nm.

Table G.22 TEM analysis on Ag TSCD-PVP NPr before SiO_2 coating. The value of λ_{max} is shown in brackets.

Sample	**Particle shape**	**%**	**Average size / nm**	***σ* / nm**	***N***
Ag TSCD-PVP NPr before SiO_2 coating (λ_{max} = 899 nm)	Triangle	63	49.13	16.17	196
Ag TSCD-PVP NPr before SiO_2 coating (λ_{max} = 899 nm)	Rounded cornered triangle	23	42.61	15.42	72
Ag TSCD-PVP NPr before SiO_2 coating (λ_{max} = 899 nm)	Other	12	33.27	20.03	36
Ag TSCD-PVP NPr before SiO_2 coating (λ_{max} = 899 nm)	Small < 10 nm	2	8.23	1.73	7

The particles after SiO_2 coating using the Stöber TEOS method were grouped differently as it was no longer possible to determine the shape of the Ag NP surrounded by SiO_2 accurately.

For the SiO_2 coated samples the total diameter of the coated samples was measured, along with the length of the silver particle (denoted as Ag inside) inside the SiO_2 coating and the coating thickness. In addition, the percentage of single-cored (containing only one silver NP), multi-cored (containing two or more silver NPs), and particles with no silver in the middle (SiO_2 only NPs) was determined along with the percentage of multi-cored versus single-cored (excluding the SiO_2 only NPs). Finally, the number and size of not SiO_2 coated Ag NP (denoted as Ag free) were measured and compared to the total number and size of the SiO_2 coated Ag NPs (Ag inside). A typical portion of a micrograph showing the different types of measurements undertaken is given in Figure G.2.

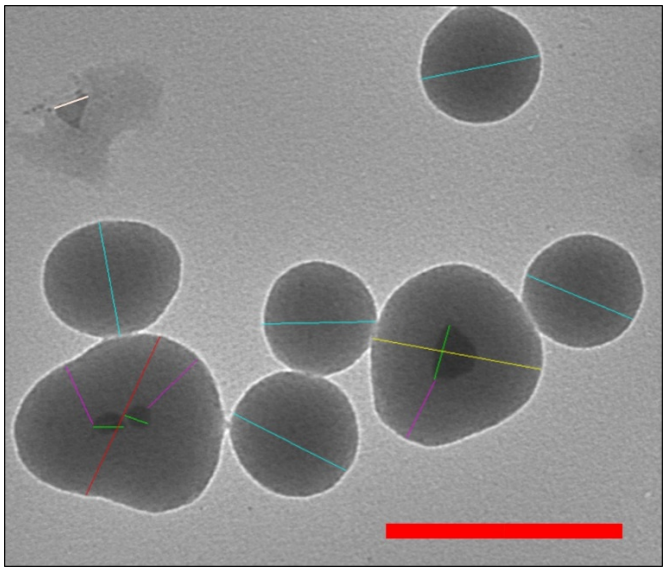

Figure G.2 Example of how the SiO_2 coated TEM measurements were undertaken. Light blue line = SiO_2 only NP, yellow line = single-cored SiO_2@Ag NP, red line = multi-cored SiO_2@Ag NP, green line = Ag inside, light orange line = Ag free (not SiO_2 coated), pink line = SiO_2 coating thickness. Thick red scale bar = 200 nm.

The TEM analysis results for the first trial utilising 16 mM TEOS (60 minutes reaction time) with 20 µM MHA capping agent are given in Table G.23. It should be noted that for this sample there was significant levels of clumping / aggregation of the NPs making the TEM micrographs difficult to analyse. For this reason the total number of particles counted in each group is low and the results obtained should be treated with caution.

Table G.23 TEM analysis on SiO_2@Ag NPr, 16 mM TEOS, 60 minutes, 20 µM MHA after SiO_2 coating to optimise the Stöber coating procedure. The λ_{max} = 895 nm.

Measurement type	**%**	**% excluding SiO_2 NPs**	**Average size / nm**	***σ* / nm**	***N***
Single-cored	19	29	280.32	87.66	6
Multi-cored	47	71	104.04	31.77	15

Measurement type	%	% excluding SiO_2 NPs	Average size / nm	σ / nm	*N*
SiO_2 only	34	-	246.95	127.30	11
SiO_2 coating thickness	-	-	46.48	35.01	52
Ag inside	92	-	37.98	10.92	54
Ag free	8	-	38.54	12.46	5

The TEM results from analysing the sample made using a lower concentration of TEOS of 10 mM the same reaction time of 60 minutes and the same (20 µM) amount of MHA are provided in Table G.24. There was less aggregation of the NPs making the TEM analysis easier and more reliable (greater value of *N* for most types of samples / measurements). There were less multi-cored NPs present and the SiO_2 coating thickness was more consistent than for the proceeding sample produced using a higher concentration of TEOS.

Table G.24 TEM analysis on SiO_2@Ag NPr, 10 mM TEOS, 60 minutes, 20 µM MHA after SiO_2 coating to optimise the Stöber coating procedure. The λ_{max} = 873 nm.

Measurement type	%	% excluding SiO_2 NPs	Average size / nm	σ / nm	*N*
Single-cored	35	62	211.45	19.24	85
Multi-cored	22	38	220.86	17.91	53
SiO_2 only	43	-	168.68	17.00	105
SiO_2 coating thickness	-	-	85.99	8.67	227
Ag inside	97	-	39.49	14.31	227
Ag free	3	-	27.33	9.57	7

When the concentration of TEOS employed was reduced to 8 mM TEOS (see Table G.25) significant aggregation of the NPs again resulted making these TEM micrographs hard to analyse. The number of multi-cored NPs increased and the coating thickness decreased and became more variable.

Table G.25 TEM analysis on SiO_2@Ag NPr, 8 mM TEOS, 60 minutes, 20 µM MHA after SiO_2 coating to optimise the Stöber coating procedure. The λ_{max} = 898 nm.

Measurement type	%	% excluding SiO_2 NPs / %	Average size / nm	σ / nm	*N*
Single-cored	16	19	135.82	58.99	3
Multi-cored	68	81	132.36	45.41	13
SiO_2 only	16	-	53.76	3.25	3
SiO_2 coating thickness	-	-	52.59	18.65	74
Ag inside	81	-	39.96	14.66	76
Ag free	19	-	10.20	7.24	18

The TEM results using an even lower concentration of TEOS (1.6 mM) are given in Table G.26. Here a thin incomplete SiO_2 coating was produced leading to a higher percentage of uncoated Ag NPs (shown as Ag free).

Table G.26 TEM analysis on SiO_2@Ag NPr, 1.6 mM TEOS, 60 minutes, 20 μM MHA after SiO_2 coating to optimise the Stöber coating procedure. The λ_{max} = 897 nm.

Measurement type	**%**	**% excluding SiO_2 NPs**	**Average size / nm**	***σ* / nm**	***N***
Single-cored	14	22	62.12	20.32	4
Multi-cored	50	78	84.94	19.41	14
SiO_2 only	36	-	52.65	47.68	10
SiO_2 coating thickness	-	-	21.89	9.47	61
Ag inside	69	-	42.41	16.10	61
Ag free	31	-	36.02	11.43	27

The TEM results obtained for a shorter reaction time of 30 minutes, using 10 mM TEOS and 20 μM MHA are provided in Table G.27. Halving the reaction time slightly reduced the coating thickness and the percentage of multi-cored NPs present (see Table G.24 and Figure L.4) but increased the percentage of uncoated Ag NPs slightly.

Table G.27 TEM analysis on SiO_2@Ag NPr, 10 mM TEOS, 30 minutes, 20 μM MHA after SiO_2 coating to optimise the Stöber coating procedure. The λ_{max} = 898 nm.

Measurement type	**%**	**% excluding SiO_2 NPs**	**Average size / nm**	***σ* / nm**	***N***
Single-cored	36	64	217.83	13.68	110
Multi-cored	21	36	229.25	18.87	63
SiO_2 only	43	-	164.61	19.19	132
SiO_2 coating thickness	-	-	84.49	10.03	169
Ag inside	90	-	42.53	13.27	170
Ag free	10	-	18.12	10.88	19

The TEM results after doubling the amount of capping agent MHA employed to 40 μM are shown in Table G.28. The number of multi-cored NPs and the percentage of uncoated Ag NPs were reduced compared to when 20 μM MHA. The thickness of the coating was also lower.

Table G.28 TEM analysis on SiO_2@Ag NPr, 10 mM TEOS, 30 minutes, 40 μM MHA after SiO_2 coating to optimise the Stöber coating procedure. The λ_{max} = 876 nm.

Measurement type	**%**	**% excluding SiO_2 NPs**	**Average size / nm**	***σ* / nm**	***N***
Single-cored	40	75	168.27	12.33	132
Multi-cored	13	25	173.23	11.21	44
SiO_2 only	47	-	113.45	18.31	156

Measurement type	%	% excluding SiO_2 NPs	Average size / nm	σ / nm	*N*
SiO_2 coating thickness	-	-	61.09	6.97	293
Ag inside	99	-	40.95	14.09	294
Ag free	1	-	56.59	25.42	3

Finally, the TEM results utilising 10 mM TEOS, 40 µM MHA and an even shorter reaction time of 15 minutes are given in Table G.29. The coating thickness obtained was less than that seen in Table G.28 but the percentage of multi-cored NPs and uncoated Ag NPrs (Ag free) increased slightly.

Table G.29 TEM analysis on SiO_2@Ag NPr, 10 mM TEOS, 15 minutes, 40 µM MHA after SiO_2 coating to optimise the Stöber coating procedure. The λ_{max} = 899 nm.

Measurement type	%	% excluding SiO_2 NPs	Average size / nm	σ / nm	*N*
Single-cored	36	69	157.26	11.56	88
Multi-cored	16	31	163.88	11.59	40
SiO_2 only	47	-	107.53	13.11	115
SiO_2 coating thickness	-	-	56.52	6.94	143
Ag inside	97	-	45.27	16.17	143
Ag free	3	-	30.30	15.54	4

G.9 As Synthesised SiO_2 Coated Silver Nanoprisms (SiO_2@Ag NPrs) Produced using Optimised Coating Procedure

In total 10 individual samples were assessed using TEM after SiO_2 coating using the optimised Stöber coating procedure. The assessment was undertaken according to the method detailed in Section 3.7.1 and in Section G.8. The results obtained are given in Table G.30 to Table G.39. One of the samples (SiO_2@Ag NPr – 7, Table G.36), produced a considerably thicker SiO_2 coating. However, this sample was manufactured using a smaller batch volume and has hence been excluded from the average results presented in the main body of the thesis (see Table 6-2).

Table G.30 TEM analysis after SiO_2 coating using the optimised Stöber TEOS procedure (SiO_2@Ag NPr - 1, 10 mM TEOS, 30 minutes, 40 µM MHA). The λ_{max} = 900 nm.

Measurement type	%	% excluding SiO_2 NPs	Average size / nm	Maximum / nm	Minimum / nm	σ / nm	*N*
Single-cored	28	96	143.01	194.23	113.99	13.29	185
Multi-cored	1	4	152.43	188.54	138.81	17.25	7
SiO_2 only	71	-	86.84	126.48	45.45	13.79	465
SiO_2 coating thickness	-	-	52.16	63.78	40.49	4.39	220

Measurement type	%	% excluding SiO_2 NPs	Average size / nm	Maximum / nm	Minimum / nm	σ / nm	*N*
Ag inside	100	-	38.90	83.68	10.31	10.41	220

Table G.31 TEM analysis after SiO_2 coating using the optimised Stöber TEOS procedure (SiO_2@Ag NPr - 2, 10 mM TEOS, 30 minutes, 40 µM MHA). The λ_{max} = 836 nm.

Measurement type	%	% excluding SiO_2 NPs	Average size / nm	Maximum / nm	Minimum / nm	σ / nm	*N*
Single-cored	45	96	142.67	186.82	89.84	11.95	234
Multi-cored	2	4	138.23	151.08	129.99	6.67	10
SiO_2 only	53	-	90.98	116.06	57.85	12.43	274
SiO_2 coating thickness	-	-	54.39	66.28	26.32	5.28	232
Ag inside	100	-	31.50	60.85	12.65	8.06	233

Table G.32 TEM analysis after SiO_2 coating using the optimised Stöber TEOS procedure (SiO_2@Ag NPr - 3, 10 mM TEOS, 30 minutes, 40 µM MHA). The λ_{max} = 836 nm.

Measurement type	%	% excluding SiO_2 NPs	Average size / nm	Maximum / nm	Minimum / nm	σ / nm	*N*
Single-cored	45	91	138.64	184.42	106.87	12.50	183
Multi-cored	5	9	138.17	168.99	120.31	11.72	19
SiO_2 only	51	-	88.91	116.45	41.60	12.53	208
SiO_2 coating thickness	-	-	52.42	62.65	41.54	3.82	192
Ag inside	100	-	34.56	71.52	14.77	9.73	192

Table G.33 TEM analysis after SiO_2 coating using the optimised Stöber TEOS procedure (SiO_2@Ag NPr - 4, 10 mM TEOS, 30 minutes, 40 µM MHA). The λ_{max} = 817 nm.

Measurement type	%	% excluding SiO_2 NPs	Average size / nm	Maximum / nm	Minimum / nm	σ / nm	*N*
Single-cored	33	93	117.28	146.68	89.04	10.75	170
Multi-cored	2	7	104.70	118.30	69.25	15.42	13
SiO_2 only	65	-	75.14	104.77	42.67	11.06	340
SiO_2 coating thickness	-	-	46.31	56.98	38.59	3.24	174
Ag inside	98	-	33.92	82.33	8.21	11.72	193
Ag free	2	-	8.93	9.39	8.56	0.42	3

Table G.34 TEM analysis after SiO_2 coating using the optimised Stöber TEOS procedure (SiO_2@Ag NPr - 5, 10 mM TEOS, 30 minutes, 40 µM MHA). The λ_{max} = 793 nm.

Measurement type	%	% excluding SiO_2 NPs	Average size / nm	Maximum / nm	Minimum / nm	σ / nm	*N*
Single-cored	37	92	117.26	168.09	98.94	10.78	120

Measurement type	**%**	**% excluding SiO_2 NPs**	**Average size / nm**	**Maximum / nm**	**Minimum / nm**	***σ* / nm**	***N***
Multi-cored	3	8	122.55	141.37	110.70	10.36	11
SiO_2 only	60	-	80.10	115.61	50.99	13.08	194
SiO_2 coating thickness	-	-	48.75	62.23	32.65	4.24	141
Ag inside	99	-	32.89	86.18	14.08	11.22	141
Ag fee	1	-	19.79	-	-	-	1

Table G.35 TEM analysis after SiO_2 coating using the optimised Stöber TEOS procedure (SiO_2@Ag NPr - 6, 10 mM TEOS, 30 minutes, 40 μM MHA). The λ_{max} = 831 nm.

Measurement type	**%**	**% excluding SiO_2 NPs**	**Average size / nm**	**Maximum / nm**	**Minimum / nm**	***σ* / nm**	***N***
Single-cored	44	94	119.80	160.04	81.13	12.30	106
Multi-cored	3	6	136.33	158.38	113.33	16.72	7
SiO_2 only	53	-	89.23	122.54	53.25	11.66	129
SiO_2 coating thickness	-	-	49.98	61.47	36.99	4.70	118
Ag inside	100	-	30.77	65.29	12.14	9.20	118

Table G.36 TEM analysis after SiO_2 coating using the optimised Stöber TEOS procedure (SiO_2@Ag NPr - 7, 10 mM TEOS, 30 minutes, 40 μM MHA). The λ_{max} = 898 nm.

Measurement type	**%**	**% excluding SiO_2 NPs**	**Average size / nm**	**Maximum / nm**	**Minimum / nm**	***σ* / nm**	***N***
Single-cored	35	51	199.05	217.03	171.18	10.95	18
Multi-cored	33	49	204.88	265.73	181.76	22.39	17
SiO_2 only	31	-	159.09	179.92	46.33	31.21	16
SiO_2 coating thickness	-	-	80.58	94.74	69.62	6.43	73
Ag inside	94	-	40.36	85.75	11.55	16.70	80
Ag free	6	-	38.03	50.15	30.48	7.59	5

Table G.37 TEM analysis after SiO_2 coating using the optimised Stöber TEOS procedure (SiO_2@Ag NPr - 8, 10 mM TEOS, 30 minutes, 40 μM MHA). The λ_{max} = 810 nm.

Measurement type	**%**	**% excluding SiO_2 NPs**	**Average size / nm**	**Maximum / nm**	**Minimum / nm**	***σ* / nm**	***N***
Single-cored	26	87	146.41	183.42	112.72	12.87	130
Multi-cored	4	13	148.35	175.69	130.00	12.69	20
SiO_2 only	70	-	98.13	131.37	35.72	14.06	346
SiO_2 coating thickness	-	-	53.45	68.46	43.20	4.80	176
Ag inside	98	-	37.49	81.70	9.23	12.71	174
Ag free	2	-	28.47	36.77	22.45	6.71	4

Table G.38 TEM analysis after SiO_2 coating using the optimised Stöber TEOS procedure (SiO_2@Ag NPr - 9, 10 mM TEOS, 30 minutes, 40 μM MHA). The λ_{max} = 906 nm.

Measurement type	**%**	**% excluding SiO_2 NPs**	**Average size / nm**	**Maximum / nm**	**Minimum / nm**	***σ* / nm**	***N***
Single-cored	50	93	138.92	185.18	112.74	17.37	77
Multi-cored	4	7	142.23	180.81	114.20	24.82	6
SiO_2 only	46	-	94.33	123.98	69.27	9.57	72
SiO_2 coating thickness	-	-	51.94	61.01	44.48	3.68	92
Ag inside	100	-	43.57	80.53	15.88	16.15	86

Table G.39 TEM analysis after SiO_2 coating using the optimised Stöber TEOS procedure (SiO_2@Ag NPr - 11, 10 mM TEOS, 30 minutes, 40 μM MHA). The λ_{max} = 876 nm.

Measurement type	**%**	**% excluding SiO_2 NPs**	**Average size / nm**	**Maximum / nm**	**Minimum / nm**	***σ* / nm**	***N***
Single-cored	29	73	140.68	190.62	110.15	18.86	55
Multi-cored	11	27	148.03	201.39	115.08	19.34	20
SiO_2 only	60	-	93.40	132.66	57.10	11.88	112
SiO_2 coating thickness	-	-	48.83	59.92	39.31	4.22	104
Ag inside	81	-	41.90	87.95	10.44	17.22	94
Ag free	19	-	16.90	29.98	7.51	7.25	22

G.9.1 Significance of differences

To ascertain if there was a difference in the thickness of the SiO_2 coating obtained for the repeat batches of SiO_2@Ag NPrs compared to the results obtained using a smaller volume in the development of the procedure (see Section G.8), ANOVA was used. Boxplots showing graphically the thickness results are provided in Figure G.3 with the results from Section G.8 given as SiO_2@ Ag NPr development. The ANOVA results are given in Table G.40. Excluding the development sample and SiO_2@Ag NPr – 7, which were both produced using a smaller batch volume and resulted in much thicker SiO_2 coating, the other 9 samples ranged in average SiO_2 coating thickness from 46.31 nm to 54.39 nm a difference of ≈ 6 nm (and approximately 4 nm between the top of the smallest thickness confidence value and the bottom of the largest thickness confidence level, samples SiO_2@Ag NPr – 4 and SiO_2@Ag NPr – 2). Hence although some of the differences between these 9 samples were significant the size of the difference was small and could be due in part to the measurement uncertainty associated with the method of ≈ 3 % (see Appendix C, Section C.4 and Appendix E, Section E.1).

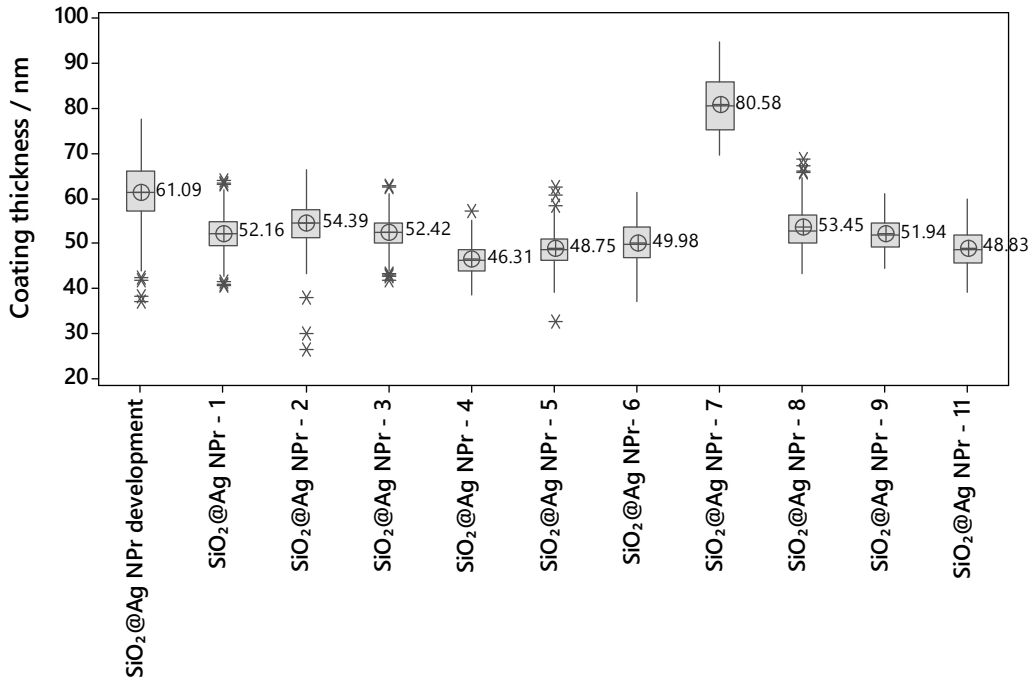

Figure G.3 Boxplots showing the TEM SiO_2 coating thickness results (the results obtained in Table G.28 is shown for comparison). All produced using 10 mM TEOS, 40 µM MHA for 30 minutes.

Table G.40 ANOVA results for the thickness of the SiO_2 coating in descending order of thickness. Both SiO_2@Ag NPr – 7 and SiO_2@Ag NPr development where produced using a smaller batch volume.

Sample	**Mean SiO_2 thickness / nm**	**Range of thickness (at 95 % confidence) / nm**	***N***	**Grouping**
SiO_2@Ag NPr - 7	80.58	79.48 to 81.72	73	A
SiO_2@Ag NPr development	61.09	60.52 to 61.66	293	B
SiO_2@Ag NPr - 2	54.39	53.75 to 55.04	232	C
SiO_2@Ag NPr - 8	53.45	52.72 to 54.19	176	C, D
SiO_2@Ag NPr - 3	52.42	51.72 to 53.12	192	D
SiO_2@Ag NPr - 1	52.16	51.50 to 52.81	220	D
SiO_2@Ag NPr - 9	51.94	50.92 to 52.95	92	D, E
SiO_2@Ag NPr - 6	49.98	49.08 to 50.88	118	E, F
SiO_2@Ag NPr - 11	48.83	47.87 to 49.78	104	F
SiO_2@Ag NPr - 5	48.75	47.93 to 49.57	141	F
SiO_2@Ag NPr - 4	46.31	45.58 to 47.05	174	G

G.10 Colloidal Stability of SiO_2 Coated Silver Nanoprisms (SiO_2@Ag NPrs) Produced using Optimised Coating Procedure

In total 3 individual SiO_2@Ag NPr samples were assessed using TEM after storage in the dark at 4 °C for ≈ 50 days. The assessment was undertaken according to the method detailed in Section 3.7.1 and in Section G.8. The results obtained are given in Table G.41, Table G.42 and Table G.43.

Table G.41 TEM analysis after storage in at 4 °C in the dark for 51 days for SiO_2@Ag NPr - 1 re-dispersed into ¼ volume of water. The λ_{max} = 804 nm.

Measurement type	**%**	**% excluding SiO_2 NPs**	**Average size / nm**	**Maximum / nm**	**Minimum / nm**	***σ* / nm**	***N***
Single-cored	32	85	132.82	173.05	81.10	17.78	88
Multi-cored	6	15	130.26	158.22	78.23	25.62	15
SiO_2 only	62	-	88.43	116.34	55.78	13.31	169
SiO_2 coating thickness	-	-	50.74	62.81	31.64	6.13	121
Ag inside	96	-	34.18	68.26	6.80	14.00	121
Ag free	4	-	22.45	31.65	8.60	9.19	5

Table G.42 TEM analysis after storage in at 4 °C in the dark for 49 days for SiO_2@Ag NPr - 2 re-dispersed into ¼ volume of water. The starting λ_{max} = 726 nm.

Measurement type	**%**	**% excluding SiO_2 NPs**	**Average size / nm**	**Maximum / nm**	**Minimum / nm**	***σ* / nm**	***N***
Single-cored	32	55	126.79	151.39	81.23	11.78	52
Multi-cored	26	45	130.06	175.74	79.15	18.45	43
SiO_2 only	42	-	92.97	118.76	63.77	12.88	70
SiO_2 coating thickness	-	-	50.84	69.94	32.35	6.20	156
Ag inside	98	-	22.27	69.71	4.41	13.04	156
Ag free	2	-	16.49	20.83	13.42	3.86	3

Table G.43 TEM analysis after storage in at 4 °C in the dark for 49 days for SiO_2@Ag NPr - 3 re-dispersed into ¼ volume of water. The starting λ_{max} = 803 nm.

Measurement type	**%**	**% excluding SiO_2 NPs**	**Average size / nm**	**Maximum / nm**	**Minimum / nm**	***σ* / nm**	***N***
Single-cored	42	85	126.18	155.19	90.23	10.15	127
Multi-cored	7	15	124.86	143.11	99.57	11.52	22
SiO_2 only	51	-	84.25	113.67	51.82	13.25	155
SiO_2 coating thickness	-	-	50.71	65.37	36.48	4.52	178
Ag inside	98	-	30.23	65.13	6.65	10.74	179
Ag free	2	-	17.80	48.17	6.35	20.33	4

G.10.1 Significance of differences

To ascertain if there was any difference in the sizes of the particles following storage in the dark at 4 °C for ≈ 50 days, unpaired t-tests were used comparing the data presented in Table 6-2 (before storage) with that presented in Table 6-4. The results that were significantly different are presented in Table G.44. When the measurement uncertainty of about 6 % (see Table E.1) is taken into consideration the difference in the size of the single-cored particles is within the measurement uncertainty (≈ 8 nm) and the average difference in the multi-cored particles is just greater at 8.67 nm. The t-test does not account for the measurement uncertainty so although these two particles appear to be smaller after storage they may in fact not be given the measurement uncertainty. However for the Ag inside NPs the 6 % uncertainty in the measurement gives a value of 2 nm for the uncertainty so the 6.97 nm average reduction in size of the NP inside the SiO_2 shell is likely to be truly significant. This suggests that the Ag NP is dissolving inside the shell on storage. The increase in the relative number of multi-cored particles also supports this hypothesis.

Table G.44 Two-sample un-paired t-test results for TEM analysis of SiO_2@Ag NPrs before and after storage in the dark at 4 °C for ≈ 50 days (where sample 2 is significantly smaller than sample 1 the average difference is shown as positive).

Sample 1	**Sample 2**	**Particle type**	**Average difference /nm**	**Range of difference (at 95 % confidence) / nm**
SiO_2@Ag NPr, ¼ volume - Initial	SiO_2@Ag NPr, ¼ volume – After ≈ 50 days in the dark at 4 °C	Single-cored	5.94	3.74 to 8.14
SiO_2@Ag NPr, ¼ volume - Initial	SiO_2@Ag NPr, ¼ volume – After ≈ 50 days in the dark at 4 °C	Multi-cored	8.67	3.04 to 14.30
SiO_2@Ag NPr, ¼ volume - Initial	SiO_2@Ag NPr, ¼ volume – After ≈ 50 days in the dark at 4 °C	Ag inside	6.97	5.67 to 8.27

G.11 Temperature Stability of SiO_2 Coated Silver Nanoprisms (SiO_2@Ag NPrs) Produced using Optimised Coating Procedure

In total 4 individual SiO_2@Ag NPr samples were evaluated using TEM after exposure to a temperature of 70 °C for 18 h. The assessment was undertaken according to the method detailed in Section 3.7.1 and in Section G.8. The results are shown in Table G.45 to Table G.48. For two of the samples measured the majority of the Ag NPs were no longer coated with SiO_2. There were the most concentrated sample tested (Table G.48) and one sample which had been diluted prior to temperature testing (Table G.47), with the other diluted SiO_2@Ag NPr NF still being SiO_2 coated (Table G.46) although there was considerable signs of porosity present in the remaining SiO_2 coatings.

Table G.45 TEM analysis after exposure to 70 °C for 18 h for SiO_2@Ag NPr - 8 re-dispersed into the same volume of water as the initial uncoated NF. Note that there were signs of porosity in the SiO_2 coating on the TEM micrographs.

Measurement type	**%**	**% excluding SiO_2 NPs**	**Average size / nm**	**Maximum / nm**	**Minimum / nm**	***σ* / nm**	***N***
Single-cored	28	95	143.02	175.45	115.50	14.01	100
Multi-cored	1	5	141.55	152.91	128.28	9.70	5
SiO_2 only	71	-	96.07	128.99	50.87	12.65	255
SiO_2 coating thickness	-	-	51.25	75.03	31.53	6.71	121
Ag inside	89	-	36.54	56.55	9.95	8.81	9.95
Ag free	11	-	23.44	76.09	5.98	19.99	14

Table G.46 TEM analysis after exposure to 70 °C for 18 h for SiO_2@Ag NPr - 10 diluted to give an Ab_{max} ≈ 0.8 au (for a 10 mm path length cuvette) prior to temperature exposure. Note that there were signs of porosity in the SiO_2 coating on the TEM micrographs.

Measurement type	**%**	**% excluding SiO_2 NPs**	**Average size / nm**	**Maximum / nm**	**Minimum / nm**	***σ* / nm**	***N***
Single-cored	28	93	134.53	174.39	86.88	18.79	83
Multi-cored	2	7	129.83	143.37	118.04	9.45	6
SiO_2 only	70	-	91.46	129.67	21.13	13.94	204
SiO_2 coating thickness	-	-	46.87	67.41	10.47	8.02	103
Ag inside	96	-	34.51	58.28	12.72	10.73	96
Ag free	4	-	26.39	37.39	14.55	9.41	4

Table G.47 TEM analysis after exposure to 70 °C for 18 h for SiO_2@Ag NPr - 12 diluted to give an Ab_{max} ≈ 0.8 au (for a 10 mm path length cuvette) prior to temperature exposure. Note that the majority of Ag NPs were no longer coated with SiO_2 and there were significant signs of porosity in the SiO_2 coating on the TEM micrographs.

Measurement type	**%**	**% excluding SiO_2 NPs**	**Average size / nm**	**Maximum / nm**	**Minimum / nm**	***σ* / nm**	***N***
Ag still SiO_2 coated	5	5	101.10	156.47	62.84	24.77	17
SiO_2 only	7	-	61.28	94.03	20.94	22.29	23
SiO_2 coating thickness	-	-	39.31	55.09	21.88	9.43	16
Ag inside	-	-	28.20	44.73	7.74	11.78	16
Ag free - triangles	6	6	48.26	63.91	32.99	8.91	20
Ag free – rounded triangles	41	44	38.59	63.03	20.08	7.87	144
Ag free - other	33	36	31.90	74.39	10.29	9.59	117
Ag free - small	9	9	7.45	11.52	4.99	1.44	31
Ag free – Ag NP thickness	-	-	5.68	8.33	4.04	1.09	28

Table G.48 TEM analysis after exposure to 70 °C for 18 h for SiO_2@Ag NPr - 8 re-dispersed into ¼ volume of water (compared to the original NF). Note that only one Ag NP was still coated with SiO_2 and there were no triangular or rounded cornered triangular free Ag NPs present on the TEM micrographs.

Measurement type	**%**	**Average size / nm**	**Maximum / nm**	**Minimum / nm**	***σ* / nm**	***N***
Ag still SiO_2 coated	< 1	Not measured	-	-	-	-
SiO_2 coating thickness (measured on 1 NP)	-	52.33	53.34	50.74	1.39	3
Ag free - other	19	12.84	24.96	8.63	4.56	23
Ag free - small	81	5.86	9.15	3.59	1.26	97

G.12 Simulated Sunlight (SSL) Stability of SiO_2 Coated Silver Nanoprisms (SiO_2@Ag NPrs) Produced using Optimised Coating Procedure

In total 3 individual samples were assessed using TEM after exposure to SSL for 6 h using set-up A in the solar simulator. The analysis was undertaken according to the method detailed in Section 3.7.1 and in Section G.8. To allow for a comparison with the before exposure TEM samples the average results for the same samples before SSL exposure are given in Table G.49. The after exposure results are given in Table G.50, Table G.51 and Table G.52. After SSL exposure the percentage of multi-cored NP had increased from 6 % to 20% - 30 % and the percentage of uncoated free Ag NPs had increased from none to 2 % – 6 %.

Table G.49 TEM analysis before exposure to SSL for 6 h for SiO_2@Ag NPr re-dispersed into ¼ volume of water (compared to the initial uncoated NF) – Average results from Table G.30, Table G.31, and Table G.32 (*N* = 3).

Measurement type	**%**	**% excluding SiO_2 NPs**	**Average size / nm**	**Maximum / nm**	**Minimum / nm**	***σ* / nm**	***N***
Single-cored	38	94	141.55	194.23	89.84	12.67	602
Multi-cored	2	6	140.96	188.54	120.31	12.87	36
SiO_2 only	60	-	88.49	126.48	41.60	13.24	947
SiO_2 coating thickness	-	-	53.04	66.28	26.32	4.69	644
Ag inside	100	-	34.93	83.68	10.31	9.90	645

Table G.50 TEM analysis after exposure to SSL for 6 h for SiO_2@Ag NPr - 1 re-dispersed into ¼ volume of water (compared to the initial uncoated NF).

Measurement type	**%**	**% excluding SiO_2 NPs**	**Average size / nm**	**Maximum / nm**	**Minimum / nm**	***σ* / nm**	***N***
Single-cored	34	78	137.76	176.49	91.38	16.45	65
Multi-cored	9	22	124.87	166.46	81.07	22.23	18
SiO_2 only	57	-	98.26	132.10	63.11	13.99	110

Measurement type	%	% excluding SiO_2 NPs	Average size / nm	Maximum / nm	Minimum / nm	σ / nm	*N*
SiO_2 coating thickness	-	-	49.30	65.02	30.02	6.03	102
Ag inside	97	-	26.38	53.40	7.21	12.07	102
Ag free	3	-	50.61	56.60	45.90	5.46	3

Table G.51 TEM analysis after exposure to SSL for 6 h for SiO_2@Ag NPr - 2 re-dispersed into ¼ volume of water (compared to the initial uncoated NF).

Measurement type	%	% excluding SiO_2 NPs	Average size / nm	Maximum / nm	Minimum / nm	σ / nm	*N*
Single-cored	37	70	133.57	163.08	102.58	12.45	46
Multi-cored	16	30	139.07	155.90	112.22	11.53	20
SiO_2 only	47	-	92.75	120.39	57.33	12.42	59
SiO_2 coating thickness	-	-	47.04	59.92	24.05	6.50	97
Ag inside	94	-	21.12	43.45	4.38	9.03	97
Ag free	6	-	33.35	74.46	14.90	24.23	6

Table G.52 TEM analysis after exposure to SSL for 6 h for SiO_2@Ag NPr - 3 re-dispersed into ¼ volume of water (compared to the initial uncoated NF).

Measurement type	%	% excluding SiO_2 NPs	Average size / nm	Maximum / nm	Minimum / nm	σ / nm	*N*
Single-cored	42	80	134.70	170.01	115.13	12.36	96
Multi-cored	10	20	138.10	167.29	91.97	16.64	24
SiO_2 only	48	-	96.91	125.15	69.56	12.30	111
SiO_2 coating thickness	-	-	49.77	65.20	37.89	5.23	153
Ag inside	98	-	27.01	59.51	10.43	9.28	153
Ag free	2	-	29.92	38.99	23.47	8.08	3

G.12.1 Significance of differences

To ascertain if there was any difference in the sizes of the particles following exposure to SSL for 6 h, unpaired t-tests were used comparing the data presented in Table G.49 (before SSL exposure) with that in Table 6-6. The results that were significantly different are given in Table G.53. When the measurement uncertainty of about 6 % (see Table E.1) is taken into consideration the difference in the size of the single-cored particles is within the measurement uncertainty (≈ 8 nm). However for the Ag inside NPs the 6 % uncertainty in the measurement gives a value of 2 nm for the uncertainty so the 9.72 nm average reduction in size of the NP inside the SiO_2 shell is likely to be truly significant. This reduction was slightly greater than the ≈ 7 nm seen after storage in the dark for ≈ 50 days (Table G.44). This suggests that the Ag NP is dissolving inside the shell on

exposure to SSL in a similar manner to the colloidal stability samples. Again, the increase in the relative number of multi-cored particles also supports this hypothesis. The thickness of the SiO_2 coating also reduced by ≈ 4 nm, suggesting that SSL is also causing the coating to dissolve. The increase in the percentage of free Ag NPs (from 0 % to 3 %) suggests that the SiO_2 coating may in addition, break apart with SSL exposure in a similar manner to the elevated temperature exposure samples.

The significant (just significant when the measurement uncertainty is taken into consideration) increase in the size of the SiO_2 only particles is interesting as it is in contrast to the idea that the SiO_2 is dissolving. However, as the Ag NPs are also dissolving inside the SiO_2 shell some of the increase in size of the SiO_2 only NPs may be due to NPs that once contained Ag cores now no longer containing Ag and being hence classified as SiO_2 only (the SiO_2 only NPs tend to be smaller than the Ag single-cored NPs).

Table G.53 Two-sample un-paired t-test results for TEM analysis of SiO_2@Ag NPrs before and after exposure to SSL for 6 h (where sample 2 is significantly smaller than sample 1 the average difference is shown as positive).

Sample 1	**Sample 2**	**Particle type**	**Average difference /nm**	**Range of difference (at 95 % confidence) / nm**
SiO_2@Ag NPr, ¼ volume - Initial	SiO_2@Ag NPr, ¼ volume – After 6 h SSL	Single-cored	6.14	4.09 to 8.19
SiO_2@Ag NPr, ¼ volume - Initial	SiO_2@Ag NPr, ¼ volume – After 6 h SSL	SiO_2 only	-8.07	-9.84 to -6.30
SiO_2@Ag NPr, ¼ volume - Initial	SiO_2@Ag NPr, ¼ volume – After 6 h SSL	Ag inside	9.72	8.41 to 11.03
SiO_2@Ag NPr, ¼ volume - Initial	SiO_2@Ag NPr, ¼ volume – After 6 h SSL	Coating thickness	4.16	3.49 to 4.83

G.13 Effect of an Extra Purification Step on the SiO_2 Coated Nanoprisms (SiO_2@Ag NPrs)

In total 2 samples produced using an initial extra purification step and 3 samples with an additional purification step at the end of the coating procedure were analysed using TEM (see Figure 3-1 and Appendix N, Section N.1 for further experimental details).

The average results obtained for the two samples produced using an initial extra purification step are shown in Table G.54. The corresponding results for an additional final purification step are given in Table G.55. In both cases there were slightly more multi-cored NPs than for the optimised

Stöber process without extra purification (13 % for initial extra purification and 24 % for final extra purification compared to 8 % - see Table 6-2).

Table G.54 TEM analysis after SiO_2 coating using the optimised Stöber procedure and an extra initial purification step (SiO_2@Ag NPr – extra initial purification – average, *N* = 2).

Measurement type	**%**	**% excluding SiO_2 NPs**	**Average size / nm**	**Maximum / nm**	**Minimum / nm**	***σ* / nm**	***N***
Single-cored	34	88	123.97	178.60	68.60	18.19	175
Multi-cored	5	13	113.92	163.17	91.80	13.08	25
SiO_2 only	61	-	97.44	130.04	44.87	14.86	319
SiO_2 coating thickness	-	-	49.92	63.97	29.41	5.81	224
Ag inside	97	-	24.84	95.87	3.18	17.36	225
Ag free	3	-	13.48	25.08	7.89	6.28	6

Table G.55 TEM analysis after SiO_2 coating using the optimised Stöber procedure and an extra final purification step (SiO_2@Ag NPr – extra final purification step – average, *N* = 3).

Measurement type	**%**	**% excluding SiO_2 NPs**	**Average size / nm**	**Maximum / nm**	**Minimum / nm**	***σ* / nm**	***N***
Single-cored	39	76	136.86	192.00	114.49	13.74	89
Multi-cored	12	24	137.06	195.73	118.49	15.70	28
SiO_2 only	48	-	102.55	131.72	70.92	9.11	109
SiO_2 coating thickness	-	-	52.15	61.20	42.96	3.39	150
Ag inside	100	-	37.82	95.83	16.99	13.11	150

G.13.1 Significance of differences

To ascertain if there was any difference in the sizes of the particles with the addition of an extra purification step either at the start of the coating procedure or at the end of the process, unpaired t-tests were used comparing the data presented in Table 6-2 (optimised method no extra purification) with that presented in firstly Table G.54 (extra initial purification) and secondly with the data in Table G.55 (extra final purification). The results that were significantly different are presented in Table G.56 for the initial extra purification and in Table G.57 for the extra final purification.

For the extra initial purification there were some differences in size that were significant even when the measurement uncertainty was taken into consideration (see Table E.1). Both the single-cored and the multi-cored particles were smaller, the SiO_2 only particles were bigger and the size of the silver inside the SiO_2 coating was smaller. However, the thickness of the SiO_2 coating although significantly different was within the uncertainty of the measurement technique (< 2 nm difference). The reduction in size of the silver NPs inside the SiO_2 shell (and the corresponding

reduction in size of the single and multi-cored samples) may have been due to the initial starting NFs employed having values of λ_{max} at the bottom end of the range for SiO_2@Ag NPrs (806 nm and 828 nm for the two samples analysed using TEM).

Table G.56 Two-sample un-paired t-test results for TEM analysis of SiO_2@Ag NPrs (optimised Stöber process, no extra purification - Table 6-2) and SiO_2@Ag NPrs produced using an initial extra purification step (where sample 2 is significantly smaller than sample 1 the average difference is shown as positive).

Sample 1	**Sample 2**	**Particle type**	**Average difference /nm**	**Range of difference (at 95 % confidence) / nm**
SiO_2@Ag NPr, ¼ volume – no extra purification	SiO_2@Ag NPr, ¼ volume extra initial purification	Single-cored	10.46	7.72 to 13.20
SiO_2@Ag NPr, ¼ volume – no extra purification	SiO_2@Ag NPr, ¼ volume extra initial purification	Multi-cored	23.42	15.01 to 31.83
SiO_2@Ag NPr, ¼ volume – no extra purification	SiO_2@Ag NPr, ¼ volume extra initial purification	SiO_2 only	-9.77	-11.50 to -8.04
SiO_2@Ag NPr, ¼ volume – no extra purification	SiO_2@Ag NPr, ¼ volume extra initial purification	Ag inside	10.69	8.88 to 12.50
SiO_2@Ag NPr, ¼ volume – no extra purification	SiO_2@Ag NPr, ¼ volume extra initial purification	SiO_2 coating thickness	1.32	0.59 to 2.05

For the final extra purification, the only difference in size that was significant and of a greater magnitude than the uncertainty associated with the measurement technique was the size of the SiO_2 only NPs, which were smaller than expected (Table G.57).

Table G.57 Two-sample un-paired t-test results for TEM analysis of SiO_2@Ag NPrs (optimised Stöber process, no extra purification - Table 6-2) and SiO_2@Ag NPrs produced using a final extra purification step (where sample 2 is significantly smaller than sample 1 the average difference is shown as positive).

Sample 1	**Sample 2**	**Particle type**	**Average difference /nm**	**Range of difference (at 95 % confidence) / nm**
SiO_2@Ag NPr, ¼ volume – no extra purification	SiO_2@Ag NPr, ¼ volume extra final purification	SiO_2 only	-14.88	-17.66 to -12.10
SiO_2@Ag NPr, ¼ volume – no extra purification	SiO_2@Ag NPr, ¼ volume extra final purification	Ag inside	-2.29	-4.33 to -0.25
SiO_2@Ag NPr, ¼ volume – no extra purification	SiO_2@Ag NPr, ¼ volume extra final purification	SiO_2 coating thickness	-0.91	-1.74 to -0.08

G.14 Effect of MHA and DMA concentration on the SiO_2 coating process for SiO_2@Ag NPrs

This subsection presents the results obtained from the TEM analysis of SiO_2@Ag NPrs synthesised using no capping agent MHA, using a higher concentration of MHA, and finally, a lower concentration of the base DMA in the base catalysed step compared to the optimised Stöber coating procedure given in Section 3.6.4.

G.14.1 Using no capping agent MHA

Although two samples were produced using no MHA in the Stöber TEOS coating process it was only possible to analyse one of these due to significant clumping of the NPs for the other sample. The sample that was analysed was produced using no MHA and ¼ the normal concentration of DMA. The results in Table G.58 show a high percentage of multi-cored NPs, and a large variation in thickness of the SiO_2 coating (average value 36.66 nm). There was also significant clumping of the NPs observed and some larger dendritic silver particles (not shown in the analysis). The clumping made the micrographs hard to analyse resulting in a lower number of measured NPs.

Table G.58 TEM analysis after SiO_2 coating using no MHA and ¼ concentration of DMA (SiO_2@Ag NPrs, 0 MHA, ¼ concentration DMA).

Measurement type	**%**	**% excluding SiO_2 NPs**	**Average size / nm**	**Maximum / nm**	**Minimum / nm**	***σ* / nm**	***N***
Single-cored	23	25	67.45	91.08	52.06	16.11	5
Multi-cored	68	75	127.38	265.22	41.82	88.53	15
SiO_2 only	9	-	16.16	16.21	16.10	0.07	2
SiO_2 coating thickness	-	-	37.63	98.74	4.62	36.66	42
Ag inside	86	-	35.15	87.77	13.83	14.41	83
Ag free	14	-	23.22	34.34	11.38	8.09	13

G.14.2 SiO_2 coated silver nanoprisms produced using a higher concentration of MHA

Three samples of SiO_2@Ag NPrs, produced using a higher concentration of 160 µM MHA were analysed using TEM. The average values obtained from these three samples are shown in Table G.59. Two sample t-tests were used to compare the results with those obtained using the normal concentration of 40 µM MHA and an initial purification at the end of the process (40 µM results in Table G.55). These showed no significant differences in the values obtained. Increasing the molarity of MHA used to 160 µM MHA has therefore not changed the morphology of the SiO_2@Ag NPrs.

Table G.59 TEM analysis after SiO_2 coating using 160 µM MHA and an additional purification step at the end of the process. Average results from 3 separate samples.

Measurement type	**%**	**% excluding SiO_2 NPs**	**Average size / nm**	**Maximum / nm**	**Minimum / nm**	***σ* / nm**	***N***
Single-cored	38	83	134.13	169.53	111.08	12.26	133
Multi-cored	8	17	138.05	168.66	115.68	17.36	28
SiO_2 only	55	-	103.45	132.83	70.76	10.68	193
SiO_2 coating thickness	-	-	51.99	63.58	39.49	4.62	202
Ag inside	98	-	38.07	73.99	12.97	12.38	194
Ag free	2	-	23.07	26.26	17.88	3.93	4

G.14.3 SiO_2 coated silver nanoprisms produced using a lower concentration of DMA

The results of undertaking TEM analysis of SiO_2@Ag NPrs produced using ¼ the concentration of DMA and the normal 40 µM MHA are shown in Table G.60. The SiO_2 coating produced was inconsistent (ranged from 6.54 nm – 74.24 nm) but on average thinner at 12.40 nm than seen at the normal DMA concentration (significant difference according to a two sample t-test), and the percentage of free (uncoated) Ag NPs was greater. The amount of SiO_2 only NPs was also considerably less than seen previously. It should be noted that aggregation of the NPs was observed on the micrographs, making them difficult to analyse accurately.

Table G.60 TEM analysis after SiO_2 coating using 40 µM MHA and ¼ volume of DMA.

Measurement type	**%**	**% excluding SiO_2 NPs**	**Average size / nm**	**Maximum / nm**	**Minimum / nm**	***σ* / nm**	***N***
Single-cored	69	73	59.65	163.83	38.30	17.26	72
Multi-cored	26	27	56.31	102.90	32.38	16.25	27
SiO_2 only	6	-	46.53	160.09	17.05	55.90	6
SiO_2 coating thickness	-	-	12.40	74.24	6.54	6.01	121
Ag inside	89	-	33.67	82.19	13.77	12.38	126
Ag free	11	-	25.44	74.25	10.80	15.03	15

The results of carrying out TEM analysis on the sample produced using the lower ¼ concentration DMA but a higher MHA concentration of 160 µM MHA are given in Table G.61. On comparing (via a t-test) with the sample produced using 40 µM MHA and the lower DMA concentration (Table G.60) there were no significant differences in the size of the NPs or the coating thickness. However, unlike previously the coating thickness was not as inconsistent (range 7.75 nm – 20.80 nm). Again aggregation of the NPs was observed making the micrographs difficult to analyse.

Table G.61 TEM analysis after SiO_2 coating using 160 μM MHA and ¼ volume of DMA.

Measurement type	**%**	**% excluding SiO_2 NPs**	**Average size / nm**	**Maximum / nm**	**Minimum / nm**	***σ* / nm**	***N***
Single-cored	46	68	63.04	96.99	32.64	14.58	53
Multi-cored	22	32	59.36	83.86	43.64	10.21	25
SiO_2 only	32	-	28.72	48.99	17.72	7.72	37
SiO_2 coating thickness	-	-	13.34	20.80	7.75	3.22	107
Ag inside	87	-	34.30	68.89	11.86	12.22	107
Ag free	13	-	22.23	35.01	8.64	9.01	16

G.15 SiO_2 Coated Silver Nanoprisms Produced Using Shorter Reaction Times

This subsection details the results obtained following the TEM analysis of SiO_2@Ag NPrs produced using shorter TEOS reaction times of 1 minute and 5 minutes. Firstly, the results obtained just after synthesis are detailed, with Table G.62 giving the results for the 1 minute reaction time and Table G.63 the 5 minute reaction time. The results following exposure to a temperature of 70 °C for 18 h for both the 1 minute and 5 minute reaction times are then given.

Varying the reaction time produced a thinner SiO_2 coating, with the 1 minute reaction time giving a coating thickness of 11.77 nm (σ = 3.79 nm, N = 187) and the 5 minute reaction time 28.40 nm (σ = 3.75 nm, N = 137). These were both significantly less (using ANOVA testing) than the average results obtained using a 30 minute reaction time of 51.24 nm (Table G.64). However, the rate of increase of the thickness was non-linear with the thickness of the coating increasing rapidly over the first 5 minutes to reach a value of ≈ ½ that obtained after 30 minutes. The percentage of multi-cored NPs appeared in both cases to be slightly greater than seen for the 30 minute reaction time at 12 % (1 minute reaction time) and 23 % (5 minute reaction time) compared to the average percentage obtained after 30 minutes of 8 %.

Table G.62 TEM analysis after SiO_2 coating using a TEOS reaction time of 1 minute, as synthesised.

Measurement type	**%**	**% excluding SiO_2 NPs**	**Average size / nm**	**Maximum / nm**	**Minimum / nm**	***σ* / nm**	***N***
Single-cored	49	88	68.93	114.71	30.81	16.04	147
Multi-cored	7	12	67.99	88.66	33.88	15.96	20
SiO_2 only	44	-	38.34	77.70	14.63	13.49	132
SiO_2 coating thickness	-	-	11.77	25.93	5.36	3.79	187
Ag inside	98	-	45.04	91.66	9.78	15.70	185

Measurement type	%	% excluding SiO_2 NPs	Average size / nm	Maximum / nm	Minimum / nm	σ / nm	*N*
Ag free	2	-	29.39	39.47	22.11	7.28	4

Table G.63 TEM analysis after SiO_2 coating using a TEOS reaction time of 5 minutes, as synthesised.

Measurement type	%	% excluding SiO_2 NPs	Average size / nm	Maximum / nm	Minimum / nm	σ / nm	*N*
Single-cored	30	77	102.79	152.09	67.18	18.00	85
Multi-cored	9	23	105.43	147.04	66.93	17.40	25
SiO_2 only	62	-	69.58	111.97	36.25	17.23	176
SiO_2 coating thickness	-	-	28.40	39.08	20.21	3.75	137
Ag inside	97	-	39.15	84.48	9.48	13.31	145
Ag free	3	-	29.71	48.48	19.49	11.06	5

Table G.64 ANOVA results for the thickness of the SiO_2 coating in descending order of thickness, for samples produced using different TEOS reaction times. The 30 minute reaction time values are from Table 6-2. Groups that do not share a letter are significantly different.

TEOS Reaction time / minutes	Mean SiO_2 thickness / nm	Range of thickness (at 95 % confidence) / nm	*N*	Grouping
30	51.24	50.99 to 51.49	1449	A
5	28.40	27.59 to 29.12	137	B
1	11.77	11.08 to 12.47	187	C

After exposure to a temperature of 70 °C for 18 h the Ag NPrs were no longer SiO_2 coated. Hence the TEM results were analysed in the same manner as used for the uncoated Ag NPrs, dividing the type of particles into four groups, triangles, rounded cornered triangles, other and small. The results for both the two reaction times of 1 minute and 5 minutes are given in Table G.65, with a graphical summary provided in Figure G.4. Also shown in Figure G.4 is the results obtained for the Ag TSCD-PVP NPr (long λ) NF after 4 h at 70 °C for comparison (temperature testing carried out with a similar but slightly larger Ab_{max} value). The results for the 1 minute and 5 minute reaction times were similar but they contained more small NPs than the long λ NF. However, some of small NPs measured may have been SiO_2 NPs from the dissolution of the SiO_2 coating rather than Ag NPs so this difference should be treated with caution.

Table G.65 TEM analysis after SiO_2 coating using a TEOS reaction time of 1 minute or 5 minutes, after 18 h at 70 °C.

Sample	Particle shape	%	Average size / nm	σ / nm	*N*
SiO_2@Ag NPrs, 1 minute TEOS, after 18 h at 70 °C	Triangle	10	54.49	13.33	60

Sample	Particle shape	%	Average size / nm	σ / nm	*N*
SiO_2@Ag NPrs, 1 minute TEOS, after 18 h at 70 °C	Rounded cornered triangle	23	35.15	11.21	140
SiO_2@Ag NPrs, 1 minute TEOS, after 18 h at 70 °C	Other	39	27.34	12.29	242
SiO_2@Ag NPrs, 1 minute TEOS, after 18 h at 70 °C	Small < 10 nm	28	6.56	1.83	175
SiO_2@Ag NPrs, 5 minutes TEOS, after 18 h at 70 °C	Triangle	9	58.89	10.89	49
SiO_2@Ag NPrs, 5 minutes TEOS, after 18 h at 70 °C	Rounded cornered triangle	30	40.46	10.24	155
SiO_2@Ag NPrs, 5 minutes TEOS, after 18 h at 70 °C	Other	34	28.20	10.69	174
SiO_2@Ag NPrs, 5 minutes TEOS, after 18 h at 70 °C	Small < 10 nm	27	6.24	1.51	140

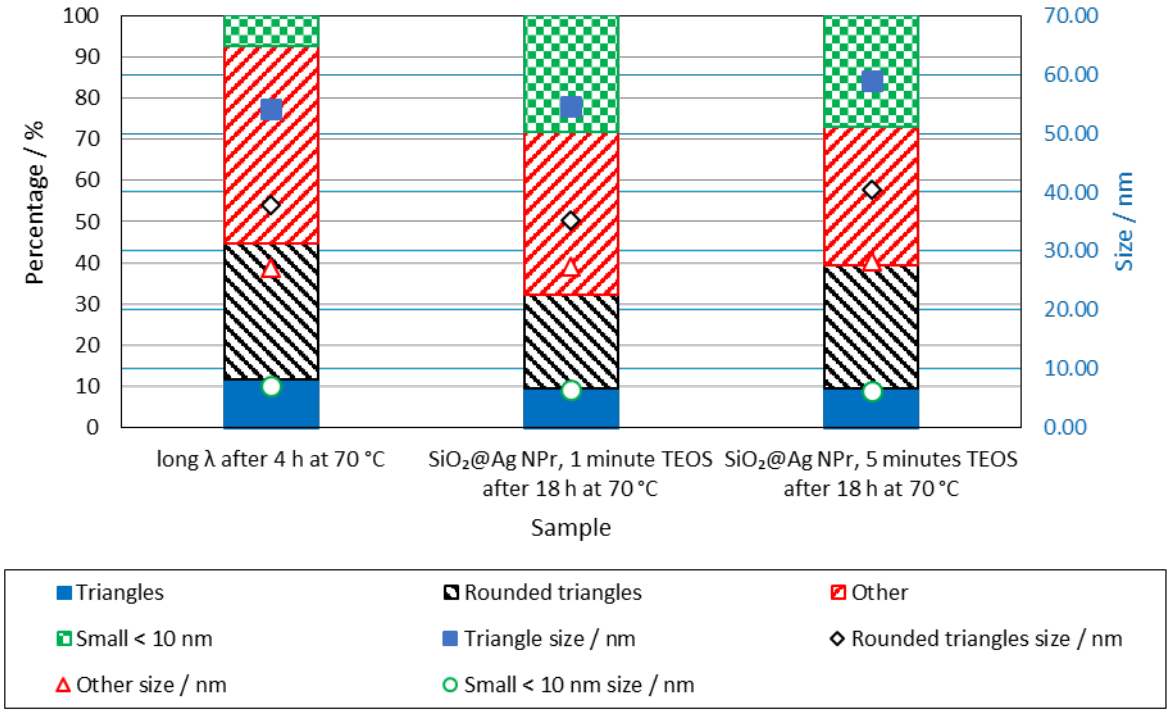

Figure G.4 Summary of TEM analysis after 18 h at 70 °C for the SiO_2@Ag NPrs produced using a TEOS reaction time of 1 minute and 5 minutes (also shown is the results for Ag TSCD-PVP NPrs (long *λ*) after 4 h at 70 °C from Figure 5-5 for comparison).

G.16 SiO_2 Coated Broadband Nanofluid (SiO_2@broadband)

The results of the TEM analysis of the SiO_2@broadband NF are given in Table G.66. Compared to the results obtained for the optimised Stöber coating procedure (Table 6-2), the percentage of multi-cored NPs was greater (52 % versus 8 %) and the amount of SiO_2 only NPs less (13 % versus 61 %).

Table G.66 TEM analysis after SiO_2 coating for the SiO_2@broadband NF.

Measurement type	**%**	**% excluding SiO_2 NPs**	**Average size / nm**	**Maximum / nm**	**Minimum / nm**	***σ* / nm**	***N***
Single-cored	42	48	113.13	169.45	91.71	11.36	70
Multi-cored	45	52	119.45	148.25	96.33	10.07	75
SiO_2 only	13	-	93.71	103.69	80.47	7.17	22
SiO_2 coating thickness	-	-	50.62	66.69	34.88	4.42	199
Ag inside	97	-	14.71	61.66	6.32	6.81	220
Ag free	3	-	11.79	15.88	9.00	2.35	6

G.16.1 Significance of differences

To ascertain if there were any differences in the size of the various classifications of NPs compared to the SiO_2@Ag NPrs, un-paired two sample t-tests were carried out comparing the results presented in Table G.66 with those given in Table 6-2. The results are given in Table G.67 (only the significantly different results are shown). The thickness of the SiO_2 coating was the same as was the size of the SiO_2 only NPs. As expected (the broadband absorber initial NF contained a greater number of smaller Ag NPs), the size of the single-cored, multi-cored, Ag inside and Ag free NPs were all significantly smaller for the SiO_2@broadband NF compared to the SiO_2@Ag NPr NF.

Table G.67 Two-sample un-paired t-test results for TEM analysis of SiO_2@broadband NF compared to SiO_2@Ag NPrs produced using the developed Stöber TEOS method (Table 6-2). Where sample 2 is significantly smaller than sample 1 the average difference is shown as positive.

Sample 1	**Sample 2**	**Particle type**	**Average difference /nm**	**Range of difference (at 95 % confidence) / nm**
SiO_2@Ag NPr, ¼ volume - Initial	SiO_2@broadband	Single-cored	21.30	17.22 to 25.38
SiO_2@Ag NPr, ¼ volume - Initial	SiO_2@broadband	Multi-cored	17.89	12.90 to 22.88
SiO_2@Ag NPr, ¼ volume - Initial	SiO_2@broadband	Ag inside	20.82	19.19 to 22.45

Appendix H Additional Information on Investigating Silver Nanoparticle Synthesis and Broadband Absorber

This Appendix presents additional results from the investigation into the Ag NP synthesis aimed at developing 2 additional recipes, one for a short λ NF ($\lambda_{max} \approx 500$ nm), the other a mid λ NF (λ_{max} = 650 nm – 750 nm). It also details the results of calculating η_{Ab} for the developed short, mid and long λ NFs. To select the optimum broadband mixture using these component NFs, η_{Ab} for a number of different combinations was estimated and the results are shown in this Appendix. To check if the synthesis method used for the short λ NF was the right choice η_{Ab} for the optimum broadband mixture using the three possible short λ NFs was then assessed. Finally, this Appendix details the results of the η_{Ab} calculations for the actual measured broadband absorber and its component NFs.

H.1 Effect of overall concentration

The experiments investigating the effect of overall concentration are detailed in Table H.1. The synthesis for the 0.1 mM Ag TSCD-PVP NPr sample was identical to the synthesis described in Section 3.5.3 except that a batch volume of 25 mL was used. This lower batch volume was utilised for all the other samples investigating concentration and the amount of each of the reagents increased proportionally to produce the other three samples. In all cases the ratio of Ag: $NaBH_4$ was kept the same at 1: 10. All other experimental parameters (for example stirring rate and timing of reagent addition) were also kept as consistent as possible.

The UV-vis results for the four samples are shown in Figure H.1. In all cases the spectrophotometer used was UV-vis-1 with a 10 mm path length 3 mL disposable cuvette. To prevent saturation of the detector samples > 0.1 mM Ag were diluted prior to measurement. The dilution and dilution ratios used are given in Table H.1.

Table H.1 Details of experiments investigating effect of overall concentration.

Sample	**0.1 mM Ag TSCD-PVP NPr 25 mL**	**0.2 mM Ag TSCD-PVP NP 25 mL**	**0.3 mM Ag TSCD-PVP NP 25 mL**	**0.4 mM Ag TSCD-PVP NP 25 mL**
Amount of Ag / mM	0.1	0.2	0.3	0.4
H_2O_2 amount in 25 mL batch / mL	0.125	0.25	0.375	0.5

Sample	**0.1 mM Ag TSCD-PVP NPr 25 mL**	**0.2 mM Ag TSCD-PVP NP 25 mL**	**0.3 mM Ag TSCD-PVP NP 25 mL**	**0.4 mM Ag TSCD-PVP NP 25 mL**
$NaBH_4$ amount / mM	1	2	3	4
TSCD amount / mM	1.5	3	4.5	6
PVP amount / mM	0.01	0.02	0.03	0.04
Dilution used for UV-vis-1 measurement	none	1.5 mL in 3 mL	1 mL in 3 mL	0.75 mL in 3 mL
Dilution ratio	1: 1	1: 2	1: 3	1: 4

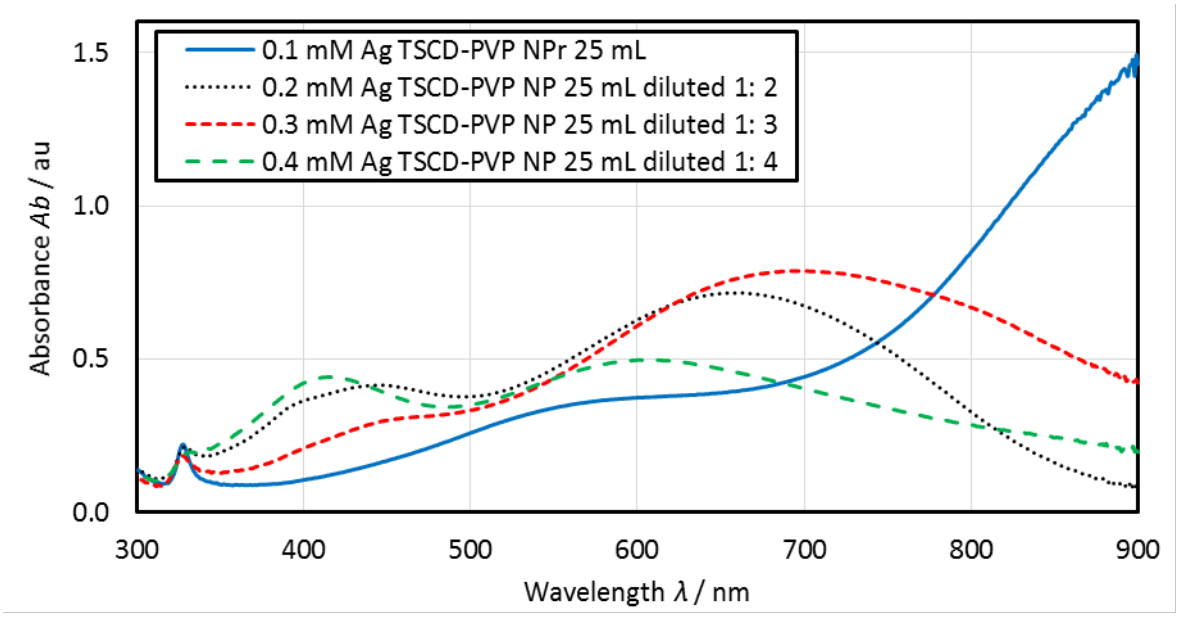

Figure H.1 UV-vis spectra showing the effect of overall reagent concentration on the resultant NPs. All measured with a 10 mm path length cuvette on UV-vis-1. Samples with a starting Ag concentration > 0.1 mM have been diluted prior to measurement.

At the initial reagent concentration of 0.1 mM Ag, λ_{max} was > 900 nm and Ab_{max} was > 1.4 au. As the concentration of reagents increased λ_{max} blue-shifted and Ab_{max} dropped with the spectra broadening. A second peak at ≈ 400 nm also started to appear when the concentration was raised. Ab_{max} for this second peak was almost as high as the primary peak at the highest reagent concentration (0.4 mM Ag). Other researchers also observed the presence of two peaks in their UV-Vis spectra when the silver reagent concentration was increased (Walshe et al., 2019), with an alternative seeded synthesis method using polyvinyl alcohol as a stabilising agent. The inability to produce nanoparticles with a λ_{max} > 800 nm at higher reagent concentrations is in contrast to the NS synthesis discussed in Section 4.3 and suggests that controlling the morphology of the resultant NPs for the NPrs synthesis to produce a peak at λ_{max} > 800 nm is likely to be problematic due to a complex relationship between each of the reagents during the synthesis, which is affected not only by the ratio of the various reagents to each other but also by their overall concentrations in the solution.

H.2 Effect of amount of hydrogen peroxide

The experimental details looking at the effect of changing the amount of H_2O_2 are given in Table H.2. The first sample is the same recipe as that detailed in Section 3.5.3 using PVP but with a batch volume of 25 mL, and the identical recipe as the first sample in Table H.1. The last sample in Table H.2 uses a similar recipe to the NS synthesis detailed in Section 3.5.2 with a starting Ag molarity of 0.1 mM, containing PVP, but with a smaller batch volume of 25 mL and a larger Ag: $NaBH_4$ ratio of 1: 10 rather than the 1: 4 ratio used in Section 3.5.2.

Table H.2 Experiments investigating changing the amount of H_2O_2 – Batch size 25 mL.

Sample	**Amount of Ag / mM**	**PVP amount / mM**	**$NaBH_4$ amount / mM**	**H_2O_2 amount / mL**	**H_2O_2 amount relative to Section 3.5.3 Ag TSCD-PVP NPr recipe / %**
0.1 mM Ag TSCD-PVP NPr 25 mL 100 % H_2O_2	0.1	0.01	1	0.125	100
0.1 mM Ag TSCD-PVP NPr 25 mL 80 % H_2O_2	0.1	0.01	1	0.100	80
0.1 mM Ag TSCD-PVP NPr 25 mL 60 % H_2O_2	0.1	0.01	1	0.075	60
0.1 mM Ag TSCD-PVP NP 25 mL 40 % H_2O_2	0.1	0.01	1	0.050	40
0.1 mM Ag TSCD-PVP NP 25 mL 20 % H_2O_2	0.1	0.01	1	0.025	20
0.1 mM Ag TSCD-PVP NP 25 mL 0 % H_2O_2 (Ag TSCD-PVP NS)	0.1	0.01	1	0.000	0

When the amount of H_2O_2 was changed, there was a blue-shift in the absorbance spectra (see Figure H.2). However, even with the 20 % H_2O_2 sample the absorption peak was still > 700 nm and Ab_{max} had dropped from 1.47 au for the 100 % H_2O_2 sample to 0.91 au. When the relationship between H_2O_2 amount and the position of λ_{max} and height of Ab_{max} were investigated further it was found that there was a linear relationship between Ab_{max} and H_2O_2 amount (R^2 = 0.99), with Ab_{max} dropping as the amount of H_2O_2 was reduced. However, although a linear line could be plotted for the λ_{max} versus H_2O_2 relationship, the line fit was extremely poor (R^2 = 0.76). It was therefore not possible to produce a NF with a high Ab_{max} at a λ_{max} of ≈ 500 nm just by varying the H_2O_2 level.

When no H_2O_2 was used, NS were produced with a λ_{max} of 399 nm and an Ab_{max} of 0.76 au. This value of λ_{max} was similar to the average value of 402 nm for the TSCD-PVP NS samples in Figure 4-1. A λ_{max} at ≈ 400 nm has been attributed by others to the formation of NS (Paramelle et al., 2014a; Zhang et al., 2011).

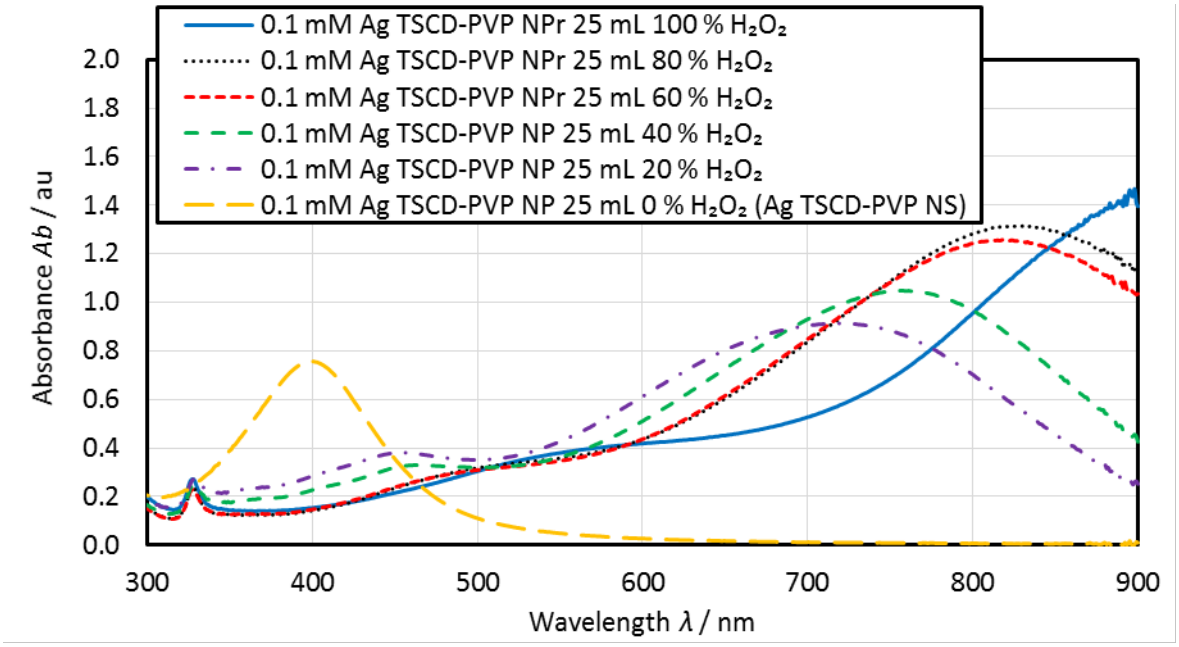

Figure H.2 Effect of varying the amount of H_2O_2 on the UV-vis spectra. All samples measured using a 10 mm path length cuvette and UV-vis-1.

H.3 Effect of varying the silver to reducing agent ratio

The experiments carried out to investigate the effect of changing the Ag: $NaBH_4$ ratio are detailed in Table H.3. Firstly, the effect of halving the Ag: $NaBH_4$ ratio from 1: 10 to 1: 5 was determined for the same range of Ag starting concentrations of 0.1 mM to 0.4 mM as used in Section H.1 (first four samples in Table H.3).

Table H.3 Details of experiments undertaken to investigate the effect of Ag: $NaBH_4$ ratio. Batch size = 25 mL.

Sample	**Amount of Ag / mM**	**PVP amount / mM**	**$NaBH_4$ amount / mM**	**Ratio of Ag: $NaBH_4$**	**H_2O_2 amount / mL**	**H_2O_2 amount relative to Section 3.5.3 Ag TSCD-PVP NPr recipe / %**
0.1 mM Ag TSCD-PVP NP, 1: 5, 100 % H_2O_2	0.1	0.01	0.5	1: 5	0.125	100
0.2 mM Ag TSCD-PVP NP, 1: 5, 100 % H_2O_2	0.2	0.02	1.0	1: 5	0.250	100
0.3 mM Ag TSCD-PVP NP, 1: 5, 100 % H_2O_2	0.3	0.03	1.5	1: 5	0.375	100
0.4 mM Ag TSCD-PVP NP, 1: 5, 100 % H_2O_2	0.4	0.04	2.0	1: 5	0.500	100
0.3 mM Ag TSCD-PVP NP, 1: 3.75, 100 % H_2O_2	0.3	0.03	1.125	1: 3.75	0.375	100
0.3 mM Ag TSCD-PVP NP, 1: 2.5, 100 % H_2O_2	0.3	0.03	0.75	1: 2.5	0.375	100

Sample	Amount of Ag / mM	PVP amount / mM	$NaBH_4$ amount / mM	Ratio of Ag: $NaBH_4$	H_2O_2 amount / mL	H_2O_2 amount relative to Section 3.5.3 Ag TSCD-PVP NPr recipe / %
0.3 mM Ag TSCD-PVP NP, 1: 5, 50 % H_2O_2	0.3	0.03	1.5	1: 5	0.185	50
0.3 mM Ag TSCD-PVP NP, 1: 5, 20 % H_2O_2	0.3	0.03	1.5	1: 5	0.075	20

Secondly, the effect of reducing the Ag: $NaBH_4$ ratio still further was investigated using a Ag starting concentration of 0.3 mM (samples 5 and 6 in Table H.3). Finally, the effect of reducing the amount of H_2O_2 added at the 1: 5 Ag: $NaBH_4$ ratio and a starting Ag molar concentration of 0.3 mM was assessed (samples 7 and 8). In all cases the batch volume used was 25 mL and the samples were measured using UV-vis-1 with a 10 mm path length, 3 mL disposable cuvette. Samples with a Ag molarity of > 0.1 mM were diluted prior to measurement in the same fashion as the samples in Table H.1.

The results for the 1: 5 Ag: $NaBH_4$ ratio samples using different starting molarities of Ag are shown in Figure H.3. When the ratio was halved at the lowest Ag starting concentration, two low peaks at λ_{max} ≈ 394 nm and 592 nm were produced. This result was very different to the result obtained with an Ag: $NaBH_4$ ratio of 1: 10 of one large peak at > 900 nm and was similar to that seen with the higher starting Ag concentration of 0.4 mM in Figure H.1. As the starting concentration of Ag was further increased there was a large blue-shift in the position of λ_{max} and an initial rise in the value of Ab_{max}. This shift in the position of λ_{max} was not consistent with the 0.2 mM sample having a λ_{max} of 778 nm (Ab_{max} = 1.540 au) and the 0.3 mM sample having a λ_{max} of 681 nm with an Ab_{max} of 1.286 au. Increasing the starting Ag concentration still further resulted in a drop in Ab_{max} to 0.739 au and a λ_{max} of 773 nm. The 0.3 mM sample would provide a suitable recipe for the mid λ NF with a λ_{max} in the 650 nm - 750 nm range and a high enough Ag concentration to allow for it to be combined without further processing.

When the Ag: $NaBH_4$ ratio was reduced further at this 0.3 mM Ag starting concentration λ_{max} blue-shifted to ≈ 400 nm (see Figure H.4) and Ab_{max} dropped to < 1 au. Again, the relationship between amount of $NaBH_4$ and λ_{max} and Ab_{max} was non-linear (linear plots of λ_{max} and Ab_{max} versus Ag: $NaBH_4$ ratio at 0.3 mM Ag concentration gave low values of R^2 of 0.61 and 0.18 respectively). This again emphasizes the complex nature of the reaction. Reducing the amount of H_2O_2 at the Ag: $NaBH_4$ ratio of 1: 5 also had the effect of initially blue-shifting λ_{max} to 616 nm, with a corresponding slight reduction in Ab_{max} to 1.22 au. Although the Ab_{max} value may make this a suitable recipe for the mid λ NF it is slightly outside the ideal range of 650 nm – 750 nm. As the amount of H_2O_2 was reduced still further to 20 % the blue-shift continued, but the height of the

primary peak reduced and a second peak at ≈ 400 nm became apparent. It was therefore not possible to identify a suitable recipe for the third short λ range NF from these experiments.

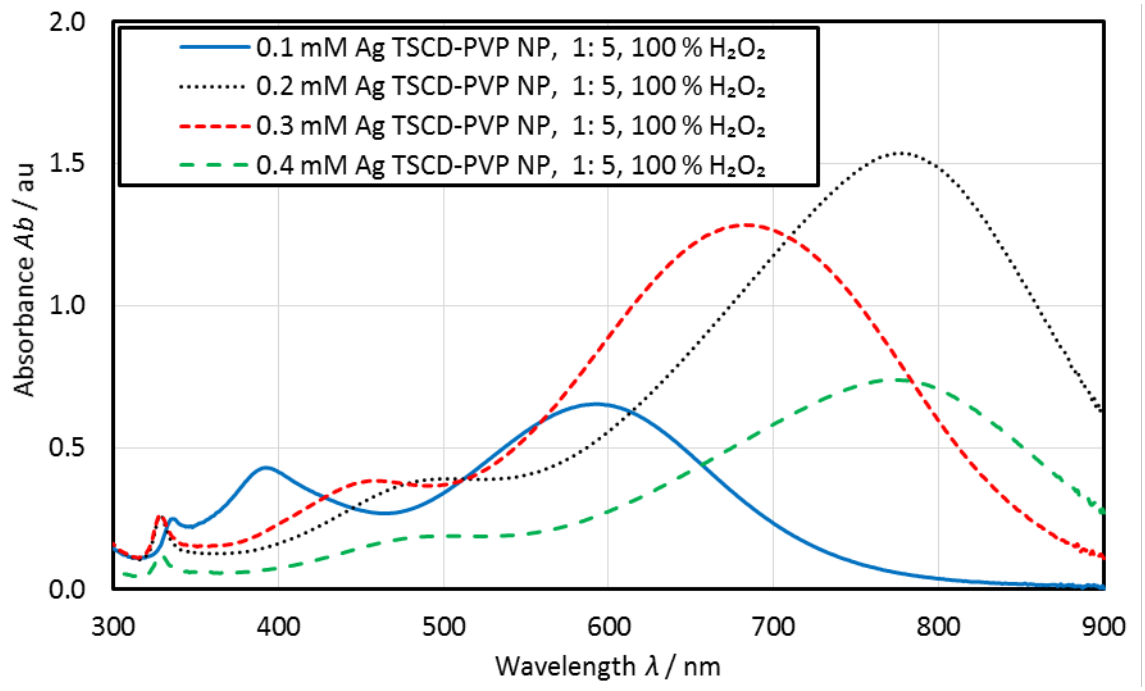

Figure H.3 Effect of a 1: 5 Ag: $NaBH_4$ ratio at different overall starting concentrations of Ag. All samples using an Ag: $NaBH_4$ ratio of 1: 5 and the same relative amount of H_2O_2 as the TSCD-PVP NPr recipe in Section 3.5.3. All measured on the UV-vis-1 spectrophotometer using a 10 mm path length 3 mL disposable cuvette. Samples with a starting Ag concentration of > 0.1 mM have been diluted.

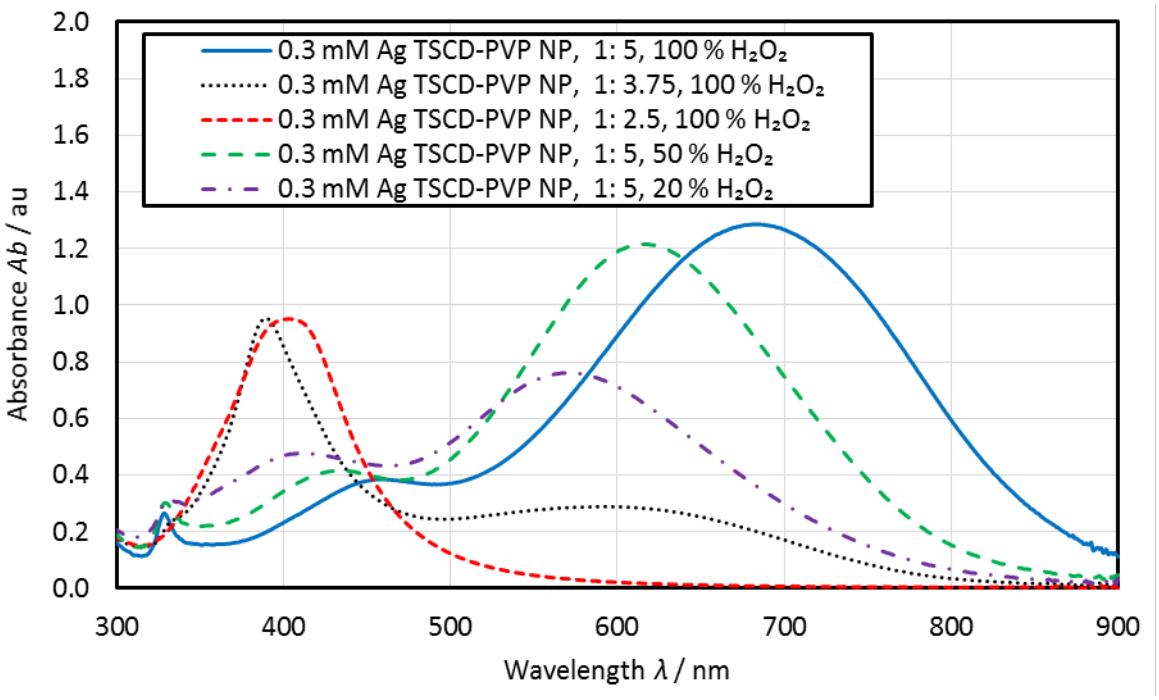

Figure H.4 UV-vis spectra showing the effect of varying the Ag: $NaBH_4$ ratio and the amount of H_2O_2 using a starting Ag concentration of 0.3 mM Ag. All measured using UV-vis-1 and a 10 mm path length 3 mL disposable cuvette. All samples diluted in the ratio 1: 3.

It was also noted that the reaction time shortened as the Ag: $NaBH_4$ ratio was reduced, with the 1: 5 ratio leading to a reaction time of ≈ 15 minutes rather than 30 minutes and the 1: 2.5

Ag: $NaBH_4$ reacting in about 8 minutes. This is consistent with the findings of Zhang et al (Zhang et al., 2011) who found that adding more $NaBH_4$ slowed the nucleation rate of the NPs leading to longer reaction times.

H.4 Timing of $NaBH_4$ Addition

To investigate the addition of more $NaBH_4$ to an already produced NF, 2 mL of the produced NF was taken and successive aliquots of 0.01 mL of 25 mM $NaBH_4$ solution were added. This had the effect of changing the final Ag and $NaBH_4$ molarity as well as the Ag: $NaBH_4$ ratio. The resultant new molarities, Ag: $NaBH_4$ ratio, λ_{max} and Ab_{max}, starting with a seed solution of 0.3 mM Ag TSCD-PVP NP, 1: 5 Ag: $NaBH_4$ ratio, 100 % H_2O_2 are given in Table H.4.

Table H.4 Details of samples investigating the timing of $NaBH_4$ addition, starting with seed = 0.3 mM Ag TSCD-PVP NP, 1: 5, 100 % H_2O_2 (mid λ). All samples have been diluted 1: 3 prior to UV-vis measurement using a 10 mm, 1 mL disposable cuvette on UV-vis-1.

Number of increments of 0.01 mL, 25 mM $NaBH_4$ solution	**Final Ag Molarity / mM**	**Final $NaBH_4$ Molarity / mM**	**Ag: $NaBH_4$ ratio**	**λ_{max} / nm**	**Ab_{max} / au**
0	0.300	1.500	1: 5	681	1.286
1	0.299	1.617	1: 5.4	618	1.208
2	0.297	1.733	1: 5.8	576	1.168
3	0.296	1.847	1: 6.3	550	1.177
4	0.294	1.961	1: 6.7	537	1.177
5	0.293	2.073	1: 7.1	529	0.957
6	0.291	2.184	1: 7.5	512	0.740
7	0.290	2.295	1: 7.9	498	0.640
8	0.288	2.404	1: 8.3	469	0.488
9	0.287	2.512	1: 8.8	450	0.508
10	0.286	2.619	1: 9.2	441	0.492

When more $NaBH_4$ was added to a seed solution comprising of 0.3 mM Ag TSCD-PVP, 1: 5 Ag: $NaBH_4$, 100 % H_2O_2 (the recipe suitable for the mid λ NF identified in Section H.3) a blue-shift in λ_{max} was observed (Figure H.5), with λ_{max} shifting from 681 to 618 nm and Ab_{max} dropping slightly from 1.286 au to 1.208 au when one aliquot of $NaBH_4$ was added.

This initial effect was surprising and similar to that obtained when less H_2O_2 was used in the recipe (compare Figure H.4 and Figure H.5). This again emphasizes the complex nature of the synthesis reaction, with $NaBH_4$ normally acting as the reducing agent, whereas H_2O_2 acts as an oxidising agent to selectively etch the surface of the developing NP. As more $NaBH_4$ was added, λ_{max} was further blue-shifted. The level of blue-shift continued as more $NaBH_4$ was added and

Ab_{max} started to reduce, with Ab_{max} more than halving to a value of 0.492 au and λ_{max} blue-shifting to a value of 441 nm after the addition of 10 aliquots of $NaBH_4$. Plots of total Ag: $NaBH_4$ ratio versus λ_{max} and versus Ab_{max} (Figure H.6) produced a reasonable linear fit (R^2 = 0.94 for λ_{max} and 0.91 for Ab_{max}). The 10 aliquot sample had reached the target value of ≈ 500 nm for the short λ NF but the reduction in Ab_{max} made this a non-ideal synthesis recipe for the production of the short λ NF with a high level of absorbance at 500 nm.

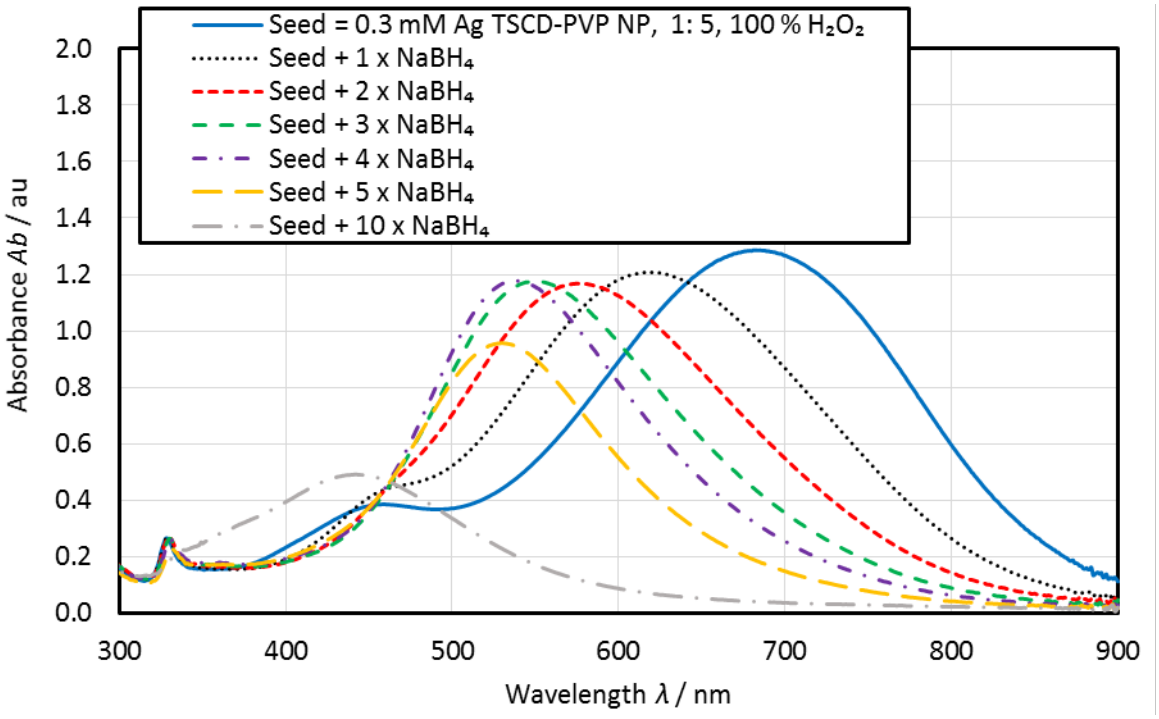

Figure H.5 Effect of adding $NaBH_4$ to an already synthesised seed NF. Seed = 0.3 mM Ag TSCD-PVP NP, 1: 5 Ag: $NaBH_4$, 100 % H_2O_2. Each aliquot of $NaBH_4$ is 0.01 mL of 25 mM solution into an original starting volume of 2 mL. Samples were diluted 1: 3 and measured using a 10 mm path length 1 mL micro cuvette using UV-vis-1.

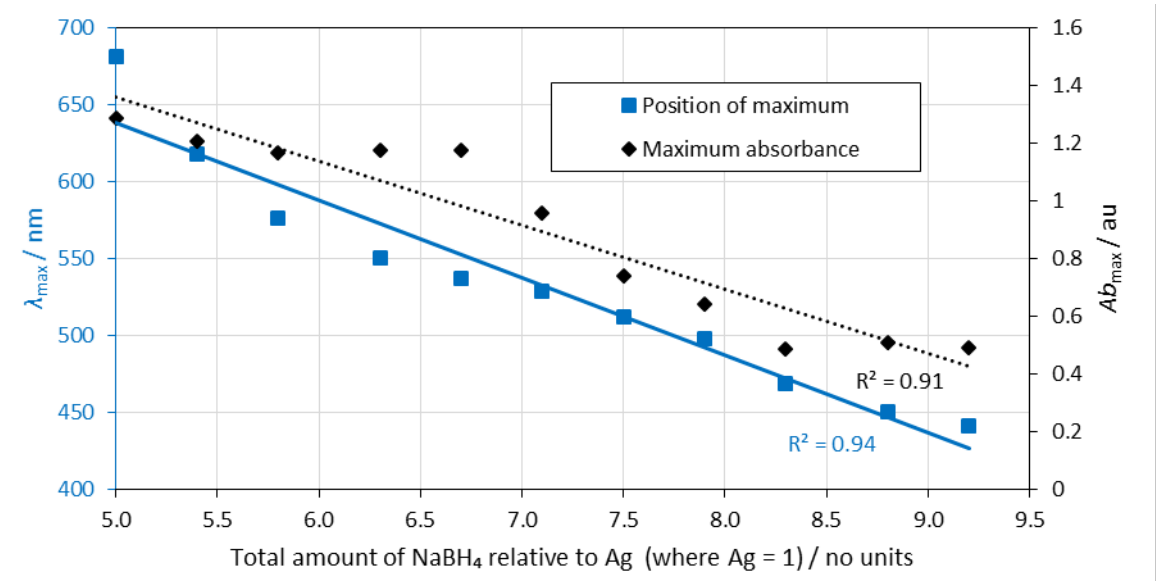

Figure H.6 The relationship between the total amount of $NaBH_4$ (relative to Ag amount), λ_{max} and Ab_{max} for a starting seed of 0.3 mM Ag TSCD-PVP NP, 1: 5, 100 % H_2O_2 (mid λ).

Adding more $NaBH_4$ to an already produced seed NF had the same effect of blue-shifting λ_{max} when different starting seeds were used (Table H.5, Figure H.7 and Figure H.8).

However, for one of the seeds (Seed Z = 0.4 mM Ag TSCD-PVP NP, 1: 5 Ag: $NaBH_4$, 100 % H_2O_2), Ab_{max} increased rather than decreased potentially due to the presence of unreacted Ag in the original NF (Figure H.8), making this seed plus 4 aliquots of $NaBH_4$ a potential recipe for the short λ NF (with λ_{max} = 523 nm and Ab_{max} = 1.121 au). Still, to give enough absorption in the 400 nm – 500 nm range a λ_{max} < 500 nm would be more suitable. Although the trends were similar the linear relationships obtained for a plot of relative $NaBH_4$ amount (i.e. Ag: $NaBH_4$ ratio) versus λ_{max} and Ab_{max} for the 0.3 mM Ag TSCD-PVP NP, 1: 5 Ag: $NaBH_4$, 100 % H_2O_2 seed (Figure H.6) was not obtained for these other seed NFs.

Table H.5 Details of samples investigating adding $NaBH_4$ to four other seed solutions. Samples using Seeds W and X have been diluted 1: 3 prior to measurement and samples using Seeds Y and Z have been diluted 1: 4. All measured with a 1 mL 10 mm path length cuvette using UV-vis-1.

Seed used	**Number of increments of 0.01 mL, 25 mM $NaBH_4$ solution**	**Final Ag Molarity / mM**	**Final $NaBH_4$ Molarity / mM**	**Ag: $NaBH_4$ ratio**	**λ_{max} / nm**	**Ab_{max} / au**
Seed W = 0.3 mM Ag TSCD-PVP NP 25 mL	0	0.3	3.0	1: 10	694	0.788
Seed W	1	0.299	3.109	1: 10.4	635	0.761
Seed W	6	0.291	3.641	1: 12.5	583	0.776
Seed X = 0.3 mM Ag TSCD-PVP NP, 1: 5 Ag: $NaBH_4$, 20 % H_2O_2	0	0.3	1.5	1: 5	571	0.761
Seed X	1	0.299	1.617	1: 5.4	523	0.707
Seed Y = 0.4 mM Ag TSCD-PVP NP 25 mL	0	0.4	4.0	1: 10	605	0.499
Seed Y	1	0.398	4.104	1: 10.3	419	0.503
Seed Z = 0.4 mM Ag TSCD-PVP NP, 1:5 Ag: $NaBH_4$, 100 % H_2O_2	0	0.4	2.0	1: 5	773	0.739
Seed Z	1	0.398	2.114	1: 5.3	589	1.097
Seed Z	2	0.396	2.228	1: 5.6	564	1.070
Seed Z	3	0.394	2.340	1: 5.9	540	1.093
Seed Z	4	0.392	2.451	1: 6.3	523	1.121

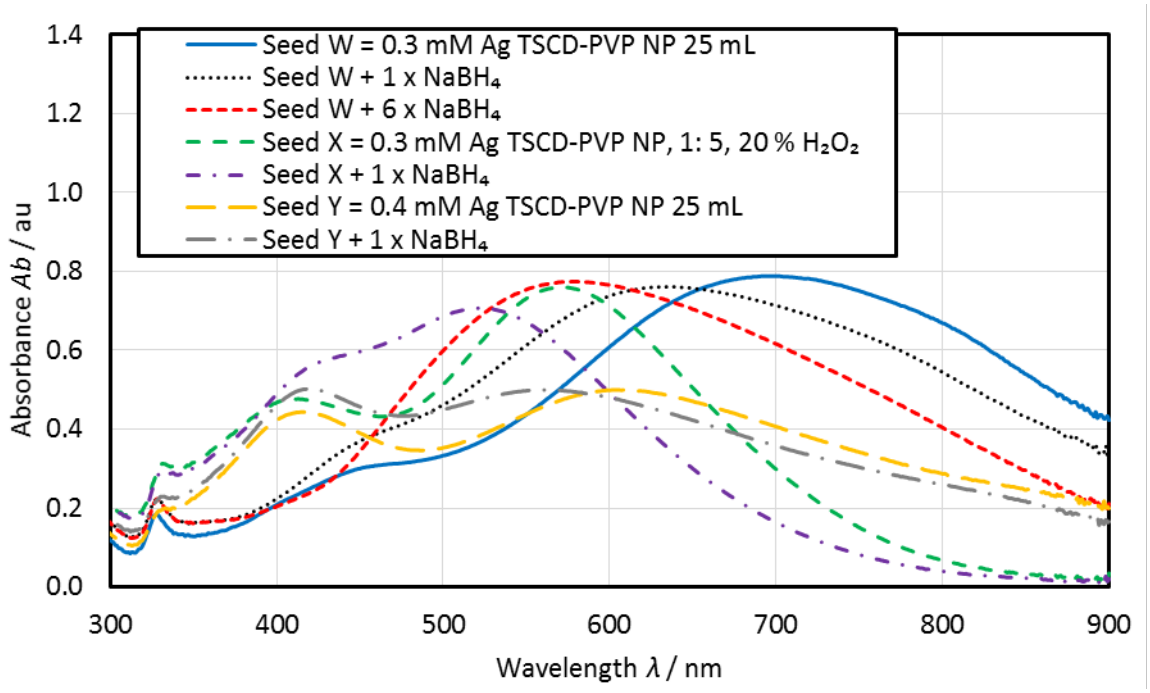

Figure H.7 UV-vis spectra investigating the addition of $NaBH_4$ to an already synthesised seed solution starting with Seeds W, X and Y (see Table H.5 for seed details). All measured using a 10 mm path length 1 mL micro cuvette with UV-vis-1. All samples diluted in ratio 1: 3 (Seeds W and X) and 1: 4 (Seed Y).

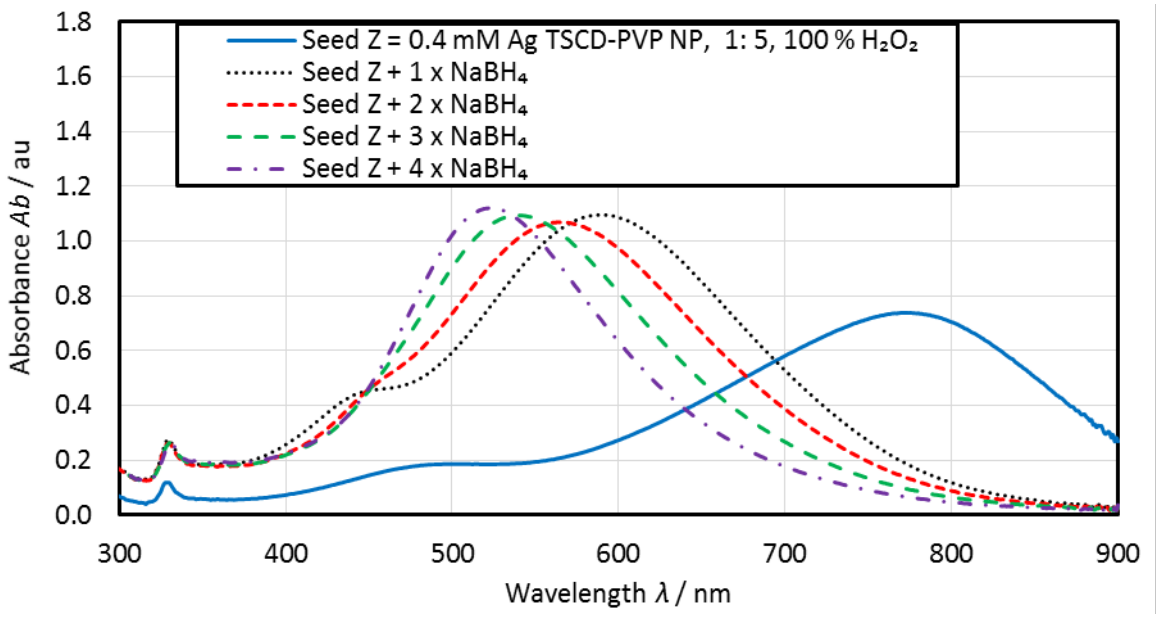

Figure H.8 UV-vis spectra showing the effect of adding successive aliquots of $NaBH_4$ to an already synthesised seed solution (Seed Z in Table H.5). All samples diluted in ratio 1: 4 and measured with a 1 mL, 10 mm path length cuvette on UV-vis-1.

The experiments investigating the addition of both $AgNO_3$ and $NaBH_4$ to an already prepared seed are detailed in Table H.6 and the resultant UV-vis spectra are shown in Figure H.9.

Initially a small amount of seed was used (3 mL and 9 mL) to check the effect of adding both reagents to an already prepared seed, this was then scaled to the normal 25 mL batch volume. The seed NF used (the fourth NF shown in Figure H.4) was chosen as it had a λ_{max} closest to the

target of 500 nm, at 616 nm but still a high Ab_{max} of 1.217 au. The effect of reducing the amount of additional $NaBH_4$ added was also investigated.

Table H.6 Details of samples produced to investigate the addition of both Ag and $NaBH_4$ to an already produced seed NF. Seed = 0.3 mM Ag TSCD-PVP NP, 1: 5 Ag: $NaBH_4$, 50 % H_2O_2. Note that the seed alone sample was diluted 1: 3 for UV-vis and all other samples were diluted 1: 5.

Sample	**Volume of seed solution / mL**	**Volume of 25 mM $AgNO_3$ solution added**	**Volume of 25 mM $NaBH_4$ solution added**	**Final Ag Molarity / mM**	**Final $NaBH_4$ Molarity / mM**	**Ag: $NaBH_4$ ratio**	**λ_{max} / nm**	**Ab_{max} / au**
Seed	25	0	0	0.3	1.5	1: 5	616	1.217
3 mL Seed + Ag + $NaBH_4$	3	0.01	0.1	0.45	2.25	1: 5	492	0.695
9 mL Seed + Ag + $NaBH_4$	9	0.03	0.3	0.45	2.25	1: 5	515	0.740
25 mL Seed + Ag + $NaBH_4$	25	0.083	0.83	0.45	2.25	1: 5	457	0.684
25 mL Seed + Ag + ½ $NaBH_4$	25	0.083	0.42	0.457	1.88	1: 4.1	455	0.658

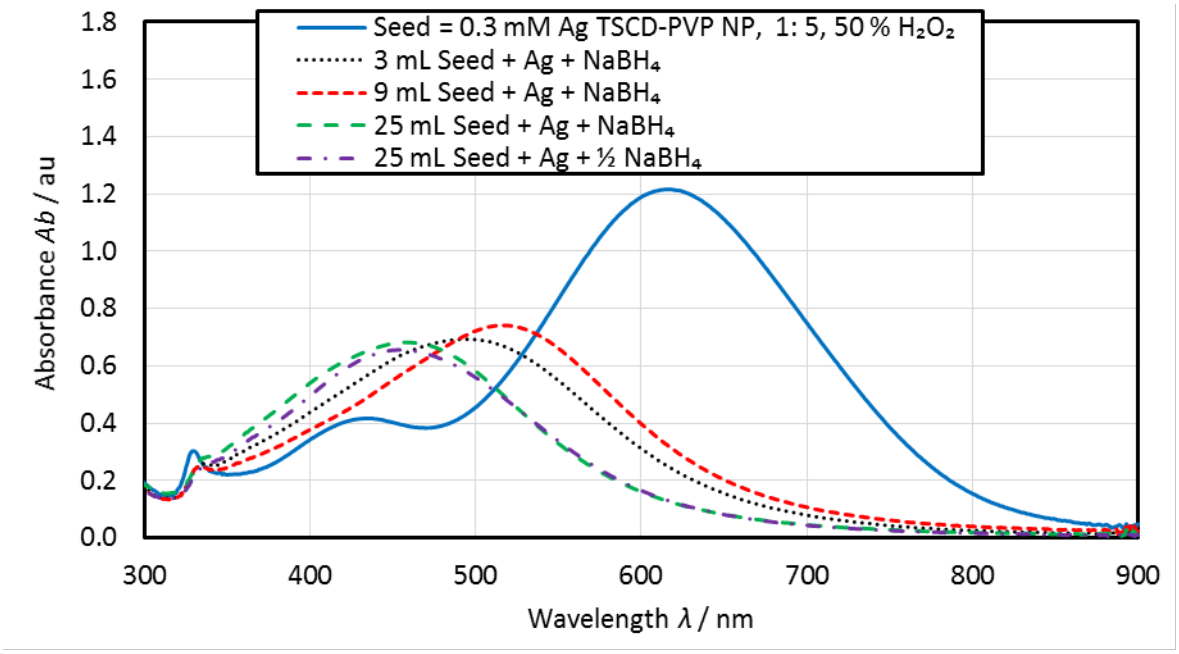

Figure H.9 UV-vis-1 spectra showing the effect of adding both $AgNO_3$ and $NaBH_4$ to an already prepared seed solution. All measured on UV-vis-1 using a 10 mm 3 mL disposable cuvette. The seed solution was diluted 1: 3 and all other solution were diluted 1: 5 prior to UV-vis measurement (details of seed solution in Table H.6).

The effect of adding both reagents was to blue-shift λ_{max} to 455 nm – 515 nm. At the same time Ab_{max} dropped to 0.658 au – 0.740 au. However, it should be noted that this value for Ab_{max} was for samples diluted 1: 5 whereas the actual Ag molarity of the samples was 0.45 mM or 0.457 mM (see Table H.6). If the samples had been diluted to give a Ag molarity of 0.1 mM the

corresponding Ab_{max} values would have been in the range 0.720 au – 0.823 au. This still represents a drop in Ab_{max}. Halving the amount of extra $NaBH_4$ added did not appear to effect either the value of λ_{max} or Ab_{max} (Figure H.9). Adding both $AgNO_3$ and $NaBH_4$ to an already synthesised seed appears to be a suitable means of producing the desired short λ NF with a λ_{max} at around 500 nm (average of 4 samples in Figure H.9 is 480 nm) even with the drop in Ab_{max} as the overall reagent concentration of Ag was higher allowing for more flexibility in the broadband mixture recipe.

H.5 Calculation of Efficiency From UV-vis-IR Spectra for Broadband Component NFs

$\eta_{Ab(300\ nm\ -\ 1350\ nm)}$ for the selected three component NFs was calculated using Equation 3-8. In addition, to allow comparison with the Ag NPr efficiency calculations given in Table 4-2, $\eta_{Ab(300\ nm\ –\ 900\ nm)}$ was calculated for a 10 mm path length using Equation 4-3. To get an estimation of the potential performance across the whole of the solar spectrum $\eta_{Ab(280\ nm\ -\ 4000\ nm)}$ was estimated assuming that there was no absorption > 900 nm using Equation 4-4 using the 300 nm - 900 nm spectra data. For completeness the performance over the whole λ range was also estimated using the 300 nm - 1350 nm spectral data and modifying Equation 4-4 to give:

$$\eta_{\mathrm{Ab(280\ nm\ –\ 4000\ nm)}} = \frac{\sum_{\lambda=300\ \mathrm{nm}}^{\lambda=1350\ \mathrm{nm}} P_{\mathrm{Ab}(\lambda)}}{\sum_{\lambda=280\ \mathrm{nm}}^{\lambda=4000\ \mathrm{nm}} P_{\mathrm{i}(\lambda)}} \times 100$$

Equation H.1

These calculations were carried out for the as measured diluted component NFs and for the NFs without dilution (Table H.7).

Table H.7 Various different efficiency calculations for the three component NFs selected for the broadband absorber. The long λ NF was not diluted prior to UV-vis measurement.

NF	$\eta_{Ab(300\ nm\ –\ 1350\ nm)}$ **/ %**	$\eta_{Ab(300\ nm\ –\ 900\ nm)}$ **/ %**	$\eta_{Ab(280\ nm\ –\ 4000\ nm)}$ **(using 300 nm – 1350 nm data/ %**	$\eta_{Ab(280\ nm\ –\ 4000\ nm)}$ **(using 300 nm – 900 nm data/ %**
Short λ -1 (diluted 1: 5)	30.69	40.62	26.93	27.02
Short λ -2 (diluted 1: 5)	27.07	35.76	23.85	23.71
Short λ -3 (diluted 1: 5)	26.59	34.92	23.42	23.15
Short λ – 1 undiluted	53.29	70.12	46.95	46.49
Short λ – 2 undiluted	50.86	66.56	44.81	44.13
Short λ – 3 undiluted	50.86	65.60	44.81	43.49
Mid λ -1 (diluted 1: 3)	56.24	72.21	49.55	47.88
Mid λ -2 (diluted 1: 3)	55.72	71.96	49.09	47.71

NF	**$\eta_{Ab(300\ nm - 1350\ nm)}$ / %**	**$\eta_{Ab(300\ nm - 900\ nm)}$ / %**	**$\eta_{Ab(280\ nm - 4000\ nm)}$ (using 300 nm – 1350 nm data/ %**	**$\eta_{Ab(280\ nm - 4000\ nm)}$ (using 300 nm – 900 nm data/ %**
Mid λ -3 (diluted 1: 3)	54.66	70.91	48.15	47.02
Mid λ – 1 undiluted	75.13	93.37	66.19	61.90
Mid λ – 2 undiluted	74.32	93.22	65.48	61.80
Mid λ – 3 undiluted	72.92	92.23	64.24	61.25
Long λ – 1	65.38	62.49	57.60	41.43
Long λ – 2	63.73	59.97	56.14	39.76
Long λ – 3	64.56	64.19	56.88	42.56

H.6 Calculation of Efficiency From UV-vis-IR Spectra to Determine Optimum Broadband Mixture

To design the broadband mixture $\eta_{Ab(300\ nm\ -\ 1350\ nm)}$ for a number of different mixtures was calculated using Equation 3-8. The results are shown in Table H.8 with the selected mixture shown in bold. All calculations are based on a 10 mm path length.

Table H.8 Calculations of optimum broadband mixture. The recipe in bold was chosen as although not the optimum in terms of $\eta_{Ab(300\ nm\ -\ 1350\ nm)}$ it contained a lower proportion of the mid λ NF and still a $\eta_{Ab(300\ nm\ -\ 1350\ nm)} > 82$ %.

% short λ	**% mid λ**	**% long λ**	**Ag / mM**	**Ag / wt. %**	**$\eta_{Ab(300\ nm\ -\ 1350\ nm)}$ / %**
10	20	70	0.176	0.0019	80.79
10	30	60	0.196	0.0021	82.20
10	40	50	0.216	0.0023	82.61
10	50	40	0.236	0.0025	82.31
20	10	70	0.191	0.0021	80.28
20	20	60	0.211	0.0023	82.45
20	30	50	0.231	0.0025	83.14
20	40	40	0.251	0.0027	82.86
30	10	60	0.227	0.0025	80.93
30	**20**	**50**	**0.247**	**0.0027**	**82.52**
30	30	40	0.267	0.0029	82.63
40	10	50	0.263	0.0028	80.33
40	20	40	0.283	0.0031	81.43
50	10	40	0.299	0.0032	78.71

To check if the selected short λ recipe chosen was the best of the three available options $\eta_{Ab(300\ nm - 1350\ nm)}$ was calculated for a 30 % short λ, 20 % mid λ and 50 % long λ mixture for all three different recipes using a 10 mm path length. The results are given in Table H.9. The selected short λ recipe is the first one shown and it can be seen that this gave a slightly greater $\eta_{Ab(300\ nm - 1350\ nm)}$ of 82.52 %. In a similar manner as for the component NFs, $\eta_{Ab(300\ nm - 900\ nm)}$ was also calculated, $\eta_{Ab(280\ nm - 4000\ nm)}$ was estimated assuming that there was no absorption > 900 nm and assuming there was no absorption > 1350 nm. Finally, to allow for direct comparison with any data obtained from monitoring the rate of change of temperature in the solar simulator $\eta_{lamp(330\ nm - 1100\ nm)}$ was also estimated using Equation 3-9. The results are given in Table H.10.

Table H.9 Effect of changing the short λ recipe on $\eta_{Ab(300\ nm - 1350\ nm)}$ for a mixture containing 30 % short λ, 20 % mid λ and 50 % long λ.

Short λ recipe	**Ag / mM**	**Ag / wt. %**	**$\eta_{Ab(300\ nm - 1350\ nm)}$ / %**
0.3 mM Ag TSCD-PVP NP, 1: 5 Ag: $NaBH_4$, 50 % H_2O_2 seed + Ag + ½ $NaBH_4$	0.247	0.0027	82.52
Seed Z = 0.4 mM Ag TSCD-PVP NP, 1: 5 Ag: $NaBH_4$, 100 % H_2O_2 + 4 x $NaBH_4$	0.230	0.0025	81.90
0.3 mM Ag TSCD-PVP NP, 1: 5 Ag: $NaBH_4$, 50 % H_2O_2 seed + Ag + $NaBH_4$	0.245	0.0026	82.35

Table H.10 Calculations of optimum broadband mixture showing various different efficiency metrics. The row in bold is the selected mixture.

% short λ	**% mid λ**	**% long λ**	**$\eta_{Ab(300\ nm - 900\ nm)}$ / %**	**$\eta_{Ab(280\ nm - 4000\ nm)}$ (using 300 nm – 1350 nm data/ %**	**$\eta_{Ab(280\ nm - 4000\ nm)}$ (using 300 nm – 900 nm data/ %**	**$\eta_{lamp(330\ nm - 1100\ nm)}$ / %**
10	20	70	86.08	71.19	57.04	86.83
10	30	60	89.08	72.43	59.03	90.35
10	40	50	90.99	72.79	60.30	92.58
10	50	40	92.25	72.52	61.13	94.05
20	10	70	85.47	70.73	56.64	86.83
20	20	60	89.50	72.65	59.31	90.72
20	**30**	**50**	**91.79**	**73.25**	**60.83**	**93.38**
20	40	40	93.13	73.01	61.72	94.95
30	10	60	87.57	71.31	58.04	88.75
30	20	50	91.09	72.71	60.37	92.74
30	30	40	92.97	72.80	61.61	94.90
40	10	50	88.30	70.78	58.52	90.07
40	20	40	91.53	71.75	60.66	93.67

% short λ	% mid λ	% long λ	$\eta_{Ab(300\ nm - 900\ nm)}$ / %	$\eta_{Ab(280\ nm - 4000\ nm)}$ (using 300 nm – 1350 nm data/ %	$\eta_{Ab(280\ nm - 4000\ nm)}$ (using 300 nm – 900 nm data/ %	$\eta_{lamp(330\ nm - 1100\ nm)}$ / %
50	10	40	88.07	69.35	58.37	90.54

H.7 Calculation of Efficiency From UV-vis-IR Spectra for the Actual Measured Broadband Mixture

The spectra obtained for the three short, mid and long λ were used to calculated the potential broadband mixture spectrum, using short λ – 1, mid λ - 1 and long λ – 1 spectra for the broadband mixture – 1, using - 2 samples for the broadband mixture – 2 and – 3 samples for broadband mixture – 3. The actual mixtures were then produced and the UV-vis-IR spectra measured. These spectra were then used to calculate the potential efficiency of the produced broadband mixture. In a similar manner as for the component NFs, $\eta_{Ab(300\ nm - 1350\ nm)}$ and $\eta_{Ab(300\ nm - 900\ nm)}$ were calculated, $\eta_{Ab(280\ nm - 4000\ nm)}$ was estimated assuming that there was no absorption > 900 nm and assuming there was no absorption > 1350 nm. Finally, to allow for direct comparison with any data obtained from monitoring the rate of change of temperature in the solar simulator $\eta_{lamp(330\ nm - 1100\ nm)}$ was also estimated using Equation 3-9. The results are given in Table H.11. Using a two-sample t-test (see Section F.1) the difference between the calculated and measured values of $\eta_{Ab(300\ nm - 1350\ nm)}$ were not significant at the 95 % confidence level.

Table H.11 Various efficiency values for the measured and calculated broadband absorber.

Sample	η_{Ab} / %	η_{Ab} / %	η_{Ab} (using 300 nm – 1350 nm data/ %	η_{Ab} (using 300 nm – 900 nm data/ %	η_{lamp} / %
Range of η calculation / nm	**300 - 1350**	**300 - 900**	**280 - 4000**	**280 - 4000**	**330 - 1100**
Calculated broadband mixture - 1	83.30	91.49	73.39	60.66	93.46
Calculated broadband mixture - 2	82.65	90.35	72.81	59.91	91.92
Calculated broadband mixture - 3	81.23	91.13	71.57	60.42	92.47
Measured broadband mixture – 1	84.36	92.14	74.32	61.09	93.25
Measured broadband mixture – 2	83.01	90.32	73.13	59.88	90.92
Measured broadband mixture – 3	81.78	90.99	72.04	60.33	91.37

Appendix I Additional Information on Consistency of Batch Synthesis

This Appendix details the UV-vis results obtained for repeating the batch synthesis methods for the short, mid and long λ NFs using a 30 mL batch volume. These UV-vis results from combining these batches are also given. The TEM results on the combined samples are provided in Appendix G, Section G.3.

I.1 Reproducibility of Short Wavelength Absorber (Short λ 30 mL Batch)

The results of repeating the short λ synthesis 12 times using a batch volume of 30 mL are shown in Figure I.1 with the full results in Table I.1. After synthesis the 12 batches were combined together and the UV-vis spectrum re-measured (the combined short λ sample in Figure I.1). The average λ_{max} was 458 nm (range = 458 nm – 470 nm, shown as the error bars), and the average Ab_{max} was 0.764 au (range 0.716 au – 0.786 au), both similar to the results obtained using a 25 mL batch volume (Figure 4-10). When combined the value of Ab_{max} appeared to drop slightly, compared to the average, to 0.721 au, and λ_{max} red-shifted slightly to 467 nm. These changes were still within the range of the results obtained for the individual samples.

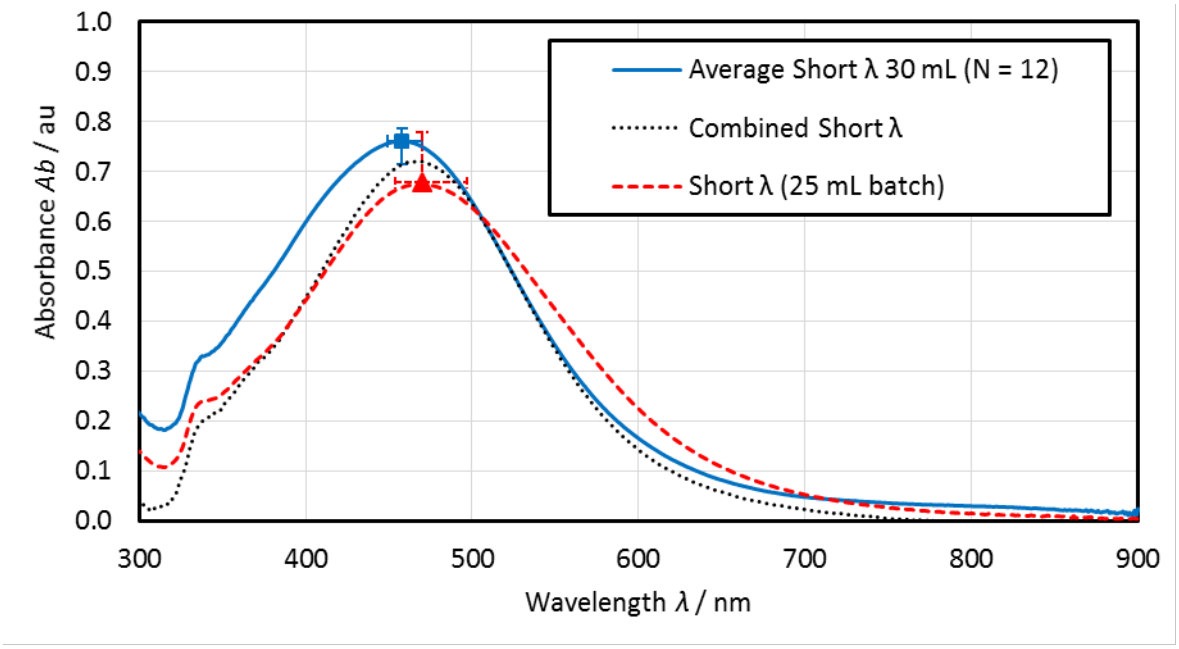

Figure I.1 UV-vis spectra for the short λ NF 30 mL samples. The error bars show the range of results obtained at the maximum absorbance for the repeat synthesis. The 30 mL batch samples were measured using UV-vis-1 and a 1 mL 10 mm path length disposable cuvette. The combined sample was measured using UV-vis-IR-1 and a 3 mL 10 mm path length cuvette. The samples have been diluted 1: 5. For ease of comparison the short λ NF from Figure 4-10 is also shown.

To test if changing the batch volume from 25 mL to 30 mL had effected the results two-sample t-tests were undertaken comparing the results for the short λ NF (25 mL batch volume) in Table 4-3 with Table I.1 (30 mL batch volume). There was no significant difference between the two sets of samples for both λ_{max} and Ab_{max}.

Table I.1 λ_{max} and Ab_{max} values for the repeat synthesis of the short λ NF with a batch size of 30 mL. All initial samples measured on UV-vis-1 using a 10 mm path length, 1 mL micro cuvette. The combined sample was measured on UV-vis-IR-1 using a 3 mL 10 mm path length disposable cuvette.

Sample	**λ_{max} / nm**	**Ab_{max} / au**
Short λ 30 mL - 1	455	0.744
Short λ 30 mL – 2	463	0.735
Short λ 30 mL – 3	458	0.748
Short λ 30 mL – 4	470	0.785
Short λ 30 mL – 5	452	0.772
Short λ 30 mL – 6	454	0.768
Short λ 30 mL – 7	459	0.786
Short λ 30 mL – 8	463	0.777
Short λ 30 mL – 9	449	0.784
Short λ 30 mL – 10	463	0.774
Short λ 30 mL – 11	456	0.776
Short λ 30 mL – 12	465	0.716
Average Short λ 30 mL	458	0.764
σ Short λ 30 mL	6	0.023
N Short λ 30 mL	12	12
Range Short λ 30 mL	449 - 470	0.716 – 0.786
Combined Short λ	467	0.721

I.2 Reproducibility of Mid Wavelength Absorber (Mid λ 30 mL Batch)

For the mid λ NF 8 repeat measurements utilising a batch volume of 30 mL (Figure I.2), there was some variation in the λ_{max} obtained. Initially the range of λ_{max} was 647 nm – 727 nm and the average value was 673 nm (error bars shown in Figure I.2 – complete results in Table I.2). The average was similar to the mid λ 25 mL samples (reproduced in Figure I.2 from Figure 4-10 for ease of comparison). However, when the same samples were re-measured after storage at 4 °C in the dark for 2 weeks (stored diluted, 0.3 mL in 1 mL), there was a blue-shift in average λ_{max} of ≈ 80 nm (full results in Table I.3).

The 8 samples were combined together and measured. Just after diluting the combined λ_{max} was similar to the initial average obtained being 659 nm. However after being stored diluted and re-measured λ_{max} had again blue-shifted by ≈ 50 nm to 610 nm. The blue-shift observed may therefore be partly due to diluting the mid λ NF to undertake UV-vis measurements. This lack of stability of the mid λ NF is discussed further in Chapter 5.

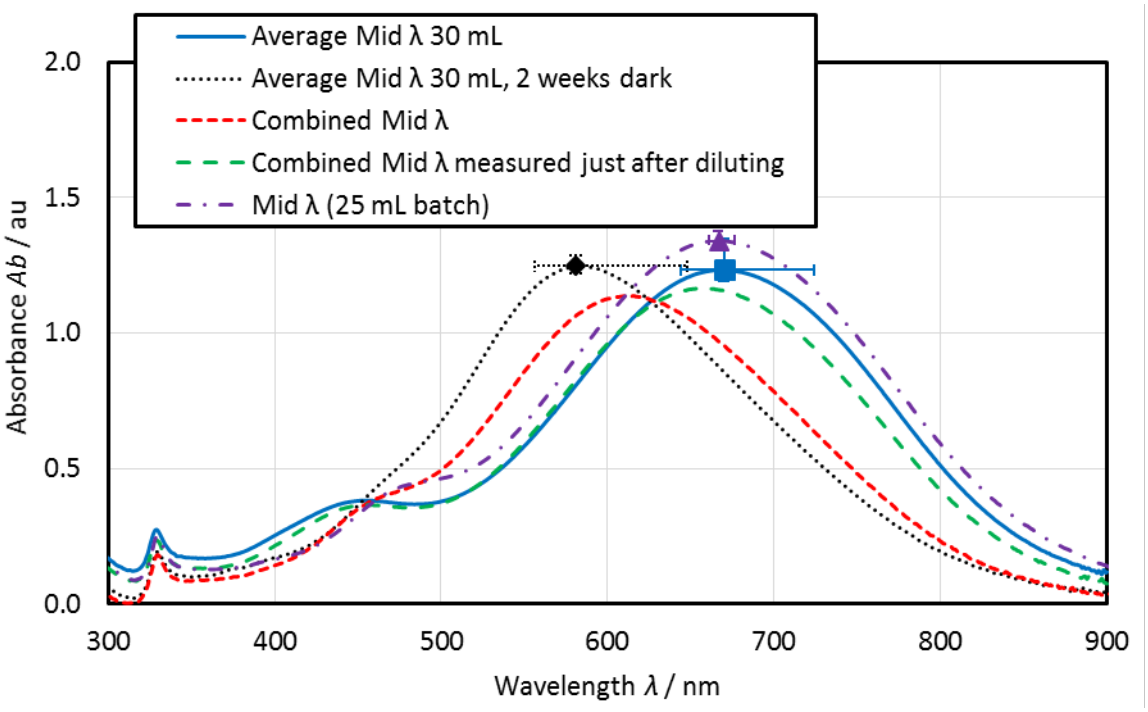

Figure I.2 UV-vis spectra for the mid λ NF 30 mL samples. The error bars show the range of results obtained at the maximum absorbance for the repeat synthesis. The 30 mL batch samples were initially measured using UV-vis-1 and a 1 mL 10 mm path length disposable cuvette. They were then re-measured after 2 weeks using UV-vis-IR-1. The combined sample was measured on UV-vis-1 just after diluting and then on UV-vis-IR-1 using a 3 mL 10 mm path length cuvette. For ease of comparison the mid λ NF from Figure 4-10 is also shown.

For Ab_{max} there was less variation in the results obtained. When compared to the 25 mL batch samples shown in Figure 4-10, the range and average were similar (note that the 8, 30 mL batch samples were diluted to 0.3 mL in 1 mL in error, the actual corrected values for comparison with the 25 mL batch samples are given in Table I.2 and Table I.3). Ab_{max} for the combined sample was, however, slightly lower than expected. The reason for this drop in Ab_{max} for the combined sample is unknown, but is unlikely to be due to insufficient mixing as the combined NF was mixed well before testing.

Table I.2 λ_{max} and Ab_{max} values for the repeat synthesis of the mid λ NF with a batch size of 30 mL. All measured on UV-vis-1 using a 10 mm path length, 1 mL micro cuvette. Note that samples were diluted to 0.3 mL in 1 mL rather than 0.33 mL in 1 mL hence Ab_{max} has been adjusted to allow comparison with the 25 mL mid λ batch samples.

Sample	**λ_{max} / nm**	**Ab_{max} / au**	**Ab_{max} adjusted for dilution/ au**
Mid λ 30 mL - 1	664	1.254	1.379
Mid λ 30 mL – 2	659	1.254	1.379

Sample	**λ_{max} / nm**	**Ab_{max} / au**	**Ab_{max} adjusted for dilution/ au**
Mid λ 30 mL – 3	670	1.252	1.377
Mid λ 30 mL – 4	659	1.248	1.373
Mid λ 30 mL – 5	647	1.263	1.390
Mid λ 30 mL – 6	727	1.400	1.540
Mid λ 30 mL – 7	648	1.241	1.366
Mid λ 30 mL – 8	713	1.362	1.498
Average Mid λ 30 mL	673	1.284	1.413
σ Mid λ 30 mL	30	0.061	0.067
N Mid λ 30 mL	8	8	8
Range Mid λ 30 mL	647 - 727	1.241 – 1.400	1.366 – 1.540

Table I.3 λ_{max} and Ab_{max} values for the repeat synthesis of the mid λ NF with a batch size of 30 mL 2 weeks after manufacture. All initial samples measured on UV-vis-IR-1 using a 10 mm path length, 1 mL micro cuvette. Note that samples were diluted to 0.3 mL in 1 mL rather than 0.33 mL in 1 mL hence Ab_{max} has been adjusted to allow comparison with the 25 mL mid λ and batch samples. The combined mid λ sample was diluted 1: 3 and measured using a 3 mL 10 mm path length cuvette.

Sample	**λ_{max} / nm**	**Ab_{max} / au**	**Ab_{max} adjusted for dilution/ au**
Mid λ 30 mL – 1, 2 weeks dark	573	1.326	1.458
Mid λ 30 mL – 2, 2 weeks dark	565	1.303	1.433
Mid λ 30 mL – 3, 2 weeks dark	579	1.304	1.435
Mid λ 30 mL – 4, 2 weeks dark	573	1.313	1.445
Mid λ 30 mL – 5, 2 weeks dark	566	1.348	1.482
Mid λ 30 mL – 6, 2 weeks dark	657	1.368	1.504
Mid λ 30 mL – 7, 2 weeks dark	574	1.349	1.484
Mid λ 30 mL – 8, 2 weeks dark	634	1.328	1.461
Average Mid λ 30 mL, 2 weeks dark	590	1.330	1.463
σ Mid λ 30 mL, 2 weeks dark	35	0.023	0.026
N Mid λ 30 mL, 2 weeks dark	8	8	8
Range Mid λ 30 mL, 2 weeks dark	565 - 657	1.303 – 1.368	1.433 – 1.504
Combined Mid λ	610	1.135	1.135
Combined Mid λ (measured using UV-vis-1 immediately after diluting to ratio of 1: 3)	659	1.167	1.167

I.2.1 Analysis of variance

To check if any of the differences between the groups of batches of the mid λ samples was significant, analysis of variance (ANOVA) was undertaken as described in Appendix F.2. This is similar to carrying out a t-test but for more than two samples (in this case 3, mid λ 25 mL, mid λ 30 mL and mid λ 30 mL after 2 weeks storage). The results are given in Table I.4 for λ_{max} and in Table I.5 for Ab_{max} (the corrected values from Table I.2 and Table I.3 have been used to allow comparison with the mid λ 25 mL samples).

Table I.4 Results of undertaking ANOVA on the mid λ, λ_{max} values. The average values and the potential range of the average value are shown along with the grouping. Groups that do not share a letter are significantly different.

Sample type	***N***	**Average λ_{max} / nm**	**Grouping**	**95 % confidence level for the mean / nm**
Mid λ 30 mL initial	8	673	A	650 to 696
Mid λ 30 mL 2 weeks dark	8	590	B	567 to 613
Mid λ 25 mL	3	667	A	630 to 704

Table I.5 Results of undertaking ANOVA on the mid λ, Ab_{max} values. The average values and the potential range of the average value are shown along with the grouping. Groups that do not share a letter are significantly different.

Sample type	***N***	**Average Ab_{max} / au**	**Grouping**	**95 % confidence level for the mean / au**
Mid λ 30 mL initial	8	1.413	A, B	1.376 to 1.449
Mid λ 30 mL 2 weeks dark	8	1.463	A	1.427 to 1.499
Mid λ 25 mL	3	1.342	B	1.282 to 1.401

After storage in the dark for 2 weeks the blue-shift in λ_{max} was significant compared to both the initial 30 mL and the 25 mL samples. The difference in λ_{max} between the two batch sizes was not significant. For Ab_{max} the 25 mL samples were significantly different (marginally lower) than the 30 mL 2 weeks dark samples, but not different to the 30 mL initial measurements. The 30 mL Ab_{max} values were not significantly different to each other.

I.3 Reproducibility of Nanoprisms Synthesis (Long λ 30 mL Batch)

The results from the 20 repeat synthesis of the long λ using a batch size of 30 mL are shown in Figure I.3 (complete results given in Table I.6). Again the error bars show the range of results for λ_{max} and Ab_{max} obtained (for clarity only the ranges for the 30 mL batch results are shown). The results of combining together all 20 batches and re-measuring the spectrum are also shown along with the results from the 50 mL batches from Figure 4-5 and the 25 mL batch size from Figure 4-10 reproduced for ease of comparison.

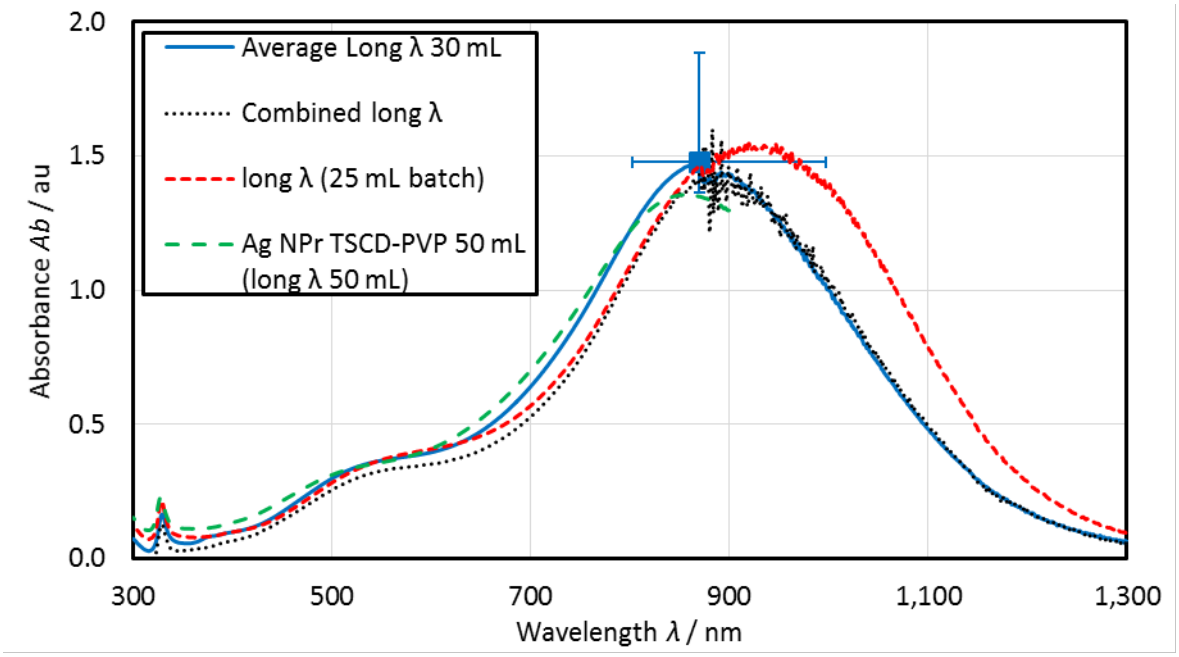

Figure I.3 UV-vis spectra for the long λ NF 30 mL samples. The error bars show the range of results obtained at the maximum absorbance for the repeat synthesis (N = 20). Measured using a 1 mL 10 mm path length cuvette on UV-vis-IR-1. For ease of comparison the long λ NFs from Figure 4-10 and Figure 4-5 is also shown.

For λ_{max} there was an almost 200 nm range of results obtained (average λ_{max} = 889 nm, range 802 nm – 997 nm). This is a large variation in λ_{max} even when the reactions were carried out as consistently as possible and illustrates clearly the problems of controlling the batch synthesis method. Others have shown numerically that a 200 nm shift in λ_{max} can occur when the corners of the prisms become rounded (Kelly et al., 2003), so the sharpness of the corners of the triangles may be influencing λ_{max}. In addition, Carboni also obtained about a 200 nm range when he repeated a similar Ag NPr batch synthesis stabilised with both TSCD and PVP using a 50 mL batch volume (Carboni, 2014).

Table I.6 λ_{max} and Ab_{max} values for the repeat synthesis of the long λ NF with a batch size of 30 mL. All measured on UV-vis-IR-1 using a 10 mm path length, 1 mL micro cuvette.

Sample	**λ_{max} / nm**	**Ab_{max} / au**
Long λ 30 mL - 1	848	1.402
Long λ 30 mL – 2	862	1.623
Long λ 30 mL – 3	932	1.559
Long λ 30 mL – 4	868	1.625
Long λ 30 mL – 5	912	1.514
Long λ 30 mL – 6	848	1.664
Long λ 30 mL – 7	802	1.381
Long λ 30 mL – 8	840	1.364
Long λ 30 mL – 9	870	1.415

Sample	**λ_{max} / nm**	**Ab_{max} / au**
Long λ 30 mL – 10	950	1.691
Long λ 30 mL – 11	832	1.638
Long λ 30 mL – 12	908	1.885
Long λ 30 ml – 13	835	1.606
Long λ 30 mL – 14	927	1.622
Long λ 30 mL – 15	915	1.731
Long λ 30 mL – 16	997	1.615
Long λ 30 mL – 17	891	1.727
Long λ 30 mL – 18	969	1.743
Long λ 30 mL – 19	942	1.532
Long λ 30 mL - 20	827	1.373
Average Long λ 30 mL	889	1.586
σ Long λ 30 mL	53	0.143
N Long λ 30 mL	20	20
Range Long λ 30 mL	802 - 997	1.364 – 1.885
Combined Long λ	883	1.593

When the 30 mL batches were combined and re-measured λ_{max} was found to be 883 nm, similar to the average for the individual batches. It should be noted that there was considerable fluctuation in the spectrum > 872 nm. This is where the lamp in the UV-vis-IR-1 spectrophotometer changes and was present on all the individual spectra leading to some uncertainty in the position of λ_{max} and the value of Ab_{max}. There was also a large range of results obtained for Ab_{max} (average 1.586 au range 1.364 au – 1.885 au). However, given the noise associated with the measurement > 872 nm this result should be treated with caution. The combined spectrum had an Ab_{max} of 1.593 au, within the range reported for the individual samples.

I.3.1 Analysis of variance

To check if the results of the 30 mL batches were similar to that obtained previously for both the 25 mL and the 50 mL batch sizes, ANOVA was undertaken using the method described in Section F.2. The results are given in Table I.7 for λ_{max} and in Table I.8 for Ab_{max}. λ_{max} was significantly blue-shifted for the 50 mL batch size compared to the 25 mL batch (same as t-test in Section 4.4), but the 30 mL batch was not significantly different from either the 25 mL or the 50 mL batch

suggesting that the difference seen between the 50 mL batch size and the 25 mL batch size may have been only due to the different number of samples in each group.

Table I.7 Results of undertaking ANOVA on the long λ, λ_{max} values. The average values and the potential range of the average value are shown along with the grouping. Groups that do not share a letter are significantly different.

Sample type	***N***	**Average λ_{max} / nm**	**Grouping**	**95 % confidence level for the mean / nm**
Ag TSCD-PVP NPr 50 mL	20	858	B	839 to 877
Long λ 25 mL	3	929	A	879 to 978
Long λ 30 mL	20	889	A, B	870 to 908

Table I.8 Results of undertaking ANOVA on the long λ, Ab_{max} values. The average values and the potential range of the average value are shown along with the grouping. Groups that do not share a letter are significantly different.

Sample type	***N***	**Average Ab_{max} / au**	**Grouping**	**95 % confidence level for the mean / au**
Ag TSCD-PVP NPr 50 mL	20	1.420	B	1.354 to 1.486
Long λ 25 mL	3	1.578	A, B	1.407 to 1.748
Long λ 30 mL	20	1.586	A	1.520 to 1.652

The long λ 30 mL batch samples had a significantly greater value of Ab_{max} than the 50 mL batches but were not significantly greater than the 25 mL batches. As the 50 mL samples were measured using UV-vis-1 (range 200 nm – 900 nm) some of the peaks may have been outside the range, leading to a lower value of Ab_{max} and hence an artificial significant difference.

Appendix J Additional Information on Performance in Simulated Sunlight (SSL) Tests

This Appendix presents additional information on the measurement of the performance using the solar simulator. Firstly, the spectrum of the lamp used in the simulator is compared to sunlight. Secondly, the results of measuring the temperature rise of water in the solar simulator are given for both set-up A and B (for details of the experimental set-up see Section 3.8.3). Finally, the results obtained for Ag NPrs, SiO_2@Ag NPrs and SiO_2 only NF using set-up A are provided and analysed using response surface analysis (see Appendix F, Section F.3).

J.1 Lamp Spectrum Versus Sunlight

The spectrum of the solar simulator lamp compared to sunlight is shown in Figure J.1. The wavelengths and absorption of the lamp is close to that of sunlight over the range measured. However, there are some large peaks in the lamps output especially the one at 825 nm. Other researchers have used similar lamps with large peaks in their output to test NFs (Gorji and Ranjbar, 2016).

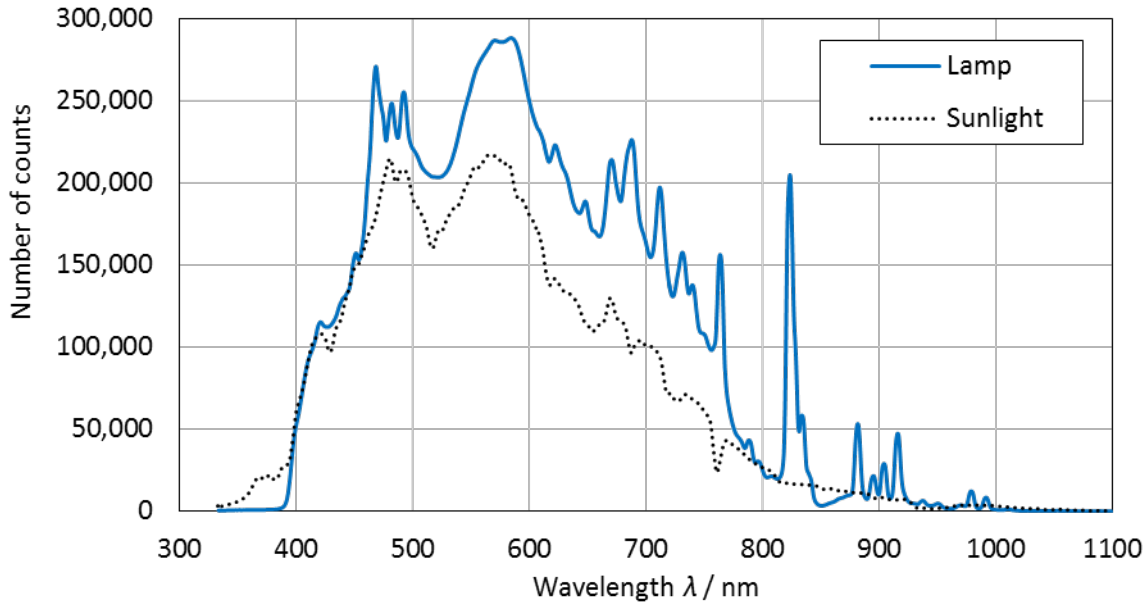

Figure J.1 Spectra obtained from the solar simulator lamp and from sunlight. The sunlight spectrum was measured at 12 noon on a sunny day. Both measured using UV-vis-IR-2 in count mode (only the Avaspec -2048 spectrophotometer and not the Hal-lamp).

J.2 Repeat tests on water

For the solar simulator set-up A, repeat tests of water were used to assess the reproducibility of the experimental set-up (using ANOVA see Appendix F.2). The results are shown in Table J.1.

Table J.1 Solar simulator results for repeat measurements on the base-fluid water for set-up A. The confidence level shows the range of possible values for the mean. The grouping shows results that are significantly different.

Position	**Back (B)**	**Front (F)**	**Middle (Md)**
N	9	9	9
Grouping	B	B	A
Mean Δ*T* after 3600 s / °C	18.75	18.68	21.83
σ Δ*T* after 3600 s / °C	1.063	0.952	1.253
95 % confidence level for mean Δ*T* after 3600 s / °C	18.00 to 19.50	17.92 to 19.43	21.08 to 22.59
Mean slope (Δ*T*/Δ*t)* / °C s^{-1}	0.017	0.016	0.020
σ slope (Δ*T*/Δ*t)* / °C s^{-1}	0.0016	0.0012	0.0017
95 % confidence level for mean slope (Δ*T*/Δ*t)* / °C s^{-1}	0.016 to 0.018	0.015 to 0.018	0.019 to 0.021

The results for the repeat measurements of water using the solar simulator set-up B are given in Table J.2. For set-up B only the middle (Md) position was used and the tests were shorter so the stagnation temperature (at *t* = 3600 s in Table J.1) was not reached so only the results for the slope Δ*T*/Δ*t* and the subsequent calculation of η_{PE} are shown. The confidence interval for the mean was calculated from undertaking ANOVA testing on all the NFs (the broadband absorber and three component NFs) evaluated using set-up B including water.

Table J.2 Solar simulator results for repeat measurements of water using Set-up B including the calculation of η_{PE} using the parameters given in Table 3-3 and Equation 3-10.

Water (Set-up B middle Md position)	**Slope Δ*T*/Δ*t* between *t* = 91 s and *t* = 211 s / °C s^{-1}**	**η_{PE} using I_L = 1191 W m^{-2} / %**
Mean	0.0058	20.51
σ	0.0003	1.17
N	3	3
Range (minimum - maximum)	0.0056 – 0.0062	19.52 to 21.79
95 % confidence level for the mean (from ANOVA)	Not calculated	14.61 to 26.34

J.3 Silver Nanoprisms (Ag NPr)

To investigate whether the experimental set-up for the solar simulator set-up A was changing with time, response surface methodology was used (see Appendix F.3). For the model, one continuous factor (time in h) and three other categorical factors were used (type, experiment and position), where "type" was the type of fluid (Ag TSCD-PVP NPrs centrifuged and re-dispersed into ¼ volume of water, or water), "experiment" denoted the sample repeat (1, 2 or 3) and "position" referred to the position of the sample in the SSL test rig (either back, front or middle see Figure 3-2). To keep the experimental set orthogonal or balanced only the results from the first 9 h of testing of each sample type were used. This equated to a total of 54 experiments. Further details are given in Table J.3. In (Kimpton et al., 2020a) the full 12 h was used for the response surface analysis and the analysis was undertaken using all 4 fluids presented together in the paper (Ag NPr, SiO_2@Ag NPrs, SiO_2 NF and water) giving a total of 108 experiments. However, the results obtained were similar. Here the results have been separated to fit with the Chapters in this thesis and reanalysed.

Table J.3 Experimental design for response surface methodology.

	Time / h	**Type**	**Experiment**	**Position**
Type of factor	continuous	categorical	categorical	categorical
Levels	9 (1 h, 2 h, 3 h, 4 h, 5 h, 6 h, 7 h, 8 h, 9 h)	1. Ag NPr ct ¼ vol 2. Water	1. Repeat 1 2. Repeat 2 3. Repeat 3	1. Back (B) 2. Front (F) 3. Middle (Md)
Number of experiments at each level	6 (3 water, 3 Ag NPr ct ¼ vol)	27	18	18
Total (levels x number of experiments at each level)	54	54	54	54

Two responses were analysed, i.e., the change in temperature (ΔT) after 3600 s or 1 h of testing and the slope of the linear portion of the graph ($\Delta T/\Delta t$) taken between t = 90 s and t = 150 s, where t = time. For ΔT after 3600 s the R^2 value obtained from the model was 99.51 % showing the model was a good fit to the data. For the slope the model fit was slightly less at 99.28 %. The main effect plots for the two responses are shown in Figure J.2. For both responses the type of fluid used and the position in the SSL were the most important factors, with the middle (Md) position giving consistently higher results for both ΔT after 3600 s and the slope $\Delta T/\Delta t$. The repeat number and the time both only changed slightly from the mean for ΔT after 3600 s showing that the experimental set-up was fairly well controlled and the repeat samples produced similar results for this response. There was more variation in the results with time for the slope but this

may have been due to spectral changes with time for the NF and is still a lower difference than that seen for either “type” or “position”.

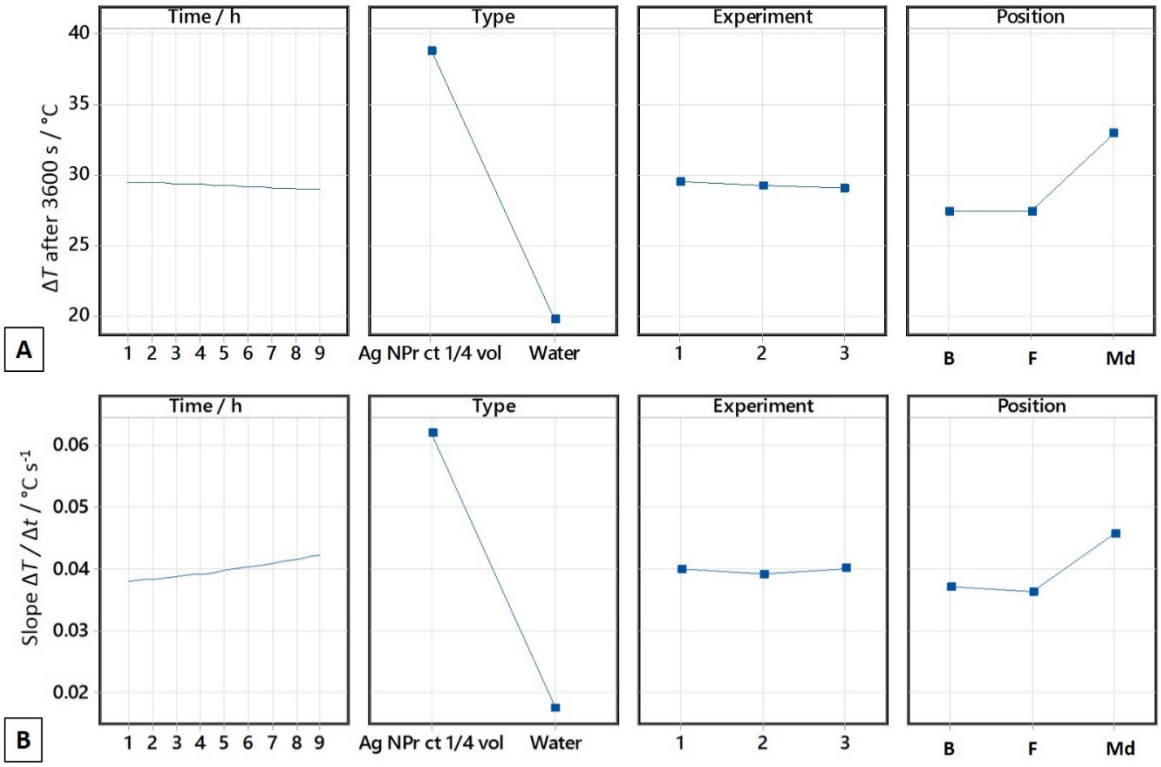

Figure J.2 Main Effect Plots for (A) Value of Δ*T* after 3600 s in SSL, and (B) The slope Δ*T*/Δ*t* taken between *t* = 90 s to *t* = 150 s. Ag NPr ct ¼ vol are Ag TSCD-PVP NPrs centrifuged and re-dispersed into ¼ volume of water. Position refers to placement in SSL apparatus where B = Back, F = front and Md = Middle.

The results analysed using ANOVA for the Ag TSCD-PVP NPrs centrifuged and re-dispersed into ¼ volume of water (for the full 12 h of testing) are given in Table J.4.

Table J.4 Solar simulator results for repeat measurements on Ag NPr ct ¼ vol NF for Set-up A. The confidence level shows the range of possible values for the mean. The grouping shows results that are significantly different.

Position	**Back (B)**	**Front (F)**	**Middle (Md)**
N	12	12	12
Grouping	B	B	A
Mean Δ*T* after 3600 s / °C	36.22	36.26	44.11
σ Δ*T* after 3600 s / °C	0.83	0.81	1.37
95 % confidence level for mean Δ*T* after 3600 s / °C	35.61 to 36.83	35.65 to 36.87	43.50 to 44.72
Mean slope (Δ*T*/Δ*t*) / °C s^{-1}	0.060	0.058	0.074
σ slope (Δ*T*/Δ*t*) / °C s^{-1}	0.004	0.007	0.006
95 % confidence level for mean slope (Δ*T*/Δ*t*) / °C s^{-1}	0.056 to 0.063	0.055 to 0.062	0.071 to 0.078

The estimation of η_{PE} for the samples measured using the solar simulator set-up A calculated by adjusting the value of η_{PE} of water to 20.51 % are given in Table J.5 along with the values obtained by estimating $\eta_{lamp(330\ nm\ -\ 900\ nm)}$ from the UV-vis spectra. As the UV-vis spectra changed with exposure, the $\eta_{lamp(330\ nm\ -\ 900\ nm)}$ calculations were undertaken using the before exposure (t = 0) and after exposure to SSL for 12 h (t =12 h) data. From Table J.5 it appears that the actual performance of the Ag NPr NF in the solar simulator was less than that predicted from calculating $\eta_{lamp(330\ nm\ -\ 900\ nm)}$. However, when the measurement uncertainties for calculating η_{PE} and $\eta_{lamp(330\ nm\ -\ 900\ nm)}$ are taken into consideration the results are similar (see Table E.4 and Table E.5). Also from Figure J.2 it can be seen that there is a small rise in the value of $\Delta T/\Delta t$ with time. If the three results for calculating η_{PE} over the time period of 11 h to 12 h in the solar simulator of 89.00 % (back, B, position), 89.67 % (front, F, position) and 95.62 % (middle, Md, position) are considered in isolation they can be seen to be a closer match to the estimated $\eta_{lamp(330\ nm\ -\ 900\ nm)}$ value obtained using the 12 h spectra.

Table J.5 Calculations of η_{PE} (using set-up A) and $\eta_{lamp(330\ nm\ -\ 900\ nm)}$ for water and Ag TSCD-PVP NPr centrifuged and re-dispersed into ¼ volume of water.

Fluid and position in solar simulator	**Mean η_{PE} or mean $\eta_{lamp(330\ nm\ -\ 900\ nm)}$ / %**	**$\sigma\ \eta_{PE}$ or σ $\eta_{lamp(330\ nm\ -\ 900\ nm)}$ / %**	***N***
η_{PE} Water middle (Md)	20.51	4.18	12
η_{PE} Water back and front (B & F)	20.51	4.55	24
η_{PE} Ag TSCD-PVP NPr ct ¼ vol middle (Md)	84.81	7.10	12
η_{PE} Ag TSCD-PVP NPr ct ¼ vol back and front (B & F)	80.00	7.86	24
$\eta_{lamp(330\ nm\ -\ 900\ nm)}$ Ag TSCD-PVP NPr ct ¼ vol calculated from t = 0 spectra	91.72	1.06	3
$\eta_{lamp(330\ nm\ -\ 900\ nm)}$ Ag TSCD-PVP NPr ct ¼ vol calculated from t = 12 h spectra	99.54	0.25	3

J.4 SiO_2 coated Silver Nanoprisms (SiO_2@Ag NPr) and SiO_2 only NF

In a similar manner to the Ag NPrs in Section J.3, response surface methodology was used to see if the experimental set up in the solar simulator was changing with time. Again one continuous factor and three categorical factors were used. However, as the SiO_2@Ag NPrs were only measured for 6 h the results for the first 6 h were used. In addition, three different levels of the "type" categorical factor was employed, SiO_2 only NF, SiO_2@Ag NPr and water. Again this equated to a total of 54 experiments. The details of the response surface analysis employed for the NFs containing SiO_2 and water are given in Table J.6.

Two responses were analysed, the change in temperature (ΔT) after 3600 s or 1 h of testing and the slope of the linear portion of the graph ($\Delta T/\Delta t$) taken between t = 90 s and t = 150 s, where t = time. For ΔT after 3600 s the R^2 value obtained from the model was 99.07 % showing the model was a good fit to the data. For the slope the model fit was slightly better at 99.43 %. The main effect plots for the two responses are shown in Figure J.3 and are similar to those seen for Ag NPrs in Figure J.2.

Table J.6 Experimental design for response surface methodology for the SiO_2 containing NFs and water.

	Time / h	**Type**	**Experiment**	**Position**
Type of factor	continuous	categorical	categorical	categorical
Levels	6 (1 h, 2 h, 3 h, 4 h, 5 h, 6 h)	1. SiO_2 NF 2. SiO_2@Ag NPrs 3. Water	1. Repeat 1 2. Repeat 2 3. Repeat 3	1. Back (B) 2. Front (F) 3. Middle (Md)
Number of experiments at each level	9 (3 water, 3 SiO_2 NF, 3 SiO_2@Ag NPr)	18	18	18
Total (levels x number of experiments at each level)	54	54	54	54

Again for both responses the type of fluid used and the position in the SSL were the most important factors, with the middle (Md) position giving consistently higher results. The repeat number and the time both only changed slightly from the mean for ΔT after 3600 s showing that the experimental set-up was fairly well controlled and the repeat samples produced similar results for this response. There was more variation in the results with time for the slope but this may have been due to spectral changes with time for the SiO_2@Ag NPr NF and is still a lower difference than that seen for either “type” or “position”.

The results analysed using ANOVA for the SiO_2 only NF (for the full 9 h of testing) are given in Table J.7 and for the SiO_2@Ag NPr (re-dispersed into ¼ volume water) in Table J.8.

Table J.7 Solar simulator results for repeat measurements on SiO_2 only NF for Set-up A. The confidence level shows the range of possible values for the mean. The grouping shows results that are significantly different.

Position	**Back (B)**	**Front (F)**	**Middle (Md)**
N	9	9	9
Grouping	B	B	A
Mean ΔT after 3600 s / °C	19.87	19.89	23.59
σ ΔT after 3600 s / °C	1.04	0.96	1.16
95 % confidence level for mean ΔT after 3600 s / °C	19.15 to 20.60	19.17 to 20.62	22.87 to 24.32

Position	Back (B)	Front (F)	Middle (Md)
Mean slope ($\Delta T/\Delta t$) / °C s^{-1}	0.018	0.017	0.021
σ slope ($\Delta T/\Delta t$) / °C s^{-1}	0.002	0.002	0.002
95 % confidence level for mean slope ($\Delta T/\Delta t$) / °C s^{-1}	0.016 to 0.019	0.016 to 0.018	0.020 to 0.023

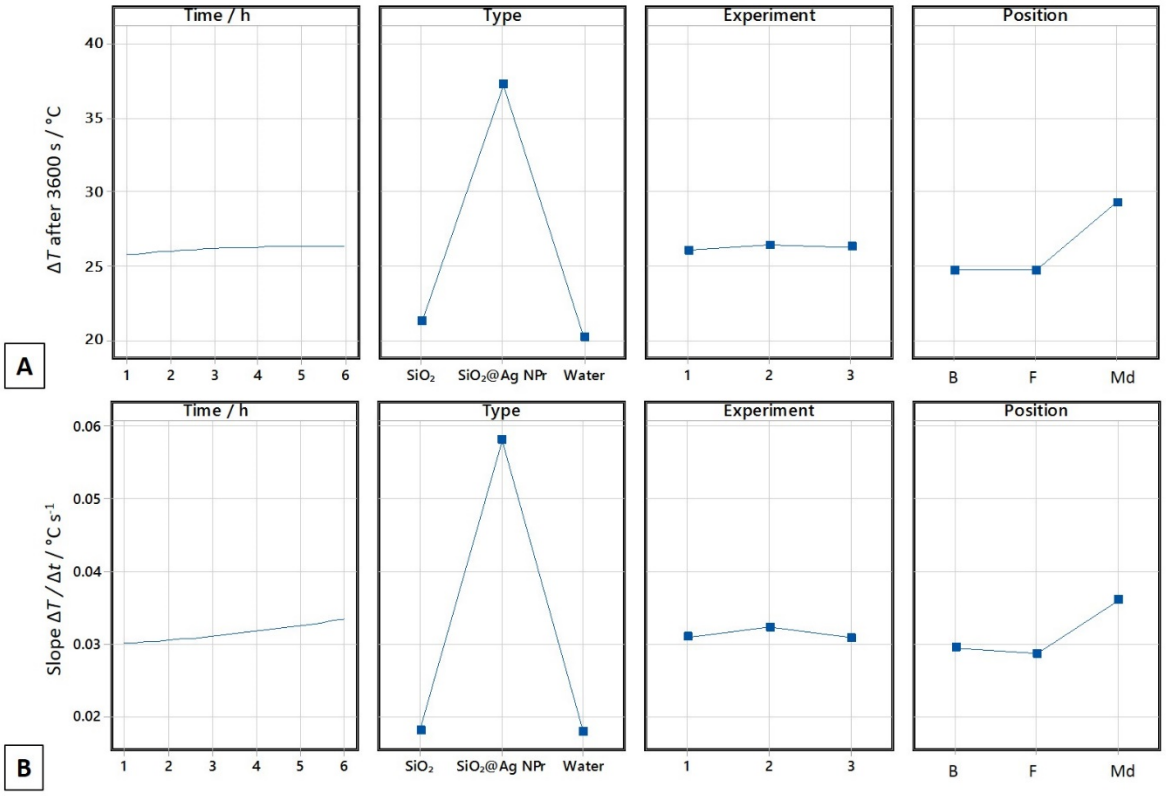

Figure J.3 Main Effect Plots for (A) Value of ΔT after 3600 s in SSL, and (B) The slope $\Delta T/\Delta t$ taken between t = 90 s to t = 150 s for SiO_2, SiO_2@Ag NPrs centrifuged and re-dispersed into ¼ volume of water, and water. Position refers to placement in SSL apparatus where B = Back, F = front and Md = Middle.

The estimation of η_{PE} for the samples measured using the solar simulator set-up A calculated by adjusting the value of η_{PE} of water to 20.51 % are given in Table J.9 along with the values obtained by estimating $\eta_{lamp(330\ nm\ -\ 900\ nm)}$ from the UV-vis spectra. As the UV-vis spectra changed with exposure, the $\eta_{lamp(330\ nm\ -\ 900\ nm)}$ calculations were undertaken using the before exposure (t = 0) and after exposure to SSL data (t = 6 h for SiO_2@Ag NPrs and t = 9 h for SiO_2 only NF). From Table J.9 it appear that the actual performance of the SiO_2@Ag NPr NF in the solar simulator was less than that predicted from calculating $\eta_{lamp(330\ nm\ -\ 900\ nm)}$. This is true even when the measurement uncertainties for calculating η_{PE} and $\eta_{lamp(330\ nm\ -\ 900\ nm)}$ are taken into consideration (see Table E.4 and Table E.5). Even when the small rise in $\Delta T/\Delta t$ with time (Figure J.3) is accounted for and the three results for calculating η_{PE} over the time period of 5 to 6 h in the solar simulator of 77.90 % (back, B, position), 70.95 % (front, F, position) and 82.05 % (middle, Md, position) are considered

in isolation they can be seen to be still lower than the estimated $\eta_{lamp(330\ nm\ -\ 900\ nm)}$ value obtained using the 6 h spectra but slight closer.

Table J.8 Solar simulator results for repeat measurements on SiO_2@Ag NPr NF for Set-up A. The confidence level shows the range of possible values for the mean. The grouping shows results that are significantly different.

Position	**Back (B)**	**Front (F)**	**Middle (Md)**
N	6	6	6
Grouping	B	B	A
Mean ΔT after 3600 s / °C	34.77	34.81	41.72
σ ΔT after 3600 s / °C	1.05	1.00	1.16
95 % confidence level for mean ΔT after 3600 s / °C	33.84 to 35.70	33.88 to 35.74	40.79 to 42.66
Mean slope ($\Delta T/\Delta t$) / °C s^{-1}	0.054	0.053	0.068
σ slope ($\Delta T/\Delta t$) / °C s^{-1}	0.005	0.002	0.004
95 % confidence level for mean slope ($\Delta T/\Delta t$) / °C s^{-1}	0.051 to 0.058	0.049 to 0.056	0.064 to 0.071

Table J.9 Calculations of η_{PE} (using set-up A) for SiO_2 NF and SiO_2@Ag NPr and $\eta_{lamp(330\ nm\ -\ 900\ nm)}$ for SiO_2@Ag NPr re-dispersed into ¼ volume of water.

Fluid and position in solar simulator	**Mean η_{PE} / % or mean $\eta_{lamp(330\ nm\ -\ 900\ nm)}$ / %**	**σ η_{PE} / % or σ $\eta_{lamp(330\ nm\ -\ 900\ nm)}$ / %**	***N***
η_{PE} SiO_2 only NF middle (Md)	24.40	2.12	9
η_{PE} SiO_2 only NF back and front (B & F)	23.51	2.89	18
η_{PE} SiO_2@Ag NPr middle (Md)	77.28	4.90	6
η_{PE} SiO_2@Ag NPr back and front (B & F)	72.66	5.02	12
$\eta_{lamp(330\ nm\ -\ 900\ nm)}$ SiO_2@Ag NPr calculated from t = 0 spectra	98.84	0.22	3
$\eta_{lamp(330\ nm\ -\ 900\ nm)}$ SiO_2@Ag NPr calculated from t = 6 h spectra	99.87	0.08	3

Comparing the η_{PE} values obtained for the SiO_2@Ag NPr NF with the results for the Ag TSCD-PVP NPr in Table J.5 using unpaired t-tests showed the η_{PE} values for SiO_2@Ag NPr to be significantly lower than those for Ag TSCD-PVP NPr NF with a mean difference of 7.34 % (back and front position) and 7.53 % (middle position). This is in contrast to both the $\eta_{lamp(330\ nm\ -\ 900\ nm)}$ and the efficiency calculations obtained directly from the UV-vis spectra (see Table 4-2, Table J.5, Table J.9 and Table M.4) which suggest that the efficiency for the SiO_2@Ag NPrs should be greater than the Ag TSCD-PVP NPr.

Appendix K Additional Information on Stability of Silver Nanofluids (Ag NFs)

This Appendix presents additional results pertaining to the stability of Ag NFs. Firstly, the available literature on stability testing of Ag NFs is presented. This literature is discussed in Chapter 5, Section 5.4. Secondly, the results of measuring the change in spectral response after storage in the dark at 4 °C (ideal conditions – colloidal stability) for various different Ag NFs is presented.

Results assessing the change in UV-vis spectra following exposure to an elevated temperature of 70 °C are then given including any significance testing undertaken. Finally, the results of assessing the change in UV-vis spectra following exposure to SSL are provided. This subsection also assesses the potential impact of any spectral changes following SSL exposure on the calculated efficiency obtained.

K.1 Literature Review on Stability

Some studies looking at exposing Ag NFs to temperature, light or looking at colloidal stability of Ag NFs are given in Table K.1.

Table K.1 Studies that have investigated the effect of time (i.e. colloidal stability), temperature or light on silver NF.

NF details	Colloidal stability	Temperature measurements	Light measurements	Reference
Ag NS in water BF	Visibly stable for ≈ 3 months no storage details	≈ 40 °C for < 10 h – no assessment of NF change	Natural sunlight for ≈ 10 h – no assessment of NF before / after exposure	(Bandarra Filho et al., 2014)
Ag nanodiscs and SiO_2 coated Ag nanodiscs in water BF (stabilised with TSCD and poly sodium 4-styrenesulfonate)	Zeta-potential measurements	Thermal cycling to 80 °C for 3 h and then cooling - 10 cycles	8 h of UV light exposure (λ = 365 nm) + 4 h in dark – ≥ 3 cycles	(Taylor et al., 2018)
SiO_2 coated Ag nanodiscs in glycerol BF	Not discussed	125 °C for up to 96 h	96 h of UV light exposure (λ = 365 nm) at room temperature and 24 h of SSL at 1300 W m^{-2}	(Hjerrild et al., 2018)

NF details	Colloidal stability	Temperature measurements	Light measurements	Reference
SiO_2 coated Ag nanodiscs in water	9 months change in λ_{max} < 5 nm. No storage conditions	-	Outdoor trials with flow – time of testing not specified	(Crisostomo et al., 2017)
Ag TSCD NPs (various NP shapes) in water BF	Not discussed	Up to 80 °C for ≤ 50 minutes	Monochromatic light of 3 different λs (457 nm, 488 nm and 514.5 nm) – temperature constant at 20 °C	(Filipczak et al., 2020)
Ag NS in water BF	1 y in dark (no storage temperature given) – 50 % reduction in Ab_{max}	-	Tested in a HP under SSL – no details of UV-vis results following testing	(Ozsoy and Corumlu, 2018)
Ag NS stabilised with either PVP or poly vinyl alcohol (PVA) in water BF	≤ 6 months stable – visual assessment, no storage details	-	-	(Garcia et al., 2020)
Ag NS stabilised with PVP in water BF	≤ 90 days – stable for 30 days but not 90 days. No storage conditions	-	-	(Mirzaei et al., 2016)
Ag NPs stabilised with TSCD and PVP (≈ λ = 770 nm)	≤ 20 days at 4 °C (in a water bath) ≈ 10 nm shift	9 h at 80 °C – change in λ_{max} to ≈ 450 nm. Lower temperatures also assessed for ≤ 20 days	-	(Zeng et al., 2010)
Ag NS stabilised with Gemini surfactants in water	-	≤ 52 h at temperatures up to 170 °C (steam stability in an autoclave) – decrease in Ab_{max}	-	(Li et al., 2019)
Ag NS and Ag / Au bimetallic NP in water BF	-	-	60 minutes SSL – no change in UV-vis spectra	(Chen, M. et al., 2017)

NF details	Colloidal stability	Temperature measurements	Light measurements	Reference
Ag nanoplates in water BF stabilised with TSCD and PVP	-	95 °C for < 5 minutes	Irradiation with a sodium lamp for ≤ 4.5 h	(Tang et al., 2013)
Ag NS in water BF with TSCD	-	-	≈ 18 h natural sunlight + ≤ 28 h SSL (500 W m^{-2})	(Tang et al., 2015)

K.2 Colloid Stability

The colloidal stability of various NFs was assessed using the protocol described in Section 3.9.2. The change in Ab_{max} following storage in the dark at 4 °C for a number of different NFs is shown in Figure K.1 and the corresponding graph for change in λ_{max} in Figure K.2.

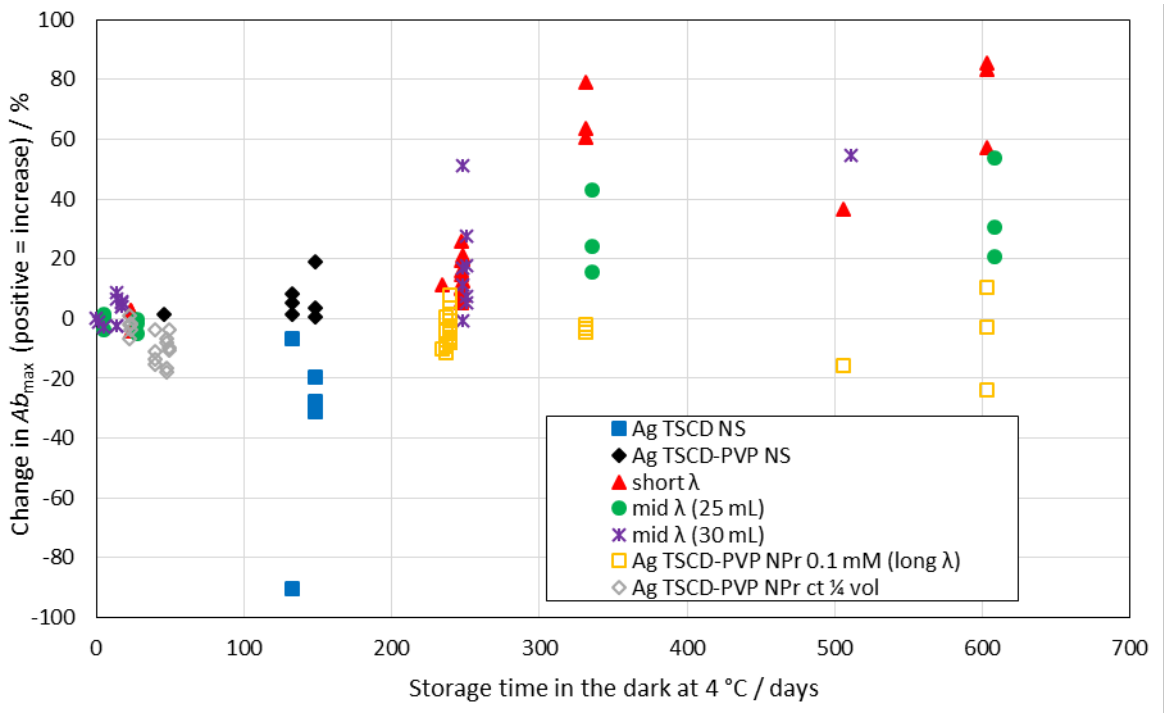

Figure K.1 Change in Ab_{max} for a number of different NF after storage in the dark at 4 °C. The short λ NF was diluted 1: 5 prior to storage, the 25 mL batch size mid λ NF was diluted 1: 3, whereas the 30 mL batch size mid λ NF was diluted 0.3 mL in 1 mL.

For the Ag NS samples the difference in stability obtained by using PVP as an additional stabilising agent was assessed. The TSCD only stabilised NS samples gave an average change in Ab_{max} of -35 % (σ = 32 %, range -7 % to -91 %, N = 5, average storage time 142 days), and for the TSCD-PVP samples the average change in Ab_{max} was 6 % (σ = 6 %, range 1 % to 19 %, N = 7, average storage time 127 days – not significantly different according to a paired t-test). This illustrates the increase in stability obtained by using PVP in addition to TSCD, especially when the fact that the TSCD-PVP samples contained a higher concentration of silver is also considered. There were not

enough samples tested to determine whether the concentration of Ag in the Ag NS NFs was affecting the stability.

The peak position for the Ag NS, λ_{max} did not change much during storage for either the samples stabilised with just TSCD or the TSCD and PVP samples (maximum change = 11 nm – see Figure K.2). According to a paired t-test (see Appendix F, Section F.1), for the samples stabilised with just TSCD the difference was significant but the mean of the difference was < 4 nm, so is likely to be within the measurement error. For the TSCD-PVP stabilised NS the difference in λ_{max} was not significant according to a paired t-test.

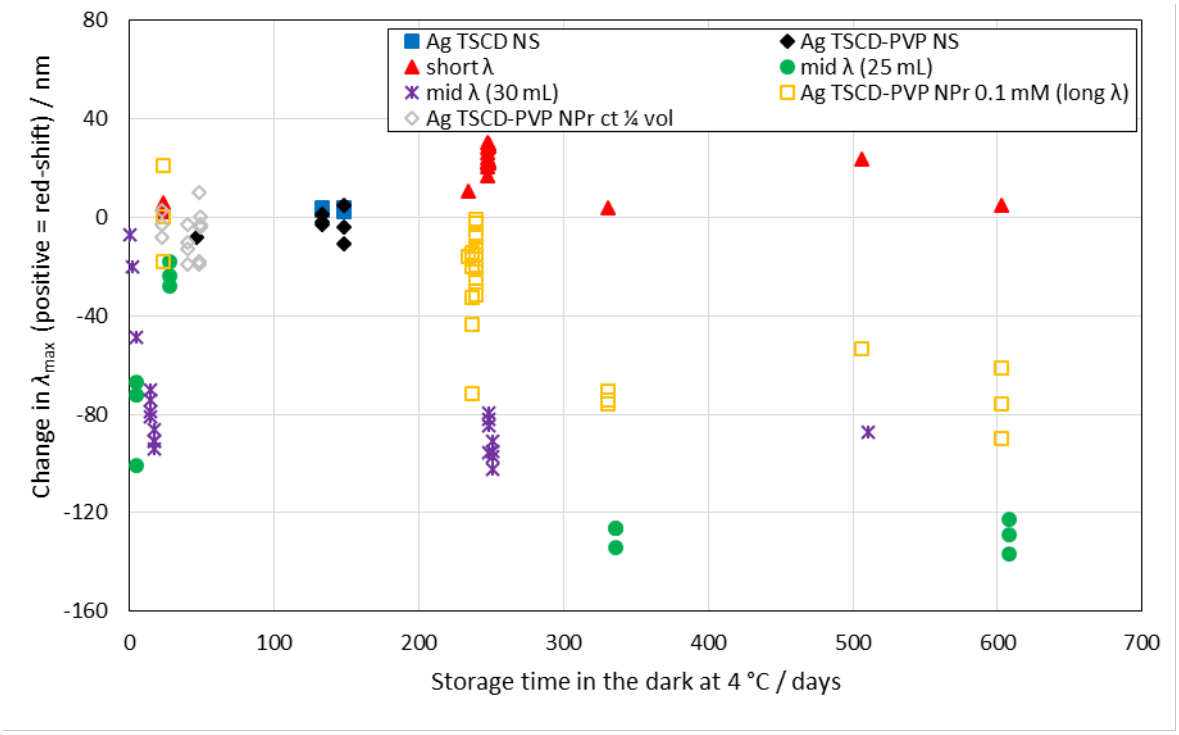

Figure K.2 Change in λ_{max} with storage in the dark at 4 °C for various different NFs. Both the short λ and mid λ NFs have been diluted prior to storage.

For the Ag NPrs both centrifuged (re-dispersed into ¼ volume of water) and non-centrifuged (0.1 mM Ag) samples were tested. All the Ag NPr samples were stabilised with both TSCD and PVP. For the centrifuged Ag NPrs after 22 days storage there was on average a very small reduction in Ab_{max}. However, a paired t-test showed this reduction to be not significant. This was the same for λ_{max} for the centrifuged Ag NPrs where there was on average a small blue-shift, which was not significant according to a paired t-test (see Figure K.2). After a further period of storage, there were more differences between the spectra, with a reduction in Ab_{max} of on average 11 % and a blue-shift in λ_{max} of 9 nm. Again although the average difference was larger after 45 days storage the value of σ and the measurement uncertainty still point to there being no change in both Ab_{max} and λ_{max} although paired t-tests did show the change in Ab_{max} and λ_{max} to be significant.

For the more dilute (0.1 mM) Ag TSCD-PVP NF (long λ) after a short storage time (23 days) there was again no change in either Ab_{max} or λ_{max} according to a paired t-test. However, when the storage time was extended λ_{max} blue-shifted while Ab_{max} remained almost unchanged (although significantly different according to a paired t-test, the size of the mean difference was < 5 %). Although there was a downward trend with storage time (i.e. a blue-shift) there was considerable variation between individual samples giving a very low value of R^2 of 0.55 for a linear trend line through the data. This makes it hard to determine the exact effect of storage time on the position of λ_{max} or even if there is a relationship between storage time and change in λ_{max}.

All the short λ NF used as one of the three component NFs in the broadband absorber the NFs were diluted 1: 5 before storage in the dark at 4 °C. After 23 days storage there was no changes in either Ab_{max} or λ_{max} (no significant change according to a paired t-test). After a further period of storage both Ab_{max} and λ_{max} increased (red-shift in λ_{max}). Again like the Ag NPrs there was considerable variation between one sample and another. When the change in Ab_{max} was plotted against storage time (see Figure K.1), there was an overall increase, however, because of the variation in the data obtained the R^2 value for the linear fit was extremely poor (0.64). Some of the increase in Ab_{max} may have been cause by evaporation of the sample with storage time (the samples were carefully sealed before storage to try and reduce this). For λ_{max} although there appeared to be a red-shift with storage time (mean value of red-shift of 26 nm, significant according to a paired t-test), the variation in data lead to an even lower value of R^2 of 0.25 (for a linear fit to the data), suggesting there was no linear relationship between storage time and change in λ_{max} for the short λ NF.

Like the short λ NFs the mid λ NFs were also diluted prior to storage. However, following dilution there was a rapid change in the position of λ_{max} for the mid λ NF. This change appeared for the 25 mL batch volume samples to be reversible over a short timeframe with λ_{max} changing by 80 nm (blue-shift) after 5 days in the dark but this change then reversed leading to a 23 nm blue-shift in λ_{max} after 28 days storage. Further investigation of the effect of storage on the mid λ NF would be needed to confirm this change in λ_{max}. After a longer period of storage (336 days) there was a further blue-shift in λ_{max} for the 25 mL batch samples of 129 nm (total change from start). The rate of change then slowed with the 25 mL samples that had been stored for 603 days still having a blue-shift in λ_{max} of 129 nm on average (σ = 17 nm, N = 3).

For the mid λ NF made using a 30 mL batch volume, this reversal in change in λ_{max} following a short storage time (≈ 20 days - 30 days) was not seen. However there was again a rapid blue-shift in λ_{max} of 83 nm after ≈ 16 days. This change in λ_{max} then slowed with the 248 day storage samples having a change in λ_{max} of -88 nm on average.

Ab_{max} for the mid λ NFs in contrast did not change by much (see Figure K.1) initially. After a further period of storage some samples showed an Ab_{max} increase of > 30 % whereas others had not increased at all. This points to incomplete sealing of the samples causing evaporation of the NF with time, leading to an increase in Ab_{max}. Further stability studies would be needed to confirm this.

K.2.1 Broadband absorber

In total 7 individual batches of the broadband absorber were measured using UV-vis using the method described in Section 3.7.3 over an extended period of storage in the dark at 4 °C. For 3 of the batches extra subsamples were removed from the main batch after ≈ 57 days - 90 days and then stored (samples 5, 6 and 7).

The first 3 broadband absorber batches were produced by combining component NFs produced using a 25 mL batch volume, whereas the other 4 batches were produced using a 30 mL batch volume for the component NFs. The UV-vis spectra initially and following storage for the 7 batches are shown in Figure K.3 - Figure K.9.

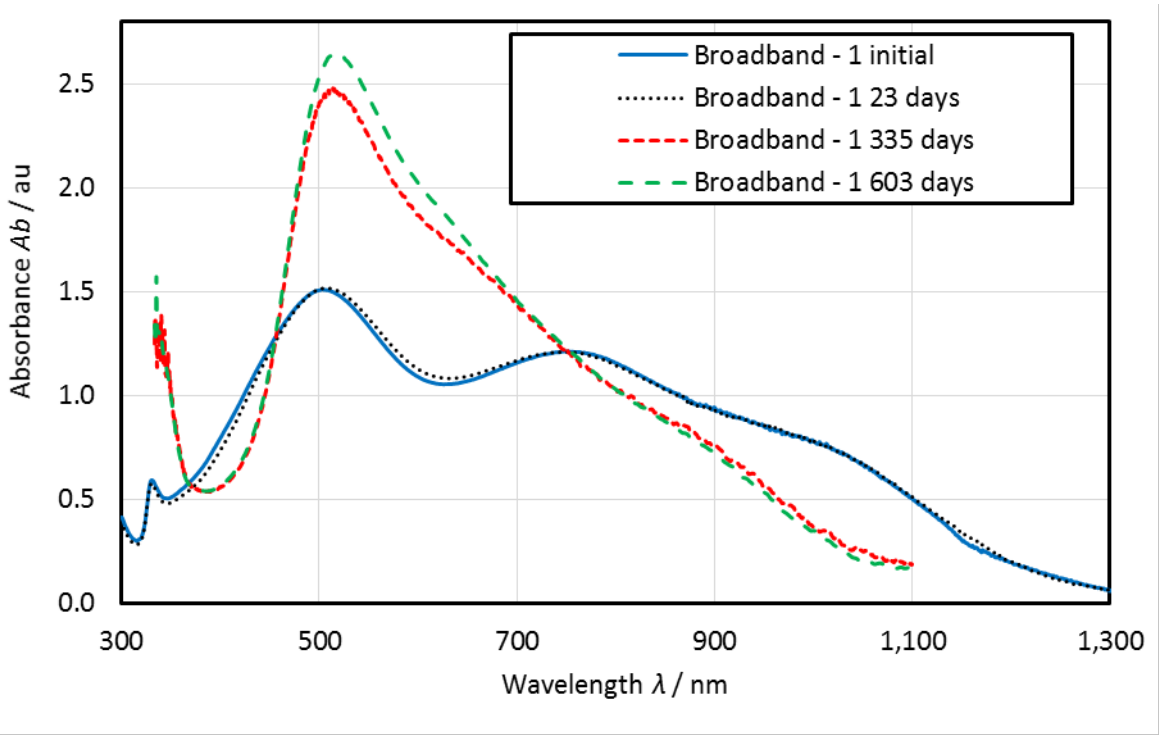

Figure K.3 UV-vis spectra of the broadband absorber (batch 1) initially and after storage in the dark at 4 °C for a maximum of 603 days. The sample was measured using UV-vis-IR-1 initially and at *t* = 23 days and using UV-vis-IR-2 after 335 days and 603 days.

For the first 3 batches the results were similar (see Figure K.3, Figure K.4 and Figure K.5), with all 3 samples being stable after 23 days storage. However, when the storage time was extended the height of the main peak increased by about 60 % and red-shifted by 10 nm – 50 nm, the shoulder corresponding to the mid λ NF became much less pronounced and the shoulder corresponding to

the long λ was blue-shifted. These changes observed reflect the changes observed for the component NFs with extended storage.

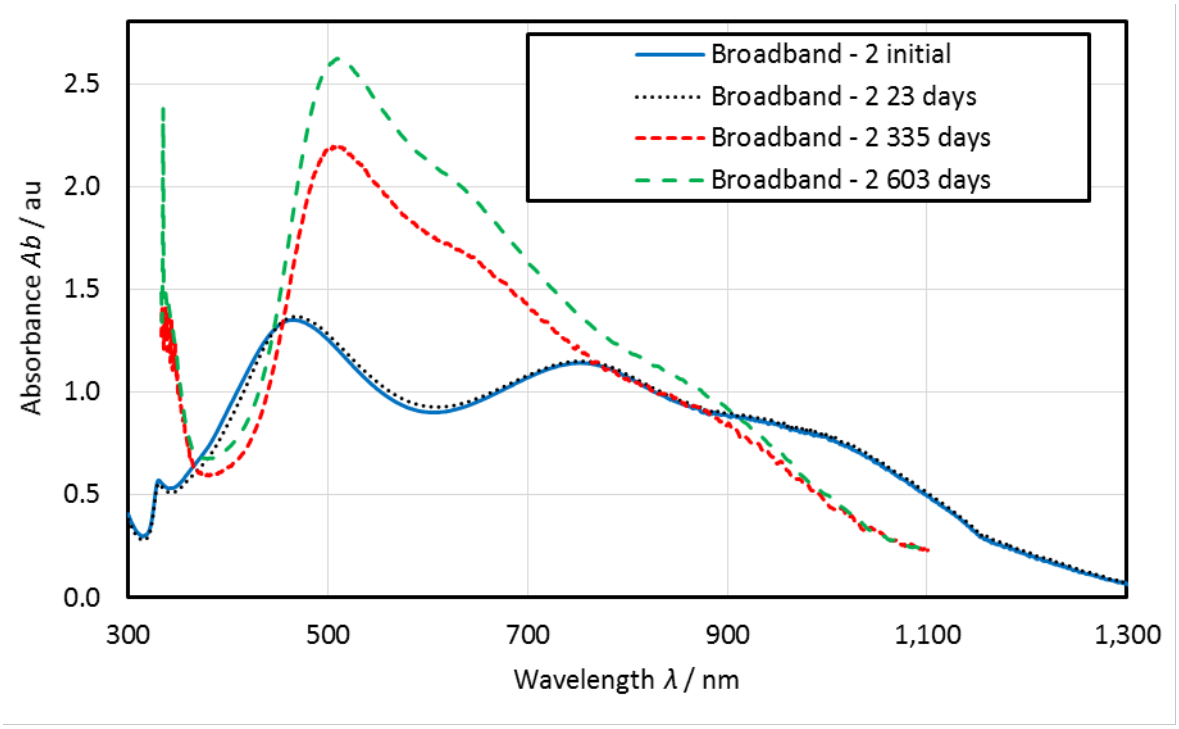

Figure K.4 UV-vis spectra of the broadband absorber (batch 2) initially and after storage in the dark at 4 °C for a maximum of 603 days. The sample was measured using UV-vis-IR-1 initially and at t = 23 days and using UV-vis-IR-2 after 335 days and 603 days.

For the fourth broadband sample (Broadband – 4 in Figure K.6), there was again an increase in height of the primary peak with extended storage (≈ 45 %) and a corresponding red-shift in λ_{max} of ≈ 50 nm. The shoulder corresponding to the mid λ NF was not as pronounced in the initial sample so it was hard to tell if this was again becoming less pronounced with storage, however it did appear to be blue-shifting. Unlike the first 3 broadband samples tested there was no blue-shift in the position of the shoulder corresponding to the long λ NF.

The other three broadband absorber batches (samples 5, 6 and 7) all exhibited similar behaviour to each other with storage in the dark at 4 °C. There was still a small increase in the height (≈ 10 %) of the primary peak and a red-shift in λ_{max} of ≈ 50 nm, however, the height increase was not as pronounced as for samples 1 – 4 and the peak also appeared to be becoming broader. Like broadband – 4 there did not appear to be much change in the position of the shoulder corresponding to the long λ NF. It is likely that the variation in stability of the mid and long λ NFs with time (see Figure K.2) may be part of the reason for the differences in the way in which the broadband absorber changes with extended storage but further studies would be needed to confirm this.

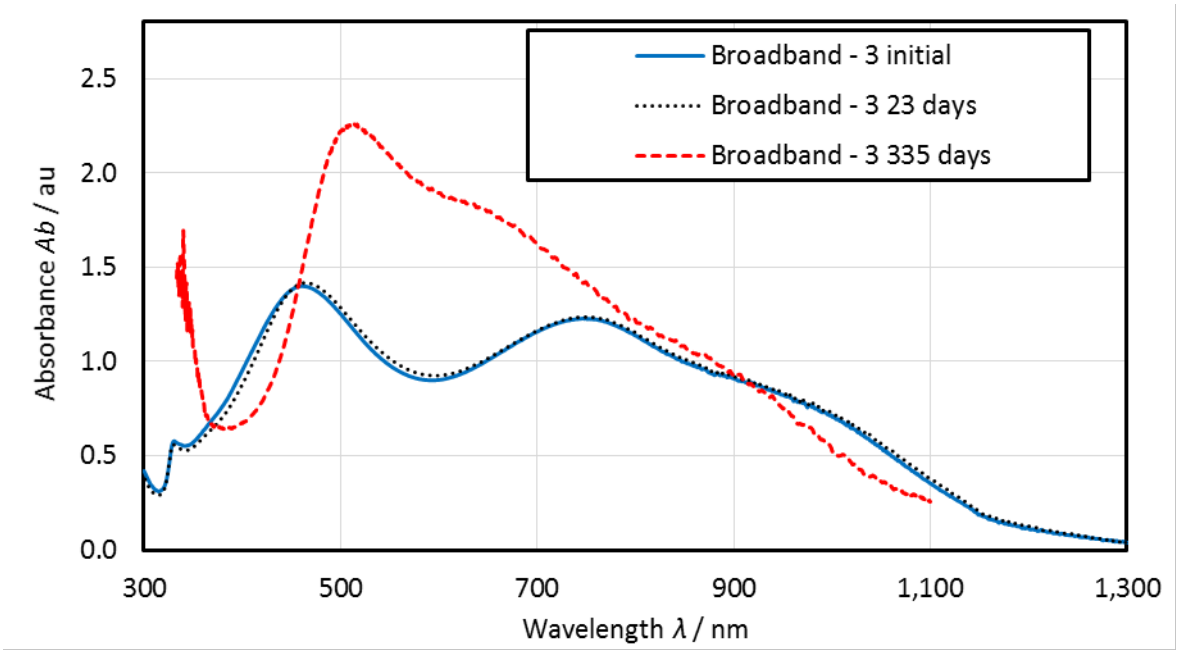

Figure K.5 UV-vis spectra of the broadband absorber (batch 3) initially and after storage in the dark at 4 °C for a maximum of 335 days. The sample was measured using UV-vis-IR-1 initially and at t = 23 days and using UV-vis-IR-2 after 335 days.

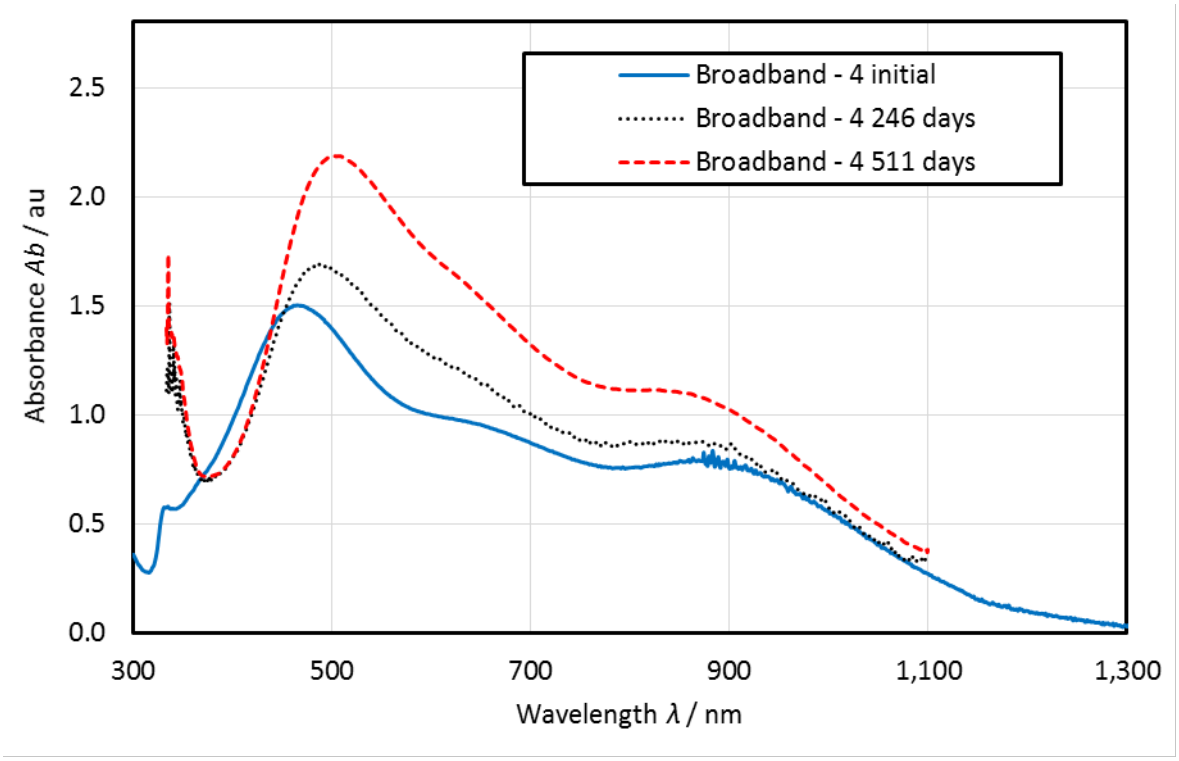

Figure K.6 UV-vis spectra of the broadband absorber (batch 4) initially and after storage in the dark at 4 °C for a maximum of 511 days. The sample was measured using UV-vis-IR-1 initially and using UV-vis-IR-2 after 246 days and 511 days.

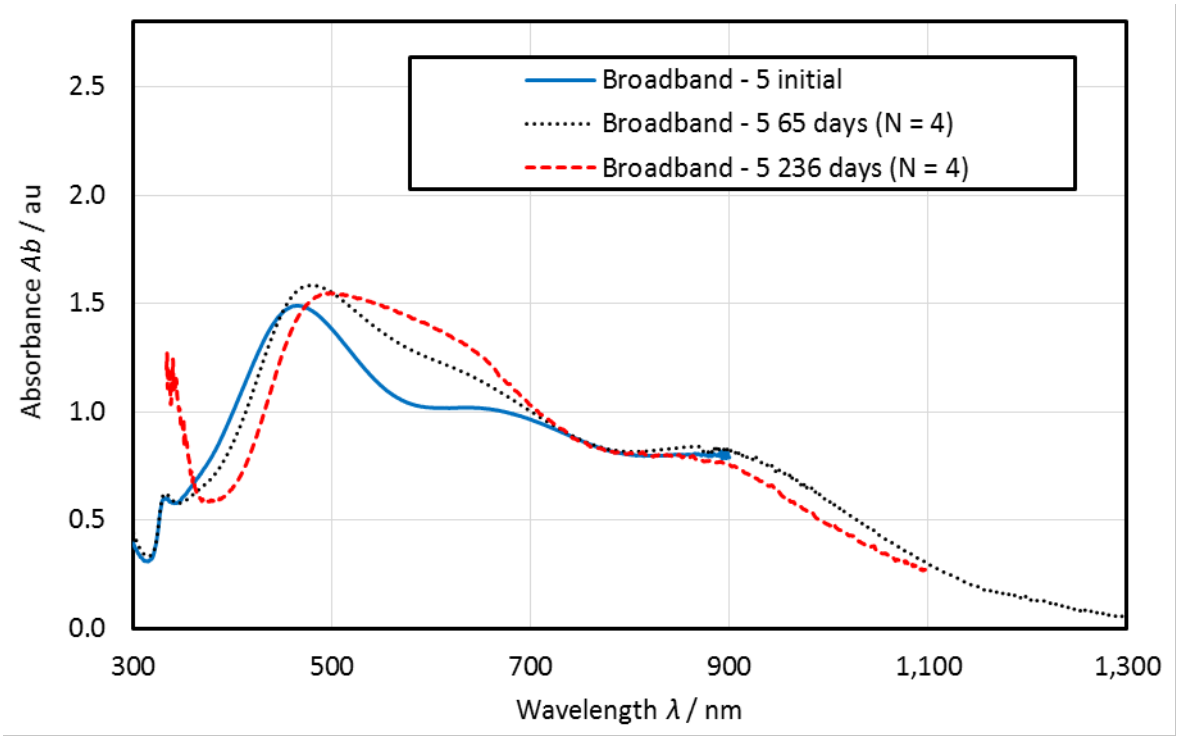

Figure K.7 UV-vis spectra of the broadband absorber (batch 5) initially and after storage in the dark at 4 °C for a maximum of 236 days.

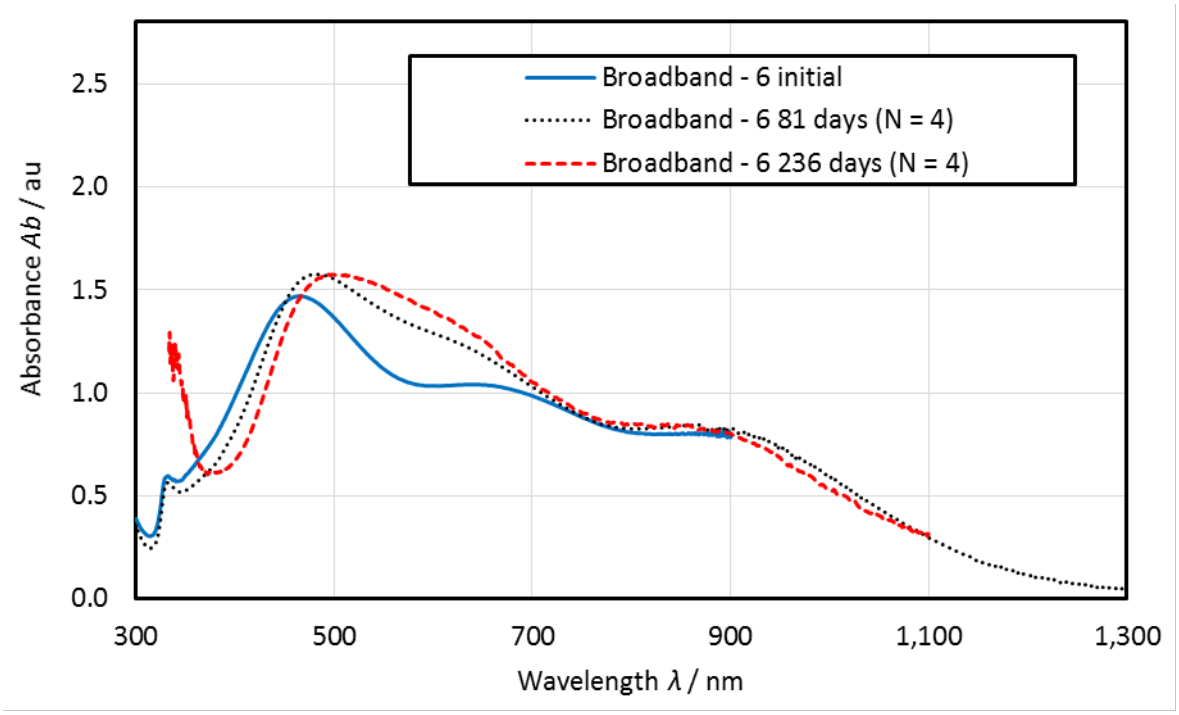

Figure K.8 UV-vis spectra of the broadband absorber (batch 6) initially and after storage in the dark at 4 °C for a maximum of 236 days.

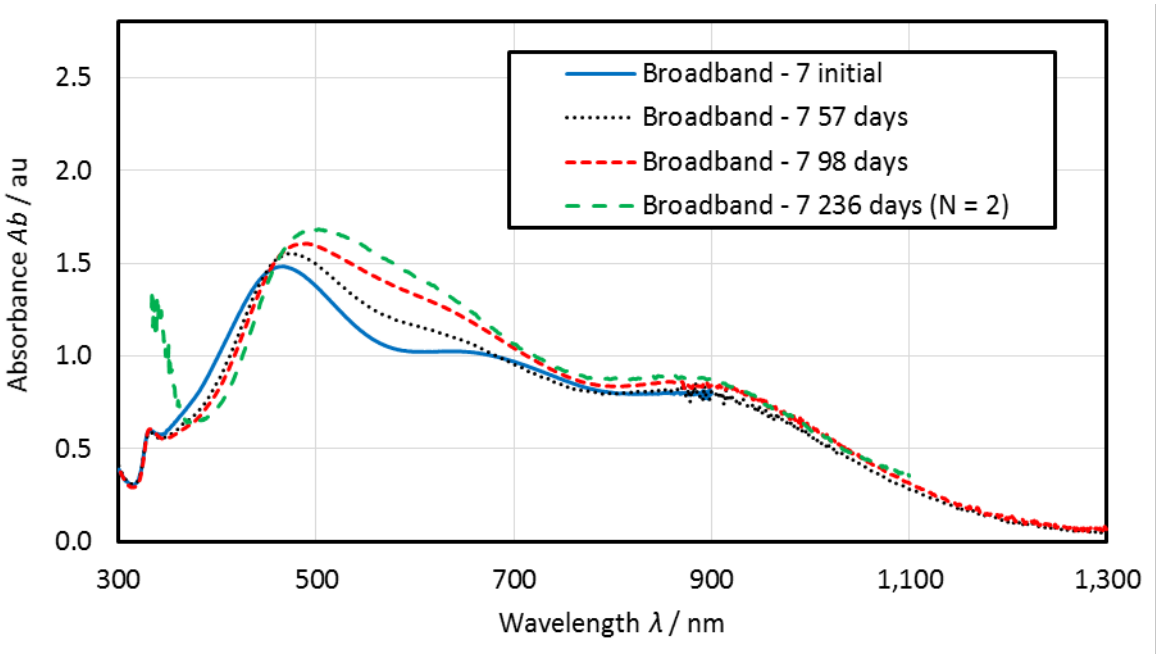

Figure K.9 UV-vis spectra of the broadband absorber (batch 7) initially and after storage in the dark at 4 °C for a maximum of 236 days.

K.3 Silver Nanofluid Stability at Elevated Temperature

The change in λ_{max} following exposure to a temperature of 70 °C for the Ag NS and the short λ NFs are shown in Figure K.10 and the corresponding change in Ab_{max} in Figure K.11. The short λ NF was diluted 1: 5 before temperature testing.

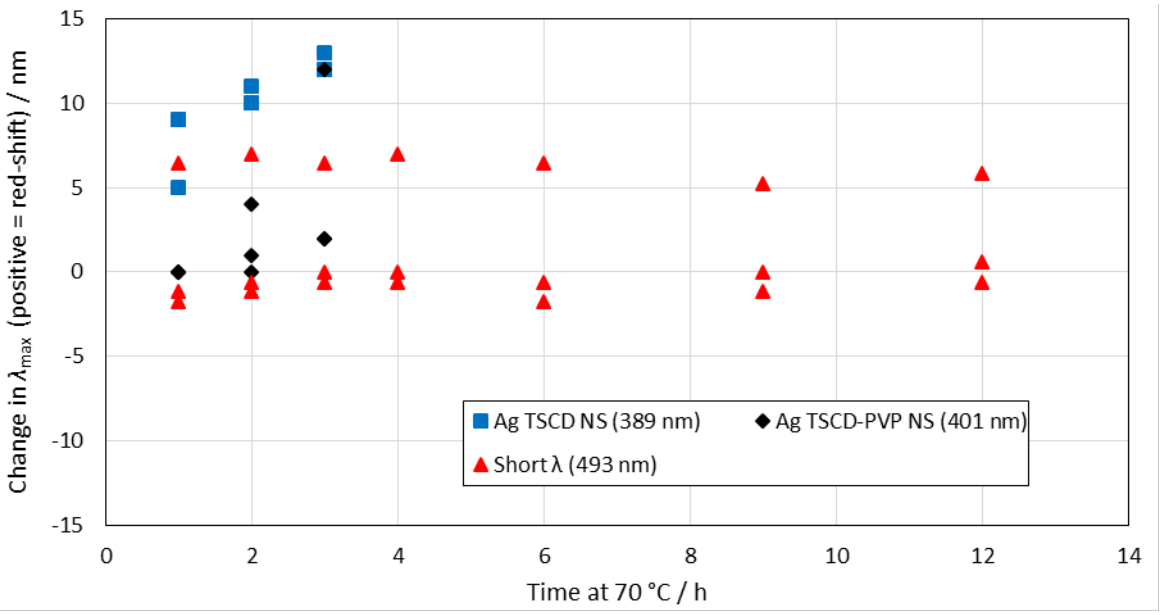

Figure K.10 Change in λ_{max} with exposure to a temperature of 70 °C for Ag NS and the short λ NF (the short λ NF has been diluted 1: 5 prior to testing). The average starting λ_{max} is shown in brackets (N = 3 in all cases).

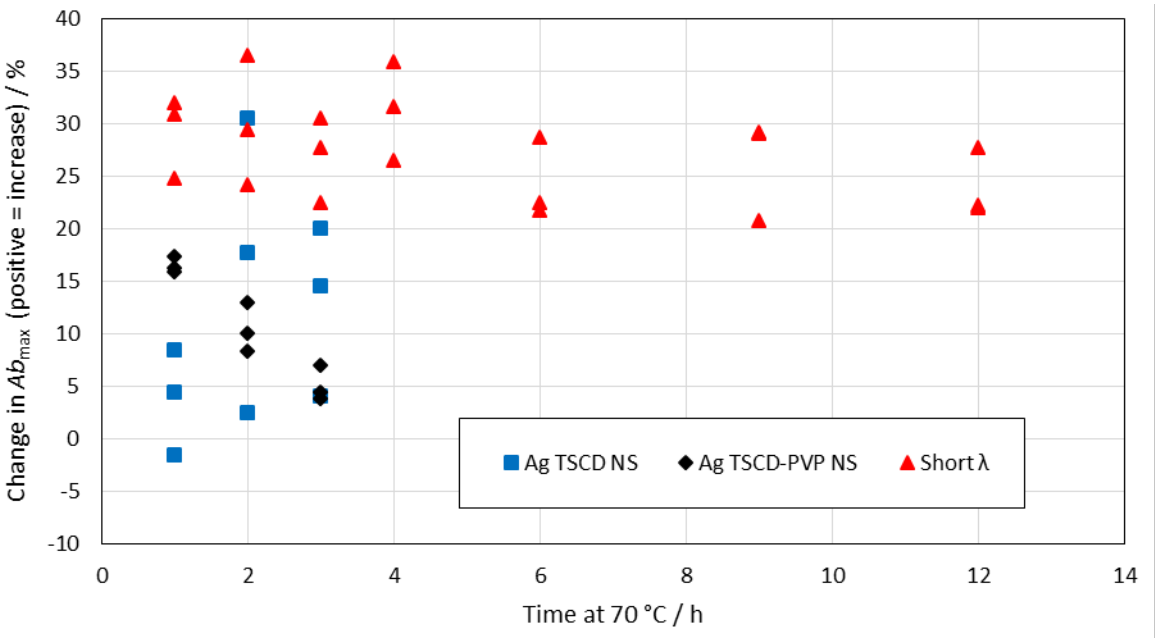

Figure K.11 Change in Ab_{max} with exposure to a temperature of 70 °C for Ag NS and the short λ NF (the short λ NF has been diluted 1: 5 prior to testing).

There was a small but significant red-shift in λ_{max} of ≈ 12 nm for the Ag TSCD NS samples combined with an increase in peak height of ≈ 13 % (confirmed by unpaired two-sample t-tests – significantly different results in Table K.2). In contrast the Ag TSCD-PVP stabilised NS NFs showed no significant change in either λ_{max} or Ab_{max} over the same 3 h test period. The short λ NF was tested for a longer time of 12 h and exhibited a larger change in Ab_{max} of ≈ 24 % but no significant change in λ_{max} over this extended testing time.

Table K.2 Two-sample t-test results for Ag NS and short λ NF before and after exposure to elevated temperature (only the significant differences shown).

Sample 1	**Sample 2**	**Variable**	**Direction of change**	**Average difference**	**Range of difference (at 95 % confidence)**
Ag TSCD NS after 3 h at 70 °C	Ag TSCD NS initial	λ_{max}	Red-shift	12.33 nm	11.41 nm to 13.26 nm
Ag TSCD NS after 3 h at 70 °C	Ag TSCD NS initial	Ab_{max}	Increase	12.7 %	0.6 % to 24.8 %
Short λ after 12 h at 70 °C	Short λ initial	Ab_{max}	Increase	24.0 %	15.5 % to 32.5 %

For the mid λ NF and the Ag NPr NFs the results obtained following exposure to a temperature of 70 °C are given in Figure K.12 (change in λ_{max}) and in Figure K.13 (change in Ab_{max}). The picture for these NFs was more complicated. The mid λ NF exhibited a rapid large blue-shift in λ_{max}. The rate of change then slowed down leading to ≈ 60 nm - 120 nm blue-shift after exposure (average difference obtained from t-test shown in Table K.3 of 96 nm). There was considerable variation in the magnitude of the blue-shift obtained. Ab_{max} increased slightly on average by ≈ 8 % over the 12 h testing period for the mid λ NF. Again there was some sample variation with one sample

showing a small decrease in Ab_{max}, so although this average rise was just significant according to an unpaired two-sample t-test it may have been caused by some evaporation of the test sample with exposure time and hence may not a real change.

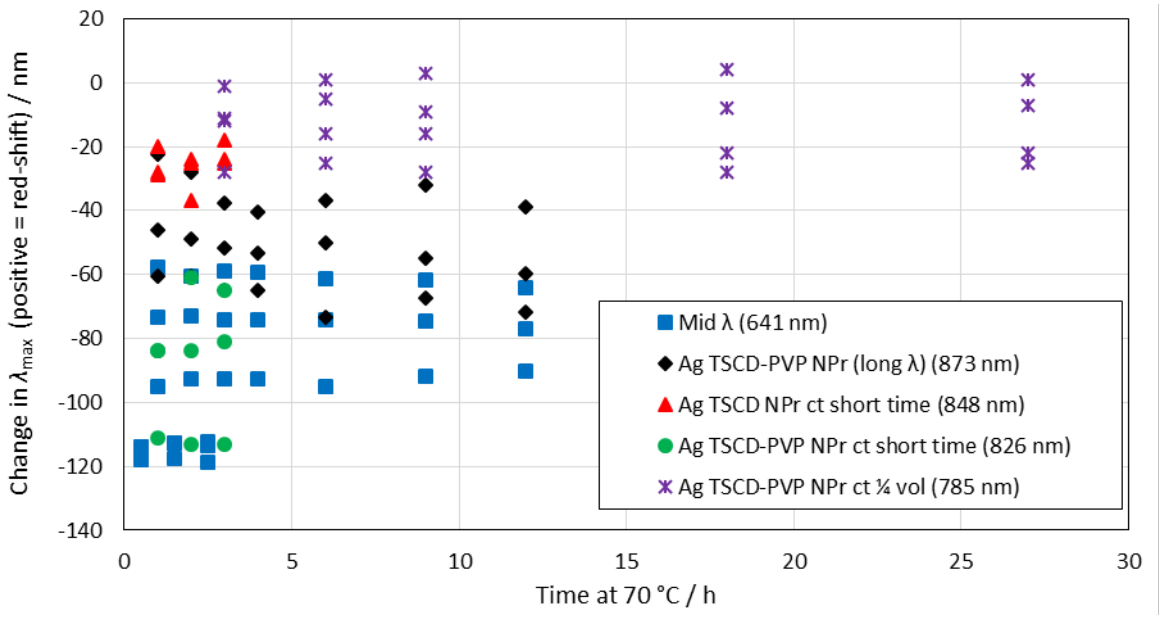

Figure K.12 Change in λ_{max} with exposure to a temperature of 70 °C for the mid λ NF and various different Ag NPr NFs (the mid λ NF has been diluted 1: 3 prior to testing). The average starting λ_{max} is shown in brackets.

More tests were undertaken using Ag NPr NFs, resulting in even more variation in the amount of blue-shift in λ_{max} obtained. In contrast there was no significant change in Ab_{max} for any of the Ag NPr NFs tested. For the as synthesised 0.1 mM Ag TSCD-PVP NPrs (long λ NF), a blue-shift in λ_{max} of 20 nm – 60 nm again occurred rapidly within the first hour of exposure. The rate of change of λ_{max} then slowed with the average change in λ_{max} being -57 nm after a total of 12 h. This change was significant according to an unpaired two-sample t-test (see Table K.3).

The centrifuged Ag TSCD NPrs exhibited a similar 20 nm - 30 nm blue-shift after 1 h of exposure. Again the rate of change of λ_{max} then slowed resulting in an average significant change of -22 nm after 3 h. These centrifuged samples were prepared by centrifuging at 12,857 r.c.f. (10,000 rpm) for 15 minutes and the supernatant removed before re-dispersing into water (shown as ct short time in Figure K.12). When the same centrifuging conditions were used on Ag TSCD-PVP NPrs (designated as ct short time), there was a larger rapid blue-shift in λ_{max} of 60 nm – 120 nm with considerable sample variation. However, when concentrated Ag TSCD-PVP NPr NFs were prepared by centrifuging using 16,168 r.c.f. (13,000 rpm) for 30 minutes (the standard centrifuging conditions given in Section 3.5.3 for Ag NPrs stabilised with both TSCD and PVP) there was no significant change in λ_{max} even over an extended testing period of 27 h.

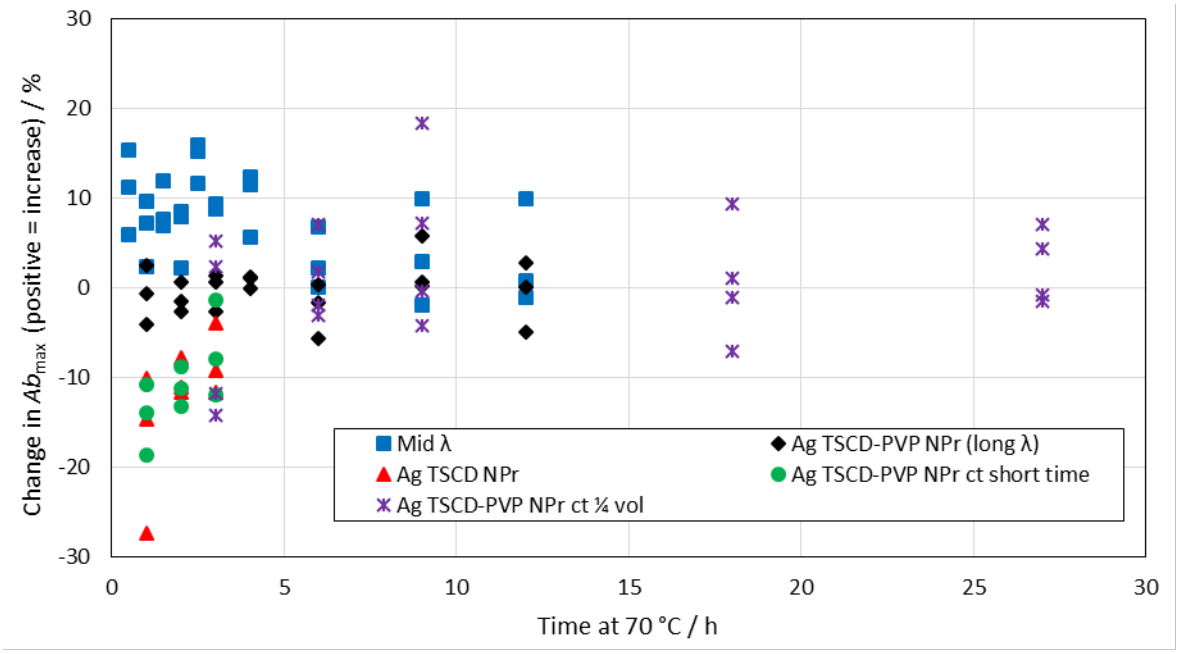

Figure K.13 Change in Ab_{max} with exposure to a temperature of 70 °C for the mid λ NF and various different Ag NPr NFs (the mid λ NF has been diluted 1: 3 prior to testing).

The level of TSCD present in the solution is known to affect the shift in λ_{max} obtained when Ag nanoplates are exposed to temperature and sunlight (Tang et al., 2015; Tang et al., 2013). It is possible therefore that the amount of centrifuging is affecting the amount of TSCD in the final NF and hence the magnitude and speed of change in λ_{max}. When all the TSCD is present (as in the case of the long λ NFs), the blue-shift in λ_{max} is ≈ 50 nm – 60 nm. When some of the TSCD is removed, but the solution is concentrated as in the case of the Ag TSCD NPrs a similar blue-shift of 20 nm – 30 nm is obtained. When there is incomplete removal of the TSCD and concentration (in the case of the Ag TSCD-PVP NPrs short centrifuge time) there is a rapid large change in λ_{max}. When all or nearly all of the TSCD is removed as in the case of the Ag TSCD-PVP NPrs centrifuged ¼ volume samples there is no significant change in λ_{max}.

It is also possible that the starting position of λ_{max} is also contributing to the level of change in λ_{max} observed. The Ag TSCD-PVP NPrs centrifuged ¼ volume samples had an initial λ_{max} of 785 nm on average already ≈ 50 nm – 100 nm blue-shifted from the initial λ_{max} of the other Ag NPr samples tested perhaps reducing any change in λ_{max} observed.

Further investigations into both the role of the TSCD and the starting value of λ_{max} would be needed to understand the relative contribution of these two factors to the shape evolution of the Ag NPrs with exposure to elevated temperature.

Table K.3 Unpaired two-sample t-test results for Ag NPrs and mid λ NF before and after exposure to elevated temperature (unpaired two-sample t-test used as the before and after samples were different sub-samples from the main sample). Only the significant differences are shown.

Sample 1	**Sample 2**	**Variable**	**Direction of change**	**Average difference**	**Range of difference (at 95 % confidence)**
Mid λ after temperature exposure	Mid λ initial	λ_{max}	Blue-shift	-95.8 nm	-113.1 nm to -78.5 nm
Mid λ after temperature exposure	Mid λ initial	Ab_{max}	Increase	8.7 %	2.4 % to 15.1 %
Ag TSCD-PVP NPr (long λ) after 12 h at 70 °C	Ag TSCD-PVP NPr (long λ) initial	λ_{max}	Blue-shift	-56.7 nm	-87.7 nm to -25.6 nm
Ag TSCD NPr centrifuged short time after 3 h at 70 °C	Ag TSCD NPr centrifuged short time initial	λ_{max}	Blue-shift	-22.3 nm	-30.2 nm to -14.4 nm
Ag TSCD-PVP NPr centrifuged short time after 3 h at 70 °C	Ag TSCD-PVP NPr centrifuged short time initial	λ_{max}	Blue-shift	-86.3 nm	-148.2 nm to -24.4 nm

K.4 Silver Nanofluids Stability With Exposure to Simulated Sunlight (SSL)

The UV-vis spectra before and after exposure to SSL for 12 h using set-up A for Ag TSCD-PVP NPrs, centrifuged and re-dispersed into ¼ volume of water are shown in Figure K.14. All three repeats exhibited a blue-shift in λ_{max} following exposure to SSL for 12 h, showing the Ag NPrs to be unstable to morphological changes with SSL exposure. Although there was some variation in Ab_{max} there was no decrease showing the NF to be stable to aggregation over the limited time tested.

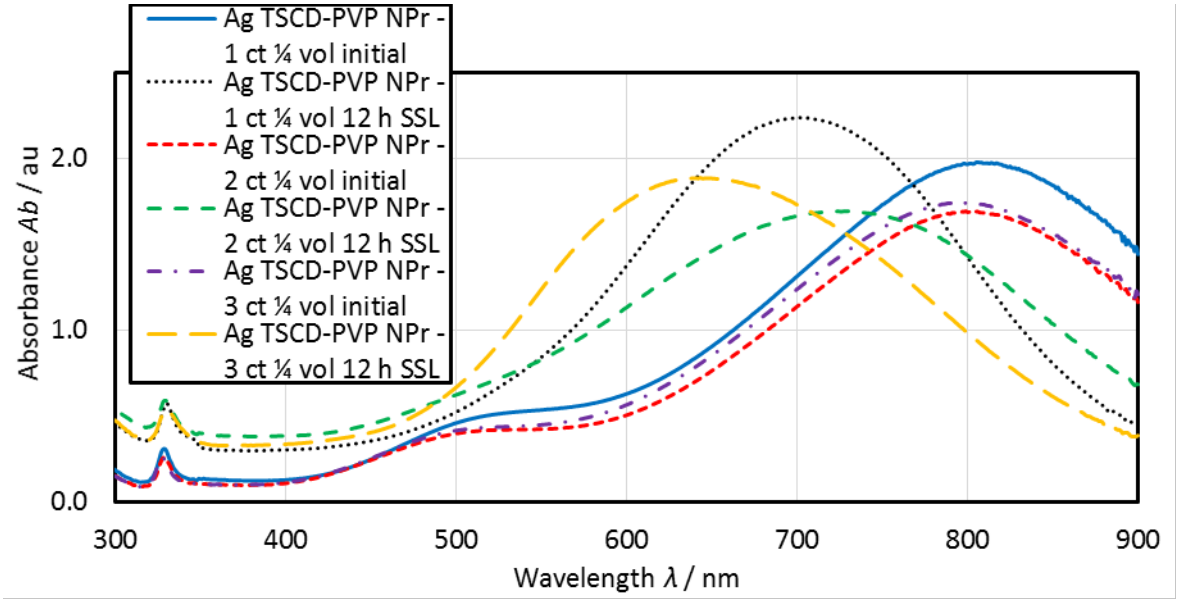

Figure K.14 UV-vis spectra of Ag TSCD-PVP NPrs centrifuged and re-dispersed into ¼ volume of water before and after SSL exposure using set-up A for 12 h. Measured using a 4 mm path length plastic cuvette and UV-vis-1.

When not centrifuged Ag TSCD-PVP NPrs were tested for a shorter time using set-up B, there was again a blue-shift in λ_{max} (see Figure K.15) and no large reduction in Ab_{max}. In contrast the short λ NF exhibited a small red-shift in λ_{max} (≈ 24 nm average value) and a significant increase in Ab_{max} following SSL exposure using set-up B for 0.5 h (see Figure K.16). The width of the absorption peak also narrowed. There was some variation between samples with one sample having no red-shift in λ_{max} (short λ – 1) and the other two samples having a red-shift of > 30 nm.

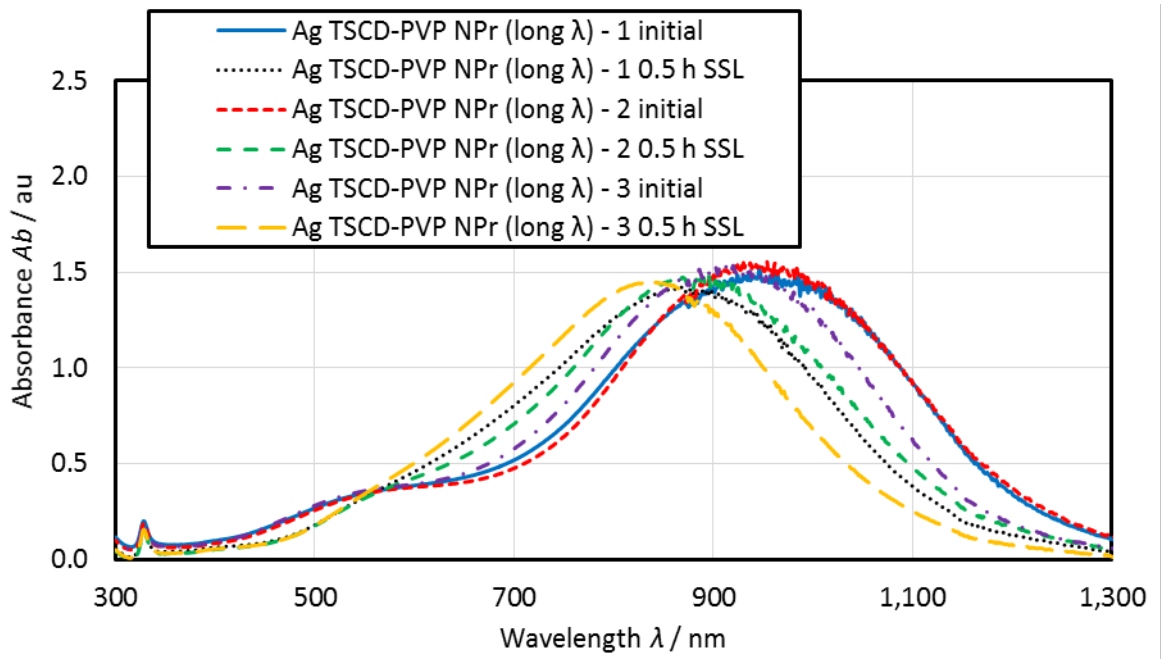

Figure K.15 UV-vis spectra of Ag TSCD-PVP NPr (long λ) before and after 0.5 h exposure to SSL using set-up B. Measured using a 10 mm path length plastic cuvette and UV-vis-IR-1.

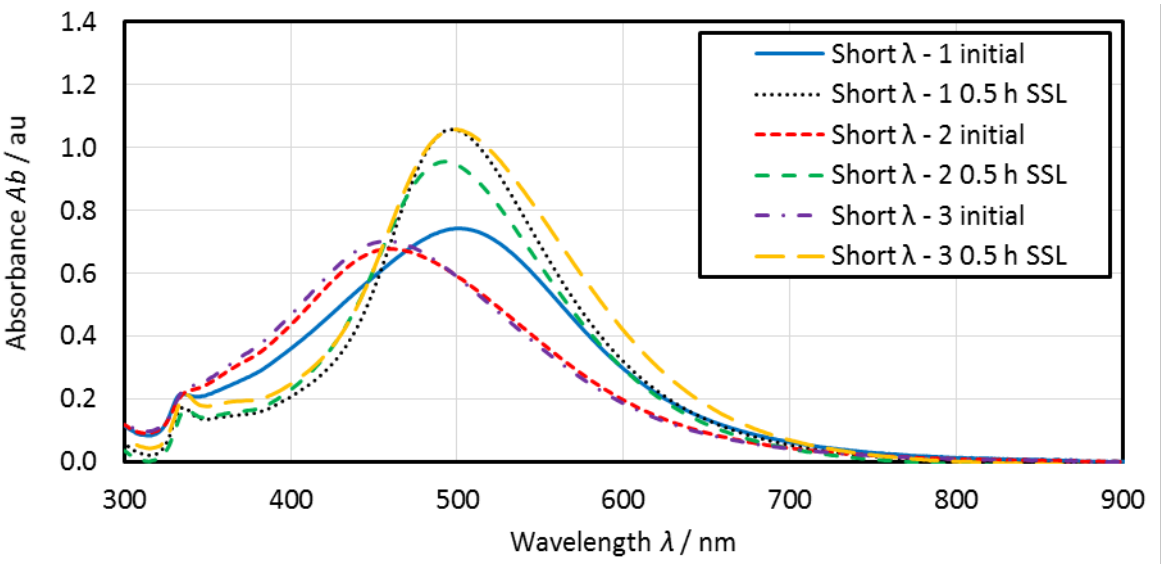

Figure K.16 UV-vis spectra of short λ before and after 0.5 h exposure to SSL using set-up B. Measured using a 10 mm path length plastic cuvette and UV-vis-IR-1. The short λ NF was diluted 1: 5 prior to testing.

The mid λ NF shown in Figure K.17, like the long λ and centrifuged Ag NPr NFs was stable to aggregation with no reduction in Ab_{max} after exposure to SSL for 0.5 h. It was, however, not stable

to morphological changes exhibiting a large blue-shift in λ_{max} and a narrowing of the width of the peak.

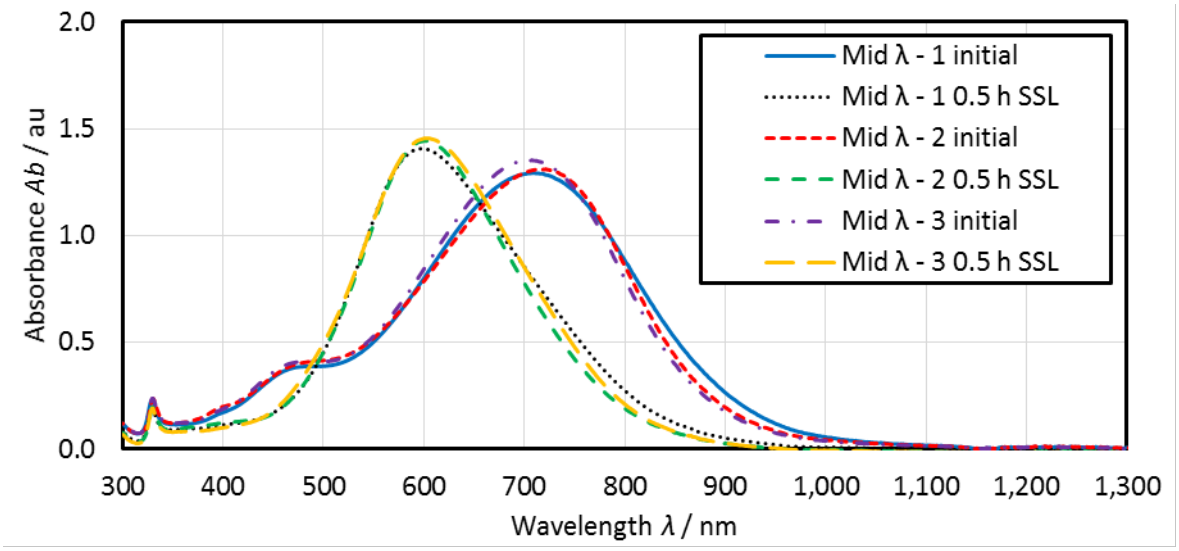

Figure K.17 UV-vis spectra of mid λ before and after 0.5 h exposure to SSL using set-up B. Measured using a 10 mm path length plastic cuvette and UV-vis-IR-1. The mid λ NF was diluted 1: 3 prior to testing.

To understand the implication of the morphological changes in the various NFs following exposure to SSL, the change in efficiency following exposure was calculated. The results for $\eta_{lamp(330\ nm\ -\ 1100\ nm)}$ are given in Table K.4 (or $\eta_{lamp(330\ nm\ -\ 900\ nm)}$ for samples not measured past 900 nm) and for two other efficiency calculations in Table K.5. It was not possible to calculate the efficiencies shown in Table K.5 for the centrifuged Ag NPrs as they were only measured over a range of 200 nm – 900 nm. It should also be noted that the before values used in both Table K.4 and Table K.5 are different to the initial values in Table H.7 and Table H.11 as for these calculations the spectra obtained just before SSL exposure was used rather than the spectra obtained immediately after synthesising.

Table K.4 Change in $\eta_{lamp(330\ nm\ -\ 1100\ nm)}$ or $\eta_{lamp(330\ nm\ -\ 900\ nm)}$ following exposure to SSL for various different NFs.

NF	**Simulator set-up and testing time / h**	**Measurement range for η_{lamp} / nm**	**Initial η_{lamp} / %**	**Final η_{lamp} / %**	**Change in η_{lamp} / % (positive = increase)**
Ag TSCD-PVP NPr centrifuged ¼ volume - 4	Set-up A 12 h	330 - 900	92.79	99.25	6.47
Ag TSCD-PVP NPr centrifuged ¼ volume - 5	Set-up A 12 h	330 - 900	90.66	99.65	8.99
Ag TSCD-PVP NPr centrifuged ¼ volume - 6	Set-up A 12 h	330 - 900	91.71	99.71	7.99
0.1 mM Ag TSCD-PVP NPr (long λ) - 1	Set-up B 0.5 h	330 - 1100	56.98	57.77	0.79

NF	Simulator set-up and testing time / h	Measurement range for η_{lamp} / nm	Initial η_{lamp} / %	Final η_{lamp} / %	Change in η_{lamp} / % (positive = increase)
0.1 mM Ag TSCD-PVP NPr (long λ) - 2	Set-up B 0.5 h	330 - 1100	55.29	55.99	0.70
0.1 mM Ag TSCD-PVP NPr (long λ) - 3	Set-up B 0.5 h	330 - 1100	58.74	59.26	0.52
Mid λ - 1	Set-up B 0.5 h	330 - 1100	73.70	72.29	-1.41
Mid λ - 2	Set-up B 0.5 h	300 - 1100	74.02	70.59	-3.43
Mid λ - 3	Set-up B 0.5 h	300 - 1100	74.56	72.13	-2.43
Short λ - 1	Set-up B 0.5 h	330 - 1100	48.67	49.74	1.07
Short λ - 1	Set-up B 0.5 h	330 - 1100	42.16	48.10	5.93
Short λ - 1	Set-up B 0.5 h	330 - 1100	41.71	53.91	12.20
Broadband absorber - 1	Set-up B 0.5 h	330 - 1100	93.34	94.51	1.17
Broadband absorber - 2	Set-up B 0.5 h	330 - 1100	91.18	94.32	3.13
Broadband absorber - 3	Set-up B 0.5 h	330 - 1100	91.66	94.77	3.11

On comparing the results obtained it can be seen that it appears that the blue-shift in λ_{max} for the centrifuged Ag NPrs increases the $\eta_{lamp(330\ nm\ –\ 900\ nm)}$ obtained. However, this result should be treated with some caution as this NF was only measured over the 200 nm – 900 nm range. Any reduction in efficiency due to the blue-shift > 900 nm would therefore not be accounted for in this calculation, potentially biasing the result obtained. This biasing of the result obtained can clearly be seen if the results for the broadband absorber from Table K.4 and Table K.5 are compared. When $\eta_{lamp(330\ nm\ –\ 1100\ nm)}$ is used to estimate the change in efficiency obtained, the efficiency for the broadband absorber increases following SSL. However, when either $\eta_{Ab(300\ nm\ -\ 1350\ nm)}$ or $\eta_{Ab(280\ nm\ -\ 4000\ nm)}$ are used the efficiency decreases (Table K.5).

In all cases the efficiency for the mid λ NF decreases following SSL. This can be explained by the narrowing of the width of the UV-vis spectra (see Figure K.17). For the short λ NF the narrowing of the absorption spectra is partly or wholly compensated for by the increase in Ab_{max} resulting in efficiency changes of -1.22 % to 12.20 % (depending on sample and calculation employed).

Table K.5 Changes in efficiencies ($\eta_{Ab(300\ nm\ -\ 1350\ nm)}$ and $\eta_{Ab(280\ nm\ -\ 4000\ nm)}$) for the broadband absorber and component NFs after exposure to SSL for 0.5 h using set-up B.

NF	**Initial η_{Ab} over range 300 nm to 1350 nm / %**	**Final η_{Ab} over range 300 nm to 1350 nm / %**	**Change in η_{Ab} / % (positive = increase)**	**Initial η_{Ab} over 280 nm to 4000 nm range (using 300 nm – 1350 nm data/ %**	**Final η_{Ab} over 280 nm to 4000 nm range (using 300 nm – 1350 nm data/ %**	**Change in η_{Ab} over 280 nm to 4000 nm range / % (positive = increase)**
0.1 mM Ag TSCD-PVP NPr (long λ) - 1	63.98	60.86	-3.11	56.36	53.62	-2.74
0.1 mM Ag TSCD-PVP NPr (long λ) - 2	62.98	60.75	-2.23	55.49	53.52	-1.96
0.1 mM Ag TSCD-PVP NPr (long λ) - 3	63.40	59.59	-3.81	55.86	52.50	-3.36
Mid λ - 1	57.01	48.54	-8.47	50.22	42.76	-7.46
Mid λ - 2	56.16	45.45	-10.71	49.48	40.04	-9.44
Mid λ - 3	56.00	46.63	-9.37	49.33	41.08	-8.25
Short λ - 1	30.06	28.85	-1.21	26.48	25.42	-1.07
Short λ - 1	26.54	27.42	0.88	23.38	24.16	0.77
Short λ - 1	26.35	31.34	4.99	23.22	27.61	4.40
Broadband absorber - 1	84.39	77.78	-6.61	74.35	68.53	-5.82
Broadband absorber - 2	83.34	78.51	-4.83	73.42	69.16	-4.26
Broadband absorber - 3	82.19	79.04	-3.15	72.41	69.64	-2.77

Appendix L Additional Information on Development of SiO_2 Coating Synthesis Methods

This Appendix presents additional information on the development of SiO_2 coating methods for the coating of Ag NPs. Firstly, further details of the experiments carried out using the water-glass SiO_2 method are given. The experiments to develop a suitable SiO_2 coating method using a Stöber TEOS method are then described.

L.1 Water-glass SiO_2 Method

In total three different experiments were undertaken using the water-glass SiO_2 coating method with three repeats being carried out for each experimental set. The first experimental group used the protocol described in Section 3.6.3, with the SiO_2 coated Ag NPrs being re-dispersed into ¼ volume of either water or PG BF. Both the water and PG samples were then assessed for their stability when exposed to an elevated temperature of 70 °C for 18 h. In addition, the water BF, NFs were evaluated for their stability when exposed to SSL for 2 h using set-up A (see Sections 3.8.3 and 3.9.4).

The second set of experiments looked at the effect of centrifuging and the coating protocol on Ab_{max} using the same sample coating protocol as used previously. This was to determine if the centrifuging or the coating protocol itself was causing the loss of product observed.

The final set of experiments looked at how the spectra and morphology changed when more (5 x) capping agent MPTMS was used. This was to see if a thicker, more consistent coating could be produced and to understand further the role of the capping agent employed.

The results of assessing the stability to an elevated temperature of 70 °C for the first set of experiments centrifuged and re-dispersed into ¼ volume of water BF are given in Table L.1 (λ_{max} results) and Table L.2 (Ab_{max} results). The corresponding results with a PG BF are given in Table L.3 and Table L.4. Two-sample t-tests (see Section F.1) showed there was no significant change in either λ_{max} or Ab_{max} following exposure to an elevated temperature in either BF. It should be noted that there was a large reduction in Ab_{max} for the samples re-dispersed into PG (a 10 mm rather than 1 mm cuvette was therefore used for these samples). There was also a large variation in Ab_{max}, both between the three different PG samples and between repeat measurements on the

same sample, due to inconsistent loss of product and any aggregation of NPs giving a non-homogeneous NF.

Table L.1 λ_{max} and change in λ_{max} with exposure to an elevated temperature of 70 °C for Ag TSCD NPrs + water-glass SiO_2 re-dispersed into ¼ volume of water BF. Measured on UV-vis-1 using a 1 mm path length quartz cuvette. Positive is a red-shift.

Time at 70 °C / h	**Ag TSCD NPrs - 1a and water-glass SiO_2 in ¼ vol water λ_{max} / nm**	**Ag TSCD NPrs - 1a and water-glass SiO_2 in ¼ vol water change in λ_{max} / nm**	**Ag TSCD NPrs – 1b and water-glass SiO_2 in ¼ vol water λ_{max} / nm**	**Ag TSCD NPrs – 1b and water-glass SiO_2 in ¼ vol water change in λ_{max} / nm**	**Ag TSCD NPrs – 1c and water-glass SiO_2 in ¼ vol water λ_{max} / nm**	**Ag TSCD NPrs – 1c and water-glass SiO_2 in ¼ vol water change in λ_{max} / nm**
0	777	0	797	0	805	0
3	783	6	802	5	802	-3
6	774	-3	797	0	807	2
9	779	2	800	3	803	-2
12	776	-1	798	1	803	-2
18	790	13	797	0	800	-5

Table L.2 Ab_{max} and change in Ab_{max} with exposure to an elevated temperature of 70 °C for Ag TSCD NPrs + water-glass SiO_2 re-dispersed into ¼ volume of water BF. Positive is an increase.

Time at 70 °C / h	**Ag TSCD NPrs - 1a and water-glass SiO_2 in ¼ vol water Ab_{max} / au**	**Ag TSCD NPrs - 1a and water-glass SiO_2 in ¼ vol water change in Ab_{max} / %**	**Ag TSCD NPrs – 1b and water-glass SiO_2 in ¼ vol water Ab_{max} / au**	**Ag TSCD NPrs – 1b and water-glass SiO_2 in ¼ vol water change in Ab_{max} / %**	**Ag TSCD NPrs – 1c and water-glass SiO_2 in ¼ vol water Ab_{max} / au**	**Ag TSCD NPrs – 1c and water-glass SiO_2 in ¼ vol water change in Ab_{max} / %**
0	0.281	0	0.320	0	0.322	0
3	0.293	4	0.305	-5	0.319	-1
6	0.278	-1	0.303	-5	0.318	-1
9	0.276	-2	0.301	-6	0.327	1
12	0.268	-5	0.296	-8	0.315	-2
18	0.266	-6	0.312	-3	0.327	-5

Table L.3 λ_{max} and change in λ_{max} with exposure to an elevated temperature of 70 °C for Ag TSCD NPrs + water-glass SiO_2 re-dispersed into ¼ volume of PG BF. Measured on UV-vis-1 using a 10 mm path length plastic micro-cuvette. Positive is a red-shift.

Time at 70 °C / h	**Ag TSCD NPrs - 1a and water-glass SiO_2 in ¼ vol PG λ_{max} / nm**	**Ag TSCD NPrs - 1a and water-glass SiO_2 in ¼ vol PG change in λ_{max} / nm**	**Ag TSCD NPrs – 1b and water-glass SiO_2 in ¼ vol PG λ_{max} / nm**	**Ag TSCD NPrs – 1b and water-glass SiO_2 in ¼ vol PG change in λ_{max} / nm**	**Ag TSCD NPrs – 1c and water-glass SiO_2 in ¼ vol PG λ_{max} / nm**	**Ag TSCD NPrs – 1c and water-glass SiO_2 in ¼ vol PG change in λ_{max} / nm**
0	835	0	828	0	800	0

Time at 70 °C / h	Ag TSCD NPrs - 1a and water-glass SiO_2 in ¼ vol PG λ_{max} / nm	Ag TSCD NPrs - 1a and water-glass SiO_2 in ¼ vol PG change in λ_{max} / nm	Ag TSCD NPrs – 1b and water-glass SiO_2 in ¼ vol PG λ_{max} / nm	Ag TSCD NPrs – 1b and water-glass SiO_2 in ¼ vol PG change in λ_{max} / nm	Ag TSCD NPrs – 1c and water-glass SiO_2 in ¼ vol PG λ_{max} / nm	Ag TSCD NPrs – 1c and water-glass SiO_2 in ¼ vol PG change in λ_{max} / nm
3	831	-4	802	-26	786	-14
6	822	-13	802	-26	788	-12
9	830	-5	791	-37	785	-15
12	818	-17	788	-40	781	-19
18	812	-23	785	-43	780	-20

Table L.4 Ab_{max} and change in Ab_{max} with exposure to an elevated temperature of 70 °C for Ag TSCD NPrs + water-glass SiO_2 re-dispersed into ¼ volume of PG BF. Measured on UV-vis-1 using a 10 mm path length plastic micro-cuvette. Positive is an increase.

Time at 70 °C / h	Ag TSCD NPrs - 1a and water-glass SiO_2 in ¼ vol PG Ab_{max} / au	Ag TSCD NPrs - 1a and water-glass SiO_2 in ¼ vol PG change in Ab_{max} / %	Ag TSCD NPrs – 1b and water-glass SiO_2 in ¼ vol PG Ab_{max} / au	Ag TSCD NPrs – 1b and water-glass SiO_2 in ¼ vol PG change in Ab_{max} / %	Ag TSCD NPrs – 1c and water-glass SiO_2 in ¼ vol PG Ab_{max} / au	Ag TSCD NPrs – 1c and water-glass SiO_2 in ¼ vol PG change in Ab_{max} / %
0	0.552	0	1.273	0	0.957	0
3	0.617	12	1.430	12	1.085	13
6	0.639	16	1.317	3	1.038	8
9	0.481	-13	1.260	-1	0.961	0
12	0.480	-13	1.202	-6	1.046	9
18	0.584	6	1.162	-9	0.980	2

The UV-vis results for the second and third group of experiments are given in Figure L.1. For the second set of experiments following using the water-glass coating method there was a red-shift in λ_{max} of 37 nm from an average of 805 nm to 842 nm (range 56 nm) and a drop in Ab_{max} of ≈ 14 %. When the NPs were centrifuged and re-dispersed into water there was a further decrease in Ab_{max} of ≈ 41 % and a small blue-shift in λ_{max} of 5 nm. This decrease in Ab_{max} was not consistent between samples, showing that there were issues with centrifuging. A longer centrifuging time or employing a greater centrifuging force may reduce this reduction, but this would require further investigation.

The third group of experiments using 5 x MPTMS level showed an even larger drop in Ab_{max} of ≈ 65 %, with a larger average red-shift in λ_{max} of 58 nm (Figure L.1). There was a large variation in both Ab_{max} and λ_{max} between the three repeat samples (error bars in Figure L.1). When

centrifuged and re-dispersed into a mixed BF of 50 % PG / water there was an almost complete loss of product.

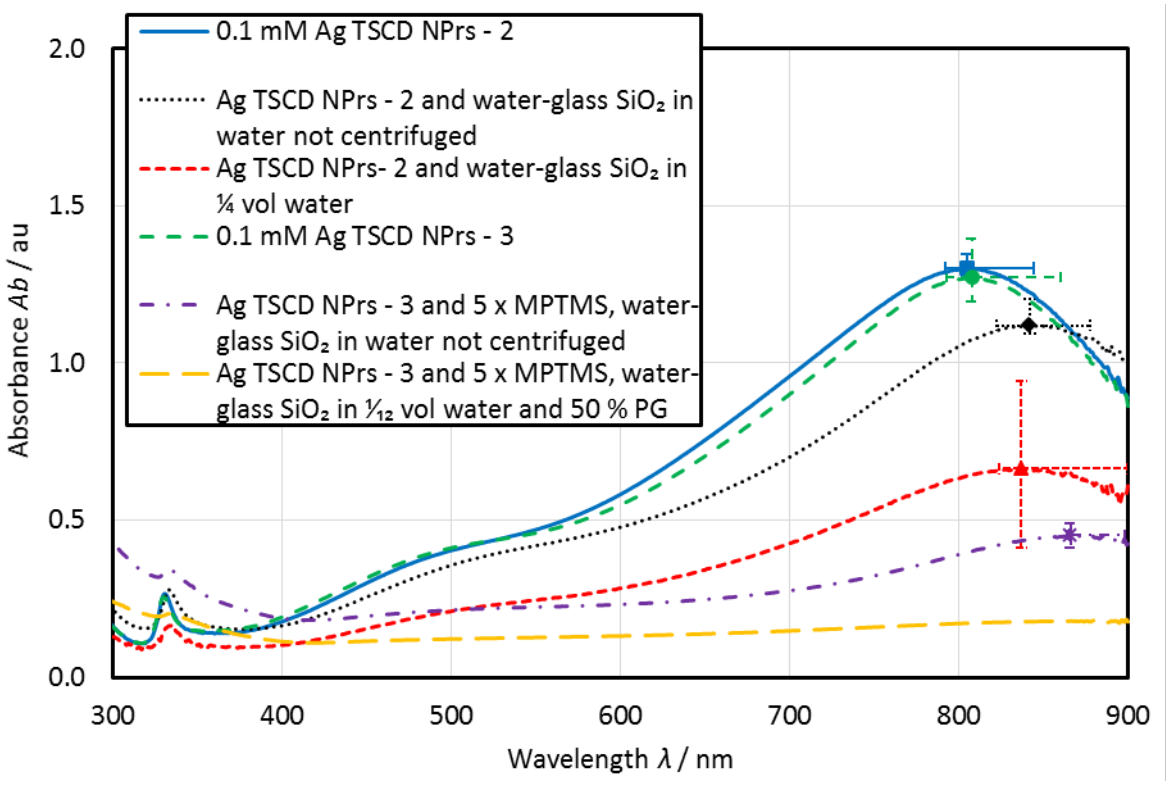

Figure L.1 UV-vis spectra before and after SiO_2 coating using the water-glass method. All measured using UV-vis-1. The after centrifuged samples have been adjusted for cuvette and concentration. Error bars show range of results obtained at the maximum absorbance (*N* = 3).

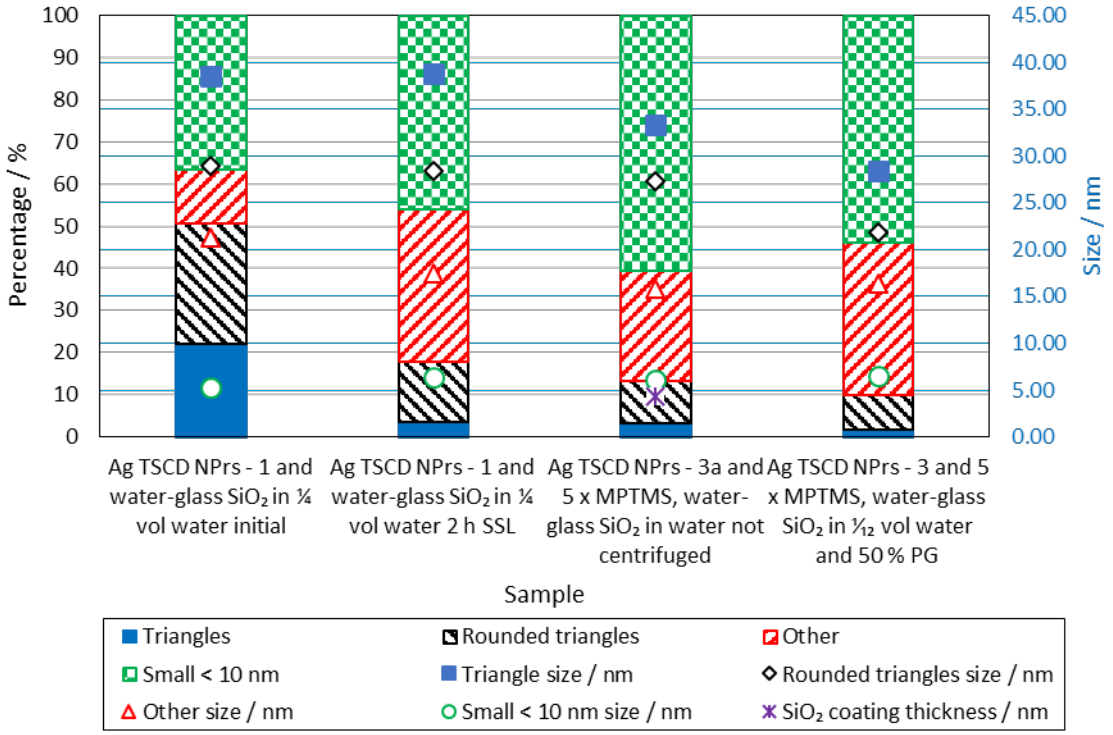

Figure L.2 Summary of the TEM analysis for the water-glass SiO_2 coating method.

A summary of the results of the TEM analysis is given in Figure L.2 with the full results being provided in Appendix G, Section G.7. Compared to the centrifuged Ag TSCD-PVP NPrs (see Figure 4-7), the size and amount of triangular particles was similar (29 %, 41.75 nm for the Ag TSCD-PVP NPrs and 22 %, 38.49 nm for the water-glass triangles) for the Ag TSCD NPrs and water-glass SiO_2 centrifuged and re-dispersed into water, but the percentage of small particles was greater (1 % for the Ag TSCD-PVP NPrs versus 36 % for the water-glass SiO_2 coated NF). This may have been due to some of the small particles being SiO_2 rather than Ag.

L.2 Stöber SiO_2 Coating Method

This subsection provides additional graphical representations of the TEM analysis results obtained for the preliminary investigations into the Stöber SiO_2 coating method. The full TEM results are given in Appendix G, Section G.8.

The variation of the SiO_2 coating thickness with concentration of TEOS employed is given in Figure L.3 and shows clearly the increase in variation in coating thickness obtained using both 16 mM and 8 mM TEOS (error bars denote the standard deviation σ). The lack of a significant change in thickness between the 60 minutes and 30 minutes, 20 µM MHA samples can also be seen (overlap of error bars).

Figure L.4 shows the percentage of multi-cored NPs (containing more than one Ag centre) as a percentage of Ag containing NPs (excluding the SiO_2 only NPs) and the percentage of Ag NPs that were not coated with SiO_2. The lowest of both these percentages was for the SiO_2@Ag NPrs produced using 40 µM MHA, 10 mM TEOS and a 30 minute reaction time. This was the chosen optimum recipe for the Stöber TEOS coating procedure.

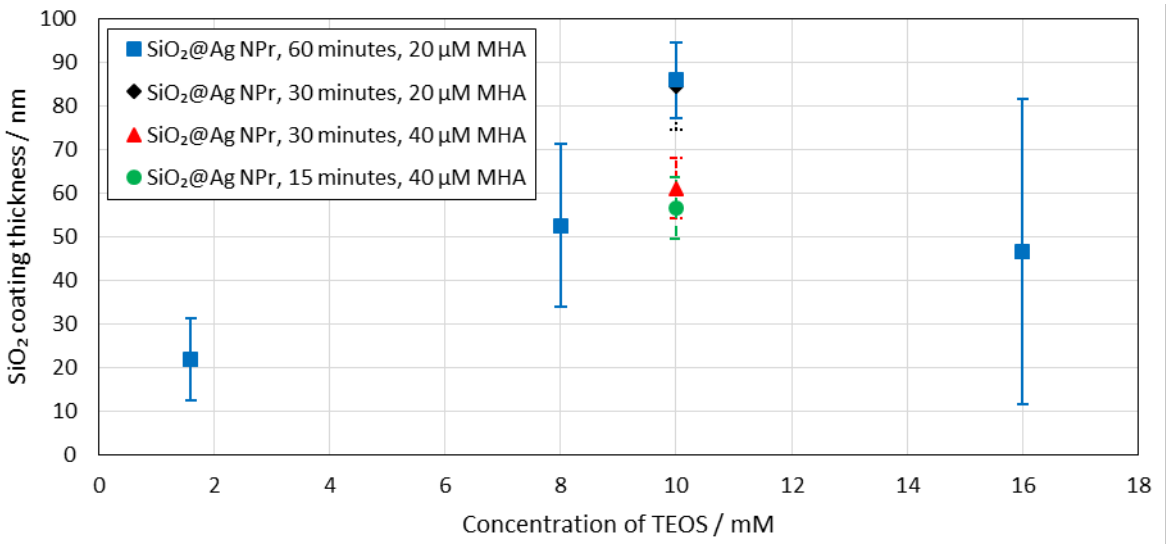

Figure L.3 Variation of the SiO_2 coating thickness obtained from the TEM analysis with concentration of TEOS used for the Stöber coating method. The error bars show the standard deviation σ.

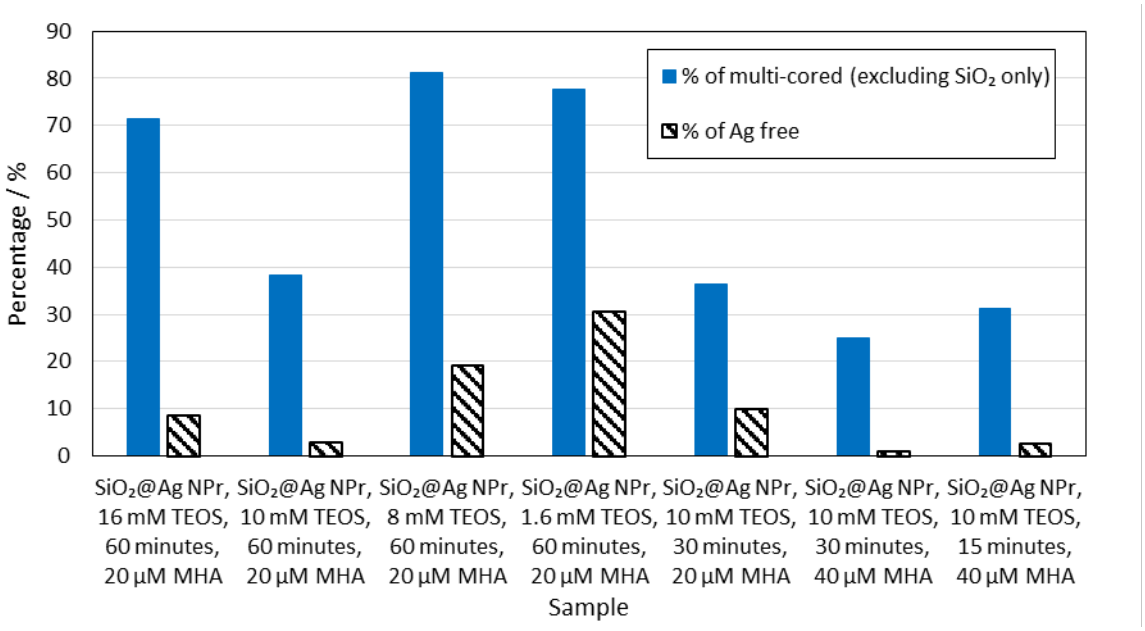

Figure L.4 Percentages of multi-cored NPs (excluding SiO_2 only NPs) and Ag free (not SiO_2 coated) obtained from the TEM analysis for the Stöber SiO_2 coating process optimisation.

Appendix M Additional Information on SiO_2 Coating of Silver Nanoprisms (Ag NPrs) Using the Optimised Stöber Process

This Appendix gives further information on the SiO_2 coating of silver nanoprisms using the developed optimised Stöber procedure detailed in Section 3.6.4. Firstly, the results obtained for the as synthesised NFs are detailed. The results of calculating the potential performance of the SiO_2@ NPrs from the UV-vis spectra are then provided. The results of assessing the stability of the SiO_2@Ag NPrs are then given, starting with the least severe testing condition, namely colloidal stability, then elevated temperature stability and finally, stability with exposure to simulated sunlight.

M.1 As Synthesised SiO_2 Coated Silver Nanoprisms (SiO_2@Ag NPrs)

The results of measuring the UV-vis spectra on the Ag TSCD-PVP NPr NFs before applying the optimised Stöber SiO_2 coating procedure are given in Table M.1. The values of Ab_{max} and λ_{max} obtained were consistent with those seen previously for Ag TSCD-PVP NPrs (Figure 4-5 and Figure I.3).

Table M.1 UV-vis results before SiO_2 coating. Measured using a 10 mm path length cuvette.

Sample	**UV-vis spectrophotometer used**	**Ab_{max} / au**	**λ_{max} / nm**
0.1 mM Ag TSCD-PVP NPr - 1	UV-vis-1	1.645	866
0.1 mM Ag TSCD-PVP NPr - 2	UV-vis-1	1.583	840
0.1 mM Ag TSCD-PVP NPr - 3	UV-vis-1	1.483	839
0.1 mM Ag TSCD-PVP NPr - 4	UV-vis-1	1.360	816
0.1 mM Ag TSCD-PVP NPr - 5	UV-vis-1	1.333	814
0.1 mM Ag TSCD-PVP NPr - 6	UV-vis-1	1.444	835
0.1 mM Ag TSCD-PVP NPr - 7	UV-vis-1	1.192	867
0.1 mM Ag TSCD-PVP NPr - 8	UV-vis-IR-2	1.653	796
0.1 mM Ag TSCD-PVP NPr - 9	UV-vis-IR-2	1.478	928
0.1 mM Ag TSCD-PVP NPr - 10	UV-vis-IR-2	1.388	895
0.1 mM Ag TSCD-PVP NPr - 11	UV-vis-IR-2	1.523	895

Sample	UV-vis spectrophotometer used	Ab_{max} / au	λ_{max} / nm
0.1 mM Ag TSCD-PVP NPr - 12	UV-vis-IR-2	1.343	798

After SiO_2 coating using the optimised Stöber method detailed in Section 3.6.4 there was a reduction in Ab_{max} for all the samples after adjusting for cuvette and volume (UV-vis results detailed in Table M.2 for the samples measured using UV-vis-1 and in Table M.3 for those measured using UV-vis-IR-2). There were also some changes in λ_{max} for some of the samples but on average there was no change (see Table 6-1). The average spectra obtained for those samples measured using UV-vis-1, before and after SiO_2 coating are shown in Figure M.1 and for those measured using UV-vis-IR-2 in Figure M.2.

Table M.2 UV-vis results after employing the optimised Stöber process. Measured using UV-vis-1. The Ab_{max} values have been adjusted for dilution and cuvette.

Sample	Ab_{max} / au (adjusted)	Change in Ab_{max} / % (positive is an increase)	λ_{max} / nm	Change in λ_{max} / nm (positive is a red-shift)
SiO_2@Ag NPr, ¼ volume - 1	1.262	-23	900	34
SiO_2@Ag NPr, ¼ volume - 2	0.978	-38	836	-4
SiO_2@Ag NPr, ¼ volume - 3	1.035	-30	836	-3
SiO_2@Ag NPr, ¼ volume - 4	0.781	-43	817	1
SiO_2@Ag NPr, ¼ volume - 5	0.740	-44	793	-21
SiO_2@Ag NPr, ¼ volume - 6	1.030	-29	831	-4
SiO_2@Ag NPr, ¼ volume - 7	0.931	-22	898	31

Table M.3 UV-vis results after employing the optimised Stöber process. Measured using UV-vis-IR-2. The Ab_{max} values have been adjusted for dilution and cuvette. The letters in the sample name refer to subsamples and the numbers the main sample.

Sample	Ab_{max} / au (adjusted)	Change in Ab_{max} / % (positive is an increase)	λ_{max} / nm	Change in λ_{max} / nm (positive is a red-shift)
SiO_2@Ag NPr, ¼ volume – 8a	1.218	-26	812	16
SiO_2@Ag NPr, ¼ volume – 8b	1.155	-30	811	15
SiO_2@Ag NPr, ¼ volume – 8c	1.159	-30	812	16
SiO_2@Ag NPr – 8d	1.153	-30	807	11
SiO_2@Ag NPr – 8e	1.169	-29	807	11
SiO_2@Ag NPr – 8f	1.142	-31	807	11
SiO_2@Ag NPr – 9a	0.733	-50	906	-22
SiO_2@Ag NPr – 9b	0.731	-51	906	-22
SiO_2@Ag NPr – 9c	0.740	-50	906	-22

Sample	Ab_{max} / au (adjusted)	Change in Ab_{max} / % (positive is an increase)	λ_{max} / nm	Change in λ_{max} / nm (positive is a red-shift)
SiO_2@Ag NPr, ¼ volume – 10	0.476	-66	871	-24
SiO_2@Ag NPr, ¼ volume – 11	0.509	-67	876	-19
SiO_2@Ag NPr, ¼ volume – 12	0.377	-72	800	2

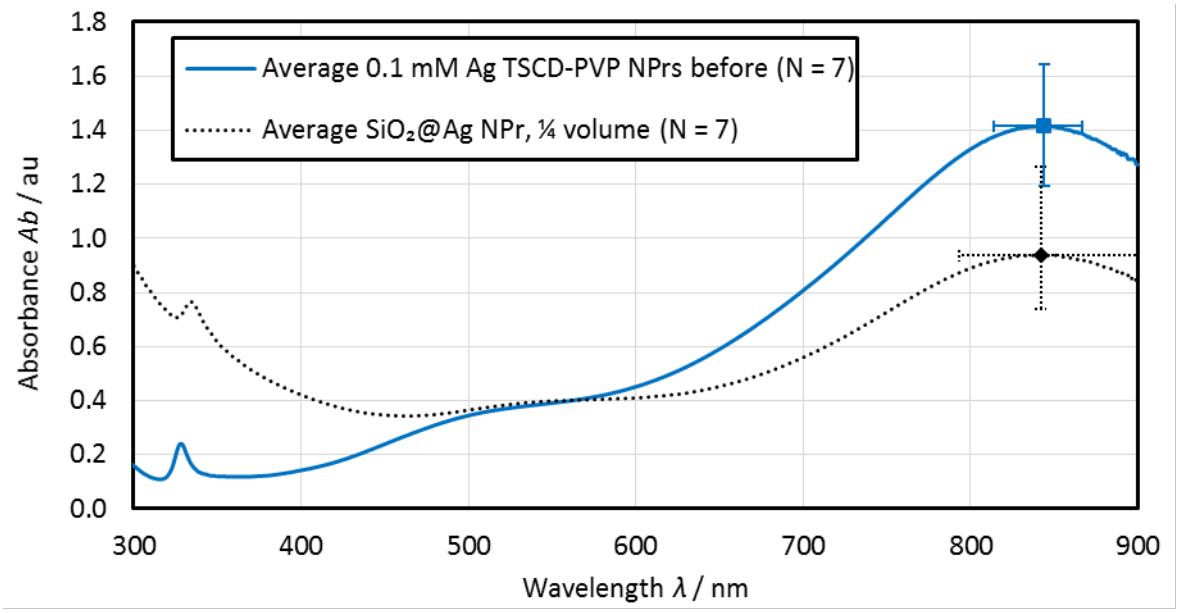

Figure M.1 UV-vis spectra before and after SiO_2 coating using the optimised Stöber process measured using UV-vis-1. The SiO_2@Ag NPrs have been adjusted for dilution and cuvette. Average values shown (*N* = 7). Error bars show range of results at the maximum absorbance.

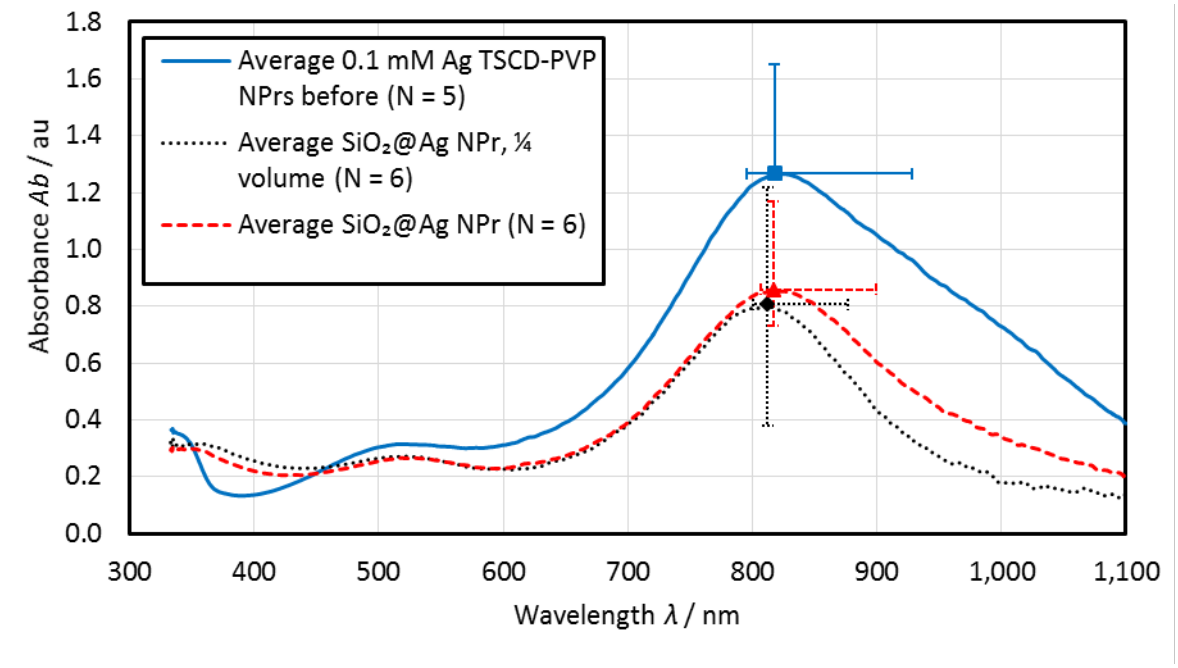

Figure M.2 UV-vis spectra before and after SiO_2 coating using the optimised Stöber process measured using UV-vis-IR-2. The SiO_2@Ag NPrs have been adjusted for dilution and cuvette. Average values shown (some SiO_2@Ag NPr samples were split for subsequent testing – hence total *N* after = 12). Error bars show range of results at the maximum absorbance.

M.1.1 TEM analysis of SiO_2 coated silver nanoprisms (SiO_2@Ag NPrs)

The morphology of the resultant SiO_2@Ag NPrs were examined using TEM. In total 10 out of the 12 samples were assessed. The results are detailed in Appendix G, Section G.9. Using a larger batch volume of 25 mL resulted in a thinner SiO_2 coating (51.24 nm average excluding SiO_2@Ag NPr – 7, produced using a smaller batch volume of 5 mL), but on average less multi-cored SiO_2@Ag NPs (8 % see Table 6-2). This reduction in multi-cored NPs was seen for the majority of samples with 2 notable exception (see Figure M.3). These were SiO_2@Ag NPr -7 (manufactured using a smaller batch volume) and SiO_2@Ag NPr – 11. The reason for the larger percentage of multi-cored NPs in this latter sample is not known, but it may have been due to incomplete sonication before final dispersal into the BF. This sample, SiO_2@Ag NPr – 10 and – 12 (not measured in the TEM) all showed a large reduction in Ab_{max} following coating supporting this hypothesis (see Table M.3). There was also a longer gap between initial preparation of the NF and analysis of the TEM sample (≈ 1 month compared to < 1 week) so there may have been some changes to the morphology in the interim in a similar manner to the changes observed for the aged broadband absorber TEM samples as discussed in Section 5.6.6. This may also account for the larger number of uncoated Ag NPs seen for this sample although some of these NPs measured as Ag free may have been SiO_2 rather than Ag.

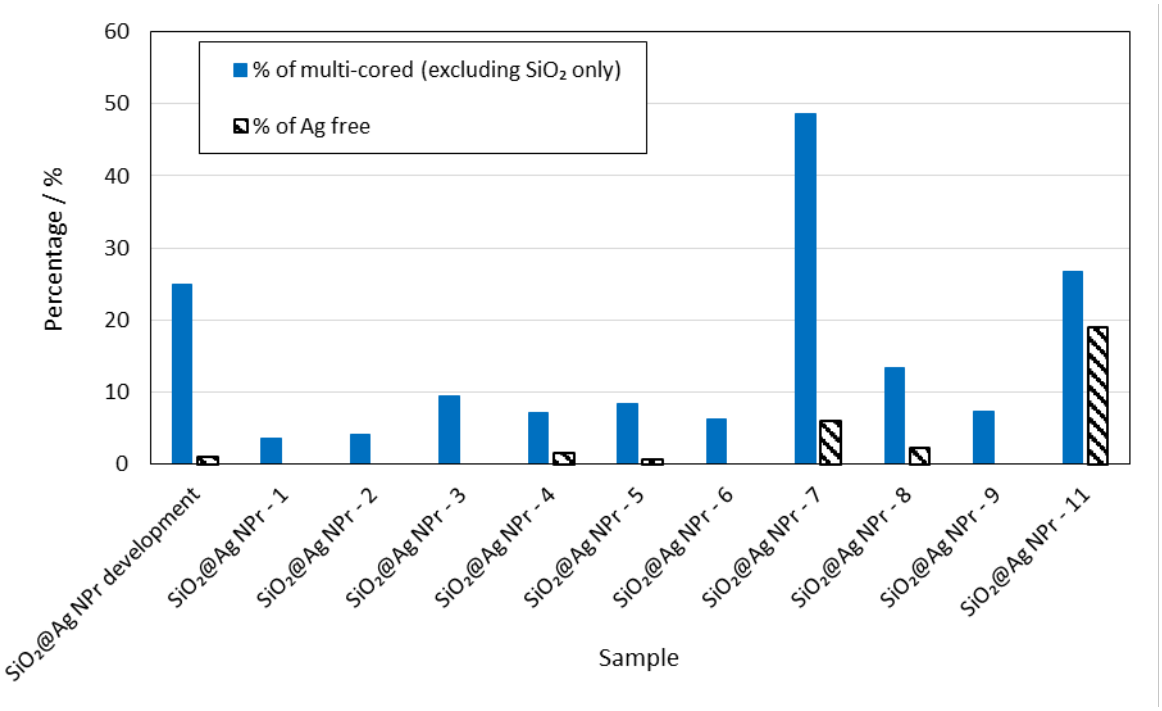

Figure M.3 Percentages of multi-cored NPs (excluding SiO_2 only NPs) and Ag free (not SiO_2 coated) obtained from the TEM analysis for the Stöber SiO_2 coating process (just synthesised). Both SiO_2@Ag NPr development and SiO_2@Ag NPr – 7 produced using a smaller batch volume.

To visualise the differences between the different samples, typical micrographs are given in Figure M.4. Figure M.4 A shows SiO_2@Ag NPr – 1, the sample with the lowest number of multi-cored NPs

and a SiO_2 coating thickness of ≈ 52 nm. Figure M.4 B shows SiO_2@Ag NPr -4, the sample with the thinnest SiO_2 coating of ≈ 46 nm. Figure M.4 C illustrates the thicker (≈ 81 nm) SiO_2 coating produced using the smaller batch volume (SiO_2@Ag NPr – 7). Finally, Figure M.4 D shows SiO_2@Ag NPr – 11. Here the degradation of the NP can be seen (as a lighter grey partly surrounding the middle NPs) along with the possible presence of a small uncoated Ag NP (in the top centre of the micrograph). Degradation could also lead to an increase in the number of multi-cored particles (when 1 central particle breaks into smaller central particles changing the NP from single-cored to multi-cored). Looking visually at Figure M.4 D it does appear that degradation of the TEM sample has occurred leading to the changes in morphology shown in Figure M.3, rather than issues with sonication. Further investigation would be needed to confirm this.

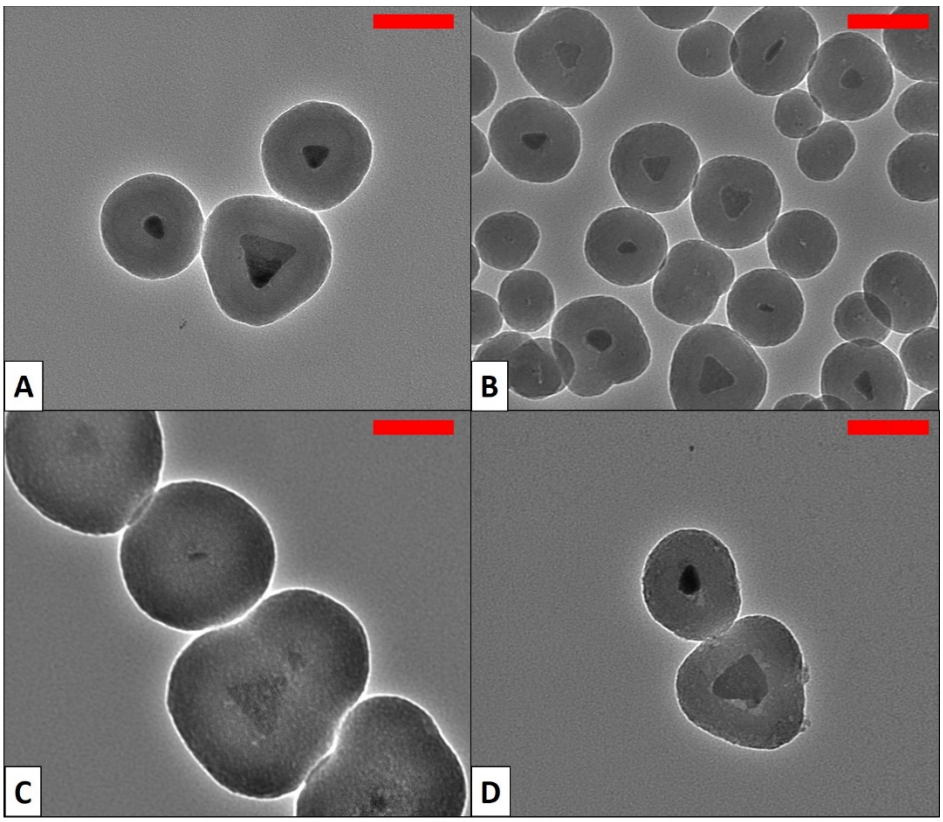

Figure M.4 Typical TEM micrographs of the as produced standard TEOS SiO_2 coating showing (A) SiO_2@Ag NPr-1, (B) SiO_2@Ag NPr-4, (C) SiO_2@Ag NPr-7, and (D) SiO_2@Ag NPr-11. All produced using 40 µM MHA and 10 mM TEOS for 30 minutes. All red scale bars = 100 nm.

M.2 Calculating Efficiency from Absorption Spectra for SiO_2 Coated Silver Nanoprisms (SiO_2@Ag NPrs)

The efficiency $\eta_{Ab(300\ nm\ -\ 900\ nm)}$ was calculated from the UV-vis spectra using Equation 4-3 and $\eta_{Ab(280\ nm\ -\ 4000\ nm)}$ was calculated assuming no absorption outside of the measured 300 nm – 900 nm range using Equation 4-4. The results for 7 of the SiO_2@Ag NPr samples re-dispersed into ¼ volume of water using a 10 mm path length are given in Table M.4.

Table M.4 Estimated η_{Ab} values for just synthesised SiO_2@Ag NPrs re-dispersed into ¼ volume of water using a 10 mm path length.

Sample	**λ_{max} / nm**	**$\eta_{Ab(300\ nm\ -\ 900\ nm)}$ / %**	**Estimated $\eta_{Ab(280\ nm\ -\ 4000\ nm)}$ / %**
SiO_2@Ag NPr, ¼ volume - 1	900	99.1	65.7
SiO_2@Ag NPr, ¼ volume - 2	836	99.3	65.8
SiO_2@Ag NPr, ¼ volume - 3	836	98.9	65.6
SiO_2@Ag NPr, ¼ volume - 4	817	96.8	62.4
SiO_2@Ag NPr, ¼ volume - 5	793	97.2	64.2
SiO_2@Ag NPr, ¼ volume - 6	831	99.6	64.5
SiO_2@Ag NPr, ¼ volume - 7	898	98.6	66.0
Average (N = 7)	844	98.5	64.9
σ (N = 7)	40	1.1	1.3

M.3 Colloidal Stability of SiO_2 Coated Silver Nanoprisms (SiO_2@Ag NPrs)

The colloidal stability of theSiO_2@Ag NPrs produced using the standard developed Stöber process was assessed using the protocol described in Section 3.9.2 with samples being stored for a maximum period of 51 days. The change in Ab_{max} and λ_{max} following storage at 4 °C in the dark are given in Table M.5. When both the change in Ab_{max} and λ_{max} were plotted against storage time there was found to be no linear relationship ($R^2 < 0.25$). Paired t-tests on the data obtained after > 38 days storage showed the difference in both Ab_{max} and λ_{max} to be significant.

Table M.5 Change in UV-vis spectra following storage in the dark at 4 °C for SiO_2@Ag NPrs re-dispersed into ¼ volume of water. Measured using UV-vis-1.

Sample	**Storage time / days**	**Change in Ab_{max} / % (positive is an increase)**	**Change in λ_{max} / nm (positive is a red-shift)**
SiO_2@Ag NPr, ¼ volume - 1	24	-15	-92
SiO_2@Ag NPr, ¼ volume - 1	51	-15	-96
SiO_2@Ag NPr, ¼ volume - 2	22	-39	-95
SiO_2@Ag NPr, ¼ volume - 2	49	-39	-110
SiO_2@Ag NPr, ¼ volume - 3	22	-5	-25
SiO_2@Ag NPr, ¼ volume - 3	49	-9	-33
SiO_2@Ag NPr, ¼ volume - 4	12	6	-24
SiO_2@Ag NPr, ¼ volume - 4	45	-5	-30
SiO_2@Ag NPr, ¼ volume - 5	5	-3	-19
SiO_2@Ag NPr, ¼ volume - 5	38	-18	-33
SiO_2@Ag NPr, ¼ volume - 6	21	-18	-26

Sample	Storage time / days	Change in Ab_{max} / % (positive is an increase)	Change in λ_{max} / nm (positive is a red-shift)
SiO_2@Ag NPr, ¼ volume - 7	5	-8	-16

M.3.1 Colloidal stability, TEM analysis

In total 3 samples were measured after storage for ≈ 50 days in the dark at 4 °C. The full results are given in Appendix G, Section G.10. The size of the Ag inside the SiO_2 shell was significantly smaller after storage and the number of multi-cored particles was greater, suggesting dissolution of the Ag with storage. Micro-graphs of the samples after storage in the dark at 4 °C for ≈ 50 days are shown in Figure M.5, where the dissolution of the Ag NPs can clearly be seen as a lighter area around the dark Ag core. In some instances the Ag NP in the centre has broken into smaller fragments, resulting in more multi-cored particles. This can be seen in Figure M.5 B and C. For ease of comparison the before storage SiO_2@Ag NPr-1 sample reproduced from Figure M.4 A is also shown.

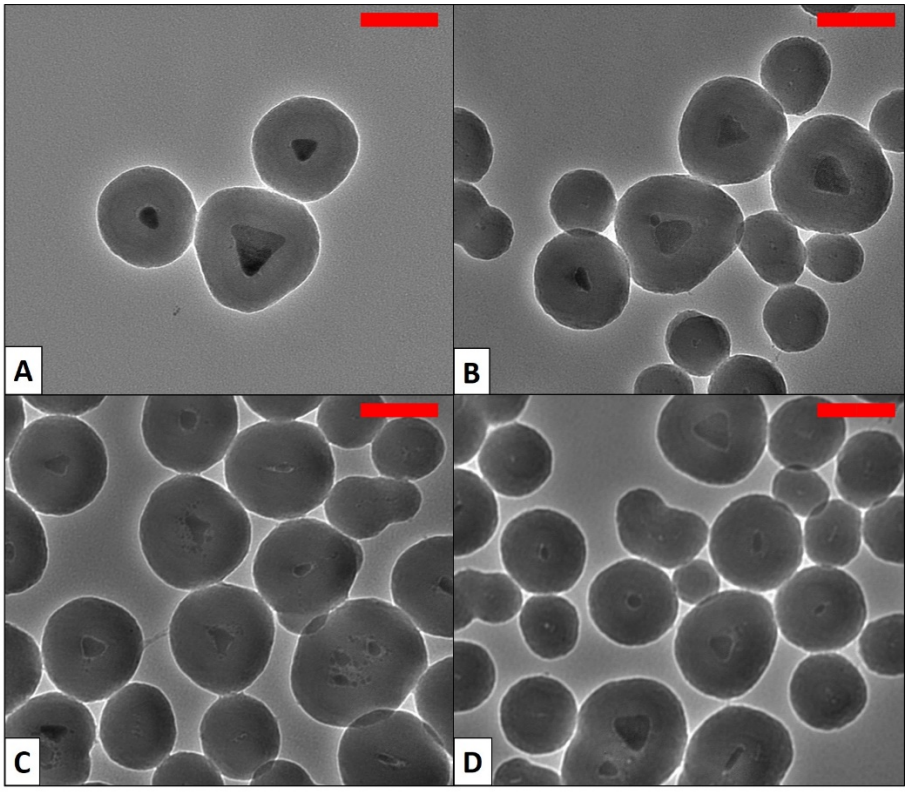

Figure M.5 Typical TEM micrographs of the standard TEOS SiO_2 coating showing (A) SiO_2@Ag NPr-1 initial, (B) SiO_2@Ag NPr-1 after 51 days, (C) SiO_2@Ag NPr-2 after 49 days, and (D) SiO_2@Ag NPr-3 after 49 days in the dark at 4 °C. All produced using 40 µM MHA and 10 mM TEOS for 30 minutes. All red scale bars = 100 nm.

M.4 SiO_2 Coated Silver Nanoprisms (SiO_2@Ag NPrs) Stability at Elevated Temperature

The SiO_2@Ag NPrs were assessed for their stability to an elevated temperature of 70 °C using the protocol described in Section 3.9.3. Three different NF concentrations were evaluated, SiO_2@Ag NPrs re-dispersed into ¼ volume, into the same volume of water and NF which were diluted to give ≈ Ab_{max} similar to the samples re-dispersed into the same volume of water (SiO_2@Ag NPr diluted). Figure M.6 shows the change in λ_{max} after exposure to an elevated temperature of 70 °C and Figure M.7 the change in Ab_{max}. For all samples there was a blue-shift in λ_{max} with exposure to an elevated temperature. To facilitate comparison with the results obtained for the uncoated Ag NFs in Section K.3 the data obtained after 9 h exposure (this time point was selected as it had the highest number of data points for all the NFs to be compared) is tabulated in Table M.6 (λ_{max} change) and Table M.7 (Ab_{max} change). The results of undertaking ANOVA testing on the 9 h data is given in Section M.4.1.

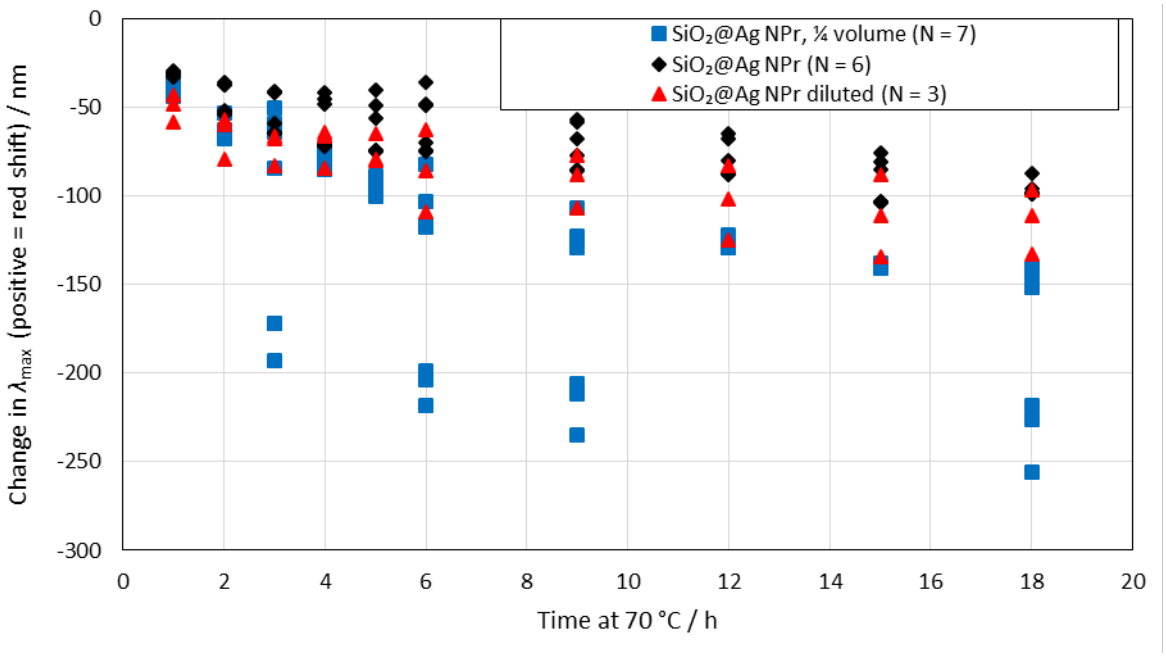

Figure M.6 Change in λ_{max} with exposure to a temperature of 70 °C for SiO_2@Ag NPr NFs with different NF concentrations.

All the SiO_2@Ag NPr samples exhibited a large blue-shift in λ_{max} with exposure to elevated temperature, with the more concentrated NF showing the greatest change. Like some of the uncoated Ag NPs in Figure K.12, there was considerable variation between samples. The size of the change increased with exposure time. However, a linear plot of exposure time versus change in λ_{max} for the more concentrated NF tested (shown as SiO_2@Ag NPr, ¼ volume) had a low R^2 value of 0.39 (no linear relationship) due to the variation between different samples. For the less

concentrated NFs the sample variation was slightly less and the corresponding linear fit for the data was better (R^2 = 0.65 for SiO_2@Ag NPr diluted and R^2 = 0.72 for SiO_2@Ag NPr).

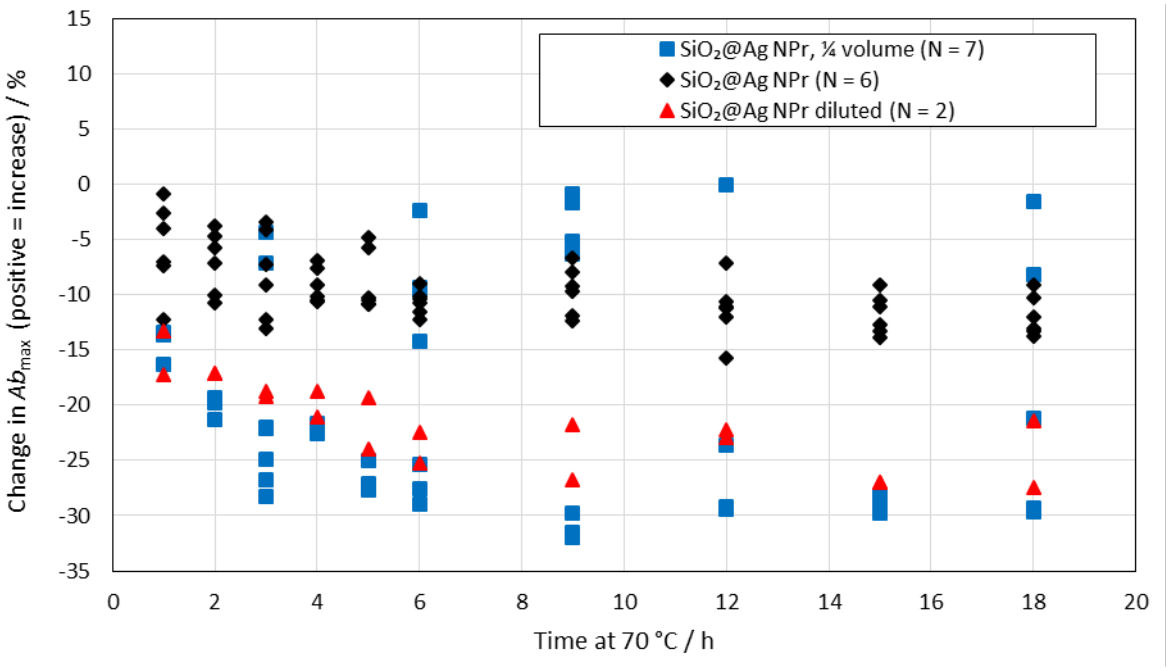

Figure M.7 Change in Ab_{max} with exposure to a temperature of 70 °C for SiO_2@Ag NPr NFs with different NF concentrations. Note that one sample was excluded from the SiO_2@Ag NPr diluted results as it was not correctly sealed resulting in a large increase in Ab_{max} due to evaporation, hence N = 2 rather than 3.

Table M.6 Change in λ_{max} after 9 h exposure to an elevated temperature of 70 °C (positive = red-shift).

Type of NF	**Average change / nm**	***σ*/ %**	**Maximum change / nm**	**Minimum change / nm**	***N***
SiO_2@Ag NPr, ¼ volume	-163	53	-235	-107	7
SiO_2@Ag NPr	-72	13	-86	-57	6
SiO_2@Ag NPr diluted	-91	15	-107	-77	3
Mid λ	-76	15	-92	-62	3
Ag TSCD-PVP NPr (long λ)	-51	18	-67	-32	3
Ag TSCD-PVP NPr centrifuged and re-dispersed into ¼ volume water	-13	13	-28	3	4

For Ab_{max}, the majority of the samples showed a reduction with exposure to temperature ranging from -2 % to -30 % after 18 h exposure (negative = reduction). There was no linear relationship between exposure time and change in Ab_{max}, with a wide variation between individual samples of the same NF.

When the 9 h data for the SiO_2@Ag NPrs are compared to the uncoated Ag NPs it appears that the more concentrated SiO_2@Ag NPr NF gave a considerable greater blue-shift in λ_{max} than the worst performing uncoated NFs (the mid λ and long λ). Analysis of variance was undertaken on the results to confirm this (see Section M.4.1).

For the change in Ab_{max} after 9 h, it appears that the SiO_2@Ag NPr NFs all showed an average reduction whereas the uncoated Ag NP NFs did not (Table M.7). Again ANOVA was undertaken to check the significance of any differences (see Section M.4.1).

Table M.7 Change in Ab_{max} after 9 h exposure to an elevated temperature of 70 °C (positive = increase).

Type of NF	**Average change / %**	***σ*/ %**	**Maximum change / %**	**Minimum change / %**	***N***
SiO_2@Ag NPr, ¼ volume	-15	15	-32	-1	7
SiO_2@Ag NPr	-10	2	-12	-7	6
SiO_2@Ag NPr diluted	-24	4	-27	-22	2
Mid λ	4	6	10	-2	3
Ag TSCD-PVP NPr (long λ)	2	3	6	0	3
Ag TSCD-PVP NPr centrifuged and re-dispersed into ¼ volume water	5	10	18	-4	4

M.4.1 Analysis of variance

To check if the results obtained after 9 h exposure to an elevated temperature of 70 °C were different for the SiO_2 coated Ag NFs compared to the uncoated Ag NPs, ANOVA was undertaken using the method described in Section F.2. The results are given in Table M.8 for the change in Ab_{max} and in Table M.9 for λ_{max}.

For Ab_{max}, the largest average reduction was for the SiO_2@Ag NPr diluted NFs, however, this reduction was not significantly different to the other two SiO_2 coated NFs or to the long λ NF. The centrifuged and re-dispersed into ¼ volume Ag NPrs showed an increase in Ab_{max} which was significantly different to 2 of the SiO_2@Ag NPr NFs.

Table M.8 Results of undertaking ANOVA on the samples after 9 h at 70 °C for the change in Ab_{max} (positive = increase). The average values and the potential range of the average value are shown along with the grouping. Groups that do not share a letter are significantly different.

Sample type	***N***	**Average change in Ab_{max} / %**	**Grouping**	**95 % confidence level for the mean / %**
SiO_2@Ag NPr, ¼ volume	7	-15.31	B, C	-22.91 to -7.72
SiO_2@Ag NPr	6	-9.61	A, B, C	-17.82 to -1.40
SiO_2@Ag NPr diluted	2	-24.21	C	-38.42 to -9.99
Mid λ	3	3.61	A, B	-7.99 to 15.22
Ag TSCD-PVP NPr (long λ)	3	2.24	A, B, C	-9.37 to -13.84
Ag TSCD-PVP NPr centrifuged and re-dispersed into ¼ volume water	4	5.20	A	-4.85 to 15.25

In contrast for λ_{max}, the most concentrated SiO_2@Ag NPr NF showed a significantly greater blue-shift in λ_{max} after 9 h exposure than all the other NFs tested, showing it to be the least morphologically stable. The Ag TSCD-PVP NPrs centrifuged and re-dispersed into ¼ volume water were the most morphologically stable but not significantly more stable than the long λ, mid λ, or the SiO_2@Ag NPrs due to the high amount of sample variation between samples of the same type.

SiO_2 coating of Ag NPrs using the developed Stöber method does not therefore seem to be a suitable method of improving the morphological temperature stability of the Ag NPrs, resulting in a reduction rather than an increase in stability.

Table M.9 Results of undertaking ANOVA on the samples after 9 h at 70 °C for the change in λ_{max} (positive = red shift).The average values and the potential range of the average value are shown along with the grouping. Groups that do not share a letter are significantly different.

Sample type	***N***	**Average change in λ_{max} / nm**	**Grouping**	**95 % confidence level for the mean / nm**
SiO_2@Ag NPr, ¼ volume	7	-162.7	C	-187.3 to -138.1
SiO_2@Ag NPr	6	-71.8	A, B	-98.4 to -45.2
SiO_2@Ag NPr diluted	2	-90.7	B	-128.3 to -53.0
Mid λ	3	-76.1	A, B	-113.8 to -38.5
Ag TSCD-PVP NPr (long λ)	3	-51.4	A, B	-89.1 to -13.8
Ag TSCD-PVP NPr centrifuged and re-dispersed into ¼ volume water	4	-12.5	A	-45.1 to 20.1

M.5 SiO_2 Coated Silver Nanoprisms (SiO_2@Ag NPrs) Stability with Simulated Sunlight Exposure

The stability with exposure to simulated sunlight (SSL) for SiO_2@Ag NPrs is presented in this subsection. The stability was assessed using UV-vis and TEM after exposure to SSL using set-up A in the solar simulator.

The average before and after exposure to SSL for 6 h spectra for SiO_2@Ag NPrs re-dispersed into ¼ volume of water (compared to original NF volume) are shown in Figure M.8. The large blue-shift in the position of λ_{max} can clearly be seen, as can the increase in the variation in the results obtained after SSL exposure (compare the relative sizes of the error bars before and after).

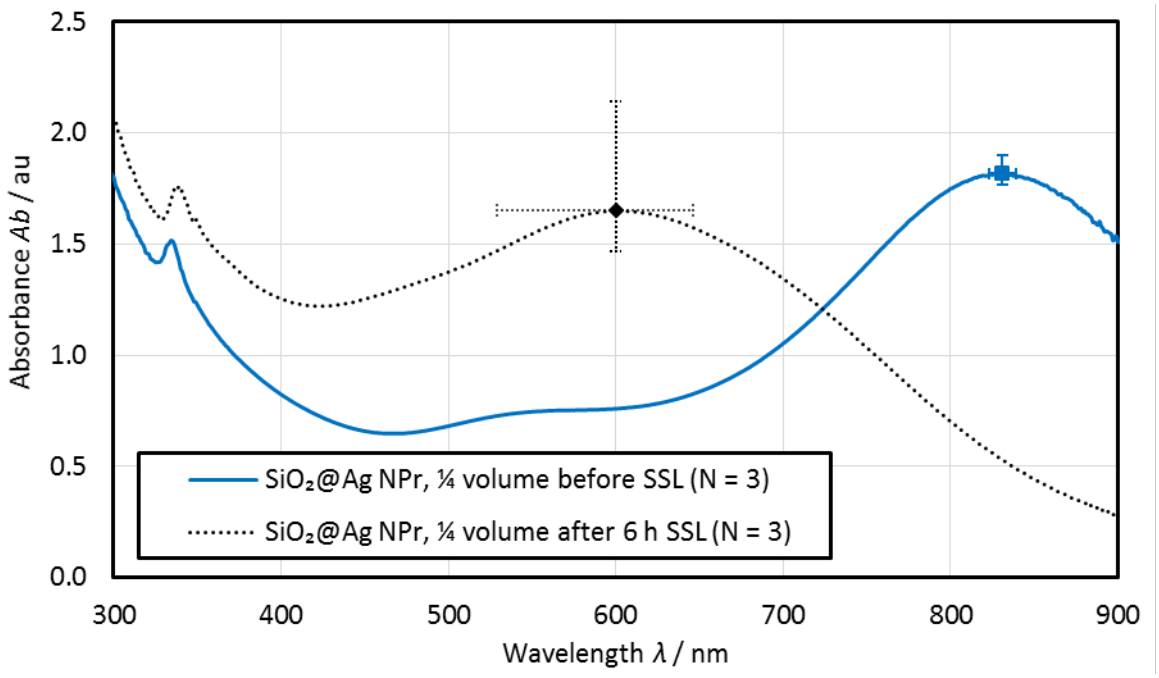

Figure M.8 Average UV-vis spectra for SiO_2@Ag NPr re-dispersed into ¼ volume of water (compared to original NF volume) before and after exposure to SSL for 6 h using set-up A in the solar simulator. The error bars show the range of results obtained at the maximum absorbance for the three repeat synthesis. Measured using UV-vis-1 and a 1 mL 4 mm path length disposable cuvette.

TEM analysis of the samples before and after exposure to SSL was undertaken. The full results are given in Appendix G, Section G.12. The size of the Ag inside the SiO_2 shell was significantly smaller after SSL exposure and the number of multi-cored particles was greater, suggesting dissolution of the Ag. The thickness of the coating was also less suggesting that this may also be dissolving. The amount of free Ag NPs had also increased so the SiO_2 coating may also be breaking apart with SSL exposure. Micro-graphs of the samples after SSL exposure are shown in Figure M.9, where the dissolution of the Ag NPs can clearly be seen as a lighter area around the dark Ag core. In some instances the Ag NP in the centre has broken into smaller fragments, resulting in more multi-cored particles. This can be seen in Figure M.5 B. The breaking up of the SiO_2 coating, releasing free Ag NPs can also be seen in Figure M.9 C. For ease of comparison the before SSL exposure SiO_2@Ag NPr-1 sample reproduced from Figure M.4 A is also shown.

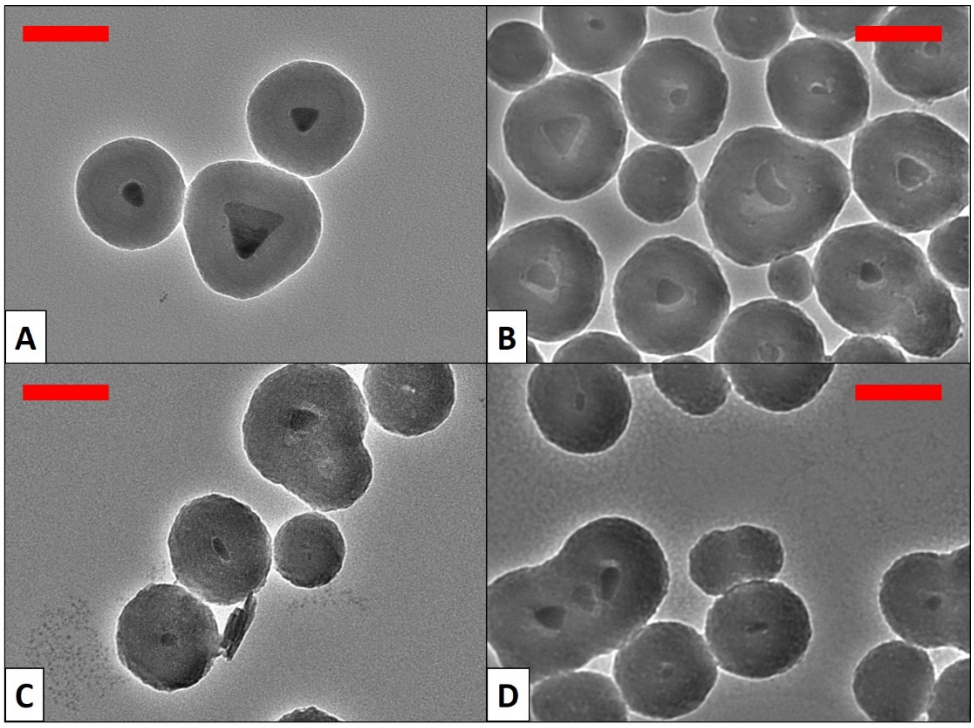

Figure M.9 Typical TEM micrographs of the standard TEOS SiO_2 coating showing (A) SiO_2@Ag NPr-1 before SSL exposure, (B) SiO_2@Ag NPr-1, (C) SiO_2@Ag NPr-2, and (D) SiO_2@Ag NPr-3 after 6 h exposure to SSL. All produced using 40 µM MHA and 10 mM TEOS for 30 minutes. All red scale bars = 100 nm.

Appendix N Additional Information on Modifications to Coating Procedure

This Appendix provide extra information on the modifications undertaken to the developed Stöber coating procedure detailed in Section 3.6.4. A schematic of the modifications investigated is given in Figure 3-1. The first subsection of this Appendix looks at the experiments conducted and the results obtained from adding an extra purification step and reducing the amount of oxygen in the final NF. The next looks at what happens when the concentration of two reagents, namely the capping agent MHA and the amount of base DMA employed in the base catalysed process were varied. The final subsection then provides details of the experiments and results obtained when the time of the base catalysed step was reduced.

In all cases elevated temperature stability was used to assess if the modification had changed the stability comparing the results to those obtained in Appendix M, Section M.4 for the optimised procedure.

N.1 Adding Extra Purification and Reducing the Amount of Oxygen

This subsection presents the results obtained from investigating the effect on the elevated temperature stability (protocol in Section 3.9.3) of either adding an extra purification step to the coating procedure or reducing the level of oxygen in the final NF. The samples were assessed both before and after exposure to a temperature of 70 °C using UV-vis. In the case of the addition of an extra purification step, initial TEM analysis using the protocol described in Section 3.7.1 was also carried out to ascertain if the addition of an extra purification step had changed the morphology of the resultant SiO_2@Ag NPrs.

An additional purification step was added at two different points in the protocol (see Figure 3-1), initially at step 3 (the first centrifuge step – extra initial purification step) and at the end of the procedure at step 9 (extra final purification step).

To add an extra initial purification step, the uncoated Ag NPrs were centrifuged for 15 minutes at 16,168 r.c.f. (13,000 rpm) and re-dispersed into Milli-Q water. They were then centrifuged for a further 15 minutes giving the same overall centrifuging time as in the standard optimised coating procedure (Section 3.6.4 and step 3 in Figure 3-1).

The final extra purification step was added by taking the NF re-dispersed into their final volume of water (step 9) and centrifuging for 15 minutes at 12857 r.c.f. (10,000 rpm) before finally, re-dispersing into water.

The amount of oxygen in the final NF was reduced by bubbling argon through the NF for 10 minutes prior to exposure to an elevated temperature of 70 °C. To allow for direct comparison with the standard optimised coating procedure each NF sample was divided into two and argon bubbled through one sub-sample.

The UV-vis results obtained for the samples with and without an extra purification step are shown in Table N.1. In all cases there was a large blue-shift in the position of λ_{max} following exposure to an elevated temperature. There was more variation in the results obtained using a final extra purification step. Two-sample t-test were undertaken on the samples comparing the effect of either an additional initial purification step or a final purification step with the samples produced using no additional purification. None of the results for either λ_{max} or Ab_{max} were significantly different either before or after exposure to an elevated temperature of 70 °C for 6 h.

The addition of an extra purification step either initially or at the end of the coating procedure therefore had no effect on the resultant temperature stability.

Table N.1 UV-vis parameters for SiO_2@Ag NPrs with and without an extra purification step (either at start of procedure or at end). All re-dispersed into ¼ volume of water compared to the original NF and measured using UV-vis-1 and a 1 mm quartz cuvette.

Parameter	**SiO_2@Ag NPr, ¼ volume**	**SiO_2@Ag NPr, ¼ volume, extra initial purification step**	**SiO_2@Ag NPr, ¼ volume, extra final purification step**
Average λ_{max} initial / nm	814	816	841
σ λ_{max} initial / nm	20	10	29
Average λ_{max} 6 h at 70 °C / nm	596	588	672
σ λ_{max} 6 h at 70 °C / nm	22	9	98
Average Ab_{max} initial / au	0.347	0.304	0.326
σ Ab_{max} initial / au	0.054	0.010	0.048
Average Ab_{max} 6 h at 70 °C / au	0.340	0.335	0.311
σ Ab_{max} 6 h at 70 °C / au	0.057	0.013	0.046
N	6	4	4

TEM analysis (full results in Appendix G, Section G.13), showed the coating thickness to be the same (within the uncertainty of the measurement technique) at ≈ 50 nm as the optimised Stöber coating procedure (Table 6-2), but the number of multi-cored (containing more than one Ag NP) particles was slightly greater (13 % for the initial purification, 24 % for the final purification versus

8 % without purification). The size of the Ag NPs was also slightly less for the NFs produced with an extra initial purification step, but this may have been due to a lower than average initial λ_{max} for these samples.

The UV-vis results obtained for the samples produced with and without a reduced oxygen level are shown in Table N.2. Un-paired two sample t-tests showed there was no significant difference between the results obtained for the samples with a reduced level of oxygen either before or after exposure to an elevated temperature of 70 °C compared to the samples with a normal level of oxygen. Hence attempting to remove the oxygen from the NFs after SiO_2 coating did not change the temperature stability of the resulting NFs.

Table N.2 UV-vis parameters for SiO_2@Ag NPrs with and without the level of oxygen in the NFs reduced. All re-dispersed into ¼ volume of water compared to the original NF and measured using UV-vis-1 and a 1 mm quartz cuvette.

Parameter	**SiO_2@Ag NPr, ¼ volume**	**SiO_2@Ag NPr, ¼ volume, oxygen reduced**
Average λ_{max} initial / nm	815	815
σ λ_{max} initial / nm	16	18
Average λ_{max} 18 h at 70 °C / nm	569	577
σ λ_{max} 18 h at 70 °C / nm	12	15
Average Ab_{max} initial / au	0.324	0.335
σ Ab_{max} initial / au	0.050	0.047
Average Ab_{max} 18 h at 70 °C / au	0.320	0.397
σ Ab_{max} 18 h at 70 °C / au	0.051	0.064
N	5	5

N.2 Understanding the Effect of Various Reagents

This subsection provides details of the experiments carried out to assess the effect of two of the reagents namely MHA and DMA in the optimised SiO_2 Stöber coating process. Firstly, the role of the two reagents is briefly evaluated by looking at their effect on uncoated Ag NPrs. Secondly, the experimental details and the results of attempts to SiO_2 coat Ag NPrs in the absence of the capping agent MHA are provided. Thirdly, experimental details and results from utilising a higher MHA concentration of 160 µM (4 x normal concentration) are given. Finally, experimental details and results for SiO_2@Ag NPrs produced using ¼ the normal concentration of DMA are provided.

To initially investigate the role of the various reagents in the SiO_2 coating procedure, the effect of the capping agent MHA and the base DMA on uncoated Ag NPr NF was determined to see if the Ag NPrs were dissolving in the presence of the reagents.

Ag TSCD-PVP NPrs (1 mL) centrifuged and re-dispersed into ¼ was taken and an appropriate volume of either MHA (0.16 mL of an ethanolic solution of 1.0 mM MHA), DMA (0.43 mL of 40 % DMA solution) or both MHA and DMA added. The UV-vis spectra was then recorded and the samples placed in the dark at 4 °C for ≈ 16 h after which the spectra was re-taken and the samples exposed to a temperature of 70 °C for 2 h using the protocol described in Section 3.9.3 (except for the Ag TSCD-PVP NPr + DMA sample). As the MHA and DMA were added to an already produced NF this had the effect of reducing the concentration of these reagents compared to the optimised procedure described in Section 3.6.4. Full details of the experiments are given in Table N.3.

Table N.3 Details of the preliminary experiments to investigate the effect of MHA and DMA on Ag TSCD-PVP NPrs.

Sample	**NF % in solution / %**	**MHA amount versus optimised procedure / %**	**DMA amount versus optimised procedure / %**	**Spectra measured**
Ag TSCD-PVP NPr ct ¼ vol	100	0	0	Initial, dark 4 °C ≈ 16 h, 2 h at 70 °C
Ag TSCD-PVP NPr ct ¼ vol + DMA	70	0	83	Initial, dark 4 °C ≈ 16 h
Ag TSCD-PVP NPr ct ¼ vol + MHA	86	86	0	Initial, dark 4 °C ≈ 16 h, 2 h at 70 °C
Ag TSCD-PVP NPr ct ¼ vol + MHA + DMA	63	63	74	Initial, dark 4 °C ≈ 16 h, 2 h at 70 °C

To further illustrate the role of MHA an attempt was made to coat Ag NPrs without using the capping agent MHA in the reaction (leaving out step 2 in Figure 3-1). Two experiments were undertaken, one using the normal amount of DMA used in the optimised Stöber process (see Section 3.6.4) and the other ¼ this concentration (both experiments used 8 mL of Ag TSCD-PVP NPr NF as the starting NF). Both samples were re-dispersed into ¼ volume of water (compared to the original NF and subjected to an elevated temperature of 70 °C for 12 h. The UV-vis results are summarised in Table N.4 and show that considerable aggregation / dissolution of the NPs had occurred during the SiO_2 coating process resulting in a large decrease in Ab_{max}. When the samples were subsequently exposed to an elevated temperature of 70 °C, Ab_{max} dropped still further resulting in an almost complete loss of absorption making it no longer possible to determine the position of λ_{max}. TEM analysis after SiO_2 coating and before temperature testing (results for SiO_2@Ag NPr, 0 MHA, ¼ concentration DMA given in Appendix G, Section G.14.1, SiO_2@Ag NPr, 0 MHA, normal DMA not analysed due to very high levels of NP aggregation) showed an inconsistent SiO_2 coating thickness of ≈ 37 nm, significant aggregation of the NPs and a high percentage of multi-cored NPs (containing more than one Ag core). The use of the MHA capping agent is therefore vital to produce consistently SiO_2 coated Ag NPrs.

Table N.4 Summarised UV-vis results for SiO_2@Ag NPrs produced using no capping agent MHA. Measured using UV-vis-1.

Parameter	**SiO_2@Ag NPr, 0 MHA, normal concentration DMA**	**SiO_2@Ag NPr, 0 MHA, ¼ concentration DMA**
Change in Ab_{max} following SiO_2 coating (positive = increase) / %	-68	-83
Change in λ_{max} after SiO_2 coating (positive = red-shift) /nm	32	28
Further change in Ab_{max} after 12 h @ 70 °C (positive = increase) / %	-15	-39

To understand better the role of MHA, additional experiments were undertaken using two different concentrations of MHA (40 µM, the normal concentration employed, and 160 µM). The starting NF used was Ag TSCD-PVP NPrs. All samples were re-dispersed into ¼ volume of water (compared to the original starting NF volume of 25 mL) and exposed to a temperature of 70 °C for 6 h. The UV-vis spectra were recorded before SiO_2 coating, after coating and after elevated temperature exposure. To allow for direct comparison with the normal optimised process the results obtained using the same batches of starting NF (Ag TSCD-PVP NPrs) are given in Table N.5 for the normal optimised process using 40 µM MHA and in Table N.6 for those produced using 160 µM MHA (all experiments also included an extra final purification). Un-paired two sample t-tests showed no significant difference between the samples (either initially after SiO_2 coating or after 6 h at 70 °C), showing that a higher level of MHA does not change the spectral response.

Table N.5 Summary of UV-vis results for SiO_2@Ag NPrs re-dispersed into ¼ volume of water (compared to the original starting NF volume) produced using 40 µM MHA and the normal concentration of DMA (the optimised Stöber process from Section 3.6.4). Measured using UV-vis-1.

Parameter	**Average**	***σ***	**maximum**	**minimum**	***N***
Change in Ab_{max} following SiO_2 coating (positive = increase) / %	-28	4	-24	-31	3
Change in λ_{max} after SiO_2 coating (positive = red-shift) /nm	4	27	35	-15	3
Further change in Ab_{max} after 6 h at 70 °C (positive = increase) / %	-27	8	-21	-35	3
Further change in λ_{max} after 6 h at 70 °C (positive = red-shift) /nm	-247	75	-163	-307	3

TEM analysis (full results in Appendix G, Section G.14.2), showed that there were no differences between the samples produced with the normal amount of MHA (40 µM) and those produced using 160 µM MHA.

Two preliminary experiments were carried out to assess the effect of reducing the concentration of the base DMA. The DMA concentration was reduced to ¼ the concentration used in the

optimised Stöber procedure (Section 3.6.4) and Ag TSCD-PVP NPrs SiO_2 coated. One experiment used a capping agent MHA concentration of 40 µM (the normal amount) and the other 160 µM. After SiO_2 coating the samples were exposed to an elevated temperature of 70 °C for 12 h using the protocol described in Section 3.9.3. TEM analysis was also undertaken after SiO_2 coating to determine if changing the DMA concentration effected the morphology (results in Appendix G, Section G.14.3).

Table N.6 Summary of UV-vis results for SiO_2@Ag NPrs re-dispersed into ¼ volume of water (compared to the original starting NF volume) produced using 160 µM MHA and the normal concentration of DMA. Measured using UV-vis-1.

Parameter	**Average**	***σ***	**maximum**	**minimum**	***N***
Change in Ab_{max} following SiO_2 coating (positive = increase) / %	-35	6	-28	-38	3
Change in λ_{max} after SiO_2 coating (positive = red-shift) /nm	1	3	4	-2	3
Further change in Ab_{max} after 6 h at 70 °C (positive = increase) / %	-29	1	-29	-30	3
Further change in λ_{max} after 6 h at 70 °C coating (positive = red-shift) /nm	-232	51	-173	-262	3

The UV-vis results, Figure N.1, show a large decrease in Ab_{max} after SiO_2 coating of 63 % (40 µM MHA) and 49 % (160 µM MHA). After exposure to an elevated temperature of 70 °C for 12 h Ab_{max} had dropped further and for the 160 µM MHA sample λ_{max} had blue-shifted by about 160 nm. It appeared that the λ_{max} for the 40 µM sample in contrast did not blue-shift, however it was not possible to accurately determine the position of λ_{max} due to the low Ab_{max} of this sample. The blue-shift for the 160 µMHA sample was greater than seen previously after 12 h at 70 °C (Figure M.6), similar to that seen after 9 h (SiO_2@Ag NPr, ¼ volume – 163 nm blue-shift, Table M.6) but the 40 µM MHA concentration appeared to have a lower blue-shift than previously.

Hence, in terms of λ_{max}, the results obtained from the elevated temperature testing of this very limited set of experiments was inconclusive. Further repeat experiments would be needed to determine the temperature stability of SiO_2@Ag NPrs produced using a lower concentration of DMA. However, given the large reduction in Ab_{max} seen on SiO_2 coating, even repeat experimentation may still prove inconclusive.

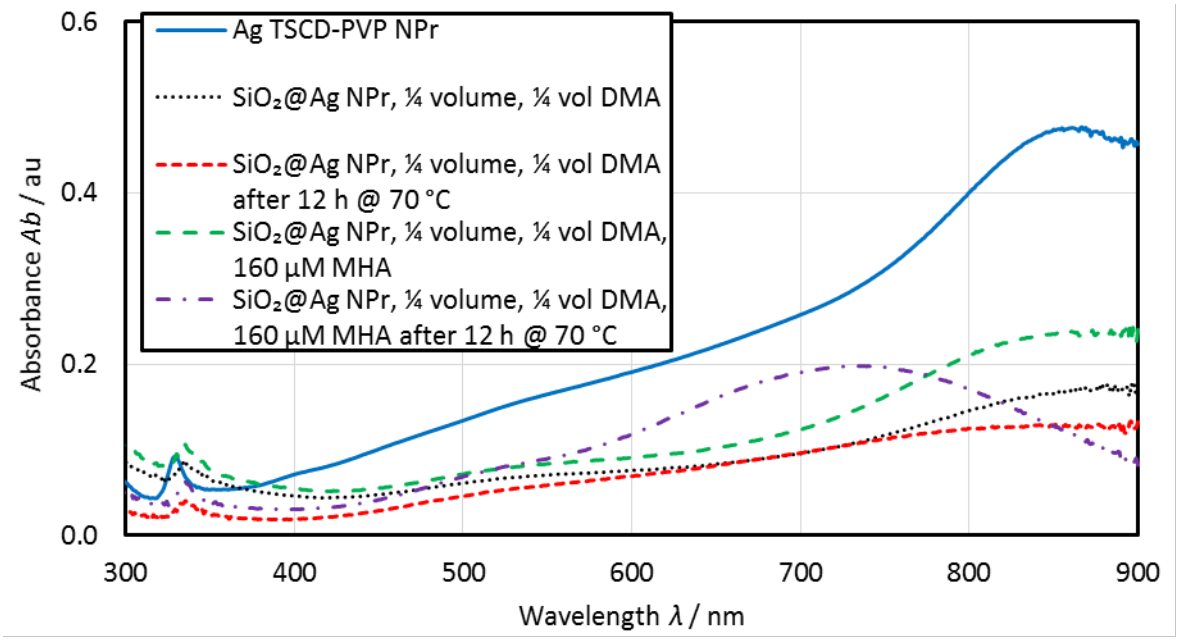

Figure N.1 UV-vis spectra before, after SiO_2 coating and after 12 h @ 70 °C for SiO_2@Ag NPrs produced using ¼ concentration of DMA. Measured using UV-vis-1. Results have been adjusted for final NF volume and cuvette employed.

N.3 Changing the Time of the TEOS Reaction Step

The production of a thinner SiO_2 coating by varying the time of the TEOS reaction step (step 6 in Figure 3-1), followed by subsequent elevated temperature stability testing (using the protocol described in Section 3.9.3) is discussed in this subsection.

Two different reaction times of 1 minute and 5 minutes were assessed (3 repeats at each reaction time) and compared to the normal reaction time of 30 minutes used in the optimised Stöber coating procedure described in Section 3.6.4.

The samples were characterised by both UV-vis and TEM, initially just after SiO_2 coating and after exposure to a temperature of 70 °C for 18 h. The TEM results are given and discussed in Appendix G, Section G.14.4. The before and after SiO_2 coating UV-vis results using reaction times of 1 minute and 5 minutes are shown in Figure N.2. For both reaction times there was a large reduction in Ab_{max} following SiO_2 coating of 68 % (σ = 4 %, N = 3) for the 5 minute reaction time and 84 % (σ = 3 %, N = 3) for the 1 minute reaction time. This reduction was greater than that seen for the standard reaction time of 30 minutes of 40 % (average of results from Table M.2 and Table M.3, σ = 15 %, N = 19). λ_{max} in contrast varied by < ± 30 nm following SiO_2 coating similar to the range obtained for the 30 minute reaction time of -24 nm to 34 nm (positive = red-shift).

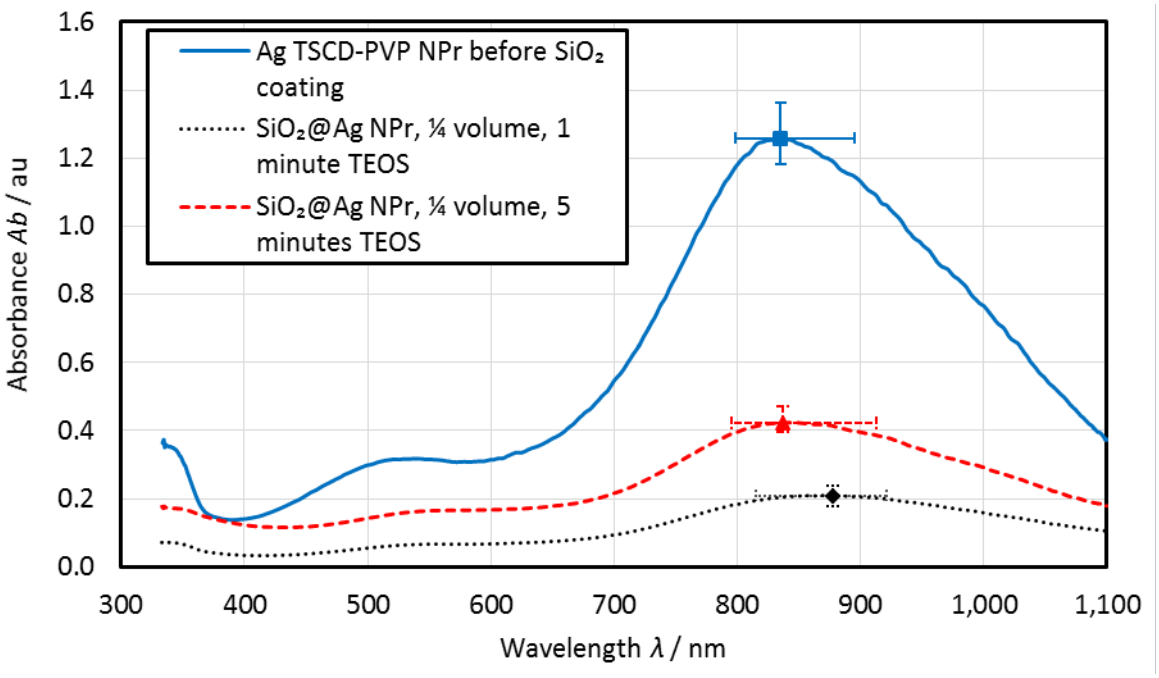

Figure N.2 UV-vis spectra before and after SiO_2 coating using a TEOS reaction time of 1 minute or 5 minutes. Measured using UV-vis-IR-2. Values have been adjusted for cuvette and dilution. Average of 3 results shown with error bars showing range of results obtained at the maximum absorbance.

The SiO_2@Ag NPrs produced using the two different reaction times were assessed for their stability to an elevated temperature of 70 °C using the protocol described in Section 3.9.3. Due to the reduction in product observed in Figure N.2, the samples were diluted to give a similar Ab_{max} of 0.8 au when measured using a 10 mm path length cuvette ≈ the same Ab_{max} as the SiO_2@Ag NPr diluted from Appendix M, Section M.4 to allow direct comparison with the optimised Stöber process with a TEOS reaction time of 30 minutes. Figure N.3 shows the change in λ_{max} after exposure to an elevated temperature of 70 °C and Figure N.4 the change in Ab_{max}. For all samples there was a blue-shift in λ_{max} with exposure to an elevated temperature. To facilitate comparison with the results obtained using the normal TEOS reaction time of 30 minutes in Section M.4 the data obtained after 9 h exposure is tabulated in Table N.7 (λ_{max} change) and Table N.8 (Ab_{max} change).

All the SiO_2@Ag NPr samples exhibited a large blue-shift in λ_{max} with exposure to elevated temperature. Although the average blue-shift was smaller for the 1 minute samples compared to the 5 minute samples ANOVA testing (including the 30 minute results) showed no significant differences between the samples produced using the different reaction times.

For Ab_{max}, all the changes apart from one sample were within ± 20 % (this one sample had an increase so may have evaporated slightly during testing). There was no relationship between exposure time and change in Ab_{max} and no significant differences (tested using ANOVA) between

the different reaction times for change in Ab_{max} (when the measurement uncertainty is also considered).

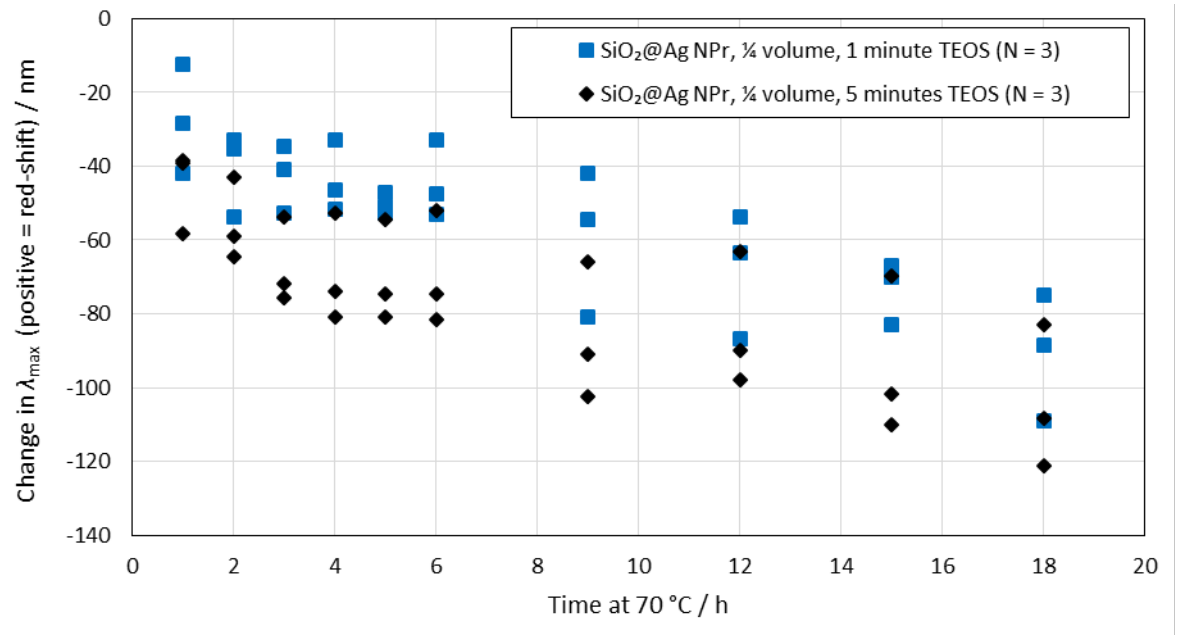

Figure N.3 Change in λ_{max} with exposure to a temperature of 70 °C for SiO_2@Ag NPr NFs produced using two different TEOS reaction times.

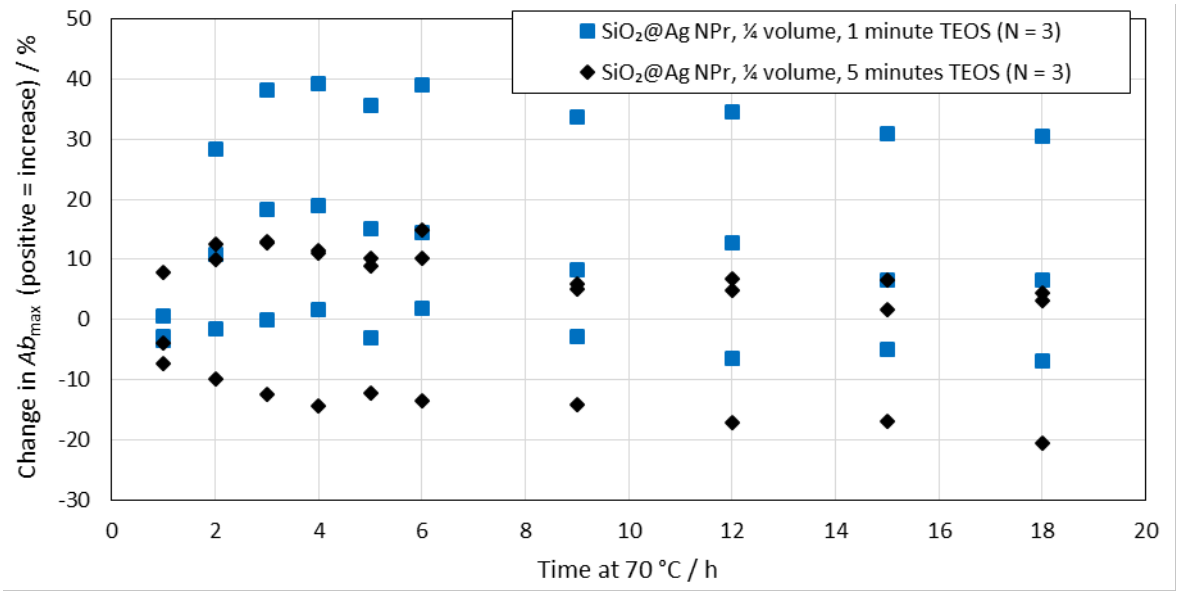

Figure N.4 Change in Ab_{max} with exposure to a temperature of 70 °C for SiO_2@Ag NPr NFs produced using two different TEOS reaction times.

Table N.7 Change in λ_{max} after 9 h exposure to an elevated temperature of 70 °C (positive = red-shift).

Type of NF	**Average change / nm**	***σ*/ %**	**Maximum change / nm**	**Minimum change / nm**	***N***
SiO_2@Ag NPr, 1 minute reaction time	-59	20	-81	-42	3
SiO_2@Ag NPr, 5 minutes reaction time	-86	19	-102	-66	3
SiO_2@Ag NPr diluted (30 minutes reaction time) – from Table M.6	-91	15	-107	-77	3

Table N.8 Change in Ab_{max} after 9 h exposure to an elevated temperature of 70 °C (positive = increase).

Type of NF	**Average change / %**	***σ*/ %**	**Maximum change / %**	**Minimum change / %**	***N***
SiO_2@Ag NPr, 1 minute reaction time	13	19	34	-3	3
SiO_2@Ag NPr, 5 minutes reaction time	-1	11	-14	6	3
SiO_2@Ag NPr diluted (30 minutes reaction time) – from Table M.7	-24	4	-27	-22	2

Appendix O Additional Information on SiO_2 Coating of the Broadband Absorber

This Appendix presents the results of calculating the potential performance of the broadband absorber NF before and after coating with SiO_2 using the measured initial UV-vis-IR spectra.

O.1 Calculation of Efficiency From UV-vis-IR Spectra

The power absorbed by the broadband absorber NF before and after SiO_2 coating is shown in Figure O.1. The SiO_2@broadband NF was slightly better at absorbing in the < 400 nm range, whereas the uncoated broadband absorber was slightly better in the > 800 nm range.

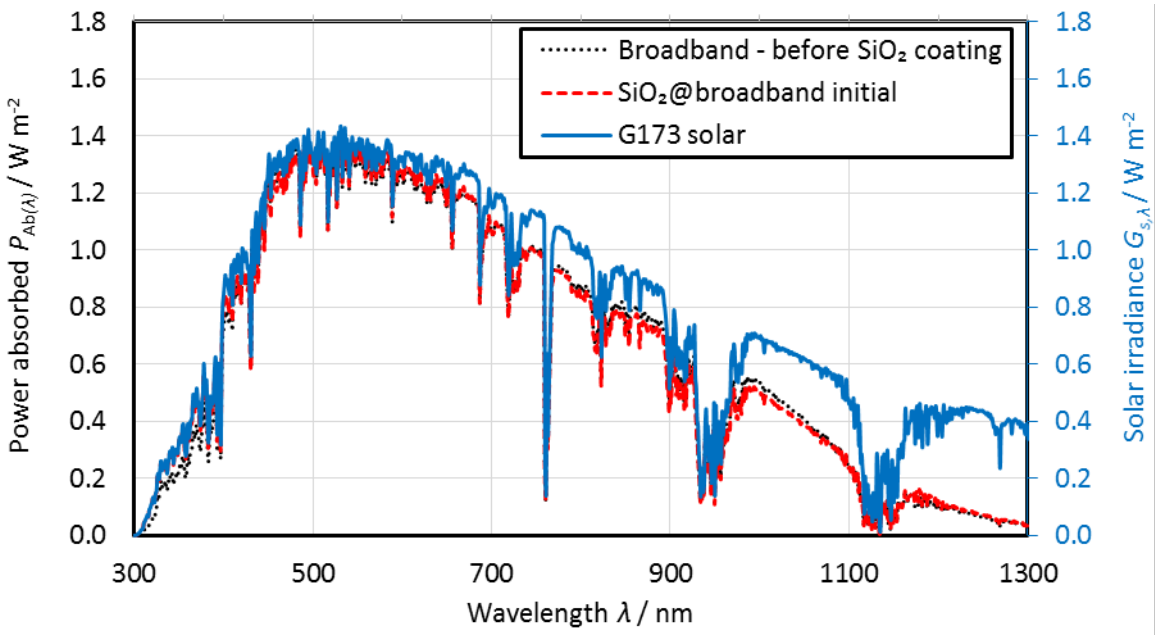

Figure O.1 Amount of power absorbed P_{Ab} of the G173 ($G_{s,\lambda(dir+cs)}$) with a 10 mm path length by the broadband absorber before and after SiO_2 coating. The secondary vertical axis is for the G173 solar spectrum taken from (ASTM, 2012).

The value of $\eta_{Ab(300\ nm\ -\ 1300\ nm)}$ for the broadband absorber before and after SiO_2 coating was calculated using Equation 3-8. In addition, to allow comparison with the Ag NPr efficiency calculations given in Table 4-2, $\eta_{Ab(300\ nm\ -\ 900\ nm)}$ was estimated for a 10 mm path length using Equation 4-3. To get an estimation of the potential performance across the whole of the solar spectrum $\eta_{Ab(280\ nm\ -\ 4000\ nm)}$ was also calculated assuming that there was no absorption > 900 nm using Equation 4-4 and the 300 nm - 900 nm spectra data. For completeness the performance over the whole λ range was also estimated using the 300 nm - 1300 nm spectral data and modifying Equation 4-4 to give (note that the broadband absorber before and after coating was

only measured over the range 300 nm – 1300 nm and not 300 nm – 1350 nm as measured previously – see Equation H.1):

$$\eta_{\mathrm{Ab(280\ nm-4000\ nm)}} = \frac{\sum_{\lambda=300\ \mathrm{nm}}^{\lambda=1300\ \mathrm{nm}} P_{\mathrm{Ab}(\lambda)}}{\sum_{\lambda=280\ \mathrm{nm}}^{\lambda=4000\ \mathrm{nm}} P_{\mathrm{i}(\lambda)}} \times 100$$

Equation O.1

The results are given in Table O.1. The $\eta_{\mathrm{Ab(300\ nm\ -\ 1300\ nm)}}$ obtained for the broadband absorber before SiO_2 coating of 81.89 % was slightly lower than the $\eta_{\mathrm{Ab(300\ nm\ -\ 1350\ nm)}}$ value of 83.05 % obtained previously (Table H.11). After SiO_2 coating the values were slightly higher than before SiO_2 coating but similar. The values for $\eta_{\mathrm{Ab(300\ nm\ -\ 900\ nm)}}$ of 91.79 % and 92.36 % were similar to those obtained previously for the broadband mixture of 91.09 % (Table H.10) and the value obtained for the centrifuged Ag TSCD-PVP NPrs re-dispersed into ¼ the volume of water of 91.7 % (Table 4-2).

Table O.1 Various different efficiency calculations for the broadband absorber before and after SiO_2 coating.

Efficiency calculation	**Broadband absorber before SiO_2 coating**	**SiO_2@broadband**
$\eta_{\mathrm{Ab(300\ nm\ -\ 1300\ nm)}}$ / %	81.89	81.95
$\eta_{\mathrm{Ab(300\ nm\ -\ 900\ nm)}}$ / %	91.79	92.36
$\eta_{\mathrm{Ab(280\ nm\ -\ 4000\ nm)}}$ (using 300 nm – 1300 nm data/ %	72.14	72.20
$\eta_{\mathrm{Ab(280\ nm\ -\ 4000\ nm)}}$ (using 300 nm – 900 nm data/ %	60.86	61.24

Bibliography

Abdelrazik, A.S., Al-Sulaiman, F.A., Saidur, R., 2019. Optical behavior of a water/silver nanofluid and their influence on the performance of a photovoltaic-thermal collector. Solar Energy Materials and Solar Cells, 201, 110054, https://doi.org/10.1016/j.solmat.2019.110054.

Abdullah, A.A., Fallatah, H.M., Lindsay, K.A., Oreijah, M.M., 2017. Measurements of the performance of the experimental salt-gradient solar pond at Makkah one year after commissioning. Solar Energy, 150, 212-219, https://doi.org/10.1016/j.solener.2017.04.040.

Abdullah, A.A., Lindsay, K.A., AbdelGawad, A.F., 2016. Construction of sustainable heat extraction system and a new scheme of temperature measurement in an experimental solar pond for performance enhancement. Solar Energy, 130, 10-24, https://doi.org/10.1016/j.solener.2016.02.005.

Abokersh, M.H., Osman, M., El-Baz, O., El-Morsi, M., Sharaf, O., 2018. Review of the phase change material (PCM) usage for solar domestic water heating systems (SDWHS). International Journal of Energy Research, 42(2), 329-357, https://doi.org/10.1002/er.3765.

Agyenim, F., Hewitt, N., Eames, P., Smyth, M., 2010. A review of materials, heat transfer and phase change problem formulation for latent heat thermal energy storage systems (LHTESS). Renewable and Sustainable Energy Reviews, 14(2), 615-628, https://doi.org/10.1016/j.rser.2009.10.015.

Aherne, D., Ledwith, D.M., Gara, M., Kelly, J.M., 2008. Optical Properties and Growth Aspects of Silver Nanoprisms Produced by a Highly Reproducible and Rapid Synthesis at Room Temperature. Advanced Functional Materials, 18(14), 2005-2016, https://doi.org/10.1002/adfm.200800233.

Ahmad, S.H.A., Saidur, R., Mahbubul, I.M., Al-Sulaiman, F.A., 2017. Optical properties of various nanofluids used in solar collector: A review. Renewable and Sustainable Energy Reviews, 73, 1014-1030, https://doi.org/10.1016/j.rser.2017.01.173.

Ahmadi, A., Ganji, D.D., Jafarkazemi, F., 2016. Analysis of utilizing Graphene nanoplatelets to enhance thermal performance of flat plate solar collectors. Energy Conversion and Management, 126, 1-11, https://doi.org/10.1016/j.enconman.2016.07.061.

Ajeena, A.M., Víg, P., Farkas, I., 2022. A comprehensive analysis of nanofluids and their practical applications for flat plate solar collectors: Fundamentals, thermophysical properties, stability, and difficulties. Energy Reports, 8, 4461-4490, https://doi.org/10.1016/j.egyr.2022.03.088.

Al-Nimr, M.d.A., Al-Dafaie, A.M.A., 2014. Using nanofluids in enhancing the performance of a novel two-layer solar pond. Energy, 68, 318-326, https://doi.org/10.1016/j.energy.2014.03.023.

Alibaba, 2020. price for potassium carbonate. https://www.alibaba.com/showroom/price-for-potassium-carbonate.html. (Accessed 08 June 2020).

Alim, M.A., Abdin, Z., Saidur, R., Hepbasli, A., Khairul, M.A., Rahim, N.A., 2013. Analyses of entropy generation and pressure drop for a conventional flat plate solar collector using different types of metal oxide nanofluids. Energy and Buildings, 66, 289-296, https://doi.org/10.1016/j.enbuild.2013.07.027.

Amjad, M., Jin, H., Du, X., Wen, D., 2018. Experimental photothermal performance of nanofluids under concentrated solar flux. Solar Energy Materials and Solar Cells, 182, 255-262, https://doi.org/10.1016/j.solmat.2018.03.044.

Amjad, M., Raza, G., Xin, Y., Pervaiz, S., Xu, J., Du, X., Wen, D., 2017. Volumetric solar heating and steam generation via gold nanofluids. Applied Energy, 206, 393-400, https://doi.org/10.1016/j.apenergy.2017.08.144.

Amouei Torkmahalleh, M., Askari, M., Gorjinezhad, S., Eroğlu, D., Obaidullah, M., Habib, A.R., Godelek, S., Kadyrov, S., Kahraman, O., Pakzad, N.Z., Ahmadi, G., 2017. Key factors impacting performance of a salinity gradient solar pond exposed to Mediterranean climate. Solar Energy, 142, 321-329, https://doi.org/10.1016/j.solener.2016.12.037.

Armand, M., Axmann, P., Bresser, D., Copley, M., Edström, K., Ekberg, C., Guyomard, D., Lestriez, B., Novák, P., Petranikova, M., Porcher, W., Trabesinger, S., Wohlfahrt-Mehrens, M., Zhang, H., 2020. Lithium-ion batteries – Current state of the art and anticipated developments. Journal of Power Sources, 479, https://doi.org/10.1016/j.jpowsour.2020.228708.

ASTM, 2012. Reference Solar Spectral Irradiance: American Standard Testing Methods (ASTM), ASTM G-173. https://rredc.nrel.gov/solar//spectra/am1.5/ASTMG173/ASTMG173.html. (Accessed 01 July 2019).

Aydin, D., Casey, S.P., Riffat, S., 2015. The latest advancements on thermochemical heat storage systems. Renewable and Sustainable Energy Reviews, 41, 356-367, https://doi.org/10.1016/j.rser.2014.08.054.

Ayompe, L.M., Duffy, A., 2013. Analysis of the thermal performance of a solar water heating system with flat plate collectors in a temperate climate. Applied Thermal Engineering, 58(1-2), 447-454, https://doi.org/10.1016/j.applthermaleng.2013.04.062.

Ayompe, L.M., Duffy, A., Mc Keever, M., Conlon, M., McCormack, S.J., 2011. Comparative field performance study of flat plate and heat pipe evacuated tube collectors (ETCs) for domestic water heating systems in a temperate climate. Energy, 36(5), 3370-3378, https://doi.org/10.1016/j.energy.2011.03.034.

Azad, E., 2012. Assessment of three types of heat pipe solar collectors. Renewable and Sustainable Energy Reviews, 16(5), 2833-2838, https://doi.org/10.1016/j.rser.2012.02.001.

Babar, H., Ali, H.M., 2019. Towards hybrid nanofluids: Preparation, thermophysical properties, applications, and challenges. Journal of Molecular Liquids, 281, 598-633, https://doi.org/10.1016/j.molliq.2019.02.102.

Bandarra Filho, E.P., Mendoza, O.S.H., Beicker, C.L.L., Menezes, A., Wen, D., 2014. Experimental investigation of a silver nanoparticle-based direct absorption solar thermal system. Energy Conversion and Management, 84, 261-267, https://doi.org/10.1016/j.enconman.2014.04.009.

Beicker, C.L.L., Amjad, M., Bandarra Filho, E.P., Wen, D., 2018. Experimental study of photothermal conversion using gold/water and MWCNT/water nanofluids. Solar Energy Materials and Solar Cells, 188, 51-65, https://doi.org/10.1016/j.solmat.2018.08.013.

Beikircher, T., Möckl, M., Osgyan, P., Streib, G., 2015. Advanced solar flat plate collectors with full area absorber, front side film and rear side vacuum super insulation. Solar Energy Materials and Solar Cells, 141, 398-406, https://doi.org/10.1016/j.solmat.2015.06.019.

Bell, S., 2001. A Beginner's Guide to Uncertainty of Measurement. NPL, UK TW11 0LW, https://www.dit.ie/media/physics/documents/GPG11.pdf. (Accessed 20 November 2019).

Brandon, M.P., Ledwith, D.M., Kelly, J.M., 2014. Preparation of saline-stable, silica-coated triangular silver nanoplates of use for optical sensing. J Colloid Interface Sci, 415, 77-84, https://doi.org/10.1016/j.jcis.2013.10.017.

British Standards Insitution (BSI), 1996. BS EN ISO 9288: 1988 Thermal insulation - Heat transfer by radiation - Physical quantities and definitions. BSI.

British Standards Insitution (BSI), 2018. BS ISO 9060-2018 Solar Energy - Specification and Classification of Instruments for Measuring Hemispherical Solar and Direct Solar Radiation. BSI.

British Standards Institution (BSI), 2013. BS EN ISO 9806: 2013 Solar energy - Solar thermal collectors - Test methods. BSI.

Budihardjo, I., Morrison, G.L., 2009. Performance of water-in-glass evacuated tube solar water heaters. Solar Energy, 83(1), 49-56, https://doi.org/10.1016/j.solener.2008.06.010.

Cabeza, L.F., Solé, A., Barreneche, C., 2017. Review on sorption materials and technologies for heat pumps and thermal energy storage. Renewable Energy, 110, 3-39, https://doi.org/10.1016/j.renene.2016.09.059.

Carboni, M., 2014. Silver Nanoprisms Embedded in a Polymeric Matrix for Energy Saving Glazing. PhD thesis, Southampton.

Carboni, M., Capretto, L., Carugo, D., Stulz, E., Zhang, X., 2013. Microfluidics-based continuous flow formation of triangular silver nanoprisms with tuneable surface plasmon resonance. Journal of Materials Chemistry C, 1(45), 7540 - 7546, https://doi.org/10.1039/c3tc31335b.

Carboni, M., Carravetta, M., Zhang, X.L., Stulz, E., 2016. Efficient NIR light blockage with matrix embedded silver nanoprism thin films for energy saving window coating. J. Mater. Chem. C, 4(8), 1584-1588, https://doi.org/10.1039/c6tc00026f.

Chaji, H., Ajabshirchi, Y., Esmaeilzadeh, E., Zeinali Heris, S., Hedayatizadeh, M., Kahani, M., 2013. Experimental Study on Thermal Efficiency of Flat Plate Solar Collector Using TiO_2/Water Nanofluid. Modern Applied Science, 7(10), 60-69, https://doi.org/10.5539/mas.v7n10p60.

Chase, M.W.J., 1998. NIST-JANAF Thermochemical Tables, Fourth Edition. Journal of Physical and Chemical Reference Data, 9, 1-1961.

Che Sidik, N.A., Mahmud Jamil, M., Aziz Japar, W.M.A., Muhammad Adamu, I., 2017. A review on preparation methods, stability and applications of hybrid nanofluids. Renewable and Sustainable Energy Reviews, 80, 1112-1122, https://doi.org/10.1016/j.rser.2017.05.221.

Chen, L., Xu, C., Liu, J., Fang, X., Zhang, Z., 2017. Optical absorption property and photo-thermal conversion performance of graphene oxide/water nanofluids with excellent dispersion stability. Solar Energy, 148, 17-24, https://doi.org/10.1016/j.solener.2017.03.073.

Chen, M., He, Y., Zhu, J., 2017. Preparation of Au–Ag bimetallic nanoparticles for enhanced solar photothermal conversion. International Journal of Heat and Mass Transfer, 114, 1098-1104, https://doi.org/10.1016/j.ijheatmasstransfer.2017.07.005.

Chen, M., He, Y., Zhu, J., Wen, D., 2016. Investigating the collector efficiency of silver nanofluids based direct absorption solar collectors. Applied Energy, 181, 65-74, https://doi.org/10.1016/j.apenergy.2016.08.054.

Chopra, K., Tyagi, V.V., Pandey, A.K., Sari, A., 2018. Global advancement on experimental and thermal analysis of evacuated tube collector with and without heat pipe systems and possible applications. Applied Energy, 228, 351-389, https://doi.org/10.1016/j.apenergy.2018.06.067.

Climate Change Committee, 2019a. Net Zero Technical Report. Crown, 7 Holbein Place, London, SW1W 8NR, https://www.theccc.org.uk/publication/net-zero-technical-report/. (Accessed 07 May 2019).

Climate Change Committee, 2019b. UK housing: Fit for the future. Crown, 7 Holbein Place, London, SW1W 8NR, https://www.theccc.org.uk/publication/uk-housing-fit-for-the-future/. (Accessed 07 May 2019).

Climate Change Committee, 2021a. CCC Joint Recommendations 2021 Report to Parliament. Crown, 1 Victoria Street, London, SW1H 0ET, https://www.theccc.org.uk/wp-content/uploads/2021/06/CCC-Joint-Recommendations-2021-Report-to-Parliament.pdf. (Accessed 01 October 2021).

Climate Change Committee, 2021b. Progress in Reducing Emissions 2021 Report to Parliament. Crown, 1 Victoria Street, London, SW1H 0ET, https://www.theccc.org.uk/wp-content/uploads/2021/06/Progress-in-reducing-emissions-2021-Report-to-Parliament.pdf. (Accessed 01 October 2021).

Cosgrove, T., 2010. Colloid Science : Principles methods and applications, Second Edition ed. John Wiley & Sons, Incorporated.

Crisostomo, F., Hjerrild, N., Mesgari, S., Li, Q., Taylor, R.A., 2017. A hybrid PV/T collector using spectrally selective absorbing nanofluids. Applied Energy, 193, 1-14, https://doi.org/10.1016/j.apenergy.2017.02.028.

Darmanin, T., Nativo, P., Gilliland, D., Ceccone, G., Pascual, C., De Berardis, B., Guittard, F., Rossi, F., 2012. Microwave-assisted synthesis of silver nanoprisms/nanoplates using a “modified polyol process”. Colloids and Surfaces A: Physicochemical and Engineering Aspects, 395, 145-151, https://doi.org/10.1016/j.colsurfa.2011.12.020.

Das, P.K., 2017. A review based on the effect and mechanism of thermal conductivity of normal nanofluids and hybrid nanofluids. Journal of Molecular Liquids, 240, 420-446, https://doi.org/10.1016/j.molliq.2017.05.071.

de Jong, A.-J., Trausel, F., Finck, C., van Vliet, L., Cuypers, R., 2014. Thermochemical Heat Storage – System Design Issues. Energy Procedia, 48, 309-319, https://doi.org/10.1016/j.egypro.2014.02.036.

de Jong, A.-J., van Vliet, L., Hoegaerts, C., Roelands, M., Cuypers, R., 2016. Thermochemical Heat Storage – from Reaction Storage Density to System Storage Density. Energy Procedia, 91, 128-137, https://doi.org/10.1016/j.egypro.2016.06.187.

Dean, J.A., Lange, N.A., 1999. Lange's Handbook of Chemistry, 15th Edition ed. McGraw-Hill, New York.

Deng, J., Ma, R., Yuan, G., Chang, C., Yang, X., 2016. Dynamic thermal performance prediction model for the flat-plate solar collectors based on the two-node lumped heat capacitance method. Solar Energy, 135, 769-779, https://doi.org/10.1016/j.solener.2016.06.060.

Department for Business Energy and Industrial Strategy, 2016. Evidence Gathering: Thermal Energy Storage (TES) Technologies. Crown, London, https://assets.publishing.service.gov.uk/government/uploads/system/uploads/attachment_data/file/545249/DELTA_EE_DECC_TES_Final__1_.pdf. (Accessed December 2021).

Department for Business Energy and Industrial Strategy, 2017a. 2016 UK Greenhouse Gas Emissions, Provisional Figures. Crown, London, https://www.gov.uk/government/statistics/provisional-uk-greenhouse-gas-emissions-national-statistics-2016. (Accessed June 2018).

Department for Business Energy and Industrial Strategy, 2017b. Energy Consumption in the UK. Crown, London, https://www.gov.uk/government/statistics/energy-consumption-in-the-uk. (Accessed June 2018).

Department for Business Energy and Industrial Strategy, 2017c. National Energy Efficiency Data-Framework Summary of Analysis using the National Energy Efficiency Data Framework (NEED). Crown, London, https://assets.publishing.service.gov.uk/government/uploads/system/uploads/attachment_data/file/633219/need-framework-summary-of-analysis-2017.pdf. (Accessed 22 November 2021).

Department for Business Energy and Industrial Strategy, 2019a. 2019 No. 1056 Climate Change, The Climate Change Act 2008 (2050 Target Amendment) Order 2019. Crown, London, http://www.legislation.gov.uk/id/uksi/2019/1056. (Accessed 19 January 2021).

Department for Business Energy and Industrial Strategy, 2019b. Digest of United Kingdom Energy Statistics 2019. Crown, London, https://www.gov.uk/government/statistics/digest-of-uk-energy-statistics-dukes-2019. (Accessed 18 March 2020).

Department for Business Energy and Industrial Strategy, 2020. National Energy Efficieny Data-Framework Summary of Analysis using the National Energy Efficiency Data Framework (NEED). Crown, London, https://assets.publishing.service.gov.uk/government/uploads/system/uploads/attachment_data/file/895140/National_Energy_Efficiency_Data_Framework_NEED_report_summary_of_analysis_2020.pdf. (Accessed 19 January 2021).

Deutsch, M., Müller, D., Aumeyr, C., Jordan, C., Gierl-Mayer, C., Weinberger, P., Winter, F., Werner, A., 2016. Systematic search algorithm for potential thermochemical energy storage systems. Applied Energy, 183, 113-120, https://doi.org/10.1016/j.apenergy.2016.08.142.

Dhimish, M., Holmes, V., Mather, P., Sibley, M., 2018. Preliminary assessment of the solar resource in the United Kingdom. Clean Energy, 2(2), 112-125, https://doi.org/10.1093/ce/zky017.

Dhinesh Kumar, D., Valan Arasu, A., 2018. A comprehensive review of preparation, characterization, properties and stability of hybrid nanofluids. Renewable and Sustainable Energy Reviews, 81, 1669-1689, https://doi.org/10.1016/j.rser.2017.05.257.

Dincer, I., 2002. On thermal energy storage systems and applications in buildings. Energy and Buildings, 34(4), 377-388, https://doi.org/https://doi.org/10.1016/S0378-7788(01)00126-8.

Dincer, I., Rosen, M., 2011. Thermal Energy Storage Systems and Applications, Second Edition ed. John Wiley and Sons, Ltd.

Dong, X., Ji, X., Jing, J., Li, M., Li, J., Yang, W., 2010. Synthesis of Triangular Silver Nanoprisms by Stepwise Reduction of Sodium Borohydride and Trisodium Citrate. J. Phys. Chem C, 114, 2070-2074, https://doi.org/10.1021/jp909964k.

Donkers, P.A.J., Pel, L., Adan, O.C.G., 2016. Experimental studies for the cyclability of salt hydrates for thermochemical heat storage. Journal of Energy Storage, 5, 25-32, https://doi.org/10.1016/j.est.2015.11.005.

Donkers, P.A.J., Sögütoglu, L.C., Huinink, H.P., Fischer, H.R., Adan, O.C.G., 2017. A review of salt hydrates for seasonal heat storage in domestic applications. Applied Energy, 199, 45-68, https://doi.org/10.1016/j.apenergy.2017.04.080.

Du, M., Tang, G.H., 2016. Plasmonic nanofluids based on gold nanorods/nanoellipsoids/nanosheets for solar energy harvesting. Solar Energy, 137, 393-400, https://doi.org/10.1016/j.solener.2016.08.029.

Duffie, J.A., Beckman, W.A., 2013. Solar Engineering of Thermal Processes, Fourth Edition. John Wiley & Sons.

Duffner, F., Mauler, L., Wentker, M., Leker, J., Winter, M., 2021. Large-scale automotive battery cell manufacturing: Analyzing strategic and operational effects on manufacturing costs. International Journal of Production Economics, 232, https://doi.org/10.1016/j.ijpe.2020.107982.

Ekhtiari, A., Flynn, D., Syron, E., 2020. Investigation of the Multi-Point Injection of Green Hydrogen from Curtailed Renewable Power into a Gas Network. Energies, 13(22), https://doi.org/10.3390/en13226047.

Energy and Climate Change Committee, 2016. 2020 Renewable Heat and Transport Targets, Second Report of Session 2016-17. Crown, UK, https://publications.parliament.uk/pa/cm201617/cmselect/cmenergy/173/173.pdf. (Accessed 22 November 2021).

Engineering Toolbox, 2004. Water - Specific Heat. https://www.engineeringtoolbox.com/specific-heat-capacity-water-d_660.html. (Accessed 21 January 2020).

Esfahani, N.N., Toghraie, D., Afrand, M., 2018. A new correlation for predicting the thermal conductivity of ZnO–Ag (50%–50%)/water hybrid nanofluid: An experimental study. Powder Technology, 323, 367-373, https://doi.org/10.1016/j.powtec.2017.10.025.

Farid, M.M., Khudhair, A.M., Razack, S.A.K., Al-Hallaj, S., 2004. A review on phase change energy storage: materials and applications. Energy Conversion and Management, 45(9-10), 1597-1615, https://doi.org/10.1016/j.enconman.2003.09.015.

Feldman, D., Margolis, R., Denholm, P., Stekli, J., 2016. Exploring the Potential Competiveness of Utility-Scale Photovoltaics plus Batteries with Concentrating Solar Power, 2015-2030. (NREL), N.R.E.L., US, https://www.nrel.gov/docs/fy16osti/66592.pdf. (Accessed December 2021).

Ferchaud, C.J., Scherpenborg, R.A.A., Zondag, H.A., de Boer, R., 2014. Thermochemical Seasonal Solar Heat Storage in Salt Hydrates for Residential Applications – Influence of the Water Vapor Pressure on the Desorption Kinetics of $MgSO_4.7H_2O$. Energy Procedia, 57, 2436-2440, https://doi.org/10.1016/j.egypro.2014.10.252.

Filipczak, P., Borkowski, M., Chudobinski, P., Bres, S., Matusiak, M., Nowaczyk, G., Kozanecki, M., 2020. Sodium citrate stabilized Ag NPs under thermal treatment, electron-beam and laser irradiations. Radiation Physics and Chemistry, 169, 107948, https://doi.org/10.1016/j.radphyschem.2018.07.020.

Flynn, C., Sirén, K., 2015. Influence of location and design on the performance of a solar district heating system equipped with borehole seasonal storage. Renewable Energy, 81, 377-388, https://doi.org/10.1016/j.renene.2015.03.036.

Frazzica, A., Brancato, V., Caprì, A., Cannilla, C., Gordeeva, L.G., Aristov, Y.I., 2020. Development of “salt in porous matrix” composites based on LiCl for sorption thermal energy storage. Energy, 208, 118338, https://doi.org/10.1016/j.energy.2020.118338.

Freeman, J., Hellgardt, K., Markides, C.N., 2015. An assessment of solar-powered organic Rankine cycle systems for combined heating and power in UK domestic applications. Applied Energy, 138, 605-620, https://doi.org/10.1016/j.apenergy.2014.10.035.

Garcia, A.M., Bizeto, M.A., Ferrari, V.B., Okamoto, D.N., de Vasconcellos, S.P., Camilo, F.F., 2020. Direct evaluation of microbial growth dynamics and colloidal stability of silver nanoparticles stabilized by poly(vinyl pyrrolidone) and poly(vinyl alcohol). Journal of Nanoparticle Research, 22(6), 137, https://doi.org/10.1007/s11051-020-04863-1.

Gil, A., Medrano, M., Martorell, I., Lázaro, A., Dolado, P., Zalba, B., Cabeza, L.F., 2010. State of the art on high temperature thermal energy storage for power generation. Part 1—Concepts, materials and modellization. Renewable and Sustainable Energy Reviews, 14(1), 31-55, https://doi.org/10.1016/j.rser.2009.07.035.

Gill, N., Osman, P., Head, L., Voyer, M., Harada, T., Waitt, G., Gibson, C., 2015. Looking beyond installation: Why households struggle to make the most of solar hot water systems. Energy Policy, 87, 83-94, https://doi.org/10.1016/j.enpol.2015.08.038.

Glasser, L., 2014a. Supporting Information - The Thermodynamics of Inorganic Hydration and of Humidity Control, with an Extensive Databasse of Salt Hydrate Pairs. Journal of Chemical & Engineering Data, 59(2), 526-530.

Glasser, L., 2014b. Thermodynamics of Inorganic Hydration and of Humidity Control, with an Extensive Database of Salt Hydrate Pairs. Journal of Chemical & Engineering Data, 59(2), 526-530, https://doi.org/10.1021/je401077x.

Goel, N., Taylor, R.A., Otanicar, T., 2020. A review of nanofluid-based direct absorption solar collectors: Design considerations and experiments with hybrid PV/Thermal and direct steam generation collectors. Renewable Energy, 145, 903-913, https://doi.org/10.1016/j.renene.2019.06.097.

Gómez-Castro, F.M., Schneider, D., Päßler, T., Eicker, U., 2018. Review of indirect and direct solar thermal regeneration for liquid desiccant systems. Renewable and Sustainable Energy Reviews, 82, 545-575, https://doi.org/10.1016/j.rser.2017.09.053.

Gondal, I.A., 2019. Hydrogen integration in power-to-gas networks. International Journal of Hydrogen Energy, 44(3), 1803-1815, https://doi.org/10.1016/j.ijhydene.2018.11.164.

Gorji, T.B., Ranjbar, A.A., 2015. Geometry optimization of a nanofluid-based direct absorption solar collector using response surface methodology. Solar Energy, 122, 314-325, https://doi.org/10.1016/j.solener.2015.09.007.

Gorji, T.B., Ranjbar, A.A., 2016. A numerical and experimental investigation on the performance of a low-flux direct absorption solar collector (DASC) using graphite, magnetite and silver nanofluids. Solar Energy, 135, 493-505, https://doi.org/10.1016/j.solener.2016.06.023.

Gorji, T.B., Ranjbar, A.A., 2017a. A review on optical properties and application of nanofluids in direct absorption solar collectors (DASCs). Renewable and Sustainable Energy Reviews, 72, 10-32, https://doi.org/10.1016/j.rser.2017.01.015.

Gorji, T.B., Ranjbar, A.A., 2017b. Thermal and exergy optimization of a nanofluid-based direct absorption solar collector. Renewable Energy, 106, 274-287, https://doi.org/10.1016/j.renene.2017.01.031.

Graf, C., Vossen, D., Imhof, A., Blaaderen, A., 2003. A General Method To Coat Colloidal Particles with Silica. Langmuir, 19, 6693-6700, https://doi.org/https://doi.org/10.1021/la0347859.

Greening, B., Azapagic, A., 2014. Domestic solar thermal water heating: A sustainable option for the UK? Renewable Energy, 63, 23-36, https://doi.org/10.1016/j.renene.2013.07.048.

Gupta, H.K., Agrawal, G.D., Mathur, J., 2015a. Experimental Evaluation of Using Nanofluid in Direct Absorption Solar Collector, Energy Technology & Ecological Concerns: A Contemporary Approach. 150-154.

Gupta, H.K., Agrawal, G.D., Mathur, J., 2015b. An experimental investigation of a low temperature Al_2O_3-H_2O nanofluid based direct absorption solar collector. Solar Energy, 118, 390-396, https://doi.org/10.1016/j.solener.2015.04.041.

Gupta, H.K., Agrawal, G.D., Mathur, J., 2015c. Investigations for effect of Al_2O_3–H_2O nanofluid flow rate on the efficiency of direct absorption solar collector. Case Studies in Thermal Engineering, 5, 70-78, https://doi.org/10.1016/j.csite.2015.01.002.

Gutierrez, A., Ushak, S., Linder, M., 2018. High Carnallite-Bearing Material for Thermochemical Energy Storage: Thermophysical Characterization. ACS Sustainable Chemistry & Engineering, 6(5), 6135-6145, https://doi.org/10.1021/acssuschemeng.7b04803.

Gutierrez, A., Ushak, S., Mamani, V., Vargas, P., Barreneche, C., Cabeza, L.F., Grágeda, M., 2017. Characterization of wastes based on inorganic double salt hydrates as potential thermal energy storage materials. Solar Energy Materials and Solar Cells, 170, 149-159, https://doi.org/10.1016/j.solmat.2017.05.036.

Haber, J., Sokolov, K., 2017. Synthesis of Stable Citrate-Capped Silver Nanoprisms. Langmuir, 33(40), 10525-10530, https://doi.org/10.1021/acs.langmuir.7b01362.

Hamdan, M.A., Rossides, S.D., Haj Khalil, R., 2013. Thermal energy storage using thermo-chemical heat pump. Energy Conversion and Management, 65, 721-724, https://doi.org/10.1016/j.enconman.2012.01.047.

Hamid, K.A., Azmi, W.H., Mamat, R., Usri, N.A., Najafi, G., 2015. Investigation of Al_2O_3 Nanofluid Viscosity for Different Water/EG Mixture Based. Energy Procedia, 79, 354-359, https://doi.org/10.1016/j.egypro.2015.11.502.

Han, W.S., Rhi, S.H., 2011. Thermal characteristics of grooved heat pipe with hybrid nanofluids. Thermal Science, 15(1), 195-206, https://doi.org/10.2298/tsci100209056h.

Hassan, M.I., Alzarooni, I.A., Shatilla, Y., 2015. The Effect of Water-Based Nanofluid Incorporating Al2O3 Nanoparticles on Heat Pipe Performance. Energy Procedia, 75, 3201-3206, https://doi.org/10.1016/j.egypro.2015.07.674.

Hawwash, A.A., Abdel Rahman, A.K., Nada, S.A., Ookawara, S., 2018. Numerical Investigation and Experimental Verification of Performance Enhancement of Flat Plate Solar Collector Using Nanofluids. Applied Thermal Engineering, 130, 363-374, https://doi.org/10.1016/j.applthermaleng.2017.11.027.

Hawwash, A.A., Hassan, H., Ahmed, M., Ookawara, S., El feky, K., 2017. Long-term Thermal Energy Storage Using Thermochemical Materials. Energy Procedia, 141, 310-314, https://doi.org/https://doi.org/10.1016/j.egypro.2017.11.111.

He, Y., Hu, Y., Li, H., 2019. An Ag@TiO_2/ethylene glycol/water solution as a nanofluid-based beam splitter for photovoltaic/thermal applications in cold regions. Energy Conversion and Management, 198, https://doi.org/10.1016/j.enconman.2019.111838.

Hesaraki, A., Holmberg, S., Haghighat, F., 2015. Seasonal thermal energy storage with heat pumps and low temperatures in building projects—A comparative review. Renewable and Sustainable Energy Reviews, 43, 1199-1213, https://doi.org/10.1016/j.rser.2014.12.002.

Hjerrild, N.E., Mesgari, S., Crisostomo, F., Scott, J.A., Amal, R., Taylor, R.A., 2016. Hybrid PV/T enhancement using selectively absorbing Ag–SiO_2/carbon nanofluids. Solar Energy Materials and Solar Cells, 147, 281-287, https://doi.org/10.1016/j.solmat.2015.12.010.

Hjerrild, N.E., Scott, J.A., Amal, R., Taylor, R.A., 2018. Exploring the effects of heat and UV exposure on glycerol-based Ag-SiO_2 nanofluids for PV/T applications. Renewable Energy, 120, 266-274, https://doi.org/10.1016/j.renene.2017.12.073.

Hoekstra, N., Pellegrini, M., Bloemendal, M., Spaak, G., Andreu Gallego, A., Rodriguez Comins, J., Grotenhuis, T., Picone, S., Murrell, A.J., Steeman, H.J., Verrone, A., Doornenbal, P., Christophersen, M., Bennedsen, L., Henssen, M., Moinier, S., Saccani, C., 2020. Increasing market opportunities for renewable energy technologies with innovations in aquifer thermal energy storage. Sci Total Environ, 709, 136142, https://doi.org/10.1016/j.scitotenv.2019.136142.

Holland, A., Kimpton, H., Cruden, A., Wills, R., 2018. CuHCF as an electrode material in an aqueous dual-ion Al^{3+}/K^{+} ion battery. Energy Procedia, 151, 69-73, https://doi.org/10.1016/j.egypro.2018.09.029.

Honnerova, P., Martan, J., Vesely, Z., Honner, M., 2017. Method for emissivity measurement of semitransparent coatings at ambient temperature. Sci Rep, 7(1), 1386, https://doi.org/10.1038/s41598-017-01574-x.

Hordy, N., Rabilloud, D., Meunier, J.-L., Coulombe, S., 2014. High temperature and long-term stability of carbon nanotube nanofluids for direct absorption solar thermal collectors. Solar Energy, 105, 82-90, https://doi.org/10.1016/j.solener.2014.03.013.

Huang, J., Han, X., Zhao, X., Meng, C., 2021. Facile preparation of core-shell Ag@SiO_2 nanoparticles and their application in spectrally splitting PV/T systems. Energy, 215, https://doi.org/10.1016/j.energy.2020.119111.

Hunter, R.J., 1981. Zeta Potential in Colloid Science, Principles and Applications. Academic Press.

Ibrahim, H., Ilinca, A., Perron, J., 2008. Energy storage systems—Characteristics and comparisons. Renewable and Sustainable Energy Reviews, 12(5), 1221-1250, https://doi.org/10.1016/j.rser.2007.01.023.

Ibrahim, N.I., Al-Sulaiman, F.A., Ani, F.N., 2018. Solar absorption systems with integrated absorption energy storage–A review. Renewable and Sustainable Energy Reviews, 82, 1602-1610, https://doi.org/10.1016/j.rser.2017.07.005.

International Energy Agency, 2014. Technology Roadmap, Energy Storage. OECD International Energy Agency, France, https://iea.blob.core.windows.net/assets/80b629ee-597b-4f79-a236-3b9a36aedbe7/TechnologyRoadmapEnergystorage.pdf. (Accessed December 2021).

International Energy Agency, 2020a. Heating. https://www.iea.org/fuels-and-technologies/heating. (Accessed 18 March 2020).

International Energy Agency, 2020b. Solar Update Newsletter, Volume 72. International Energy Agency Solar Heating and Cooling Programme, https://www.iea-shc.org/Data/Sites/1/publications/IEA_SHC_Solar_Update_Newsletter-Issue72-December_2020.pdf. (Accessed December 2021).

International Energy Agency, 2021. Net Zero by 2050 A Roadmap for the Global Energy Sector (4th revision). International Energy Agency, France, https://iea.blob.core.windows.net/assets/deebef5d-0c34-4539-9d0c-10b13d840027/NetZeroby2050-ARoadmapfortheGlobalEnergySector_CORR.pdf. (Accessed 18 November 2021).

International Renewable Energy Agency (IRENA), 2013. Technology Brief E17 Thermal Energy Storage. International Energy Agency IRENA and ETSAP,

https://www.irena.org/publications/2013/Jan/Thermal-energy-storage. (Accessed December 2021).

Iyahraja, S., Rajadurai, J.S., 2015. Study of thermal conductivity enhancement of aqueous suspensions containing silver nanoparticles. AIP Advances, 5(5), 057103, https://doi.org/10.1063/1.4919808.

Jeon, J., Park, S., Lee, B.J., 2014. Optical property of blended plasmonic nanofluid based on gold nanorods. Opt Express, 22 Suppl 4, A1101-1111, https://doi.org/10.1364/OE.22.0A1101.

Jeon, J., Park, S., Lee, B.J., 2016. Analysis on the performance of a flat-plate volumetric solar collector using blended plasmonic nanofluid. Solar Energy, 132, 247-256, https://doi.org/10.1016/j.solener.2016.03.022.

Jin, H., Lin, G., Bai, L., Amjad, M., Bandarra Filho, E.P., Wen, D., 2016. Photothermal conversion efficiency of nanofluids: An experimental and numerical study. Solar Energy, 139, 278-289, https://doi.org/10.1016/j.solener.2016.09.021.

Jin, R., Cao, C., Hao, E., Metraux, G.S., Schalz, G., Mirkin, C.A., 2003. Controlling anisotropic nanoparticle growth through plasmon excitation. Nature, 425(6957), 487-490, https://doi.org/10.1038/nature02014.

Jin, R., Cao, Y., Mirkin, C.A., Kelly, K., Schalz, G., Zheng, J., 2001. Photoinduced Coversion of Silver Nanospheres to Nanoprisms. Science, 294, 1901-1904, https://doi.org/https://doi.org/10.1126/science.1066541.

Jorgenson, J., Mehos, M., Denholm, P., 2016. Comparing the net cost of CSP-TES to PV deployed with battery storage. 1734, 080003, https://doi.org/10.1063/1.4949183.

Kakaç, S., Pramuanjaroenkij, A., 2009. Review of convective heat transfer enhancement with nanofluids. International Journal of Heat and Mass Transfer, 52(13-14), 3187-3196, https://doi.org/10.1016/j.ijheatmasstransfer.2009.02.006.

Kang, J., Li, Y., Chen, Y., Wang, A., Yue, B., Qu, Y., Zhao, Y., Chu, H., 2015. Core–shell Ag@SiO_2 nanoparticles of different silica shell thicknesses: Preparation and their effects on photoluminescence of lanthanide complexes. Materials Research Bulletin, 71, 116-121, https://doi.org/10.1016/j.materresbull.2015.07.017.

Karami, M., Akhavan-Bahabadi, M.A., Delfani, S., Raisee, M., 2015. Experimental investigation of CuO nanofluid-based Direct Absorption Solar Collector for residential applications. Renewable and Sustainable Energy Reviews, 52, 793-801, https://doi.org/10.1016/j.rser.2015.07.131.

Kaygusuz, K., Ayhan, T., 1999. Experimental and theoretical investigation of combined solar heat pump system for residential heating. Energy Conversion and Management, 40, 1377-1396, https://doi.org/https://doi.org/10.1016/S0196-8904(99)00026-6.

Kazemi-Beydokhti, A., Heris, S.Z., Moghadam, N., Shariati-Niasar, M., Hamidi, A.A., 2014. Experimental Investigation of Parameters Affecting Nanofluid Effective Thermal Conductivity. Chemical Engineering Communications, 201(5), 593-611, https://doi.org/10.1080/00986445.2013.782291.

Kelly, K., Coronado, E., Zhao, L., Schatz, G., 2003. The Optical Properties of Metal Nanoparticles: The Influence of SIze, Shape, and Dielectric Environment. Journal of Physical Chemistry B, 107, 668-677, https://doi.org/10.1021/jp026731y.

Khlebtsov, B.N., Khlebtsov, N.G., 2011. On the measurement of gold nanoparticle sizes by the dynamic light scattering method. Colloid Journal, 73(1), 118-127, https://doi.org/10.1134/s1061933x11010078.

Khullar, V., Tyagi, H., Hordy, N., Otanicar, T.P., Hewakuruppu, Y., Modi, P., Taylor, R.A., 2014. Harvesting solar thermal energy through nanofluid-based volumetric absorption systems. International Journal of Heat and Mass Transfer, 77, 377-384, https://doi.org/10.1016/j.ijheatmasstransfer.2014.05.023.

Kim, D., Jeong, S., Moon, J., 2006. Synthesis of silver nanoparticles using the polyol process and the influence of precursor injection. Nanotechnology, 17(16), 4019-4024, https://doi.org/10.1088/0957-4484/17/16/004.

Kimpton, H., Cristaldi, D.A., Stulz, E., Zhang, X., 2020a. Thermal performance and physicochemical stability of silver nanoprism-based nanofluids for direct solar absorption. Solar Energy, 199, 366-376, https://doi.org/10.1016/j.solener.2020.02.039.

Kimpton, H., Stulz, E., Zhang, X., 2020b. Silver nanofluids based broadband solar absorber through tuning nanosilver geometries. Solar Energy, 208, 515-526, https://doi.org/10.1016/j.solener.2020.08.018.

Kimpton, H., Zhang, X., Stulz, E., 2020c. Decarbonising heating and hot water using solar thermal collectors coupled with thermal storage: The scale of the challenge. Energy Reports, 6, 25-34, https://doi.org/10.1016/j.egyr.2020.02.024.

Kimpton, H., Zhang, X., Stulz, E., 2021. The temperature stability and development of a broadband silver nanofluid for solar thermal applications. Energy Reports, 7, 87-96, https://doi.org/10.1016/j.egyr.2021.02.049.

Kittler, S., Greulich, C., Diendorf, J., Köller, M., Epple, M., 2010. Toxicity of Silver Nanoparticles Increases during Storage Because of Slow Dissolution under Release of Silver Ions. Chemistry of Materials, 22(16), 4548-4554, https://doi.org/10.1021/cm100023p.

Kiyabu, S., Lowe, J.S., Ahmed, A., Siegel, D.J., 2018. Computational Screening of Hydration Reactions for Thermal Energy Storage: New Materials and Design Rules. Chemistry of Materials, 30(6), 2006-2017, https://doi.org/10.1021/acs.chemmater.7b05230.

Knoll, C., Müller, D., Artner, W., Welch, J.M., Werner, A., Harasek, M., Weinberger, P., 2017. Probing cycle stability and reversibility in thermochemical energy storage – $CaC_2O_4{\cdot}H_2O$ as perfect match? Applied Energy, 187, 1-9, https://doi.org/10.1016/j.apenergy.2016.11.053.

Kuang, Y.H., Wang, R.Z., Yu, L.Q., 2003. Experimental study on solar assisted heat pump system for heat supply. Energy Conversion and Management, 44, 1089-1098, https://doi.org/https://doi.org/10.1016/S0196-8904(02)00110-3.

Kumar, S., Chander, N., Gupta, V.K., Kukreja, R., 2021. Progress, challenges and future prospects of plasmonic nanofluid based direct absorption solar collectors - A state-of-the-art review. Solar Energy, 227, 365-425, https://doi.org/10.1016/j.solener.2021.09.008.

Kumar, S.S., Kumar, K.M., Kumar, S.R.S., 2017. Design of Evacuated Tube Solar Collector with Heat Pipe. Materials Today: Proceedings, 4(14), 12641-12646, https://doi.org/10.1016/j.matpr.2017.10.075.

Ledwith, D.M., Whelan, A.M., Kelly, J.M., 2007. A rapid, straight-forward method for controlling the morphology of stable silver nanoparticles. Journal of Materials Chemistry, 17(23), 2459, https://doi.org/10.1039/b702141k.

Lee, S.Y., Jin, S.H., Kim, S.M., Kim, J.W., 2016. Solution plasma process to synthesize silver nanofluids and their thermal conductivity behaviors. Metals and Materials International, 20(4), 695-699, https://doi.org/10.1007/s12540-014-4014-1.

Lele, A., 2016. Chapter 2: State-of-Art of Thermochemical Storage Systems. Springer International Publishing, Switzerland.

Lewis, N.S., 2007. Toward Cost-Effective Solar Energy Use. Science, 315(5813), 798-801, https://doi.org/https://doi.org/10.1126/science.1137014.

Li, D., Fang, W., Feng, Y., Geng, Q., Song, M., 2019. Stability properties of water-based gold and silver nanofluids stabilized by cationic gemini surfactants. Journal of the Taiwan Institute of Chemical Engineers, 97, 458-465, https://doi.org/10.1016/j.jtice.2019.02.017.

Li, H., He, Y., Liu, Z., Huang, Y., Jiang, B., 2017. Synchronous steam generation and heat collection in a broadband Ag@TiO_2 core–shell nanoparticle-based receiver. Applied Thermal Engineering, 121, 617-627, https://doi.org/10.1016/j.applthermaleng.2017.04.102.

Li, Q., Zheng, C., Mesgari, S., Hewkuruppu, Y.L., Hjerrild, N., Crisostomo, F., Rosengarten, G., Scott, J.A., Taylor, R.A., 2016. Experimental and numerical investigation of volumetric versus surface solar absorbers for a concentrated solar thermal collector. Solar Energy, 136, 349-364, https://doi.org/10.1016/j.solener.2016.07.015.

Li, X., Chen, W., Zou, C., 2020. An experimental study on β-cyclodextrin modified carbon nanotubes nanofluids for the direct absorption solar collector (DASC): Specific heat capacity and photo-thermal conversion performance. Solar Energy Materials and Solar Cells, 204, https://doi.org/10.1016/j.solmat.2019.110240.

Linnow, K., Niermann, M., Bonatz, D., Posern, K., Steiger, M., 2014. Experimental Studies of the Mechanism and Kinetics of Hydration Reactions. Energy Procedia, 48, 394-404, https://doi.org/10.1016/j.egypro.2014.02.046.

Lismont, M., Paez, C.A., Dreesen, L., 2015. A one-step short-time synthesis of Ag@SiO_2 core-shell nanoparticles. J Colloid Interface Sci, 447, 40-49, https://doi.org/10.1016/j.jcis.2015.01.065.

Liu, C., Rao, Z., 2017. Challenges in various thermal energy storage technologies. Science Bulletin, 62(4), 231-233, https://doi.org/10.1016/j.scib.2017.01.019.

Liu, C., Zhang, L., He, Y., Yu, W., 2020. Enhancement of Photo-Thermal Conversion Performance of the Nanofluids Through Spectral Complementarity between Silver and Cesium Tungstate Oxide Nanoparticles. Journal of Thermal Science, 29(5), 1322-1332, https://doi.org/10.1007/s11630-020-1306-2.

Liu, G., Cao, H., Xu, J., 2018. Solar evaporation of a hanging plasmonic droplet. Solar Energy, 170, 184-191, https://doi.org/10.1016/j.solener.2018.05.069.

Liu, Z.-H., Hu, R.-L., Lu, L., Zhao, F., Xiao, H.-s., 2013. Thermal performance of an open thermosyphon using nanofluid for evacuated tubular high temperature air solar collector. Energy Conversion and Management, 73, 135-143, https://doi.org/10.1016/j.enconman.2013.04.010.

Lu, L., Liu, Z.-H., Xiao, H.-S., 2011. Thermal performance of an open thermosyphon using nanofluids for high-temperature evacuated tubular solar collectors. Solar Energy, 85(2), 379-387, https://doi.org/10.1016/j.solener.2010.11.008.

Luo, Z., Wang, C., Wei, W., Xiao, G., Ni, M., 2014. Performance improvement of a nanofluid solar collector based on direct absorption collection (DAC) concepts. International Journal of Heat and Mass Transfer, 75, 262-271, https://doi.org/10.1016/j.ijheatmasstransfer.2014.03.072.

MacKay, D., 2008. Sustainable Energy - without the hot air. UIT Cambridge.

Mahian, O., Kianifar, A., Kalogirou, S.A., Pop, I., Wongwises, S., 2013. A review of the applications of nanofluids in solar energy. International Journal of Heat and Mass Transfer, 57(2), 582-594, https://doi.org/10.1016/j.ijheatmasstransfer.2012.10.037.

Mallah, A.R., Kazi, S.N., Zubir, M.N.M., Badarudin, A., 2018. Blended morphologies of plasmonic nanofluids for direct absorption applications. Applied Energy, 229, 505-521, https://doi.org/10.1016/j.apenergy.2018.07.113.

Mallah, A.R., Mohd Zubir, M.N., Alawi, O.A., Salim Newaz, K.M., Mohamad Badry, A.B., 2019. Plasmonic nanofluids for high photothermal conversion efficiency in direct absorption solar collectors: Fundamentals and applications. Solar Energy Materials and Solar Cells, 201, https://doi.org/10.1016/j.solmat.2019.110084.

Mamani, V., Gutiérrez, A., Ushak, S., 2018. Development of low-cost inorganic salt hydrate as a thermochemical energy storage material. Solar Energy Materials and Solar Cells, 176, 346-356, https://doi.org/10.1016/j.solmat.2017.10.021.

Mehrali, M., Ghatkesar, M.K., Pecnik, R., 2018. Full-spectrum volumetric solar thermal conversion via graphene/silver hybrid plasmonic nanofluids. Applied Energy, 224, 103-115, https://doi.org/10.1016/j.apenergy.2018.04.065.

Mehta, J.R., Rane, M.V., 2013. Liquid Desiccant based Solar Air Conditioning System with Novel Evacuated Tube Collector as Regenerator. Procedia Engineering, 51, 688-693, https://doi.org/10.1016/j.proeng.2013.01.098.

Mellor, A., Alonso Alvarez, D., Guarracino, I., Ramos, A., Riverola Lacasta, A., Ferre Llin, L., Murrell, A.J., Paul, D.J., Chemisana, D., Markides, C.N., Ekins-Daukes, N.J., 2018. Roadmap for the next-generation of hybrid photovoltaic-thermal solar energy collectors. Solar Energy, 174, 386-398, https://doi.org/10.1016/j.solener.2018.09.004.

Metraux, G.S., Mirkin, C.A., 2005. Rapid Thermal Synthesis of SIlver Nanoprisms with Chemically Tailorable Thickness. Advanced Materials, 17(4), 412-415, https://doi.org/10.1002/adma.200401086.

Milanese, M., Colangelo, G., Cretì, A., Lomascolo, M., Iacobazzi, F., de Risi, A., 2016a. Optical absorption measurements of oxide nanoparticles for application as nanofluid in direct absorption solar power systems – Part I: Water-based nanofluids behavior. Solar Energy Materials and Solar Cells, 147, 315-320, https://doi.org/10.1016/j.solmat.2015.12.027.

Milanese, M., Colangelo, G., Cretì, A., Lomascolo, M., Iacobazzi, F., de Risi, A., 2016b. Optical absorption measurements of oxide nanoparticles for application as nanofluid in direct absorption solar power systems – Part II: ZnO, CeO_2 , Fe_2O_3 nanoparticles behavior. Solar Energy Materials and Solar Cells, 147, 321-326, https://doi.org/10.1016/j.solmat.2015.12.030.

Minardi, J.E., Chuang, H.N., 1975. Performance of a "black" liquid flat-plate solar collector. Solar Energy, 17(3), 179-183, https://doi.org/https://doi.org/10.1016/0038-092X(75)90057-2.

Mirzaei, A., Janghorban, K., Hashemi, B., Bonyani, M., Leonardi, S.G., Neri, G., 2016. Characterization and optical studies of PVP-capped silver nanoparticles. Journal of Nanostructure in Chemistry, 7(1), 37-46, https://doi.org/10.1007/s40097-016-0212-3.

Modest, M., 2003. Radiative Heat transfer, 2nd Edition ed. Academic press, USA.

Moreira, L.M., Carvalho, E.A., Bell, M.J.V., Anjos, V., Sant'Ana, A.C., Alves, A.P.P., Fragneaud, B., Sena, L.A., Archanjo, B.S., Achete, C.A., 2013. Thermo-optical properties of silver and gold

nanofluids. Journal of Thermal Analysis and Calorimetry, 114(2), 557-564, https://doi.org/10.1007/s10973-013-3021-7.

Muhammad, M.J., Muhammad, I.A., Sidik, N.A.C., Yazid, M.N.A.W.M., Mamat, R., Najafi, G., 2016. The use of nanofluids for enhancing the thermal performance of stationary solar collectors: A review. Renewable and Sustainable Energy Reviews, 63, 226-236, https://doi.org/10.1016/j.rser.2016.05.063.

Murshed, S.M.S., Leong, K.C., Yang, C., 2008. Investigations of thermal conductivity and viscosity of nanofluids. International Journal of Thermal Sciences, 47(5), 560-568, https://doi.org/10.1016/j.ijthermalsci.2007.05.004.

Murshed, S.M.S., Nieto de Castro, C.A., Lourenço, M.J.V., Lopes, M.L.M., Santos, F.J.V., 2011. A review of boiling and convective heat transfer with nanofluids. Renewable and Sustainable Energy Reviews, 15(5), 2342-2354, https://doi.org/10.1016/j.rser.2011.02.016.

N'Tsoukpoe, K.E., Mazet, N., Neveu, P., 2016. The concept of cascade thermochemical storage based on multimaterial system for household applications. Energy and Buildings, 129, 138-149, https://doi.org/10.1016/j.enbuild.2016.07.047.

N'Tsoukpoe, K.E., Schmidt, T., Rammelberg, H.U., Watts, B.A., Ruck, W.K.L., 2014. A systematic multi-step screening of numerous salt hydrates for low temperature thermochemical energy storage. Applied Energy, 124, 1-16, https://doi.org/10.1016/j.apenergy.2014.02.053.

Nasrin, R., Alim, M.A., 2014. Finite Element Simulation of Forced Convection in a Flat Plate Solar Collector: Influence of Nanofluid with Double Nanoparticles. Journal of Applied Fluid Mechanics, 7(3), 543-556, https://doi.org/https://doi.org/10.36884/jafm.7.03.21416.

Nasrin, R., Parvin, S., Alim, M.A., 2015. Heat Transfer and Collector Efficiency through a Direct Absorption Solar Collector with Radiative Heat Flux Effect. Numerical Heat Transfer, Part A: Applications, 68(8), 887-907, https://doi.org/10.1080/10407782.2015.1023122.

Noghrehabadi, A., Hajidavaloo, E., Moravej, M., 2016. Experimental investigation of efficiency of square flat-plate solar collector using SiO_2 /water nanofluid. Case Studies in Thermal Engineering, 8, 378-386, https://doi.org/10.1016/j.csite.2016.08.006.

Oliveira, L.R.d., Ribeiro, S.R.F.L., Reis, M.H.M., Cardoso, V.L., Bandarra Filho, E.P., 2019. Experimental study on the thermal conductivity and viscosity of ethylene glycol-based nanofluid containing diamond-silver hybrid material. Diamond and Related Materials, 96, 216-230, https://doi.org/10.1016/j.diamond.2019.05.004.

Otanicar, T., Hoyt, J., Fahar, M., Jiang, X., Taylor, R.A., 2013. Experimental and numerical study on the optical properties and agglomeration of nanoparticle suspensions. Journal of Nanoparticle Research, 15(11), https://doi.org/10.1007/s11051-013-2039-x.

Otanicar, T.P., Golden, J.S., 2009. Comparative Environmental and Economic Analysis of Conventional and Nanofluid Solar Hot Water Technologies. Environ Sci Technol, 43, 6032-6037, https://doi.org/https://doi.org/10.1021/es900031j.

Otanicar, T.P., Phelan, P.E., Golden, J.S., 2009. Optical properties of liquids for direct absorption solar thermal energy systems. Solar Energy, 83(7), 969-977, https://doi.org/10.1016/j.solener.2008.12.009.

Otanicar, T.P., Phelan, P.E., Prasher, R.S., Rosengarten, G., Taylor, R.A., 2010. Nanofluid-based direct absorption solar collector. Journal of Renewable and Sustainable Energy, 2(3), 033102, https://doi.org/10.1063/1.3429737.

Otanicar, T.P., Phelan, P.E., Taylor, R.A., Tyagi, H., 2011. Spatially Varying Extinction Coefficient for Direct Absorption Solar Thermal Collector Optimization. Journal of Solar Energy Engineering, 133(2), 024501, https://doi.org/10.1115/1.4003679.

Otari, S.V., Yadav, H.M., Thorat, N.D., Patil, R.M., Lee, J.K., Pawar, S.H., 2016. Facile one pot synthesis of core shell Ag@SiO_2 nanoparticles for catalytic and antimicrobial activity. Materials Letters, 167, 179-182, https://doi.org/10.1016/j.matlet.2015.12.134.

Ozsoy, A., Corumlu, V., 2018. Thermal performance of a thermosyphon heat pipe evacuated tube solar collector using silver-water nanofluid for commercial applications. Renewable Energy, 122, 26-34, https://doi.org/10.1016/j.renene.2018.01.031.

Panzarasa, G., 2015. Just What Is It That Makes Silver Nanoprisms so Different, so Appealing? Journal of Chemical Education, 92(11), 1918-1923, https://doi.org/10.1021/acs.jchemed.5b00320.

Paramelle, D., Sadovoy, A., Gorelik, S., Free, P., Hobley, J., Fernig, D.G., 2014a. A rapid method to estimate the concentration of citrate capped silver nanoparticles from UV-visible light spectra. Analyst, 139(19), 4855-4861, https://doi.org/10.1039/c4an00978a.

Paramelle, D., Sadovoy, A., Gorelik, S., Free, P., Hobley, J., Fernig, D.G., 2014b. Supplementary Information: Rapid method to estimate the concentration of citrate capped silver nanoparticles from UV - visible light spectra. Electronic Supplementary material (ESI) for Analyst, 139, 4855-4861, https://doi.org/https://doi.org/10.1039/c4an00978a.

Park, K.H., Im, S.H., Park, O.O., 2011. The size control of silver nanocrystals with different polyols and its application to low-reflection coating materials. Nanotechnology, 22(4), 045602, https://doi.org/10.1088/0957-4484/22/4/045602.

Pashley, R.M., Karaman, M.E., 2004. Applied Colloids and Surface Chemistry. John Wiley & Sons, Ltd, England.

Pathak, A.D., Nedea, S.V., Zondag, H.A., Rindt, C.C.M., Smeulders, D.M.J., 2016. A DFT based equilibrium study of a chemical mixture Tachyhydrite and their lower hydrates for long term heat storage. Journal of Physics: Conference Series, 745, 032003, https://doi.org/10.1088/1742-6596/745/3/032003.

Pathak, A.D., Tranca, I., Nedea, S.V., Zondag, H.A., Rindt, C.C.M., Smeulders, D.M.J., 2017. First-Principles Study of Chemical Mixtures of $CaCl_2$ and $MgCl_2$ Hydrates for Optimized Seasonal Heat Storage. J Phys Chem C Nanomater Interfaces, 121(38), 20576-20590, https://doi.org/10.1021/acs.jpcc.7b05245.

Pellegrini, M., Bloemendal, M., Hoekstra, N., Spaak, G., Andreu Gallego, A., Rodriguez Comins, J., Grotenhuis, T., Picone, S., Murrell, A.J., Steeman, H.J., 2019. Low carbon heating and cooling by combining various technologies with Aquifer Thermal Energy Storage. Sci Total Environ, 665, 1-10, https://doi.org/10.1016/j.scitotenv.2019.01.135.

Polte, J., 2015. Fundamental growth principles of colloidal metal nanoparticles – a new perspective. CrystEngComm, 17(36), 6809-6830, https://doi.org/10.1039/c5ce01014d.

Polvongsri, S., Kiatsiriroat, T., 2014. Performance Analysis of Flat-Plate Solar Collector Having Silver Nanofluid as a Working Fluid. Heat Transfer Engineering, 35(13), 1183-1191, https://doi.org/10.1080/01457632.2013.870003.

Posern, K., Kaps, C., 2010. Calorimetric studies of thermochemical heat storage materials based on mixtures of $MgSO_4$ and $MgCl_2$. Thermochimica Acta, 502(1-2), 73-76, https://doi.org/10.1016/j.tca.2010.02.009.

Posern, K., Osburg, A., 2017. Determination of the heat storage performance of thermochemical heat storage materials based on $SrCl_2$ and $MgSO_4$. Journal of Thermal Analysis and Calorimetry, 131(3), 2769-2773, https://doi.org/10.1007/s10973-017-6861-8.

Prieto, C., Cooper, P., Fernández, A.I., Cabeza, L.F., 2016. Review of technology: Thermochemical energy storage for concentrated solar power plants. Renewable and Sustainable Energy Reviews, 60, 909-929, https://doi.org/10.1016/j.rser.2015.12.364.

Rad, F.M., Fung, A.S., 2016. Solar community heating and cooling system with borehole thermal energy storage – Review of systems. Renewable and Sustainable Energy Reviews, 60, 1550-1561, https://doi.org/10.1016/j.rser.2016.03.025.

Radloff, C., Halas, N.J., 2001. Enhanced thermal stability of silica-encapsulated metal nanoshells. Applied Physics Letters, 79(5), 674-676, https://doi.org/10.1063/1.1389322.

Rammelberg, H.U., Myrau, M., Schmidt, T., Ruck, W.K.L., 2013. An Optimization of Salt Hydrates for Thermochemical Heat Storage, Innovative Materials for Processes in Energy Systems. Fukuaka, Japan, pp. 550-555.

Rammelberg, H.U., Osterland, T., Priehs, B., Opel, O., Ruck, W.K.L., 2016. Thermochemical heat storage materials – Performance of mixed salt hydrates. Solar Energy, 136, 571-589, https://doi.org/10.1016/j.solener.2016.07.016.

Ranga Babu, J.A., Kumar, K.K., Srinivasa Rao, S., 2017. State-of-art review on hybrid nanofluids. Renewable and Sustainable Energy Reviews, 77, 551-565, https://doi.org/10.1016/j.rser.2017.04.040.

Reddy, K.S., Mudgal, V., Mallick, T.K., 2018. Review of Latent Heat Thermal Energy Storage for Improved Material Stability and Effective Load Management. Journal of Energy Storage, 15, 205-227, https://doi.org/10.1016/j.est.2017.11.005.

Romero, I., 2013. An Experimental Investigation of an Electrical Storage Heater in the Context of Storage Technologies. University of Strathclyde.

Rosenow, J., Guertler, P., Sorrell, S., Eyre, N., 2018. The remaining potential for energy savings in UK households. Energy Policy, 121, 542-552, https://doi.org/10.1016/j.enpol.2018.06.033.

Roy, S., Asirvatham, L., Kunhappan, D., Cephas, E., Wongwises, S., 2015. Heat Transfer Performance of Silver/Water Nanofluid in a Solar Flat-Plate Collector. Journal of Thermal Engineering, 1(2), 104-112, https://doi.org/https://doi.org/10.18186/jte.29475.

Salehi, J.M., Heyhat, M.M., Rajabpour, A., 2013. Enhancement of thermal conductivity of silver nanofluid synthesized by a one-step method with the effect of polyvinylpyrrolidone on thermal behavior. Applied Physics Letters, 102(23), 231907, https://doi.org/10.1063/1.4809998.

Sani, E., Ninni, P.D., Colla, L., Barison, S., Agresti, F., 2015. Optical properties of mixed nanofluids containing carbon nanohorns and silver nanoparticles for solar energy applications. Journal of Nanoscience and Nanotechnology, 15, 3568-3573, https://doi.org/10.1166/jnn.2015.9838.

Sansom, R., 2012. The Impact of Future Heat Demand Pathways on the Economics of Low Carbon Heating Systems, BIEE- 9th Academic Conference. Oxford, UK.

Sarathkumar, P., Sivaram, A.R., Rajavel, R., Praveen Kumar, R., Krishnakumar, S.K., 2017. Experimental Investigations on The Performance of A Solar Pond by using Encapsulated Pcm with Nanoparticles. Materials Today: Proceedings, 4(2), 2314-2322, https://doi.org/10.1016/j.matpr.2017.02.080.

Sarsam, W.S., Amiri, A., Shanbedi, M., Kazi, S.N., Badarudin, A., Yarmand, H., Bashirnezhad, K., Zaharinie, T., 2017. Synthesis, stability, and thermophysical properties of aqueous colloidal dispersions of multi-walled carbon nanotubes treated with beta-alanine. International Communications in Heat and Mass Transfer, 89, 7-17, https://doi.org/10.1016/j.icheatmasstransfer.2017.09.006.

Scapino, L., Zondag, H.A., Van Bael, J., Diriken, J., Rindt, C.C.M., 2017a. Energy density and storage capacity cost comparison of conceptual solid and liquid sorption seasonal heat storage systems for low-temperature space heating. Renewable and Sustainable Energy Reviews, 76, 1314-1331, https://doi.org/10.1016/j.rser.2017.03.101.

Scapino, L., Zondag, H.A., Van Bael, J., Diriken, J., Rindt, C.C.M., 2017b. Sorption heat storage for long-term low-temperature applications: A review on the advancements at material and prototype scale. Applied Energy, 190, 920-948, https://doi.org/10.1016/j.apenergy.2016.12.148.

Selvakumar, N., Barshilia, H.C., Rajam, K.S., 2010. Review of sputter deposited mid- to high-temperature solar selective coatings for flat plat/evacuated tube collectors and solar thermal power generation applications. Bangalore, India, https://www.researchgate.net/publication/277327602_Review_of_sputter_deposited_mid-_to_high-_temperature_solar_selective_coatings_for_Flat_PlateEvacuated_tube_collectors_and_solar_thermal_power_generation_applications. (Accessed December 2021).

Shafieian, A., Khiadani, M., Nosrati, A., 2019. Thermal performance of an evacuated tube heat pipe solar water heating system in cold season. Applied Thermal Engineering, 149, 644-657, https://doi.org/10.1016/j.applthermaleng.2018.12.078.

Sharaf, O.Z., Rizk, N., Joshi, C.P., Abi Jaoudé, M., Al-Khateeb, A.N., Kyritsis, D.C., Abu-Nada, E., Martin, M.N., 2019. Ultrastable plasmonic nanofluids in optimized direct absorption solar collectors. Energy Conversion and Management, 199, https://doi.org/10.1016/j.enconman.2019.112010.

Sharafeldin, M.A., Gróf, G., 2018. Experimental investigation of flat plate solar collector using CeO_2 -water nanofluid. Energy Conversion and Management, 155, 32-41, https://doi.org/10.1016/j.enconman.2017.10.070.

Sharafeldin, M.A., Gróf, G., Mahian, O., 2017. Experimental study on the performance of a flat-plate collector using WO_3 /Water nanofluids. Energy, 141, 2436-2444, https://doi.org/10.1016/j.energy.2017.11.068.

Sharma, P., Baek, I.-H., Cho, T., Park, S., Lee, K.B., 2011. Enhancement of thermal conductivity of ethylene glycol based silver nanofluids. Powder Technology, 208(1), 7-19, https://doi.org/10.1016/j.powtec.2010.11.016.

Sheffield Hallam University, 2019. Beer's Law. https://teaching.shu.ac.uk/hwb/chemistry/tutorials/molspec/beers1.htm. (Accessed 09 October 2019).

Shkatulov, A., Aristov, Y., 2015. Modification of magnesium and calcium hydroxides with salts: An efficient way to advanced materials for storage of middle-temperature heat. Energy, 85, 667-676, https://doi.org/10.1016/j.energy.2015.04.004.

Shkatulov, A., Krieger, T., Zaikovskii, V., Chesalov, Y., Aristov, Y., 2014. Doping magnesium hydroxide with sodium nitrate: a new approach to tune the dehydration reactivity of heat-storage materials. ACS Appl Mater Interfaces, 6(22), 19966-19977, https://doi.org/10.1021/am505418z.

Shukla, D.L., Modi, K.V., 2017. A technical review on regeneration of liquid desiccant using solar energy. Renewable and Sustainable Energy Reviews, 78, 517-529, https://doi.org/10.1016/j.rser.2017.04.103.

Sibbitt, B., McClenahan, D., Djebbar, R., Paget, K., 2015. Case Study Drake Landing Solar Community, Groundbreaking Solar. https://www.dlsc.ca/reports/JUL2015/Goundbreaking_Solar_Case_Study.pdf. (Accessed December 2021).

Sibbitt, B., McClenahan, D., Djebbar, R., Thornton, J., Wong, B., Carriere, J., Kokko, J., 2012. The Performance of a High Solar Fraction Seasonal Storage District Heating System – Five Years of Operation. Energy Procedia, 30, 856-865, https://doi.org/10.1016/j.egypro.2012.11.097.

Silvert, P.-Y., Herrera-Urbina, R., Duvauchelle, N., Vijayakrishnan, V., Tekaia-Elhsissen, K., 1996. Preparation of colloidal silver dispersions by the polyol process Part 1 - Synthesis and characterization. Journal of Materials Chemistry, 6(4), 573-577, https://doi.org/10.1039/JM9960600573.

Silvert, P.-Y., Herrera-Urbina, R., Tekaia-Elhsissen, K., 1997. Preparation of colloidal silver dispersions by the polyol process Part 2 - Mechanism of particle formation. Journal of Materials Chemistry, 7(2), 293-299, https://doi.org/10.1039/A605347E.

Simic, M., George, J., 2017. Design of a System to Monitor and Control Solar Pond: A Review. Energy Procedia, 110, 322-327, https://doi.org/10.1016/j.egypro.2017.03.147.

Singh, N., Khullar, V., 2019. Efficient Volumetric Absorption Solar Thermal Platforms Employing Thermally Stable - Solar Selective Nanofluids Engineered from Used Engine Oil. Sci Rep, 9(1), 10541, https://doi.org/10.1038/s41598-019-47126-3.

Sögütoglu, L.C., Donkers, P.A.J., Fischer, H.R., Huinink, H.P., Adan, O.C.G., 2018. In-depth investigation of thermochemical performance in a heat battery: Cyclic analysis of K_2CO_3 , $MgCl_2$ and Na_2S. Applied Energy, 215, 159-173, https://doi.org/10.1016/j.apenergy.2018.01.083.

Solar Ratings and Certification Corporation, 2020. Solar Ratings and Certification summary page. https://secure.solar-rating.org/Certification/Ratings/RatingsSummaryPage.aspx. (Accessed 19 March 2020).

SPECIFIC, 2021. Solar Heat Storage: Eliminating Gas Heating. https://www.specific.eu.com/assets/downloads/casestudy/Solar_Heat_Storage_FINAL.pdf. (Accessed 22 November 2021).

Spyridonos, A.V., Argiriou, A.A., Nickoletatos, J.K., 2003. Thermal storage efficiencies of two solar saltless water ponds. Solar Energy, 75(3), 207-216, https://doi.org/10.1016/j.solener.2003.08.003.

Sreekumar, S., Joseph, A., Sujith Kumar, C.S., Thomas, S., 2020. Investigation on influence of antimony tin oxide/silver nanofluid on direct absorption parabolic solar collector. Journal of Cleaner Production, 249, https://doi.org/10.1016/j.jclepro.2019.119378.

Sreekumar, S., Shah, N., Mondol, J.D., Hewitt, N., Chakrabarti, S., 2022. Broadband absorbing mono, blended and hybrid nanofluids for direct absorption solar collector: a comprehensive review. Nano Futures, 6(2), https://doi.org/10.1088/2399-1984/ac57f7.

Stamplecoskie, K.G., Scaiano, J.C., 2010. Light Emitting Diode Irradiation Can Control the Morphology and Optical Properties of Silver Nanoparticles. Journal of the American Chemical Society - Communications, 132, 1825-1827, https://doi.org/https://doi.org/10.1021/ja910010b.

Statista, 2022. Lithium-ion Battery pack Costs Worldwide between 2011 and 2030. https://www.statista.com/statistics/883118/global-lithium-ion-battery-pack-costs/. (Accessed 23 May 2022).

Steiger, M., 2018. Thermodynamic properties of $SrCl_2$ (aq) from 252 K to 524 K and phase equilibria in the $SrCl_2$ –H_2O system: Implications for thermochemical heat storage. The Journal of Chemical Thermodynamics, 120, 106-115, https://doi.org/10.1016/j.jct.2018.01.017.

Sutton, R., Jewell, E., Searle, J., Elvins, J., 2018. Discharge performance of blended salt in matrix materials for low enthalpy thermochemical storage. Applied Thermal Engineering, 145, 483-493, https://doi.org/10.1016/j.applthermaleng.2018.09.052.

Tam, N.T., Van Trinh, P., Anh, N.N., Hong, N.T., Hong, P.N., Minh, P.N., Thang, B.H., 2018. Thermal Conductivity and Photothermal Conversion Performance of Ethylene Glycol-Based Nanofluids Containing Multiwalled Carbon Nanotubes. Journal of Nanomaterials, 2018, 1-8, https://doi.org/10.1155/2018/2750168.

Tang, B., Sun, L., Li, J., Zhang, M., Wang, X., 2015. Sunlight-driven synthesis of anisotropic silver nanoparticles. Chemical Engineering Journal, 260, 99-106, https://doi.org/10.1016/j.cej.2014.08.044.

Tang, B., Xu, S., Hou, X., Li, J., Sun, L., Xu, W., Wang, X., 2013. Shape evolution of silver nanoplates through heating and photoinduction. ACS Appl Mater Interfaces, 5(3), 646-653, https://doi.org/10.1021/am302072u.

TATA Steel, 2021. Active Solar Air Heating, Unglazed Transpired Solar Collector. https://www.tatasteeleurope.com/construction/products/renewables/active-solar-air-heating/unglazed-transpired-solar-collector. (Accessed 22 November 2021).

Tawfik, M.M., 2017. Experimental studies of nanofluid thermal conductivity enhancement and applications: A review. Renewable and Sustainable Energy Reviews, 75, 1239-1253, https://doi.org/10.1016/j.rser.2016.11.111.

Taylor, B.N., Kuyatt, C.E., 1994. NIST Technical Note 1297 - Guidelines for Evaluating and Expressing the Uncertainty of NIST Measurement Results. NIST, https://nvlpubs.nist.gov/nistpubs/Legacy/TN/nbstechnicalnote1297.pdf. (Accessed 25 February 2021).

Taylor, R., Coulombe, S., Otanicar, T., Phelan, P., Gunawan, A., Lv, W., Rosengarten, G., Prasher, R., Tyagi, H., 2013. Small particles, big impacts: A review of the diverse applications of nanofluids. Journal of Applied Physics, 113(1), 011301, https://doi.org/10.1063/1.4754271.

Taylor, R.A., Hjerrild, N., Duhaini, N., Pickford, M., Mesgari, S., 2018. Stability testing of silver nanodisc suspensions for solar applications. Applied Surface Science, 455, 465-475, https://doi.org/10.1016/j.apsusc.2018.05.201.

The Renewable Energy Hub, 2021. A Complete Guide to Heat Pumps in 2021. https://www.renewableenergyhub.co.uk/main/heat-pumps-information/. (Accessed 04 January 2022).

Tian, Y., Zhao, C.Y., 2013. A review of solar collectors and thermal energy storage in solar thermal applications. Applied Energy, 104, 538-553, https://doi.org/10.1016/j.apenergy.2012.11.051.

Tiwari, A., Uzun, L., 2015. Carbon-Based Hybrid Composites as Advanced Electrodes for Supercapacitors, Advanced Functional Materials. Wiley, 399-432.

Torres, V., Popa, M., Crespo, D., Calderón Moreno, J.M., 2007. Silver nanoprism coatings on optical glass substrates. Microelectronic Engineering, 84(5-8), 1665-1668, https://doi.org/10.1016/j.mee.2007.01.262.

Trausel, F., de Jong, A.-J., Cuypers, R., 2014. A Review on the Properties of Salt Hydrates for Thermochemical Storage. Energy Procedia, 48, 447-452, https://doi.org/10.1016/j.egypro.2014.02.053.

Tsuji, M., Gomi, S., Maeda, Y., Matsunaga, M., Hikino, S., Uto, K., Tsuji, T., Kawazumi, H., 2012. Rapid transformation from spherical nanoparticles, nanorods, cubes, or bipyramids to triangular prisms of silver with PVP, citrate, and H_2O_2. Langmuir, 28(24), 8845-8861, https://doi.org/10.1021/la3001027.

Turkyilmazoglu, M., 2016. Performance of direct absorption solar collector with nanofluid mixture. Energy Conversion and Management, 114, 1-10, https://doi.org/10.1016/j.enconman.2016.02.003.

Tyagi, H., Phelan, P., Prasher, R., 2009. Predicted Efficiency of a Low-Temperature Nanofluid-Based Direct Absorption Solar Collector. Journal of Solar Energy Engineering, 131(4), 041004, https://doi.org/10.1115/1.3197562.

UK Government, 2008. Climate Change Act 2008, Chapter 27. Her Majestry's Stationary Office and Queen's Printer of Acts of Parliament.

UK Government, 2021a. Heat and Buildings Strategy. Crown, UK, https://assets.publishing.service.gov.uk/government/uploads/system/uploads/attachment_data/file/1032119/heat-buildings-strategy.pdf. (Accessed 22 November 2021).

UK Government, 2021b. Net Zero Strategy: Build Back Greener. Crown, UK, https://assets.publishing.service.gov.uk/government/uploads/system/uploads/attachment_data/file/1028157/net-zero-strategy.pdf. (Accessed 02 November 2021).

Ulset, E.T., Kosinski, P., Balakin, B.V., 2018. Solar steam in an aqueous carbon black nanofluid. Applied Thermal Engineering, 137, 62-65, https://doi.org/10.1016/j.applthermaleng.2018.03.038.

Ung, T., Liz-Marzan, L., Mulvaney, P., 1998. Controlled Method for Silica Coating of Silver Colloids. Influence of Coating on the Rate of Chemical Reactions. Langmuir, 14, 3740-3748, https://doi.org/https://doi.org/10.1021/la980047m.

USP Technologies, 2021. H_2O_2 Equivalent Values of Concentration. https://www.h2o2.com/technical-library/physical-chemical-properties/physical-properties/default.aspx?pid=13&name=Equivalent-Values-of-Concentration. (Accessed 18 February 2021).

Vallejo, J.P., Sani, E., Żyła, G., Lugo, L., 2019. Tailored silver/graphene nanoplatelet hybrid nanofluids for solar applications. Journal of Molecular Liquids, 296, https://doi.org/10.1016/j.molliq.2019.112007.

Walsh, S., Reynolds, J., Abbas, B., Woods, R., Searle, J., Jewell, E., Elvins, J., 2020. Assessing the Dynamic Performance of Thermochemical Storage Materials. Energies, 13(9), https://doi.org/10.3390/en13092202.

Walshe, J., Amarandei, G., Ahmed, H., McCormack, S., Doran, J., 2019. Development of poly-vinyl alcohol stabilized silver nanofluids for solar thermal applications. Solar Energy Materials and Solar Cells, 201, https://doi.org/10.1016/j.solmat.2019.110085.

Wang, X.-Q., Mujumdar, A.S., 2007. Heat transfer characteristics of nanofluids: a review. International Journal of Thermal Sciences, 46(1), 1-19, https://doi.org/10.1016/j.ijthermalsci.2006.06.010.

Wang, X., He, Y., Liu, X., Shi, L., Zhu, J., 2017. Investigation of photothermal heating enabled by plasmonic nanofluids for direct solar steam generation. Solar Energy, 157, 35-46, https://doi.org/10.1016/j.solener.2017.08.015.

Wilson, I.A.G., Rennie, A.J.R., Ding, Y., Eames, P.C., Hall, P.J., Kelly, N.J., 2013. Historical daily gas and electrical energy flows through Great Britain's transmission networks and the decarbonisation of domestic heat. Energy Policy, 61, 301-305, https://doi.org/10.1016/j.enpol.2013.05.110.

Xie, H., Yu, W., Li, Y., Chen, L., 2011. Discussion on the thermal conductivity enhancement of nanofluids. Nanoscale Res Lett, 6(1), 124, https://doi.org/10.1186/1556-276X-6-124.

Xu, R., 2008. Progress in nanoparticles characterization: Sizing and zeta potential measurement. Particuology, 6(2), 112-115, https://doi.org/10.1016/j.partic.2007.12.002.

Xuan, Y., Duan, H., Li, Q., 2014. Enhancement of solar energy absorption using a plasmonic nanofluid based on TiO_2/Ag composite nanoparticles. RSC Advances, 4(31), 16206, https://doi.org/10.1039/c4ra00630e.

Xue, C., Chen, X., Hurst, S.J., Mirkin, C.A., 2007. Self-Assembled Monolayer Mediated Silica Coating of Silver Triangular Nanoprisms. Advanced Materials, 19(22), 4071-4074, https://doi.org/10.1002/adma.200701506.

Xue, C., Metraux, G.S., Millstone, J.E., Mirkin, C.A., 2008. Mechanistic Study of Photomediated Triangular Silver Nanoprism Growth. J Am Chem Soc, 130, 8337-8344, https://doi.org/https://doi.org/10.1021/ja8005258.

Yan, S., Sun, D., Gong, Y., Tan, Y., Xing, X., Mo, G., Chen, Z., Cai, Q., Li, Z., Yu, H., Wu, Z., 2016. Temperature-driven directional coalescence of silver nanoparticles. J Synchrotron Radiat, 23(Pt 3), 718-728, https://doi.org/10.1107/S1600577516002253.

Yu, W., Xie, H., 2012. A Review on Nanofluids: Preparation, Stability Mechanisms, and Applications. Journal of Nanomaterials, 2012, 1-17, https://doi.org/10.1155/2012/435873.

Yu, X., Xuan, Y., 2018. Investigation on thermo-optical properties of CuO/Ag plasmonic nanofluids. Solar Energy, 160, 200-207, https://doi.org/10.1016/j.solener.2017.12.007.

Zagabathuni, A., Ghosh, S., Pabi, S.K., 2016. The difference in the thermal conductivity of nanofluids measured by different methods and its rationalization. Beilstein J Nanotechnol, 7, 2037-2044, https://doi.org/10.3762/bjnano.7.194.

Zalba, B., Marin, J., Cabeza, L.F., Mehling, H., 2003. Review on thermal energy storage with phase change: materials, heat transfer analysis and applications. Applied Thermal Engineering, 23, 251-283, https://doi.org/https://doi.org/10.1016/S1359-4311(02)00192-8.

Zambolin, E., Del Col, D., 2010. Experimental analysis of thermal performance of flat plate and evacuated tube solar collectors in stationary standard and daily conditions. Solar Energy, 84(8), 1382-1396, https://doi.org/10.1016/j.solener.2010.04.020.

Zayed, M.E., Zhao, J., Du, Y., Kabeel, A.E., Shalaby, S.M., 2019. Factors affecting the thermal performance of the flat plate solar collector using nanofluids: A review. Solar Energy, 182, 382-396, https://doi.org/10.1016/j.solener.2019.02.054.

Zeiny, A., Jin, H., Bai, L., Lin, G., Wen, D., 2018. A comparative study of direct absorption nanofluids for solar thermal applications. Solar Energy, 161, 74-82, https://doi.org/10.1016/j.solener.2017.12.037.

Zeng, J., Roberts, S., Xia, Y., 2010. Nanocrystal-based time-temperature indicators. Chemistry, 16(42), 12559-12563, https://doi.org/10.1002/chem.201002665.

Zeng, J., Xuan, Y., 2018. Enhanced solar thermal conversion and thermal conduction of MWCNT-SiO_2 /Ag binary nanofluids. Applied Energy, 212, 809-819, https://doi.org/10.1016/j.apenergy.2017.12.083.

Zhang, Q., Li, N., Goebl, J., Lu, Z., Yin, Y., 2011. A systematic study of the synthesis of silver nanoplates: is citrate a "magic" reagent? J Am Chem Soc, 133(46), 18931-18939, https://doi.org/10.1021/ja2080345.

Zhang, X., Li, M., Shi, W., Wang, B., Li, X., 2014. Experimental investigation on charging and discharging performance of absorption thermal energy storage system. Energy Conversion and Management, 85, 425-434, https://doi.org/10.1016/j.enconman.2014.05.100.

Zhao, D., Qian, X., Gu, X., Jajja, S.A., Yang, R., 2016. Measurement Techniques for Thermal Conductivity and Interfacial Thermal Conductance of Bulk and Thin Film Materials. Journal of Electronic Packaging,, 138(4), 040802, https://doi.org/https://doi.org/10.1115/1.4034605.

Zmijan, R., Carboni, M., Capretto, L., Stulz, E., Zhang, X., 2014. In situ microspectroscopic monitoring within a microfluidic reactor. RSC Adv., 4(28), 14569-14572, https://doi.org/10.1039/c4ra01650e.